



Introduction to the Themed Section: 'Revisiting Sverdrup's Critical Depth Hypothesis' Introduction

Revisiting Sverdrup's critical depth hypothesis

Shubha Sathyendranath^{1*}, Rubao Ji², and Howard I. Browman³

¹Plymouth Marine Laboratory, Prospect Place, Plymouth PL1 3DH, UK

²Department of Biology, Woods Hole Oceanographic Institution, Woods Hole, MA 02543, USA

³Institute of Marine Research, Austevoll Research Station, Marine Ecosystem Acoustics Research Group, 5392 Storebø, Norway

*Corresponding author: tel: +44 1752 633 164; fax: +44 1752 633 101; e-mail: shubha@dal.ca

Sathyendranath, S., Ji, R., and Browman, H. I. Revisiting Sverdrup's critical depth hypothesis. – ICES Journal of Marine Science, 72: 1892 – 1896.

Received 23 May 2015; accepted 24 May 2015.

Published more than 60 years ago in this Journal, the article in which Sverdrup proposed the concept of critical depth to explain the initiation of the spring bloom in the North Atlantic has accrued an exceptionally large number of citations and continues to be cited more than 50 times per year. The framework provided by Sverdrup has now been applied, adapted, and tested across many aquatic systems worldwide. Datasets have been collected; models have been built on the framework: these studies have generated new insights into phytoplankton dynamics and interesting debates on the relative importance of the various factors responsible for phytoplankton blooms. This article theme set presents some of the most recent efforts to discuss and test Sverdrup's critical depth hypothesis using a diverse set of approaches, ranging from controlled experiments to field observations as well as numerical and analytical models. The set of papers celebrates an elegant and powerful hypothesis that has had long-lasting influence. It is to be expected that it will also stimulate future research, adding even more to our understanding of one of the most fundamental processes in biological oceanography.

Keywords: bloom onset, light attenuation, mixed layer, mixing depth, phytoplankton, primary production, stratification, turbulence.

Background

More than 60 years ago, Sverdrup (1953) published an article in this Journal laying down the theoretical framework for analysing spring phytoplankton bloom initiation in the North Atlantic. It inspired a generation of oceanographers, and continues to do so to this day. In a world where it has become fashionable to cite the most recent author to advance an idea, rather than the first, Sverdrup's article remains one of the most cited publications in the field (see below). This is a testament to its importance.

What is the secret of its longevity? Probably, the answers to this question would be as varied as the backgrounds and interests of the scientists to whom it might be posed, but we will try to list a few aspects that we find important. First of all, Sverdrup provided a rigorous, mathematical formalism to concepts and observations that had been aired before (e.g. Gran and Braarud, 1935), thereby making it possible to test hypotheses regarding phytoplankton blooms in a quantitative way. Although he addressed the specific case of spring blooms, the model presented by Sverdrup was built on the broad and strong general principle of mass balance for

phytoplankton in a layer of the water column, such that the model was readily applicable to the study of any type of phytoplankton dynamics just about anywhere. The model, which is deceptively simple, is rich in potential applications, providing a master class on how to construct a general model and how to simplify it for a specific case: that of the spring bloom initiation in the North Atlantic. The simplifications led to an analytic result that provided insights into the processes that determine spring blooms. Even in the current oceanographic era when numerical modelling is the norm and the aspiration, analytic solutions remain the method of choice for interpretation of model solutions.

It is useful to recognize the two distinct parts of the critical depth concept that Sverdrup introduced: the first part, that uses the principle of conservation of mass in a layer of the water column to study net change in phytoplankton concentration, is axiomatic, and may be recognized as a theory that cannot be violated: it provides the framework for constructing details of a model. The second part, which identifies the major factors responsible for the formation of blooms, belongs more in the realm of hypotheses that can be tested. And, the model has been tested, again and again.

When authors have criticized the Sverdrup model, most of the criticisms have been levelled at the specific case with which Sverdrup chose to illustrate his model, pointing to additional processes or different parameterizations that might have been invoked to render the model more suitable for situations and locations not considered, or perhaps not relevant, to the particular case Sverdrup studied. In so doing, some authors overlooked a deeper message in Sverdrup's paper: biological dynamics in the ocean can be described by rigorous equations based on first principles (in this case, the principle of mass balance) to yield original results testable by observations at sea. It was a revolutionary view when the paper was published. In our opinion, the paper remains a thing of beauty, as useful now as it was then, whose importance matures as one or another criticism makes us realize how easily the Sverdrup model can be adapted to a variety of situations.

The paper introduced a biological depth horizon—the critical depth—that has remained arguably the most important reference depth for the study of phytoplankton dynamics, on a par with the mixed layer depth (or mixing depth) in the physical domain and euphotic depth in the optical domain. Importantly, Sverdrup brought the biological and the physical reference depths in juxtaposition, and discussed the implications. In this regard, his was among the first models to explore biological–physical interactions in the ocean. The work has also led to interesting discussions on the nuances that differentiate a mixed layer from an actively mixing layer [see Franks (2015)], which helped explain apparent contradictions that seemed to violate the very foundations of the concept of critical depth: instances when biological fields appeared to show vertical structure in a surface layer notwithstanding that the physical properties indicated a deeper mixed layer. Interestingly, in such instances, one might argue that vertical profiles of some easily measured biological or bio-optical properties could provide excellent measures of mixing depth, in the absence of direct measurements of turbulence. One might also argue that such studies, discussing apparent contradictions between biological and physical fields, have provided impetus to physical oceanographers to delve deeper into processes that govern the development and evolution of mixed layer and mixing layers, to assess which of these would be more appropriate for interpretation of biological processes.

Quantifying the impact of Sverdrup (1953)

The bibliographic database Web of Science (WoS), Thomson Reuters, was used to trace the influence of Sverdrup (1953) in the literature. Sverdrup's publications are not indexed as primary literature in the WoS. Therefore, citations to the articles from the indexed literature were traced using the WoS's cited reference search in which the author names and publication year are used to identify cited references. We searched for citations to "HU Sverdrup 1953" in journals that are indexed in WoS from 1945 onwards. The searches were carried out in April 2015. The retrieved citing publications were analysed according to bibliographic parameters such as publication year, journal, and nationality of citing authors. A quantitative bibliometric analysis does not yield any information about the reasons why an article or author's work continues to be cited. To provide more insights into that question, we conducted a citation context analysis by analysing the textual passages in which Sverdrup (1953) is referred to in the citing documents [*sensu* Small (1982)]. We made an arbitrary choice to look only at citing articles that in turn have been highly cited. Using this approach, we were able to assess the influence of Sverdrup's work on other high impact publications within the field. We limited the

study to the top 20 articles, all of which have been cited >200 times. Thus, the context analysis should be considered illustrative rather than systematic.

In total, 1082 unique citations of Sverdrup (1953) were identified (including citations from 1953 to April 2015). Those articles have themselves been cited >43 000 times. The top five highly cited articles that refer to Sverdrup (1953) have accrued between 488 and 881 citations themselves. Google Scholar listed 1543 cites to Sverdrup (1953).

The number of citations has increased over time, with Sverdrup (1953) currently being cited an impressive 30–60 times per year (Figure 1). Very few publications, in any field, attain total citation numbers as high as this and the current citation rate is exceptional for a 62-year-old scientific publication. The typical scientific article is poorly cited the first year after publication; and a citation peak is reached ~3 years after publication, followed by decreasing citedness (Aksnes, 2003). In oceanographic research, the rise typically takes longer, although it rarely reaches a level anywhere near as high as has Sverdrup (1953). Aksnes (2003) defined different temporal citation patterns of highly cited articles. One category, termed "delayed rise, no decline", is characterized by a relatively slow rise in citation frequencies and a stable or increasing citation level thereafter. The citation curve of Sverdrup (1953) resembles this category of highly cited articles (Figure 1). Such a citation pattern indicates that Sverdrup (1953) reports research–concepts–theories that are of continuing interest to researchers.

When interpreting the citation life cycle of Sverdrup's work, it must be noted that there has been a large increase in the overall volume of research in marine science since 1953. Thus, the number of articles that could cite Sverdrup (1953) is much larger today than in the past. However, this does not account for the rise in citations to Sverdrup (1953), since they have risen from ~2–5 per year before 1980 to >30 per year since 2000, an increase that is much greater than the overall growth in marine science publications during the same period (i.e. a factor of ~3).

Garfield (1977) identified 15 reasons why a particular article might be cited. At least two of them seem particularly relevant for Sverdrup (1953): paying homage to pioneers and identifying original publications in which an idea or concept was discussed. The second, more specific type of referencing, "identifying original

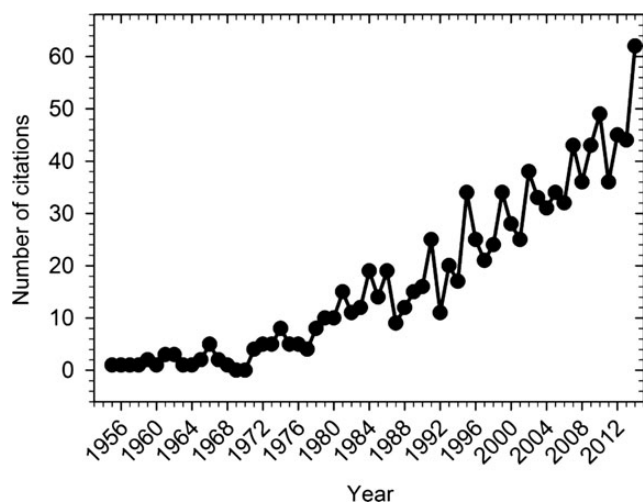


Figure 1. The absolute number of citations to Sverdrup (1953) per year (1953–2014).

the articles. Typically, the introduction of a scientific article is structured as a progression from the general to the particular and often starts with references to the more general or basic works within a field. Consistent with this, references to Sverdrup (1953) are often found at the beginning of the text. Moreover, there are several instances of the work having been the basis for other notable hypotheses in marine science, for example Cushing's match–mismatch hypothesis, “The hypothesis assumed that during the spring peak, plankton production followed Sverdrup's (1953) model, and that during the autumn peak the same principles applied, but in reverse—spring and autumn are the periods of mixing or weak stratification” (Cushing 1990, p. 251, lines 8–11). In another example, Platt *et al.* (2003a, b) found it illuminating to place their model on phytoplankton biomass and residual nitrate in the mixed layer in the context of Sverdrup's critical depth. They pointed out that, if environmental conditions remain stable, changes in phytoplankton concentration will draw the critical depth towards the mixed layer depth, and the maximum biomass that can be attained will be dictated by the mixed layer depth and the bio-optical properties of the system: a bio-optical homeostasis that guards against runaway blooms (Sathyendranath and Platt, 2007). More recently, the concept of bloom initiation timing has been placed into the more general topic of plankton phenology under a changing climate (e.g. Ji *et al.*, 2010).

It is worth noting that teachers still use Sverdrup's work to stimulate student engagement and discussion of topical issues in biological oceanography. A paper that emerged from such a course (Fischer *et al.*, 2014) points out that Sverdrup's model provided a framework against which new observations could be compared with garner new insights into the functioning of the marine ecosystem.

The articles in this theme set

The papers that make up this theme set of the *ICES Journal of Marine Sciences* provide a cross section of the various types of research that are still stimulated by Sverdrup's work. New datasets from both field observations of many different regional oceans, along with theoretical analyses based on different types of models, are included.

Franks (2015) points out that we may have sometimes been lax in “testing” Sverdrup's carefully laid-out critical depth hypothesis. Step by careful step, he lays out the different physical processes that have a potential influence on phytoplankton dynamics, and discusses the associated scales and their implications for bloom formation. Lewandowska *et al.* (2015) focus on the importance of phytoplankton traits such as growth rates, photoadaptation to low light, nutrient kinetics, and grazing resistance for the formation of phytoplankton blooms.

Different types of models are used to examine various aspects of bloom dynamics associated with the critical depth hypothesis. Enriquez and Taylor (2015) use a theoretical approach to explore the contrasting roles of wind mixing and surface heating on the timing of spring blooms. Levy (2015) uses a nitrogen–phytoplankton–zooplankton simulation model that is run with varying degrees of complexity in how the biological and physical processes are expressed in the model to examine conditions under which one process or another has a dominant role in dictating bloom formation. Lindemann *et al.* (2015) use a Lagrangian model that follows a population of individual cells to illustrate the importance of plasticity of phytoplankton physiological rates in determining phytoplankton community structure and dynamics.

Regional coverage and spatial scale of the studies in this theme set is also broad. Smith and Jones (2015) examine phytoplankton

growth in the Ross Sea in the context of the critical depth criterion and wind mixing, and conclude that periods of calm, favouring shallow mixed layers interspersed with deep wind mixing events favoured accumulation of high biomass in the mixed layer. Brody and Lozier (2015) use *in situ* data from the Labrador Sea and the North Atlantic to study blooms, and conclude that the transition of oceanographic conditions in Spring from buoyancy-driven to wind-driven mixing conditions marks the onset of blooms. Llorca *et al.* (2015), Sallée *et al.* (2015), and Thomalla *et al.* (2015) focused their work on understanding bloom dynamics in the Southern Ocean. Marra *et al.* (2015) use mooring data from the Iceland Basin in the North Atlantic and from the central Arabian Sea to study factors that determine bloom dynamics and conclude that changes in water column stratification were important at all mooring sites as a factor responsible for bloom formation. Cole *et al.* (2015) examine bloom-favouring processes at the basin scale in the North Atlantic, and contrast them with the Southern Ocean and the North Pacific. Aksnes (2015) studied the coastal waters off Norway, pointing out the importance of water clarity, unrelated to phytoplankton concentration, in dictating the light environment in the surface layers and hence bloom dynamics. Fieldwork at small-scales is presented by Diehl *et al.* (2015) who studied the onset of blooms in a controlled mesocosm experiment in a lake. Walter *et al.* (2015) examine the potential effects of temperature and light during deep convection on phytoplankton growth, using laboratory experiments on growth of a single species of phytoplankton (*Thalassiosira weissflogii*).

The articles comprising this theme set, and the many relevant articles cited by them, attest to the great progress that oceanography has made since the days of Sverdrup. Some of the discussions of today, for example surrounding parameterization of the physical conditions that dictate bloom dynamics, or over the intricacies of phytoplankton growth and loss terms, would not have been possible in the days of Sverdrup. Technologically as well, we have made great strides, with moorings, drifters, gliders, and satellites generating huge quantities of data. Modelling has also developed rapidly as computing power has increased and become readily available to researchers. And yet, the simple concept of critical depth still provides the underpinning for many efforts to understand the ephemeral world of phytoplankton.

The breadth of oceanographic regions and oceanographic processes investigated in this theme set within the framework of Sverdrup's critical depth hypothesis, the new theoretical developments presented, the innovative observational technologies brought to bear on the problem, and the variety of laboratories and countries engaged in the investigations, all bode well for the continued influence of Sverdrup's work on the oceanographic community.

Acknowledgements

This initiative began with an e-mail from Alf Håkon Hoel, who in September 2013 alerted HIB to the 60th anniversary of Sverdrup's 1953 article and suggested that it would be appropriate to commemorate it. We are grateful to the authors who accepted our invitation to contribute. SS's work was supported by the National Centre for Earth Observations of the United Kingdom's Natural Environmental Research Council. RJ worked on this article theme set as a Cooperative Institute for the North Atlantic Region Fellow and also received funding from the United States National Science Foundation (PLR-1417677 and PLR-1341558) and NASA (NNX14AH74G) for phenology-related projects. HB's contribution to this article

was supported by Projects # 81529 (“Fine scale interactions in the plankton”) and 83741 (“Scientific publishing and editing”) from the Institute of Marine Research, Norway.

References

- Aksnes, D. L. 2015. Sverdrup critical depth and the role of water clarity in Norwegian Coastal Water. *ICES Journal of Marine Science*, 72: 2041–2050.
- Aksnes, D. W. 2003. Characteristics of highly cited papers. *Research Evaluation*, 12: 159–170.
- Brody, S. R., and Lozier, M. S. 2015. Characterizing upper-ocean mixing and its effect on the spring phytoplankton bloom with in situ data. *ICES Journal of Marine Science*, 72: 1961–1970.
- Cole, H. S., Henson, S., Martin, A. P., and Yool, A. 2015. Basin-wide mechanisms for spring bloom initiation: how typical is the North Atlantic? *ICES Journal of Marine Science*, 72: 2029–2040.
- Cushing, D. H. 1990. Plankton production and year-class strength in fish populations: An update of the match/mismatch hypothesis. *Advances in Marine Biology*, 26: 249–293.
- Diehl, S., Berger, S. A., Soissons, Q., Giling, D. P., and Stibor, H. 2015. An experimental demonstration of the critical depth principle. *ICES Journal of Marine Science*, 72: 2051–2060.
- Enriquez, R. M., and Taylor, J. R. 2015. Numerical simulations of the competition between wind-driven mixing and surface heating in triggering spring phytoplankton blooms. *ICES Journal of Marine Science*, 72: 1926–1941.
- Fischer, A. D., Moberg, E. A., Alexander, H., Brownlee, E. F., Hunter-Cevera, K. R., Pitz, K. J., Rosengard, S. Z., et al. 2014. Sixty years of Sverdrup. A retrospective of progress in the study of phytoplankton blooms. *Oceanography*, 27: 222–235.
- Franks, P. J. S. 2015. Has Sverdrup’s critical depth hypothesis been tested? Mixed layers vs. turbulent layers. *ICES Journal of Marine Science*, 72: 1897–1907.
- Garfield, E. 1977. Can citation indexing be automated? *In* *Essay of an Information Scientist*, vol. 1 (Vol. 1). ISI Press, Philadelphia.
- Gran, H. H., and Braarud, T. 1935. A quantitative study of the Phytoplankton in the Bay of Fundy and the Gulf of Maine. *Journal of the Biological Board of Canada*, 1: 279–467.
- Ji, R., Edwards, M., Mackas, D. L., Runge, J., and Thomas, A. C. 2010. Marine plankton phenology and life history in a changing climate: Current research and future directions. *Journal of Plankton Research*, 32: 1355–1368.
- Lévy, M. 2015. Exploration of the critical depth hypothesis with a simple NPZ model. *ICES Journal of Marine Science*, 72: 1916–1925.
- Lewandowska, A. M., Striebel, M., Feudel, U., Hillebrand, H., and Sommer, U. 2015. The importance of phytoplankton trait variability in spring bloom formation. *ICES Journal of Marine Science*, 72: 1908–1915.
- Lindemann, C., Backhaus, J. O., and St John, M. A. 2015. Physiological constraints on Sverdrup’s Critical-Depth-Hypothesis: the influences of dark respiration and sinking. *ICES Journal of Marine Science*, 72: 1942–1951.
- Llort, J., Lévy, M., Sallée, J.-B., and Tagliabue, A. 2015. Onset, intensification, and decline of phytoplankton blooms in the Southern Ocean. *ICES Journal of Marine Science*, 72: 1971–1984.
- Marra, J. F., Dickey, T. D., Plueddemann, A. J., Weller, R. A., Kinkade, C. S., and Stramska, M. 2015. Phytoplankton bloom phenomena in the North Atlantic Ocean and Arabian Sea. *ICES Journal of Marine Science*, 72: 2021–2028.
- Platt, T., Broomhead, D. S., Sathyendranath, S., Edwards, A. M., and Murphy, E. J. 2003b. Phytoplankton biomass and residual nitrate in the pelagic ecosystem. *Proceedings of the Royal Society of London A* 459: 1063–1073.
- Platt, T., Sathyendranath, S., Edwards, A. M., Broomhead, D. S., and Ulloa, O. 2003a. Nitrate supply and demand in the mixed layer of the ocean. *Marine Ecology Progress Series* 254: 3–9.
- Sallée, J.-B., Llort, J., Tagliabue, A., and Lévy, M. 2015. Characterisation of distinct bloom phenology regimes in the Southern Ocean. *ICES Journal of Marine Science*, 72: 1985–1998.
- Sathyendranath, S., and Platt, T. 2007. Spectral effects in bio-optical control on the ocean system. *Oceanologia*, 49: 5–39.
- Small, H. 1982. Citation context analysis. *In* *Progress in Communication Sciences*, 3, pp. 287–310. Ed. by B. Dervin, and M. Voigt. Ablex, Norwood.
- Smith, W. O., and Jones, R. M. 2015. Vertical mixing, critical depths, and phytoplankton growth in the Ross Sea. *ICES Journal of Marine Science*, 72: 1952–1960.
- Sverdrup, H. 1953. On conditions for the vernal blooming of phytoplankton. *Journal du Conseil/Conseil Permanent International pour l’Exploration de la Mer* 18: 287–295.
- Thomalla, S., Racault, M.-F., Swart, S., and Monteiro, P. 2015. High-resolution view of the spring bloom initiation and net community production in the Subantarctic Southern Ocean using glider data. *ICES Journal of Marine Science*, 72: 1999–2020.
- Walter, B., Peters, J., van Beusekom, J. E. E., and St John, M. A. 2015. Interactive effects of temperature and light during deep convection: a case study on growth and condition of the diatom *Thalassiosira weissflogii*. *ICES Journal of Marine Science*, 72: 2061–2071.



Contribution to the Themed Section: 'Revisiting Sverdrup's Critical Depth Hypothesis' Food for Thought

Has Sverdrup's critical depth hypothesis been tested? Mixed layers vs. turbulent layers

Peter J. S. Franks*

Scripps Institution of Oceanography, University of California, San Diego, La Jolla, CA 92093-0218, USA

*Corresponding author: e-mail: pfranks@ucsd.edu

Franks, P. J. S. Has Sverdrup's critical depth hypothesis been tested? Mixed layers vs. turbulent layers. – ICES Journal of Marine Science, 72: 1897 – 1907.

Received 27 May 2014; revised 17 September 2014; accepted 17 September 2014; advance access publication 17 October 2014.

Sverdrup (1953. On conditions for the vernal blooming of phytoplankton. *Journal du Conseil International pour l'Exploration de la Mer*, 18: 287 – 295) was quite careful in formulating his critical depth hypothesis, specifying a “thoroughly mixed top layer” with mixing “strong enough to distribute the plankton organisms evenly through the layer”. With a few notable exceptions, most subsequent tests of the critical depth hypothesis have ignored those assumptions, using estimates of a hydrographically defined mixed-layer depth as a proxy for the actual turbulence-driven movement of the phytoplankton. However, a closer examination of the sources of turbulence and stratification in turbulent layers shows that active turbulence is highly variable over time scales of hours, vertical scales of metres, and horizontal scales of kilometres. Furthermore, the mixed layer as defined by temperature or density gradients is a poor indicator of the depth or intensity of active turbulence. Without time series of coincident, *in situ* measurements of turbulence and phytoplankton rates, it is not possible to properly test Sverdrup's critical depth hypothesis.

Keywords: critical depth, diffusivity, dissipation, mixed layer, mixing, stratification, Sverdrup, turbulence.

Introduction

Sverdrup's critical depth hypothesis

More than 60 years ago, Sverdrup formulated his critical depth hypothesis (SCD: Sverdrup, 1953) to explain the well-documented North Atlantic spring phytoplankton bloom. The SCD hypothesis is a simple model based on the premise that winter phytoplankton growth is limited by the amount of available light: strong turbulence in the upper layer of the ocean moves phytoplankton rapidly through the water column. These conditions result in each phytoplankton receiving the average amount of light over the depth of the mixed layer, which—since light decays exponentially with depth—is significantly less light than would be available if the phytoplankton were stationary within the euphotic zone. Sverdrup (1953) postulated that there existed a particular depth—the *critical depth*—at which the vertically integrated phytoplankton growth (assumed proportional to the exponentially decreasing local irradiance) equalled the vertically integrated phytoplankton losses (assumed to have no depth dependence). When the mixed layer is shallower than the critical depth, integrated growth outweighs the losses, and a bloom can occur. This was hypothesized to occur through a spring shoaling of the mixed layer, driven by surface heating.

Since its formulation, this hypothesis has served as a basis for understanding bloom dynamics throughout the world's oceans (e.g. Fischer *et al.*, 2014). Over the decades, many studies have attempted to test the SCD hypothesis with mixed results. Using satellite imagery and mixed-layer climatologies, Obata *et al.* (1996), Siegel *et al.* (2002), Brody *et al.* (2013), Brody and Lozier (2014), and Chiswell *et al.* (2013) found evidence supporting the SCD hypothesis (though that support was qualified in some cases), while Behrenfeld (2010), Boss and Behrenfeld (2010), Behrenfeld and Boss (2014), and Behrenfeld *et al.* (2013) rejected the SCD hypothesis based on the observation that net phytoplankton growth was positive and increasing in the middle of winter.

Before proceeding, it is important to clarify some terms. Technically “mixing” refers to the homogenization of gradients of a property. Once those gradients disappear, there is nothing left to mix, thus “mixing” stops, although the water may still be turbulent. Since we are concerned with the movement of phytoplankton through a light gradient, the strength of turbulent motions of the water is the more relevant quantity, and care will be taken to use the term “turbulence” or “dissipation” (see below) to refer to the turbulent motions of the water, rather than “mixing”. A “mixed layer”, on

the other hand, is hydrographically defined as the region in which the temperature or density difference is less than a given amount (see below).

In formulating his model (both conceptual and mathematical), Sverdrup's first explicit assumption was that "there exists a thoroughly mixed top layer of thickness D ". His second assumption was, "Within the top layer the turbulence is strong enough to distribute the plankton organisms evenly through the layer". The turbulent displacement of a particle can be expressed mathematically using an eddy diffusivity, which I will denote K (units: $\text{m}^2 \text{s}^{-1}$). In the SCD model, Sverdrup made the following assumptions: (i) the diffusivity was strong enough that over a day, every phytoplankter spent an equal amount of time at every depth in the mixed layer, and (ii) this movement resulted in phytoplankton experiencing the average irradiance within the mixed layer over the course of a day. Interestingly, because of his assumptions, neither the magnitude nor the vertical structure of K appears in Sverdrup's (1953) equations.

The central issue to testing the SCD hypothesis is understanding the meaning of a "thoroughly mixed" layer. In this context, "thoroughly mixed" means that every phytoplankter in the turbulent layer receives the same average amount of irradiance over some time interval: a photoperiod or a growth period, for example. To first order, the average time τ_L it takes for a particle to move a distance $\pm L$ from its present depth with a local diffusivity $K(z)$ is given by

$$\tau_L = \frac{L}{2K(z)}. \quad (1)$$

To build our intuition, τ_L can be thought of as a residence time of a particle in a layer $2L$ thick, centred on the particle's present depth. It is clear from (1) that the residence time is inversely proportional to the diffusivity $K(z)$: larger diffusivities (stronger turbulence) lead to shorter residence times. Thus, a vertical gradient in diffusivity—or turbulence—would also result in a vertical gradient in residence time of phytoplankton with depth, thus affecting the amount of light they are exposed to.

In his paper, Sverdrup (1953) clearly states, "... a phytoplankton population may increase independently of the thickness of the mixed layer if the turbulence is moderate" (page 290, my italics). Sverdrup was clearly aware of the distinction between a mixed layer (defined hydrographically by a vertical temperature or density difference) and the intensity of turbulence in that mixed layer. This is the basis of Huisman *et al.*'s (1999) formulation of the "critical turbulence" hypothesis: if K is weak enough, turbulent motions will still occur, but the residence time of the phytoplankton in the euphotic zone will be long enough to cause net positive growth. Townsend *et al.* (1992), Ellertsen (1993), and Chiswell (2011), for example, observed the initiation of shallow spring blooms in apparently unstratified water columns, that is, water columns with deep mixed layers. Chiswell (2011) concluded that the upper mixed layer in which the bloom occurred was not turbulent enough to satisfy the SCD criterion of a "thoroughly mixed layer".

Huisman *et al.* (1999) point out that it is not sufficient to simply define a mixed layer: it is also necessary to specify how vigorously that mixed layer is mixing, i.e. to quantify the strength of the turbulence. This point has been echoed and amplified in subsequent studies (e.g. Ebert *et al.*, 2001; Chiswell, 2011; Taylor and Ferrari, 2011; Brody and Lozier, 2014). Sverdrup (1953) avoided the necessity of including the vertical diffusivity, K , by explicitly assuming it

was large enough to be ignored. But he clearly understood the ramifications of weaker turbulence—he just chose not to include it in his model. Huisman *et al.* (1999) explicitly include a vertically constant diffusivity K in their model. Brody and Lozier (2014) parameterized vertical overturning time scales for the turbulent layer based on large-scale hydrographic properties and atmospheric forcings; again, they assumed that the turbulent motions were vertically uniform. Using higher-order turbulence closure models, Taylor and Ferrari (2011) and Mahadevan *et al.* (2012) are among the only studies to have employed a vertically varying diffusivity in their analyses of the SCD hypothesis. One of the points I make in this synthesis is that it is crucial to know not only the intensity of the turbulence, but also its vertical structure and temporal variability. That is, to test the SCD hypothesis, we must find the part of the water column that is consistent with the assumptions of the SCD hypothesis: "a thoroughly mixed top layer". This requires measurements of the actual turbulence, rather than the hydrographic results of the mixing: the mixed layer.

As I will show below, vertical gradients of turbulence can, and often do, exist even when the turbulence is strong enough to homogenize hydrographic properties such as temperature and density. Thus, if the "thoroughly mixed" layer is defined by uniform temperature or density, as is commonly the case (see below), and this layer contains a vertical gradient in turbulence, Sverdrup's first assumption is not met and the SCD hypothesis is not properly being tested. Intuitively, then, the details of the vertical and temporal structures of the turbulence are fundamental to our definition of "thoroughly mixed", regardless of the vertical distribution of other hydrographic properties like temperature or density. In other words, the presence of a mixed, homogenous, layer in temperature or density does not imply either that turbulence is ongoing or that turbulence is strong enough to move the phytoplankton completely and rapidly (relative to temporal changes in the light field) through the (hydrographically defined) mixed layer, as required by the SCD hypothesis.

As the debate concerning the validity of the SCD hypothesis continues, this paper explores the physics and the spatial and temporal dynamics of one of the foundations of the SCD hypothesis: turbulence within the mixed layer. I will show that the vertical structure and intensity of turbulence depends strongly on the source of energy that drives the turbulence, and the sources of stratification that can suppress it. I will show that restratification—the formation of vertical density gradients through heating, freshwater fluxes or slumping of horizontal density gradients—can occur on time scales of hours and spatial scales of kilometres. Even extremely weak restratification can inhibit turbulence, and this can occur rapidly (hours). Furthermore, I will show that including this short-time scale variability has important consequences for understanding dynamics in the upper ocean. In particular, I hope to demonstrate that a deeper understanding of the spatial and temporal dynamics of turbulent layers may help to reconcile the various studies supporting and rejecting the SCD hypothesis, and to further the investigation of the mechanisms underlying the spring bloom.

Mixed layer vs. turbulent layer

Sverdrup (1953) wrote about a "mixed layer", though he was clearly referring to a "turbulent layer"—the waters that are kept in motion through turbulence. This distinction has largely been forgotten, and most subsequent tests of the SCD hypothesis have used measures of the mixed layer, not the turbulent layer. Brainerd and Gregg (1995) may have been the first to formally distinguish a mixed layer from a turbulent layer. As they note, "The distinction is significant, because

it is often important to match the mixed layer time scale to that of the process being studied". As we will see below, the time scales of variability of turbulence and biological time scales (~ 1 d) are often well matched when considering phytoplankton photosynthesis and growth.

Mixed layers are typically defined operationally as the shallowest depth at which a difference in temperature or density, measured from the surface (or 10 m in some cases), reaches a given threshold (see Kara *et al.*, 2000; De Boyer Montégut *et al.*, 2004; Lorbacher *et al.*, 2006; Holte and Talley, 2009, for summaries of the various thresholds used). These thresholds are often instrument-dependent, with larger thresholds for lower-resolution sensors. A typical temperature threshold is 0.2°C less than the surface value, or a density increase of 0.125 kg m^{-3} above the surface value. These criteria give the location of the seasonal pycnocline, and time series of mixed-layer depths will usually produce well-behaved, smooth annual cycles (e.g. Holte and Talley, 2009). The mixed-layer depth in temperate waters deepens from late fall into winter, and then shoals gradually from winter into spring. Mixed-layer depths during winter can reach several hundred metres (or more than 1000 m in regions of strong convection and deep water formation), and are typically a few tens of metres during summer.

As discussed above, the issue of relevance to the SCD hypothesis is not the depth of the mixed layer, but more precisely, the depth (and intensity) of active turbulence—the *turbulent layer*. Turbulence is usually measured in the field in terms of the dissipation rate of turbulent kinetic energy, ε (units: $\text{m}^2\text{ s}^{-3}$ or W kg^{-1} , often just called “dissipation” for short). Large values of ε indicate strong turbulence: there is a great deal of kinetic energy from turbulence being dissipated at small (mm–cm) scales. Unfortunately, there is no ε -based criterion for operationally identifying the base of the turbulent layer, partly because ε is very difficult to measure, requiring specialized instrumentation and expertise, and partly because any such criterion would depend on the problem at hand (e.g. phytoplankton or temperature might have different criteria). Brainerd and Gregg (1995) show that a density step as small as $0.0025\text{--}0.005\text{ kg m}^{-3}$ would often mark the base of the actively turbulent surface layer—the region of surface-enhanced ε . For most instruments, a density change this small would be considered noise. Indeed, Brainerd and Gregg (1995) pointed out that there were many density steps of this magnitude in their vertical profiles; in the absence of coincident dissipation measurements, it was impossible to say which one would mark the base of the turbulent layer. The strongly turbulent layer was almost always equal to or shallower than the mixed layer; on some occasions, “remnant turbulence” could still be intense below a newly forming mixed layer.

Since it is the turbulence—not the depth of the mixed layer—that is of relevance to the SCD hypothesis, it is worth building some intuition about the dynamics that control it. When mixing occurs in a stably stratified ocean, light water is pushed down and heavy water brought up, both moving against gravity. This vertical mixing actually raises the centre of gravity of the water column, thus increasing its potential energy. The gain in potential energy comes at the expense of kinetic energy, which is dissipated in the process of moving water up and down. Thus, to have vertical turbulence, one has to have a source of kinetic energy that is strong enough to overcome the existing density stratification. Turbulence in the surface boundary layer, then, is a trade-off between the kinetic (and sometimes potential—see the “Convectively driven turbulence” section) energy available to drive the turbulence, and the density stratification that can suppress it.

In the sections to follow, I first present and discuss some sources of energy that drive turbulence, and then sources of stratification that suppress it. These sources are presented not to be comprehensive, but more as vehicles to enhance our intuition concerning the time and space scales of changes in turbulence and restratification. A careful consideration of these time and space scales is essential to proper testing of the SCD hypothesis.

Sources of turbulence

To mix fluid across a density gradient requires energy. This can be kinetic energy transferred across the ocean's surface by wind, waves, Langmuir circulations, or gravitational instability caused by a cooling of the ocean's surface (convection).

Wind-driven turbulence

When the wind blows on the ocean's surface, it imparts kinetic energy to the ocean. Whether this kinetic energy goes into accelerating the surface waters horizontally (the Ekman layer) or into turbulence depends largely on the ambient density stratification. If the stratification is weak enough, kinetic energy from the wind will cause mixing of the density gradient. A criterion for determining whether the wind-driven shear will cause mixing in the face of stratification is given by the gradient Richardson number:

$$Ri = \frac{N^2}{(\partial u/\partial z)^2}, \quad (2)$$

where N is the buoyancy frequency,

$$N^2 = \frac{g}{\rho} \frac{\partial \rho}{\partial z}. \quad (3)$$

u is the horizontal velocity, z the vertical coordinate, g the acceleration due to gravity, and ρ the density. The numerator of Ri is a measure of the vertical stratification $\partial \rho/\partial z$, while the denominator quantifies the vertical shear. When $Ri < 0.25$, that is, when the vertical shear squared is greater than four times the buoyancy frequency squared, turbulent mixing is likely to occur. Strong shear or weak stratification (low buoyancy frequency) will allow turbulence and will generate vertical mixing of the density gradient.

The intensity of wind-driven turbulence varies with the strength of the wind. This is usually given through the friction velocity, u^* :

$$u^* = \sqrt{\frac{\tau}{\rho}}, \quad (4)$$

where τ is the surface windstress and ρ the water density. The dissipation rate of turbulent kinetic energy ε is then found from the “law of the wall” through the scaling

$$\varepsilon = \frac{u^{*3}}{\kappa z}, \quad (5)$$

where κ is von Karman's constant (0.4, dimensionless). Examination of (5) shows that the dissipation rate—the intensity of turbulence—is predicted to decay with depth away from the surface as z^{-1} (i.e. $1/\text{depth}$, Figure 1). This decay with depth is less sharp than, say, the exponential decrease in irradiance with depth, but still leads to a surface-intensified distribution of turbulence.

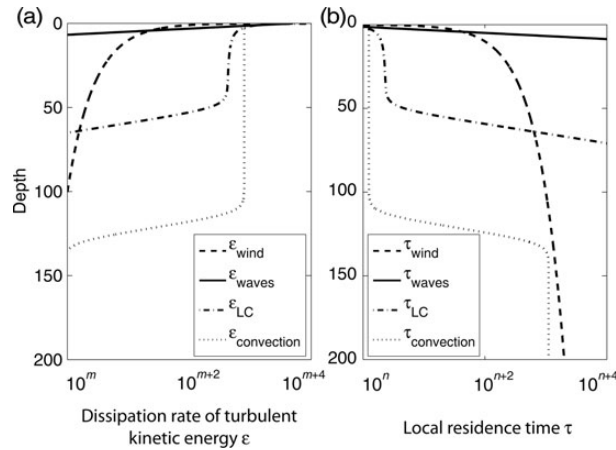


Figure 1. (a) Schematic of the vertical structure of the dissipation rate of turbulent kinetic energy, ϵ , generated by wind, waves, Langmuir circulations, and convective mixing. (b) Schematic of the vertical structure of the local residence time τ in the various types of turbulent layers in (a). Note that the actual values of dissipation and residence time are strongly dependent on the conditions: the magnitudes of these profiles should not be interpreted literally. The horizontal axes give the order-of-magnitude changes of the variables.

One implication from (4) and (5) is that wind-driven turbulence increases exponentially with the windstress; thus, small changes in windstress will drive proportionately larger changes in dissipation. These changes in dissipation can occur on very short time scales—when the source of energy changes, the dissipation changes within hours or less (e.g. Brainerd and Gregg, 1993a; D’Asaro, 2001).

The eddy diffusivity, K , which parameterizes the strength of the mixing in stratified waters is usually calculated from the dissipation and the buoyancy frequency following Osborn (1980):

$$K = \frac{0.2\epsilon}{N^2}. \quad (6)$$

The “constant” of 0.2 is not technically a constant, but represents the “mixing efficiency”: only 20% of the available energy dissipated by turbulence actually drives mixing. Eddy diffusivities for momentum (more properly called an eddy viscosity), density, temperature, salt, and phytoplankton could all be different, though typically the diffusivity for density is used as the diffusivity for plankton. From (6), we can see that the diffusivity will be higher when dissipation (ϵ) is stronger, and weaker when the density gradient (N^2) is stronger. It is clear from this formulation that the turbulence and stratification work against each other to give the resultant rate of mixing of the property. Note that this formulation is not applicable to turbulence driven by convection (Osborn, 1980) or in a mixed layer: the density gradient is zero ($N = 0$) or negative, and the predicted diffusivity is infinite (see the “Convectively driven turbulence” section).

A first-order estimate of the depth of the wind-mixed layer L_{wind} can be found from (Price and Sundermeyer, 1999; Wang and Huang, 2004)

$$L_{\text{wind}} = \frac{u^*}{2f}, \quad (7)$$

where f is the Coriolis frequency. Though this estimate does not account for variations in the strength of turbulence through the

layer, it is clear that the turbulent layer will be thicker with a stronger wind or at more equatorward latitudes for a given windstress.

The local (with depth) residence time of a particle in a turbulent layer will vary inversely with the dissipation rate, regardless of the source of dissipation. For wind-driven turbulence, the residence time τ_{wind} increases rapidly with depth (Figure 1), suggesting that phytoplankton not far from the surface will experience relatively long periods of constant irradiance. Thus, windforcing alone will not necessarily lead to a deep “thoroughly mixed layer”.

Wave-driven turbulence

Comparisons of field data with the z^{-1} depth scaling of wind-driven dissipation sometimes agree (e.g. Harcourt and D’Asaro, 2008; D’Asaro, 2014). More often, though, the profiles of ϵ show significant enhancement near the surface that cannot be accounted for by the z^{-1} depth dependence of wind-forced turbulence (e.g. Anis and Moum, 1992, 1995; Brainerd and Gregg, 1993a). Part of this surface-enhanced dissipation is due to the actions of the surface wave field.

Turbulence driven by surface waves typically falls off exponentially from the surface (Huang and Qiao, 2010; Huang *et al.*, 2012; Sutherland *et al.*, 2013; Figure 1). The dissipation ϵ is proportional to both the friction velocity u^* (and thus the windstress) and the Stokes velocity u_{S0} at the surface:

$$\epsilon = Cu_{S0}u^{*2}e^{-2kz}, \quad (8)$$

where C is an empirical constant and k is the horizontal wave number ($=2\pi/\text{wavelength}$) characterizing the surface wave field. The wave-driven turbulence thus depends strongly on the windstress (though less so than the wind-driven turbulence), but it decays more rapidly with depth than wind-driven turbulence, with a depth scale of $1/2k$. This exponential decay with depth often gives a strongly surface-intensified dissipation field (e.g. Anis and Moum, 1995; Huang *et al.*, 2012; McWilliams *et al.*, 2012; Sutherland *et al.*, 2013) with dissipation levels orders of magnitude higher than those due to wind alone (Figure 1). This wave effect on surface mixed layer turbulence is particularly apparent in the open ocean (Huang *et al.*, 2012).

Because of the rapid decrease in wave-driven turbulence with depth, the residence time τ_{wave} of particles increases very rapidly with depth (Figure 1). Thus, it is unlikely that waves alone could cause strong turbulence over a sufficiently deep layer to keep phytoplankton well mixed through any significant portion of the euphotic zone.

Langmuir circulations

Research in the last two decades has identified the importance of Langmuir circulations to mixing and turbulence in the upper ocean. D’Asaro and Dairiki (1997) showed that excess dissipation in the surface turbulent layer over that predicted by the law of the wall (i.e. windstress alone) could be accounted for by Langmuir circulations—or more specifically, the Craik–Leibovich vortex force (Craik and Leibovich, 1976), which dominates near the surface during large waves (D’Asaro *et al.*, 2014). Harcourt (2013) showed that the Craik–Leibovich vortex force gave dissipation rates well above the law of the wall scaling [z^{-1} , Equation (5)], generating surface-intensified and significantly enhanced dissipation rates in the turbulent surface layer (Figure 1).

McWilliams *et al.* (1997) characterized the importance of Langmuir circulations through a turbulent Langmuir number

$$La_t = \sqrt{\frac{u^*}{u_{S0}}}, \quad (9)$$

which is the ratio of the friction velocity (4) to the Stokes velocity at the surface. Harcourt and D'Asaro (2008) modified this to include the vertical gradient of the Stokes velocity:

$$La_{SL} = \sqrt{\frac{u^*}{\Delta u_{SL}}}. \quad (10)$$

Here, Δu_{SL} takes the Stokes drift averaged over the top 25% of the mixed layer and subtracts from it the value near the base of the mixed layer, thus decreasing the sensitivity of (9) to the surface value. This scaling gave excellent representations of the turbulence intensity as a function of friction velocity (e.g. Harcourt and D'Asaro, 2008; D'Asaro, 2014).

The vertical distribution of dissipation driven by Langmuir circulations has mostly been studied through models. Skyllingstad and Denbo (1995), McWilliams *et al.* (1997), and Grant and Belcher (2009) found dissipation rates that decreased with depth at about the same rate as wind-driven turbulence [z^{-1} , Equation (5)]. Recently, Harcourt (2013) performed a fairly thorough modelling analysis of the vertical structure of dissipation in Langmuir circulations, and found a surface region in which dissipation decreased as z^{-1} (though more slowly than wind-driven turbulence), lying above a thicker layer of relatively constant dissipation (Figure 1). Dissipation decreased rapidly below the mixed layer. This suggests that Langmuir circulations are quite efficient at moving particles vertically through the mixed layer—more efficient than wind- or wave-driven turbulence, but less efficient than convectively driven turbulence.

Particle residence times in Langmuir turbulence, τ_{LC} , are relatively constant through an upper layer (usually corresponding to the mixed layer), increasing rapidly below (Figure 1). With strong Langmuir circulations, these residence times could be short enough to satisfy the conditions for the SCD hypothesis of a “thoroughly mixed top layer”. The intense turbulence driven by the Craik–Leibovich vortex force (of which Langmuir circulations are an example) is often strong enough to inhibit restratification through heating (Kukulka *et al.*, 2013). D'Asaro and Dairiki (1997) showed rapid deepening of the turbulent layer (25 m over 10 h) presumably driven by Langmuir circulations, followed by a similarly rapid restratification after the wind died. D'Asaro (2014) points out that the effects of Langmuir circulations are still poorly understood, and their scalings are not well developed. It is clear, however, that they are an important source of turbulence in the upper ocean, though they probably do not extend as deep as turbulence driven by convection.

Convectively driven turbulence

When the ocean loses heat through its surface, the top layers of the ocean become colder. Similarly, evaporation can increase the surface salinity; both these processes increase the density of the surface water. If these changes are great enough, the surface water can become denser than the water below it. This is gravitationally unstable: the surface water must sink, and in the process generates

convectively driven turbulence. Because of the sinking of dense water to an equilibrium level, convectively driven turbulence is very efficient.

Convectively driven turbulence was first quantified in the ocean surface layer by Shay and Gregg (1984) in a Gulf Stream eddy during winter cooling. They showed intense dissipation throughout the surface turbulent layer, with an abrupt, two to three orders of magnitude decrease in dissipation at the base of the turbulent layer. While the dissipation due to windforcing decreases as z^{-1} (5), convectively driven dissipation tends to be constant throughout the turbulent layer (e.g. Shay and Gregg, 1986; Lombardo and Gregg, 1989; Anis and Moum, 1994) with a magnitude scaled by the buoyancy flux J_b (Lombardo and Gregg, 1989; D'Asaro, 2014; Figure 1). The depth at which the relative contributions of wind- and convection-driven turbulence are equal is given by the Monin–Obukhov length L_{MO} (Shay and Gregg, 1986):

$$L_{MO} = \frac{u^{*3}}{\kappa J_b}. \quad (11)$$

At depths shallower than L_{MO} , turbulence is likely dominated by wind; dissipation due to convection is particularly apparent at depths $>L_{MO}$. The strong turbulence caused by convection tends to extend to the base of the mixed layer, and defines the seasonal pycnocline.

During convective mixing, the vertical temperature gradient can be negative, giving a negative buoyancy frequency. In this situation, Equation (6) cannot be used to calculate the diffusivities used to model particle and tracer motions. A better approach is the use of a turbulence closure model such as the K-profile parameterization (KPP—Large *et al.*, 1994) or Mellor and Yamada (1974) to model vertical profiles of diffusivities driven by boundary forcing. The strong, relatively uniform turbulence driven by convection leads to a constant vertical profile of plankton residence times, $\tau_{\text{convection}}$, in the convecting layer (Figure 1). These strongly turbulent layers are the most likely to satisfy the SCD hypothesis, with short residence times of plankton at any given irradiance in the upper layer. As I show below, however, small changes in stratification can rapidly (hours) shut down convective turbulence, leaving a well mixed but quiescent layer in which a bloom could form.

Measurements have shown that the intensity of dissipation, ε , tends to have a lognormal distribution, characterized by a few extremely intense events, with many much weaker occurrences. This lognormal distribution of dissipation leads to skewed distributions of diffusivities (6), with frequent occurrences of weak turbulence, and rare occurrences of intense turbulence events. These intense patches of turbulence can then drive infrequent, large fluxes over short time and space scales. Stevens *et al.* (2011) showed that the measured mean and median diffusivities were very different—the mean was biased towards large values by the rare occurrence of extremely high diffusivities. The biased mean would give a very different picture of the mixing climate for the phytoplankton: rather than experiencing weak turbulence most of the time with a few rare bursts of strong turbulence as suggested by the median diffusivity (the more accurate view), the mean diffusivity would suggest fairly strong turbulence all the time.

Relevance to the SCD hypothesis

Each of the turbulence-generating mechanisms described above has a different vertical distribution of turbulence intensity or dissipation (Figure 1). From (1), this means that phytoplankton would have

different residence times in different parts of the water column, affecting their local net growth and potentially allowing blooms in the presence of a much deeper (hydrographically measured) mixed layer. Wind- and wave-driven turbulence is strongly surface-intensified, giving longer residence times in deeper waters that are potentially still well within the euphotic zone. Convectively driven turbulence tends to move water in the turbulent layer most evenly, and would be the closest to satisfying the assumptions of the SCD hypothesis. Convection is a common source of turbulence during winter at temperate and high latitudes. As we shall see, however, convectively driven turbulence is relatively easy to suppress through extremely small changes in stratification.

Sources of stratification

Waters in an unstratified ocean would be easy to move via turbulence, as vertical motions would not be inhibited by any density gradient. This is seldom the case, however, as there are many sources of density stratification that are constantly operating. As stratification increases, more kinetic energy is needed to create the same turbulent mixing. Here, I discuss three main sources of stratification in the ocean: heat flux, freshwater flux, and horizontal density gradients.

Heat flux

The surface buoyancy flux J_b has two main components: the surface sensible heat flux Q_s , and the latent heat flux Q_l :

$$J_b = \frac{g}{\rho} \left(\frac{\alpha}{c_p} Q_s + \frac{\beta S}{(1-S)H} Q_l \right), \quad (12)$$

where α is the thermal expansion coefficient, c_p the specific heat of seawater, β the haline contraction coefficient, S the salinity, and H the latent heat of vaporization (e.g. Brainerd and Gregg, 1993a). When the first term on the right is positive (depending on the orientation of your vertical coordinate), the surface of the ocean will heat, leading to enhanced vertical stratification. The second term on the right determines the change in density through evaporation (and consequent increases in salinity: see the “Freshwater flux” section).

The heat flux through the ocean’s surface varies a great deal, both seasonally and daily. In many regions of the ocean, the heat flux will change from positive (net heating) to negative (net cooling) over a few hours during the course of the day, due to the sun’s position in the sky. A negative night-time heat flux can drive deep convection, which is subsequently shut down by heat-induced stratification during the day (Figure 2). This daily cycle of heat flux strongly modulates the daily cycles of surface-layer turbulence.

Surface-driven turbulence is very sensitive to heating. Brainerd and Gregg (1993a) and Shay and Gregg (1986), for example, showed that a $<0.2^\circ\text{C}$ step in temperature or a $<0.005 \text{ kg m}^{-3}$ step in density was sufficient to shut down dissipation below the diurnal turbulent layer (but above the seasonal mixed layer). The dissipation decayed with a time scale of $\sim 2 \text{ h}$ (Caldwell *et al.*, 1997), giving decreases in the vertical diffusivity of a factor of 100 over a few hours (Brainerd and Gregg, 1993a; Peters *et al.*, 1994). The short time scales for changes in the intensity and vertical distribution of turbulence have been appreciated for many decades. Mellor and Durbin (1975) found that turbulent mixing decayed with a time scale of 20% of an inertial period ($<1 \text{ d}$) in their mixed-layer model. Shay and Gregg (1986) observed dissipation to decrease in $<1 \text{ d}$ with changes in surface forcing, while Brainerd and Gregg (1993a) measured a $40\times$ decrease in ε over 4 h when convective turbulence was suppressed. D’Asaro and

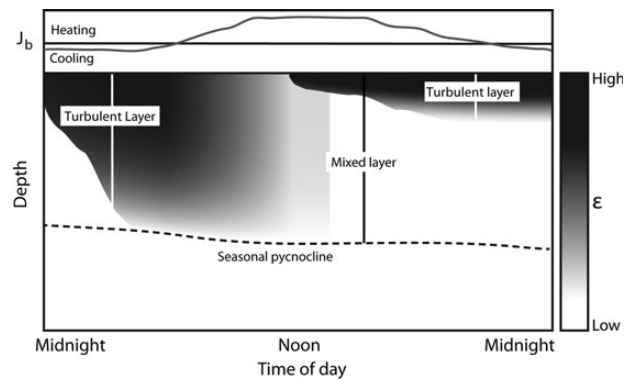


Figure 2. Schematic view of diel cycle of dissipation (grey scale, bottom panel) during net heating and net cooling at the surface (grey line, top panel). Cooling at night creates dense water at the surface that sinks, causing rapid convectively driven turbulence down to the seasonal pycnocline. Heating during the day can cause restratification that suppresses the turbulence from the surface, leading to a shallow turbulent layer with a remnant (non-mixing) mixed layer below (dashed line). A surface freshwater flux can similarly restrict the vertical extent of turbulence.

Dairiki (1997) observed restratification in 10 h after a storm passed their coastal study site.

Stramska and Dickey (1993) showed that including the absorption of heat by phytoplankton could cause a 0.2°C increase in temperature relative to a water column without phytoplankton in a model of the North Atlantic during winter–spring transition. This phytoplankton-driven temperature increase could be sufficient to shut down convective turbulence, stabilizing the water column. Indeed, Stramska and Dickey (1994) showed that including the heating due to phytoplankton led to local blooms before large-scale stratification of the water column: the heating decreased the local turbulence, allowing blooms in the sense of the SCD hypothesis.

A few recent studies have compared diel-resolved fluctuations in surface heat flux J_b and windstress τ to more averaged fluctuations in global models. Kamenkovich (2005) found that the high-frequency forcing led to shallower mixed layers in high-latitude regions in winter. Bernie *et al.* (2007) found that including the diurnal cycle led to trapping of momentum fluxes from the surface windstress near the surface in the time mean, leading to a reduction in vertical mixing and shallower turbulent layers. Kawai and Wada (2007) reviewed the literature and concluded that including diurnal variability is important, and that diurnal variations at high latitude, in particular, have been poorly studied.

Freshwater flux

Changes in salinity at the ocean’s surface can occur through evaporation, rain, or horizontal advection of waters of different salinity. Price (1979) was one of the first to detail the changes in vertical density distributions over the course of a rain event. He showed that the surface salinity decreased by 0.25, which was coincidentally similar to the change seen by Brainerd and Gregg (1997) in another study. The low-salinity signal was quickly (a few hours) mixed throughout the surface turbulent layer, decreasing its average density. This increased the density contrast at the base of the turbulent layer, which inhibited further mixed-layer deepening. The relatively static mixed layer could then accumulate more heat, which further enhanced the density step at the base of the mixed layer.

The inhibition of vertical turbulence by a low-salinity layer was also seen by Peters *et al.* (1994) and Wijesekera and Gregg (1996), who showed that the low-salinity “puddles” created by a rainstorm had a horizontal scale of ~ 10 km, and a vertical scale of 1 m. The salinity-induced barrier to turbulence was almost instantaneous, and lasted almost a day. This is consistent with observations of Hosegood *et al.* (2006) who found considerable vertical structure above the mixed layer after a rainfall, indicating decreased vertical turbulence due to salinity stratification.

Vertical variations in salinity through the interleaving of different water masses can have a profound effect on vertical turbulence. For example, Christensen and Pringle (2012) showed that a subsurface low-salinity layer in the Gulf of Maine offset the increased density of surface waters due to cooling, causing less turbulence than might be expected through convective heat loss alone. Shay and Gregg (1984) found a similar salt-stabilized temperature inversion in a Gulf Stream ring, which caused a 2–3 order of magnitude drop in dissipation at the base of the strongly turbulent layer. Long *et al.* (2012) found that wind-driven horizontal advection of low-salinity water was sufficient to stabilize the water column, allowing a bloom to form. Similarly, Ji *et al.* (2007, 2008) found that the timing and spatial pattern of the spring bloom in the Gulf of Maine depended on the freshwater flux into the Gulf from the Scotian Shelf: increased freshening caused earlier blooms.

In developing a data-based mixed-layer climatology, De Boyer Montégut *et al.* (2004) found that including salinity effects in the definition of the mixed layer led to shallower estimates of mixed layers during January, February, and March in the North Pacific and western North Atlantic, but deeper estimated mixed layers in the eastern North Atlantic due to salinity compensation of temperature gradients. This study re-emphasizes the point that neglecting salinity effects will affect estimates of mixed-layer depth, which are commonly used in tests of the SCD hypothesis. Furthermore, salinity variations are another factor causing differences between a mixed-layer depth and the actual depth of turbulent mixing.

Horizontal stratification

With a few notable exceptions (e.g. Taylor and Ferrari, 2011; Mahadevan *et al.*, 2012), most studies examining SCD have assumed a one-dimensional (vertical) trade-off of turbulence and stratification. However, we have known since at least the 1990s (e.g. Brainerd and Gregg, 1993a, b) that the tilting (flattening or slumping) of horizontal density gradients can cause vertical density gradients that will decrease vertical turbulence (Figure 3). The tilting of isopycnals from near vertical to horizontal is known as “restratification”: horizontal density gradients become vertical density gradients. Brainerd and Gregg (1993a, b, 1997) showed that horizontal gradients could cause restratification over the course of a few hours, during which the buoyancy frequency N could increase by a factor of 10. Caldwell *et al.* (1997) found that $\sim 40\%$ of the restratification they observed was due to the relaxation of horizontal gradients, rather than local vertical processes. Hosegood *et al.* (2006, 2008) found that most of the restratification they observed in the surface mixed layer was through the tilting of existing horizontal density gradients. Stevens *et al.* (2011) also noted stratification induced by the slumping of horizontal density gradients during a Southern Ocean iron fertilization experiment, while Long *et al.* (2012) found horizontal advection-driven restratification to dominate turbulence, allowing phytoplankton blooms.

In addition to windforcing (Ekman flux), there appear to be two main mechanisms that cause horizontal density gradients to slump

in the mixed layer: baroclinic (and other, often smaller-scale) instabilities, and the vertical shear of near-inertial waves. Hosegood *et al.* (2006) found a great deal of horizontal structure in temperature, salinity, and density at scales down to 2 km (the resolution of their vehicle). These structures occur at the “submesoscale” (e.g. Lévy *et al.*, 2012), and are often surface-intensified. A variety of instabilities can act on these horizontal gradients to cause them to slump, restratifying the mixed layer (Figure 3). Hosegood *et al.* (2006) concluded that near-surface baroclinic instabilities were responsible for the observed restratification, and that these dynamics occurred at horizontal scales that are not resolved in most models of ocean physics (but see Taylor and Ferrari, 2011; Mahadevan *et al.*, 2012 for counterexamples).

Tandon and Garrett (1994, 1995) showed that near-inertial waves can cause restratification. These low-frequency waves generated mainly by wind events propagate almost vertically, causing horizontal layers of water to oscillate horizontally relative to each other. This creates a vertical shear that can flatten existing horizontal

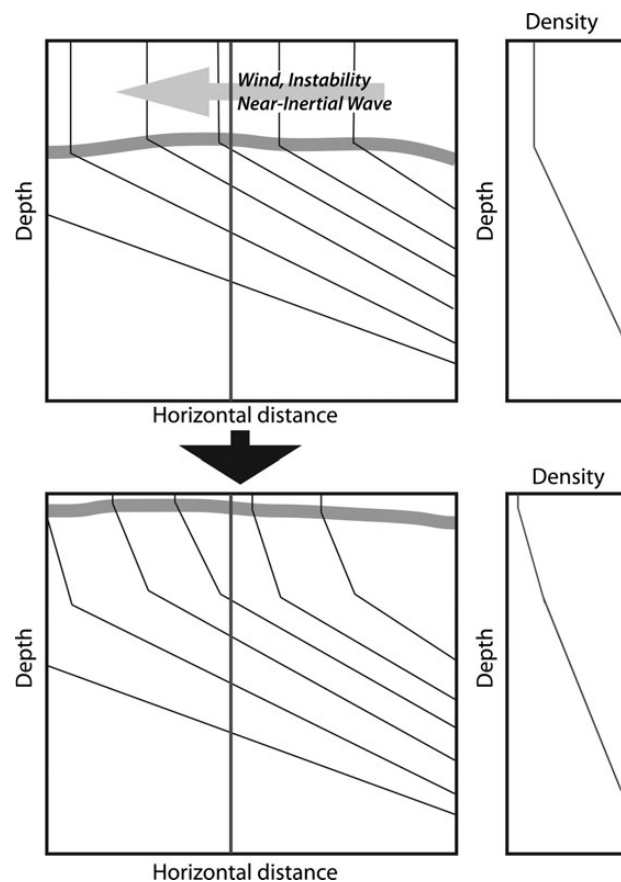


Figure 3. Schematic showing how a horizontal density gradient can slump to create a vertical density gradient that suppresses vertical turbulence. (Upper left) A horizontal density gradient in a region with deep turbulent layers is perturbed by a forcing with a vertical shear such as a baroclinic instability or a near-inertial wave. (Upper right) The vertical density profile taken at the vertical grey line in the upper-left panel, showing the deep mixed layer. (Lower left) The horizontal density gradient in the mixed layer has tilted, creating vertical density gradients that suppress turbulence (turbulent layer shown by thick grey line). (Lower right) The vertical density profile taken at the vertical grey line in the lower left panel, showing the shallow mixed layer after slumping.

density gradients, causing restratification (e.g. Hosegood *et al.*, 2008). The waves can also tilt horizontal gradients upwards, decreasing the local vertical density gradients, depending on the phase of the wave and the geostrophic currents.

Vertical shear of horizontal density gradients is thus a rapid and efficient mechanism to increase vertical stratification and damp vertical turbulence. It will occur wherever there are horizontal density gradients, and cannot be accounted for in one-dimensional models.

Relevance to the SCD hypothesis

The sources of stratification determine how the kinetic energy of turbulence is distributed in time and space. Surprisingly small steps in density can suppress turbulence, leaving a well mixed but quiescent layer below an actively turbulent layer. Changes in density arise from heat flux, freshwater flux, and the slumping of horizontal density gradients, showing that the temporal and spatial structures of turbulence must be studied in a three-dimensional framework. The short time scales (hours) and small horizontal spatial scales (kilometres) of turbulence are likely to drive patchiness of phytoplankton growth on similar scales. This suggests that phytoplankton spring blooms should be patchy, transient, local phenomena, such as seen by Mahadevan *et al.* (2012).

Discussion

In formulating his critical depth hypothesis, Sverdrup (1953) assumed a “thoroughly mixed top layer” with turbulence “strong enough to distribute the plankton organisms evenly through the layer”. Subsequent tests of the SCD hypothesis have generally ignored the turbulence, and have instead used the operationally defined “mixed-layer depth” as a (very inadequate) proxy for turbulence intensity and vertical structure. The smooth seasonal cycles of mixed layers—averaged over weeks to months in time and 10–1000 km in space—used by most researchers remove most of the important aspects of turbulence that are essential to understanding the timing and location of a spring bloom. Bernie *et al.* (2007, 2008) included diel variability in forcing in a global circulation model focusing on atmosphere–ocean coupling in the tropics, and found significant changes in heating due to the diel rectification of the daily mean sea surface temperature. These hourly fluctuations propagated up to cause changes in seasonal and interannual cycles of both the ocean and atmosphere. In their review, Kawai and Wada (2007) underscore the importance of including diel variability in heat fluxes and windstress when exploring larger-scale problems: the short-time scale variability affects the long-term behaviour of the system. This problem is particularly acute at high latitudes where we have a paucity of high-frequency observations (but see Martin *et al.*, 2011; Cetinic *et al.*, 2012; Mahadevan *et al.*, 2012 for notable exceptions). Fundamentally, even if mixed-layer depths reflected the depth of strong turbulence, weekly or monthly estimates of mixed-layer depth should be used with caution and some scepticism when testing the SCD hypothesis.

Time averages of surface mixed-layer dynamics remove a great deal of important structure. One basic feature of turbulent layers is that they do not gradually move upwards in the water column as heating increases or wind decreases. Rather, they reform at the surface, leaving a remnant layer below. Tiny increases in temperature or density ($<0.02^{\circ}\text{C}$ or $<0.005\text{ kg m}^{-3}$) can be sufficient to shut down wind-forced or convectively driven turbulence below. This shut down can occur over a few hours, leaving an unstratified but quiescent remnant mixed layer below a shallow, actively turbulent layer. At a local scale, then (and the scale that is relevant to the

phytoplankton), the depth of the turbulent layer is highly variable, deepening when kinetic energy is available, and reforming at the surface when stratifying fluxes overcome the sources of turbulence. This leads to a discontinuity in the turbulent-layer depth: it deepens and then re-forms at the surface, often over the course of a day. This discontinuity has important implications for understanding the turbulent environment experienced by the phytoplankton: it is highly variable in intensity and vertical structure over relatively small horizontal spatial scales. From one hour to the next, the turbulent layer could shoal from 100 to 20 m due to some local heating, a rainstorm, or slumping of horizontal gradients, giving a newly quiescent environment for phytoplankton photosynthesis.

It is becoming increasingly clear from observations and models that vertical turbulence is intimately tied to submesoscale horizontal gradients in density. In their surveys, Hosegood *et al.* (2006) found horizontal density gradients on the scale of 1–2 km (the smallest scales they could resolve); these gradients significantly affected the intensity and distribution of vertical turbulence in the study area. Patchiness of surface salinity due to rain was estimated to have 10 km horizontal scales (Wijesekera and Gregg, 1996), and we would expect significant horizontal density structure at oceanic mesoscales (10–100 km) that would affect vertical turbulence. The horizontal wavelength of near-inertial waves is <10 km, similar to many mixed-layer instabilities. These horizontal density gradients and vertical shears should drive variations in turbulent layer depth on the same horizontal scales. It is clear then, that 100–1000 km horizontal averages of mixed-layer depth will smooth over a great deal of variability that is fundamental to understanding the local growth of the phytoplankton.

In this synthesis, I have tried to make the point that turbulence varies locally with time scales of hours and spatial scales of kilometres. One might ask then, how this local view of turbulence and consequent phytoplankton response can be reconciled with the large-scale (many weeks, 1000s of km) view of a spatially and temporally coherent spring bloom. As Chiswell *et al.* (2013) notes, “13 years of data suggest that this spring bloom initiation progresses smoothly, [while] uncomposited images of surface chlorophyll show that at any given time, surface chlorophyll is dominated by seemingly near chaotic processes”. In this view, then, the coherence of the spring bloom arises from averaging away the small-scale variability. The large-scale forcings and conditions are modulated by the local forcings and conditions to determine the local timing and intensity of the bloom: the large-scale forcings indicate when a bloom *might* occur; the local dynamics indicate whether it *will* occur. A local bloom could occur earlier or later than large-scale forcings would indicate, due to local winds, local freshwater flux, a local change in the heat flux (less cloud, for example), and mesoscale or submesoscale changes in the turbulent-layer depth, etc.

An obvious question then is, “Can large-scale averages of properties (e.g. temperature, mixed-layer depth, chlorophyll) and forcings (e.g. heat flux, wind, irradiance) be used to test the SCD hypothesis?” Upper-ocean turbulence is, after all, driven largely by surface forcings, as indicated in the synthesis above. Is it reasonable to use averaged forcings to infer averaged dynamics to compare with averaged data to test what is essentially a local hypothesis? Many of the properties being averaged (turbulence, mixed-layer depth, phytoplankton growth) have very non-linear responses to their forcings. The average of a non-linear variable depends greatly on the time- or space-scale of the averaging. Furthermore, the average of products of non-linear variables, for example, is not the same as the product of the averages, which is what is normally used to test

the SCD hypothesis. I do not believe we can definitively answer the question posed here. But I do believe that we should approach such averaged analyses with healthy scepticism until we have better measurements (both remote and *in situ*), and better means of analysing the observations.

In reviewing mixed layers and turbulent layers, I have shown that both the sources of energy that drive vertical turbulence and the sources of stratification that suppress vertical turbulence are extremely patchy in time and space. The key point, however, is that to properly test the SCD hypothesis one must obtain coincident measurements of the turbulence and the phytoplanktonic rates, as it is the turbulent water motions that move the phytoplankton through the vertical light gradient. Drawing conclusions about the movement of phytoplankton in a mixed layer whose depth is determined by vertical profiles of temperature or density is potentially very misleading. Furthermore, using large-scale averages of properties to infer dynamics can easily lead to incorrect conclusions. Sverdrup (1953) was quite explicit about the requirement of a "thoroughly mixed layer"; currently, the only accurate measure of the existence of such a layer is through measurements of turbulence, *in situ*. I would maintain, therefore, that with the possible exception of Mahadevan *et al.* (2012), the SCD hypothesis has yet to be thoroughly tested in the field. Perhaps quantifying the turbulent layer rather than the mixed layer will lead to a deeper understanding of the timing and structure of spring phytoplankton blooms, and a reconciliation of the various tests of the SCD hypothesis.

Summary

- (i) Because of the variety of mechanisms creating turbulence in the surface turbulent layer, the mixed-layer depth (defined by temperature or density) is usually a poor indicator of the depth of turbulence, the vertical structure of turbulence, and the intensity of turbulence.
- (ii) Different forcing mechanisms drive very different vertical distributions of turbulence intensity, from surface-intensified, to relatively uniform with depth.
- (iii) Forcings that increase stratification can shut down active turbulence in hours, with density steps as small as $<0.005 \text{ kg m}^{-3}$.
- (iv) Turbulent layers do not shoal monotonically, but rather tend to re-form at the surface, and then entrain downwards with time.
- (v) Fluctuations in turbulence occur over time scales of hours and spatial scales of kilometres.
- (vi) It is essential to include the short time scale and small spatial scale variations of turbulence in analyses when testing the SCD hypothesis. The depth of the mixed layer is an insufficient and usually inaccurate measure of the turbulent layer depth.
- (vii) Inclusion of the structure and intensity of turbulence may lead to a reconciliation of the various tests of the SCD hypothesis.

Acknowledgements

I would like to thank my students and postdoc Fanny Chenillat, Christian Briseño, Alain de Verneil, Stephanie Snyder, Bryce Inman, Jessica Carrière-Garwood, and Ruth Musgrave for

extremely useful advice and editorial help during the writing of this synthesis. In particular, I would like to thank two anonymous reviewers whose comments, suggestions, and criticisms both improved the manuscript, and got me thinking about further issues related to SCD and turbulence.

References

- Anis, A., and Moum, J. N. 1992. The superadiabatic surface layer of the ocean during convection. *Journal of Physical Oceanography*, 22: 1221–1227.
- Anis, A., and Moum, J. N. 1994. Prescriptions for heat flux and entrainment rates in the upper ocean during convection. *Journal of Physical Oceanography*, 24: 2142–2155.
- Anis, A., and Moum, J. N. 1995. Surface wave–turbulence interactions: scaling $\epsilon(z)$ near the sea surface. *Journal of Physical Oceanography*, 25: 2025–2045.
- Behrenfeld, M. J. 2010. Abandoning Sverdrup's critical depth hypothesis on phytoplankton blooms. *Ecology*, 91: 977–989.
- Behrenfeld, M. J., and Boss, E. S. 2014. Resurrecting the ecological underpinnings of ocean plankton blooms. *Annual Review of Marine Science*, 6: 167–194.
- Behrenfeld, M. J., Doney, S. C., Lima, I., Boss, E. S., and Siegel, D. A. 2013. Annual cycles of ecological disturbance and recovery underlying the subarctic Atlantic spring plankton bloom. *Global Biogeochemical Cycles*, 27: 526–540.
- Bernie, D. J., Guilyardi, E., Madec, G., Slingo, J. M., and Woolnough, S. J. 2007. Impact of resolving the diurnal cycle in an ocean–atmosphere GCM. Part 1: a diurnally forced OGCM. *Climate Dynamics*, 29: 575–590.
- Bernie, D. J., Guilyardi, E., Madec, G., Slingo, J. M., Woolnough, S. J., and Cole, J. 2008. Impact of resolving the diurnal cycle in an ocean–atmosphere GCM. Part 2: a diurnally coupled CGCM. *Climate Dynamics*, 31: 909–925.
- Boss, E., and Behrenfeld, M. 2010. In situ evaluation of the initiation of the North Atlantic phytoplankton bloom. *Geophysical Research Letters*, 37: L18603. doi:10.1029/2010GL044174.
- Brainerd, K. E., and Gregg, M. C. 1993a. Diurnal restratification and turbulence in the oceanic surface mixed layer 1. Observations. *Journal of Geophysical Research*, 98: 22645–22656.
- Brainerd, K. E., and Gregg, M. C. 1993b. Diurnal restratification and turbulence in the oceanic surface mixed layer 2. Modeling. *Journal of Geophysical Research*, 98: 22657–22664.
- Brainerd, K. E., and Gregg, M. C. 1995. Surface mixed and mixing layer depths. *Deep Sea Research I*, 42: 1521–1543.
- Brainerd, K. E., and Gregg, M. C. 1997. Turbulence and stratification on the tropical ocean—global atmosphere-coupled ocean–atmosphere response experiment microstructure pilot cruise. *Journal of Geophysical Research*, 102: 10437–10455.
- Brody, S. R., and Lozier, M. S. 2014. Changes in dominant mixing length scales as a driver of subpolar phytoplankton bloom initiation in the North Atlantic. *Geophysical Research Letters*, 41: 3197–3203.
- Brody, S. R., Lozier, M. S., and Dunne, J. P. 2013. A comparison of methods to determine phytoplankton bloom initiation. *Journal of Geophysical Research*, 118: 2345–2357.
- Caldwell, D. R., Lien, R.-C., Moum, J. N., and Gregg, M. C. 1997. Turbulence decay and restratification in the equatorial ocean surface layer following nighttime convection. *Journal of Physical Oceanography*, 27: 1120–1132.
- Cetinic, I., Perry, M. J., Briggs, N. T., Kallin, E., D'Asaro, E. A., and Lee, C. M. 2012. Particulate organic carbon and inherent optical properties during 2008 North Atlantic bloom experiment. *Journal of Geophysical Research*, 117: C06028. doi:10.1029/2011JC007771.
- Chiswell, S. M. 2011. Annual cycles and spring blooms in phytoplankton: don't abandon Sverdrup completely. *Marine Ecology Progress Series*, 443:39–50.

- Chiswell, S. M., Bradford-Grieve, J., Hadfield, M. G., and Kennan, S. C. 2013. Climatology of surface chlorophyll *a*, autumn–winter and spring blooms in the southwest Pacific Ocean. *Journal of Geophysical Research*, 118:1003–1018.
- Christensen, M. K., and Pringle, J. M. 2012. The frequency and cause of shallow winter mixed layers in the Gulf of Maine. *Journal of Geophysical Research*, 117: C01025. doi:10.1029/2011JC007358.
- Craik, A. D. D., and Leibovich, S. 1976. A rational model for Langmuir circulations. *Journal of Fluid Mechanics*, 73: 401–426.
- D’Asaro, E. 2014. Turbulence in the upper-ocean mixed layer. *Annual Review of Marine Science*, 6: 101–115.
- D’Asaro, E., and Dairiki, G. T. 1997. Turbulence intensity measurements in a wind-driven mixed layer. *Journal of Physical Oceanography*, 27: 2009–2022.
- D’Asaro, E., Thomson, J., Shcherbina, A. Y., Harcourt, R. R., Cronin, M. F., Hemer, M. A., and Fox-Kemper, B. 2014. Quantifying upper ocean turbulence driven by surface waves. *Geophysical Research Letters*, 41: 102–107.
- D’Asaro, E. A. 2001. Turbulent vertical kinetic energy in the ocean mixed layer. *Journal of Physical Oceanography*, 31:3530–3537.
- De Boyer Montégut, C., Madec, G., Fischer, A. S., Lazar, A., and Iudicone, D. 2004. Mixed layer depth over the global ocean: an examination of profile data and a profile-based climatology. *Journal of Geophysical Research*, 109: C12003. doi:10.1029/2004JC002378.
- Ebert, U., Arrayás, M., Temme, N., and Sommeijer, B. 2001. Critical conditions for phytoplankton blooms. *Bulletin of Mathematical Biology*, 63:1095–1124.
- Ellertsen, H. C. 1993. Spring blooms and stratification. *Nature*, 363:24.
- Fischer, A. D., Moberg, E. A., Alexander, H., Brownlee, E. F., Hunter-Cevera, K. R., Pitz, K. J., Rosengard, S. Z., *et al.* 2014. Sixty years of Sverdrup: a retrospective of progress in the study of phytoplankton blooms. *Oceanography*, 27: 222–235.
- Grant, A. L. M., and Belcher, S. E. 2009. Characteristics of Langmuir turbulence in the ocean mixed layer. *Journal of Physical Oceanography*, 39: 1871–1887.
- Harcourt, R. R. 2013. A second-moment closure model of Langmuir turbulence. *Journal of Physical Oceanography*, 43: 673–697.
- Harcourt, R. R., and D’Asaro, E. 2008. Large-eddy simulation of Langmuir turbulence in pure wind seas. *Journal of Physical Oceanography*, 38: 1542–1562.
- Holte, J., and Talley, L. 2009. A new algorithm for finding mixed layer depths with applications to Argo data and subantarctic mode water formation. *Journal of Atmospheric and Oceanic Technology*, 26: 1920–1939.
- Hosegood, P., Gregg, M. C., and Alford, M. H. 2006. Sub-mesoscale lateral density structure in the oceanic surface mixed layer. *Geophysical Research Letters*, 33: L22604. doi:10.1029/2006GL026797.
- Hosegood, P., Gregg, M. C., and Alford, M. H. 2008. Restratification in the surface mixed layer with submesoscale lateral density gradients: diagnosing the importance of the horizontal dimension. *Journal of Physical Oceanography*, 38: 2438–2460.
- Huang, C. J., and Qiao, F. 2010. Wave–turbulence interaction and its induced mixing in the upper ocean. *Journal of Geophysical Research*, 115: C04026. doi:10.1029/2009JC005853.
- Huang, C. J., Qiao, F., Dai, D., Ma, H., and Guo, J. 2012. Field measurement of upper ocean turbulence dissipation associated with wave–turbulence interaction in the South China Sea. *Journal of Geophysical Research*, 117: C00J09. doi:10.1029/2011JC007806.
- Huisman, J., van Oostveen, P., and Weissing, F. J. 1999. Critical depth and critical turbulence: two different mechanisms for the development of phytoplankton blooms. *Limnology and Oceanography*, 44:1781–1787.
- Ji, R., Davis, C. S., Chen, C. S., Townsend, D. W., Mountain, D. G., and Beardsley, R. C. 2007. Influence of ocean freshening on shelf phytoplankton dynamics. *Geophysical Research Letters*, 34: doi:10.1029/2007/GL032010.
- Ji, R., Davis, C. S., Chen, C. S., Townsend, D. W., Mountain, D. G., and Beardsley, R. C. 2008. Modeling the influence of low-salinity water inflow on winter–spring phytoplankton dynamics in the Nova Scotian Shelf—Gulf of Maine region. *Journal of Plankton Research*, 30:1399–1416.
- Kamenkovich, I. M. 2005. Role of daily surface forcing in setting the temperature and mixed layer structure of the Southern Ocean. *Journal of Geophysical Research*, 110: C07006. doi:10.1029/2004JC002610.
- Kara, A. B., Rochford, P. A., and Hurlburt, H. E. 2000. An optimal definition for ocean mixed layer depth. *Journal of Geophysical Research*, 105: 16803–16821.
- Kawai, Y., and Wada, A. 2007. Diurnal sea surface temperature variation and its impact on the atmosphere and ocean: a review. *Journal of Oceanography*, 63: 721–744.
- Kukulka, T., Plueddemann, A. J., and Sullivan, P. P. 2013. Inhibited upper ocean restratification in nonequilibrium swell conditions. *Geophysical Research Letters*, 40: 3672–3676.
- Large, W. G., McWilliams, J. C., and Doney, S. C. 1994. Oceanic vertical mixing: a review and a model with a nonlocal boundary layer parameterization. *Reviews of Geophysics*, 32: 363–403.
- Lévy, M., Ferrari, R., Franks, P. J. S., Martin, A. P., and Rivière, P. 2012. Bringing physics to life at the submesoscale. *Geophysical Research Letters*, 39: L14602. doi:10.1029/2012GL052756.
- Lombardo, C. P., and Gregg, M. C. 1989. Similarity scaling during nighttime convection. *Journal of Geophysical Research*, 94: 6273–6284.
- Long, M. C., Thomas, L. N., and Dunbar, R. B. 2012. Control of phytoplankton bloom inception in the Ross Sea, Antarctica, by Ekman restratification. *Global Biogeochemical Cycles*, 26: GB1006. doi:10.1029/2010GB003982.
- Lorbacher, K., Dommenges, D., Niiler, P. P., and Köhl, A. 2006. Ocean mixed layer depth: a subsurface proxy of ocean–atmosphere variability. *Journal of Geophysical Research*, 111: C07010. doi:10.1029/2003JC002157.
- Mahadevan, A., D’Asaro, E., Lee, C., and Perry, M. J. 2012. Eddy-driven stratification initiates North Atlantic spring phytoplankton blooms. *Science*, 337: 54–58.
- Martin, P., Lampitt, R. S., Perry, M. J., Sanders, R., Lee, C., and D’Asaro, E. 2011. Export and mesopelagic particle flux during a North Atlantic spring diatom bloom. *Deep Sea Research I*, 58: 338–349.
- McWilliams, J. C., Huckle, E., Liang, J.-H., and Sullivan, P. P. 2012. The wavy Ekman layer: Langmuir circulations, breaking waves, and Reynolds stresses. *Journal of Physical Oceanography*, 42: 1793–1816.
- McWilliams, J. C., Sullivan, P., and Moeng, C. 1997. Langmuir turbulence in the ocean. *Journal of Fluid Mechanics*, 334: 1–30.
- Mellor, G. L., and Durbin, P. A. 1975. The structure and dynamics of the ocean surface mixed layer. *Journal of Physical Oceanography*, 5: 718–728.
- Mellor, G. L., and Yamada, T. 1974. A hierarchy of turbulent closure models for planetary boundary layers. *Journal of Atmospheric Sciences*, 31: 1791–1806.
- Obata, A., Ishizaka, J., and Endoh, M. 1996. Global verification of critical depth theory for phytoplankton bloom with climatological in situ temperature and satellite ocean color data. *Journal of Geophysical Research*, 10: 20657–20667.
- Osborn, T. R. 1980. Estimates of the local rate of vertical diffusion from dissipation measurements. *Journal of Physical Oceanography*, 10: 83–89.
- Peters, H., Gregg, M. C., and Sanford, T. B. 1994. The diurnal cycle of the upper equatorial ocean: turbulence, fine-scale shear, and mean shear. *Journal of Geophysical Research*, 99: 7707–7723.
- Price, J. F. 1979. Observations of a rain-formed mixed layer. *Journal of Physical Oceanography*, 9: 643–649.
- Price, J. F., and Sundermeyer, M. A. 1999. Stratified Ekman layers. *Journal of Geophysical Research*, 104: 20467–20494.

- Shay, T. J., and Gregg, M. C. 1984. Turbulence in an oceanic convective mixed layer. *Nature*, 310: 282–285.
- Shay, T. J., and Gregg, M. C. 1986. Convectively driven turbulent mixing in the upper ocean. *Journal of Physical Oceanography*, 16: 1777–1798.
- Siegel, D. A., Doney, S. C., and Yoder, J. A. 2002. The North Atlantic spring phytoplankton bloom and Sverdrup's critical depth hypothesis. *Science*, 296: 730–733.
- Skyllingstad, E. S., and Denbo, D. W. 1995. An ocean large-eddy simulation of Langmuir circulations and convection in the surface mixed layer. *Journal of Geophysical Research*, 100: 8501–8522.
- Stevens, C., Ward, B., Law, C., and Walkington, M. 2011. Surface layer mixing during the SAGE ocean fertilization experiment. *Deep Sea Research II*, 58:776–785.
- Stramska, M., and Dickey, T. 1993. Phytoplankton bloom and the vertical thermal structure of the upper ocean. *Journal of Marine Research*, 51:819–842.
- Stramska, M., and Dickey, T. 1994. Modeling phytoplankton dynamics in the northeast Atlantic during the initiation of the spring bloom. *Journal of Geophysical Research*, 99: 10241–10253.
- Sutherland, G., Ward, B., and Christensen, K. H. 2013. Wave-turbulence scaling in the ocean mixed layer. *Ocean Science*, 9: 597–608.
- Sverdrup, H. U. 1953. On conditions for the vernal blooming of phytoplankton. *Journal du Conseil International pour l'Exploration de la Mer*, 18: 287–295.
- Tandon, A., and Garrett, C. 1994. Mixed layer restratification due to a horizontal density gradient. *Journal of Physical Oceanography*, 24: 1419–1424.
- Tandon, A., and Garrett, C. 1995. Geostrophic adjustment and restratification of a mixed layer with horizontal gradients above a stratified layer. *Journal of Physical Oceanography*, 25: 2229–2241.
- Taylor, J. R., and Ferrari, R. 2011. Shutdown of turbulent convection as a new criterion for the onset of spring phytoplankton blooms. *Limnology and Oceanography*, 56: 2293–2307.
- Townsend, D. W., Keller, M. D., Sieracki, M. E., and Ackleson, S. G. 1992. Spring phytoplankton blooms in the absence of vertical water column stratification. *Nature*, 360: 59–62.
- Wang, W., and Huang, R. X. 2004. Wind energy input to the Ekman layer. *Journal of Physical Oceanography*, 34: 1267–1275.
- Wijesekera, H. W., and Gregg, M. C. 1996. Surface layer response to weak winds, westerly bursts, and rain squalls in the western Pacific warm pool. *Journal of Geophysical Research*, 101: 977–997.

Handling editor: Rubao Ji



Contribution to the Themed Section: 'Revisiting Sverdrup's Critical Depth Hypothesis' Food for Thought

The importance of phytoplankton trait variability in spring bloom formation

Aleksandra M. Lewandowska^{1,2*}, Maren Striebel², Ulrike Feudel³, Helmut Hillebrand², and Ulrich Sommer⁴

¹German Centre for Integrative Biodiversity Research (iDiv) Halle-Jena-Leipzig, Deutscher Platz 5e, Leipzig 04103, Germany

²Institute for Chemistry and Biology of the Marine Environment (ICBM-Terramare), Carl-von-Ossietzky University Oldenburg, Schleusenstrasse 1, Wilhelmshaven 26382, Germany

³Institute for Chemistry and Biology of the Marine Environment (ICBM), Carl-von-Ossietzky University Oldenburg, Carl von Ossietzky Strasse 9-11, Oldenburg 26111, Germany

⁴Marine Ecology, GEOMAR Helmholtz Center for Ocean Research Kiel, Düsterbrookweg 20, Kiel 24105, Germany

*Corresponding author: tel: +49 44219448209; fax: +49 4421944299; e-mail: aleksandra.lewandowska@uni-oldenburg.de

Lewandowska, A. M., Striebel, M., Feudel, U., Hillebrand, H., and Sommer, U. The importance of phytoplankton trait variability in spring bloom formation. – ICES Journal of Marine Science, 72: 1908–1915.

Received 4 August 2014; revised 15 March 2015; accepted 19 March 2015; advance access publication 9 April 2015.

About 60 years ago, the critical depth hypothesis was proposed to describe the occurrence of spring phytoplankton blooms and emphasized the role of stratification for the timing of onset. Since then, several alternative hypotheses appeared focusing on the role of grazing and mixing processes such as turbulent convection or wind activity. Surprisingly, the role of community composition—and thus the distribution of phytoplankton traits—for bloom formation has not been addressed. Here, we discuss how trait variability between competing species might influence phytoplankton growth during the onset of the spring bloom. We hypothesize that the bloom will only occur if there are species with a combination of traits fitting to the environmental conditions at the respective location and time. The basic traits for formation of the typical spring bloom are high growth rates and photoadaptation to low light conditions, but other traits such as nutrient kinetics and grazing resistance might also be important. We present concise ideas on how to test our theoretical considerations experimentally. Furthermore, we suggest that future models of phytoplankton blooms should include both water column dynamics and variability of phytoplankton traits to make realistic projections instead of treating the phytoplankton bloom as an aggregate community phenomenon.

Keywords: critical depth, light spectrum, phytoplankton, spring bloom, trait.

Introduction

The spring phytoplankton bloom is a ubiquitous phenomenon in temperate to boreal aquatic ecosystems, and the timing and magnitude of the spring bloom triggers much of the dynamics in these ecosystems throughout the year (Platt *et al.*, 2003; Edwards and Richardson, 2004). Consequently, it has been a major task of plankton ecology to explain the mechanisms driving the onset of the phytoplankton spring bloom and its dynamics. Since the 1920s, researchers have emphasized the role of light and mixing processes in bloom formation (Gran and Braarud, 1935; Atkins, 2009). In the early 1940s, Riley (1942) introduced the compensation depth concept—the depth at which photosynthesis exactly matches

respiration rate. By incorporating these concepts, Sverdrup (1953) proposed the first quantitative explanation of the occurrence of the spring phytoplankton bloom. In the following years, several theories were advanced to explain the spring bloom formation, highlighting the role of turbulence, grazing, and nutrients in phytoplankton blooms, but the critical depth hypothesis (Sverdrup, 1953) remains the most cited and widely accepted. A comprehensive review on the research following Sverdrup's critical depth hypothesis was recently published by Fischer *et al.* (2014).

According to Sverdrup (1953), there is a critical mixing depth for any given time and location at which light availability in the mixed water column is sufficient to allow photosynthetic production to

compensate for losses. This depth is estimated to be 5–10 times the compensation depth as defined by Riley (1942). The phytoplankton bloom can only occur if the actual mixing depth is less than the critical mixing depth, assuming that net photosynthesis and growth rates of phytoplankton are positive. Sverdrup argued that during spring warming, stratification compresses the mixing depth and the moment when the mixing depth becomes shallower than the critical mixing depth marks the onset of the phytoplankton bloom. The subsequent dynamics of the bloom are then governed by the stability and extent of the stratification.

Sverdrup's theory makes a number of simplifying assumptions, which might limit its application to natural systems. First, Sverdrup's hypothesis assumes that community respiration is constant with depth, whereas in reality respiration is species-specific and does not stay constant with depth (Smetacek and Passow, 1990; Williams, 1998; Robinson *et al.*, 2002). Second, the critical depth theory is based on light intensity alone, but the quality of the spectral availability of light changes as well with depth. These changes in available components (wavelengths) of solar radiation potentially create light niches for phytoplankton species, which are able to use different parts of the available light spectrum depending on the accessory pigments they contain (Polimene *et al.*, 2014). Third, Sverdrup's hypothesis assumes a thoroughly mixed water layer in which the phytoplankton cells are evenly distributed. In reality, mixing processes depend on wind activity and local hydrography which are not uniform (Taylor and Ferrari, 2011), leading to a rather patchy distribution of organisms (Chiswell, 2011). Furthermore, some species are able to actively migrate within the water column, also leading to an uneven distribution. Comparing phytoplankton blooms in the absence of vertical stratification in the Gulf of Maine (Townsend *et al.*, 1992) with the hypothesis proposed by Sverdrup (1953), Huisman *et al.* (1999a) formulated the critical turbulence hypothesis. Here, the focus is not on stratification but turbulence: if turbulence is below a species-specific threshold, phytoplankton can bloom in the euphotic upper water column before being transported deeper where light is insufficient.

Sverdrup himself was aware of some weaknesses of his hypothesis, especially emphasizing the role of community composition in bloom formation. He noted that the irradiance at the compensation depth must depend on plankton composition, including species composition within the phytoplankton as well as the interaction between phyto- and zooplankton (Sverdrup, 1953). As a replacement of the critical depth hypothesis, Behrenfeld (2010) proposed a dilution-recoupling hypothesis according to which physical processes like water column mixing affect the balance between phytoplankton growth and grazing by zooplankton. He defined the bloom as a combined effect of the decoupling between phytoplankton growth and losses due to the mixed layer deepening (Behrenfeld, 2010). According to Behrenfeld (2010), a deepening of the mixed layer 'dilutes' the grazing pressure on phytoplankton and allows a bloom to begin. This hypothesis does not necessarily require water column stratification to occur, but is rather based on changes in predator–prey interactions.

Alternative or amended theories to explain the bloom formation emphasized the role of grazers (Smetacek and Passow, 1990; Behrenfeld, 2010), stratification onset (Chiswell, 2011), and turbulent convection (Huisman *et al.*, 1999a; Taylor and Ferrari, 2011), but the role of phytoplankton trait composition has so far largely been omitted from the discussion of phytoplankton spring bloom formation. This is surprising, as phytoplankton succession can clearly be linked to interspecific variation in resource use.

Although the theory on species coexistence describes competition for resources at steady state (Tilman *et al.*, 1982), it might also be helpful in defining resource requirements for certain species. Tilman *et al.* (1982) showed that species can form a stable population only if they have enough limiting resource for their specific growth, such that mortality is balanced by reproduction. This minimal resource concentration was termed R^* and the best competitor should be the species with the lowest requirement for the limiting resource (lowest R^*). For light, this theory has been modified, such that competitive interactions are mediated by self-shading whereby a species with the highest tolerance to self-shading (lowest critical light requirement I^*) survives in competition for light (Huisman and Weissing, 1994). In Tilman's terminology, the onset of the spring phytoplankton bloom is triggered when light availability becomes larger than I^* for light during spring, when light is a limiting resource for most of the phytoplankton species, but mortality through grazing is low. Such conditions favour low light-adapted species with high chlorophyll concentration as shown in the modelling study by Polimene *et al.* (2014). These authors suggest that pigment-mediated photoadaptation plays a primary role in shaping phytoplankton communities during the winter–spring transition.

Based on this background, we propose that the onset of the spring phytoplankton bloom depends on both allogenic factors (water column mixing, temperature, grazing by zooplankton, etc.) and autogenic factors (species physiology and traits, life history, etc.). Both allogenic and autogenic factors affect the balance between reproduction and mortality, allogenic factors being additionally responsible for resource supply. We hypothesize that the match of environmental change at the winter–spring transition and an optimal trait combination of the phytoplankton community are required to allow rapid phytoplankton growth and bloom formation.

The role of hydrodynamics

Hydrodynamic flow patterns in the oceans play a pivotal role for the formation of plankton blooms. While horizontal flow patterns like eddies, fronts, and jets are responsible for the redistribution of nutrients and plankton on intermediate spatial scales (Abraham, 1998; Martin, 2003; Tél *et al.*, 2005), vertical flows often account for turbulent mixing on small spatial scales (Mann and Lazier, 1991; Kiørboe, 1993; Denman and Gargett, 1995; Prairie *et al.*, 2012). The vertical flow patterns are approximately one order of magnitude smaller in strength than the horizontal ones. The structure of hydrodynamic flows on all scales leads to an incomplete mixing of the water column which has a large impact on plankton communities.

Vertical flows

Depending on their density compared with the density of water, plankton cells rise or sink. Turbulent diffusion resolving small-scale turbulence interacts with the sinking motion and influences strongly the vertical distribution of phytoplankton. Sverdrup's critical depth hypothesis (Sverdrup, 1953) focuses on light-dependent growth and does not account for the implications of sinking and turbulent diffusion. In contrast, the critical turbulence hypothesis by Huisman *et al.* (1999a, b, 2002) takes the interplay between light-dependent growth and turbulent diffusion into account. They showed that the critical depth depends on the turbulence level. On the other hand, each species possesses a critical turbulence level at which growth rates exceed the vertical mixing rate, leading to a phytoplankton bloom independently of the critical depth. Since critical depth and critical turbulence are independent

phenomena, one can expect that different phytoplankton communities favour those different strategies leading to different species compositions depending on the strength of turbulent mixing. Whereas low turbulence conditions favour buoyant phytoplankton species, well-mixed waters benefit species with low light requirement. Huisman *et al.* (1999b) assumed a homogeneous turbulent diffusion across the whole water column, whereas more recent studies show how a depth-dependent turbulent diffusion would influence the location of the chlorophyll maximum (Jäger *et al.*, 2010; Ryabov *et al.*, 2010; Peeters *et al.*, 2013). To estimate the impact of turbulent mixing in more detail one has to take its depth dependence into account, instead of relying on simple two-layer models. Moreover, active movement of plankton organisms can also be important (Mellard *et al.*, 2012).

Horizontal flows

Looking at the horizontal mixing, the situation can be quite different with respect to the time-scales involved. Horizontal transport is much faster than the time needed for plankton growth. Therefore, redistribution of nutrients due to horizontal transport would not be able to have a visible effect in shaping plankton communities. However, there exist mesoscale hydrodynamic structures (Lagrangian coherent structures) of size of about 10–100 km in the ocean, which have a lifetime of several days to weeks. Such long-lived structures like eddies and fronts can have an important influence on the growth of plankton, since close to these structures biological time-scales of growth become comparable to the time-scale of the flow. As a result, stirring and mixing are essential determinants of plankton patterns occurring in the ocean (Abraham, 1998). Particularly, vortices in the flow can act as incubators for plankton growth giving rise to plankton blooms inside vortices. The emergence of the plankton blooms within mesoscale eddies can occur due to two different mechanisms. They can entrain nutrient-rich waters (i) from upwelling events close to the coast and transport them over long distances in the ocean or (ii) from deeper layers in the open ocean by rotation. In both cases, the transport barriers, which are formed around the eddies, decrease substantially the exchange of water masses between inside and outside. Owing to this confinement of the plankton, “hot spots” of their growth are maintained for a rather long time (Martin *et al.*, 2002; Sandulescu *et al.*, 2008; d’Ovidio *et al.*, 2013). Other structures like fronts and jets also play an important role in the formation of plankton blooms (López *et al.*, 2001; Hernández-García and López, 2004; Taylor and Ferrari, 2011; Levy *et al.*, 2012).

The heterogeneous distribution of nutrients mediated by mesoscale hydrodynamic structures can not only give rise to particular mechanisms of the formation of plankton blooms, but can also induce different species dominance patterns and hence different plankton communities across the ocean (Bastine and Feudel, 2010; d’Ovidio *et al.*, 2010). Eddies typically persist for weeks, but may in some instances persist for several months (Kang and Curchitser, 2013). Therefore, eddies may strongly influence the development of different communities. In fact, incomplete mixing can promote the coexistence of species (Bracco *et al.*, 2000; Scheuring *et al.*, 2000, 2003) and can be considered as one possible solution of the paradox of plankton (Hutchinson, 1961).

The role of solar irradiance

Besides temporal and spatial changes in mixing processes, during winter-spring transition phytoplankton experience rapid changes in solar irradiance (in intensity, as well as spectral

characteristic) caused by changing solar angle and meteorological conditions (e.g. cloud cover). The light spectrum within the pelagic environment changes temporarily on a diel rhythm following the daily spectral shifts of light entering a water column and spatially by selective absorption of light (specific wavelength) with water depth. Phytoplankton responds to mixing processes and changing irradiance by varying the amounts and proportions of photosynthetic pigments, enzymatic activities, and cell volumes (Barlow *et al.*, 2013). These adjustments are species-specific. Some species are best adapted to high or low light intensities, while others are more competitive under well-mixed conditions (Strzepek and Harrison, 2004). Hickman *et al.* (2009) demonstrated that chromatic adaptations along with cell size markedly contribute to the balance of growth and loss rates for phytoplankton taxa and determine their distribution along light and nutrient gradients.

At high latitudes, daylight is considerable longer during summer than in winter (Kirk, 1994) and the lower solar angle in winter results in higher reflectance from the water surface (Runcie and Riddle, 2006). Low light conditions in winter strongly favour large diatoms which have high requirement for nutrients, especially silicate, but are good competitors for light (low I^* for light). Dramatically changing light conditions on the onset of stratification in spring favour fast-growing diatoms adapted to variable light, which can form the spring phytoplankton bloom (Widdicombe *et al.*, 2010; Polimene *et al.*, 2014). The low light-adapted species still significantly contribute to the bloom biomass because of their size and high chlorophyll content. At lower latitudes, changes in solar irradiance are less seasonal and the ecosystem is limited by nutrients and grazing rather than by light (Siegel *et al.*, 2002). High light availability allows phytoplankton to reach relatively high biomass even in winter (Moustaka-Gouni *et al.*, 2014). Thus, phytoplankton traits related to nutrient uptake (and nitrogen fixation) and grazing resistance (e.g. toxin production) might be more important in lower latitudes than in irradiance-related traits.

The role of phytoplankton traits

Recently, the trait-based approach has been successfully used in phytoplankton ecology, mainly to model community structure in response to global change (Litchman *et al.*, 2012). A characterization of functional traits (growth rate, cell size, and composition of photosynthetic pigments) can help in predicting what group of species is likely to dominate the bloom (Margalef, 1978). Using information on traits to parameterize population dynamic models, it is possible to predict which species can coexist under which environmental conditions (Litchman and Klausmeier, 2008; Edwards *et al.*, 2012; Litchman *et al.*, 2012). However, it should be kept in mind that most phytoplankton traits (growth rate, cell size, and nitrogen uptake kinetics) are plastic to some extent and depend on physical factors like temperature and irradiance (Eppley, 1972).

At any time and location, there will be a limited number of species with optimal traits (well adapted to low light–high turbulence conditions and characterized by a high growth rate) that can form the spring phytoplankton bloom. Here, to better understand the role of traits (in particular growth rates and photoadaptation), we use data on natural marine phytoplankton communities from an indoor mesocosm experiment which addressed the impact of warming and mixing depth on the spring phytoplankton bloom [for details, see Lewandowska and Sommer (2010)].

Selection for high growth rates

We assume that the spring phytoplankton bloom is a rapid event which selects for fast growing species. Slow growing species do not multiply fast enough to exceed losses (grazing and sinking) and therefore they cannot rapidly increase their biomass.

Figure 1a represents maximum observed growth rates of phytoplankton species from the Baltic Sea under light-limiting conditions (~ 6 mol photons $\text{m}^{-2} \text{d}^{-1}$) during winter–spring transition (16th February–6th April 2008). Phytoplankton biomass peaked around 4th March and was dominated by species having growth rates at least two times higher than the average community. Emphasizing the role of species-specific traits, community response depended on those species (Figure 1b).

If such fast growing species are absent, a spring bloom might not occur despite favourable hydrodynamic conditions. There already is ample evidence of this: warming and wind changes altered phytoplankton community composition and lead to disappearance of the typical spring diatom bloom in Narragansett Bay (Nixon and Fulweiler, 2009), Bahia Blanca Estuary (Guinder *et al.*, 2010), Mediterranean Sea (Goffart *et al.*, 2002), and coccolithophorid bloom in the Western English Channel (Garcia-Soto *et al.*, 2011). Always, the abundance of a usually dominant species dramatically decreased and the remaining species were not able to form a bloom.

Selection for low light adaptations

We propose that the occurrence of the spring phytoplankton bloom depends not only on stratification onset and mixed layer depth, but also on the balance of available resources in concert with phytoplankton community composition. The initiation of the bloom is determined by the light dose which has to be sufficient for the fast-growing species with the lowest I^* for light. A bloom cannot start without good competitors for light and species with high growth rates. These conclusions place a major emphasis on the role of overwintering for the spring phytoplankton bloom as well as the match between stratification- and mixing-mediated resource supply and phytoplankton community structure. In winter, when light is a limiting factor for most of the phytoplankton species, low light-adapted species with high cellular chlorophyll concentrations become dominant, followed by fast-growing species adapted to variable light conditions (Widdicombe *et al.*, 2010). Experiments on phytoplankton monocultures converge on the conclusion that cellular chlorophyll concentrations increase with low irradiances (maximizing photon capture), but decrease with increasing light availability (Falkowski and Owens, 1980; Iriarte and Purdie, 1993; Dubinsky and Stambler, 2009)—a pattern also reflected in our sample dataset on natural phytoplankton community (Lewandowska and Sommer, 2010; Figure 2). The bloom of these species is possible, because mortality (mainly via grazing) is still low in relation to reproduction rates, whereas with the seasonal increase of zooplankton biomass, traits such as the resistance to grazing become more important.

Diatoms typically have high cellular chlorophyll concentrations and often dominate spring phytoplankton blooms at temperate latitudes. In our example datasets, diatoms dominating the bloom (*Skeletonema*, *Thalassiosira*, and *Chaetoceros*) had high growth rates under low light conditions (Figure 3a). In contrast, picoplankton with low tolerance to limiting light increased growth rates with increased light (Figure 3a). Since they possibly also suffered from high losses to heterotrophic protists, they did not achieve high abundances during the spring bloom (cf. Figure 1b). Similar examples of

growth-irradiance relationships were presented for bloom forming haptophyte species isolated from the Bay of Biscay (Seoane *et al.*, 2009; Figure 3b), which in contrast to diatoms form blooms under high light conditions.

Efficient use of light spectrum

Rapid changes in solar irradiance, mixing depth, and turbidity during the winter–spring transition affect spectral attenuation coefficients of seawater. Increasing self-shading by growing phytoplankton further alters the underwater light spectrum, because available light is partitioned by phytoplankton with different pigment compositions. Consequently, the underwater light spectrum substantially changes selecting for different phytoplankton groups. Therefore, besides general light requirement and specific growth rate, the pigment composition can be a basic trait shaping the phytoplankton community during the spring bloom (Polimene *et al.*, 2014). Pigment composition determines not only adaptation to low or high light conditions, but also the light use efficiency across the wavelength spectrum and thereby the “spectral niche” used. Besides chlorophyll, xanthophyll pigments play a pivotal role in phytoplankton physiology, especially with respect to photoacclimation. They are involved in both light harvesting (acting as antenna pigments) and photoprotection mechanisms being an indicator of photoadaptation (Meyer *et al.*, 2000; Polimene *et al.*, 2014). Some phytoplankton species can regulate which parts of the spectrum they utilize by adjusting their pigment composition, depending on the availability of different wavelengths of light (Ting *et al.*, 2002; Stomp *et al.*, 2004). Therefore, phytoplankton community structure during winter–spring transition might not only depend on species-specific growth rates, but also on phytoplankton traits related to pigment composition. Specific light absorption by phytoplankton species should shift the competitive advantage towards species being able to use the remaining part of the light spectrum, which however has rarely been assessed during spring phytoplankton blooms. Wall and Briand (1979) showed in a field experiment that long wavelength radiation increased the relative proportion of cyanobacteria and diatoms and reduced the proportion of dinoflagellates. Thus, cyanobacteria and diatoms might have an advantage in the upper part of the water column, where the red wavelengths are mostly confined, in contrast to dinoflagellates, which should prefer lower parts of the water column.

Phytoplankton seasonal succession

A trait-based approach might not only help explaining the occurrence of the spring bloom, but inform our understanding of phytoplankton seasonal succession in general. Later in the season, increased zooplankton grazing rates select for different sets of traits, including grazing resistance, competition for limiting mineral nutrients, and efficient utilization of nutrient pulses induced by storms, upwelling, and turbulent mixing. It has been argued that much of the variation in aggregated phytoplankton biomass and cell size structure can be organized along turbulence and nutrient supply axes (Cullen *et al.*, 2002). Recently, Lewandowska *et al.* (2014) related seasonal differences in plankton community composition to nutrient supply, with cell size and grazing resistance as emerging important traits. More general, a trait-based approach can also serve as a mechanistic underpinning of the—recently revised—PEG-model on plankton succession (Sommer *et al.*, 2012).

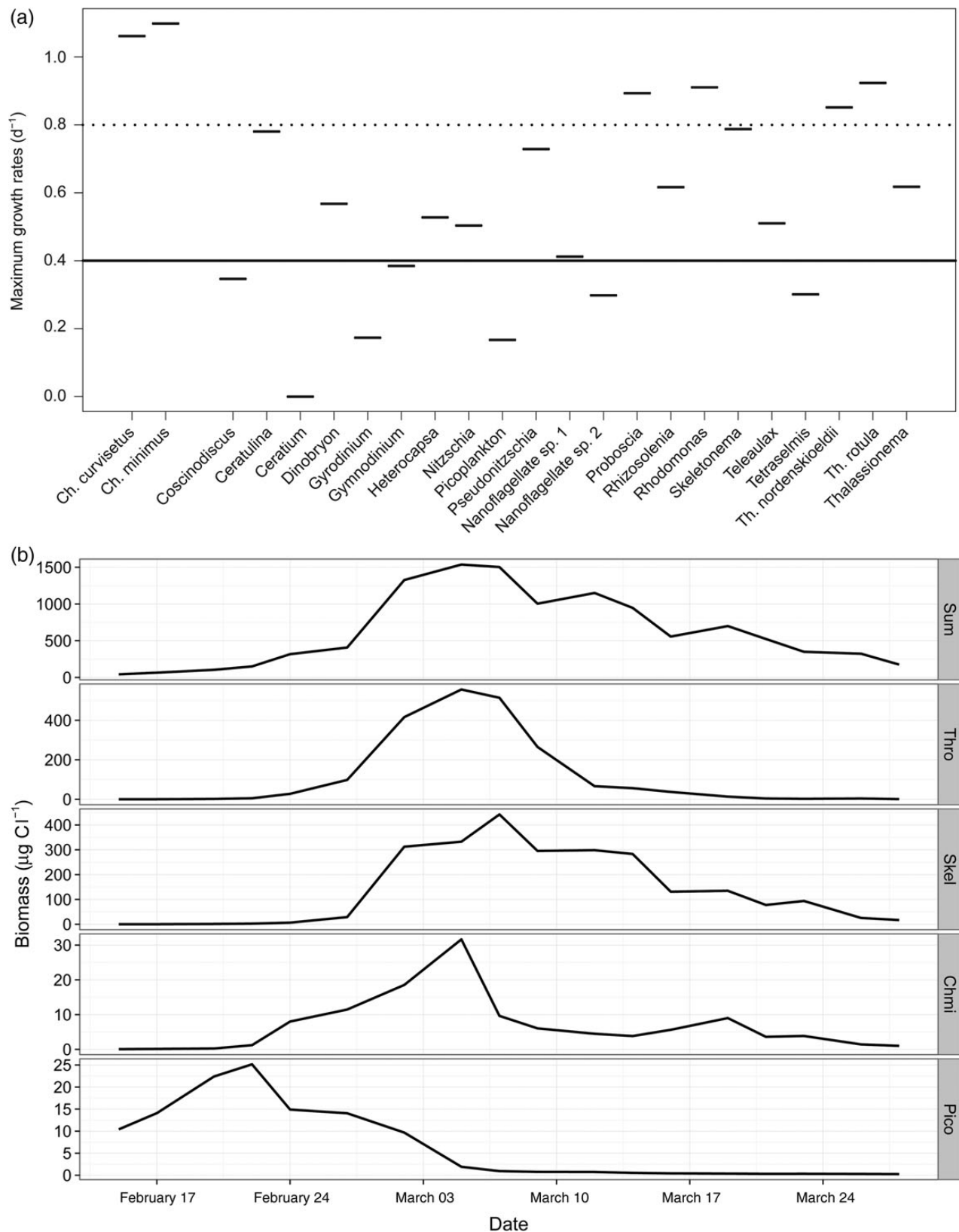


Figure 1. (a) Maximum growth rates of phytoplankton species under limited light conditions during winter–spring transition. The maximum growth rate of the whole community is represented by the solid line, and dashed line represents a threshold line: two times the maximum community growth rate. Species above or close to the threshold line are able to form the bloom. (b) Time course of phytoplankton species. Good competitors show high synchrony with the total community biomass (data source: [Lewandowska and Sommer 2010](#)). Sum, total phytoplankton biomass; Thro, *Thalassiosira rotula*; Skel, *Skeletonema costatum*; Chmi, *Chaetoceros minimum*; Pico, picoplankton.

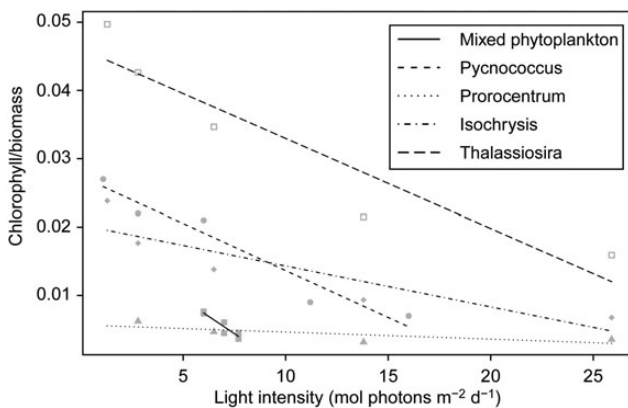


Figure 2. Impact of light intensity on cellular chlorophyll content. Data from Iriarte and Purdie (1993), Dubinsky and Stambler (2009), and Lewandowska and Sommer (2010).

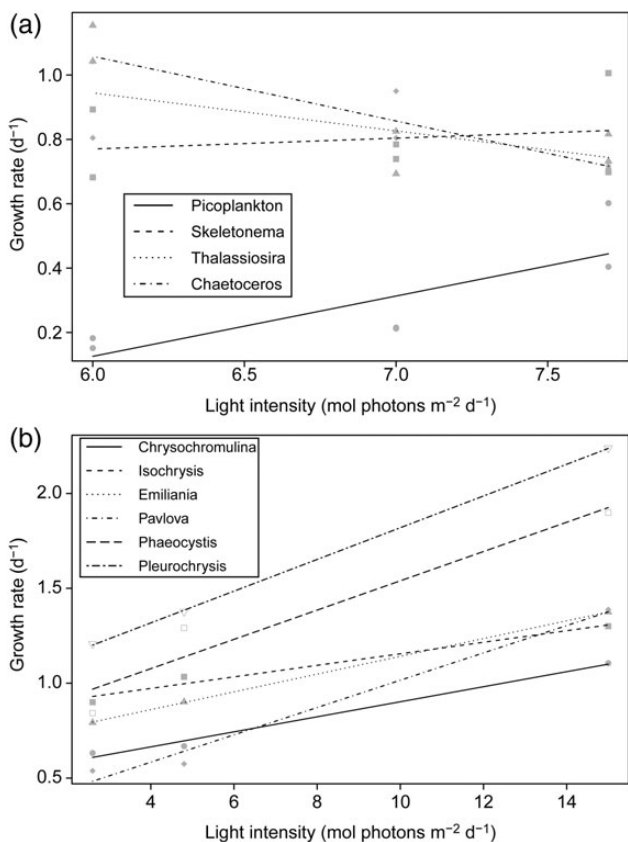


Figure 3. Impact of light intensity on maximum growth rates of selected key species in the natural Baltic Sea community (a) and bloom forming haptophyte species isolated from the Bay of Biscay (b). The less steep (or more negative) the slope, the better competitor for light. Data from Seoane *et al.* (2009), and Lewandowska and Sommer (2010).

Summary

The critical depth hypothesis has been used to explain the occurrence of the spring phytoplankton bloom for decades and is still widely accepted despite ongoing criticisms and alterations. Extending ideas presented by Sverdrup (1953), Huisman *et al.*

(1999a), and Behrenfeld (2010), we propose a hypothesis that each phytoplankton species has its own specific critical depth (SCD) which depends on its set of traits. A species with the most favoured traits and the highest SCD in given location and time will growth first and can form a bloom. The bloom will not occur if there is no species with set of traits matching environmental requirements as it happens in the high nutrients–low chlorophyll ocean regions which are lacking iron. The basic traits for detrainment blooms such as classical spring bloom in temperate latitudes are high growth rates and photoadaptation to low irradiance level in the red light spectrum. For other bloom types (e.g. upwelling blooms), other traits such as nutrient kinetics and grazing resistance might be more important.

Future directions

We do not abandon Sverdrup's hypothesis, but rather suggest that it can be made more robust by including information on hydrodynamic and functional traits of phytoplankton. Observational studies provide one way forward assessing the variation in phytoplankton bloom phenology in response to changing environment, but they do not necessarily address the effect of species identity in bloom formation. We need a new generation of experiments that target how community composition influences the dynamics of phytoplankton blooms. To better understand the role of phytoplankton traits in bloom formation, it will be useful to combine laboratory experiments investigating species-specific traits under controlled conditions with large field experiments using natural phytoplankton communities and manipulating temperature, light availability (intensity and spectral composition), or grazing. One possible approach is to use mesocosms that differ in their hydrodynamic and optical properties and contain natural plankton in combination with laboratory experiments that assess species-specific traits. Such multiscale experimental approaches provide the information needed to include phytoplankton traits and interspecific interactions between species into models predicting phytoplankton blooms. These experiments should also help in understanding mechanisms of species coexistence in fluctuating environment. Including both variability in resource supply and competition mechanisms, it should be possible to predict not only the start and magnitude of the phytoplankton bloom, but also which group of species will dominate the bloom. Such an approach, linking dynamic ecosystem models and experiments is urgently needed if we are to accurately understand and predict changes in marine phytoplankton.

Acknowledgements

The authors thank Daniel Boyce and two anonymous reviewers for their thoughtful comments on the previous versions of the manuscript.

References

- Abraham, E. R. 1998. The generation of plankton patchiness by turbulent stirring. *Nature*, 391: 577–580.
- Atkins, W. R. G. 2009. The phosphate content of Sea Water in relation to the growth of the Algal Plankton. Part III. *Journal of the Marine Biological Association of the United Kingdom*, 14: 447.
- Barlow, R., Lamont, T., Britz, K., and Sessions, H. 2013. Mechanisms of phytoplankton adaptation to environmental variability in a shelf ecosystem. *Estuarine, Coastal and Shelf Science*, 133: 45–57.

- Bastine, D., and Feudel, U. 2010. Inhomogeneous dominance patterns of competing phytoplankton groups in the wake of an island. *Nonlinear Processes in Geophysics*, 17: 715–731.
- Behrenfeld, M. J. 2010. Abandoning Sverdrup's critical depth hypothesis on phytoplankton blooms. *Ecology*, 91: 977–989.
- Bracco, A., Provenzale, A., and Scheuring, I. 2000. Mesoscale vortices and the paradox of the plankton. *Proceedings of the Royal Society of London, Series B: Biological Sciences*, 267: 1795–1800.
- Chiswell, S. 2011. Annual cycles and spring blooms in phytoplankton: don't abandon Sverdrup completely. *Marine Ecology Progress Series*, 443: 39–50.
- Cullen, J. J., Franks, P. S., Karl, D. M., and Longhurst, A. 2002. Physical influences on marine ecosystem dynamics. *In The Sea*, pp. 297–336. Ed. by A. Robinson, J. McCarthy, and B. J. Rothschild. John Wiley & Sons, New York.
- d'Ovidio, F., De Monte, S., Alvain, S., Dandonneau, Y., and Lévy, M. 2010. Fluid dynamical niches of phytoplankton types. *Proceedings of the National Academy of Sciences of the United States of America*, 107: 18366–18370.
- d'Ovidio, F., De Monte, S., Penna, A. D., Cotté, C., and Guinet, C. 2013. Ecological implications of eddy retention in the open ocean: a Lagrangian approach. *Journal of Physics A: Mathematical and Theoretical*, 46: 254023.
- Denman, K. L., and Gargett, A. E. 1995. Biological-physical interactions in the upper ocean: the role of vertical and small scale transport processes. *Annual Review of Fluid Mechanics*, 27: 225–256.
- Dubinsky, Z., and Stambler, N. 2009. Photoacclimation processes in phytoplankton: mechanisms, consequences, and applications. *Aquatic Microbial Ecology*, 56: 163–176.
- Edwards, K. F., Thomas, M. K., Klausmeier, C. A., and Litchman, E. 2012. Allometric scaling and taxonomic variation in nutrient utilization traits and maximum growth rate of phytoplankton. *Limnology and Oceanography*, 57: 554–566.
- Edwards, M., and Richardson, A. J. 2004. Impact of climate change on marine pelagic phenology and trophic mismatch. *Nature*, 430: 881–884.
- Eppley, R. W. 1972. Temperature and phytoplankton growth in the sea. *Fishery Bulletin*, 4: 1063–1085.
- Falkowski, P., and Owens, T. 1980. Light—shade adaptation. Two strategies in marine phytoplankton. *Plant Physiology*, 66: 592–595.
- Fischer, A., Moberg, E., Alexander, E., Brownlee, K., Hunter-Cevera, K., Pitz, K., Rosengard, S., et al. 2014. Sixty years of Sverdrup: A retrospective of progress in the study of phytoplankton blooms. *Oceanography*, 27: 222–235.
- García-Soto, C., Ferndndez, E., Pingree, R. D., and Harbour, D. S. 2011. Evolution and structure of a shelf coccolithophore bloom in the Western English Channel. *Journal of Plankton Research*, 17: 2011–2036.
- Goffart, A., Hecq, J., and Legendre, L. 2002. Changes in the development of the winter-spring phytoplankton bloom in the Bay of Calvi (NW Mediterranean) over the last two decades: a response to changing climate? *Marine Ecology Progress Series*, 236: 45–60.
- Gran, H., and Braarud, T. 1935. A quantitative study of the phytoplankton in the Bay of Fundy and the Gulf of Maine (including Observations on Hydrography, Chemistr5r and Turbiditfi). *Journal of the Biological Board of Canada*, 1: 279–467.
- Guinder, V., Popovich, C., Molinero, J., and Perillo, G. 2010. Long-term changes in phytoplankton phenology and community structure in the Bahía Blanca Estuary, Argentina. *Marine Biology*, 157: 2703–2716.
- Hernández-García, E., and López, C. 2004. Sustained plankton blooms under open chaotic flows. *Ecological Complexity*, 1: 253–259.
- Hickman, A. E., Holligan, P. M., Moore, C. M., Sharples, J., Krivtsov, V., and Palmer, M. R. 2009. Distribution and chromatic adaptation of phytoplankton within a shelf sea thermocline. *Limnology and Oceanography*, 54: 525–536.
- Huisman, J., Arrayas, M., Ebert, U., and Sommeijer, B. 2002. How do sinking phytoplankton species manage to persist? *American Naturalist*, 159: 245–254.
- Huisman, J., van Oostveen, P., and Weissing, F. 1999a. Critical depth and critical turbulence: two different mechanisms for the development of phytoplankton blooms. *Limnology and Oceanography*, 44: 1781–1787.
- Huisman, J., van Oostveen, P., and Weissing, F. 1999b. Species dynamics in phytoplankton blooms: incomplete mixing and competition for light. *American Naturalist*, 154: 46–68.
- Huisman, J., and Weissing, F. 1994. Light-limited growth and competition for light in well-mixed aquatic environments: an elementary model. *Ecology*, 75: 507–520.
- Hutchinson, G. E. 1961. The paradox of the plankton. *American Naturalist*, 95: 137–145.
- Iriarte, A., and Purdie, D. A. 1993. Photosynthesis and growth response of the oceanic picoplankter *Pycnococcus provasoli* Guillard (clone $\Omega 48-23$) (Chlorophyta) to variations in irradiance, photoperiod and temperature. *Journal of Experimental Marine Biology and Ecology*, 168: 239–257.
- Jäger, C. G., Diehl, S., and Emans, M. 2010. Physical determinants of phytoplankton production, algal stoichiometry, and vertical nutrient fluxes. *American Naturalist*, 175: E91–E104.
- Kang, D., and Curchitser, E. N. 2013. Gulf Stream eddy characteristics in a high-resolution ocean model. *Journal of Geophysical Research: Oceans*, 118: 4474–4487.
- Kjørboe, T. 1993. Turbulence, phytoplankton cell size, and the structure of pelagic food webs. *Advances in Marine Biology*, 29:1–72.
- Kirk, J. T. O. 1994. Light and photosynthesis in aquatic ecosystems. Cambridge university press, Cambridge.
- Levy, M., Ferrari, R., Franks, P. J., Martin, A. P., and Riviere, P. 2012. Bringing physics to life at the submesoscale. *Geophysical Research Letters*, 39, L14602.
- Lewandowska, A., and Sommer, U. 2010. Climate change and the spring bloom: a mesocosm study on the influence of light and temperature on phytoplankton and mesozooplankton. *Marine Ecology Progress Series*, 405: 101–111.
- Lewandowska, A. M., Boyce, D. G., Hofmann, M., Matthiessen, B., Sommer, U., and Worm, B. 2014. Effects of sea surface warming on marine plankton. *Ecology Letters*, 17: 614–623.
- Litchman, E., Edwards, K., Klausmeier, C., and Thomas, M. 2012. Phytoplankton niches, traits and eco-evolutionary responses to global environmental change. *Marine Ecology Progress Series*, 470: 235–248.
- Litchman, E., and Klausmeier, C. A. 2008. Trait-based community ecology of phytoplankton. *Annual Review of Ecology, Evolution, and Systematics*, 39: 615–639.
- López, C., Neufeld, Z., Hernández-García, E., and Haynes, P. H. 2001. Chaotic advection of reacting substances: Plankton dynamics on a meandering jet. *Physics and Chemistry of the Earth, Part B: Hydrology, Oceans and Atmosphere*, 26: 313–317.
- Mann, K., and Lazier, J. 1991. Dynamics of marine ecosystems: biological-physical interactions in the oceans. Blackwell Scientific Publications, Boston.
- Margalef, R. 1978. Life-forms of phytoplankton as survival alternatives in an unstable environment. *Oceanologica Acta*, 1: 493–509.
- Martin, A. P. 2003. Phytoplankton patchiness: the role of lateral stirring and mixing. *Progress in Oceanography*, 57: 125–174.
- Martin, A. P., Richards, K. J., Bracco, A., and Provenzal, A. 2002. Patchy productivity in the open ocean. *Global Biogeochemical Cycles*, 16: 9-1–9-9.
- Mellard, J., Yoshiyama, K., Klausmeier, C. A., and Litchman, E. 2012. Experimental test of phytoplankton competition for nutrients and light in poorly mixed water columns. *Ecological Monographs*, 82: 239–256.

- Meyer, A., Tackx, M., and Daro, N. 2000. Xanthophyll cycling in *Phaeocystis globosa* and *Thalassiosira* sp.: a possible mechanism for species succession. *Journal of Sea Research*, 43: 373–384.
- Moustaka-Gouni, M., Michaloudi, E., and Sommer, U. 2014. Modifying the PEG model for Mediterranean lakes—no biological winter and strong fish predation. *Freshwater Biology*, 59: 1136–1144.
- Nixon, S., and Fulweiler, R. 2009. The impact of changing climate on phenology, productivity, and benthic–pelagic coupling in Narragansett Bay. *Estuarine, Coastal and Shelf Science*, 82: 1–18.
- Peeters, F., Kerimoglu, O., and Straile, D. 2013. Implications of seasonal mixing for phytoplankton production and bloom development. *Theoretical Ecology*, 6: 115–129.
- Platt, T., Fuentes-Yaco, C., and Frank, K. T. 2003. Spring algal bloom and larval fish survival. *Nature*, 423: 398–399.
- Polimene, L., Brunet, C., Butenschon, M., Martinez-Vicente, V., Widdicombe, C., Torres, R., and Allen, J. I. 2014. Modelling a light-driven phytoplankton succession. *Journal of Plankton Research*, 36: 214–229.
- Prairie, J. C., Sutherland, K. R., Nickols, K. J., and Kaltenberg, A. M. 2012. Biophysical interactions in the plankton: A cross-scale review. *Limnology and Oceanography: Fluids and Environments*, 2: 121–145.
- Riley, G. 1942. The relationship of vertical turbulence and spring diatom flowerings. *Journal of Marine Research*, 5: 67–87.
- Robinson, C., Serret, P., Tilstone, G., Teira, E., Zubkov, M. V., Rees, A. P., and Woodward, E. M. S. 2002. Plankton respiration in the Eastern Atlantic Ocean. *Deep Sea Research Part I: Oceanographic Research Papers*, 49: 787–813.
- Runcie, J. W., and Riddle, M. J. 2006. Photosynthesis of marine macroalgae in ice-covered and ice-free environments in East Antarctica. *European Journal of Phycology*, 41: 223–233.
- Ryabov, A. B., Rudolf, L., and Blasius, B. 2010. Vertical distribution and composition of phytoplankton under the influence of an upper mixed layer. *Journal of Theoretical Biology*, 263: 120–133.
- Sandulescu, M., Lopez, C., Hernandez-Garcia, E., and Feudel, U. 2008. Plankton blooms in vortices: The role of biological and hydrodynamic time scales. *Nonlinear Processes in Geophysics*, 14: 443–454.
- Scheuring, I., Károlyi, G., Pentek, A., Tél, T., and Toroczka, Z. 2000. A model for resolving the plankton paradox: coexistence in open flows. *Freshwater Biology*, 45: 123–132.
- Scheuring, I., Károlyi, G., Toroczka, Z., Tél, T., and Péntek, Á. 2003. Competing populations in flows with chaotic mixing. *Theoretical Population Biology*, 63: 77–90.
- Seoane, S., Zapata, M., and Orive, E. 2009. Growth rates and pigment patterns of haptophytes isolated from estuarine waters. *Journal of Sea Research*, 62: 286–294.
- Siegel, D. A., Maritorena, S., Nelson, N. B., Hansell, D. A., and Lorenzi-Kayser, M. 2002. Global distribution and dynamics of colored dissolved and detrital organic materials. *Journal of Geophysical Research: Oceans*, 107: 21-1–21-14.
- Smetacek, V., and Passow, U. 1990. Spring bloom initiation and Sverdrup's critical-depth model. *Limnology and Oceanography*, 35: 228–234.
- Sommer, U., Adrian, R., De Senerpont Domis, L., Elser, J. J., Gaedke, U., Ibelings, B., Jeppesen, E., *et al.* 2012. Beyond the Plankton Ecology Group (PEG) model: Mechanisms driving plankton succession. *Annual Review of Ecology, Evolution, and Systematics*, 43: 429–448.
- Stomp, M., Huisman, J., De Jongh, F., Veraart, A. J., Gerla, D., Rijkeboer, M., Ibelings, B. W., *et al.* 2004. Adaptive divergence in pigment composition promotes phytoplankton biodiversity. *Nature*, 432: 104–107.
- Strzepek, R. F., and Harrison, P. J. 2004. Photosynthetic architecture differs in coastal and oceanic diatoms. *Nature*, 403: 689–692.
- Sverdrup, H. U. 1953. On conditions for the vernal blooming of phytoplankton. *Journal du Conseil International pour l'Exploration de la Mer*, 18: 287–295.
- Taylor, J. R., and Ferrari, R. 2011. Shutdown of turbulent convection as a new criterion for the onset of spring phytoplankton blooms. *Limnology and Oceanography*, 56: 2293–2307.
- Tél, T., de Moura, A., Grebogi, C., and Károlyi, G. 2005. Chemical and biological activity in open flows: a dynamical system approach. *Physics Reports*, 413: 91–196.
- Tilman, D., Kilham, S. S., and Kilham, P. 1982. Phytoplankton community ecology: The role of limiting nutrients. *Annual Review of Ecology and Systematics*, 13: 349–372.
- Ting, C., Rocap, G., King, J., and Chisholm, S. 2002. Cyanobacterial photosynthesis in the oceans: the origins and significance of divergent light-harvesting strategies. *Trends in Microbiology*, 10: 134–142.
- Townsend, D. W., Keller, M. D., Sieracki, M. E., and Ackleson, S. G. 1992. Spring phytoplankton blooms in the absence of vertical water column stratification. *Nature*, 360: 59–62.
- Wall, D., and Briand, F. 1979. Response of lake phytoplankton communities to in situ manipulations of light intensity and colour. *Journal of Plankton Research*, 1: 103–112.
- Widdicombe, C. E., Eloire, D., Harbour, D., Harris, R. P., and Somerfield, P. J. 2010. Long-term phytoplankton community dynamics in the Western English Channel. *Journal of Plankton Research*, 32: 643–655.
- Williams, P. J. 1998. The balance of plankton respiration and photosynthesis in the open oceans. *Nature*, 394: 55–57.

Handling editor: Rubao Ji



Contribution to the Themed Section: 'Revisiting Sverdrup's Critical Depth Hypothesis' Food for Thought

Exploration of the critical depth hypothesis with a simple NPZ model

Marina Lévy*

Sorbonne Université (UPMC, Paris 6)/CNRS/UPMC/IRD/MNHN, Laboratoire d'Océanographie et du Climat (LOCEAN), Institut Pierre, Simon Laplace (IPSL), Paris Cedex 05 75252, France

*Corresponding author: e-mail: marina.levy@upmc.fr

Lévy, M. Exploration of the critical depth hypothesis with a simple NPZ model. – ICES Journal of Marine Science, 72: 1916–1925.

Received 15 September 2014; revised 7 January 2015; accepted 12 January 2015; advance access publication 16 February 2015.

The critical depth hypothesis (CDH) is a predictive criteria for the onset of phytoplankton blooms that comes from the steady-state analytical solution of a simple mathematical model for phytoplankton growth presented by Sverdrup in 1953. Sverdrup's phytoplankton-only model is very elementary compared with state-of-the-art ecosystem models whose numerical solution in a time-varying environment do not systematically conform to the CDH. To highlight which model ingredients make the bloom onset deviate from the CDH, the complexity of Sverdrup's model is incrementally increased, and the impact that each new level of complexity introduced is analysed. Complexity is added both to the ecosystem model and to the parameterization of physical forcing. In the most complete experiment, the model is a one-dimensional Nutrient-Phytoplankton-Zooplankton model that includes seasonally varying mixed layer depth and surface irradiance, light and nutrient limitation, variable grazing, self-shading, export, and remineralization. When complexity is added to the ecosystem model, it is found that the model solution only marginally deviates from the CDH. But when the physical forcing is also changed, the model solution can conform to two competing theories for the onset of phytoplankton blooms—the critical turbulence hypothesis and the disturbance recovery hypothesis. The key roles of three physical ingredients on the bloom onset are highlighted: the intensity of vertical mixing at the end of winter, the seasonal evolution of the mixed-layer depth from the previous summer, and the seasonal evolution of surface irradiance.

Keywords: bloom onset, critical depth, critical turbulence, disturbance recovery, NPZ model.

Introduction

More than 60 years ago, Sverdrup (1953) presented a simple, water column-based, mathematical model that tied together the roles of vertical mixing, light attenuation with depth and seasonally increasing light into a predictive criteria for the onset of the spring bloom. The critical depth hypothesis (CDH) is this model's solution. The CDH predicts that blooms start when the seasonal mixed-layer shoals above a critical depth (D_C), and offers a simple analytical expression for this depth.

In more recent years, observational evidence that biomass could start accumulating before restratification (Townsend *et al.*, 1994; Boss and Behrenfeld, 2010) led researchers to revisit the CDH. Two other hypotheses were subsequently proposed to explain winter, rather than spring, bloom onsets. The critical turbulence hypothesis (CTH) attributes winter blooms to physical drivers (Huisman *et al.*, 1999; Chiswell, 2011; Taylor and Ferrari, 2011; Brody and Lozier,

2014; Ferrari *et al.*, 2014) and states that, rather than a critical depth, there should exist a critical level of turbulence (parameterized by a turbulent diffusivity κ_c) below which blooms occur. The emphasis of the CTH is on the distinction between apparently mixed layers (i.e. where density is homogeneous on the vertical but the turbulence is not necessarily strong) and regions with active vertical mixing (active mixing layers, characterized by large values of turbulent diffusivity κ) (Brainerd and Gregg, 1995; Franks, 2015). Note that the CTH has also been described as the "stratification-onset model" (Chiswell, 2011). On the other hand, the disturbance recovery hypothesis (DRH) highlights the importance of grazing control on bloom dynamics (Evans and Parslow, 1985; Banse, 1994; Marra and Barber, 2005; Behrenfeld, 2010; Boss and Behrenfeld, 2010; Behrenfeld and Boss, 2014). In essence, the DRH posits that winter entrainment of plankton-free water dilutes plankton populations, leading to reduced grazer encounters, and consequently net growth in the integrated population.

Though Sverdrup did not pose it this way originally, his model can be understood in terms of a differential equation for the time evolution of phytoplankton concentration (P)

$$\partial_t P = (\mu - l)P + \partial_z(\kappa \partial_z P). \quad (1)$$

The parameters μ and l are the phytoplankton growth and loss rates, respectively. The last term accounts for vertical mixing, and $\kappa = \kappa(z)$ is the vertical mixing coefficient. Note that in this equation, transport processes other than vertical mixing are omitted and P is assumed to vary only with depth and time. Sverdrup solves this equation at steady-state, resulting in a necessary condition for the depth-integrated phytoplankton growth to exceed its losses. Importantly, Sverdrup makes a number of assumptions before solving this equation, among which are a constant loss rate l , and of a value of κ large enough to ensure homogeneous distribution of phytoplankton within the surface mixed layer. This last assumption allows him to circumvent the details of vertical mixing by focusing on integral properties in an homogeneous surface layer. Hence, by construction, Sverdrup's model solution does not account for variable grazing, or for low values of κ , and thus cannot reproduce the CTH or DRH.

Contemporary ecosystem models basically follow the foundation of Equation (1), but allow for more flexibility in the description of μ and l than Sverdrup's model. This flexibility is allowed by the consideration of additional state variables that feedback on P through their contribution to μ and l , such as resources (N) and predators (Z). Models vary in complexity in terms of the number of variables, as well as in their expressions for μ and l . Importantly, they are also embedded in a physical model, with explicit representation of vertical mixing.

Numerical solutions of these models do not always conform to the CDH. Using a Sverdrup-like one-variable (i.e. phytoplankton only) ecosystem model embedded in a high-resolution three-dimensional upper-ocean turbulence model, Taylor and Ferrari (2011) showed departure from the CDH when turbulent mixing was below a critical turbulence level, which supports the CTH. On the other hand, in a one-dimensional 15-variable ecosystem model for the western Subarctic Pacific, Yoshie *et al.* (2003) found an increase in the integrated phytoplankton biomass as the mixed layer deepened due to a decrease of the grazing pressure by dilution. A similar result was obtained for the Subarctic Atlantic with the more complex 24-variable Biogeochemical Element Cycling Community Climate System Model (Behrenfeld *et al.*, 2013). Along the same line, the 24-variable ecosystem model PISCES, in an idealized one-dimensional setup for the Southern Ocean (Llort *et al.*, 2015) also supported the DRH. Finally, other models, such as the four-variable ecosystem model embedded in a coarse-resolution ocean general circulation model used by Dutkiewicz *et al.* (2001) to simulate the subpolar North-Atlantic bloom onset, supported the CDH. The above studies, in aggregate, highlight that each of these seemingly competing spring bloom drivers may be achieved depending on the form of the model. However, the models are too different to identify how specific biological and physical factors influence bloom onset.

In this note, I examine the bloom onset problem with a one-dimensional Nutrient-Phytoplankton-Zooplankton (NPZ) model (Franks, 2002), forced by vertical mixing in a time-varying mixed layer. The NPZ model, with only three state variables, is one of the simplest ecosystem models. Yet this set-up, which allows for variable grazing and variable κ , is sufficiently complex to explore the CDH, CTH, and DRH in one framework. Using a unified framework

allows me to identify the model ingredients that make the bloom onset deviate from the CDH. I start from the simplest model of Sverdrup, and progressively add complexity. This enables me to explore the impact that each new level of complexity introduces in a series of incremental numerical experiments. Complexity is added both to the ecosystem model (number of state variables, formulation of μ and l) and to the parameterization of physical forcing (from a mixed layer at steady-state to a mixed layer following a full seasonal cycle, and from constant incident irradiance to seasonal irradiance). This illustrative set of experiments is far from exhaustive. The intention is to shed light on the important roles of both the physical forcing and model structure, as well as to bridge the gap between Sverdrup's model solution and the different solutions obtained with more sophisticated ecosystem models.

After recalling the details of Sverdrup's model and presenting the NPZ model, Sverdrup's model assumptions are relaxed one by one, thus progressively adding complexity in both the model and physical forcing. The most complete experiment is obtained with a time-variable 1D-NPZ model, which, unlike Sverdrup's model, accounts for time-variable self-shading, explicit grazing, nutrient and light limitation, variable vertical mixing, and time-variable mixed-layer depth. Model solutions are presented at each step of the process; the bloom onset is diagnosed as the time at which water column growth and losses come in balance.

Method

Sverdrup's model

Sverdrup's model is based on an earlier model proposed by Riley (1946). It considers that the phytoplankton growth rate μ is proportional to light I that the light-extinction coefficient k is constant and that the phytoplankton loss rate l is equal to a constant mortality rate m_p . Under these assumptions, μ and l in Equation (1) are

$$\mu = \alpha I, \quad (2)$$

$$l = m_p \quad (3)$$

with

$$I = I_0 e^{-kz}, \quad (4)$$

where I_0 is the fraction of surface irradiance usable for photosynthesis. Assuming that vertical mixing κ is strong enough to distribute the organisms evenly within a surface mixed layer allows one to integrate Equation (1) from the surface to the bottom ($D > 0$) of the mixed layer, resulting in the expression

$$\partial_t \bar{P} = \frac{\alpha I_0}{kD} (1 - e^{-kD}) \bar{P} - m_p \bar{P} \quad (5)$$

with

$$\bar{P} = \int_0^D P \, dz \quad (6)$$

the total phytoplankton biomass within the mixed layer. Setting $\partial_t \bar{P} = 0$ results in an equation for a critical mixed-layer depth D_C for which depth-integrated growth equals depth-integrated losses, i.e.

$$\frac{\alpha I_0}{kD_C} (1 - e^{-kD_C}) = m_p. \quad (7)$$

The value of D_C depends on the three model parameters α , m_p , and k , and on the surface irradiance I_0 . In Sverdrup's paper, the number

Table 1. Sverdrup's model parameters.

Parameter name	Symbol	Value	Unit
Phytoplankton growth rate per unit light	α	3.66×10^{-7}	$\text{s}^{-1} \text{W}^{-1} \text{m}^2$
Phytoplankton mortality rate	m_p	5.80×10^{-7}	s^{-1}
Light attenuation	k	0.05	m^{-1}
Surface irradiance	I_0	50	W m^{-2}
Compensation irradiance	I_C	1.58	W m^{-2}
Critical depth	D_C	270	m

of parameters is reduced by assuming that the compensation irradiance $I_C = m_p/\alpha$ is known, where I_C is defined as the irradiance at the depth for which $\mu(z) = l(z)$ (see Siegel *et al.*, 2002, for the evaluation of the compensation irradiance from ocean colour observations). We assign these parameters such that both k and I_C are close to the values proposed by Sverdrup in his paper (Table 1). Note that Sverdrup uses different values for k and we choose a value in the lower range, which leads to a critical depth of $D_C = 270$ m from Equation (7). Results with a larger value of k , leading to a shallower critical depth, will also be presented.

NPZ model

Complexity is added to Sverdrup's model by introducing two extra state variables, nutrients (N) and zooplankton (Z). In the context of the bloom onset, introducing Z enables the model to account for time-dependent phytoplankton losses, which is necessary to allow the emergence of a model solution that satisfies the DRH. The need to introduce N is not as straightforward since the bloom always appears during the winter-to-spring transition when nutrients are plentiful. However, as we will see, a complete description of the bloom requires one to integrate the model over the full seasonal cycle. Hence, the seasonal cycling of nutrients—essentially the entrainment between fall and winter followed by export and remineralization between spring and summer—must also be accounted for.

The phytoplankton and zooplankton equations follow the general form of Equation (1), and are given by

$$\partial_t P = (\mu_p - l_p)P + \partial_z(\kappa \partial_z P) \quad (8)$$

$$\partial_t Z = (\mu_z - l_z)Z + \partial_z(\kappa \partial_z Z) \quad (9)$$

with plankton growth and loss terms given by

$$\mu_p = \alpha K_i (1 - e^{-(I/K_i)}) \frac{N}{N + K_n} \quad (10)$$

$$l_p = m_p + g_z Z \quad (11)$$

$$\mu_z = g_z P \quad (12)$$

$$l_z = \tau_z + m_z Z + (1 - a_z)g_z P. \quad (13)$$

We note that the phytoplankton growth rate μ_p incorporates two limitation terms that were absent in Sverdrup's model and which vary between 0 and 1: light saturated growth ($1 - e^{-(I/K_i)}$) and nutrient limitation ($N/(N + K)$). Moreover, the phytoplankton loss rate l_p includes a term due to grazing $g_z Z$ which depends on the abundance of zooplankton. The zooplankton loss rate l_z includes excretion (τ_z), mortality ($m_z Z$) and non-assimilated grazing

Table 2. NPZ model parameters.

Parameter name	Symbol	Value	Unit
Phytoplankton growth rate per unit light	α	3.66×10^{-7}	$\text{s}^{-1} \text{W}^{-1} \text{m}^2$
Nutrient limitation half-saturation	K_n	0.7	mmol m^{-3}
Light limitation half-saturation	K_i	33.	W m^{-2}
Phytoplankton mortality rate	m_p	5.80×10^{-7}	s^{-1}
Background light attenuation	k_b	0.05/0.15	m^{-1}
light attenuation by phytoplankton	k_p	0.03	$\text{m}^{-1} \text{mmol}^{-1} \text{m}^3$
Zooplankton maximal grazing rate	g_z	9.26×10^{-6}	s^{-1}
Assimilated food fraction by zooplankton	a_z	0.7	
Zooplankton excretion rate	τ_z	5.80×10^{-7}	s^{-1}
Zooplankton mortality rate	m_z	2.31×10^{-6}	$\text{s}^{-1} \text{mmol}^{-1} \text{m}^3$
Export ratio	f_e	0.2	
Euphotic layer depth	z_b	150	m
Remineralization exponential decay	r	0.858	

$((1 - a_z)g_z P)$. Light is attenuated with depth as in Equation (4), but unlike in Sverdrup's model, the light attenuation coefficient depends on P ,

$$k = k_b + k_p P. \quad (14)$$

The nutrient pool is depleted by photosynthesis ($-\mu_p P$) and resupplied by the combined losses of phytoplankton and zooplankton after they are remineralized (R). There are no external sources of N . To implicitly account for the export of organic material out the euphotic layer by the sinking of particles, only a fraction $(1 - f_e)R$ of the remineralized material is locally resupplied to the nutrient pool; the rest of the remineralized material is vertically integrated ($f_e \int_0^H R dz$, with H the depth of the water column) and redistributed below the euphotic depth z_b , following the Martin curve $f(z)$ (Martin *et al.*, 1987). The resulting equation for N is

$$\partial_t N = -\mu_p P + (1 - f_e)R + \partial_z f \left(f_e \int_0^H R dz \right) + \partial_z(\kappa \partial_z N) \quad (15)$$

with

$$R = l_z Z + l_p P \quad (16)$$

and

$$f(z) = \min \left(1, \left(\frac{z}{z_b} \right)^{-r} \right), \quad f(H) = 0. \quad (17)$$

The NPZ model presented above is a common tool in oceanographic research, and has many variants (Franks, 2002). The functional forms of the growth and loss terms (Equations (10)–(13)) and model parameters (Table 2) used here come from of the more complex Locean Ocean Biogeochemical System for Ecosystem and Resources model, which has been calibrated against biogeochemical data of the Northeast Atlantic spring bloom (Karleskind *et al.*, 2011).

This NPZ model can be reduced to Sverdrup’s model by setting to zero the grazing rate g , the phytoplankton light attenuation k_p , the nutrient half-saturation constant K_n , and by replacing the light limitation term $(1 - e^{-I/K_i})$ with its first order expansion at low light, I/K_i . The consequences of these simplifications will be investigated incrementally in the set of experiments with label ‘B’, described below.

Equations (8), (9), and (15) are solved with an implicit-in-time scheme, using a time-step of 1 h. The vertical resolution is 5 m, and there are 70 equally spaced vertical layers. Initial conditions for N , P , and Z are set to 4, 0.1, and 0.01 mmol m⁻³, respectively, homogeneously over the whole column; these values correspond to winter conditions.

Bloom onset diagnostics

The bloom onset is assessed by examining the seasonal evolution of the total phytoplankton growth ($\bar{\mu}$, green lines in Figure 1) and loss (\bar{l} , blue lines in Figure 1) rates. The onset is defined as the time at

which phytoplankton net growth ($\bar{\mu} - \bar{l}$) switches from negative to positive value. As noted by Chiswell (2013), integrating over the depth of the mixed layer (as in Sverdrup, 1953; Behrenfeld, 2010; Behrenfeld et al., 2013) does not account for the phytoplankton biomass which is detrained, diffused and slowly decays below the mixed layer when the mixed-layer shallows. Thus here, the phytoplankton growth and loss rates are integrated over the whole depth H of the water column rather than over the mixed-layer depth D [as in Equation (6)], e.g.

$$\bar{\mu} = \frac{1}{P} \int_0^H \mu_p P \, dz \tag{18}$$

$$\bar{l} = \frac{1}{P} \int_0^H l_p P \, dz \tag{19}$$

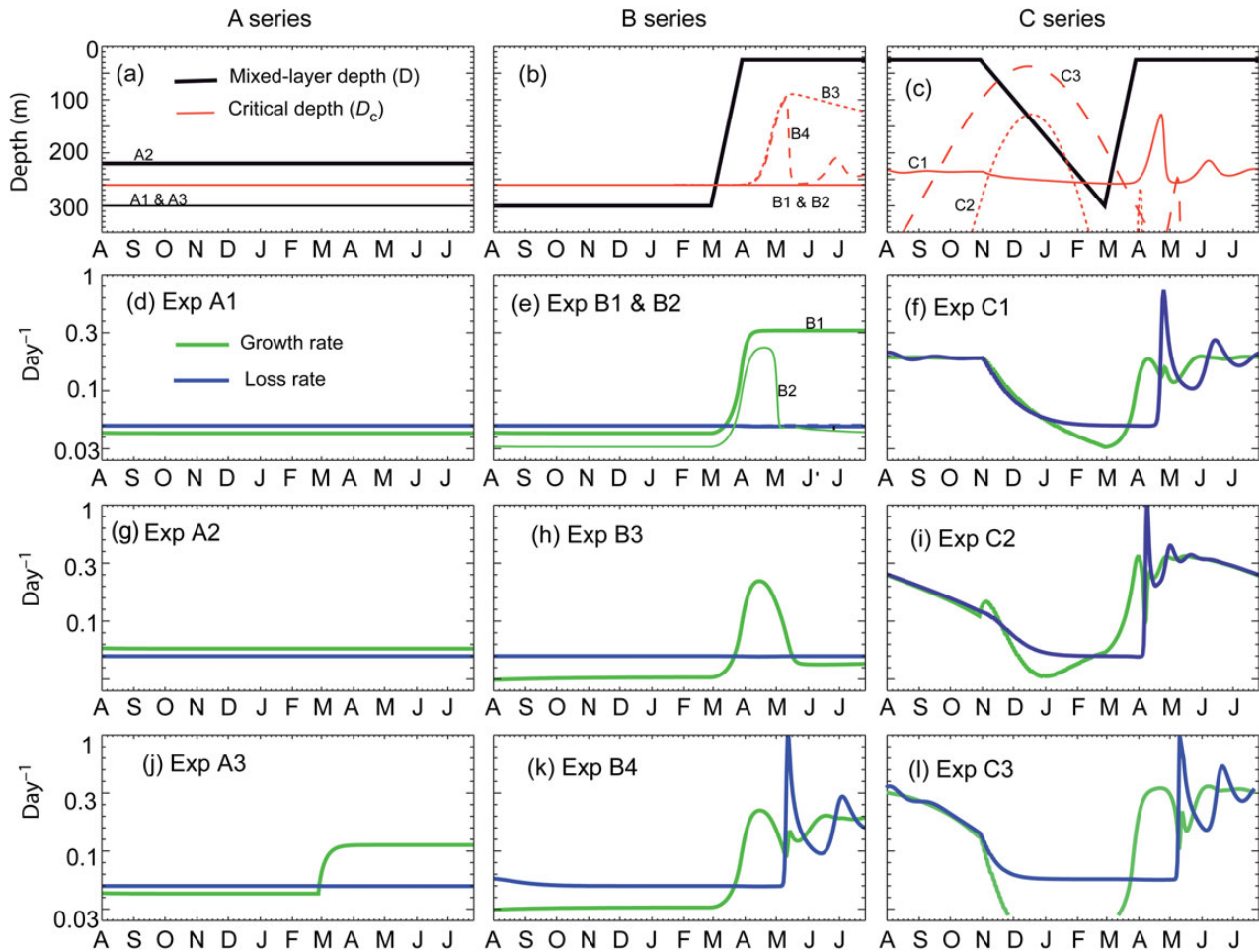


Figure 1. For each series of experiments A (left hand column), B (middle column), and C (right hand column), the first line (a–c) shows the seasonal evolution of the mixed-layer depth D (in black) and critical depth D_C (in red). The other lines show the seasonal evolution of the total water-column phytoplankton growth rate ($\bar{\mu}$, in green) and loss rate (\bar{l} , in blue) for each experiment in the corresponding series. The actual bloom onset occurs when net growth is positive, i.e. when the green curve comes above the blue one. The theoretical bloom onset predicted by the CDH occurs when the black curve comes above the red one (indicated by the dotted vertical lines in the B and C series). In (a), the thick black line shows D for experiment A2 and the thin black line shows D in A1 and A3; D_C is the same for A1, A2, and A3. In (b), D is the same for the four experiments B1–B4; the plain red line is D_C for B1 and B2, the dotted line for B3 and the dashed line for B4. In (c), D is the same for the three experiments C1–C3; the plain red line is D_C in C1, the dotted line in C2, and the dashed line in C3. In (e), the thick green line is the growth rate in B1, and the thin green line is the growth rate in B2; the loss rate is identical in B1 and B2.

such that

$$\frac{1}{\bar{P}} \partial_t \bar{P} = \bar{\mu} - \bar{l} \quad (20)$$

with

$$\bar{P} = \int_0^H P \, dz. \quad (21)$$

With these definitions, the total stock of biomass in the water column, \bar{P} , increases as soon as $\bar{\mu}$ exceeds \bar{l} .

Relaxing Sverdrup's hypothesis

The analytical expression for a critical depth relies on a number of assumptions, clearly identified in Sverdrup's 1953 paper, and used to construct his model. Paraphrasing Sverdrup, these assumptions are:

1. Phytoplankton develops in a thoroughly mixed layer at the surface of the ocean where turbulence is large enough to distribute the organisms evenly on the vertical.
2. Inorganic nutrients are fully available in the mixed layer and do not limit productivity.
3. Productivity is proportional to the light energy available for photosynthesis.
4. The light-extinction coefficient is constant in the mixed layer.
5. Grazers are not yet present in pre-bloom conditions.

It should be noted that these assumptions greatly facilitate the analytical derivation of the critical depth but are not necessary to simulate a bloom numerically. Here, using a set of numerical experiments (Table 3), the CDH is challenged by relaxing the above assumptions, one by one.

Physical forcing

The physical drivers of the model are the vertical mixing coefficient κ and surface irradiance I_0 . In all experiments, κ is set to κ_{\max} inside an upper mixed layer of depth D and to a minimum value of $10^{-5} \text{ m}^2 \text{ s}^{-1}$ below.

Three series of experiments (labelled A, B, and C) are conducted in which three different time evolutions of the mixed layer are considered (Figure 1a–c, black curves). These experiments are characteristic of the situation in the North Atlantic. In the A series, the mixed-layer depth is kept constant in time. In the B series, the winter-to-spring transition of the mixed layer is included. Finally

in the C series, the seasonal cycle of the mixed layer from the previous summer is included. Surface irradiance is kept constant in time, except in the last two experiments of the C series (C2 and C3) where seasonal variations are also included (see Table 3).

Results

Series A: Constant mixed-layer depth

In the A series of experiments (Figure 1, left hand column), the mixed-layer depth is kept constant in time and Sverdrup's model is used. This series corresponds to the analytical solution of Sverdrup and serves to test that the numerical model solution is faithful to the analytical solution. The turbulent diffusivity κ_{\max} is set to $1 \text{ m}^2 \text{ s}^{-1}$, such that assumption #1 is met. This value is typical of a convective situation and corresponds to a time scale of the order of 0.1 d for a mixed-layer depth of 100 m. To achieve the test, two experiments are compared, one (A1) where D is slightly deeper than D_C , the other (A2) where D is slightly shallower. Results for A1 and A2 confirm that our numerical model reproduces the situation explored by Sverdrup: in A2, $\bar{\mu}$ is larger than \bar{l} (Figure 1g): the condition for a bloom onset is satisfied; this is not the case in A1 (Figure 1d). Note that in A1 and A2, the net growth is constant and positive, so phytoplankton biomass would grow indefinitely with time.

To relax assumption #1 and test how the strength of turbulence in the mixed layer affects the bloom, we conduct experiment A3, similar to A1 except that κ_{\max} switches to a smaller value in spring ($10^{-2} \text{ m}^2 \text{ s}^{-1}$ after 1 March). This value now corresponds to a time scale of 10 d for a mixed-layer depth of 100 m. Experiment A3 mimics a situation where the mixed layer remains deep but turbulence decreases. Such a decrease has been attributed to net cooling subsidence at the end of winter (Taylor and Ferrari, 2011) and lowered windstress (Chiswell, 2011). We found that in A3, $\bar{\mu}$ becomes larger than \bar{l} as soon as vertical mixing is reduced (Figure 1j). In this situation, the vertical phytoplankton distribution is no longer homogeneous in the mixed layer, but exhibits a marked surface maxima (not shown). A situation similar to this, where density was fairly homogeneous within the top 300 m and phytoplankton developed in a thin surface layer was observed by Chiswell (2011) in the bloom East of New Zealand. Experiment A3 thus breaks the CDH but satisfies the CTH: net growth becomes positive when vertical turbulence falls below a critical value. Repeating this experiment with different values of κ_{\max} would allow one to determine the critical turbulent diffusivity numerically. Note that the value of κ_{\max} that I have used here is quite high, and lower critical turbulence levels would be obtained

Table 3. Set of experiments.

	D_{\max} (m)	D_{\min} (m)	κ_{\max} ($\text{m}^2 \text{ s}^{-1}$)	I_0^{\min} (W m^{-2})	I_0^{\max} (W m^{-2})	self-shading	Grazing	I and N limitations	k_b (m^{-1})
A1	300	300	1.	50.	50.	N	N	N	0.05
A2	220	220	1.	50.	50.	N	N	N	0.05
A3	300	300	1e^{-2}	50.	50.	N	N	N	0.05
B1	300	25	1.	50.	50.	N	N	N	0.05
B2	300	25	1.	50.	50.	N	N	Y	0.05
B3	300	25	1.	50.	50.	Y	N	Y	0.05
B4	300	25	1.	50.	50.	Y	Y	Y	0.05
C1	300	25	1.	50.	50.	Y	Y	Y	0.05
C2	300	25	1.	25.	200.	Y	Y	Y	0.05
C3	300	25	1.	25.	200.	Y	Y	Y	0.15

The first six columns are the parameters of the physical forcing (see also Figure 1), the last three are the parameters of the biogeochemical model. The A series uses Sverdrup's model (no self-shading, no grazing, no nutrient-N and light-I limitation terms). The C series uses the full NPZ model (i.e. with self-shading, grazing, and nutrients). In the B series, the model progressively transits from Sverdrup's to NPZ.

with a larger light attenuation coefficient (Huisman *et al.*, 1999, their Fig. 4).

Series B: Winter-to-spring transition of the mixed layer

The idea behind the CDH is that the mixed layer crosses the critical depth between winter and spring, which initiates the bloom. Implicitly, this suggests time variations in the mixed-layer depth, but in the steady-state analytical derivation of the critical depth, this effect is not explicitly accounted for. The B series of experiments focuses on a transient winter-to-spring transition: starting from unfavourable winter conditions, the mixed layer crosses the critical depth and shoals from D_{\max} to D_{\min} over time t_s , with $D_{\min} < D_C < D_{\max}$. The four experiments B1–B4 of this series share this transient physical forcing (Figure 1, central column), whereas the ecosystem model is progressively complexified from Sverdrup's model (B1) to the NPZ model (B4).

In B1, the ecosystem model is the same as in the A series (i.e. Sverdrup's model), which enables the transient and steady-state solution of the same equation to be compared. As expected, the shoaling causes $\bar{\mu}$ to increase above \bar{l} , in agreement with the CDH. To further assess the CDH, we compare the exact timing of the theoretical and actual bloom onsets in B1. The theoretical onset (marked by the thin vertical lines) occurs when the mixed-layer depth (Figure 1, in black) and critical depth (in red) intersect. The actual onset occurs when the growth rate (green curve) and loss rate (blue curve) intersect. Our B1 experiment reveals a time shift of ~ 1 week between the theoretical and actual bloom onset dates, and thus highlights a small deviation from the CDH (Figure 1e). Interestingly, this deviation does not come from the model assumptions, but from the way the original model of Sverdrup was solved, i.e. at steady state. It is worth noting that the magnitude of this deviation (1 week) is much smaller than the precision in the bloom onset detection date from satellite data (1 month, Cole *et al.*, 2012; Brody *et al.*, 2013). We also note that, as in the A series, the post-bloom situation in B1 is unrealistic since net phytoplankton growth is not arrested, due to the lack of nutrient limitation.

Next, in B2, B3, and B4, Sverdrup's assumptions #2–#5 regarding the form of the ecosystem model are relaxed sequentially. In B2, light saturated growth and nutrient limitation are accounted for, this is equivalent to an NP model. The time shift between the theoretical and actual onsets is extended by another week compared with B1 (Figure 1e). The larger shift is due to a reduced winter growth rate in response to both the nutrient limitation term (which is slightly < 1) and more complex light dependence of growth (by a fairly similar amount, not shown). We also note that the post-bloom situation in B2 is more realistic than in B1, since $\bar{\mu}$ goes back to low values after the bloom, due to nutrient limitation. Assumptions #2 and #3 do, therefore, cause moderate deviation from the CDH.

Experiment B3 allows for active self-shading (k_p is no longer 0), leading to time-variations in the critical depth (since k increases with increasing levels of phytoplankton). We find that k deviates from its background value mostly after the bloom onset, once biomass has had time to significantly accumulate. This change in k is reflected in the post-bloom shoaling of the critical depth, from 270 to 80 m (Figure 1b). The shape of the growth rate is also marginally affected compared with B2 during post-bloom conditions, in response to changes in light penetration (Figure 1h). Overall, however, the bloom onset in B3 is fairly similar to that in B2, justifying Sverdrup's constant-light-extinction hypothesis (#4).

Finally, accounting for grazing (experiment B4) significantly increases the loss rate after the bloom, but not before and therefore

has little consequence on the actual onset (Figure 1k). We also note out-of-phase oscillations of the growth and loss rates in post-bloom conditions, which are typical of predator–prey interactions, with the signature of an oscillating critical depth.

A preliminary conclusion from the B set of experiments is that, at least in the chosen set of model parameters, Sverdrup's assumptions about the very simple formulations of μ and l do not seriously challenge the CDH. At most, there is a time shift of 1–2 weeks between the theoretical and actual onset, and this time shift mainly ensues from bloom dynamics. Most importantly, accounting for explicit grazing (assumption #5) is not sufficient to significantly deviate from the CDH or to conform to the DRH. As shown next, this is not the case when the full seasonal is included.

Series C: Full seasonal cycle of the mixed layer

Because of the absence of disturbance in winter, spring shoaling of the mixed layer is the only physical factor that can trigger the bloom in the A and B experiments. To address this issue, the NPZ ecosystem model is forced with a repeating seasonal cycle of the mixed layer in the C set of experiments. Starting from summer, when the mixed layer is at its shallowest (D_{\min}), the mixed layer progressively deepens through fall and winter until it reaches D_{\max} , then shallows more rapidly during spring (in time t_s) until it comes back to its initial summer value D_{\min} (Figure 1c). The model is integrated for 2 years so that the summer initial conditions of the second year are consistent with the physical forcing. Results from the second year are shown in the right hand column of Figure 1. Both the model and the physical forcing are identical in B4 and C1 after 1 March (i.e. after the deepest mixed layer is reached); the two experiments differ in their physical forcing during the summer-to-winter transition.

In experiment C1, phytoplankton growth and losses are in close balance during summer, when the mixed layer is stratified and the physical forcing is steady. Phytoplankton and zooplankton are confined within the mixed layer, and there is a strong vertical gradient in nutrients (Figure 2). The deepening of the mixed layer on model date November 1 creates a disturbance that drives the system out of this summer equilibrium. Nutrients are entrained within the mixed layer, and the phytoplankton and zooplankton populations are diluted. A remarkable consequence of this perturbation is the increase in phytoplankton biomass seen in November and December (solid curve, Figure 2). This increase is not seen in the surface phytoplankton concentration (dashed curve, Figure 2), which, on the contrary, decreases in response to dilution. This situation is reminiscent of the winter situation observed in the Sub-Arctic Atlantic with profiling floats (Boss and Behrenfeld, 2010). Clearly, in C1, the winter onset of net growth is associated with the dilution and decrease of the zooplankton biomass (Figure 2). Both $\bar{\mu}$ and \bar{l} decrease, with the decrease in \bar{l} slightly larger than that of $\bar{\mu}$ (Figure 1f). This slight imbalance between $\bar{\mu}$ and \bar{l} enables the increase of the phytoplankton biomass: dilution decreases the grazing rate at a rate faster than it decreases the growth rate. Thus the winter situation in C1 satisfies the DRH: biomass starts accumulating in November, at a time when the mixed-layer depth is still above the critical depth, and thus disagrees with the CDH.

However, unlike the situation described by Behrenfeld (2010), biomass accumulation does not extend throughout winter; after January, grazing becomes negligible and the phytoplankton loss rate saturates (at the value of the mortality rate) while $\bar{\mu}$ continues to decrease, causing net growth to eventually become negative. Chiswell (2011) suggested that the CDH could perhaps be used to explain such negative net growth in winter. For experiment C1 to

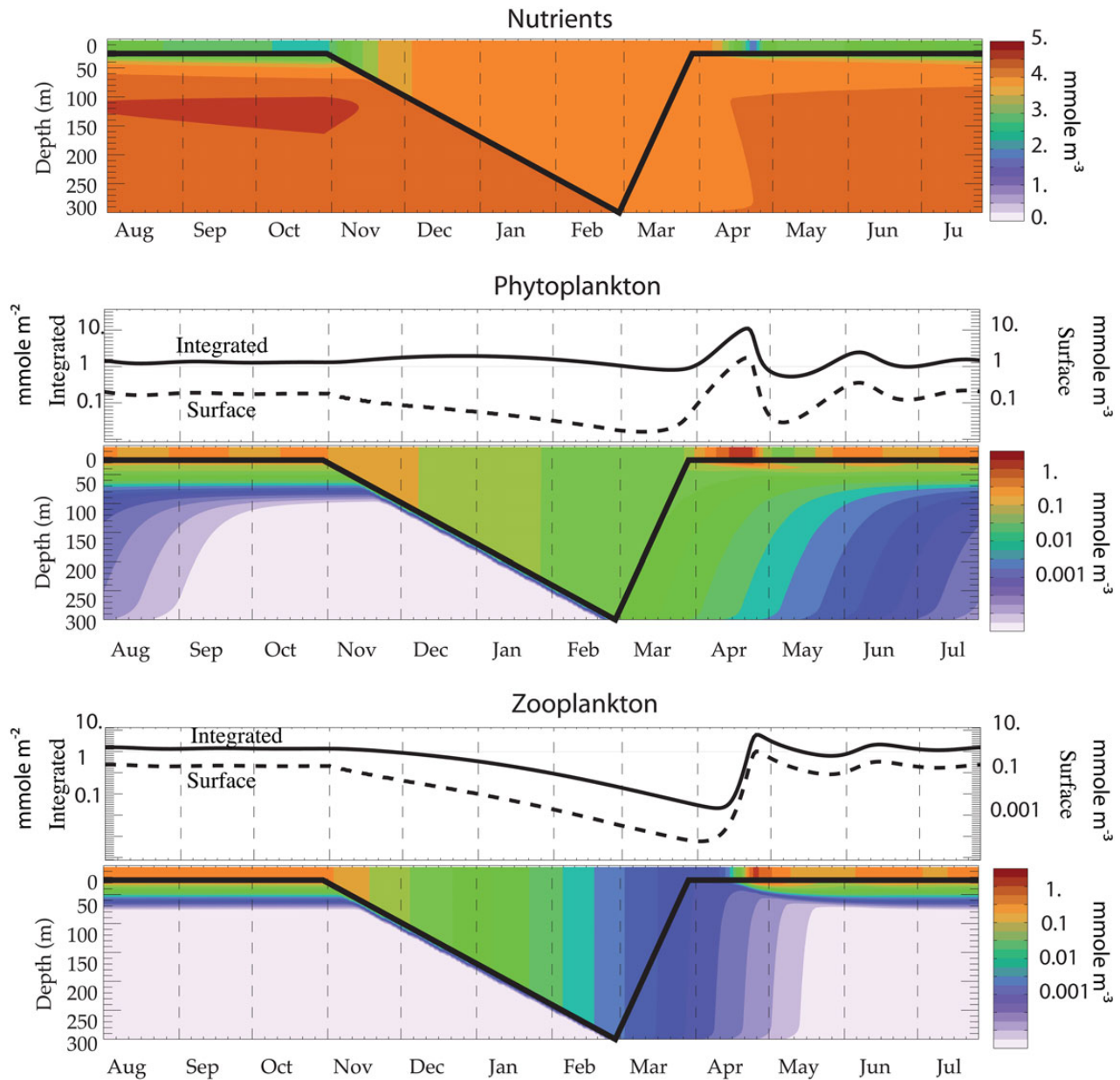


Figure 2. Seasonal evolution of the vertical distribution of nutrients, phytoplankton, and zooplankton in experiment C1 (colour contours). The overlaid thick black line shows the mixed-layer depth D . For phytoplankton and zooplankton, also shown are the seasonal evolution of the total depth-integrated biomass (solid line, top panel, in mmol m^{-2}) and of the surface biomass (dashed line, top panel, in mmol m^{-3}).

be consistent with Chiswell's hypothesis, we would expect this negative net growth to be driven by the deepening of the mixed layer below the critical depth; however, the mixed layer crosses the critical depth in February, 1 month after negative net growth has initiated.

From March onward, when the mixed layer stratifies, the evolution becomes very similar to that in experiment B4 with the occurrence of a second growth period in spring, in closer agreement with the CDH. It should be noted that, as expected, the shoaling of the mixed layer induces the detrainment of phytoplankton and zooplankton biomass below the mixed layer, such that, during the onset and climax of the bloom, phytoplankton biomass is not confined to the mixed layer, as hypothesized by Sverdrup, but shows a slowly decaying profile below the mixed layer (Figure 2). We also

note that a peculiarity of C1 is that nutrients are never exhausted from the surface layer (Figure 1). This is due to the weak surface illumination I_0 which is held constant at a low winter value. Thus the fall and winter conditions in C1 are close to those described by Sverdrup, i.e. not nutrient limited.

In C2, we add another degree of realism by allowing I_0 to vary seasonally in a sinusoidal manner between winter (I_0^{\min} , 21 December) and summer (I_0^{\max} , 21 June) extrema. The generally larger values of I_0 lead to notably deeper critical depths, such that in C2 the mixed layer is almost always above the critical depth (Figure 1c). The larger surface illumination in spring and summer (compared with all previous experiments) now allows more efficient exhaustion of mixed-layer nutrients by summer (not shown). In C2, growth and loss rates are in equilibrium in summer, and both decrease, due to

the decreasing amount of light (Figure 1i). Most notably in C2, the disturbance driven by the deepening of the mixed layer on November 1 causes a rapid increase of the growth rate, in contrast to C1 where the growth rate decreased (Figure 1f). This increase ensues from the resupply of nutrients by entrainment, which alleviates nutrient limitation (not shown), and leads to a positive net growth. However, as in C1, this increase is short lived. As the mixed layer continues to deepen, light limitation increases until the date of the winter solstice (21 December) causing a rapid decay of the growth rate. In consequence, this first growth period is limited to fall (to the month of November), while in C1 it covered fall and winter (until January). Moreover, unlike in C1, this fall bloom satisfies neither the DRH nor the CDH: it is closer to a so-called entrainment bloom (i.e. Lévy *et al.*, 2005; Martínez *et al.*, 2011; Chiswell and Grieve, 2013).

The seasonal increase in surface light in experiment C2 drives a slow increase in the growth rate that starts at the winter solstice (21 December), i.e. much earlier than in C1 where the increase of $\bar{\mu}$ followed the mixed-layer stratification (1 March). Incidentally, this leads to a theoretical spring bloom onset in closer agreement with the CDH than in any other case: the actual bloom onset, which was late by 2 weeks in most of the previous experiments, now occurs less than a week before the theoretical bloom onset date. Accounting for variable surface irradiance thus adds a degree of freedom which counterbalances the deviations from the CDH identified before. Note that an experiment similar to C2 but with a more rapid restratification time scale t_s (2 d instead of 30 d), intended to mimic the rapid decrease of turbulence in the mixed layer following the spring sign change in surface buoyancy flux (Taylor and Ferrari, 2011), has the main consequence of a more abrupt bloom onset, and even closer agreement between the actual and theoretical bloom onsets (not shown).

Finally in C3, the conditions are identical with those of C2 except that a stronger background light absorption coefficient is used (0.15 m^{-1} instead of 0.05 m^{-1}), leading to a critical depth shallower by $\sim 100 \text{ m}$. The overall stronger light absorption leads to a stronger light limitation in fall which prevents the appearance of the fall bloom; in November, the growth rate decreases abruptly when the mixed layer started deepening. In this last experiment, there was only one growth period, in spring, that satisfied the CDH, although the bloom started ~ 2 weeks after the mixed layer became shallower than the critical depth.

Experiments C1, C2, and C3 thus illustrate three different fall/winter situations: one (C1) characteristic of the DRH, with a decrease of the loss rate that exceeds the decrease of the growth rate; one (C2) characteristic of a fall bloom, with an increase of the growth rate due to the entrainment of nutrients; and one (C3) characteristic of the CDH, with a sharp decrease of the growth rate as soon as the mixed layer became deeper than the critical depth. The spring situations, however, are more similar, with a bloom that starts shortly after the mixed layer shallowed in all three cases.

Conclusions

The analytical expression for a critical maximum mixed-layer depth for bloom onset was formulated by Sverdrup (1953) from a phytoplankton-only model, solved at steady state. Since then, both *in situ* and satellite observations have revealed many instances where the bloom occurred before the onset of seasonal stratification, thus challenging the CDH (Townsend *et al.*, 1994; Behrenfeld, 2010; Boss and Behrenfeld, 2010). These observations have led to a wide debate regarding Sverdrup's model assumptions (a recent review

of the debate is provided by Lindemann and St John, 2014) and to the formulation of two alternative theories that challenged some aspects of Sverdrup's hypothesis.

More precisely, the CTH recognizes that apparently mixed layers (i.e. where temperature and salinity are fairly homogeneous) are not always regions of intense vertical mixing. This situation occurs frequently at the end of winter, when the mixed layer is well established, and when cessation of surface cooling and reduction of wind-stress reduces significantly vertical mixing within this layer compared with winter values. On the other end, the DRH challenges Sverdrup's assumption of a constant loss (mortality) rate. In particular, Behrenfeld (2010) suggests that a decrease in the loss rate is as plausible as an increase in the growth rate in initiating the bloom. In winter, such a decrease could be initiated by the dilution of predators and prey when the mixed layer entrains plankton-free waters.

Conceptual models of the bloom now incorporate all three hypotheses (Chiswell, 2011; Lindemann and St John, 2014). In parallel, numerical models have shown their ability to simulate them all (e.g. Dutkiewicz *et al.*, 2001; Behrenfeld *et al.*, 2013). It is uncertain which is more likely occurring in nature, but understanding is critical if one wants to project how phytoplankton dynamics will evolve in a changing ocean (Lindemann and St John, 2014).

Beyond all debate, Sverdrup's approach was indisputably pedagogical: it illustrated for the first time how a basic ecosystem model could be used to address a key ecological problem, namely the onset of phytoplankton blooms. In this regard, building on Sverdrup's approach, I presented a unifying framework in which the different concepts could be tested and rationalized. The framework is a one-dimensional NPZ model, forced by vertical mixing in a time-varying mixed layer. It builds on the initial phytoplankton model of Sverdrup's and adds the ingredients necessary for testing the CTH and DRH, i.e. explicit vertical mixing with variable strength κ and variable loss through incorporation of grazing. In addition, this framework also tested other assumptions of Sverdrup, i.e. steady state, constant-light absorption, the absence of nutrient limitation, and a productivity proportional to light.

The set of experiments presented here demonstrates that all three mechanisms for stimulating phytoplankton blooms can be modelled within this 1D-NPZ framework. It showed that adding complexity to the ecosystem model is not sufficient to make the model solution deviate from the CDH: the understanding of bloom dynamics requires a comprehensive representation of the physical drivers, and this representation was oversimplified in Sverdrup's model. The following lessons have been learned, and it is to be hoped will be useful for future bloom studies.

First, it is crucial to make a clear distinction between the mixed layer and the mixing layer, particularly when analysing observations; a number of prior studies have pointed that the seasonal thermocline (defined on a density criteria) is not always a good proxy of the mixing layer (Franks, 2015). This distinction is probably more natural to modellers, who can easily access to the model vertical mixing coefficient. Observational estimates of vertical mixing are sparse, though it may be possible to use the large array of Argo floats, from which the mixed-layer depth can be extracted, in conjunction with satellite observations of the bloom (Sallée *et al.*, 2015). An interesting alternative is to compare the bloom onset with the surface net heat flux rather than to a critical depth (Ferrari *et al.*, 2014).

Second, it is crucial to account for the evolution of the physical parameters from the previous summer—and thus of the full seasonal cycle—to understand bloom dynamics. Many of the recent studies on

the bloom onset focus on the winter-to-spring transition (Brody and Lozier, 2014; Ferrari *et al.*, 2014). However, as nicely illustrated by the conceptual model of Chiswell (2011), the summer-to-winter transition can also be associated with the accumulation of phytoplankton biomass. These early onsets may arise from a diverse set of processes, such as entrainment of nutrient (Chiswell, 2011), dilution of grazers (Behrenfeld, 2010), or increasing levels of solar radiation (Llort *et al.*, 2015). In the experiments presented here, the fall/winter production period is clearly separated from the spring bloom by a period of negative net growth in winter. However, the two periods can also merge in a single, long period of net growth and this has been reported both from observations (Lévy *et al.*, 2005; Behrenfeld, 2010; Sallée *et al.*, 2015) and from different sets of model experiments (Karleskind *et al.*, 2011; Behrenfeld *et al.*, 2013; Llort *et al.*, 2015).

Third, the seasonal evolution of surface irradiance is a key, and often neglected ingredient of the bloom timing. It is puzzling that in our most realistic experiments, when seasonal variations of solar radiation are accounted for, the actual onset is in closer agreement with Sverdrup's theoretical onset date, whereas these variations were not accounted for in the derivation of the critical depth. We find that this good agreement is due to counter-balancing effects, where solar radiation shifts the bloom onset toward the winter solstice, i.e. before the theoretical CDH date, while unsteady bloom dynamics shift the onset past this theoretical date.

Finally, variable loss—through incorporation of grazing—is necessary but not sufficient to conform to the DRH. In fact in all of our experiments, the loss rate is constant from winter to spring, in agreement with Sverdrup's assumption that grazers play a minor role on the onset of blooms in spring. Winter bloom conforming to the DRH only emerges in the specific situation where nutrients are still available at the end of summer and light levels are low, a situation that can be found at subpolar latitudes. Within the parameter range explored here, this winter onset disappears as soon as the seasonal evolution of surface irradiance is accounted for.

To finish, I remind the reader that the conclusions drawn from this illustrative set of experiments are limited by the fact that neither the physical nor the biological parameter spaces have been exhaustively explored, and that the role of other potentially important mechanisms such as acclimatation of the cells to external conditions or the physiology of sinking (Lindemann and St John, 2014) has not been addressed.

Acknowledgements

I thank the Center for Atmosphere Ocean Science, Courant Institute of Mathematical Sciences, New York University, and in particular Shafer Smith, for inviting me to give lectures in their department, which provided the inspiration for this note. Many thanks also to J. Llort, J.-B. Sallée, L. Bopp, J.-M. Andre, and A. Tagliabue for their insightful comments, to R. Ferrari for lively discussions on the bloom onset and to three anonymous reviewers for their helpful comments.

References

- Banase, K. 1994. Grazing and zooplankton production as key controls of phytoplankton production in the open ocean. *Oceanography*, 7: 13–20.
- Behrenfeld, M. 2010. Abandoning Sverdrup's Critical Depth Hypothesis on phytoplankton blooms. *Ecology*, 91: 977–989.
- Behrenfeld, M. J., and Boss, E. S. 2014. Resurrecting the ecological underpinnings of ocean plankton blooms. *Annual Review of Marine Science*, 6: 167–194.
- Behrenfeld, M. J., Doney, S. C., Lima, I., Boss, E. S., and Siegel, D. A. 2013. Annual cycles of ecological disturbance and recovery underlying the subarctic Atlantic spring plankton bloom. *Global Biogeochemical Cycles*, 27: 526–540.
- Boss, E., and Behrenfeld, M. 2010. In situ evaluation of the initiation of the North Atlantic phytoplankton bloom. *Geophysical Research Letters*, 37: L18603.
- Brainerd, K. E., and Gregg, M. C. 1995. Surface mixed and mixing layer depths. *Deep Sea Research Part I*, 42: 1521–1543.
- Brody, S. R., and Lozier, M. S. 2014. Changes in dominant mixing length scales as a driver of subpolar phytoplankton bloom initiation in the North Atlantic. *Geophysical Research Letters*, 41, doi:10.1002/2014GL059707.
- Brody, S. R., Lozier, M. S., and Dunne, J. P. 2013. A comparison of methods to determine phytoplankton bloom initiation. *Journal of Geophysical Research-Oceans*, 118: 2345–2357.
- Chiswell, S. 2011. Annual cycles and spring blooms in phytoplankton: don't abandon Sverdrup completely. *Marine Ecology-Progress Series*, 443: 39–50.
- Chiswell, S. M. 2013. Comment on “Annual cycles of ecological disturbance and recovery underlying the subarctic Atlantic spring plankton bloom”. *Global Biogeochemical Cycles*, doi: 10.1002/2013GB004681.
- Chiswell, S. M., and Grieve, J. B. 2013. Climatology of surface chlorophyll a, autumn-winter and spring blooms in the south-west Pacific Ocean. *Journal of Geophysical Research: Oceans*, 118: 1003–1018.
- Cole, H., Henson, S., Martin, A., and Yool, A. 2012. Mind the gap: the impact of missing data on the calculation of phytoplankton phenology metrics. *Journal of Geophysical Research*, 117: C08030.
- Dutkiewicz, S., Follows, M., Marshall, J., and Gregg, W. 2001. Interannual variability of phytoplankton abundances in the North Atlantic. *Journal of Geophysical Research*, 48: 2323–2344.
- Evans, T. G., and Parslow, J. S. 1985. A model of annual plankton cycles. *Biological Oceanography*, 3: 327–347.
- Ferrari, R., Merrifield, S., and Taylor, J. 2014. Shutdown of convection triggers increase of surface chlorophyll. *Journal of Marine Systems*, S0924-7963(14)00038-4, doi: 10.1016/j.jmarsys.2014.02.009.
- Franks, P. J. 2002. NPZ models of plankton dynamics: their construction, coupling to physics, and application. *Journal of Oceanography*, 58: 379–387.
- Franks, P. J. 2015. Has Sverdrup's critical depth hypothesis been tested? Mixed layers vs. turbulent layer. *ICES Journal of Marine Science Journal*, 72: 1897–1907.
- Huisman, J., van Oostveen, P., and Weissing, F. J. 1999. Critical depth and critical turbulence: two different mechanisms for the development of phytoplankton blooms. *Limnology and Oceanography*, 44: 1781–1787.
- Karleskind, P., Lévy, M., and Memery, L. 2011. Subduction of carbon, nitrogen, and oxygen in the northeast Atlantic. *Journal of Geophysical Research*, 116: C02025.
- Lévy, M., Lehahn, Y., André, J., Memery, L., Loisel, H., and Heifetz, E. 2005. Production regimes in the Northeast Atlantic: a study based on Sea-viewing Wide Field-of-view Sensor (SeaWiFS) chlorophyll and ocean general circulation model mixed layer depth. *Journal of Geophysical Research*, 110: 1998–2006.
- Lindemann, C., and St John, M. A. 2014. A seasonal diary of phytoplankton in the North Atlantic. *Frontiers in Marine Science*, 1: 1–6.
- Llort, J., Lévy, M., Sallée, J.-B., and Tagliabue, A. 2015. Onset, intensification, and decline of phytoplankton blooms in the Southern Ocean. *ICES Journal of Marine Science*, 72: 1971–1984.
- Marra, J., and Barber, R. T. 2005. Primary productivity in the Arabian Sea: a synthesis of JGOFS data. *Progress in Oceanography*, 65: 159–175.

- Martin, J. H., Knauer, G. A., Karl, D. M., and Broenkow, W. W. 1987. VERTEX: carbon cycling in the northeast Pacific. *Deep Sea Res.*, 34: 267–285.
- Martinez, E., Antoine, D., D’Ortenzio, F., and de Boyer Montégut, C. 2011. Phytoplankton spring and fall blooms in the North Atlantic in the 1980s and 2000s. *Journal of Geophysical Research*, 116: C11029.
- Riley, G. A. 1946. Factors controlling phytoplankton populations on Georges Bank. *Journal of Marine Research*, 6: 54–73.
- Sallée, J. B., Llorc, J., Tagliabue, A., and Lévy, M. 2015. Characterisation of distinct bloom phenology regimes in the Southern Ocean. *ICES Journal of Marine Science*, 72: 1985–1998.
- Siegel, D., Doney, S., and Yoder, J. 2002. The North Atlantic spring phytoplankton bloom and Sverdrup’s critical depth hypothesis. *Science*, 296: 730.
- Sverdrup, H. 1953. On conditions for the vernal blooming of phytoplankton. *Journal du Conseil / Conseil Permanent International pour l’Exploration de la Mer*, 18: 287–295.
- Taylor, J. R., and Ferrari, R. 2011. Shutdown of turbulent convection as a new criterion for the onset of spring phytoplankton blooms. *Limnology and Oceanography*, 56: 2293–2307.
- Townsend, D., Cammen, L., Holligan, P., Campbell, D., and Pettigrew, N. 1994. Causes and consequences of variability in the timing of spring phytoplankton blooms. *Deep Sea Research Part I*, 41: 747.
- Yoshie, N., Yamanaka, Y., Kishi, M. J., and Saito, H. 2003. One dimensional ecosystem model simulation of the effects of vertical dilution by the winter mixing on the spring diatom bloom. *Journal of Oceanography*, 59: 563–571.

Handling editor: Rubao Ji



Contribution to the Themed Section: 'Revisiting Sverdrup's Critical Depth Hypothesis' Original Articles

Numerical simulations of the competition between wind-driven mixing and surface heating in triggering spring phytoplankton blooms

Rica Mae Enriquez and John R. Taylor*

Department of Applied Mathematics and Theoretical Physics, University of Cambridge, Cambridge, Cambridgeshire CB3 0WA, UK

*Corresponding author: tel: +44 1223 337030; fax: +44 1223 765900; e-mail: j.r.taylor@damtp.cam.ac.uk

Enriquez, R. M., and Taylor, J. R. Numerical simulations of the competition between wind-driven mixing and surface heating in triggering spring phytoplankton blooms. – ICES Journal of Marine Science, 72: 1926–1941.

Received 4 August 2014; revised 18 March 2015; accepted 4 April 2015; advance access publication 12 May 2015.

About 60 years ago, Sverdrup formalized the critical depth hypothesis to explain the timing of the spring phytoplankton bloom in terms of the depth of the surface mixed layer. In recent years, a number of refinements and alternatives to the critical depth hypothesis have been proposed, including the critical turbulence hypothesis which states that a bloom can occur when turbulent mixing is sufficiently weak, irrespective of the mixed layer depth. Here, we examine the relative influence of wind-driven mixing and net surface heating on phytoplankton growth. Of particular interest is whether wind-driven mixing can delay the spring bloom after winter convection gives way to net surface warming. We address these questions using high-resolution large-eddy simulations (LES) coupled with a simple phytoplankton model. We also describe an analytical phytoplankton model with a formulation for the turbulent mixing based on the LES results. For a constant, prescribed surface heat flux, net phytoplankton growth is seen when the windstress is smaller than a critical value. Similarly, for a constant windstress, a critical heat flux separates cases with growing and decaying phytoplankton populations. Using the LES results, we characterize the critical windstress and critical heat flux in terms of other physical and biological parameters and propose a simple expression for each based on the analysis of the analytical model. Phytoplankton growth begins when the mixing depth shoals above the critical depth, consistent with the critical depth hypothesis. Our results provide a framework to interpret blooms in other conditions where both the depth and the intensity of turbulent mixing might be crucial factors in influencing phytoplankton growth.

Keywords: critical depth, critical turbulence, large-eddy simulation, mixing depth, phytoplankton bloom, turbulent diffusivity.

Introduction

The striking scene of phytoplankton amassing in the surface boundary layer during spring—the spring bloom—has fascinated scientists for decades. Early work by [Gran and Braarud \(1935\)](#) and [Riley \(1946\)](#) suggested that the spring bloom begins when the mixed layer depth first shoals above a critical depth. About 60 years ago, [Sverdrup \(1953\)](#) formalized the “critical depth hypothesis” and derived an expression for the critical mixed layer depth based on several assumptions. Among these, he assumed that: phytoplankton cells are uniformly distributed in the mixed layer; phytoplankton growth at the onset of the bloom is not limited by nutrient availability; the depth-dependent cellular growth rate is proportional to the available light which decreases

exponentially with depth from a surface maximum; and the combined loss rate, which incorporates all sources of phytoplankton loss, including mortality due to grazing, and losses due to sinking, viral infection, and parasitism, is independent of depth.

Prompted by observations of phytoplankton blooms preceding mixed layer shoaling ([Townsend *et al.*, 1994](#); [Behrenfeld, 2010](#); [Boss and Behrenfeld, 2010](#)), several recent studies have proposed refinements or alternatives to the critical depth hypothesis involving physical and/or biological triggers of the spring bloom ([Huisman *et al.*, 1999](#); [Behrenfeld, 2010](#); [Chiswell, 2011](#); [Taylor and Ferrari, 2011a, b](#); [Mahadevan *et al.*, 2012](#)). Here, we will consider only physical mechanisms, specifically wind-driven turbulence and the development of stratification through net surface heating. We do not

attempt to rule out biological drivers of the spring bloom, such as the dilution-recoupling hypothesis proposed by Behrenfeld (2010). Our goal is not to reproduce a given spring bloom event, but instead to examine the possible role of physical drivers on phytoplankton growth during the spring bloom.

Although Sverdrup (1953) used the mixed layer depth, defined using measured temperature and salinity profiles, as a proxy for the depth of active mixing, these depths are not always equal (Brainerd and Gregg, 1995). The mixed layer depth is often defined in terms of a fixed density or temperature difference from the surface and reflects the maximum depth of past mixing, whereas the “mixing depth” is the depth to which currently active turbulence penetrates. When the mixing depth is shallower than the mixed layer depth, the former is a more appropriate choice for comparison with the critical depth (Brody and Lozier, 2014).

Huisman *et al.* (1999) considered a scenario where the rate of mixing is not sufficient to maintain a uniform phytoplankton concentration in the mixing layer. Using a one-dimensional column model with the rate of change of phytoplankton concentration balanced by growth, losses, and diffusion, they showed that a bloom could be triggered either by a reduction in the mixing depth or by a reduction in the strength of mixing within this layer. When the mixing depth is significantly deeper than the critical depth, blooms occur in their model when the turbulent diffusivity, κ_T , is less than a critical value, κ_c , the so-called “critical turbulence hypothesis”. This scenario was anticipated by Sverdrup (1953) who stated: “a phytoplankton population may increase independently of the thickness of the mixed layer if the turbulence is moderate”.

The “critical turbulence” hypothesis can also be interpreted in terms of characteristic time-scales (Taylor and Ferrari, 2011b). Mixing occurs on a time-scale that depends on the size and intensity of the turbulent motions responsible for stirring phytoplankton cells down from the ocean surface. On the other hand, phytoplankton cells accumulate in regions where local growth outweighs losses with a characteristic growth time-scale. When the mixing time-scale is very fast relative to the growth time-scale, the phytoplankton concentration is expected to remain relatively uniform, in agreement with Sverdrup’s assumption. On the other hand, when mixing is slow compared with the growth time-scale, this assumption may no longer be valid, and a bloom can occur through the critical turbulence mechanism.

Taylor and Ferrari (2011b) applied the critical turbulence hypothesis to study phytoplankton blooms following a period of thermal convection. In the absence of lateral processes, such as eddy-induced slumping (Taylor and Ferrari, 2011a; Mahadevan *et al.*, 2012), they asserted that the spring bloom could be triggered by a shutdown of thermal convection. This hypothesis was supported by Ferrari *et al.* (2014) using satellite observations of near-surface Chlorophyll concentration and heat flux from an atmospheric reanalysis dataset from the North Atlantic. Taylor and Ferrari (2011b) assumed that in winter, turbulence in the mixed layer is driven primarily by thermal convection, whereas winds play a secondary role.

After the shutdown of thermal convection, phytoplankton growth could still be suppressed as long as wind-driven mixing is sufficiently strong. Chiswell (2011) suggested that strong winds could delay the spring bloom, with a bloom occurring only after the windstress drops below a critical threshold. Since density stratification generally suppresses turbulence, the level of windforcing needed to suppress a bloom is expected to increase with increasing net surface heating. This suggestion was supported by Brody *et al.*

(2013) who found that a stabilizing heat flux was not always sufficient to trigger a bloom. An important open question remains: what is the value of the critical windstress and how does it change in response to a stabilizing surface heat flux?

Here, we will seek to identify how the critical windstress depends on important parameters including the stabilizing surface heat flux and the critical depth. We will address this question using large-eddy simulations (LES) that resolve the largest turbulent overturns in a wind-driven Ekman layer. By systematically varying the surface windstress and the stabilizing heat flux across a suite of simulations, we will examine when phytoplankton blooms develop. We will then use the results from the LES to develop an analytical model, extending previous work by Huisman *et al.* (1999), Ebert *et al.* (2001), and Taylor and Ferrari (2011b) to explicitly include the effects of wind-forcing and surface heating. The analytical model could help predict how a given seasonal progression of surface wind and heat fluxes might lead to the onset of the spring bloom and provides a framework to interpret blooms in observations and models with more complicated biogeochemistry.

This paper is divided into the following main sections: a description of the setup and results of the LES and an overview of the development of an analytical model in a heated, wind-driven Ekman layer. After discussion and conclusions, an appendix contains a comparison of LES and analytical phytoplankton model results.

Large-eddy simulations

Setup

To study the influence of wind-driven mixing and surface heating on phytoplankton growth, we use high-resolution, three-dimensional LES of the wind-forced turbulent Ekman layer, as illustrated in Figure 1. In each simulation, turbulence is generated by imposing a constant surface windstress, τ_{wind} . Some simulations also include a constant, positive net surface heat flux, Q_0 . Note that since we do not explicitly include a diurnal cycle in our model, Q_0 is intended to represent the time-averaged net surface heat flux. Taylor and Ferrari (2011b) simulated the mixing due to a typical diurnal cycle using LES and found that it was insufficient to prevent a phytoplankton bloom. The complete list of simulation parameters is listed in Table 1. Our parameter space for Q_0 ranges from 0 to 75 W m⁻² whereas our parameter space for τ_{wind} ranges from 0.01 to 0.2 Pa. Although we focus on the coupling effects of surface heating and winds, our parameter space covers typical spring values.

LES explicitly resolve the largest, most energetic three-dimensional turbulent motions and model the influence of smaller scales. In this methodology, a spatial filter, denoted here by an overbar, $\bar{\cdot}$, is applied to the governing equations. The LES then time-steps the following filtered equations for the three components of velocity, $\bar{\mathbf{u}}$, buoyancy, \bar{b} , phytoplankton cell concentration, \bar{P} , and the continuity equation:

$$\frac{\partial \bar{\mathbf{u}}}{\partial t} + \bar{\mathbf{u}} \cdot \nabla \bar{\mathbf{u}} + f \hat{\mathbf{k}} \times \bar{\mathbf{u}} = -\frac{1}{\rho_0} \nabla \bar{p} + b \hat{\mathbf{k}} - \nabla \cdot \tau^{\text{SGS}} + \nu \nabla^2 \bar{\mathbf{u}}, \quad (1)$$

$$\frac{\partial \bar{b}}{\partial t} + \bar{\mathbf{u}} \cdot \nabla \bar{b} = -\nabla \cdot \lambda_b^{\text{SGS}} + \kappa_b \nabla^2 \bar{b}, \quad (2)$$

$$\frac{\partial \bar{P}}{\partial t} + \bar{\mathbf{u}} \cdot \nabla \bar{P} = (\mu(z) - m) \bar{P} - \nabla \cdot \lambda_p^{\text{SGS}} + \kappa_p \nabla^2 \bar{P}, \quad (3)$$

$$\nabla \cdot \bar{\mathbf{u}} = 0. \quad (4)$$

The left hand sides of Equations (1)–(3) include advection by the resolved three-dimensional velocity field. Unresolved subgrid-scale (SGS) processes are represented through τ^{SGS} , λ_b^{SGS} , and λ_p^{SGS} , which denote the SGS stress, buoyancy flux, and phytoplankton flux, respectively. The form of the SGS contributions is described below. The molecular viscosity, ν , is set to $10^{-6} \text{ m}^2 \text{ s}^{-1}$. The Prandtl numbers of phytoplankton and buoyancy, Pr_p and Pr_b , are equal to 1 and 7 (Taylor and Ferrari, 2010), respectively, such that $\kappa_p = \nu$ and $\kappa_b = \nu/7$. However, since the molecular transport is negligible in all simulations, our results are insensitive to the value of these parameters. We apply the Boussinesq approximation and symbolize the background density as ρ_0 .

Since our focus is on the influence of turbulent mixing on phytoplankton growth, we use a highly simplified phytoplankton model in Equation (3). In particular, we follow Sverdrup (1953) and Taylor and Ferrari (2011a, b) in assuming that the local growth rate, $\mu(z)$, is a prescribed function of depth only and that the loss rate, $m = 0.1 \text{ d}^{-1}$, is constant in space and time. The prescribed

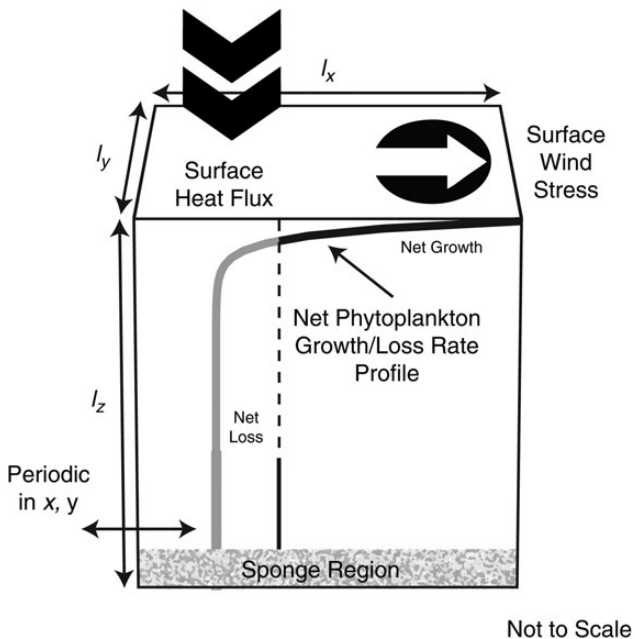


Figure 1. Schematic of the LES domain. The domain lengths, l_x , l_y , and l_z , are listed in Table 1. The lateral boundary conditions are periodic and the bottom boundary includes a sponge region. For each simulation, a constant surface windstress and/or a surface heat flux is applied. The growth model assumes that phytoplankton cell concentration growth is light-limited and that the biological parameters are constant in time.

local growth rate is $\mu(z) = \mu_0 e^{-z/h_L}$ where $\mu_0 = 1 \text{ d}^{-1}$ is the maximum growth rate at the ocean surface, and $h_L = \{5 \text{ m}, 10 \text{ m}\}$ is the e -folding depth associated with light penetration. The values of the biological parameters used in this study, μ_0 , m , and h_L , can be found in Tables 1 and 2. The growth rate is a function of the average light availability from the past day. Phytoplankton cells are allowed to move vertically and they instantly adapt to the light availability at each depth. The instantaneous growth rate is a function of depth alone and so we neglect phytoadaptation (Cullen and Lewis, 1988) or growth rate dependence on past history. Both effects can be included if a particle-based Lagrangian approach is taken instead of an Eulerian model (Broekhuizen, 1999; Nagai et al., 2004; Ross and Sharples, 2004; Yamazaki et al., 2014). For simplicity, the local growth and loss rates, μ_0 and m , are assumed to be constant in time. As a result, we do not consider interactions between phytoplankton, nutrients, and zooplankton, which would modulate the growth and loss rates. We also neglect other processes including cell sinking/buoyancy and motility, since phytoplankton cell capacities are too weak to counteract the mixing intensity. Despite these simplifications, the response of the three-dimensional phytoplankton concentration to resolved and SGS turbulence is non-trivial.

The values for the biological parameters, μ_0 , m , and h_L (Table 2), are selected for comparison with simulations that examine the beginning of phytoplankton blooms with steady convection, without a surface windstress, and a critical depth of 50 m (Taylor and Ferrari, 2011b). We include an additional value of $h_L = 10 \text{ m}$ to study if and how the critical wind changes for a critical depth of 100 m.

Details of the numerical method are given in Taylor (2008) and we use the same method as Taylor and Ferrari (2011b), except that we use a different model for the SGS terms. The stable wind-driven boundary layer, typical in spring and summer, is much shallower than the convective boundary layer found in winter. The depth of the stable wind-driven boundary is subject to the strengths of the surface wind and the surface heating. Although wind deepens the boundary layer by approximately the Ekman depth, the surface heating provides stability and shallows the boundary layer. Previously, Mason and Derbyshire (1990) demonstrated that the constant Smagorinsky model, used in Taylor and Ferrari (2011b), might not be appropriate for simulating stable boundary layers where stratification can suppress turbulent production. This led to the development of SGS models suitable for the stable boundary layer (e.g. Kosović and Curry, 2000; Basu and Porté-Agel, 2006; Beare et al., 2006; Zhou and Chow, 2011; Enriquez, 2013). Here, we use the dynamic Wong–Lilly model, which has been previously applied to study the stable atmospheric boundary layer (Zhou and Chow, 2011, 2012), where the dynamics are analogous to the stable wind-driven boundary layer considered here (Lien and

Table 1. Parameters for LES.

l_x, l_y, l_z (m)	n_x, n_y, n_z	h_L (m)	h_c (m)	τ_{wind} (Pa)	Q_0 (W m^{-2})
100, 100, 150	128, 128, 120	5	50	0.001*, 0.01	0
100, 100, 150	64, 64, 120	5	50	0.02, 0.04, 0.06	0
100, 100, 150	64, 64, 120	5	50	0.08, 0.10	0, 5, 25, 50, 75
150, 150, 225	64, 64, 120	10	100	0.10, 0.15, 0.20	0, 5, 25, 50, 75

The simulations use a domain size of l_x, l_y, l_z , using n_x, n_y, n_z computational grid-points. The simulations vary the light e -folding depth, h_L , the critical depth, h_c , the windstress, τ_{wind} , and the surface heat flux, Q_0 . The first set of simulations includes unheated cases forced with a surface windstress. The LES with $\tau_{\text{wind}} = 0.001 \text{ Pa}$ is an extremely low windstress case that is only used in Figure A3. The second set of simulations includes cases forced with surface heating and windstress.

Table 2. Chosen physical, biological, and numerical parameters for LES.

	Symbol	Value
Physical parameter		
Coriolis parameter	f	10^{-4} s^{-1}
Background density	ρ_0	1000 kg m^{-3}
Specific heat capacity	c_p	$4 \times 10^3 \text{ J kg}^{-1} \text{ }^\circ\text{C}^{-1}$
Thermal expansion coefficient	α	$1.65 \times 10^{-4} \text{ }^\circ\text{C}^{-1}$
Gravitational acceleration	g	9.81 m s^{-2}
Biological parameter		
Maximum specific growth rate	μ_0	1 d^{-1}
Specific loss rate	m	0.1 d^{-1}
e -folding depth associated with light penetration	h_L	5, 10 m
Numerical parameter		
Molecular viscosity	ν	$10^{-6} \text{ m}^2 \text{ s}^{-1}$
Molecular diffusivity	κ	$10^{-6} \text{ m}^2 \text{ s}^{-1}$
Buoyancy Prandtl number	Pr_b	7
Phytoplankton Prandtl number	Pr_p	1

Sanford, 2004). The SGS stress tensor is modelled as:

$$\tau^{\text{SGS}} = -2\nu_{\text{SGS}}\bar{\mathbf{S}}, \quad (5)$$

where $\bar{\mathbf{S}} = (\nabla\mathbf{u} + \nabla\mathbf{u}^T)/2$ is the rate of strain tensor. The dynamic eddy viscosity, ν_{SGS} , is given by $\nu_{\text{SGS}} = C_\epsilon\Delta_f^{4/3}$. The local horizontal test filter width, Δ_f , is equal to twice the grid spacing, Δ_g . The dynamic coefficient C_ϵ is determined using the least-squares method of Lilly (1992), which results in an eddy viscosity that varies in space and time. The SGS buoyancy and phytoplankton flux terms in Equations (2) and (3) are modelled as:

$$\lambda_b^{\text{SGS}} = -\kappa_{\text{SGS}}\nabla\bar{b}, \quad (6)$$

$$\lambda_p^{\text{SGS}} = -\kappa_{\text{SGS}}\nabla\bar{P}, \quad (7)$$

where κ_{SGS} is the SGS diffusivity. We set the SGS Prandtl numbers of phytoplankton and buoyancy, equal to 1 such that $\kappa_{\text{SGS}} = \nu_{\text{SGS}}$.

Windforcing is represented by applying a constant stress boundary condition at the top of the domain. Here, the x -axis is aligned with the windstress, and (u, v, w) will denote the velocity in the downwind, cross-wind, and vertical directions, respectively. Surface heating is represented by applying a uniform buoyancy flux as a boundary condition to Equation (2). Since the smallest mixing depth in our simulations is ~ 25 m, the added buoyancy is quickly mixed down from the surface. To limit the number of parameters in this study, we do not include penetrative heating. However, it would be interesting to include this process in future work. Although the LES model solves for buoyancy, if we assume a linear equation of state and neglect freshwater inputs at the surface, the surface buoyancy flux, B_0 , can be related to an equivalent surface heat flux, Q_0 :

$$B_0 = \frac{Q_0\alpha g}{c_p\rho_0}, \quad (8)$$

where α is the thermal expansion coefficient, g the gravitational acceleration, c_p the specific heat capacity, and ρ_0 a background density (see Table 2 for values).

We use a computational domain size of $l_x = 100$, $l_y = 100$, and $l_z = 150$ m for simulations with $h_L = 5$ m, and a domain of $l_x = 150$, $l_y = 150$, and $l_z = 225$ m for simulations with $h_L = 10$ m. For both domains, we use $n_x = 64$, $n_y = 100$, and $n_z = 120$ m grid-points. The resolution of the simulation with a windstress, τ_{wind} , equal to 0.01 Pa and $Q_0 = 0 \text{ W m}^{-2}$, is higher to ensure that we resolve the largest turbulent motions in the thinner Ekman layer. The domain size is comparable with previous simulations of an unstratified wind-driven Ekman layer (Zikanov *et al.*, 2003). The grid is stretched in the vertical direction to resolve small-scale turbulence near the surface. For the smaller domain, the minimum and maximum vertical grid spacings are 0.3 and 2.3 m, respectively. For the larger domain, the minimum and maximum vertical grid spacings are 0.4 and 3.5 m, respectively. Following Taylor and Ferrari (2011b), we use boundary conditions that approximate an unbounded domain without large-scale horizontal gradients. Specifically, periodic boundary conditions are applied in the horizontal directions. A sponge region is placed in the lower 15% of the domain to prevent interactions between the flow and the lower boundary.

For each case, there is a 12-h initialization period. At the start of this period, we prescribe a uniform buoyancy profile, and the velocity is initialized by applying random fluctuations with an amplitude of 0.001 m s^{-1} with no mean flow. During the first 9 h of the initialization period, the windstress and surface heat flux are increased linearly from zero to the value specified in Table 1. The windstress and surface heat flux remain at this value for the remaining 3 h of the initialization period and the remaining 8 d of each simulation. After the 12 h initialization period, we initialize the phytoplankton concentration with a uniform profile and reset the simulation time to $t = 0$ d. Mean values are calculated by averaging over horizontal planes and are denoted by $\langle \rangle$. Phytoplankton concentrations are normalized by the initial concentration, P_0 , or the average surface concentration at a given time, $\langle P_{s,t} \rangle$.

Results

Before discussing the effects of surface windstress and heating flux on phytoplankton dynamics, we briefly describe the mean velocity and buoyancy fields. Figure 2a and b depicts the mean horizontal velocities, $\langle \bar{u} \rangle$ and $\langle \bar{v} \rangle$, for $\tau_{\text{wind}} = 0.08 \text{ Pa}$ and $Q_0 = 0, 25, 75 \text{ W m}^{-2}$, averaged from $t = 0$ to $t = 8$ d. Our simulations in the cases with $Q_0 = 0 \text{ W m}^{-2}$ have been validated by comparing with results from Zikanov *et al.* (2003), and our mean velocity profiles closely match their results. As the level of heating increases, the Ekman flow becomes confined to a shallower region and the maximum magnitude of the cross-wind component, $\langle \bar{v} \rangle$, increases. This is consistent with the confinement effects in a stable bottom Ekman layer reported in Taylor and Sarkar (2008).

Mean buoyancy profiles, $\langle \bar{b} \rangle$, are shown in Figure 2c. For the case in which $Q_0 = 0$, the buoyancy remains zero since there is no source of buoyancy. However, the addition of surface heating leads to a non-uniform buoyancy profile. The warm (buoyant) fluid is confined to a layer near the surface, and this layer is shallower with stronger heating. Note that the non-uniform profiles of buoyancy translate to relatively small changes in temperature. The mixed layer depth is often defined in terms of a fixed density or temperature difference from the surface. For example, a metric used to define the mixed layer depth is a temperature change of 0.8°C (Kara *et al.*, 2000). From Figure 2c, the buoyancy change from the surface for the $\tau_{\text{wind}} = 0.08 \text{ Pa}$, $Q_0 = 75 \text{ W m}^{-2}$ case is $\sim 5.0 \times 10^{-4} \text{ m s}^{-2}$, which corresponds to a temperature change of just 0.3°C , smaller

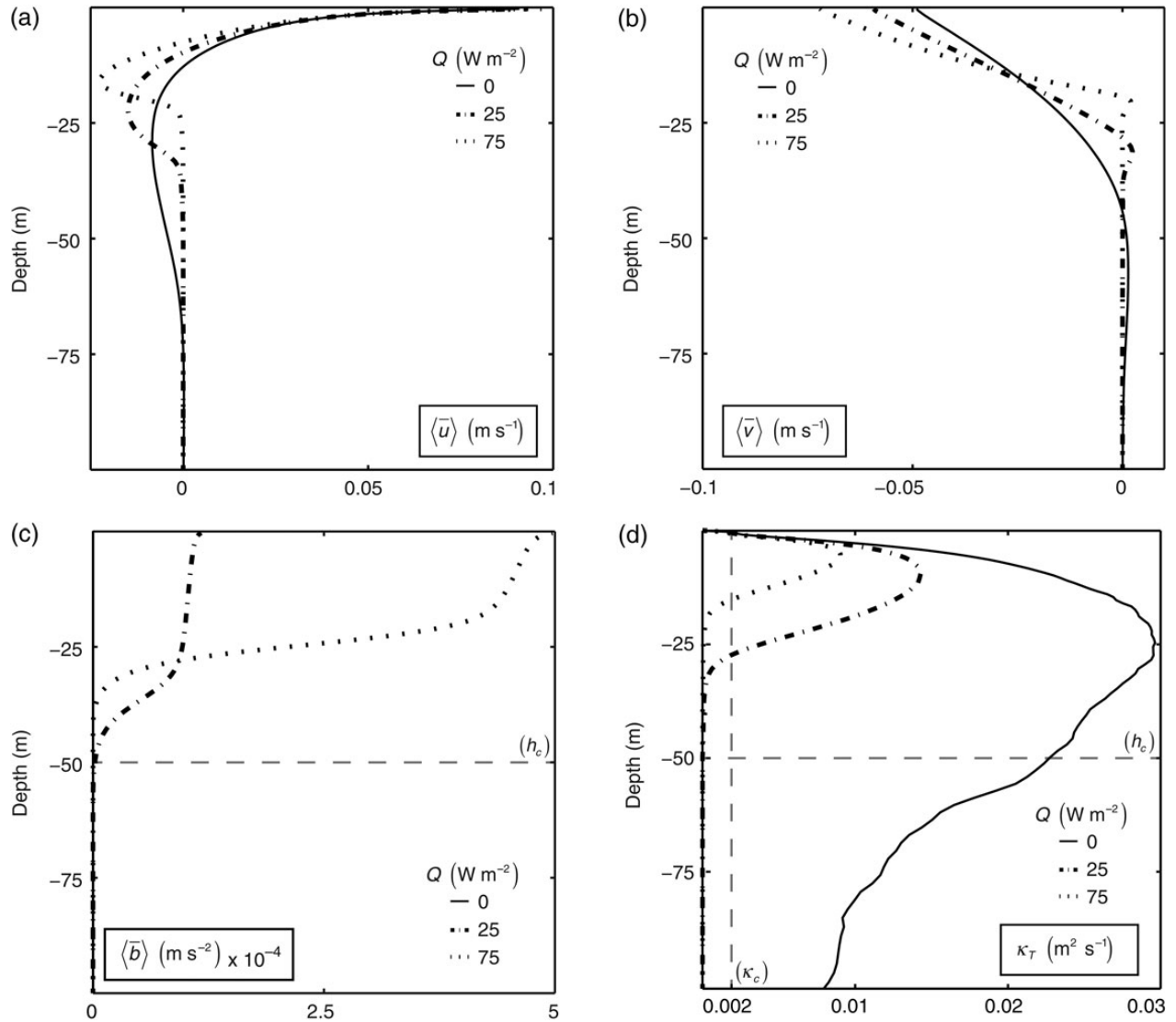


Figure 2. Profiles of the resolved mean velocities, (a) $\langle \bar{u} \rangle$ and (b) $\langle \bar{v} \rangle$, (c) buoyancy, $\langle \bar{b} \rangle$, and (d) total turbulent diffusivity, κ_T , from the LES with $\tau_{\text{wind}} = 0.08$ Pa and $Q_0 = 0, 25$, and 75 W m^{-2} . Profiles are averaged from $t = 0$ to $t = 8$ d. For these cases, the critical depth, h_c , is 50 m, and the critical diffusivity, κ_c , is 0.002 $\text{m}^2 \text{s}^{-1}$.

than the Kara *et al.* (2000) mixed layer depth criterion. Similarly, other methods to find the mixed layer depth (e.g. Holte and Talley, 2009) would also classify our full domain as the mixed layer.

Profiles of the turbulent diffusivity of phytoplankton, κ_T , shown in Figure 2d, highlight how a stabilizing surface heat flux limits the vertical extent of phytoplankton mixing. Here, the turbulent diffusivity is defined as the sum of the mean SGS diffusivity, $\langle \kappa_{\text{SGS}} \rangle$, and the resolved turbulent diffusivity diagnosed from the LES fields:

$$\kappa_T = \frac{\langle \kappa_{\text{SGS}} \rangle - \langle \bar{w} \bar{P} \rangle}{\partial \langle \bar{P} \rangle / \partial z}. \quad (9)$$

For all cases, the SGS diffusivity accounts for less than 10% of the total diffusivity. For the LES here, the largest SGS diffusivity contributions are located near the surface. Additionally, the SGS contribution increases with surface heating since the length scales become smaller. As the level of heating increases, the magnitude of κ_T

decreases and the mixing depth shallows. Note that in the case with $Q_0 = 0$, mixing extends well below the critical depth, $h_c \equiv h_L \mu_0 / m = 50$ m. Taylor and Ferrari (2011b) derived a useful approximate expression for the critical turbulent diffusivity:

$$\kappa_c \simeq \frac{h_c^2}{m} (\mu_0 - m)^2. \quad (10)$$

In all three cases shown in Figure 2d, the maximum turbulent diffusivity is larger than the critical turbulent diffusivity, $\kappa_c \simeq 0.002$ $\text{m}^2 \text{s}^{-1}$.

Figure 3 shows a three-dimensional snapshot of the phytoplankton concentration for the simulation with $\tau_{\text{wind}} = 0.08$ Pa and $Q_0 = 5$ W m^{-2} . In this case, the phytoplankton are largely confined to the warm layer near the surface, although three-dimensional fluctuations in the phytoplankton concentration are still clearly visible. The level of variability in the three-dimensional phytoplankton concentration at each depth can be quantified with the horizontal variance, shown in Figure 4. Here, the square root of the variance is

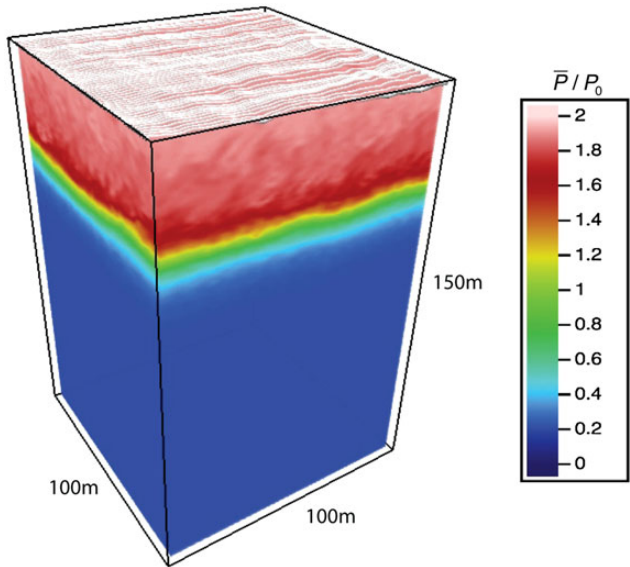


Figure 3. Resolved phytoplankton concentration from the LES simulation with $\tau_{\text{wind}} = 0.08$ Pa and $Q_0 = 5$ W m⁻². Phytoplankton concentrations are normalized by P_0 , the initial phytoplankton concentration at $t = 0$ d. White lines show instantaneous streaklines at the sea surface. In this simulation, the phytoplankton concentration is highly confined to a relatively thin mixing layer, although fluctuations in the phytoplankton concentration are still visible within the mixing layer itself.

normalized by the local mean concentration to aid comparison between the cases. Without heating, fluctuations in the phytoplankton concentration are relatively small. The normalized variance in this case increases somewhat with depth, although this is partly a reflection of a decrease in the mean concentration with depth. With surface heating, the normalized phytoplankton variance is large at the base of the active mixing layer.

Figure 5 shows the evolution of the horizontally averaged phytoplankton concentration as a function of depth for the three simulations shown in Figure 2d. Profiles are at $t = 0, 2, 4, 6, 8$ d. For these cases, the critical depth, h_c , is 50 m, and the corresponding e -folding depth associated with light penetration, h_L , is 5 m. The suppression of turbulent mixing and the restriction of the mixing depth cause a regime change in the phytoplankton response. In the case with $Q_0 = 0$, the phytoplankton concentration decreases in time at all depths and the concentration is modestly surface-intensified. The lack of a bloom is consistent with strong mixing with $\kappa_T > \kappa_c$ over a layer deeper than the critical depth. In contrast, the cases with a positive surface heat flux exhibit phytoplankton growth.

In the positive surface heat flux cases shown in Figure 5, the mixing depths inferred from the vertical phytoplankton flux profiles are shallower than the critical depth, and the mixing depths clearly delineate regions of high and low phytoplankton concentration. The simulations with $h_c = 100$ and $h_L = 10$ m show comparable behaviour to the simulations with $h_c = 50$ and $h_L = 5$ m; If the windstress is above a critical threshold, phytoplankton cell concentration decays over time. Additional surface heating may suppress the turbulence and allow phytoplankton cell concentration to increase.

To quantify the mixing depth from the LES, we calculate the depth at which the vertical phytoplankton flux is less than 5% of the maximum vertical phytoplankton flux, $\langle w'P' \rangle / \langle w'P' \rangle_{\text{max}} = 0.05$.

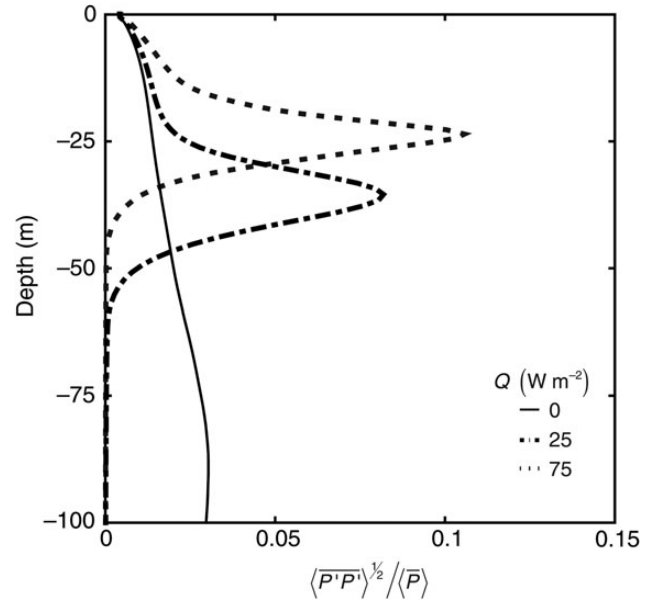


Figure 4. Profiles of the ratio of the square root of the averaged phytoplankton concentration variance to mean phytoplankton concentration, $\langle P'P' \rangle^{1/2} / \langle \bar{P} \rangle$ from the LES with $\tau_{\text{wind}} = 0.08$ Pa and $Q_0 = 0$ W m⁻². Profiles are averaged from $t = 0$ to $t = 8$ d. For this case, the critical depth, h_c is 50 m.

The mixing depth diagnosed from the LES using this threshold allows us to identify the influence of mixing depth on bloom initiation. Figure 6 displays the calculated mixing depths as a function of surface windstress and heat flux for $h_L = 5$, $h_c = 50$ m (a) and $h_L = 10$, $h_c = 100$ m (b). As the windstress increases the mixing depth increases. For a given windstress, the mixing depth decreases with additional surface heating. Filled symbols in Figure 6 indicate simulations with positive net phytoplankton growth. Net growth occurs where the mixing depth is shallower than the critical depth, consistent with the critical depth hypothesis if the mixing depth is used instead of the mixed layer depth.

The mixing depth diagnosed from the LES output can also be used to quantify the net phytoplankton growth rates. The evolution of the depth-averaged phytoplankton concentration from the LES for all cases with $h_L = 5$ m (corresponding to $h_c = 50$ m) is shown in Figure 7. Here, the phytoplankton concentration was averaged over horizontal planes and within the diagnosed mixing depth and normalized by the initial concentration:

$$P_{\text{avg},t} = -\frac{1}{L} \int_{-L}^0 \frac{\langle \bar{P} \rangle}{P_0} dz, \quad (11)$$

where L is the mixing depth diagnosed from the LES using the method described above. For all cases shown with $Q_0 = 0$, the depth-averaged phytoplankton concentration decreases in time. On the other hand, sufficiently large surface heat fluxes can lead to net growth (Figure 7b).

The net phytoplankton growth rates from the LES can be calculated from the depth-averaged phytoplankton concentration:

$$\sigma = \ln \frac{P_{\text{avg},t_2} / P_{\text{avg},t_1}}{t_2 - t_1}. \quad (12)$$

We calculate the exponential growth rates using $P_{\text{avg},t}$ at $t_1 = 4$ and $t_2 = 8$ d and plot them for all cases in Figure 8. Increasing the

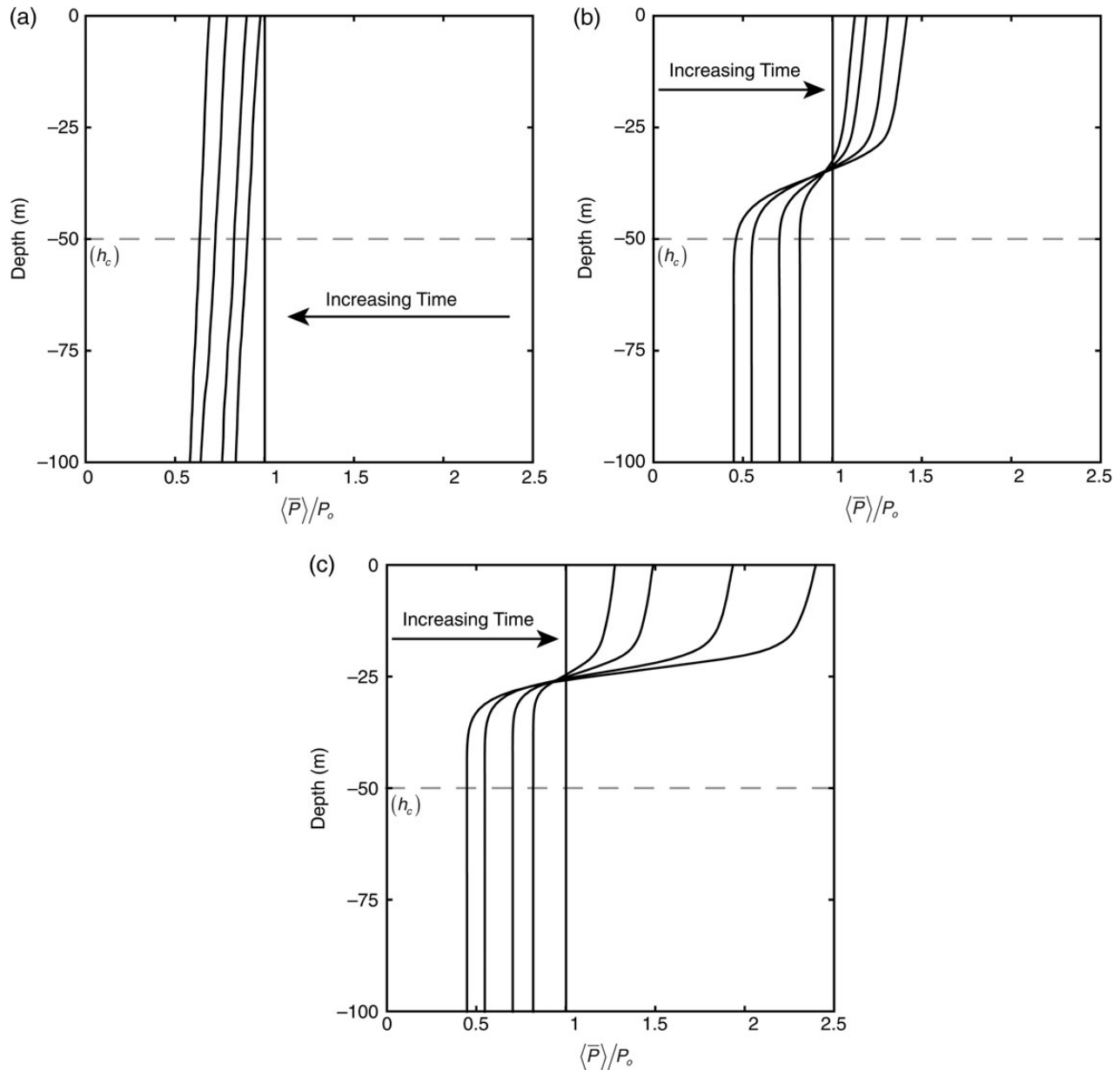


Figure 5. Profiles of the resolved mean phytoplankton cell concentration, $\langle \bar{P} \rangle / P_0$, at $t = 0, 2, 4, 6,$ and 8 d from the LES with $\tau_{\text{wind}} = 0.08 \text{ Pa}$ and (a) $Q_0 = 0 \text{ W m}^{-2}$, (b) $Q_0 = 25 \text{ W m}^{-2}$, and (c) $Q_0 = 75 \text{ W m}^{-2}$. Phytoplankton concentrations are normalized by P_0 , the initial phytoplankton concentration at $t = 0 \text{ d}$. The critical depth, h_c , is 50 m , and the corresponding e -folding depth associated with light penetration, h_e , is 5 m for these simulations.

surface windstress leads to slightly lower growth rates, whereas increasing the surface heat flux leads to higher growth rates. If the resulting growth rate is positive, it is classified as growth, and negative if otherwise. Additionally, Figure 6 shows that there is growth when the mixing depths are shallower than the critical depth and decay if the mixing depth is greater than the critical depth.

Analytical phytoplankton concentration model

Although the LES simulates the response of phytoplankton to wind-driven turbulence and surface heating, the computations are

expensive, which limits our ability to explore the influence of various parameters. In this section, we will develop an analytical model for the phytoplankton concentration in a heated, wind-driven Ekman layer using a method similar to that described in Taylor and Ferrari (2011b). The analytical model will be used to derive approximate expressions for the critical windstress and critical surface heat flux in terms of other physical and biological parameters. In this section, we will first introduce the form of the analytical model, then describe parameterizations for the mixing depth and turbulent diffusivity for the wind-driven and surface-heated cases. Results of the new model are described in the “Results from the analytical model” section.

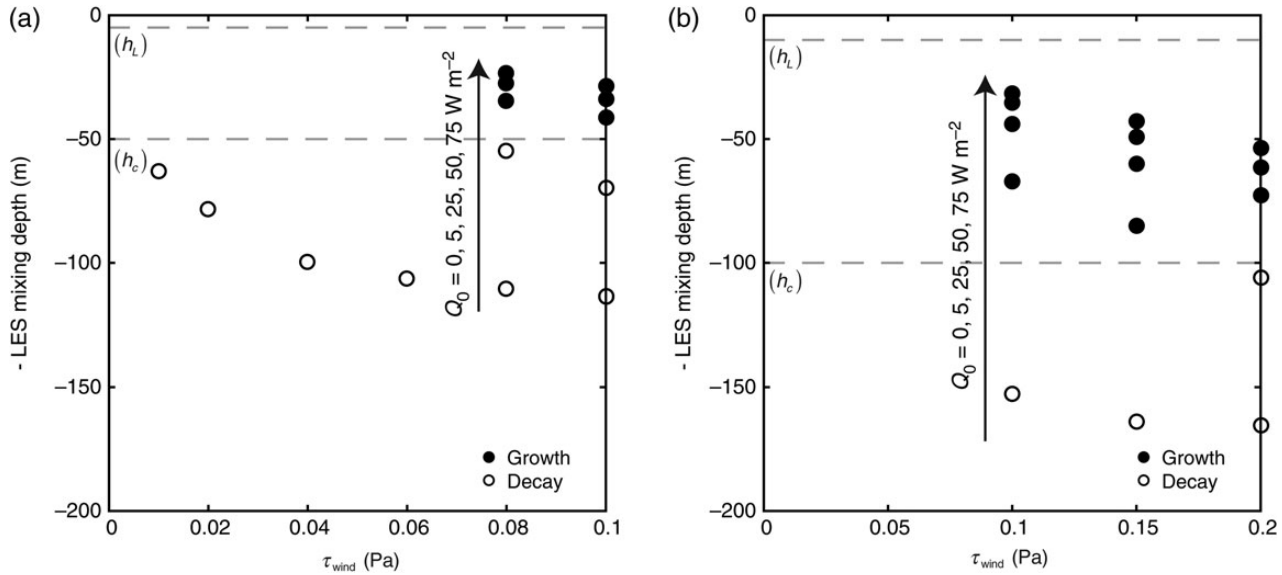


Figure 6. LES mixing depths as a function of the surface windstress for (a) $h_c = 50$ m ($h_L = 5$ m) and (b) $h_c = 100$ m ($h_L = 10$ m). The surface heat flux varied from 0 to 75 W m^{-2} . For a given windstress, increasing the surface heat flux leads to shallower mixing depths. The light e -folding depth, h_L , and the critical depth, h_c , are indicated with grey dashed lines. Filled circles symbolize an LES exhibits phytoplankton growth and empty circles symbolize an LES exhibits phytoplankton decay.

Following Taylor and Ferrari (2011b), we begin by averaging the three-dimensional phytoplankton concentration equation [Equation (3)] across horizontal planes to obtain:

$$\frac{\partial}{\partial t} P(z, t) = (\mu(z) - m)P(z, t) + \tilde{\kappa}_T \frac{d^2}{dz^2} P(z, t), \quad (13)$$

where $P(z, t)$ is the horizontally averaged phytoplankton concentration, and $\tilde{\kappa}_T$ represents mixing by resolved and SGS turbulence. Here, a uniform turbulent diffusivity profile is used and is symbolised by $\tilde{\kappa}_T$ to distinguish it from the turbulent diffusivity diagnosed from the LES, κ_T . Next, we seek exponentially growing/decaying solutions of the form $P(z, t) = \hat{P}(z)e^{\sigma t}$, in which σ is the net phytoplankton growth rate. Using this ansatz results in the following eigenvalue problem:

$$\sigma P(z, t) = (\mu(z) - m)\hat{P}(z) + \tilde{\kappa}_T \frac{d^2}{dz^2} \hat{P}(z). \quad (14)$$

Solving Equation (14) yields a set of eigenvalues, σ_n , and corresponding eigenvectors, \hat{P}_n . The evolution of an arbitrary initial profile can then be expressed as a linear combination of the eigenvectors:

$$P(z, t) = \sum_n A_n^0 e^{\sigma_n t} \hat{P}_n(z), \quad (15)$$

with the coefficients, A_n^0 , chosen to match the initial conditions.

For a given set of parameters, we can compute the corresponding eigenvalues and eigenvectors with a uniform turbulent diffusivity profile within the mixing depth, L , and with no phytoplankton flux boundary conditions at $z = 0$ and $z = -L$. Under bloom conditions, when the phytoplankton population grows exponentially, we expect the most rapidly growing mode to dominate so that the growth rate eventually asymptotes to the largest eigenvalue,

$\sigma \rightarrow \max(\sigma_n)$, regardless of the initial condition. If the largest growth rate is positive, $\max(\sigma_n) > 0$, a bloom may develop under the specified conditions. However, before we can interpret the dependence of the results on surface forcing, we need to develop formulations for the mixing depth, L , and the turbulent diffusivity, $\tilde{\kappa}_T$, as functions of the surface windstress and the heat flux.

Mixing depth and turbulent diffusivity scales

To express the mixing depth in terms of the surface forcing, we adapt the following form from Zilitinkevich and Baklanov (2002), which includes the effects of surface stress and a stabilizing surface buoyancy flux:

$$\frac{1}{L^2} = \frac{f^2}{(C_1 u_*^2)^2} + \frac{f B_0}{(C_2 u_*^2)^2}, \quad \text{for } B_0 \geq 0. \quad (16)$$

Where C_1 and C_2 are prescribed constants, f the Coriolis parameter, $u_* \equiv (\tau_{\text{wind}}/\rho_o)^{1/2}$ the friction velocity, and B_0 the surface buoyancy flux. Note that an increase in windstress will result in an increase in u^* and hence an increase in the mixing depth, L . Conversely, as the magnitude of the surface heat and buoyancy flux increase, the mixing depth will shallow.

The formulation in Equation (16) effectively interpolates between the turbulent Ekman depth, $\delta_{\text{Ekman}} = u^*/f$, seen in the first term on the right hand side of Equation (16), and the depth of a stable boundary layer affected by a surface buoyancy flux and rotation, $\delta_{\text{SBL}} = u_*^2/(fB_0)^{1/2}$ (Zilitinkevich, 1972), represented through the second term on the right hand side of Equation (16). Brody and Lozier (2014) specify separate and discontinuous mixing depths for small heat fluxes and large heat fluxes, whereas Equation (16) provides a continuous formulation for the mixing depth that is applicable from neutral to strongly stable regimes.

Recall from Figure 2d that the turbulent diffusivity and mixing depth both depend on the surface forcing. This distinguishes the

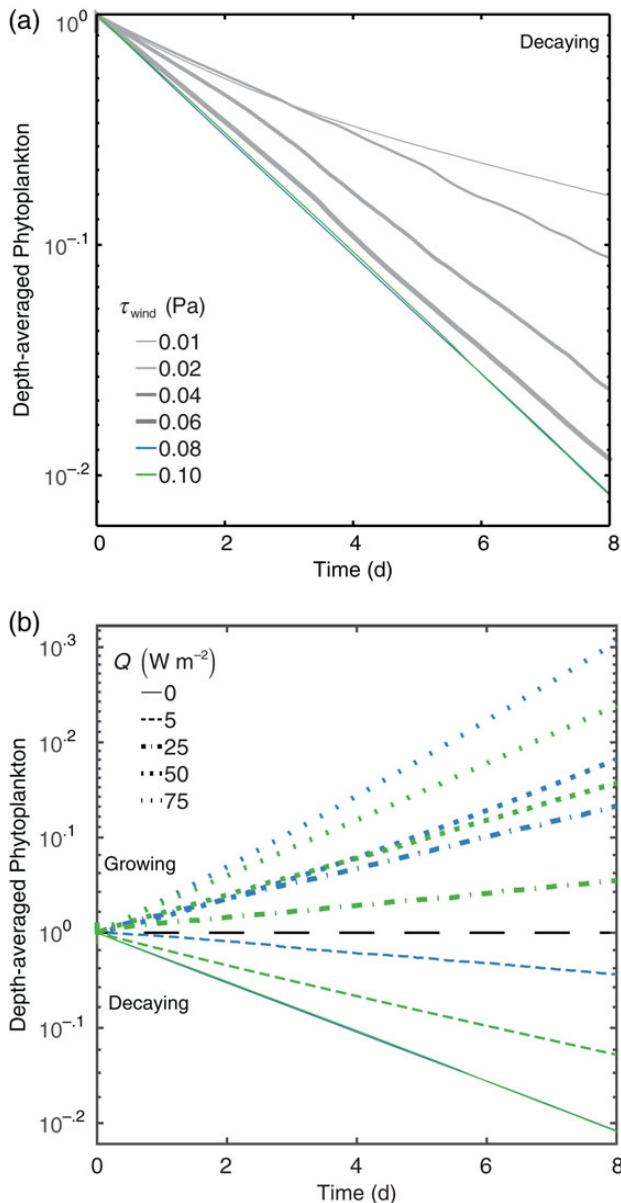


Figure 7. The evolution of the LES depth-averaged phytoplankton cell concentration within the mixing depth, L , normalized by the initial concentration, P_0 . Cases at various (a) surface windstresses, τ_{wind} , with $Q_0 = 0$ and (b) surface heat fluxes, Q_0 , are shown with the varying τ_{wind} shown in (a). Linestyles differentiate the values of Q_0 whereas colours distinguish the values of τ_{wind} . The plots shown are for the cases with $h_c = 50$ m (corresponding to $h_L = 5$ m).

dynamics of a heated, wind-forced boundary layer from scenarios considered in previous studies. For example, in considering thermal convection, Taylor and Ferrari (2011b) found that turbulence extends throughout the existing mixed layer, and varying the magnitude of the surface cooling influenced the intensity but not the depth of mixing. Here, we seek to develop a formulation for the turbulent diffusivity that captures the inter-dependence of the mixing depth and mixing intensity for the heated, wind-forced boundary layer.

To formulate a scaling for the turbulent diffusivity, $\tilde{\kappa}_T$, we use standard mixing length theory (e.g. Wyngaard, 2010). First, we

define the eddy turnover time, $\tau = d/v$, using a characteristic turbulent length scale, d , and velocity scale, v . We assume that turbulence is generated by the surface windstress, in which case the friction velocity, u^* , provides a characteristic turbulent velocity scale. We further assume that the largest turbulent motions dominate mixing and that their size scales with the mixing depth such that $d = L$ and $\tau = L/u^*$. On dimensional grounds, the turbulent diffusivity will then scale with $\tilde{\kappa}_T \sim L^2/\tau$, or

$$\tilde{\kappa}_T = C_3 u_* L. \quad (17)$$

Three coefficients, C_1 , C_2 , and C_3 , are then needed to relate the mixing depth and turbulent diffusivity to the surface forcing. To determine the values of these coefficients, we use turbulent diffusivity profiles diagnosed from the LES. The coefficients are selected to produce a uniform $\tilde{\kappa}_T$ that best represents κ_T for a range of τ_{wind} and Q_0 . Specifically, C_1 and C_2 are first chosen to produce the best collapse of the κ_T profiles. Then, C_3 is chosen so that the uniform $\tilde{\kappa}_T$ is representative of a depth-averaged κ_T .

Figure 9 shows the profiles of the normalized turbulent diffusivity, $\kappa_T^* = \kappa_T/(u_* L)$, plotted against the normalized depth, z/L , for the wind-only cases (Figure 9a) and the cases with surface heating (Figure 9b). In this figure, the approximate corresponding wind-speed at 10 m above the sea surface for each windstress value is given for reference. Values are approximated with $\tau_{\text{wind}} = \rho_{\text{air}} C_D U_{10}^2$, where $\rho_{\text{air}} = 1.3 \text{ kg m}^{-3}$ is air density, and $C_D = 0.0013$ is the drag coefficient. These figures represent our choice of the pair of C_1 and C_2 that best collapse the κ_T^* profiles for all the cases, using the suggested range of $C_2 = 0.51 \pm 0.06$ (Zilitinkevich *et al.*, 2007). Setting $C_1 = 1$ and $C_2 = 0.57$ minimizes the error between all the κ_T^* profiles. We choose not to set C_1 based solely on the mixing depth of the wind-only simulations since there is a large spread in the resulting value of C_1 . If the mixing depths of the wind-only simulations are used, the average value of C_1 is 1.45 with a standard deviation of 0.29. As seen in Figure 9b, the turbulent diffusivity profiles collapse well when normalized by u^* and L for all cases with $Q_0 \neq 0$. After selecting C_1 and C_2 , we average the κ_T profiles from $z = 0$ to $z = -L$ and arrive at $C_3 = 0.02$, which is shown as vertical lines in Figure 9. Values of the analytical model coefficients used in this study are summarized in Table 3. Using a uniform diffusivity profile may affect the mean growth rates. The growth rates from the analytical solution are compared with LES results in the Appendix.

Comparing the normalized turbulent diffusivity profiles in Figure 9a and b, it is worth noting that the turbulent diffusivity extends deeper in the cases with $Q_0 = 0$ than in the cases with surface heating. We are unable to identify a set of coefficients C_1 , C_2 , and C_3 that produce the same mixing depth in the heated and unheated cases. We believe that this discrepancy is due to the development of a stable stratification at the base of the mixing layer in the heated cases, as seen in Figure 2c. This stable stratification inhibits mixing and somewhat reduces the mixing depth in cases with $Q_0 > 0$. It would be possible to explicitly include the effects of stratification (e.g. Zilitinkevich and Baklanov, 2002), but this would require solving an additional prognostic equation for the buoyancy. In an effort to keep the analytical model as simple as possible, our formulation depends only on the surface forcing. As will be shown in the next section, the analytical model produces an excellent agreement with the LES when $Q_0 > 0$, although when $Q_0 = 0$, the analytical model underestimates the mixing depth and consequently, overestimates the phytoplankton growth rate.

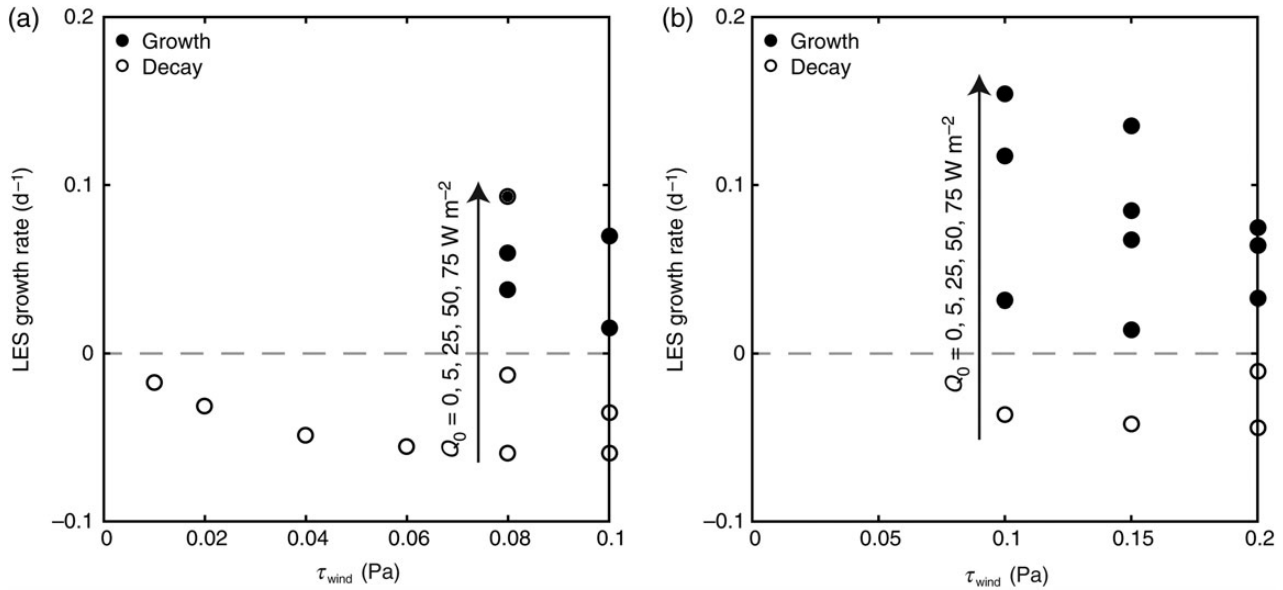


Figure 8. LES growth rates as a function of the surface windstress for (a) $h_c = 50$ m ($h_L = 5$ m) and (b) $h_c = 100$ m ($h_L = 10$ m). The surface heat flux varied from 0 to 75 W m^{-2} . For a given windstress, increasing the surface heat flux leads to higher growth rates. The grey dashed lines indicate zero growth. Filled circles symbolize an LES exhibits phytoplankton growth and empty circles symbolize an LES exhibits phytoplankton decay.

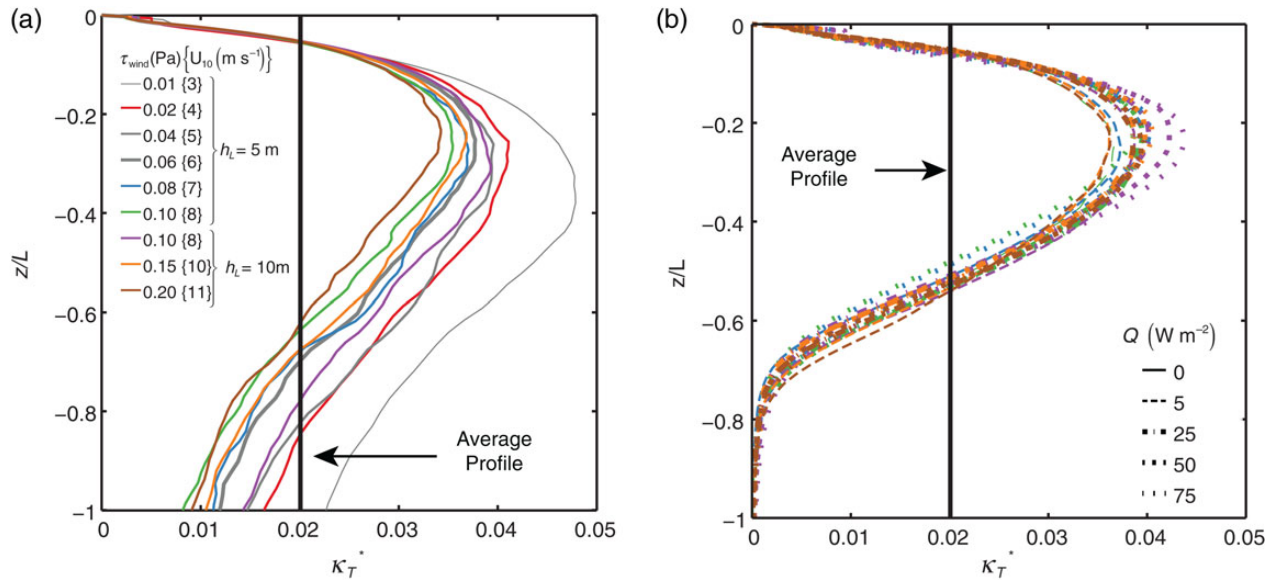


Figure 9. Normalized turbulent diffusivity profiles, $\kappa_T^* = \kappa_T / (u * L)$, diagnosed from the LES for various windstress, τ_{wind} , and surface heat flux, Q_0 . Panel (a) shows cases with $Q_0 = 0$, and panel (b) shows profiles for various positive surface heat fluxes. Vertical lines indicate the average turbulent diffusivity from all the LES, which is used to acquire the coefficient C_3 for a uniform phytoplankton diffusivity model Equation (17). The corresponding wind at 10 m above the sea surface, U_{10} , is written next to the windstress values. Values are approximated with $\tau_{wind} = \rho_{air} C_D U_{10}^2$, where $\rho_{air} = 1.3 \text{ kg m}^{-3}$ is air density, and $C_D = 0.0013$ is the drag coefficient.

Results from the analytical model

In this section, we describe the predictions of the analytical model and compare the results with the LES and the critical depth and critical hypotheses. We solve Equation (14) using the formulation for the mixing depth and turbulent diffusivity described in the previous section. For comparison, we will start with the same biological

Table 3. Non-dimensional parameters for the mixing depth and vertical phytoplankton diffusivity model.

Parameter	Value
C_1	1.0
C_2	0.57
C_3	0.02

parameters as the LES, although the analytical model allows us to explore a much wider range of physical forcing and to derive expressions for the critical heat flux and critical windstress. Details of the parameter space used for the analytical model are in Table 4. In the first part of this section, we apply the same biological parameter values as in the LES, but use a wider range of surface windstress and heat flux. The sensitivity analysis that follows varies the biological parameters μ_0 and h_L , in addition to the wider range of surface windstress and heat flux.

Table 4. Parameters for the analytical model that complement the LES.

Δ_z (m)	μ_0 (d^{-1})	h_L (m)	Chl ($mg\ m^{-3}$)	h_c (m)	τ_{wind} (Pa)	Q_0 ($W\ m^{-2}$)
0.1	1	5	4	50	0.001–0.1	0–100
0.1	1	10	0.2	100	0.001–0.4	0–100
0.1	0.5	5	4	25	0.001–0.1	0–100
0.1	0.5	10	0.2	50	0.001–0.4	0–100
0.1	0.5	15	0.05	75	0.001–1.0	0–100
0.1	1	5	4	50	0.001–0.1	0–100
0.1	1	10	0.2	100	0.001–0.4	0–100
0.1	1	15	0.05	150	0.001–1.0	0–100
0.1	1.5	5	4	75	0.001–0.1	0–100
0.1	1.5	10	0.2	150	0.001–0.4	0–100
0.1	1.5	15	0.05	225	0.001–1.0	0–100

Varying parameters for simulations include the maximum growth rate, μ_0 , light limiting depth, h_L , the critical depth, h_c , the windstress, τ_{wind} , and the surface heat flux, Q_0 . The corresponding chlorophyll (Chl) concentration for each h_L value is noted in the table. The windstress is described as a range with a spacing of 0.001 Pa. The surface heat flux also covers a range. The spacing used is $5\ W\ m^{-2}$. The simulations in the top section are compared directly with LES results. The simulations on the bottom section are used for testing the sensitivity of μ_0 and h_L on the solution.

The resulting normalized net growth rate from the analytical model, $\sigma^* = \max(\sigma_n/m)$, is shown as a function of surface windstress and surface heat flux in Figures 10 and 11. The $\sigma^* = 0$ curve separates growing and decaying solutions and indicates the critical windstress for a given heat flux. In general, the normalized growth curves show that increasing the surface windstress leads to slower growth rates and that increasing surface heating promotes faster growth, as expected. Figure 10 shows contours of the growth rate for $h_c = 50\ m$ (corresponding to $h_L = 5\ m$), whereas Figure 11 uses $h_c = 100\ m$ (corresponding to $h_L = 10\ m$). When $Q_0 = 0$, the model predicts a critical windstress of $\sim 0.03\ Pa$ when $h_L = 5\ m$, whereas a higher critical windstress ($\sim 0.13\ Pa$) is predicted when $h_L = 10\ m$.

For comparison, symbols also indicate whether a specific LES exhibited growth (filled circle) or decay (open square) of phytoplankton concentration averaged over L for a given surface windstress and a heat flux. In general, the $\sigma^* = 0$ contour predicted from the analytical model delineates the growing and decaying cases from the LES. However, when $Q_0 = 0$, the critical windstress is somewhat overpredicted by the model.

One interpretation of the critical depth hypothesis is that net phytoplankton growth should occur when the mixing depth is shallower than the critical depth. When the mixing depth is equal to the critical depth, $L = h_c$, no growth should occur. We can evaluate this hypothesis using the analytical model which includes the effects of limited turbulent mixing by comparing the $L = h_c$ contour with the $\sigma^* = 0$ contour, as shown in Figure 10a. In this case, the critical depth is $h_c = 50\ m$, and indeed, the $L = 50\ m$ contour follows the $\sigma^* = 0$ contour relatively closely. The discrepancy between the two can largely be explained by the slight overestimate of the mixing depth in the cases with $Q \neq 0$. Similarly, the $L = 100\ m$ contour closely coincides with the zero growth rate contour for the case $h_c = 100\ m$ (Figure 11a).

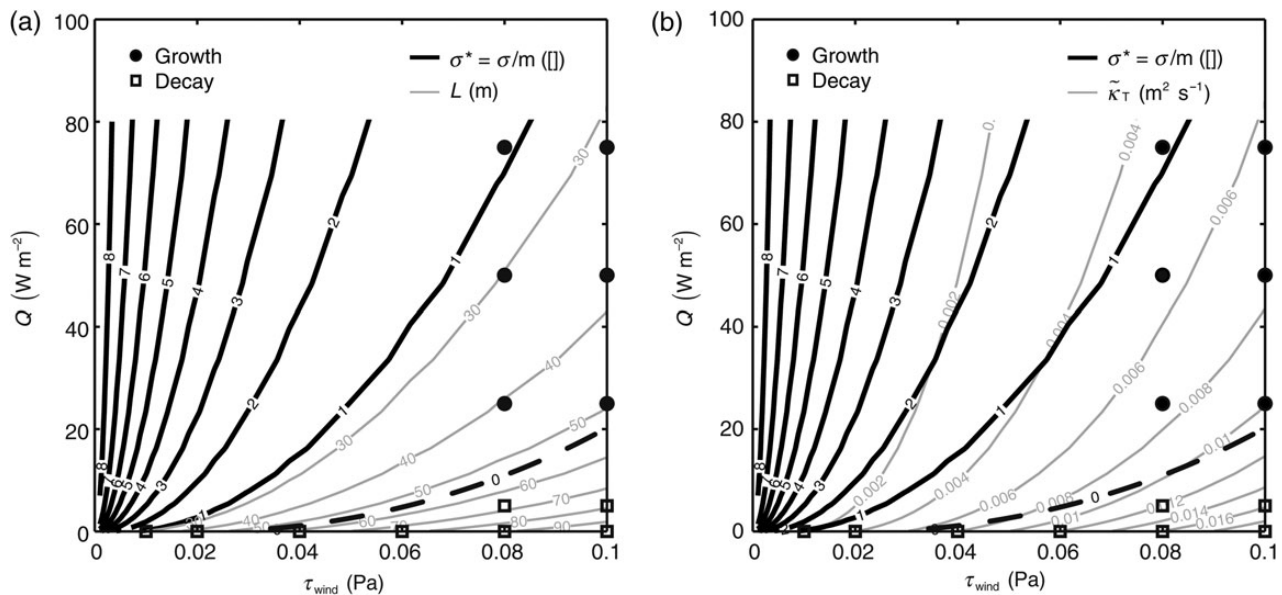


Figure 10. Normalized net growth rate, $\sigma^* \equiv \sigma/m$, curves from the analytical model as a function of the surface windstress, τ_{wind} , and surface heating, Q_0 , with a critical depth, h_c , of 50 m (black). This critical depth corresponds to $h_L = 5\ m$. The zero growth curve (dashed black lines) indicates the boundary between phytoplankton cell concentration growth and decay. The resulting growth (filled circle) or decay (open square) of phytoplankton cell concentration averaged over L from the LES is also shown. Contours of mixing depth, L (a), and phytoplankton turbulent diffusivity, $\tilde{\kappa}_T$ (b), are shown in grey.

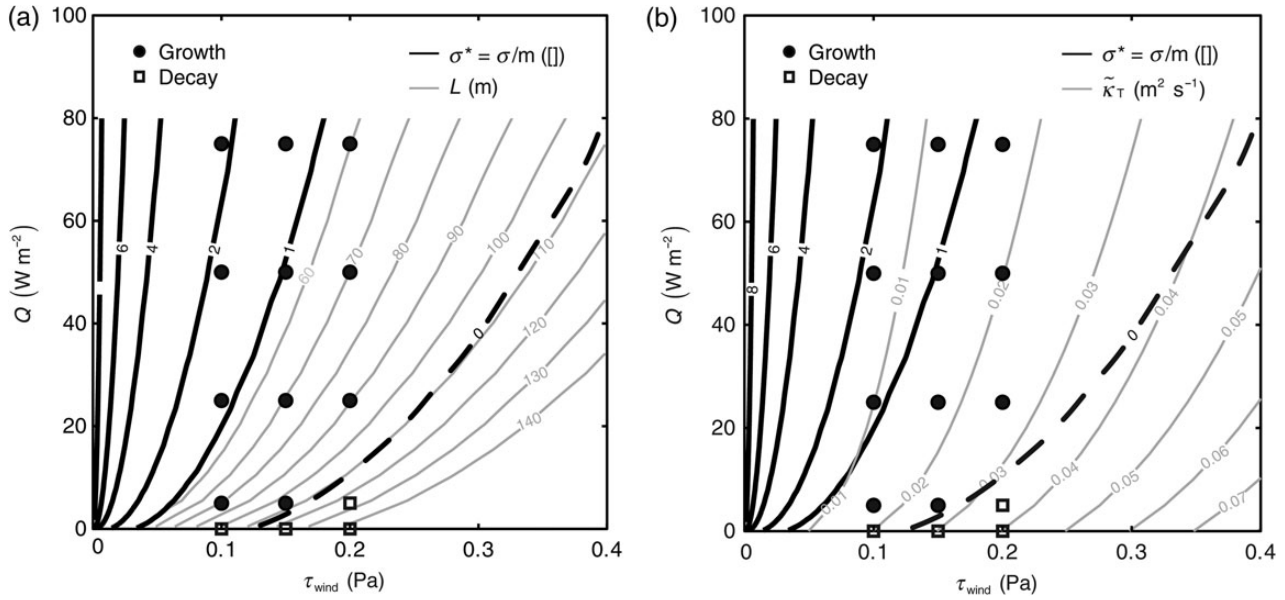


Figure 11. Same as Figure 10 but for $h_c = 100$ m (corresponding to $h_L = 10$ m). The scale of τ_{wind} is larger than Figure 10.

The magnitude of the turbulent diffusivity, estimated using Equations (16) and (17), is shown along with the growth rate contours in Figures 10b and 11b. To evaluate the critical turbulence hypothesis for a heated wind-driven boundary layer, we can compare the $\tilde{\kappa}_T = \kappa_c$ contour to the marginal stability contour ($\sigma^* = 0$). For $h_L = 5$ m, the critical turbulent diffusivity is $\kappa_c = 0.002 \text{ m}^2 \text{ s}^{-1}$, and the $\tilde{\kappa}_T = \kappa_c$ contour intersects the zero heat flux axis at ~ 0.01 Pa, which is less than the critical windstress ~ 0.03 Pa, predicted by the analytical model. For $h_L = 10$ m, the critical turbulent diffusivity is $\kappa_c = 0.009 \text{ m}^2 \text{ s}^{-1}$, and the $\tilde{\kappa}_T = \kappa_c$ contour intersects the zero heat flux axis below the critical windstress ~ 0.13 Pa predicted by the analytical model. When $Q_0 > 0$ the $\tilde{\kappa}_T = \kappa_c$ and $\sigma^* = 0$ contours diverge further, indicating that the critical turbulence becomes less significant with increased surface heating.

Analytical expressions for the critical windstress and the critical heat flux can be obtained by solving Equation (14) for a range of surface windstress and heat flux values. For a given surface windstress or a given surface heat flux, the corresponding critical surface condition can be estimated. To do this, we will use the approximate expression for the critical turbulent diffusivity from Equation (10) and substitute Equations (16) and (17) for the turbulent diffusivity. Without surface heating ($Q_0 = 0$), the critical windstress is

$$\frac{\tau_{\text{crit}}}{\rho_0} = \frac{f}{C_1 C_3} \frac{h_L^2}{m} (\mu_0 - m)^2. \quad (18)$$

When the surface heating and windstress are both non-zero, the analytical solutions are somewhat more complicated. The critical buoyancy flux is

$$B_{\text{crit}} = \left(\frac{\tau_{\text{wind}}}{\rho_0} \right)^3 \frac{C_2^2 C_3^2 m^2}{h_L^4 (\mu_0 - m)^4 f} - \left(\frac{\tau_{\text{wind}}}{\rho_0} \right) \frac{C_2^2 f}{C_1^2}. \quad (19)$$

From this expression, the critical surface heat flux can be calculated using $Q_{\text{crit}} = B_{\text{crit}} c_p \rho_0 / (\alpha g)$, where c_p and α are the heat capacity and thermal expansion coefficient, respectively. It is less simple to isolate an expression for the critical windstress with surface heating which

satisfies the following cubic equation

$$C_3^2 m^2 \frac{\tau_{\text{crit}}}{\rho_0} = h_L^4 (\mu_0 - m)^4 \left(\frac{f^2 \rho_0}{C_1^2 \tau_{\text{crit}}} + \frac{\rho_0^2 f B_0}{C_2^2 \tau_{\text{crit}}^2} \right), \quad (20)$$

where B_0 is the surface buoyancy flux. This equation can be readily solved numerically, but the closed form expression for τ_{crit} is cumbersome. However, we can rewrite Equation (20) in terms of the Ekman layer depth, δ_{Ekman} , and the stable boundary layer depth, δ_{SBL} , defined in the ‘‘Mixing depth and turbulent diffusivity sales’’ section:

$$C_3^2 m^2 \frac{\tau_{\text{crit}}}{\rho_0} = h_L^4 (\mu_0 - m)^4 \left(\frac{1}{C_1^2 \delta_{\text{Ekman}}^2} + \frac{1}{C_2^2 \delta_{\text{SBL}}^2} \right). \quad (21)$$

Although δ_{Ekman} and δ_{SBL} both depend implicitly on the windstress, we can examine limits when one is much smaller than the other. When surface heating is small and $\delta_{\text{Ekman}} \ll \delta_{\text{SBL}}$, we recover the expression given in Equation (18). In the other limit, when heating is large enough to confine mixing to a depth much shallower than the Ekman depth, i.e. when $\delta_{\text{SBL}} \ll \delta_{\text{Ekman}}$, the critical windstress is

$$\frac{\tau_{\text{crit}}}{\rho_0} = \left(f B_0 h_L^4 \frac{(\mu_0 - m)^4 C_2^2}{m^2 C_3^2} \right)^{1/3}. \quad (22)$$

Note that large stabilizing surface buoyancy fluxes increase the critical windstress. The critical windstress also depends strongly on h_L , μ_0 , and m .

Numerical solutions of Equation (20) are shown in Figure 12 for various values of the critical depth. Each curve traces out solutions with no net growth as a function of the windstress and the surface heat flux. The figure can therefore be used to find the critical surface heat flux for a given windstress, or conversely the critical windstress for a given surface heat flux. We expand on the simulations presented above by adding an additional value of $h_L + 15$ m and allowing μ_0 to vary from 0.5, 1.0, and 1.5 d^{-1} . This causes the critical depth, h_c , to vary over a wide range from 25 to 225 m. Figure 12 shows that as the critical depth increases, the critical

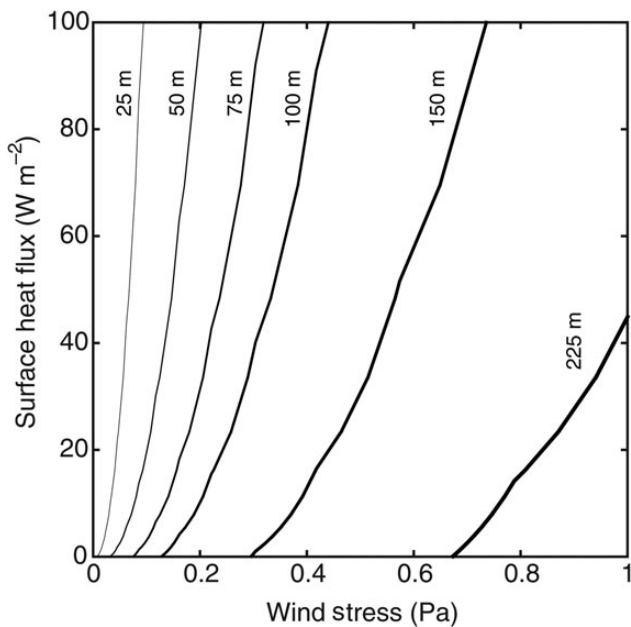


Figure 12. Normalized analytical critical growth, σ^* , curves as a function of the surface windstress and surface heat fluxes. These curves represent the sensitivity of the critical growth curve to the critical depth, $h_c = h_L(\mu_0/m)$. Each curve represents a solution for a given critical depth, which results from varying $\mu_0 = 0.5, 1, \text{ and } 1.5 \text{ d}^{-1}$ and the e -folding depth associated with light penetration, $h_L = 5, 10, \text{ and } 15 \text{ m}$. The loss rate, m , is constant and is set to 0.1 d^{-1} . From right to left, the critical depths increase from 25 to 225 m, indicating that a higher critical depth requires a higher critical windstress for a given heat flux.

growth curve shifts towards higher windstresses and lower surface heat fluxes. In other words, a larger critical depth requires a stronger wind to suppress a bloom.

Discussion and conclusions

In this paper, LES were used to study the response of phytoplankton to wind-driven mixing and surface heating. Results from a series of LES runs forced with various constant values of the windstress and surface heat flux were used to develop parameterizations for the mixing depth and turbulent diffusivity and assess the analytical model that was based on these parameterizations. We then presented analytical solutions to extend the LES results to a wider range of parameter values and obtained expressions for the critical windstress and the critical heat flux in terms of other physical and biological parameters.

The LES results indicate that the depth and intensity of mixing are each capable of influencing phytoplankton growth. In the absence of positive heating averaged over a day, net phytoplankton growth occurs in the LES when the windstress is below a critical threshold. The LES results agree with the critical depth hypothesis; phytoplankton growth occurs when the mixing depth first becomes shallower than the critical depth. In this case, wind-driven mixing maintains a relatively uniform phytoplankton concentration in the mixing layer, and growth conditions are consistent with the critical depth hypothesis based on the mixing layer depth rather than the mixed layer depth. During this period, there is a decoupling between the mixed and the mixing layer.

The critical windstress predicted by our analytical model depends strongly on the surface heat flux and the critical depth

(Figure 12). In the absence of heating and when the critical depth is relatively small ($h_c \leq 50 \text{ m}$), the critical windstress is very small ($< 0.05 \text{ Pa}$). In this case, very little wind is sufficient to mix phytoplankton out of the euphotic layer and prevent a bloom. This is consistent with the conclusion drawn by Taylor and Ferrari (2011b) who found that very low levels of surface cooling were sufficient to prevent blooms. However, Figure 12 also shows that the critical windstress is highly sensitive to the critical depth. This is a new result and was not seen under convective conditions. Unlike convection which extends throughout the mixed layer, wind-driven mixing cannot extend far below the Ekman layer depth in the absence of surface heat fluxes. Therefore, a large windstress is required to keep phytoplankton cells well-mixed below a deep critical depth. The addition of surface heating strongly restricts the depth of mixing and results in a sharp increase in the critical windstress.

We can interpret the sensitivity of phytoplankton growth to winds and heating using the parameterizations for the mixing depth and turbulent diffusivity introduced in Equations (16) and (17). First, consider a case with no net heat flux ($Q_0 = 0$), where $L \propto u_*^2/f$ and $\kappa_T \propto u_*^2/f$. If the windstress is reduced by an amount $\Delta\tau_{\text{wind}}$, the mixing depth, L , will be reduced by a factor proportional to $\sqrt{\Delta\tau_{\text{wind}}}$, whereas the turbulent diffusivity, κ_T , will decrease by a factor of $\Delta\tau_{\text{wind}}$. Depending on the particular physical and biological conditions, it is therefore possible for κ_T to drop below the critical turbulence threshold before the mixing depth shoals above the critical depth. Conversely, when the mixing depth is strongly influenced by the stabilizing effect of surface heating and $L \propto u_*^2/\sqrt{B_0 f}$, an increase in the surface heat flux will reduce L and κ_T by the same factor. Therefore, if the turbulent diffusivity associated with wind-driven mixing alone is much larger than the critical turbulence threshold, it is unlikely that increasing the surface heating will trigger a bloom through the critical turbulence criterion before the mixing depth shoals above the critical depth.

In an effort to isolate the influence of various physical mechanisms on the timing of the spring bloom, we used a highly simplified phytoplankton model. We neglected several factors that could be important in the timing of the spring bloom, including phytoplankton/zooplankton interactions (Behrenfeld, 2010), nutrient availability (Moore *et al.*, 2006), and eddy-driven restratification (Taylor and Ferrari, 2011a; Mahadevan *et al.*, 2012). The results of our model are therefore best interpreted not as a prediction for the timing of a given bloom event, but rather an indication of the sensitivity of phytoplankton growth to winds and surface heating. Part of the rationale for considering a simplified phytoplankton model is that LES simulations are very costly, which makes exploring a vast parameter space extremely challenging. However, the analytical model that we presented could be expanded to include a more complex biogeochemical model and used to study how a complex ecosystem responds to changes in physical forcing.

Acknowledgements

We thank Stephanie Henson, Marina Lévy, Joan Llorc, and Anna Rumyantseva for their helpful discussions on spring blooms. We would also like to express our gratitude to an anonymous reviewer for the many constructive critiques. This work was supported through a Newton International Fellowship from the Royal Society to RME. JRT was supported by a grant from the Natural Environment Research Council, award NE/J010472/1.

References

- Basu, S., and Porté-Agel, F. 2006. Large-eddy simulation of stably stratified atmospheric boundary layer turbulence: a scale-dependent dynamic modeling approach. *Journal of the Atmospheric Sciences*, 63: 2074–2091.
- Beare, R. J., Macvean, M. K., Holtslag, A. A. M., Cuxart, J., Esau, I., Golaz, J.-C., Jimenez, M. A., *et al.* 2006. An intercomparison of large-eddy simulations of the stable boundary layer. *Boundary-Layer Meteorology*, 118: 247–272.
- Behrenfeld, M. J. 2010. Abandoning Sverdrup's critical depth hypothesis on phytoplankton blooms. *Ecology*, 91: 977–989.
- Boss, E., and Behrenfeld, M. 2010. In situ evaluation of the initiation of the North Atlantic phytoplankton bloom. *Geophysical Research Letters*, 37: 1–5.
- Brainerd, K. E., and Gregg, M. C. 1995. Surface mixed and mixing layer depths. *Deep Sea Research I: Oceanographic Research Papers*, 42: 1521–1543.
- Brody, S. R., and Lozier, M. S. 2014. Changes in dominant mixing length scales as a driver of subpolar phytoplankton bloom initiation in the North Atlantic. *Geophysical Research Letters*, 41: 3197–3203.
- Brody, S. R., Lozier, M. S., and Dunne, J. P. 2013. A comparison of methods to determine phytoplankton bloom initiation. *Journal of Geophysical Research: Oceans*, 118: 2345–2357.
- Broekhuizen, N. 1999. Simulating motile algae using a mixed Eulerian-Lagrangian approach: does motility promote diatom persistence or co-existence with diatoms? *Journal of Plankton Research*, 21: 1191–1216.
- Chiswell, S. M. 2011. Annual cycles and spring blooms in phytoplankton: don't abandon Sverdrup completely. *Marine Ecology Progress Series*, 443: 39–50.
- Cullen, J. J., and Lewis, M. R. 1988. The kinetics of algal photoadaptation in the context of vertical mixing. *Journal of Plankton Research*, 10: 1039–1063.
- Ebert, U., Arrayás, M., Temme, N., Sommeijer, B., and Huisman, J. 2001. Critical conditions for phytoplankton blooms. *Bulletin of Mathematical Biology*, 63: 1095–1124.
- Enriquez, R. M. 2013. Subgrid-scale turbulence modeling for improved large-eddy simulation of the atmospheric boundary layer. PhD Dissertation, Stanford University, 207 pp.
- Ferrari, R., Merrifield, S. T., and Taylor, J. R. 2014. Shutdown of convection triggers increase of surface chlorophyll. *Journal of Marine Systems*. doi:10.1016/j.jmarsys.2014.02.009.
- Gran, H. H., and Braarud, T. 1935. A quantitative study of the phytoplankton in the Bay of Fundy and the Gulf of Maine (including observations on hydrography, chemistry and turbidity). *Journal of the Biological Board of Canada*, 1: 279–467.
- Holte, J., and Talley, L. 2009. A new algorithm for finding mixed layer depths with applications to argo data and subantarctic mode water formation. *Journal of Atmospheric and Oceanic Technology*, 26: 1920–1939.
- Huisman, J., van Oostveen, P., and Weissing, F. 1999. Critical depth and critical turbulence: two different mechanisms for the development of phytoplankton blooms. *Limnology and Oceanography*, 44: 1781–1787.
- Kara, A. B., Rochford, P. A., and Hurlburt, H. E. 2000. An optimal definition for ocean mixed layer depth. *Journal of Geophysical Research*, 105: 16803.
- Kosović, B., and Curry, J. A. 2000. A large eddy simulation study of a quasi-steady, stably stratified atmospheric boundary layer. *Journal of the Atmospheric Sciences*, 57: 1052–1068.
- Lien, R.-C., and Sanford, T. B. 2004. Turbulence spectra and local similarity scaling in a strongly stratified oceanic bottom boundary layer. *Continental Shelf Research*, 24: 375–392.
- Lilly, D. K. 1992. A proposed modification of the Germano subgrid-scale closure method. *Physics of Fluids A*, 4: 633–635.
- Mahadevan, A., D'Asaro, E., Lee, C., and Perry, M. J. 2012. Eddy-driven stratification initiates North Atlantic spring phytoplankton blooms. *Science*, 337: 54–58.
- Mason, P. J., and Derbyshire, S. H. 1990. Large-eddy simulation of the stably-stratified atmospheric boundary layer. *Boundary-Layer Meteorology*, 53 (1–2): 117–162.
- Moore, C. M., Mills, M. M., Milne, A., Langlois, R., Achterberg, E. P., Lochte, K., Geider, R. J., *et al.* 2006. Iron limits primary productivity during spring bloom development in the central North Atlantic. *Global Change Biology*, 12: 626–634.
- Nagai, T., Yamazaki, H., and Kamykowski, D. 2004. A Lagrangian photoresponse model coupled with 2nd-order turbulence closure. *Marine Ecology Progress Series*, 265: 17–30.
- Riley, G. A. 1946. Factors controlling phytoplankton populations on Georges Bank. *Journal of Marine Research*, 6: 54–73.
- Ross, O. N., and Sharples, J. 2004. Recipe for 1-d Lagrangian particle tracking models in space-varying diffusivity. *Limnology and Oceanography: Methods*, 2: 289–302.
- Sverdrup, H. 1953. On conditions for the vernal blooming of phytoplankton. *Journal du Conseil International pour l'Exploration de la Mer*, 18: 287–2985.
- Taylor, J. R. 2008. Numerical simulations of the stratified oceanic bottom boundary layer. PhD Thesis, University of California, San Diego.
- Taylor, J. R., and Ferrari, R. 2010. Buoyancy and wind-driven convection at mixed layer density fronts. *Journal of Physical Oceanography*, 40: 1222–1242.
- Taylor, J. R., and Ferrari, R. 2011a. Ocean fronts trigger high latitude phytoplankton blooms. *Geophysical Research Letters*, 38: 1–5.
- Taylor, J. R., and Ferrari, R. 2011b. Shutdown of turbulent convection as a new criterion for the onset of spring phytoplankton blooms. *Limnology and Oceanography*, 56: 2293–2307.
- Taylor, J. R., and Sarkar, S. 2008. Direct and large eddy simulations of a bottom Ekman layer under an external stratification. *International Journal of Heat and Fluid Flow*, 29: 721–732.
- Townsend, D. W., Cammen, L. M., Holligan, P. M., Campbell, D. E., and Pettigrew, N. R. 1994. Causes and consequences of variability in the timing of spring phytoplankton blooms. *Deep Sea Research I: Oceanographic Research Papers*, 41: 747–765.
- Wyngaard, J. C. 2010. *Turbulence in the Atmosphere*. Cambridge University Press, New York. 393 pp.
- Yamazaki, H., Locke, C., Umlauf, L., Burchard, H., Ishimaru, T., and Kamykowski, D. 2014. A Lagrangian model for phototaxis-induced thin layer formation. *Deep Sea Research II: Topical Studies in Oceanography*, 101: 193–206.
- Zhou, B., and Chow, F. K. 2011. Large-eddy simulation of the stable boundary layer with explicit filtering and reconstruction turbulence modeling. *Journal of the Atmospheric Sciences*, 68: 2142–2155.
- Zhou, B., and Chow, F. K. 2012. Turbulence modeling for the stable atmospheric boundary layer and implications for wind energy. *Flow, Turbulence and Combustion*, 88: 255–277.
- Zikanov, O., Slinn, D. N., and Dhanak, M. R. 2003. Large-eddy simulations of the wind-induced turbulent Ekman layer. *Journal of Fluid Mechanics*, 495: 343–368.
- Zilitinkevich, S., and Baklanov, A. 2002. Diagnostic and prognostic equations for the depth of the stably stratified Ekman boundary layer. *Quarterly Journal of the Royal Meteorological Society*, 128: 25–46.
- Zilitinkevich, S., Esau, I., and Baklanov, A. 2007. Further comments on the equilibrium height of neutral and stable planetary boundary layers. *Quarterly Journal of the Royal Meteorological Society*, 133: 265–271.
- Zilitinkevich, S. S. 1972. On the determination of the height of the Ekman boundary layer. *Boundary-Layer Meteorology*, 3: 141–145.

Appendix

Comparison of LES and analytical model results

In this section, we compare the calculated mixing depth and phytoplankton growth rate results from the LES and analytical model to understand any model biases.

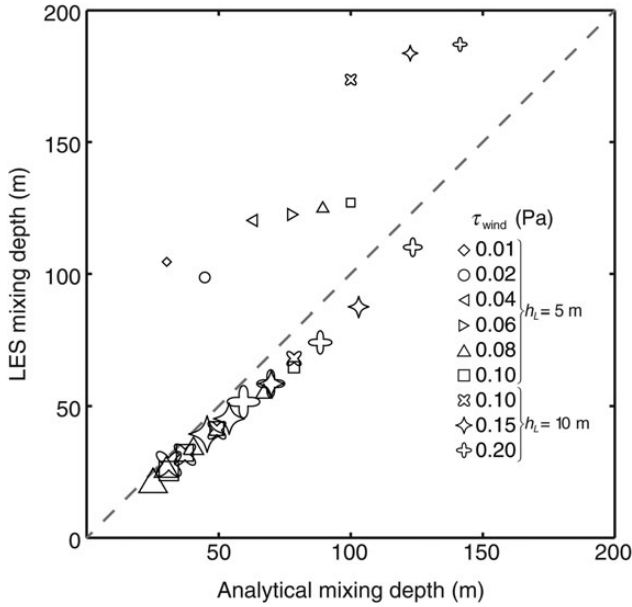


Figure A1. Comparison of mixing depths from LES and analytical solutions for various windstress, τ_{wind} , and surface heating, Q_0 , cases. Symbols depict individual values of τ_{wind} . Larger symbols indicate higher levels of Q_0 .

The values of the mixing depth from the analytical model and the LES are shown in Figure A1. The analytical model underpredicts the mixing depth for the unheated cases and slightly overpredicts the mixing depth for the heated cases. This is because the coefficient C_1 in Equation (16) tended to be higher than the chosen value for the

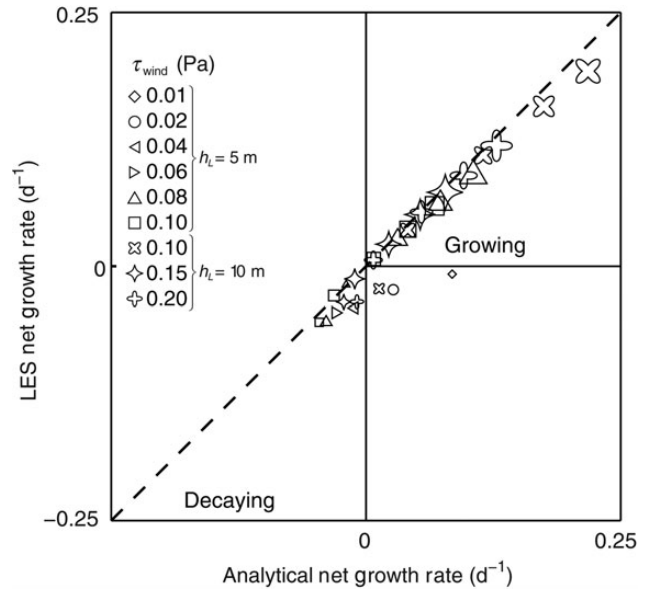


Figure A2. Comparison of net growth rates from LES and analytical solutions for various windstress, τ_{wind} , and surface heating, Q_0 , cases. Symbols depict individual values of τ_{wind} . Larger symbols indicate higher levels of Q_0 .

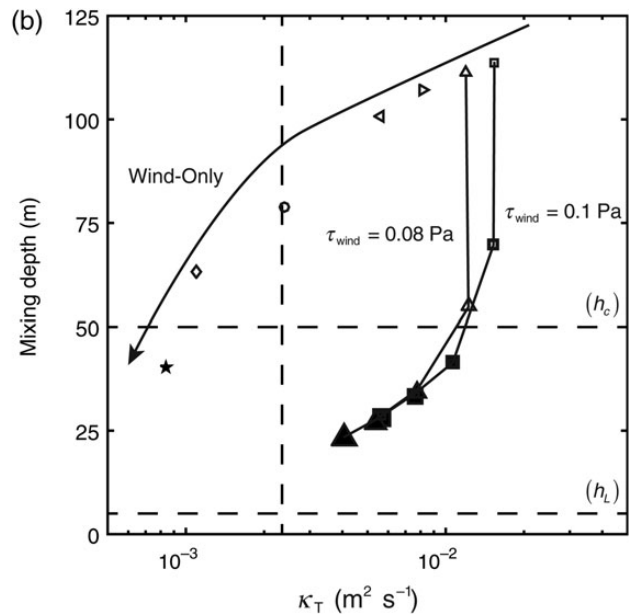
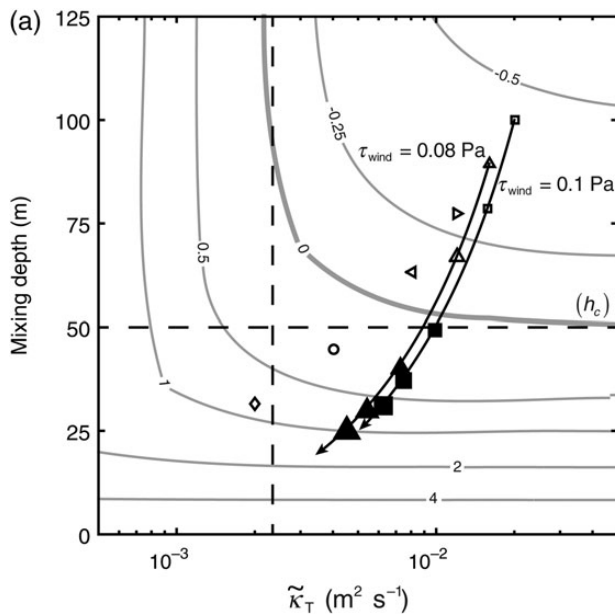


Figure A3. Normalized analytical growth, σ^* , curves (grey) as a function of the turbulent diffusivity, $\tilde{\kappa}_T$, and mixing depth, L (a). Arrows indicate the movement from an unheated case to higher surface heating, Q_0 , cases for a given τ_{wind} . The mixing depth and turbulent diffusivity from the LES are shown in (b). Lines connect the cases with the same τ_{wind} . Dashed lines indicate the critical turbulent diffusivity, κ_c and the critical depth, h_c . Symbols depict individual values of τ_{wind} : star, 0.001 Pa; diamond, 0.01 Pa; circle, 0.02 Pa; left-pointing pointer, 0.04 Pa; right-pointing pointer, 0.06 Pa; triangle, 0.08 Pa; square, 0.10 Pa. Filled symbols correspond to phytoplankton cell concentration growth.

wind-only cases. Rather than using distinct values of the coefficients in the heated and unheated cases, we chose a combination of C_1 and C_2 that led to the smallest standard deviation in the normalized eddy diffusivity profiles across all cases.

Figure A2 shows a comparison of the growth rates from the analytical model and the LES. Overall, the analytical model captures the growth rate inferred from the LES well, although there are some differences, notably in the unheated case with $\tau_{\text{wind}} = 0.01$ Pa. For this case, the model predicts significant phytoplankton growth, but the LES shows weak decay for the period examined, although the growth rates are small in magnitude in both models. The overprediction of the growth rates from the analytical model when $Q_0 = 0$ appears to be due to an underestimate in the mixing depth for these cases.

Figure A3 shows contours of the normalized growth rate from the analytical model (σ^*) as a function of κ_T and L for the cases with $h_L = 5$ m (corresponding to $h_c = 50$ m). The critical turbulent diffusivity and critical depth thresholds are depicted as dashed lines. Symbols indicate the values of the turbulent diffusivity and mixing depth calculated for the analytical model with values of Q and τ_{wind} corresponding to each LES run. Arrows indicate the direction of increasing surface heat flux, Q_0 , for a constant windstress, τ_{wind} . When following along a series with $\tau_{\text{wind}} = 0.08$ or 0.1 Pa, and increasing the surface heat flux, the trajectory crosses the $\sigma^* = 0$ contour when the mixing depth is very close to the critical depth.

The turbulent diffusivity and mixing depth diagnosed directly from the LES with $h_L = 5$ m (corresponding to $h_c = 50$ m) are shown in Figure A3. Comparing Figure A3, it is clear that the model significantly underpredicts L for the cases with $Q_0 = 0$. However, the turbulent diffusivity from the analytical model matches the turbulent diffusivity diagnosed from the LES more closely. The coefficients for the analytical model were selected to predict the eddy diffusivity more accurately than the mixing depth. Additionally, there is more disagreement in the normalized eddy diffusivity profiles for the unheated cases than the heated cases. Therefore, it is also expected that there would be more agreement between the analytical model and LES eddy diffusivities for the heated cases. Following the series with $Q_0 = 0$ in Figure A3 from high to low windstress, growth does not begin when the critical turbulence threshold is crossed. The LES also demonstrates that phytoplankton growth occurs when the mixing depth is less than the critical depth. To see this trajectory, we add a special $\tau_{\text{wind}} = 0.001$ Pa wind-only case to this figure.

The results shown are for cases with $h_c = 50$ m. However, the results are qualitatively similar for the cases with $h_c = 100$ m. By comparing Figures 10 and 11, we see that higher values of windstress are needed to suppress growth for deeper critical depths. The analytical model and LES results for the cases with $h_c = 100$ m also show that phytoplankton growth occurs when the mixing depth is less than the critical depth.

Handling editor: Shubha Sathyendranath



Contribution to the Themed Section: 'Revisiting Sverdrup's Critical Depth Hypothesis' Original Article

Physiological constraints on Sverdrup's Critical-Depth-Hypothesis: the influences of dark respiration and sinking

Christian Lindemann^{1*}, Jan O. Backhaus², and Michael A. St John¹

¹National Institute of Aquatic Resources – DTU Aqua, Technical University of Denmark, Jægersborg Allé 1, Charlottenlund 2920, Denmark

²Institute of Oceanography, University of Hamburg, Bundesstraße 53, Hamburg 20146, Germany

*Corresponding author: tel: +45 35 88 34 47; fax: +45 35 88 33 33; e-mail: chrli@aqu.dtu.dk

Lindemann, C., Backhaus, J. O., and St John, M. A. Physiological constraints on Sverdrup's Critical-Depth-Hypothesis: the influences of dark respiration and sinking. – ICES Journal of Marine Science, 72: 1942–1951.

Received 11 June 2014; revised 25 February 2015; accepted 1 March 2015; advance access publication 24 March 2015

Discussions on the controls initiating the onset of the phytoplankton spring bloom in particular in the North Atlantic have since Sverdrup been dominated by the role of physical and biological drivers. Undoubtedly, these drivers play an important role in phytoplankton dynamics and thus the onset of the spring bloom. However, they neglect the cells ability to modify vital rates in response to changes in the external environment. In this study, we use a non-hydrostatic convection model coupled to an Individual-Based-Model to simulate changes phytoplankton cells during the transition from winter conditions as driven by convective mixing, and the onset of thermal stratification resulting in the spring bloom. The comparison between a simulation using a standard fixed rate approach in line with the original Sverdrup hypothesis and a simulation parameterized to include variable respiration and sinking rates showed that the latter approach was able to capture the observed phytoplankton concentration during deep convective mixing, the timing and magnitude of the spring bloom as well as simulating realistic physiological rates. In contrast, the model employing fixed rate parameterizations could only replicate field observations when employing unrealistic parameter values. These results highlight the necessity to consider not only the physical and biological external controls determining phytoplankton dynamics but also the cells ability to modify critical physiological rates in response to external constraints. Understanding these adaptive qualities will be of increasing importance in the future as species assemblages and physical controls change with changing climate.

Keywords: cell sinking, dark respiration, deep convection, phytoplankton spring bloom.

Introduction

The onset of the North Atlantic phytoplankton spring bloom has received a significant amount of attention due in part its influence on the dynamics of higher trophic levels (Houde, 2008) and its role for the biological carbon pump (Sanders *et al.*, 2014). The “Critical-Depth-Hypothesis” (Sverdrup, 1953) with its foundations in the works of Gran and Braarud (1935) and Riley (1946) has served as the starting point for predicting the onset of the spring bloom. It has been widely discussed, criticized, and extended based on increased understanding of the role of abiotic and biotic mechanisms. For example, Eilertsen *et al.* (1995) based on the role of light on phytoplankton proposed photoperiod control as a driving mechanism for the onset of the spring bloom. Moreover, the “Critical-Turbulence-Hypothesis” (Huisman *et al.*, 1999) predicts bloom

conditions based on turbulent diffusivity, light-limited growth, and mixed-layer depth. Following this mechanism, low levels of turbulent diffusivity are not able to counteract cell sinking, while high levels of turbulence mix cells out of the euphotic zone. At an intermediate level, sinking is balanced by turbulent mixing, retaining the cells in the euphotic zone where they receive sufficient light to generate a surface phytoplankton bloom. The “Convection-Shutdown-Hypothesis” (Ferrari *et al.*, 2014) builds upon earlier findings by Townsend *et al.* (1994) and Taylor and Ferrari (2011a) and suggested that the shutdown of winter convective mixing could serve as a better indicator for the onset of the spring bloom than the mixed-layer depth, the basis of the “Critical-Depth-Hypothesis”. This approach has subsequently been interpreted as an extension of Huisman's “Critical-Turbulence-Hypothesis”

(Behrenfeld and Boss, 2014). Furthermore, processes such as frontal systems (Taylor and Ferrari, 2011b) and vertical processes (Mahadevan *et al.*, 2012) can play an important role in creating stratification and thus initiating surface blooms without a change in net surface heat flux. All of these mechanisms infer physical controls as the primary cause of the rapid increase in surface chlorophyll observed in early spring. A more biologically based interpretation of the controls on the spring bloom has been presented by Behrenfeld (2010). The “Disturbance-Recovery-Hypothesis” suggesting that phytoplankton blooming is predominately controlled by biological interaction, namely the release of grazing pressure due to dilution of microzooplankton grazers (Landry and Hassett, 1982; Behrenfeld and Boss, 2014).

Given the multiple and interrelated mechanisms acting to influence the phytoplankton community, it is unlikely that one dominant mechanism, biological or physical in nature controls phytoplankton growth and the onset of the spring bloom. More likely, these dynamics are controlled by an interplay between the aforementioned mechanisms with one or the other dominating spatially and or temporally and leading to the heterogeneous manifestation of the bloom as seen in satellite (Lindemann and St John, 2014).

An omission in the discussion to date has been the basic physiological ability of phytoplankton to modify their vital rates relative to their external conditions. The Critical-Depth-Hypothesis (Sverdrup, 1953) assumes a constant respiration rate, encompassing grazing, sinking and cell respiration, independent of depth and the diurnal cycle. This does not reflect the cells ability to modify critical rates such as respiration and sinking, which potentially lead to a change in the critical depth (Smetacek and Passow, 1990).

Cell respiration is a highly variable internal process influenced by environmental conditions such as temperature (Verity, 1982), nutrients (Laws and Bannister, 1980), and light (Falkowski and Owens, 1980) as well as cellular growth. Light-limited low growth rates can induce a reduction of metabolic rates and thus dark respiration (Jochem, 1999). Based on laboratory studies, Falkowski and Owens (1980) determined that for cells acclimatized to a specific light level, the ratio of maximum production and dark respiration remained the same over a wide variety of light intensities suggesting that the maximum growth and respiration rates can be equally affected by light. This observation was supported in subsequent studies, e.g. Cosper (1982), Verity (1982), Langdon (1988), and Sakshaug *et al.* (1989).

However, in the North Atlantic during winter, within the deep convective layer, cells can be exposed to rapidly changing light levels, thus not conforming to the assumption of constant light or a steady state. Investigations on short-term dark respiration responses to changing light conditions have shown that dark respiration increases rapidly with photosynthesis (Weger *et al.*, 1989). As light declines, photosynthesis declines commensurate with the reduction in light; however, dark respiration does not react instantaneously but decreased gradually to a minimum (Weger *et al.*, 1989; Xue *et al.*, 1996). This decoupling of photosynthesis and respiration results in proportionally higher rates of respiration after light exposure (Falkowski *et al.*, 1985).

Phytoplankton cells have been observed to exhibit a wide range of different sinking rates, from several meters per day (Smayda, 1970) to positive buoyancy (Acuña *et al.*, 2010). For cells of similar shape and density, the sinking speed can be estimated using Stokes law (Miklasz and Denny, 2010). However, density is influenced by the species-specific cell composition and growth phase. Cells can maintain density levels close to neutral buoyancy, or even achieve positive

buoyancy (Acuña *et al.*, 2010) via active regulation of inorganic (Anderson and Sweeney, 1977) and organic material (Boyd and Gradmann, 2002). Buoyancy regulation and hence the sinking rate of phytoplankton cells has been related to growth (Waite *et al.*, 1992; Brookes and Ganf, 2001). Fast growing cells typically are found to show lower sinking rates than cells growing under conditions of limiting light (Waite *et al.*, 1992), nutrients (Bienfang *et al.*, 1982) or iron (Waite and Nodder, 2001), independent of cell size. These observations suggest that growth conditions are more important in controlling cell sinking than cell size (Bienfang *et al.*, 1982; Peperzak and Colijn, 2003).

To assess the importance of the cells ability to modify dark respiration and sinking, we developed and employed an Individual-Based-Model (IBM) for phytoplankton cells. IBM models have proven to be a useful tool for understanding the growth dynamics of phytoplankton cells (Hellweger and Kianirad, 2007). One of the advantages of the Lagrangian approach relative to the Eulerian approach is that an individual particle can be followed through space and time. Thus, the individual history of one particle cannot only be stored for analysis, but particle properties can depend on the “life history” as well as the abiotic and biotic constraints impacting on the individual. In this study, using a non-hydrostatic convection model (CM) coupled to a Lagrangian IBM, we investigate the effect of the cells natural ability to adjust their respiration and sinking in relation to changes in environmental conditions over the course of the onset of the spring bloom.

Material and methods

Non-hydrostatic convection model

The non-hydrostatic CM utilized has been employed in several studies (Kämpf and Backhaus, 1998; Backhaus *et al.*, 1999; Wehde and Backhaus, 2000; Wehde *et al.*, 2001; Große *et al.*, 2014) and is set on an isotropic, equidistant grid. The model uses Boussinesq-equations for an incompressible fluid to describe a 2.5 dimensional ocean slice. The ocean slice itself is two dimensional (x, z); however, fluxes are calculated for all three dimensions (x, y, z). The equations for conservation of movement are as follows:

$$\frac{\partial U}{\partial t} + U \frac{\partial U}{\partial x} + W \frac{\partial U}{\partial z} - fV + f^\circ W = -\frac{1}{\rho_0} \frac{\partial P}{\partial x} + \frac{\partial}{\partial x} \left(\nu_t \frac{\partial U}{\partial x} \right) + \frac{\partial}{\partial z} \left(\nu_t \frac{\partial U}{\partial z} \right), \quad (1)$$

$$\frac{\partial V}{\partial t} + U \frac{\partial V}{\partial x} + W \frac{\partial V}{\partial z} + fU = \frac{\partial}{\partial x} \left(\nu_t \frac{\partial V}{\partial x} \right) + \frac{\partial}{\partial z} \left(\nu_t \frac{\partial V}{\partial z} \right), \quad (2)$$

$$\frac{\partial W}{\partial t} + U \frac{\partial W}{\partial x} + W \frac{\partial W}{\partial z} - f^\circ U = -\frac{1}{\rho_0} \frac{\partial P}{\partial x} - \frac{\rho'}{\rho_0} g + \frac{\partial}{\partial x} \left(\nu_t \frac{\partial W}{\partial x} \right) + \frac{\partial}{\partial z} \left(\nu_t \frac{\partial W}{\partial z} \right), \quad (3)$$

where U , V , and W are the velocity components for the three dimensions (x, y, z). The variable P denotes the non-hydrostatic part of the pressure, g represents the gravity, ν_t the eddy viscosity, ρ' the reduced density, and ρ_0 represents the reference density. The variables f and f° are the complete Coriolis parameters. The turbulent eddy viscosity (ν_t) is parameterized by the zero-order turbulence closure by Kochergin (1987). The numerical stability is ensured by the CFL stability criteria with a physical time steps for advection of temperature, salinity, and momentum set to a maximum of 1 min.

The equations of conservation for temperature (T) and salinity (S) are:

$$\frac{\partial T}{\partial t} + U \frac{\partial T}{\partial x} + W \frac{\partial T}{\partial z} = \frac{\partial}{\partial x} \left(K_T \frac{\partial T}{\partial x} \right) + \frac{\partial}{\partial z} \left(K_T \frac{\partial T}{\partial z} \right) + \frac{\delta E_T}{\partial t}, \quad (4)$$

$$\frac{\partial S}{\partial t} + U \frac{\partial S}{\partial x} + W \frac{\partial S}{\partial z} = \frac{\partial}{\partial x} \left(K_S \frac{\partial S}{\partial x} \right) + \frac{\partial}{\partial z} \left(K_S \frac{\partial S}{\partial z} \right) + \frac{\delta E_S}{\partial t}, \quad (5)$$

where $\delta E_T/\partial t$ and $\delta E_S/\partial t$ are the thermal and saline sea surface forcing, respectively. The variables K_T and K_S are the eddy diffusivities for heat and salt, respectively, and are set equal to the eddy viscosity (ν_t).

The thermal surface forcing changes according to

$$\frac{\delta E_T}{\partial t} = \frac{-Q_{\text{net}}}{\rho c_{\text{sw}}}, \quad (6)$$

where c_{sw} is the specific heat of seawater. The variable Q_{net} denotes the net surface heat flux calculated by

$$Q_{\text{net}} = \Delta Q_{\text{lw}} + Q_{\text{sw}} + Q_{\text{lat}} + Q_{\text{nses}}, \quad (7)$$

where ΔQ_{lw} is the difference between the atmospheric long-wave radiation and the long-wave radiation from the sea surface, Q_{sw} is the incoming short wave radiation, Q_{lat} is the latent heat flux, and Q_{nses} is the sensible heat flux.

Light intensity (I) in the water column at depth (z) is described by

$$I(z) = I_0 \times \exp^{-(k_c + s)z}, \quad (8)$$

where I_0 is the incoming radiation at the sea surface, z is the depth, k_c is the extinction coefficient due to turbidity, and s the self-shading of phytoplankton estimated by

$$s = k_{\text{phy}} C, \quad (9)$$

where k_{phy} , the extinction coefficient of phytoplankton, is 0.03 (Große et al., 2014) and C is the phytoplankton concentration in (mmol C m^{-3}).

For further details of the physical model, see Kämpf and Backhaus (1998) and Wehde and Backhaus (2000). Deviating from the older versions of this model, this version uses the equation of state proposed by McDougall et al. (2003), which uses potential temperature instead of the *in situ* temperature (UNESCO, 1981).

Biological Individual-Based-Model

The biological IBM consists of Lagrangian tracers depicting phytoplankton cells of indefinite biomass within the ocean slice where the biological time step is set to 5 min.

Phytoplankton growth during winter and early spring in the North Atlantic is not believed to be nutrient limited, therefore it does not account for nutrient limitation. Grazing is not accounted for explicitly, but it is parameterized by a biomass-dependent mortality rate (m). All biological parameter values are given in Table 1.

Cell growth

Net phytoplankton concentration depends on the cells growth rate μ , the cells sinking rate ν , and advection and diffusion in the three dimensions:

$$\frac{DC}{Dt} = \frac{\partial C}{\partial t} - \nabla \cdot (UC) + \nabla \cdot (\nu_t \nabla C) - \nu \frac{\partial C}{\partial z} + \mu C, \quad (10)$$

where $U = (U, V, W)$. The growth rate is estimated by

$$\mu = P^C - r - m, \quad (11)$$

where P^C is the photosynthesis, r is the respiration, and m is the mortality.

Photosynthesis is calculated according to:

$$P^C = P_{\text{max}}^C \left[1 - \exp\left(-\frac{\alpha^{\text{chl}} I \theta^C}{P_{\text{max}}^C}\right) \right], \quad (12)$$

where P_{max}^C is the maximum specific photosynthesis rate, α^{chl} is the initial slope of the function, and θ^C is the chlorophyll-to-carbon ratio. Changes in chlorophyll are described following Geider et al. (1997):

$$\frac{d\text{Chl}}{dt} = \rho^{\text{chl}} P^C C - r\text{Chl}, \quad (13)$$

where ρ^{chl} is the biosynthesis of chlorophyll according to

$$\rho^{\text{chl}} = \theta_m^C \left(\frac{P^C}{\alpha^{\text{chl}} I \theta^C} \right), \quad (14)$$

where θ_m^C is the maximum chlorophyll-to-carbon ratio.

Table 1. Biological model parameters and scaling coefficients.

Description	Symbol	Value	Unit	Source
Maximum specific carbon fixation rate	P_{max}^C	3	d^{-1}	Geider et al. (1998)
Chl-specific initial slope of PI curve	α^{chl}	0.5	$10^{-5} \text{ gC m}^{-2} (\text{gChl mmol photons})^{-1}$	Geider et al. (1997)
Maximum Chl-to-carbon ratio	θ_m^{chl}	0.05	gChl (gC)^{-1}	Cloern et al. (1995)
Cost of biosynthesis	Z	0.23	gC (gC)^{-1}	Geider et al. (1998)
Mortality rate	m	0.05	d^{-1}	Wehde et al. (2001)
Specific respiration reduction in dark	α^r	0.0455	h^{-1}	Weger et al. (1989)
Maintenance cost	r^0	0.02	gC (gC)^{-1}	Geider and Osborne (1989)
Maximum sinking velocity	ν^{max}	6.8	m d^{-1}	Smayda (1970) ^a
Sinking rate scaling coefficient	α^{ν}	4.15	–	Waite et al. (1992)

^aOnly considering alive cells.

The values for the specific respiration reduction in the dark and the sinking rate scaling coefficient were extracted from Weger et al. (1989) and Waite et al. (1992), respectively.

Cell respiration

In this model, cell respiration rate consists of maintenance metabolism (r^0) and the cost of biosynthesis which, under the influence of light, is proportionally related to photosynthesis. However, when photosynthesis ceases, biosynthesis does not stop immediately, but decays over time (e.g. Walter *et al.*, 2015). Weger *et al.* (1989) investigated short-term acclimation of phytoplankton dark respiration to variable light conditions. While the shutdown of light led to a gradual decrease of respiratory loss, moving from dark to light conditions showed an almost instantaneous return of high respiration rates. Here, the respiration rate is modelled accounting for these dynamics through:

$$r = \max\left(\zeta P^C + r^0, r \times \exp^{-\alpha' t}\right), \quad (15)$$

where the upper term represents respiration in light with ζ being the cost of biosynthesis. The second expresses the decrease of respiration in the dark, where α' is the rate of decrease with time, which was extracted from Weger *et al.* (1989).

Cell sinking

The sinking rate of each cell is modelled based on the concept of Waite *et al.* (1992), who coupled the sinking rate to the overall metabolic state of the cell. They found that when cells were transferred from light into darkness, their sinking rate could be described as a negative function of their respiration rate.

The sinking rate can therefore be described by the maximum sinking velocity v_{\max} and a scaling factor (α'') of the relative respiration (r'), which was extracted from Waite *et al.* (1992):

$$v = v_{\max}^{-\alpha'' r'}, \quad (16)$$

where

$$r' = \frac{r}{\zeta P_{\max}^C + r^0}. \quad (17)$$

Model setup and initial conditions

The model was set up to simulate conditions at Ocean Weather Station Mike (OWM) (66°N 02°E), the same station where the observations by Sverdrup (1953) were used to develop the Critical-Depth-Hypothesis. Three hourly meteorological forcing for the period was obtained from the Norwegian Meteorological Office (METNO) and was used for the simulation from 5 April to 10 May 1997 (yearday 95–130) with the first 5 d considered as spin-up. The simulation was initialized with vertical profiles from Ocean Weatherstation Mike. This period was chosen since it encompassed the period from pre-bloom conditions with typical deep convective mixing to stratified conditions with shallow wind-driven mixing towards the end of the simulation. Here (and in the following) we refer to deep convection as convection that is not driven by nocturnal cooling, but extends over a longer period, hence leading to deeper convective mixing. The simulation was not continued throughout the full spring bloom as our assumptions (e.g. no nutrient limitation) would be invalid. Field observations of the further development of the spring bloom after our simulation period showed the maximum chlorophyll concentration occurred on

23 May (yearday 143) with values of over 3 mg Chl m^{-3} (Niehoff *et al.*, 1999).

In our study, Lagrangian tracers (20 000 particles) were randomly distributed from 10 to 400 m depth at the beginning of the simulation. The model domain was set to 1000 × 1500 m with a grid size of 5 × 5 m.

Model simulations

To demonstrate the effect of the cells ability to modify rates of both sinking and respiration, we compared the model simulation, using the variable parameterizations for respiration and sinking as described above, to simulations using fixed values. Other than employing the variable parameterizations, both the fixed value simulations and the adaptive simulation are identical. The values used in the simulations with fixed parameter values were chosen to encompass the range of values found in the adaptive simulation. These fixed values were 0.02, 0.135, 0.25, and 0.47 for the daily average carbon-specific respiration (d^{-1}) and 0, 2.25, 4.5, and 6.8 sinking (m d^{-1}), respectively. We compared the adaptive run to runs with each of the 4 × 4 combinations of these fixed respiration and sinking rates. The outputs of these fixed value simulations and the respective fixed parameter combinations are presented in Figure 5.

Results

The beginning of the simulation is characterized by a negative net surface heat flux (Figure 1a), with minimal values of ca. -350 W m^{-2} . This led to strong convective mixing as indicated by the turbulent kinetic energy (TKE) (Figure 1b). The initial

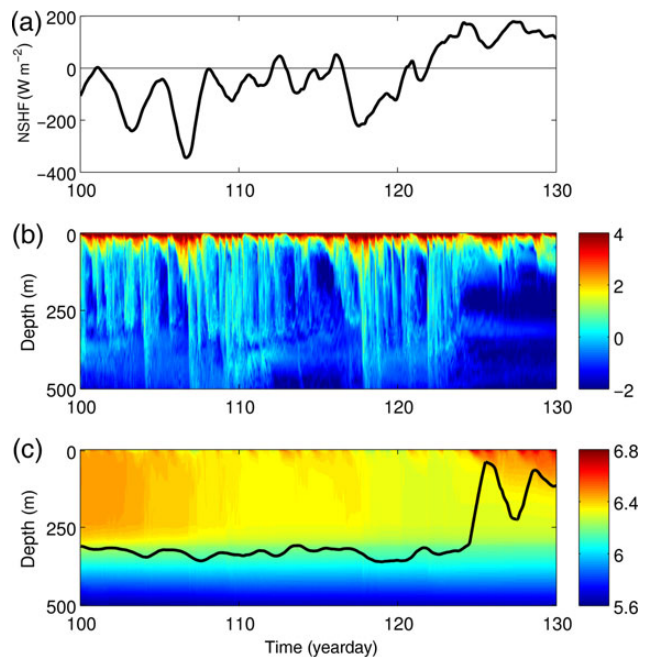


Figure 1. Physical water properties as predicted by the non-hydrostatic CM over the course of the simulation at Ocean Weatherstation Mike. (a) Simulated net surface heat flux (W m^{-2}). (b) Hovmöller diagram showing simulated water column TKE ($\text{cm}^2 \text{s}^{-1}$) on a log scale. (c) Simulated temperature within the water column ($^{\circ}\text{C}$). The black line indicates the estimated mixed-layer depth.

period of strong mixing was followed by a reduction in net surface heat loss (-100 – 70 W m^{-2}) causing a reduction in convective mixing, followed by a stabilization of the water column (~ 5 May, yearday 125) as indicated by the temperature profile (Figure 1c). This resulted in changes in the mixed-layer depth, defined here as the depth range over which the temperature deviates by $<0.2^\circ\text{C}$ from 10 m below the surface. This value is on the lower range of values commonly used to define the MLD (de Boyer Montégut *et al.*, 2004). The temperature within the surface layer (~ 6.3 – 6.5°C) as predicted by the model compares well with observations and the onset of stratification was captured by the model both with regard to the timing (~ 5 May, yearday 125) and stratification depth (~ 50 m) (Irigoien *et al.*, 1998).

Adaptive simulations

The simulated biomass and dynamics of the winter phytoplankton community using the adaptive parameterization compares well with the published 100 m integrated values of Irigoien *et al.* (1998) and Niehoff *et al.* (1999), showing an increase in biomass of $\sim 200\%$ (Figure 2) over the period of the simulation.

Until the onset of stratification, the integrated chlorophyll over the mixed layer showed a decreasing trend (Figure 2). The onset of stratification was marked by a short lived drop in mixed-layer integrated phytoplankton biomass after which the mixed-layer integrated phytoplankton concentration started to increase similar to that of the 100 m integrated chlorophyll. The drop can be attributed to cells being “left behind” below the now stratifying mixed layer, thus reducing the integrated biomass due to a decrease in the water column depth now defining as the mixed layer.

Depending on their position within the water column, the phytoplankton “particles” were either retained within the mixed layer or where “detrained” (Behrenfeld and Boss, 2014) into deeper waters as

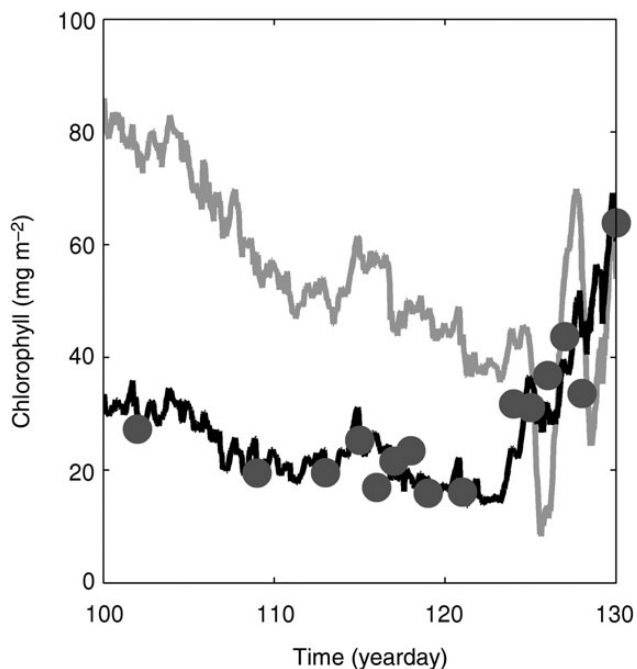


Figure 2. Integrated chlorophyll at Ocean Weathership Mike over the course of the simulation. The solid lines show chlorophyll integrated over the upper 100 m. Grey dots are observations of 100 m integrated chlorophyll. The dashed line shows chlorophyll integrated over the mixed-layer depth and hence over the varying convective layer depth.

has been suggested earlier by Evans and Parslow (1985). Our simulations illustrate that during deep convective mixing all tracers are generally homogeneously distributed throughout the mixed layer (Figure 3c). However, occasionally increased production occurred in agreement with the Critical-Turbulence-Hypothesis (Huisman *et al.*, 1999) leading to an increased phytoplankton biomass near the surface. This biomass was however subsequently quickly mixed throughout the convective mixed layer (CML) as result of an increase in turbulent mixing.

A reduction in net surface heat flux after 28 April (yearday 118) (Figure 1a) led to reduced cooling of surface water and thus to a reduction in convection depth. Thereafter, primary production in the upper ~ 50 m increased with reduced mixing towards the end of the simulation (Figure 3c). The simulated chlorophyll-to-carbon ratio varied between 0.05 and 0.018 with surface values being the lowest, in particular toward the end of the simulation. These values are at the higher end of the range of values reported in the literature (Cloern *et al.*, 1995; Geider *et al.*, 1997), which is however not surprising given the overall low light levels. Dark respiration generally followed the same pattern as primary production. However, because the increase in production did not occur instantaneously, it showed a wider spread over time and space (Figure 3a). Within the euphotic zone, defined as 1% of surface light level, the ratio of integrated daily carbon-specific gross production and integrated daily carbon-specific respiration rate varied in between ~ 28 and 39% (Figure 4), which compares well with value reported in the literature. Geider (1992) summarized several earlier measurements on phytoplankton respiration finding a range of 26–65% carbon being respired over 24 h. Laws and Bannister (1980) found night losses in between 10 and 20% of daytime production and a more theoretical approach (Marra and Barber, 2004) yielded values of ~ 35 – 40% of daily respiratory losses.

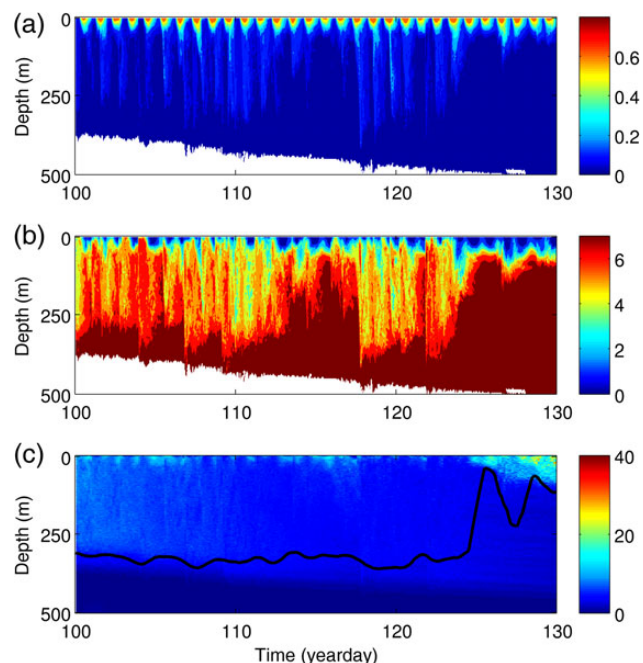


Figure 3. Phytoplankton properties simulated by the non-hydrostatic CM over the course of the simulation at Ocean Weathership Mike. Hovmöller diagrams show the (a) carbon-specific respiration rate (d^{-1}), (b) sinking rate (m d^{-1}), and (c) phytoplankton concentration (mg C m^{-3}).

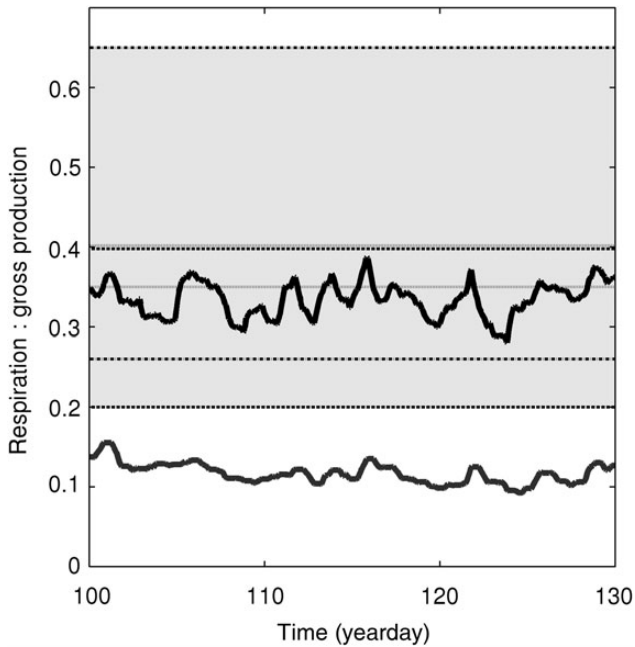


Figure 4. Simulated ratio of daily average respiration rate to daily gross production rate. The thick black line indicates the result as simulated by the adaptive model. The thick gray line indicates the result as simulated using a fixed specific respiration rate of 0.135 d^{-1} and a sinking rate of 4.5 m d^{-1} . The shaded area indicates that the range of values reported in the literature. Vertical lines indicate that limits of range reported by Laws and Bannister (1980) (dash-dotted), Geider (1992) (dashed), and Marra and Barber (2004) (dotted).

Sinking rates were lowest at the surface during this period with rates as low as 0.13 m d^{-1} . Generally, sinking rates increased with depth and were highest below the mixed layer reaching ν^{max} of 6.8 m d^{-1} (Figure 3b).

Adaptive vs. fixed parameterizations

We compared the adaptive run to runs with different combinations of fixed respiration and sinking rates (Figure 5). In general, changes in respiration rates had a bigger influence on phytoplankton biomass than sinking rates. Runs with respiration set to the minimum value ($r^0 = 0.02 \text{ d}^{-1}$) systematically overestimated the phytoplankton biomass regardless of the sinking rate applied. Runs using respiration rates of 0.25 and 0.47 d^{-1} always underestimated phytoplankton concentrations. In the runs using a fixed respiration rate of 0.135 d^{-1} , the simulated phytoplankton concentration showed a much better fit with observations (Figure 5).

The impact of the sinking rate on phytoplankton biomass was more pronounced towards the end of the simulations, despite remaining less important than the respiration rate. In these simulations, using fixed rates, the ratio of daily carbon-specific gross production to respiration within the euphotic zone varied in between 0.09 and 0.15 d^{-1} (Figure 4) which is lower than the lowest values than the values reported in the literature.

Discussion

Phytoplankton biomass

Traditionally, it has been assumed that the peak integrated phytoplankton biomass is associated with the spring bloom. During this period, cells experience sufficient light for growth due to a

reduced mixing depth while not under the influence of nutrient limitation, that is, the classical critical-depth model (Sverdrup, 1953). However, the concept of “phyto-convection” (Backhaus *et al.*, 1999) suggests that deep convective mixing can sustain a homogeneously distributed viable phytoplankton biomass within the deep winter mixing zone on the same order of magnitude as during the spring bloom (Backhaus *et al.*, 2003). In our simulation, phytoplankton cells are generally homogeneously distributed during deep convection which was closely followed by the onset of stratification and an increase in surface phytoplankton biomass (Figure 3c). However, before the onset of stratification around 25 April, a reduction in surface cooling resulted in a net surface heat flux of around zero (Figure 1a). During this period, no change in mixed-layer depth was observed a minor increase in phytoplankton surface concentration occurred (Figure 3c). Similar dynamics have been observed in the North Atlantic (Townsend *et al.*, 1992) and support the hypothesis that the shutdown of deep convective mixing is a better indicator for growth conditions than the hydrostatic vertical water column profile (Townsend *et al.*, 1994; Taylor and Ferrari, 2011a). This pulse of productivity also indicates that the cells contained in an actively mixed layer represent the potentially photosynthetic active phytoplankton. Phytoplankton biomass within the deep CML was observed by Backhaus *et al.* (2003) to be similar to estimates of biomass occurring during the spring bloom. Our model shows similar dynamics with the total standing stock over the CML being on the same order as that after the onset of stratification (Figure 2). Hence, the upper 100 m, a traditional approach for estimating integrated biomass, has the potential to underestimate the standing stock during winter.

Given these observations, the question then arises as to the mechanisms allowing phytoplankton cells to survive and maintain a viable phytoplankton stock in a deep mixed layer where they spend a large period below the euphotic zone. Over the course of winter, the release from micro-zooplankton grazing pressure has been suggested to compensate for the reduction in light exposure as the mixed layer deepens (Behrenfeld and Boss, 2014). Our model does not include an explicit representation of zooplankton grazing pressure; hence, we were not able to address this question. However, the adaptive simulation showed a good fit with field observations without a detailed representation of grazing, suggesting that physiological acclimation could play an equally important role.

Individual physiology of phytoplankton growth

The ability of a phytoplankton cell to react to changing environmental conditions, although a key determinant of biomass production and community structure has received little attention in relation to the onset of the spring bloom.

For an individual cell, the internal growth is dependent upon nutrients, the photosynthetically active radiation for growth and the loss terms such as sinking and respiration, which become proportionally more important under conditions of low growth (Sakshaug *et al.*, 1991).

Sinking

Phytoplankton sinking rates are highly variable and depend on species, cell shape, life stage, growth condition, and particle aggregation (Smayda, 1970; Miklasz and Denny, 2010). Sinking velocities of phytoplankton cells rarely exceed a few tens of meters per day, while actively growing cells have been shown to have much lower sinking velocities and can even achieve positive buoyancy (Moore and Villareal, 1996; Acuña *et al.*, 2010). In a convective regime vertical,

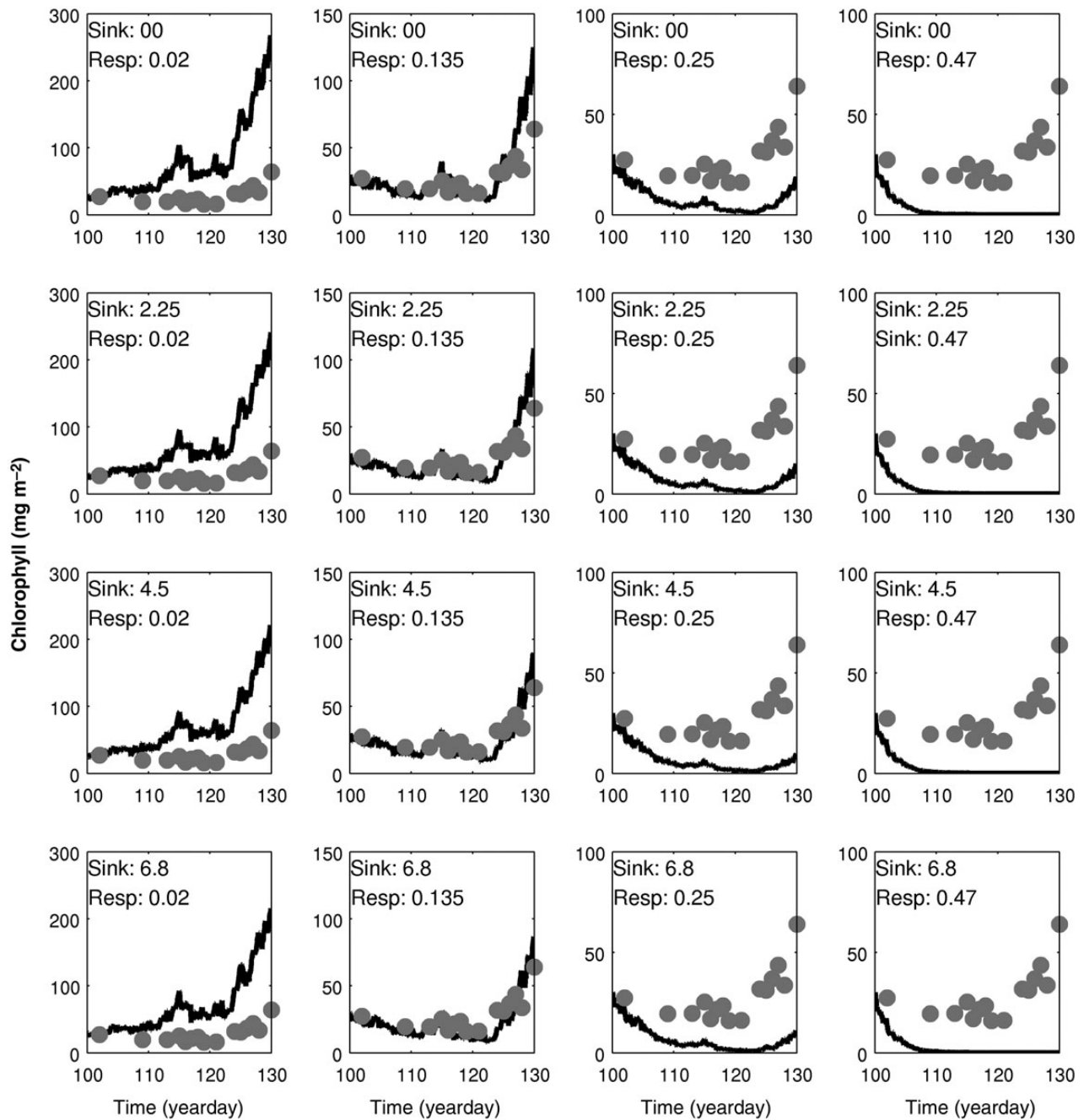


Figure 5. Simulated 100 m integrated chlorophyll at Ocean Weathership Mike using different combinations of fixed values for carbon-specific respiration rate (0.02, 0.135, 0.35, 0.47 d^{-1}) and fixed sinking rates (0.0, 2.25, 4.5, 6.8 m d^{-1}). The grey dots indicated measured values.

velocities can be approximately several hundred meters per day (Marshall and Schott, 1999; D'Asaro, 2008) thus greatly exceeding sinking rates. Nevertheless, sinking can remain an important aspect, since cells may still sink out at the bottom of the mixed, especially during periods of reduced winter deep convection which is of varying depth and temporal duration (Marshall and Schott, 1999). This is captured in our simulation (Figure 1b). Hence, cells can experience periods without convective mixing, causing increased sinking, and increased detrainment of cells at the base of the convective layer. Convective layer deepening, due to stronger winds and cooling, can lead to an entrainment of previous “lost”

cells back into the CML depending on the interaction between sinking rate and convective mixing. For example, D'Asaro (2008) found that the maximum sinking velocity for cells to be successfully re-incorporated into the CML to be 7 m d^{-1} . In this study, lower sinking rates (0.13–3.7 m d^{-1}) were recorded near the surface, generally staying below 2 m d^{-1} .

Towards the end of the simulation when environmental conditions became more favourable for growth and stratification had commenced, sinking rates in the upper 50 m ranged between 0.13 and 1.1 m d^{-1} (Figure 3b). Sinking rates below the mixed-layer depth remained relatively constant at the maximum of 6.8 m d^{-1} .

These rates cover a wide range of sinking rates reported for different taxa and environmental conditions (Smayda, 1970) incorporating the assumption of lower sinking rates for growing cells (Waite *et al.*, 1992). Our model was not able to reproduce positive buoyancy as reported for large fast growing diatoms (Moore and Villareal, 1996; Acuña *et al.*, 2010). However, in field samples taken during the simulated period diatoms represented only a minor fraction of the phytoplankton composition (Irigoien *et al.*, 1998). Given our simulated values and observed and predicted convective velocities, it is suggested that phytoplankton sinking rates play only a minor role in the loss terms during periods of deep convection. However, it may be of significance for cells during periods of weakening convection. Here phytoplankton cells can be detained below the convective mixing thus having the potential to be lost from the system and sequestered at depth.

Dark respiration

Dark respiration can be highly variable and is known to change with growth and physiological condition of the cell (Waite *et al.*, 1992; Jochem, 1999). In the classical critical-depth model (Sverdrup, 1953) however, as in most models, it is treated as a constant, potentially leading to significant errors (Smetacek and Passow, 1990).

As growth during winter is normally limited by light due to shorter photoperiod and deeper mixing, dark respiration holds the potential to be an important physiology component, impacting on the onset of the spring bloom as well as the winter stock.

Using variable respiration rates, the model estimated higher values of respiration closer to the surface (Figure 3a), where cells exhibit positive growth rates. This is in agreement with our mechanistic understanding of dark respiration (Falkowski and Owens, 1980; Jochem, 1999) and with the reported ratios of respiration to gross growth (Laws and Bannister, 1980; Geider, 1992; Marra and Barber, 2004).

A reduction of the respiratory losses with depth can allow cells to prolong the availability of energetic reserves and thus survival in the dark. During winter in a deep convective layer, this can be an important survival strategy (McMinn and Martin, 2013), potentially playing an important role in determining the seed population for the spring bloom (Backhaus *et al.*, 1999).

Fixed vs. flexible parameterizations

In this study, we contrasted simulations with variable respiration and sinking rates with those using fixed values to highlight the potential importance of the cells response to environmental conditions. Usually in our simulations, comparisons of fixed respiration and sinking rates over the range of values encompassed by our flexible parameterizations were unable to reproduce the observed concentrations (Figure 5). Applying a specific respiration rate of 0.135 d^{-1} showed a similarly good fit to observations. However, this fixed respiration rate, when expressed as respiration in percentage loss per gross growth (Figure 4) is below the value reported for growing cells (Laws and Bannister, 1980; Geider, 1992; Marra and Barber, 2004). Conversely, the adaptive model was able to simulate a realistic gross growth to respiration ratio (Figure 4). This resulted in higher respiration rates near the surface, which needed to be compensated by lower respiration rates at depth (Figure 3a) to achieve similar biomass to the observations (Figure 2). Thus, to reproduce the observed concentrations, the model required employing fixed parameter values of respiration not substantiated in the literature. This indicates that during the winter and the spring transition

period acclimation of physiological rates can be an important process to sustain the phytoplankton community.

Conclusion

In this study, we showed, using a Lagrangian phytoplankton IBM which allowed cells to modify physiological rates, that plasticity of physiological rates can play an important role for the persistence and composition of the North Atlantic phytoplankton community.

When using variable respiration and sinking rates, the model was able to capture the observed phytoplankton concentration during deep convective mixing and the timing and magnitude of the onset of the spring bloom (Figure 2), while simulating realistic physiological rates. In contrast, the model with fixed rates was only able to produce the observations when employing unrealistic parameter values. These results highlight the importance of considering variable parameterization in modelling approaches and suggest that the cells ability to adjust physiological rates to environmental conditions may play an important role in the onset of classical phytoplankton spring bloom. The adaptive model was able to maintain a viable phytoplankton biomass over the convective layer during winter similar to that observed by Backhaus *et al.* (2003), with potentially important implications for the carbon budget. Furthermore, minor phytoplankton surface blooms during winter occurred in the absence of stratification due to a reduction in deep convective mixing. Similar features have been observed in the North Atlantic (Townsend *et al.*, 1992) supporting the hypothesis that active mixing can be more important in controlling growth (Taylor and Ferrari, 2011a) than the hydrostatic conditions employed in the classical critical-depth model (Sverdrup, 1953).

Clearly, the biophysical environment sets the boundaries on phytoplankton dynamics and thus plays a central role in phytoplankton community dynamics. However, an organisms ability to acclimatize to these constraints cannot be neglected, as it allows the organism to find loopholes to escape these controls (Chisholm, 1992). To gain a more realistic understanding of phytoplankton dynamics, the interplay between physical and biological controls needs to be merged with advances in our understanding of the physiologically determined adaptive capacities of phytoplankton cells.

Acknowledgements

The observational phytoplankton data used for the validation was kindly provided by X. Irigoien. Meteorological data from station “Mike” was kindly provided by the Norwegian Meteorological Office (METNO). This publication was partly financially supported by the 7th EU-framework project EURO-BASIN (Contract Nr 264933) and the DTU Aqua PhD School.

References

- Acuña, J., López-Alvarez, M., Nogueira, E., and González-Taboada, F. 2010. Diatom flotation at the onset of the spring phytoplankton bloom: an in situ experiment. *Marine Ecology Progress Series*, 400: 115–125.
- Anderson, L., and Sweeney, B. 1977. Diel changes in sedimentation characteristics of *Ditylum brightwelli*: changes in cellular lipid and effects of respiratory inhibitors and ion-transport modifiers. *Limnology and Oceanography*, 22: 539–552.
- Backhaus, J., Hegseth, E., Wehde, H., Irigoien, X., Hatten, K., and Logemann, K. 2003. Convection and primary production in winter. *Marine Ecology Progress Series*, 251: 1–14.

- Backhaus, J., Wehde, H., Hegseth, E., and Kämpf, J. 1999. Phyto-convection: the role of oceanic convection in primary production. *Marine Ecology Progress Series*, 189: 77–92.
- Behrenfeld, M. J. 2010. Abandoning Sverdrup's critical depth hypothesis on phytoplankton blooms. *Ecology*, 91: 977–989.
- Behrenfeld, M. J., and Boss, E. S. 2014. Resurrecting the ecological underpinnings of ocean plankton blooms. *Annual Review of Marine Science*, 6: 167–194.
- Bienfang, P., Harrison, P., and Quarmby, L. 1982. Sinking rate response to depletion of nitrate, phosphate and silicate in four marine diatoms. *Marine Biology*, 67: 295–302.
- Boyd, C., and Gradmann, D. 2002. Impact of osmolytes on buoyancy of marine phytoplankton. *Marine Biology*, 141: 605–618.
- Brookes, J., and Ganf, G. 2001. Variations in the buoyancy response of *Microcystis aeruginosa* to nitrogen, phosphorus and light. *Journal of Plankton Research*, 23: 1399–1411.
- Chisholm, S. 1992. Phytoplankton size. In *Primary Productivity and Biogeochemical Cycles in the Sea Environmental Science Research*, 43, pp. 213–237. Ed. by P. G. Falkowski, A. D. Woodhead, and K. Vivirito. Plenum Press, New York.
- Cloern, J. E., Grenz, C., and Videgar-Lucas, L. 1995. An empirical model of the phytoplankton chlorophyll: carbon ratio—the conversion factor between productivity and growth rate. *Limnology and Oceanography*, 40: 1313–1321.
- Cosper, E. 1982. Influence of light intensity on diel variations in rates of growth, respiration and organic release of a marine diatom: comparison of diurnally constant and fluctuating light. *Journal of Plankton Research*, 4: 705–724.
- D'Asaro, E. 2008. Convection and the seeding of the North Atlantic bloom. *Journal of Marine Systems*, 69: 233–237.
- De Boyer Montégut, C., Madec, G., Fischer, A. S., Lazar, A., and Iudicone, D. 2004. Mixed layer depth over the global ocean: an examination of profile data and a profile-based climatology. *Journal of Geophysical Research*, 109: C12003.
- Eilertsen, H., Sandberg, S., and Tollefsen, H. 1995. Photoperiodic control of diatom spore growth: a theory to explain the onset of phytoplankton blooms. *Marine Ecology Progress Series*, 116: 303–307.
- Evans, G., and Parslow, J. 1985. A model of annual plankton cycles. *Biological Oceanography*, 3: 327–347.
- Falkowski, P., Dubinsky, Z., and Wyman, K. 1985. Growth-irradiance relationships in phytoplankton. *Limnology and Oceanography*, 30: 311–321.
- Falkowski, P., and Owens, T. 1980. Light-shade adaptation two strategies in marine phytoplankton. *Plant Physiology*, 66: 592–595.
- Ferrari, R., Merrifield, S. T., and Taylor, J. R. 2014. Shutdown of convection triggers increase of surface chlorophyll. *Journal of Marine Systems*, in press.
- Geider, R. J., and Osborne, B. A. 1989. Respiration and microalgal growth: a review of the quantitative relationship between dark respiration and growth. *New Phytologist*, 112: 327–341.
- Geider, R. 1992. Respiration: taxation without representation? In *Primary Productivity and Biogeochemical Cycles in the Sea Environmental Science Research*, 43, pp. 333–360. Ed. by P. Falkowski, A. Woodhead, and K. Vivirito. Springer, USA.
- Geider, R. J., MacIntyre, H. L., and Kana, T. M. 1997. Dynamic model of phytoplankton growth and acclimation: responses of the balanced growth rate and the chlorophyll a: carbon ratio to light, nutrient-limitation and temperature. *Marine Ecology Progress Series*, 148: 187–200.
- Geider, R. J., MacIntyre, H. L., and Kana, T. M. 1998. A dynamics regulatory model of phytoplanktonic acclimation to light, nutrients, and temperature. *Limnology and Oceanography*, 43: 679–694.
- Gran, H., and Braarud, T. 1935. A quantitative study of the phytoplankton in the Bay of Fundy and the Gulf of Maine (including observations on hydrography, chemistry and turbidity). *Journal of the Biological Board of Canada*, 1: 219–467.
- Große, F., Lindemann, C., Pätsch, J., and Backhaus, J. O. 2014. The influence of winter convection on primary production: a parameterisation using a hydrostatic three-dimensional biogeochemical model. *Journal of Marine Systems*, Elsevier BV, in press.
- Hellweger, F. L., and Kianirad, E. 2007. Individual-based modeling of phytoplankton: evaluating approaches for applying the cell quota model. *Journal of Theoretical Biology*, 249: 554–565.
- Houde, E. D. 2008. Emerging from Hjort's Shadow. *Journal of Northwest Atlantic Fishery Science*, 41: 53–70.
- Huisman, J., van Oostveen, P., and Weissing, F. 1999. Critical depth and critical turbulence: two different mechanisms for the development of phytoplankton blooms. *Limnology and Oceanography*, 44: 1781–1787.
- Irigoien, X., Head, R., Klenke, U., Meyer-Harms, B., Harbour, D., Niehoff, B., Hirche, H., et al. 1998. A high frequency time series at weathership M, Norwegian Sea, during the 1997 spring bloom: feeding of adult female *Calanus finmarchicus*. *Marine Ecology Progress Series*, 172: 127–137.
- Jochem, F. 1999. Dark survival strategies in marine phytoplankton assessed by cytometric measurement of metabolic activity with fluorescein diacetate. *Marine Biology*, 135: 721–728.
- Kämpf, J., and Backhaus, J. O. 1998. Shallow, brine-driven free convection in polar oceans: Nonhydrostatic numerical process studies. *Journal of Geophysical Research*, 103: 5577.
- Kochergin, V. P. 1987. Three dimensional prognostic models. *Coastal and Estuarine Sciences*, 4: 201–208.
- Landry, M. R., and Hassett, R. P. 1982. Estimating the grazing impact of marine micro-zooplankton. *Marine Biology*, 67: 283–288.
- Langdon, C. 1988. On the causes of interspecific differences in the growth-irradiance relationship for phytoplankton. II. A general review. *Journal of Plankton Research*, 10: 1291–1312.
- Laws, E. A., and Bannister, T. T. 1980. Nutrient- and light-limited growth of *Thalassiosira fluviatilis* in continuous culture, with implications for phytoplankton growth in the ocean. *Limnology and Oceanography*, 25: 457–473.
- Lindemann, C., and St John, M. A. 2014. A seasonal diary of phytoplankton in the North Atlantic. *Frontiers in Marine Science*, 1: 00037.
- Mahadevan, A., D'Asaro, E., Lee, C., and Perry, M. J. 2012. Eddy-driven stratification initiates North Atlantic spring phytoplankton blooms. *Science*, 337: 54–58.
- Marra, J., and Barber, R. T. 2004. Phytoplankton and heterotrophic respiration in the surface layer of the ocean. *Geophysical Research Letters*, 31: 1–4.
- Marshall, J., and Schott, F. 1999. Open ocean convection: observations, theory, and models. *Reviews of Geophysics*, 37: 1–64.
- McDougall, T., Jackett, D., Wright, D., and Feistel, R. 2003. Accurate and computationally efficient algorithms for potential temperature and density of seawater. *Journal of Atmospheric and Oceanic Technology*, 20: 730–741.
- McMinn, A., and Martin, A. 2013. Dark survival in a warming world. *Proceedings of the Royal Society B: Biological Sciences*, 280: 20122909.
- Miklasz, K., and Denny, M. 2010. Diatom sinking speeds: improved predictions and insight from a modified Stokes' law. *Limnology and Oceanography*, 55: 2513–2525.
- Moore, J. K., and Villareal, T. A. 1996. Size-ascent rate relationships in positively buoyant marine diatoms. *Limnology and Oceanography*, 41: 1514–1520.
- Niehoff, B., Klenke, U., Hirche, H., Irigoien, X., Head, R., and Harris, R. 1999. A high frequency time series at weathership M, Norwegian Sea, during the 1997 spring bloom?: the reproductive biology of *Calanus finmarchicus*. *Marine Ecology Progress Series*, 176: 81–92.
- Peperezak, L., and Colijn, F. 2003. Phytoplankton sinking rates in the Rhine region of freshwater influence. *Journal of Plankton Research*, 25: 365–383.
- Riley, G. A. 1946. Factors controlling phytoplankton populations on Georges Bank. *Journal of Marine Research*, 6: 54–73.

- Sakshaug, E., Andresen, K., and Kiefer, D. 1989. A steady state description of growth and light absorption in the marine planktonic diatom *Skeletonema costatum*. *Limnology and Oceanography*, 34: 198–205.
- Sakshaug, E., Johnsen, G., Andresen, K., and Vernet, M. 1991. Modeling of light-dependent algal photosynthesis and growth: experiments with the Barents Sea diatoms *Thalassiosira nordenskioldii* and *Chaetoceros furcellatus*. *Deep Sea Research Part A: Oceanographic Research Papers*, 38: 415–430.
- Sanders, R., Henson, S. A., Koski, M., De La Rocha, C. L., Painter, S. C., Poulton, A. J., Riley, J., *et al.* 2014. The Biological Carbon Pump in the North Atlantic. *Progress in Oceanography*. Elsevier Ltd.
- Smayda, T. 1970. The suspension and sinking of phytoplankton in the sea. *Oceanography and Marine Biology: An Annual Review*, 8: 353–414.
- Smetacek, V., and Passow, U. 1990. Spring bloom initiation and Sverdrup's critical-depth model. *Limnology and Oceanography*, 35: 228–234.
- Sverdrup, H. 1953. On conditions for the vernal blooming of phytoplankton. *Journal du Conseil*, 18: 287–295.
- Taylor, J. R., and Ferrari, R. 2011a. Shutdown of turbulent convection as a new criterion for the onset of spring phytoplankton blooms. *Limnology and Oceanography*, 56: 2293–2307.
- Taylor, J. R., and Ferrari, R. 2011b. Ocean fronts trigger high latitude phytoplankton blooms. *Geophysical Research Letters*, 38: L23601.
- Townsend, D., Keller, M., Sieracki, M., and Ackleson, S. 1992. Spring phytoplankton blooms in the absence of vertical water column stratification. *Nature*, 360: 59–62.
- Townsend, D. W., Cammen, L. M., Holligan, P. M., Campbell, D. E., and Pettigrew, N. R. 1994. Causes and consequences of variability in the timing of spring phytoplankton blooms. *Deep Sea Research Part I: Oceanographic Research Papers*, 41: 747–765.
- UNESCO, I. W. G. 1981. The practical salinity scale 1978 and the international equation of state of seawater 1980. UNESCO Technical Report Papers in Marine Science.
- Verity, P. 1982. Effects of temperature, irradiance, and daylength on the marine diatom *Leptocylindrus danicus* Cleve. III. Dark respiration. *Journal of Experimental Marine Biology and Ecology*, 60: 197–207.
- Waite, A. M., and Nodder, S. D. 2001. The effect of in situ iron addition on the sinking rates and export flux of Southern Ocean diatoms. *Deep-Sea Research Part II: Topical Studies in Oceanography*, 48: 2635–2654.
- Waite, A. M., Thompson, P. A., and Harrison, P. J. 1992. Does energy control the sinking rates of marine diatoms? *Limnology and Oceanography*, 37: 468–477.
- Walter, B., Peters, J., van Beusekom, J. E. E., and St John, M. A. 2015. Interactive effects of temperature and light during deep convection: a case study on growth and condition of the diatom *Thalassiosira weissflogii*. *ICES Journal of Marine Science*, 72: 2061–2071.
- Weger, H., Herzig, R., Falkowski, P., and Turpin, D. 1989. Respiratory losses in the light in a marine diatom: measurements by short-term mass spectrometry. *Limnology and Oceanography*, 34: 1153–1161.
- Wehde, H., and Backhaus, J. 2000. The fate of Lagrangian tracers in oceanic convective conditions: on the influence of oceanic convection in primary production. *Nonlinear Analysis: Real World Applications*, 1: 3–21.
- Wehde, H., Backhaus, J. O., and Nøst Hegseth, E. 2001. The influence of oceanic convection in primary production. *Ecological Modelling*, 138: 115–126.
- Xue, X., Gauthier, D. A., Turpin, D. H., and Weger, H. G. 1996. Interactions between photosynthesis and respiration in the green alga *Chlamydomonas reinhardtii* (characterization of light-enhanced dark respiration). *Plant Physiology*, 112: 1005–1014.

Handling editor: Shubha Sathyendranath



Contribution to the Themed Section: 'Revisiting Sverdrup's Critical Depth Hypothesis' Original Article

Vertical mixing, critical depths, and phytoplankton growth in the Ross Sea

Walker O. Smith, Jr* and Randolph M. Jones

Virginia Institute of Marine Science, College of William & Mary, Gloucester Point, VA 23062, USA

*Corresponding author: tel: +1 804 684 7709; fax: +1 804 684 7399; e-mail: wos@vims.edu

Smith, W. O. Jr, and Jones, R. M. Vertical mixing, critical depths, and phytoplankton growth in the Ross Sea. – ICES Journal of Marine Science, 72: 1952 – 1960.

Received 4 June 2014; revised 27 October 2014; accepted 29 November 2014; advance access publication 23 December 2014.

Phytoplankton growth and biomass accumulation vary spatially and temporally in the Ross Sea, largely as a function of ice concentrations, vertical mixing depths, and iron concentrations. To assess the role of vertical mixing in bloom initiation, we used a high-resolution numerical model to estimate changes in mixed layer depths from October 1 through early December, the period where phytoplankton growth begins and biomass accumulates, and estimate critical depths for this period. Mixed layers in October ranged from the complete water column (>600 m) to ca. 200 m; over a 60-day period, the mixed layers decreased on average by 70%. Estimated critical depths were exceeded in October, but would allow growth to proceed in late October due to shoaling of mixed layer depths, consistent with the known onset of the spring bloom in the Ross Sea. We also analysed a series of stations sampled near the Ross Ice Shelf during January 2012. Mean vertical profiles for the stations indicated deep vertical mixing; mixed layer depths averaged 60 m and ranged up to 96 m. Chlorophyll concentrations within the mixed layer averaged $6.60 \mu\text{g l}^{-1}$, and the pigment contributions were dominated by *Phaeocystis antarctica*. We suggest that this mesoscale region near the ice shelf is elevated in phytoplankton biomass due to frequent mixing events that redistribute biomass to depth and replenish nutrients, which in turn are utilized by an assemblage capable of utilizing low mean irradiance levels. Thus, the deep mixed layers and high biomass concentrations represent growth over long periods under reduced mixing punctuated by short periods of deeper vertical mixing that redistribute biomass. Water column vertical mixing and phytoplankton biomass in the Ross Sea are consistent with the critical depth concept as originally proposed by Sverdrup.

Keywords: biomass, chlorophyll, irradiance, phytoplankton, Ross Sea, vertical mixing.

Introduction

Southern Ocean phytoplankton experience exceptionally large variations in physical forcing variables, such as irradiance, vertical water column stratification, and nutrient supply, and also have relatively low growth rates due to low temperatures. The classical concepts formalized by Sverdrup (1953) have long been applied to Southern Ocean phytoplankton (Mitchell and Holm-Hansen, 1991; Nelson and Smith, 1991), in that it has largely been assumed that vertical mixing is deep in winter, and mixed layers shoal as less saline water from ice melt and heat from increased solar irradiance in spring increases vertical stratification in spring and summer. These concepts have been questioned by Behrenfeld (2010), who suggested that blooms in the North Atlantic were regulated by the tight coupling between grazers and phytoplankton, as well as the

dilution effect due to increased vertical mixing in winter. This “dilution-recoupling” hypothesis was further supported by drifter data from the North Atlantic (Boss and Behrenfeld, 2010). Mahadevan *et al.* (2012) suggested that eddy-derived mesoscale variations in mixed layer depths provided a mosaic of environments in which phytoplankton growth proceeded, and thus generated a bloom in spring that preceded one derived from temperature-induced stratification. Behrenfeld (2010) largely used satellite data to support his argument, as there are few direct observations collected during the onset of spring blooms in any environment. This is especially true in the Southern Ocean and its most southerly seas, such as the Ross Sea, where thick ice cover makes it difficult for ships to sample during the winter–spring transition.

Assessments of the role of irradiance on phytoplankton growth have shown the importance of vertical mixing in the Southern Ocean. Mitchell and Holm-Hansen (1991) suggested that mixed layers >40 m precluded phytoplankton growth and accumulation in the West Antarctic Peninsula; Nelson and Smith (1991) calculated critical depths for the Ross Sea and concluded that the critical depth concept indeed was applicable in describing phytoplankton growth and biomass accumulation. Smith *et al.* (2000) combined data from a series of cruises with a large range of mixed layer depths (some with mixed layers >600 m) and confirmed the conclusion of Mitchell and Holm-Hansen (1991) that growth was largely restricted to locations where mixed layers were <40 m. This was strong circumstantial evidence of the validity of the critical depth concept, but none of these studies sampled during early spring or conducted a time series of plankton development. Hence, while a relationship between vertical mixing and phytoplankton was established, a complete test of the Sverdrup concepts was lacking.

The Ross Sea is a heterogeneous system that becomes nearly completely ice covered in winter, with ice growing to ca. 1 m in thickness. There are regions near the coast, such as in Terra Nova Bay and near the central Ross Ice Shelf, where intense winds blow ice away from the coast and reduce ice concentrations in small areas. These areas continue to produce ice due to the very low air temperatures (ca. -60°C); ice formation results in brine rejection, the sinking of which in turn drives deep vertical mixing. The spatial extent of such mixing is, however, unknown. Indeed, very few observations on the water column are available for the winter and early spring period, given the difficulty of gaining access to the region at that time.

The waters close to the Ross Ice Shelf are different from those over much of the rest of the continental shelf, in that they often exhibit deep mixed layers throughout the year. They also are the sites of large blooms of the haptophyte *Phaeocystis antarctica* (El-Sayed *et al.*, 1983). In other parts of the Ross Sea, *P. antarctica* blooms appear early in spring (ca. late October; Smith and Gordon, 1997) and reach very high biomass (up to $15\ \mu\text{g l}^{-1}$ chlorophyll) by mid-December, after which the colonial forms disappear rapidly from the water column (Smith *et al.*, 2011). After *Phaeocystis* biomass is reduced, diatoms often grow, occasionally reaching chlorophyll concentrations that are equal to those of the primary *Phaeocystis* bloom (Smith *et al.*, 2006, 2011). The presence of *Phaeocystis* near the ice shelf is unusual, but also is quite predictable.

We present data from two sets of experiments. The first is the result of a model of Ross Sea circulation (Dinniman *et al.*, 2003, 2011) that accurately represents the essential physical processes on the continental shelf at a resolution that is relevant to phytoplankton growth and accumulation. The second is a set of measurements taken near the Ross Ice Shelf where deep mixed layers were detected along with enhanced concentrations of phytoplankton biomass. We use both of these to suggest that the concepts developed by Sverdrup (1953) indeed are applicable to the Ross Sea (and by extension, to much of the Southern Ocean), and to suggest a mechanism by which extensive accumulations of phytoplankton biomass can accumulate in the deep mixed layer despite the likely irradiance limitation.

Material and methods

Numerical model

The numerical model uses an implementation of the Regional Ocean Modeling System (Haidvogel *et al.*, 2008) for the Ross Sea

(Dinniman *et al.*, 2003, 2011). The circulation model uses a 5-km horizontal grid spacing with 24 terrain-following vertical layers, and its domain extends from 67.5°S to under the Ross Ice Shelf. The model includes a dynamic sea ice model (Budgell, 2005) that prognostically calculates sea ice concentration and thickness

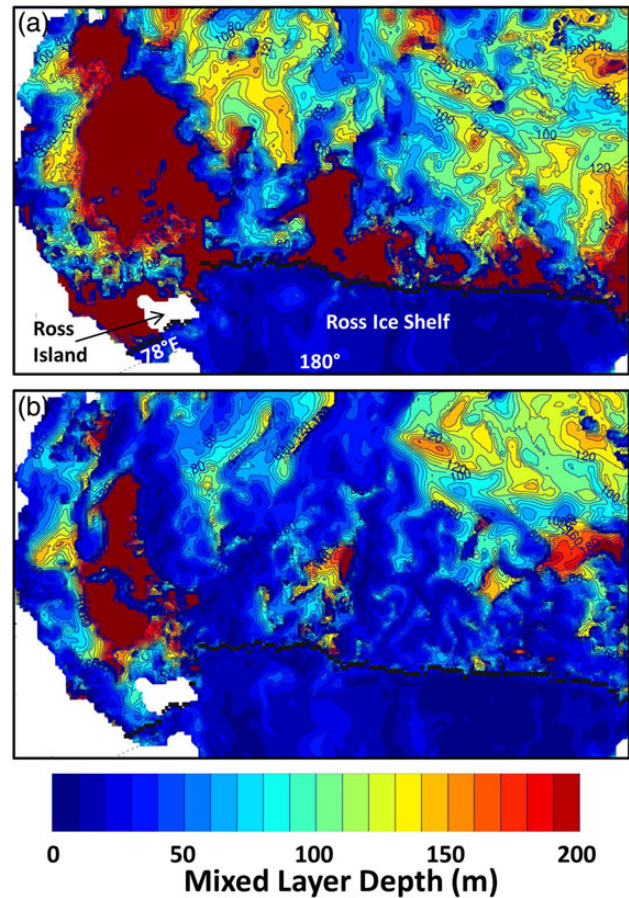


Figure 1. Modelled spatial distributions of the depth of mixing (m) in the Ross Sea from (a) October 1 and (b) November 27.

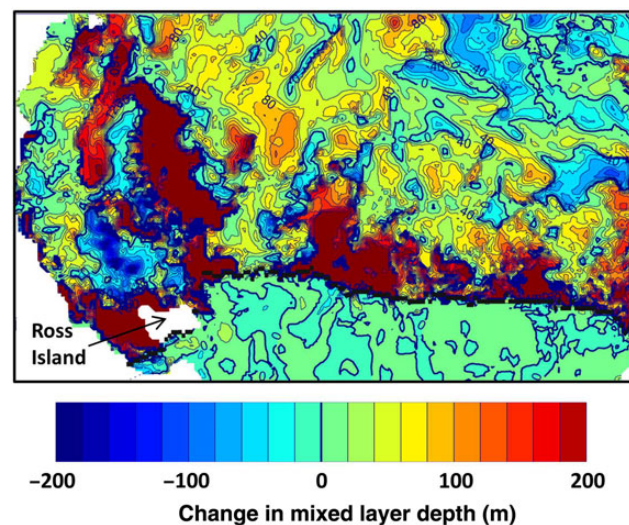


Figure 2. Modelled changes in the mixed layer depth between October 1 and November 27.

(Stern *et al.*, 2013) and accurately depicts circulation, shelf-water formation, and ice distribution (Dinniman *et al.*, 2007, 2011; Smith *et al.*, 2014a). Winds and air temperatures were taken every 6 h from the ERA-Interim (Dee *et al.*, 2011). The model also simulates the mechanical and thermodynamic interactions between the Ross Ice Shelf and the waters below (Holland and Jenkins, 1999; Dinniman *et al.*, 2011). Ocean tides are included. Mixed layers were derived from October 1 through November 27 at 2-week intervals. Mixed layers are defined by a change in σ_t of 0.01 kg m^{-3} from a stable surface layer (Thompson and Fine, 2003), as were observational mixed layers (see below).

Observations

Observations in the Ross Sea were collected as part of Processes Regulating Iron Supply at the Mesoscale (PRISM) in January–February 2012 from the *R/VIB Nathaniel B. Palmer* cruise NBP12-01. Hydrographic information was obtained using a Seabird 911+ CTD that was fitted with a WETLabs fluorometer and SeaTech transmissometer. Mixed layer depths were determined as with the model; that is, changes in σ_t from the stable surface layer (generally from 10 m) of 0.01 kg m^{-3} (Thompson and Fine, 2003; Sedwick *et al.*, 2011; Smith *et al.*, 2011, 2013). Kaufman *et al.* (2014) compared a number of independent methods of determining mixed layer depths and found no substantial difference among them, and also used a 0.01 kg m^{-3} threshold. Irradiance data (both surface and

submarine) were measured using BioSpherical Instruments quantum sensors. Water was collected from 12 depths in the upper 150 m for nutrients, phytoplankton biomass (chlorophyll *a*,

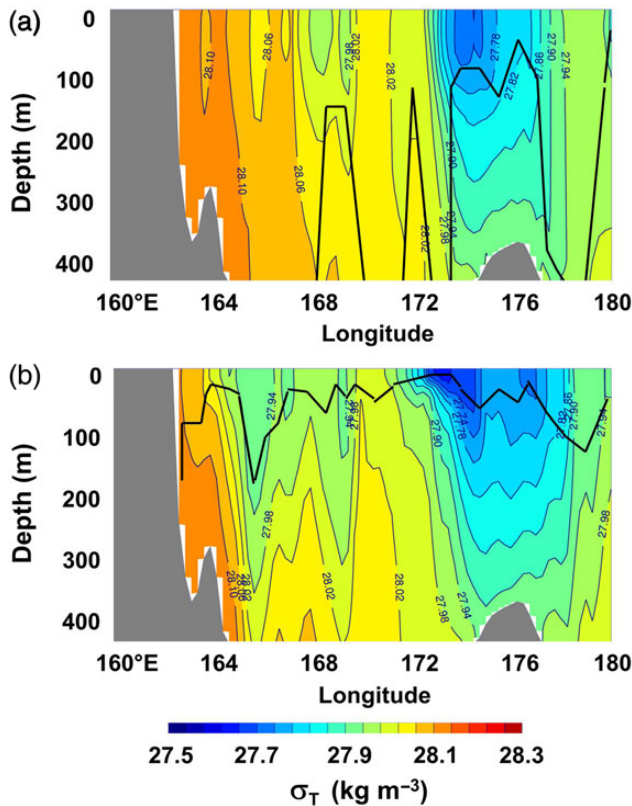


Figure 3. Modelled density distributions from the coast of Victoria Land to 180° along 77°S on (a) October 1 and (b) November 27. The mixed layer depth is indicated by the solid black line. Critical depths in October were 27 m, assuming an $\sum E_o$ of $5 \text{ mol photons m}^{-2} \text{ d}^{-1}$ and a $K_{\text{PAR}} = 0.048 \text{ m}^{-1}$, and in late November equalled 218 m, when $\sum E_o$ was assumed to increase to $40 \text{ mol photons m}^{-2} \text{ d}^{-1}$.

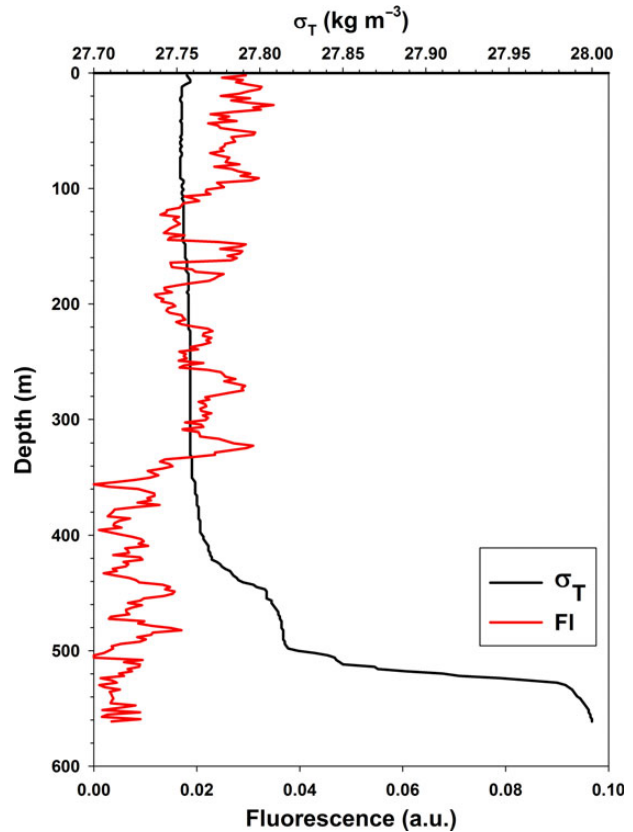


Figure 4. Vertical distribution of density (σ_t) and fluorescence in the entire water column ($z = 561 \text{ m}$) at St. 12 (occupied on 27 October 1996; 78.02°S , 175.91°E) within 20 km of the Ross Ice Shelf.

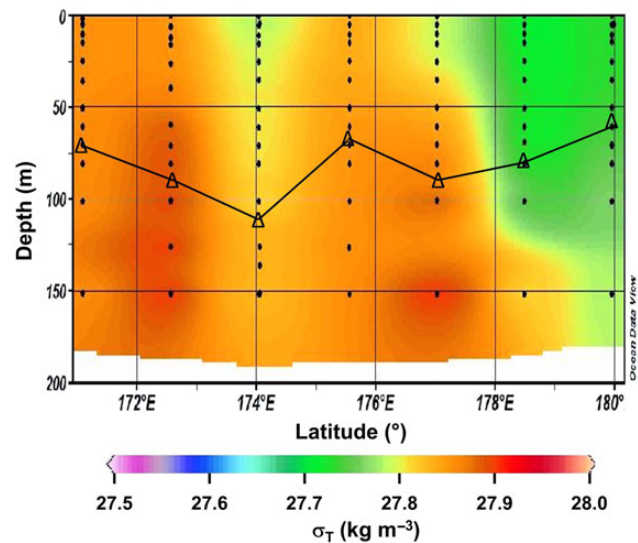


Figure 5. Distribution of density (σ_t) along 77°S on 16–17 November 2006 (Smith *et al.*, 2013). Mixed layer depths indicated by triangles and solid line.

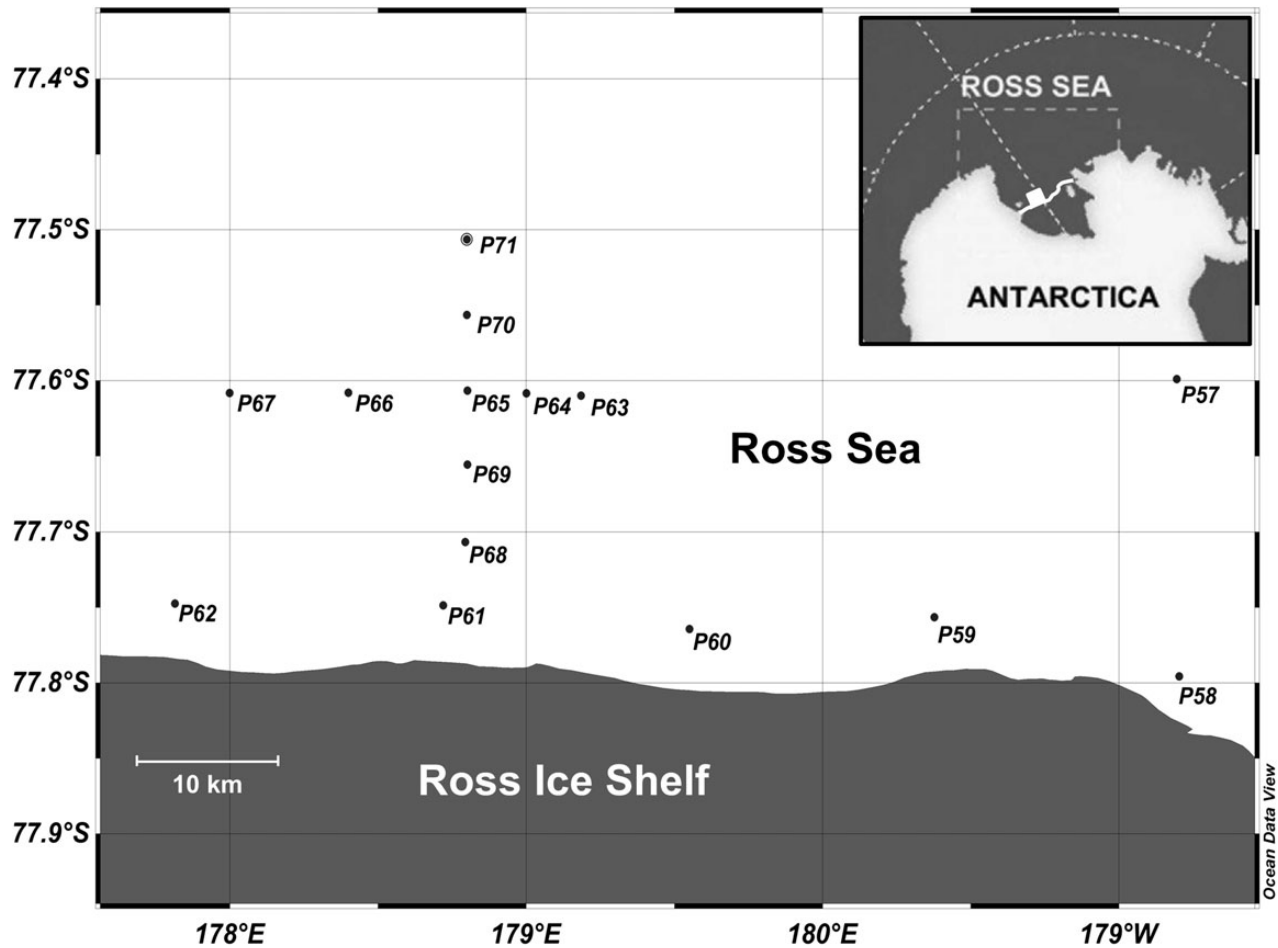


Figure 6. Location of the stations occupied near the Ross Ice Shelf in January 2012 during *NBP12-01*. White square in inset shows the location of the PRISM ice shelf stations.

Table 1. Calculated critical depths [from Equation (1)] and measured euphotic zone (1% isolume) depths, mixed layer depths, and mean mixed layer chlorophyll concentrations for PRISM stations located near the Ross Ice Shelf.

Station number	Mixed layer depth (m)	Euphotic zone depth (m)	Critical depth (m)	Mixed layer chlorophyll concentration ($\mu\text{g L}^{-1}$)
57	39	28	32	8.71
58	45	25	29	8.22
59	42	29	33	5.67
60	91	29	33	6.00
61	51	30	35	7.38
62	47	29	33	4.97
63	54	25	29	7.79
64	70	25	29	6.26
65	93	26	30	5.81
66	58	26	30	6.24
67	36	31	36	3.53
68	96	30	35	6.41
69	79	29	33	8.69
70	54	28	32	8.30
71	47	31	36	5.07
Mean \pm SD	60.1 \pm 20.5	28.1 \pm 2.15	32.2 \pm 2.47	6.60 \pm 1.53

Surface irradiance assumed to be 20 mol photons $\text{m}^{-2} \text{d}^{-1}$.

Table 2. Mean and SD of oceanographic variables at stations near the Ross Ice Shelf ($n = 15$).

Variable	Mean \pm SD
Mixed layer depth (m)	60.1 \pm 20.5
Euphotic zone depth (m)	28.1 \pm 2.15
Nitrate concentration (μM)	18.1 \pm 1.38
Silicic acid concentration (μM)	72.1 \pm 1.55
Chlorophyll <i>a</i> concentration ($\mu\text{g l}^{-1}$)	6.60 \pm 1.53
POC concentration ($\mu\text{mol l}^{-1}$)	35.1 \pm 7.83

particulate organic carbon (POC) and nitrogen, pigment, and biogenic silica concentrations; only chlorophyll *a* data are used in this analysis), and phytoplankton composition using Teflon-coated, external closure Niskin bottles. Methods for the determination of all variables are described in detail elsewhere (DiTullio and Smith, 1996; Gardner *et al.*, 2000; Smith *et al.*, 2006).

Critical depths (Z_c) were calculated using a reformulation of the Sverdrup (1953) equation (Nelson and Smith, 1991) or

$$Z_c = \frac{\sum E_0}{3.78K_{PAR}}, \quad (1)$$

where $\sum E_0$ is the surface photosynthetically active radiation (PAR) integrated over 24 h, K_{PAR} is the diffuse attenuation coefficient of PAR, and 3.78 is a combination of constants and conversion factors. Equation (1) was derived from the original Sverdrup (1953) formulation, but with slight changes with regard to photo-compensation depths and irradiance units. Specifically, Nelson and Smith (1991) used water column PAR values to avoid the assumptions of reflectance and differential absorption of wavelengths, and used more recent estimates of photocompensation depths from temperate regions.

The variable K_{PAR} was estimated as the slope of the line determined by regressing the natural logarithm of PAR values with depth, and the depth of the euphotic zone (1% of surface irradiance) calculated from K_{PAR} . Since the ship never was at a single location for 24 h, we estimated the minimum and maximum integrated irradiance values by fitting observed values for a clear sky at solar noon and local midnight to a sinusoidal function and a 24-h photoperiod (Hiscock *et al.*, 2003). We estimated that clouds reduced incident irradiance by 50%, although cloud-cover reductions can range 30–97%.

Results

Model and supporting observations

Modelled mixed layers in the Ross Sea are spatially variable and are a function of the magnitude and duration of brine rejection from the pack ice. For example, near the Ross Ice Shelf where southerly winds blow off the shelf and advect the pack ice to the north, new ice is continually generated in the polynya, and brine is continuously released, driving extremely deep mixing (Figure 1). Deep mixing also occurs over the shallow banks that parallel the coast of Victoria Land; conversely, lesser mixing occurs in the troughs where warmer water enters onto the shelf from the Ross Gyre. Changes in mixed layer depth over this 8-week period were large, and most areas had mixed layers that shoaled by 100 m or more, except in areas where pack ice remained (Figure 2). The modelled distribution of density along 77°S demonstrates the large temporal changes in mixed layer depths (Figure 3). Critical depths along this transect, assuming a constant irradiance, are shallower than the mixed layer depths in early October, but largely greater than the mixed layers in late November. Specifically, if a daily irradiance of $5 \text{ mol photons m}^{-2} \text{ d}^{-1}$ and chlorophyll concentrations of $<0.1 \mu\text{g l}^{-1}$ are assumed in early October, critical depths equal 27 m [derived from Equation (1)]; when daily integrated irradiance increases by late November and approaches 40 mol

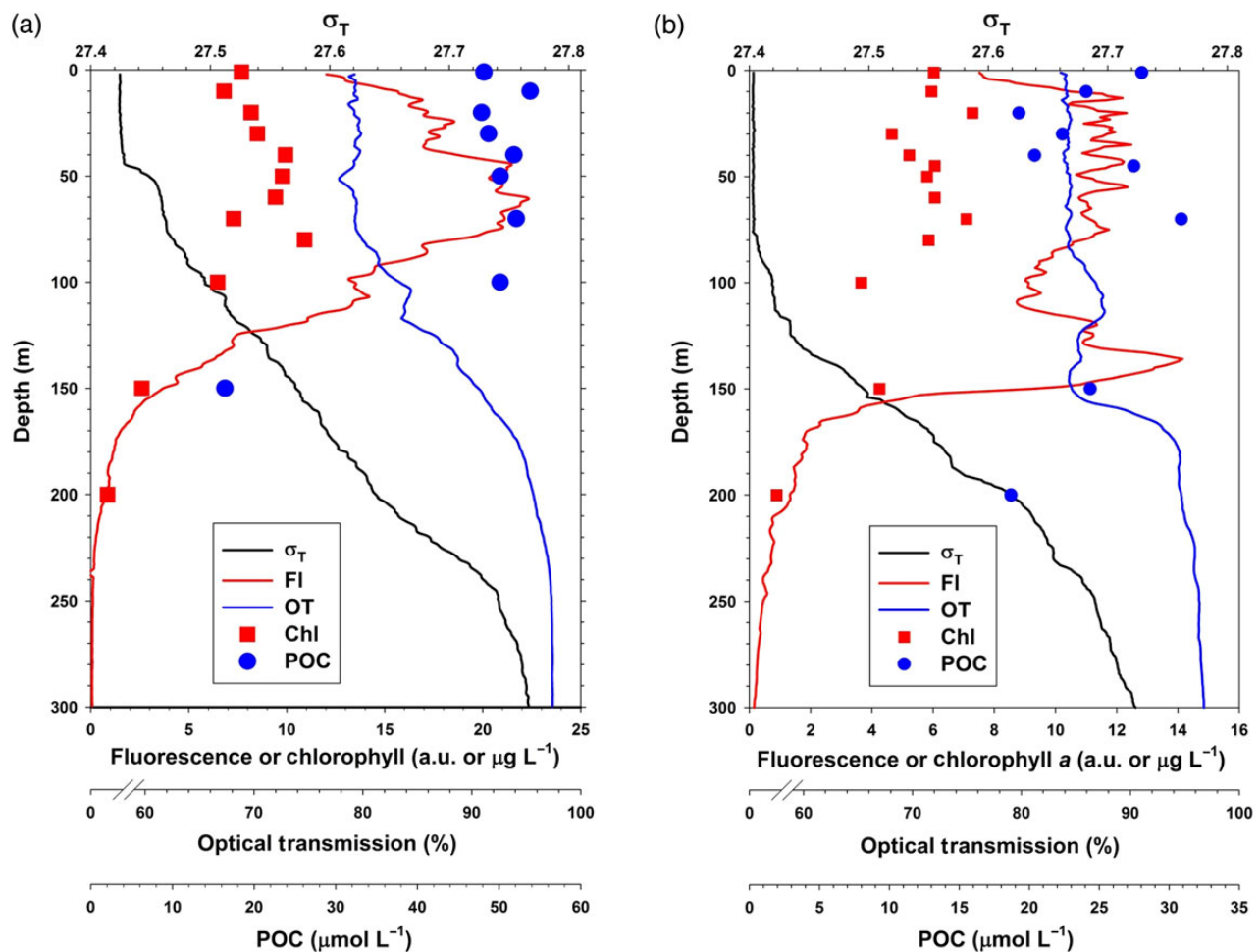


Figure 7. Vertical distribution of density, fluorescence, and optical transmission of two stations (a: St. 58 and b: St. 60) occupied during NBP12-01. Solid squares represent extracted chlorophyll concentrations, and solid circles represent POC concentrations.

photons $\text{m}^{-2} \text{d}^{-1}$ (but again with chlorophyll concentrations $< 0.1 \mu\text{g l}^{-1}$), critical depths exceed 200 m. As such, the model results and estimated critical depths are consistent with Sverdrup's (1953) original hypothesis.

Only limited numbers of oceanographic investigations have sampled the Ross Sea polynya in late winter or early spring. One station (at 78.02°S , 175.91°E) near the ice shelf was sampled on 27 October 1997 (http://usjgofs.who.edu/jg/dir/jgofs/southern/nbp96_4A/; Figure 4), and it showed a deep mixed layer ($> 400 \text{ m}$) with no enhanced phytoplankton biomass. Other stations during the same cruise near 76.5°S showed that mixed layers reached completely to the shelf floor. Another series of stations were completed from 16 to 17 November 2006 (Figure 5; Smith *et al.*, 2013), where mixed layers ranged from 58 to 112 m and where chlorophyll levels were $> 1 \mu\text{g l}^{-1}$. Thus, the limited observations in late winter–early spring support the modelled mixed layer depths, as well as the progression of reduced mixed layers associated with increasing phytoplankton biomass within the winter–spring transition.

Observations near the Ross Ice Shelf

Water columns near the Ross Ice Shelf (Figure 6) were characterized by deep mixed layers and large phytoplankton biomass. Mixed layer depths for the 15 PRISM stations near the ice shelf averaged $60.1 \pm 20.5 \text{ m}$ (Table 1); surface nitrate concentrations at these stations averaged $18.1 \mu\text{M}$. Mean euphotic zone depths and silicic acid, chlorophyll, and POC concentrations were 28.1 m, $72.1 \mu\text{M}$, $6.60 \mu\text{g l}^{-1}$, and $35.1 \mu\text{mol l}^{-1}$ (Table 2). Numerically, the phytoplankton assemblages were dominated by *Phaeocystis antarctica*, a condition also observed some 35 years earlier by El-Sayed *et al.* (1983).

Two stations (Sts 58 and 60), both similar in distance from the ice shelf, can be contrasted with respect to vertical density structure, fluorescence, optical transmission, and distributions of nitrate, chlorophyll, and POC (Figure 7). The mixed layer of St. 58 ($Z_{\text{mix}} = 45 \text{ m}$) was slightly less than the mean for all stations (60.1 m; Table 1), and exhibited not only large phytoplankton biomass within the mixed layer, but also substantial concentrations below, which extended to 150 m. Optical transmission values supported the same conclusion of a large biomass through the upper 150 m. The depth of the euphotic zone was 25 m. St. 60 exhibited a deeper Z_{mix} (96 m), with large biomass accumulations within the mixed layer and below (again, through 150 m), as indicated by the large fluorescence and transmission values. St. 60's euphotic depth was 29 m.

Calculated critical depths strongly suggested that growth during sampling was largely limited by irradiance (Table 1); that is, critical depths were shallower in all cases than the mixed layer depths. We recognize that Sverdrup's original contribution was designed to predict the onset of a bloom rather than growth under high biomass conditions, but estimates of critical depths emphasize the primary role of irradiance in both growth initiation, biomass accumulation, and growth limitation. Critical depth estimates are highly dependent on integrated daily irradiance estimates (Table 3), which can vary greatly over space and time. Much of our sampling near the ice shelf was conducted under very cloudy skies, with substantial snow and strong winds. Our estimates of critical depths (Table 1) assumed a daily $\sum E_o$ of approximately half the maximum clear sky irradiance, but if the meteorological conditions that were encountered during sampling continued for 24 h or more, integrated irradiance would likely be substantially less, resulting in even more modest critical depths. Similarly, since spring conditions

Table 3. Dependence of estimated critical depths on surface irradiance.

Integrated daily surface irradiance (mol photons $\text{m}^{-2} \text{d}^{-1}$)	Calculated critical depths (m)
5	8.0
10	16.1
15	24.1
20	32.2
25	40.2
30	48.3
40	64.3
50	80.4
60	96.5
80	128

Critical depths calculated assuming a euphotic depth of 28 m and a K_{PAR} of 0.164 m^{-1} , values similar to those measured during NBP12-01.

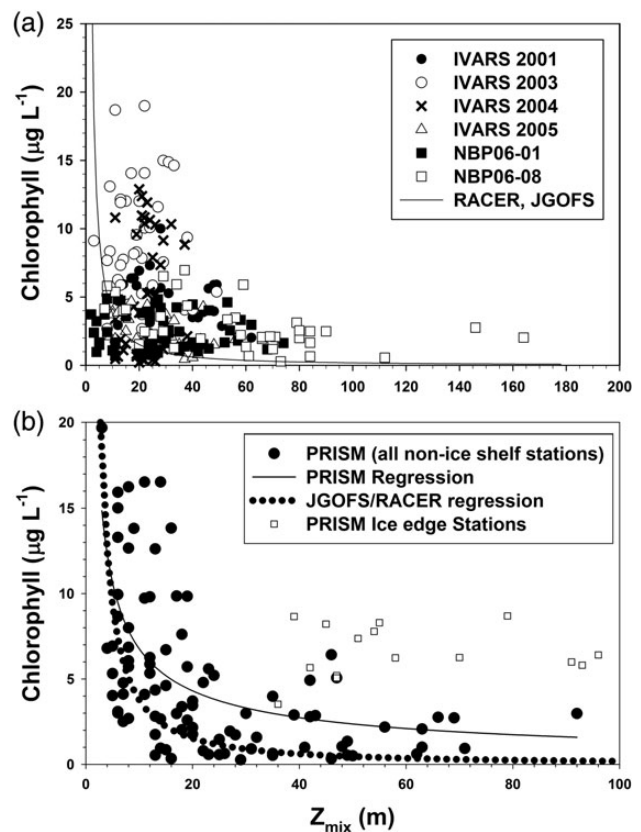


Figure 8. Relationship of mixed layer depth (Z_{mix}) and mean chlorophyll concentration in the mixed layer from (a) six cruises from 2000 to 2006 in the Ross Sea and (b) PRISM (both ice-shelf and non-ice-shelf stations). Included in both is the relationship determined by Mitchell and Holm-Hansen (1991), and in (b) the power relationship of PRISM non-ice-shelf stations ($\text{CHL} = 30.4Z_{\text{m}}^{-0.65}$; $R^2 = 0.31$, $p < 0.001$).

often are extremely cloudy, $\sum E_o$ values in spring would likely be reduced by far $> 50\%$.

Discussion

Although there are no data from the Southern Ocean to directly test Sverdrup's (1953) hypothesis, the Ross Sea appears to be an excellent region where these concepts can be verified. Our model results show

that for most of the continental shelf, mixed layers are very deep in winter and spring (driven by ice formation and brine rejection); furthermore, estimated critical depths for early spring (ca. 27 m assuming a euphotic depth of 95 m and 5 mol photons $\text{m}^{-2} \text{d}^{-1}$) remain far less than the mixed layer depths (Figure 3). As solar radiation increases seasonally and mixed layers become shallower, critical depths become deeper (ca. 211 m) and exceed the mixed layer depths. The critical depth concept appears completely consistent with phytoplankton temporal patterns observed in the past (Smith *et al.*, 2014b) and predicts the onset of growth (in late October; Smith and Gordon, 1997) well.

The role of vertical mixing and irradiance limitation has long been recognized as a dominant factor in controlling the annual productivity of the Southern Ocean (Smith *et al.*, 2014b). This remains true even with the realization that iron concentrations are exceptionally low throughout much of the Antarctic realm, even on continental shelves (Sedwick *et al.*, 2011). Mitchell and Holm-Hansen (1991) emphasized the importance of vertical mixing and suggested that mixed layers >40 m effectively precluded phytoplankton growth and biomass accumulation, a conclusion also supported by extensive data from the Ross Sea collected in the 1990s (Smith *et al.*, 2000). Many additional investigations have been completed in the past 15 years, and those suggest that the absolute depth of mixing is indeed important in regulating biomass, but that some environments support an elevated biomass in mixed layers up to 60 m (Figure 8a). Regardless of the absolute depth of mixing, the inverse relationship between mixing and chlorophyll concentration remains, emphasizing the importance of irradiance on the

regulation of phytoplankton biomass (Figure 8a). Mitchell and Holm-Hansen (1991) also emphasized that the duration of stratification was important to allow growth to proceed in a high-irradiance environment and permit biomass to accumulate. As such, loss terms from the surface mixed layer are important, and the stations where elevated biomass is observed in mixed layers deeper than 40 m may reflect a reduced loss rate. Data from the Ross Sea demonstrating substantial chlorophyll in deeper mixed layers suggest that these large accumulations may result from reduced loss rates when compared with the west Antarctic Peninsula. Conversely, there are many stations where shallow mixed layers support relatively low chlorophyll concentrations, and we suggest that these represent locations that have had stratification for substantial periods of time and the biomass levels have been reduced due to losses (grazing, sinking) and reduced growth rates from iron limitation (Sedwick *et al.*, 2011).

Data from the PRISM cruise, and specifically from the ice shelf stations (Figure 8b), are also markedly different from the relationship developed by Mitchell and Holm-Hansen (1991). Specifically, there are a substantial number of stations that exhibit elevated chlorophyll concentrations in mixed layers deeper than 40 m. This is especially true of the ice shelf stations, where there are extremely high chlorophyll concentrations that are nearly independent of mixed layer depth (Figure 8b). Based on our analysis of critical and euphotic depths, it is unlikely that these large biomass levels are the direct result of growth at depths below the euphotic zone. Such large concentrations of phytoplankton must have a different mechanism of generation.

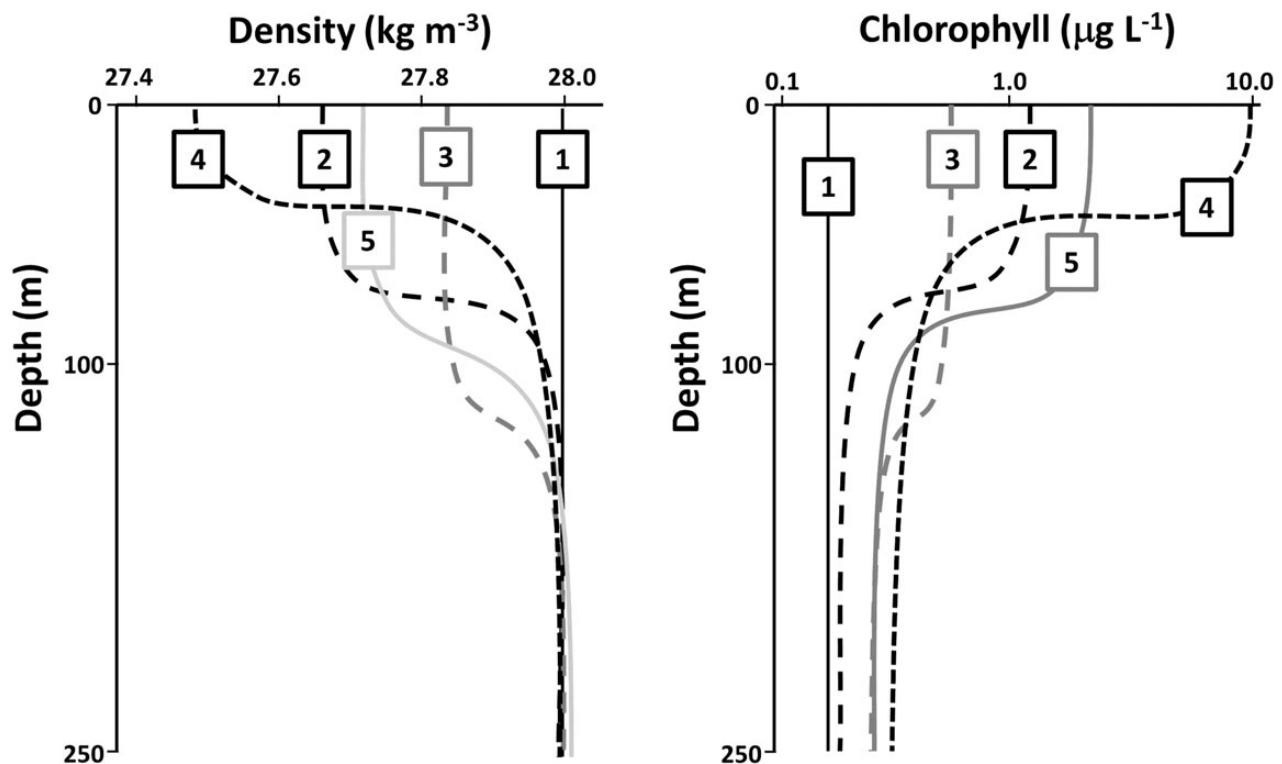


Figure 9. Schematic diagram of the generation of high biomass, deep mixing stations. Numbers indicate periods within the spring bloom: 1—initial, spring condition with deep mixing and low biomass; 2—generation of elevated biomass under relatively quiescent, stratified conditions; 3—redistribution of biomass and salt/heat during a wind event; 4—further growth and accumulation of biomass under quiescent, stratified conditions; and 5—redistribution of biomass and salt/heat during a wind event. Scales on axes are approximate.

We suggest the following as a means of accumulation of such large phytoplankton standing stocks (Figure 9): extensive growth during periods of significant water column stratification, followed by biomass redistribution by mixing induced by wind events, followed by further restratification of the surface water column, and followed by another redistribution of biomass during an intense wind event. Therefore, the growth/redistribution events would be driven by the timescales of local wind events. Furthermore, these blooms would be largely confined to the region near the ice shelf, as they are frequently the location of katabatic winds that blow off the continent over water. These katabatic winds likely only blow for ca. 20 km from the ice shelf, thus restricting the spatial extent of these blooms. Phytoplankton are dominated by the colonial haptophyte *Phaeocystis antarctica*, a species that is known to acclimate to low irradiances (Kropuenske *et al.*, 2009) and thrive in more deeply mixed water columns. It has also been suggested that the growth of *P. antarctica* becomes iron limited at the end of December in much of the Ross Sea (Smith *et al.*, 2000); however, the deep vertical mixing near the ice shelf, coupled with ice shelf iron inputs, likely precludes any iron limitation and allows mesoscale blooms to continue throughout summer.

In summary, phytoplankton growth in the Ross Sea in spring is clearly controlled by low irradiance levels imposed by surface pack ice and deep vertical mixing. While no data are available to directly test Sverdrup's (1953) critical depth hypothesis, model results are consistent with previous observations and confirm the validity of the classical paradigm in the Southern Ocean. An unusual region near the ice shelf is also irradiance limited, but the timescales of mixing likely allow for the development of a deeply mixed surface layer that maintains an elevated, though irradiance limited, phytoplankton biomass. Thus, irradiance can play a critical role in regulating phytoplankton growth in the Ross Sea at a variety of time and space scales, and the region would be an excellent location for an explicit observational test of Sverdrup's hypothesis.

Acknowledgements

This research was supported by the National Science Foundation (Grant ANT-0944254). We thank M. Dinniman and S. Mack for their assistance in the simulations and plotting of model results, as well as our PRISM colleagues for their assistance at sea. This is VIMS Contribution number 3428.

References

Behrenfeld, M. J. 2010. Abandoning Sverdrup's critical depth hypothesis on phytoplankton blooms. *Ecology*, 91: 977–989.

Boss, E., and Behrenfeld, M. 2010. In situ evaluation of the initiation of the North Atlantic phytoplankton bloom. *Geophysical Research Letters*, 37: L18603, doi:10.1029/2010GL044174.

Budgell, W. P. 2005. Numerical simulation of ice-ocean variability in the Barents Sea region: towards dynamical downscaling. *Ocean Dynamics*, 55: 370–387.

Dee, D. P., Uppala, S. M., Simmons, A. J., Berrisford, P., Poli, P., Kobayashi, S., Andrae, U., *et al.* 2011. The ERA-Interim reanalysis: configuration and performance of the data assimilation system. *Quarterly Journal of the Royal Meteorological Society*, 137: 553–597.

Dinniman, M. S., Klinck, J. M., and Smith, W. O., Jr. 2003. Cross shelf exchange in a model of the Ross Sea circulation and biogeochemistry. *Deep-Sea Research II*, 50: 3103–3120.

Dinniman, M. S., Klinck, J. M., and Smith, W. O., Jr. 2007. The influence of sea ice cover and icebergs on circulation and water mass formation

in a numerical circulation model of the Ross Sea, Antarctica. *Journal of Geophysical Research*, 112: C05S93, doi:10.1029/2007JC004251.

Dinniman, M. S., Klinck, J. M., and Smith, W. O., Jr. 2011. A model study of Circumpolar Deep Water on the West Antarctic Peninsula and Ross Sea continental shelves. *Deep-Sea Research II*, 58: 1508–1523.

DiTullio, G. R., and Smith, W. O., Jr. 1996. Spatial patterns in phytoplankton biomass and pigment distributions in the Ross Sea. *Journal of Geophysical Research*, 101: 18467–18477.

El-Sayed, S. Z., Biggs, D. C., and Holm-Hansen, O. 1983. Phytoplankton standing crop, primary productivity, and near-surface nitrogenous nutrient fields in the Ross Sea, Antarctica. *Deep-Sea Research*, 30: 871–886.

Gardner, W. D., Richardson, M. J., and Smith, W. O., Jr. 2000. Seasonal patterns of water column particulate organic carbon and fluxes in the Ross Sea, Antarctica. *Deep-Sea Research II*, 47: 3423–3449.

Haidvogel, D. B., Arango, H., Budgell, W. P., Cornuelle, B. D., Curchitser, E., Di Lorenzo, E., Fennel, K., *et al.* 2008. Ocean forecasting in terrain-following coordinates: formulation and skill assessment of the regional ocean modeling system. *Journal of Computational Physics*, 227: 3595–3624.

Hiscock, M. R., Marra, J., Smith, W. O., Jr, Goericke, R., Meausres, C., Vink, S., Olson, R. J., *et al.* 2003. Primary productivity and its regulation in the Pacific Sector of the Southern Ocean. *Deep-Sea Research II*, 50: 533–558.

Holland, D. M., and Jenkins, A. 1999. Modeling thermodynamic ice-ocean interactions at the base of an ice shelf. *Journal of Physical Oceanography*, 29: 1787–1800.

Kaufman, D. E., Friedrichs, M. A. M., Smith, W. O., Jr, Queste, B. Y., and Heywood, K. J. 2014. Biogeochemical variability in the southern Ross Sea as observed by a glider deployment. *Deep-Sea Research I*, 92: 93–106.

Kropuenske, L. R., Mills, M. M., van Dijken, G. L., Bailey, S., Robinson, D. H., Welschmeyer, N. A., and Arrigo, K. R. 2009. Photophysiology in two major Southern Ocean phytoplankton taxa: photoprotection in *Phaeocystis antarctica* and *Fragilariopsis cylindrus*. *Limnology and Oceanography: Methods*, 54: 1176–1196.

Mahadevan, A., D'Asaro, E., Lee, C., and Perry, M. J. 2012. Eddy-driven stratification initiates North Atlantic spring phytoplankton blooms. *Science*, 337: 54–58.

Mitchell, B. G., and Holm-Hansen, O. 1991. Observations and modeling of the Antarctic phytoplankton crop in relation to mixing depth. *Deep-Sea Research*, 38: 981–1007.

Nelson, D. M., and Smith, W. O., Jr. 1991. Sverdrup revisited: critical depths, maximum chlorophyll levels and the control of Southern Ocean productivity by the irradiance/mixing regime. *Limnology and Oceanography*, 36: 1650–1661.

Sedwick, P. N., Marsay, C. M., Aguilar-Islas, A. M., Lohan, M. C., Sohst, B. M., Long, M. C., Arrigo, K. R., *et al.* 2011. Early-season iron depletion in the Ross Sea polynya: implications for iron dynamics on the Antarctic continental shelf. *Journal of Geophysical Research*, 116: C12019, doi:10.1029/2010JC006553.

Smith, W. O., Jr, Ainley, D. G., Arrigo, K. R., and Dinniman, M. S. 2014b. The oceanography and ecology of the Ross Sea. *Annual Review of Marine Science*, 6: 469–487.

Smith, W. O., Jr, Asper, V., Tozzi, S., Liu, X., and Stammerjohn, S. E. 2011. Continuous fluorescence measurements in the Ross Sea, Antarctica: scales of variability. *Progress in Oceanography*, 88: 28–45.

Smith, W. O., Jr, Dinniman, M. S., Hoffman, E. E., and Klinck, J. 2014a. The effects of changing winds and temperatures on the oceanography of the Ross Sea in the 21st century. *Geophysical Research Letters*, 41, doi:10.1002/2014GL059311.

Smith, W. O., Jr, and Gordon, L. I. 1997. Hyperproductivity of the Ross Sea (Antarctica) polynya during austral spring. *Geophysical Research Letters*, 24: 233–236.

- Smith, W. O., Jr, Marra, J., Hiscock, M. R., and Barber, R. T. 2000. The seasonal cycle of phytoplankton biomass and primary productivity in the Ross Sea, Antarctica. *Deep-Sea Research II*, 47: 3119–3140.
- Smith, W. O., Jr, Shields, A. R., Peloquin, J. A., Catalano, G., Tozzi, S., Dinniman, M. S., and Asper, V. 2006. Biogeochemical budgets in the Ross Sea: variations among years. *Deep-Sea Research II*, 53: 815–833.
- Smith, W. O., Jr, Tozzi, S., Sedwick, P. W., DiTullio, G. R., Peloquin, J. A., Long, M., Dunbar, R., *et al.* 2013. Spatial and temporal variations in variable fluorescence in the Ross Sea (Antarctica): oceanographic correlates and bloom dynamics. *Deep-Sea Research I*, 79: 141–155.
- Stern, A. A., Dinniman, M. S., Zagorodnov, V., Tyler, S. W., and Holland, D. M. 2013. Intrusion of warm surface water beneath the McMurdo Ice Shelf, Antarctica. *Journal of Geophysical Research*, 118: 7036–7048.
- Sverdrup, H. U. 1953. On conditions for the vernal blooming of phytoplankton. *Journal du Conseil International pour l'Exploration de la Mer*, 18: 287–295.
- Thompson, R. E., and Fine, I. V. 2003. Estimating mixed layer depth from oceanic profile data. *Journal of Atmospheric and Oceanic Technology*, 20: 319–329.

Handling editor: Shubha Sathyendranath



Contribution to the Themed Section: 'Revisiting Sverdrup's Critical Depth Hypothesis' Original Article

Characterizing upper-ocean mixing and its effect on the spring phytoplankton bloom with *in situ* data

Sarah R. Brody* and M. Susan Lozier

Department of Earth and Ocean Sciences, Duke University, Durham, NC 27708, USA

*Corresponding author: tel/fax: +1 919 613 2115; e-mail: sarah.brody@duke.edu

Brody, S. R., and Lozier, M. S. Characterizing upper-ocean mixing and its effect on the spring phytoplankton bloom with *in situ* data. – ICES Journal of Marine Science, 72: 1961–1970.

Received 29 May 2014; revised 2 January 2015; accepted 5 January 2015; advance access publication 4 February 2015.

Since publication, the Sverdrup hypothesis, that phytoplankton are uniformly distributed within the ocean mixed layer and bloom once the ocean warms and stratifies in spring, has been the conventional explanation of subpolar phytoplankton spring bloom initiation. Recent studies have sought to differentiate between the actively mixing section of the upper ocean and the uniform-density mixed layer, arguing, as Sverdrup implied, that decreases in active mixing drive the spring bloom. In this study, we use *in situ* data to investigate the characteristics and depth of active mixing in both buoyancy- and wind-driven regimes and explore the idea that the shift from buoyancy-driven to wind-driven mixing in the late winter or early spring creates the conditions necessary for blooms to begin. We identify the bloom initiation based on net rates of biomass accumulation and relate changes in the depth of active mixing to changes in biomass depth profiles. These analyses support the idea that decreases in the depth of active mixing, a result of the transition from buoyancy-driven to wind-driven mixing, control the timing of the spring bloom.

Keywords: Lagrangian floats, North Atlantic Bloom experiment, Ocean turbulence, phytoplankton, spring bloom, Sverdrup hypothesis.

Introduction

The timing of the subpolar spring phytoplankton bloom has long been of interest to oceanographers due to its impact on carbon export (Stramska *et al.*, 1995; Sabine *et al.*, 2004; Lutz *et al.*, 2007) and upper trophic level species recruitment (Platt *et al.*, 2003; Edwards and Richardson, 2004; Koeller *et al.*, 2009). In his seminal 1953 paper, Harald Sverdrup hypothesized that because phytoplankton are uniformly distributed within the ocean mixed layer, the spring shoaling of this mixed layer increases available light to a level at which the phytoplankton population can grow (Sverdrup, 1953). While Sverdrup defined the term “mixed layer” as the section of the water column exhibiting both active turbulence and homogenous density, contemporary studies in support of the Sverdrup Hypothesis have generally used density-based criteria only to define the mixed layer (e.g. Follows and Dutkiewicz, 2001; Siegel *et al.*, 2002; Henson *et al.*, 2009), and have linked the timing of the spring bloom to ocean surface warming (Follows and Dutkiewicz, 2001; Henson *et al.*, 2006). More recent work has focused on the possibility that decreases in active turbulence within the mixed layer, rather than decreases in the mixed layer

itself, create the conditions necessary for bloom onset (Huisman *et al.*, 1999; Chiswell, 2011; Taylor and Ferrari, 2011; Chiswell *et al.*, 2013). This decrease has been attributed to the shutdown of turbulent convection after heat fluxes become positive (Taylor and Ferrari, 2011) and also to decreases in the local wind strength (Chiswell, 2011; Chiswell *et al.*, 2013). Because phytoplankton blooms that occur when the ocean mixed layer is deep encounter reduced barriers to sinking and thus export higher amounts of carbon than blooms that occur in shallow mixed layers (Stramska *et al.*, 1995), this distinction has important consequences for the marine carbon cycle.

Other recent work has focused on localized increases in water column stratification by means other than warming as a driver of blooms. Specifically, it has been suggested that lateral density gradients are converted to vertical density gradients by submesoscale eddies within the mixed layer, and that this increase in stratification can initiate blooms (Mahadevan *et al.*, 2012). Finally, while contemporary bloom phenology studies typically use surface chlorophyll from satellite data to examine the phytoplankton seasonal cycle (Platt *et al.*, 2009; Cole *et al.*, 2012; Racault *et al.*, 2012; Sapiano

et al., 2012; Brody *et al.*, 2013), a series of studies (Behrenfeld, 2010; Boss and Behrenfeld, 2010; Behrenfeld *et al.*, 2013) has drawn attention to the fact that the original work by Sverdrup focused on the rate of net biomass accumulation within the water column. The use of this metric has led to an alternative hypothesis regarding the phytoplankton seasonal cycle (Behrenfeld, 2010; Boss and Behrenfeld, 2010; Behrenfeld *et al.*, 2013): positive net accumulation rates are driven by the deepening of the mixed layer in winter, dilution of the plankton population, and consequent decreases in zooplankton grazing pressure.

Brody and Lozier (2014) (hereafter BL14) investigated several proposed drivers of the subpolar spring bloom in the North Atlantic: shoaling seasonal mixed layers (Follows and Dutkiewicz, 2001; Siegel *et al.*, 2002; Henson *et al.*, 2009), the onset of positive heat fluxes (Taylor and Ferrari, 2011), and decreases in wind strength (Chiswell, 2011; Chiswell *et al.*, 2013). BL14 compared these mechanisms to a new framework for the North Atlantic bloom initiation: that blooms begin when the dominant mixing length scale (L_{mix}), or depth of active mixing, in the upper ocean decreases. BL14 found that decreases in L_{mix} are a better predictor of bloom initiation than decreases in the mixed layer depth, the onset of positive heat fluxes, or decreases in wind strength. They also found that decreases in L_{mix} generally occur after the shift from buoyancy-driven to wind-driven mixing in the upper ocean, likely because strongly negative surface buoyancy fluxes generate larger, more coherent vertical eddies compared with those generated by wind forcing, which then reduce the light exposure of phytoplankton within the upper ocean. Essentially, BL14 clarified and expanded upon the light-limitation-based explanation of bloom initiation described in the Sverdrup hypothesis by estimating a depth of turbulent mixing that differs at times from the density-defined mixed-layer depth, and providing a mechanism for bloom initiation that does not depend on the onset of positive heat fluxes (net ocean surface warming).

The BL14 framework was tested using satellite data to identify the spring bloom and surface reanalysis data to estimate mixing length scales, thus leaving open questions regarding how well the L_{mix} model estimates the depth of active mixing, and whether the shift from buoyancy-driven to wind-driven mixing causes the active mixing depth to shoal. *In situ* datasets provide a unique opportunity to more closely examine the BL14 framework by allowing for the estimation of mixing from measurements in the upper ocean rather than relying on information from surface forcing fields. Specifically, we use *in situ* data to (i) assess whether surface forcing data can be used to accurately estimate the depth of L_{mix} under different conditions; (ii) further characterize differences and similarities in buoyancy-driven and wind-driven mixing to determine whether and how buoyancy forcing drives deeper mixing than wind forcing; and (iii) investigate whether decreases in L_{mix} precede the initiation of the spring bloom, as measured using depth-resolved biomass records.

To answer the first two questions, we employ data from autonomous Lagrangian floats. Because these floats are designed to be neutrally buoyant (D'Asaro *et al.*, 1996), they can follow the three-dimensional motions of water parcels and have been used to examine turbulence within the upper ocean during a variety of mixing regimes. For this study, we use data from the Labrador Sea Experiment (Krahmann *et al.*, 2003), when deep convection drove turbulent mixing (Steffen and D'Asaro, 2002), and from the North Atlantic Bloom 2008 experiment (Fennel *et al.*, 2011), during which mixing was primarily wind-driven (Mahadevan

et al., 2012). By assuming that these Lagrangian floats simulate the trajectories of particles within the upper ocean (Harcourt *et al.*, 2002; D'Asaro, 2008), we use their vertical paths to observe the strength and depth of active mixing in the ocean in buoyancy-driven and wind-driven mixing environments. To answer the third question, we examine changes in depth-integrated biomass using biological data collected during a subpolar spring bloom as part of the North Atlantic Bloom 2008 experiment.

Data and methods

Data

Float data

We utilize data from two field programmes. The Labrador Sea Deep Convection Experiment (Krahmann *et al.*, 2003) deployed 25 Lagrangian floats during winters of 1997/1998 in the Labrador Sea (52–56°W, 56–59°N). Floats drifted for ~2 months, recording temperature and pressure at 5 min intervals, and position at 4 h intervals (see Steffen and D'Asaro, 2002 for further details on float mechanics and experiment design). We additionally use data from 36 PALACE floats (Davis *et al.*, 1992; Lavender *et al.*, 2000), also deployed during the Labrador Sea Experiment, which parked at varying depths in the Labrador Sea (400, 700, and 1500 m) and periodically surfaced to record temperature and salinity profiles.

In the North Atlantic Bloom 2008 Experiment (NAB08), one Lagrangian float was deployed during the months of April and May 2008 in the subpolar North Atlantic south of Iceland (58.5–62.5°N, 18–28°W) (Fennel *et al.*, 2011; Mahadevan *et al.*, 2012). This float alternated between drifting within the mixed layer, profiling, and autoballasting. During all modes, the float recorded temperature, salinity, and position data every 50–60 s. In both Lagrangian float experiments, the floats were designed to be neutrally buoyant through adjustable compressibility and high drag (D'Asaro *et al.*, 1996; D'Asaro, 2003).

Gliders data

The NAB08 experiment deployed four Seagliders (Eriksen *et al.*, 2001) on paths following the Lagrangian float. The Seagliders continuously profiled the upper ocean, collecting approximately four profiles per day between 0 and 1000 m. The Seagliders measured temperature, salinity, and pressure, as well as chlorophyll *a* fluorescence, and backscatter at 700 nm wavelength calibrated to ship-based observations (see Briggs *et al.*, 2011 for further details on the Seaglider instrumentation). Consistent with previous work on the NAB08 data (e.g. Briggs *et al.*, 2011; Cetinic *et al.*, 2012), we use both the chlorophyll *a* fluorescence and backscatter at 700 nm (bbp(700)) as proxies for phytoplankton biomass (Behrenfeld *et al.*, 2005).

To facilitate comparison between derived physical variables (e.g. mixed layer depths) and derived biological variables (e.g. net biomass accumulation rates), we process the physical (temperature, salinity, density) and biological (chlorophyll fluorescence and bbp(700)) observations from the gliders using the same methods. Following Briggs *et al.* (2011), we process the data by first smoothing the profiles using sequential five-point running median filters and seven-point running mean filters. For ease of comparison with surface forcing data, which has a 1-d temporal resolution, and to highlight variability in biomass and density at the scale of the water column, we average the data into 1-d, 10-m bins, then smooth with 2-d, 50-m running means to further filter out submesoscale

variability (Briggs *et al.*, 2011). We then average daily data from all gliders.

Surface forcing data

We use three surface forcing products containing both winds and heat fluxes: Objectively Analyzed Air-Sea Fluxes (OAFlux) (Yu and Weller, 2007; oafux.whoi.edu), NCEP-NCAR reanalysis 2 (Kanamitsu *et al.*, 2002; <http://www.esrl.noaa.gov/psd>), and ECMWF-ERA-Interim daily fields (data-portal.ecmwf.int). All heat flux and wind products are at daily resolution, with spatial resolution varying from 0.75 to 2.6°. We also use one wind-only product from the NOAA WaveWatch III hindcast data (<http://polar.ncep.noaa.gov/waves>), which is available at a higher spatial and temporal resolution (0.5°, 3-h resolution). Finally, we use photosynthetically available radiation (PAR) obtained from 9-km, 8-d SeaWiFS data, via the Giovanni data portal (<http://disc.sci.gsfc.nasa.gov/giovanni/>). We obtained all surface forcing data for the period of the NAB08 experiment. Because the daily averaged distance between the float and the averaged position of the four Seagliders (maximum distance of 1.1°; mean distance of 0.41°) is comparable with both the spatial resolution of the surface forcing data and the distance between any two gliders on a given day (maximum distance of 2.3°; mean distance of 0.49°), we linearly interpolate the gridded values of the surface forcing data to the position of the Lagrangian float.

Upper-ocean vertical velocities

Observed

For both Lagrangian float datasets (Labrador Sea and NAB08), we calculate vertical velocities, w , at each time step using centred differencing of the depth and time records. We calculate turbulent vertical velocities using $w' = w - \bar{w}$. Because we focus on changes in vertical velocities at the timescale of phytoplankton growth (days) \bar{w} is computed as a daily mean. For the NAB08 data, we additionally calculate the daily rms-vertical velocity, w_{rms} , for n daily measurements using $w_{\text{rms}} = \sqrt{\sum (w_n - \bar{w})^2 / n}$. In the Labrador Sea Experiment, Lagrangian floats were placed below the mixed layer in fall, and were entrained into the mixed layer as surface cooling strengthened and mixing deepened (Steffen and D'Asaro, 2002); we therefore exclude data collected before the entrainment of the floats into the convective layer (approximately the first half of the 1998 float records, as seen in Steffen and D'Asaro, 2002, figures 6 and 7) and after heat fluxes became positive (after 8 March for 1997, after 2 March for 1998) to ensure that upper-ocean mixing was buoyancy-driven during the period of analysis. Given these two conditions, no data from the 1998 floats were used in our analysis. For the NAB08 experiment, to ensure that we are examining wind-driven mixing, we exclude the period of the record during which heat fluxes were negative (before Day 13) for the analysis in Figure 2c. However, we use the entire NAB08 float depth record in to calculate w_{rms} in Figure 3b.

Estimated

We estimate the wind-driven vertical velocity, w^* , from 10-m wind speeds (U_{10}), using $w_*^2 = \rho_a / \rho_w C_D U_{10}^2$, derived from the definition of windstress, where ρ_a and ρ_w are the densities of the air and the surface water, respectively, and C_D is the drag coefficient, calculated as a function of wind speed (Hersbach, 2011). We estimate buoyancy-driven vertical velocity, w_b , during periods of negative heat flux, using the relationship, verified in laboratory (Deardorff and Willis, 1985; Fernando *et al.*, 1991), field

(Steffen and D'Asaro, 2002), and modelling (Deardorff, 1972; Molemaker and Dijkstra, 1997) studies, between w_b and surface buoyancy forcing (B_0). Steffen and D'Asaro (2002) tested several models relating w_b and B_0 and found the best predictive skill with the model $w_b = a(HB_0)^{1/3} + w_o$, where H is the mixed-layer depth and a and w_o are empirical constants. Following Steffen and D'Asaro (2002), we calculated a and w_o using a linear fit of $(HB_0)^{1/3}$ onto w_{rms} to obtain values of $a = 0.46$ and $w_o = 0.009$.

Mixed layer depth, H , and buoyancy frequency (N^2)

For both the Labrador Sea and NAB08 experiments, we calculate H using a density difference from the surface criteria, or density threshold. Because many different density thresholds have been used in previous studies to calculate mixed layer depths (see Holte and Talley, 2009 for a review), we choose two thresholds, 0.03 and 0.125 kg m⁻³, to ensure that our findings are not sensitive to the choice of mixed layer depth definition. Mixed layer depths calculated with the 0.03 and 0.125 kg m⁻³ density thresholds are comparable with mixed layer depths calculated using the Holte and Talley (2009) density algorithm and a density gradient method (Figure 1), so our results using these two thresholds are likely insensitive to the method for determining the mixed layer depth. We use the PALACE floats to calculate daily mixed layer depths during the Labrador Sea experiment, with the surface density taken from the 13-m PALACE measurement. We average all H measurements derived from PALACE profiles recorded within the temporal and spatial range of the Lagrangian floats to create a mixed layer depth time series for the segment of the Lagrangian float record used in this study. Because 23 February and 5 March did not contain reliable PALACE profiles, we estimate H on those dates by the average of the surrounding days. For the NAB08 experiment, we use the binned daily density profiles from

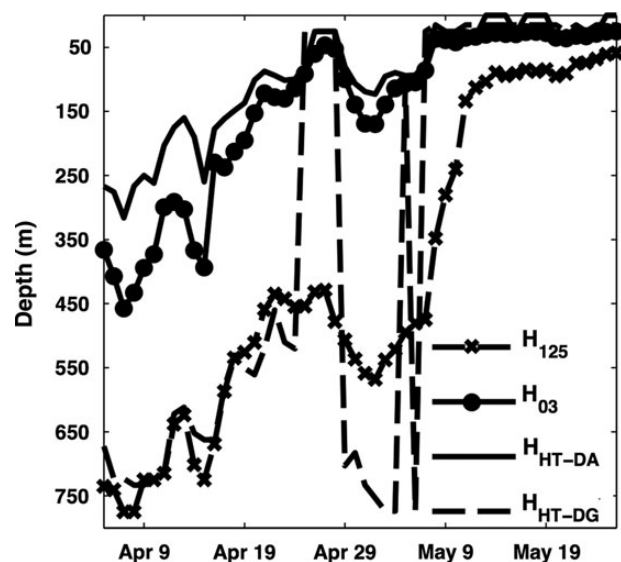


Figure 1. Mixed layer depths (H) calculated using the 0.03 and 0.125 kg m⁻³ density difference criteria (H_{03} and H_{125}) compared with mixed layer depths calculated using the Holte – Talley density algorithm (H_{DA} ; Holte and Talley, 2009) and a maximum density gradient method, also from Holte and Talley (2009), H_{DG} , all calculated over the period of the North Atlantic Bloom 2008 experiment.

the glider records to calculate H , determining the surface density from the top bin (0–10 m).

We calculate the daily average N^2 for the NAB08 data over the maximum daily depth of the NAB08 Lagrangian float using the GSW MATLAB oceanographic toolbox (McDougall and Barker, 2011) and the binned glider temperature and salinity profiles.

Active mixing depth, L_{mix}

We calculate L_{mix} for the NAB08 period using the method outlined in BL14 for each of the three surface forcing products, and for each of the two mixed layer depth definitions, creating a total of six L_{mix} estimates. We define L_{mix} for three cases. In Case 1, where buoyancy-driven mixing dominates, L_{mix} is equal to the mixed layer depth (Taylor and Ferrari, 2011), H . In Case 2, where wind-driven mixing dominates in the presence of weak buoyancy forcing, L_{mix} is equal to the Ekman length scale (Denman and Gargett, 1983; Wang and Huang, 2003), L_{EK} . To calculate L_{EK} , we use $L_{\text{EK}} = \gamma(w_*)/f$, where f is the Coriolis parameter ($1.27 \times 10^{-4} \text{ s}^{-1}$) and γ is an empirical constant, for which we use a value of 0.5 (Wang and Huang, 2003). Finally, in Case 3, where wind-driven mixing dominates in the presence of strongly positive buoyancy forcing, L_{mix} is equal to the Ozmidov length scale (Denman and Gargett, 1983; Riley and Lelong, 2000), $L_{\text{OZ}} = (2\pi)\epsilon^{1/2}N^{-3/2}$, where ϵ is the rate of turbulent kinetic energy dissipation and is equal to $w_*^3/\kappa z$ at depth z , where $\kappa = 0.41$ is the Von Kármán constant. We base the transition between these cases on the relative strengths of wind and buoyancy forcing, as parameterized by the magnitude of the Obukhov length scale, $L_{\text{OB}} = -w_*^3/\kappa B_o$, where B_o is the surface buoyancy flux and is directly proportional to the surface heat flux (Phillips, 1977; Taylor and Ferrari, 2011).

Phytoplankton accumulation rates (r) and bloom period

We use both the daily chlorophyll fluorescence and bbp(700) profiles from the binned and processed NAB08 Seaglider data to calculate phytoplankton net accumulation rates, r , from the daily biomass rate of change (Behrenfeld, 2010; Boss and Behrenfeld, 2010; Behrenfeld *et al.*, 2013). Briefly, the definition of r we use accounts for phytoplankton growth occurring below the surface of the ocean and at times occurring deeper than the mixed layer depth by using three criteria for r . When mixed layers are deep and constant or deepening, r is calculated from biomass integrated to the depth of the mixed layer, consistent with the original Sverdrup hypothesis. When mixed layers are shallow, r is calculated from biomass integrated to the depth of a threshold isolume, above which phytoplankton have sufficient light to grow, to account for phytoplankton growth below a shallow mixed layer. Finally, when mixed layers are deep but shoaling, r is calculated from biomass averaged within the mixed layer, to exclude the portion of the phytoplankton population being detrained from the mixed layer and thus no longer actively growing. Further details can be found in Boss and Behrenfeld (2010).

We use H_{03} to calculate r : r calculated with H_{125} shows qualitatively similar patterns, but with slightly more variability in terms of whether r is positive or negative on any given day. We calculate the depth of the threshold isolume (z_{415}) as $z_{415} = \log(0.415/0.98\text{PAR})(z_{\text{eu}}/\log(0.01))$ (Boss and Behrenfeld, 2010), where $0.415 \text{ mol quanta m}^{-2} \text{ d}^{-1}$ is the lowest PAR value that can support phytoplankton growth (Letelier *et al.*, 2004), and z_{eu} is the depth of the euphotic layer, calculated using surface chlorophyll concentrations (Morel *et al.*, 2007).

We then use the r record to identify the period of the spring bloom captured in the NAB08 record. Several methods exist to define the initiation of the subpolar spring phytoplankton bloom, and the selection of the method can depend on the question being asked (Brody *et al.*, 2013). To capture the start of a seasonal, rather than transient, bloom, we define the bloom as the period of sustained positive rates of biomass accumulation (Brody and Lozier, 2014), meaning that r calculated either with chlorophyll fluorescence or bbp(700) cannot be negative for >1 consecutive day during the bloom period. Therefore, we set the bloom initiation date to occur immediately after the last instance in which r is negative for two consecutive days, and the bloom termination date to occur immediately before r again becomes negative for two consecutive days.

Uncertainty in the calculation of r comes from the fact that the 0.415 threshold PAR value was derived from measurements in the tropical Pacific Ocean, and thus likely represents a shallow estimate of the threshold isolume for subpolar phytoplankton (Boss and Behrenfeld, 2010). However, because the threshold isolume is only used in the r calculation once the mixed layer depth has become very shallow, this uncertainty only affects the end of the r record. We compared the threshold isolume with the euphotic depth (z_{eu}) and found very small differences between the two depths (see Figure 4). Additionally, r calculated with z_{eu} only differs from r calculated with z_{415} after Day 33 of the NAB08 record, within 1 day of the bloom termination, and only differs in magnitude, rather than sign. The choice of z_{415} to calculate r therefore has no effect on the date of the bloom initiation and termination.

Results

Assessment of estimated L_{mix}

We first use Lagrangian float paths to assess the BL14 estimate of the active mixing layer (L_{mix}) during buoyancy-driven mixing, where L_{mix} is equal to the mixed layer depth, H , and wind-driven mixing, where L_{mix} is equal to the Ekman depth, L_{EK} . In both cases, we use the daily maximum depth recorded by the Lagrangian floats (D_{max}) to estimate the depth of the active mixing layer from the float data. Although these datasets were collected at different times and at different locations in the subpolar North Atlantic, they each provide an example of what mixing might look like under buoyancy-driven and wind-driven conditions.

In the wind-driven case (the NAB08 record after 17 April, Figure 2a), we find a close correspondence between D_{max} and L_{EK} , except a short period centered around May 14 (shaded area in Figure 2a; with generally high r^2 values ($r^2 = 0.66$ over the non-shaded portion of the record) and low root mean square differences, (rmsd) between D_{max} and L_{EK} (22.2 m, compared with an average D_{max} of 48.7 m and a range in D_{max} over the float record of 150.0 m.)

In the buoyancy-driven case (the 1997 Labrador Sea record over 20 February to 7 March, Figure 2b), D_{max} is of comparable magnitude with H , but only when H is defined using the 0.03 kg m^{-3} density difference criterion. Again, the rmsd between H and D_{max} is small (279 m) compared with the average depth of D_{max} (635 m) and range over the period and floats (754 m). The correlation between D_{max} and H on any given day is low ($r^2 = 0.024$), but because H is calculated using density profiles from PALACE floats, which are close to, but not at, the position of the Lagrangian floats, D_{max} is averaged from several Lagrangian float records, and the Labrador Sea record is relatively short and does not record large changes in D_{max} or H , this low correlation can be

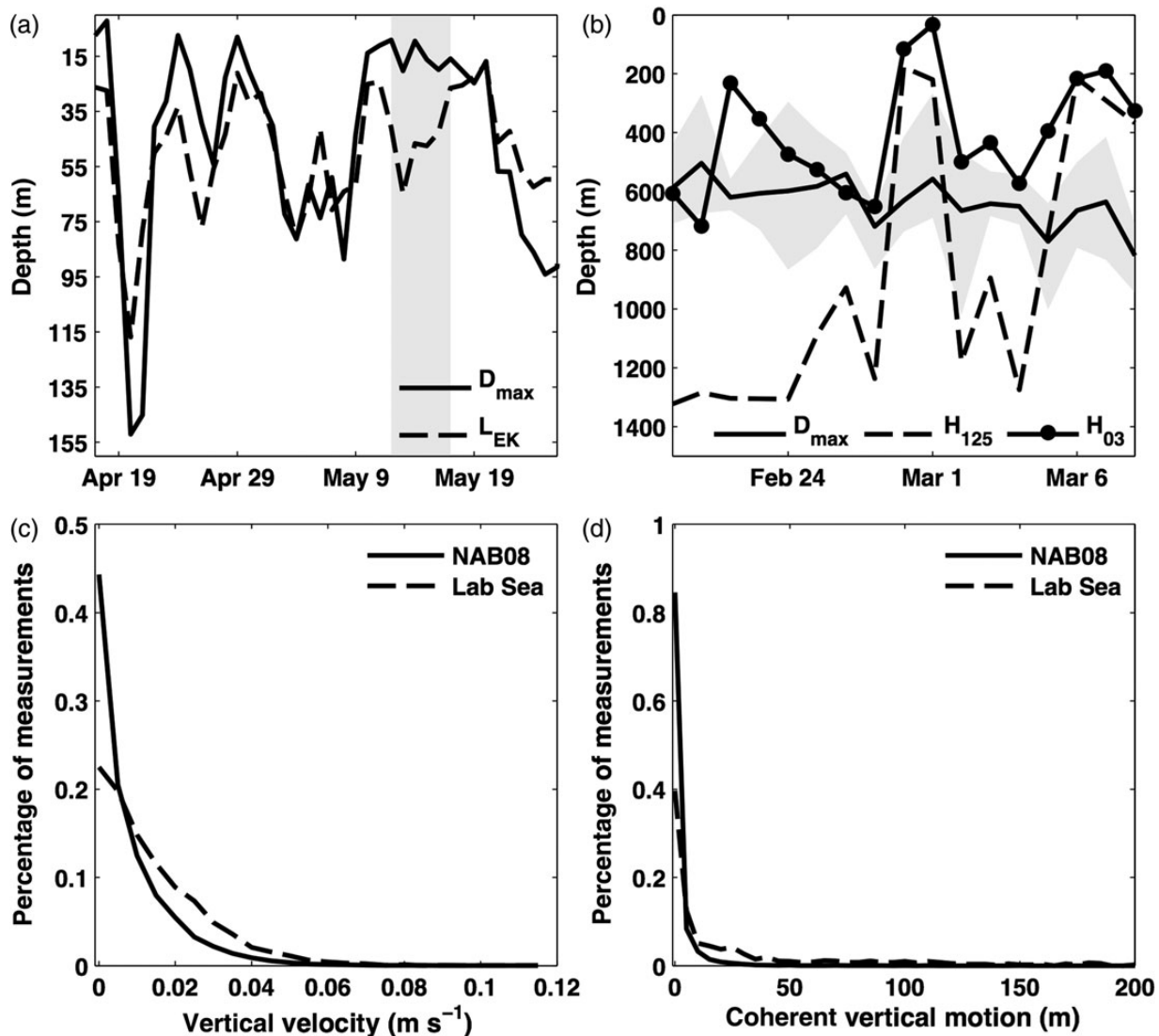


Figure 2. (a) Daily maximum depths attained by the NAB08 float (D_{max}), compared with the Ekman depth (L_{EK}). Grey shading is as in Figure 3c. (b) Daily maximum depths averaged over the four Lab Sea floats with complete records (Floats 8, 12, 16, and 21) (D_{max}), compared with the mixed layer depths H_{03} and H_{125} . The grey shading denotes the daily minimum/maximum of D_{max} out of the four floats. (c) Normalized distributions of the magnitude of float vertical velocities for the Labrador Sea and NAB08 data. Distributions were created using bin sizes of 0.005, ranging from 0 to 0.115 $m s^{-1}$, with open boundaries. (d) Normalized distributions of the magnitude of coherent vertical motions recorded by the floats. Distributions were created using bin sizes of 5, ranging from 0 to 300 m, with open boundaries. For all distributions in (c, d), the Labrador Sea distribution is composed of the four Labrador Sea floats shown in (b).

expected. Nonetheless, in both the wind-driven and buoyancy-driven case, we find support for the BL14 estimation of the active mixing depth.

Comparison of buoyancy- and wind-driven mixing

We next explore whether the large difference between the depth of the active mixing layer in the buoyancy-driven and the wind-driven mixing regimes (Figure 2a and b) is accompanied by differences in the magnitude of the vertical velocities, and the size of coherent vertical motions. The distributions of the magnitude of turbulent vertical velocity measurements, $|w|$ (Figure 2c), in the two experiments show that floats in the buoyancy-driven mixing environment have a higher mean $|w|$ (0.016 $m s^{-1}$ compared with 0.010 $m s^{-1}$)

and a larger variance ($1.97 \times 10^{-4} m s^{-1}$ compared with $1.26 \times 10^{-4} m s^{-1}$).

The distributions of the coherent vertical motions, i.e. the magnitude of the vertical distance travelled by a float before changing directions, for both the buoyancy-driven and wind-driven mixing environments (Figure 2d), show that in the buoyancy-driven case, the floats more frequently record large vertical motions. In this case, the variance of the buoyancy-driven distribution is several orders of magnitude greater than the wind-driven distribution (8.82×10^{-3} vs. 4.28×10^{-5} m). The mean of the buoyancy-driven vertical motions is also much greater (47.8 vs. 2.81 m). For both the distributions of $|w|$ and the coherent vertical motions, Kolmogorov–Smirnov tests (Massey, 1951) show that the distributions of the NAB08 and Lab Sea data are significantly different at the

95% confidence level. These comparisons support the idea that the deep active mixing layers observed in the buoyancy-driven mixing environment result from large coherent convective cells, in contrast to the smaller motions that characterize the wind-driven regime.

Analysis of L_{mix} and bloom initiation

The NAB08 record provides the opportunity to examine changes in turbulent vertical velocities and the depth of L_{mix} before and during the initiation of a subpolar spring bloom. The bloom initiation date occurs on Day 12 of the NAB08 record (16 April, Figure 3a), approximately 2 d before heat fluxes become positive (Figure 3a). This timing is consistent with the analysis of Mahadevan *et al.*

(2012), who approximated the NAB08 bloom initiation date from the biomass record, and with BL14, who found positive satellite-derived chlorophyll rates of change in the subpolar North Atlantic to occur when heat fluxes were weakening but still negative.

As noted in Mahadevan *et al.* (2012), and as seen at other study sites (D'Asaro, 2003), daily rms-vertical velocities calculated from the Lagrangian float data (w_{rms}) and turbulent vertical velocities calculated from wind stress (w^*) are generally in very good agreement (Figure 3b), indicating the dominance of wind-driven mixing during the bloom initiation. However, this correspondence is weak during approximately the first 9 d of the time series, before the bloom initiation, when w_{rms} is significantly larger than and less correlated with w^* as compared with the remainder of the

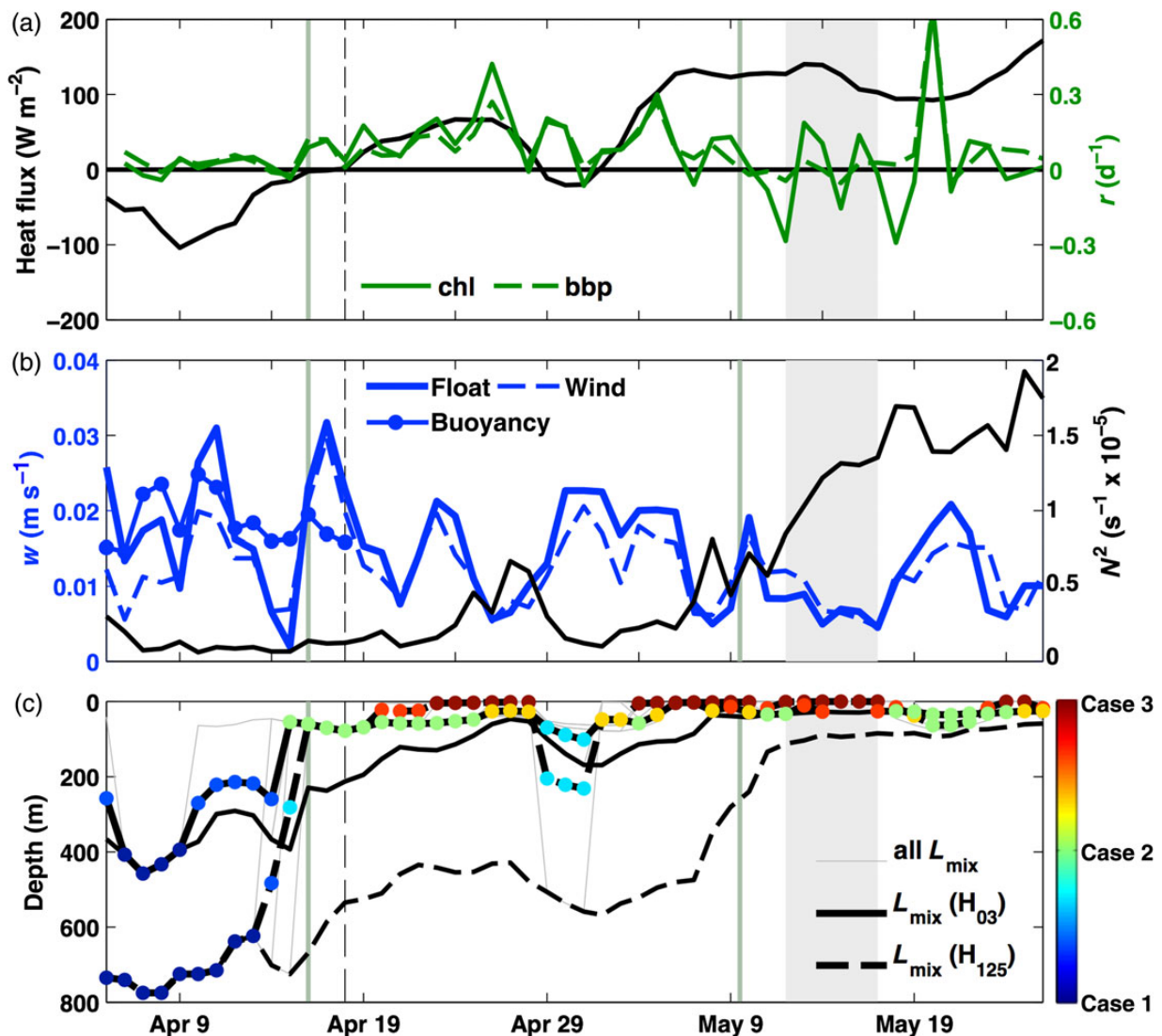


Figure 3. (a) Daily rates of change (r) of depth-integrated chlorophyll fluorescence and bbp(700) measured from NAB08 glider profile data, plotted with heat fluxes averaged from the OAFUX, NCEP-NCAR, and ECMWF-ERA products. The vertical green lines show the dates on which r becomes consistently positive (the bloom initiation) and negative (the bloom termination). The vertical black line shows the date on which the averaged heat flux time series becomes positive. (b) Turbulent vertical velocities calculated from the WaveWatch III windstress record, the daily averaged buoyancy flux record, and derived from rms daily averaged vertical float velocities. (c) L_{mix} depth measurements shown calculated for all possible combinations of the OAFUX, NCEP-NCAR, and ECMWF-ERA heat flux/wind products and mixed layer depth definitions, then averaged for H_{03} and H_{125} . Marker colours refer to the case (1, 2, or 3) of L_{mix} at each day, averaged for the L_{mix} measurements calculated from all three surface forcing products. The H_{03} and H_{125} are also shown as the non-marked solid and dashed lines.

NAB08 record (Table 1). This period coincides with a period of relatively strong loss of heat to the atmosphere (Figure 3a); thus, buoyancy forcing is potentially playing a role in the turbulent mixing during this time. We estimate buoyancy-driven vertical velocities (w_b) for the entire period of negative heat fluxes (the first 14 d of the float record, Figure 3b). Because of the lower spatial resolution of the heat flux data when compared with the wind data, and because of the additional uncertainty introduced by the glider-derived mixed layer depths in the calculation of w_b , we expect generally lower correlations between w_b and w_{rms} than between w^* and w_{rms} . However, we do see that during the first 9 d of the record, the correlation between w_b and w_{rms} is higher than during the bloom initiation (Days 10–14), when heat fluxes are weak, while the correlation between w^* and w_{rms} is higher during Days 10–14 than Days 1–9 (Table 1). The rmsd between w_b and w_{rms} is also lower during the first 9 d of the record compared with the rmsd between w^* and w_{rms} during this period (Table 1). These patterns support the hypothesis that mixing is not wind-driven, and may be buoyancy-driven, before the bloom initiation.

A shift from buoyancy-driven to wind-driven mixing occurring 3 d before the start of the bloom would be consistent with the bloom initiation framework developed in BL14. Moreover, the average stratification over the portion of the water column in which the Lagrangian float travels stays very low until well after the bloom initiation (Figure 3b), also consistent with the BL14 idea that the bloom begins during Case 2 mixing (wind-driven mixing in unstratified conditions). We note, however, that the relatively short period during which heat fluxes were strongly negative and stratification was low, as well as the small number of days in which heat fluxes were weakly negative, precludes a definitive assessment of the drivers of mixing before the bloom.

The hypothesis that a shift from buoyancy-driven to wind-driven mixing creates the conditions in which a bloom can begin rests on the assumption that this shift decreases the depth of active mixing. The model for this active mixing depth, L_{mix} , contains different parameterizations for buoyancy-driven mixing (Case 1, $L_{mix} = H$) and wind-driven mixing (Case 2, $L_{mix} = L_{EK}$). We next examine whether L_{mix} calculated over the period of the NAB08 record transitions from Case 1 to Case 2 synchronously with the observed shift in the w_{rms} record from w_b -correlated with w^* -correlated, and, if so, whether this transition causes L_{mix} to shoal. All L_{mix} estimates show a clear shift from Case 1 to Case 2 coincident with bloom initiation (Figure 3c) and with the beginning of increased correspondence between w^* and w_{rms} (Figure 3b). This shift from Case 1 to Case 2 is accompanied by a large decrease in L_{mix} , consistent with the idea that such a decrease leads to an increase in light availability for phytoplankton and thus drives the spring

bloom. During the same period, mixed layers generally remain very deep, and do not show the same pronounced shoaling seen in the L_{mix} record (Figure 3c).

During most of the remainder of the bloom period, the close correspondence between w^* and w_{rms} (Figure 3b), the relatively weak heat fluxes (Figure 3a), the strong agreement between the float-derived D_{max} and estimated L_{EK} (Figure 3a), and the weak stratification (Figure 3b) indicate that Case 2 conditions prevail. During the period of approximately 12 May through 18 May (after the bloom termination, shaded area in Figure 3c), the overestimation of D_{max} by L_{EK} (Figure 2a), the slight overestimation of w_{rms} by w^* (Figure 3b), and the relatively high stratification (Figure 3b) indicate that L_{mix} is in Case 3, or stratified wind-driven mixing. While L_{mix} calculated using H_{03} generally follows this pattern, L_{mix} calculated using H_{125} transitions to Case 3 well before 12 May, indicating that H_{03} is the more appropriate definition of the mixed layer depth for the calculation of L_{mix} in the NAB08 location and period.

The depth-resolved NAB08 glider data provide additional evidence that the phytoplankton bloom initiation corresponds to the shoaling of L_{mix} , rather than to the shoaling of the mixed layer. We compare L_{mix} calculated using H_{03} with both H_{03} and with the depths of the euphotic depth and threshold isolume (z_{eu} , z_{415}), again using depth-time profiles of both chlorophyll fluorescence and bbp(700) as proxies for phytoplankton biomass (Figure 4). Before the initiation of the spring bloom, H and L_{mix} are equal and very deep. Phytoplankton biomass, as measured by both chlorophyll fluorescence (Figure 4a) and bbp(700) (Figure 4b), is distributed fairly evenly over the top 300–400 m of the water column. At this point, H_{03} and L_{mix} both approximate the bottom boundary of biomass accumulation, as expected for pre-bloom, buoyancy-mixed conditions. At and directly after the bloom initiation date, the chlorophyll fluorescence and bbp(700) depth profiles noticeably increase in concentration within the top 50–100 m. L_{mix} , which has shoaled considerably, generally tracks these horizons. Though H_{03} shoals during this period, it remains deeper than the highest concentrations of biomass.

As the bloom progresses and reaches its termination date, chlorophyll fluorescence and bbp(700) concentrations are approximately uniform and high within the top 50–150 m of the record (Figure 4). While L_{mix} and H_{03} intermittently shoal above these concentration horizons, the euphotic depth and threshold isolume begin to delineate the bottom boundary of significant biomass growth and accumulation. The records during this period also show evidence of sinking biomass, particularly in the elevated bbp(700) concentrations after 1 May (dashed line in Figure 4b) and in the chlorophyll fluorescence and bbp(700) spike at 300–400 m on 9 May, which was analysed by Briggs *et al.* (2011) for its role in carbon export. Because sinking biomass creates a vertical profile that indicates increased concentration at depth, yet that concentration includes the non-growing population, we place greater emphasis on the match between L_{mix} and biomass at the beginning of the bloom.

Table 1. Correlation (r^2) and difference (rmsd) information for wind-estimated and buoyancy-estimated vertical velocities compared with the observed vertical velocities (w_{rms}) for different segments of the NAB08 record.

	Days 1–9	Days 10–14	Days 10–52
w^*	0.51, 0.0078	0.97, 0.0029	0.82, 0.0032
w_b	0.24, 0.0058	0.14, 0.0107	NA

^aThe first number in each box denotes the r^2 value for each velocity and time segment; the second number denotes the rmsd value (units ms^{-1}).

^bThere is no value for buoyancy-estimated vertical velocities during Days 10–52 because buoyancy-estimated velocities are only computed when heat fluxes are negative.

Discussion

In this study, we used *in situ* data to further examine the light-limitation-based mechanisms for subpolar bloom initiation first formalized by the Sverdrup Hypothesis. Specifically, we examined the idea that phytoplankton are uniformly mixed to the depth of the dominant mixing length scale, or active mixing depth (L_{mix}), which shoals during the transition from buoyancy- to wind-driven

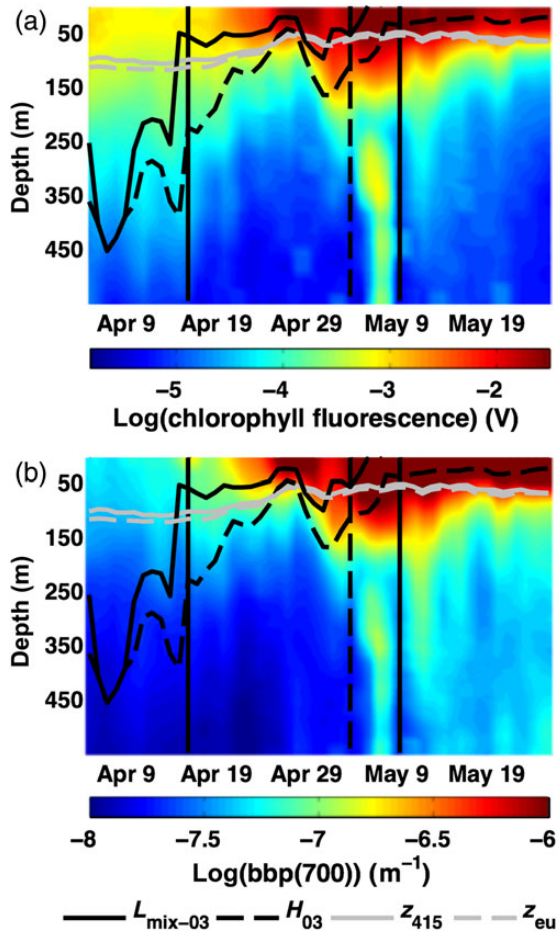


Figure 4. Daily chlorophyll fluorescence (a) and $bbp(700)$ concentration (b) depth-time records from the NAB08 glider data. Both records are plotted on a log scale. In both plots, the time span shown is the same as in Figure 3, the black vertical solid lines correspond to the bloom initiation and termination dates shown as green lines in Figure 3, and the black vertical dashed lines highlight the beginning of apparent biomass sinking (1 May). The threshold isolume (z_{415}) used to calculate r and euphotic depth (z_{eu}) are also shown.

mixing, thus alleviating light limitation and prompting a bloom. This idea is consistent with previous observations made of blooms occurring when heat fluxes are negative (Mahadevan *et al.*, 2012) and when the water column is unstratified (Townsend *et al.*, 1992).

We first examined whether the BL14 estimation of L_{mix} from surface forcing data accurately estimates the depth of active mixing in buoyancy- and wind-driven mixing regimes. According to the BL14 framework, L_{mix} should be equal to the mixed-layer depth, H , during buoyancy-driven mixing and equal to the Ekman depth, L_{EK} , during wind-driven mixing. We found that the daily maximum depths attained by the Lagrangian floats in these regimes are consistent with H_{03} for buoyancy-driven regimes and with L_{EK} for wind-driven regimes (Figure 2a and b).

A further investigation of the wind-driven record in the context of the spring bloom shows that the daily maximum float depth corresponds very closely to L_{EK} , or Case 2 mixing, during the initiation and duration of the bloom (17 April–9 May). The daily maximum depths then become more shallow than L_{EK} for a brief period after the bloom termination (12 May–18 May), indicating a shift to

Case 3 mixing. This shift is also seen in the relatively high heat fluxes (Figure 3a), low observed turbulent vertical velocities (Figure 3b), and high stratification (Figure 3b) at this time. That this shift is mirrored in the L_{mix} record, which briefly transitions to Case 3 from Case 2 on these days (Figure 3c), provides further support for L_{mix} as an estimator of the depth of active mixing.

We explored in more detail the differences and similarities between buoyancy-driven and wind-driven mixing, as seen in the Lagrangian float records. The deep maximum depths, high vertical velocities, and large coherent vertical motions experienced by floats in the buoyancy-driven environment, compared with those in the wind-driven environment (Figure 2), support the hypothesis that coherent convective cells within the mixed-layer drive deeper mixing of particles when mixing is generated by buoyancy forcing.

Further, we found evidence to support the idea that mixing transitions from buoyancy-driven to wind-driven in the NAB08 record shortly before the bloom begins. Wind-estimated turbulent vertical velocities (w^*) underestimate observed vertical velocities (w_{rms}) before the bloom initiation. During the same period, heat fluxes are negative and the correspondence between w_{rms} and buoyancy-estimated velocities (w_b) is relatively high (Table 1, Figure 3b).

Finally, we find significant shoaling of L_{mix} to coincide with both the increased synchrony between the wind-estimated and observed vertical velocities and the beginning of the spring bloom, in contrast to the density-defined mixed layer during this period (Figure 3c). We find further evidence of this synchrony in depth-resolved biomass time series (Figure 4), in which L_{mix} better delineates the lower boundary of increased surface biomass concentrations at the onset of the bloom than does the density-defined mixed layer.

Our results thus support the underlying ideas of the Sverdrup hypothesis—that phytoplankton are uniformly mixed to deep depths in winter, with little available light, then begin to bloom in spring as mixing weakens and the population concentrates in the light-filled upper ocean. At the same time, we propose that decreases in the dominant mixing length scales operating in the upper ocean (L_{mix}), driven by the transition from buoyancy-driven to wind-driven mixing, better predict the onset of the spring bloom than the surface warming and consequent decreases in the density-defined mixed layer typically attributed to the Sverdrup hypothesis. Given that the Sverdrup hypothesis is predicated on the phytoplankton mixing depth shoaling above the critical depth (where integrated phytoplankton photosynthesis equals integrated respiration) before the bloom, the critical depth during the NAB08 experiment might be located between 250 and 50 m, the approximate depths of L_{mix} before and after it shoals.

We further note that at and after the bloom termination, depth-resolved profiles show high concentrations of biomass deeper than either the density-defined mixed layer or L_{mix} would predict (Figure 4). It has been suggested that in stratified, high-light conditions, phytoplankton grow to the depth of the euphotic zone, deeper at these times than the depth of surface mixing (Behrenfeld, 2010; Boss and Behrenfeld, 2010). Our results confirm this idea, providing justification for integrating biomass to the depth of a threshold isolume to calculate rates of change during these periods (Behrenfeld, 2010), as we do here to calculate r , and suggesting that the highest phytoplankton growth does not occur within the active mixing layer year-around. Additionally, our analysis makes it apparent that, for both the Labrador Sea and NAB08 data, the

mixed layer based on the 0.03 kg m^{-3} density threshold, and by extension the Holte-Talley algorithm mixed layer depth, is noticeably more appropriate for the active mixing depth estimation than the 0.125 kg m^{-3} threshold. While this may not be the case for all datasets and regions, the mixed-layer depth definition used to calculate L_{mix} must always be chosen deliberately.

While our work provides evidence for the idea that the shift from buoyancy-driven to wind-driven mixing, reflected in the shoaling of L_{mix} , provides the necessary mechanism for bloom initiation at the NAB08 site, recent studies have offered different explanations for the subpolar spring bloom. Mahadevan *et al.* (2012) also used the NAB08 data and, noting the appearance of a bloom before heat fluxes became positive, used the record of shallow vs. deep stratification, as well as a numerical model, to propose that mixed-layer eddies, arising from horizontal density gradients, drive stratification, and bloom initiation before the warming of the ocean surface. We use the same *in situ* data, though with stratification measured over a different part of the water column, to propose that changes in surface forcing and one-dimensional mixing alone are sufficient to drive bloom initiation. However, perhaps both of these proposed mechanisms could be at play at different times and to different extents throughout the subpolar oceans in the early spring. We note that the stratification signature observed by Mahadevan *et al.* (2012) in the NAB08 record—a concurrent, small increase in shallow and deep stratification while heat fluxes are negative followed by a large increase in shallow stratification only after heat fluxes become positive, is consistent with a stratification scenario that might be observed in the transition from Case 2 to Case 3 mixing in our formulation.

A theory of bloom initiation based on top-down control of phytoplankton has also been proposed (Behrenfeld, 2010; Boss and Behrenfeld, 2010; Behrenfeld *et al.*, 2013): that deep mixed-layers dilute plankton populations, reduce encounters between zooplankton grazers and phytoplankton, and thus promote growth in the integrated population. This theory has been tested *in situ* as well, using data from an optical profiling float released in the North Atlantic between 2004 and 2007 between 45 and 55°N (Boss *et al.*, 2008; Boss and Behrenfeld, 2010). However, two factors prevent a direct comparison with the NAB08 data. First, this float profiled an area of the North Atlantic 5–10° southward of the NAB08 experiment site, where the average PAR over the course of a year is significantly higher than at the NAB08 site, and productivity patterns are indicative of the transition zone between subtropical and subpolar waters, where light limitation is not the sole driver of phytoplankton blooms (Brody *et al.*, 2013). Relatedly, the mixed layers recorded by that float, determined using the 0.125 kg m^{-3} density difference criterion, never exceeded 160 m, and usually stayed $> 100 \text{ m}$, vastly increasing the winter light exposure of the biomass in that area compared with the biomass experiencing the 700–800 m mixed layers observed at the beginning of the NAB08 record. While it is possible that, had the NAB08 experiment started during winter, rather than at the beginning of April, it would have recorded growth in the integrated population as mixed layers deepened, it is equally possible that light limitation becomes a more important factor than dilution and grazing in setting the timing of the phytoplankton bloom in areas of deep mixed layers and low winter PAR.

Thus, from available data, there is strong *in situ* evidence for decreases in L_{mix} driven by a shift from buoyancy-driven to wind-driven mixing, as one of the primary drivers of the subpolar spring phytoplankton bloom. This formulation of the light-limitation-

based theory for subpolar blooms raises the possibility that changes in ocean-atmosphere forcing conditions on interannual to decadal timescales, as they affect the timing of the transition from buoyancy to wind-driven mixing, could affect the timing of the spring phytoplankton bloom in a predictable manner.

References

- Behrenfeld, M. 2010. Abandoning Sverdrup's critical depth hypothesis on phytoplankton blooms. *Ecology*, 91: 977–989.
- Behrenfeld, M., Boss, E., Siegel, D., and Shea, D. 2005. Carbon-based ocean productivity and phytoplankton physiology from space. *Global Biogeochemical Cycles*, 19: GB1006.
- Behrenfeld, M., Doney, S., Lima, I., Boss, E., and Siegel, D. 2013. Annual cycles of ecological disturbance and recovery underlying the subarctic Atlantic spring plankton blooms. *Global Biogeochemical Cycles*, 27: 526–540.
- Boss, E., and Behrenfeld, M. 2010. *In situ* evaluation of the initiation of the North Atlantic phytoplankton bloom. *Geophysical Research Letters*, 37: L18603.
- Boss, E., Swift, L., Taylor, L., Brickley, P., Zaneveld, R., Riser, S., Perry, M., *et al.* 2008. Observations of pigment and particle distributions in the western north Atlantic from an autonomous float and ocean color satellite. *Limnology and Oceanography*, 53: 2112–2122.
- Briggs, N., Perry, M., Cetinic, I., Lee, C., D'Asaro, E., Gray, A., and Rehm, E. 2011. High-resolution observations of aggregate flux during a subpolar North Atlantic spring bloom. *Deep-Sea Research Part I*, 58: 1031–1039.
- Brody, S., and Lozier, M. 2014. Changes in dominant mixing length scale as a driver of phytoplankton bloom initiation in the North Atlantic. *Geophysical Research Letters*, 41: 3197–3206.
- Brody, S., Lozier, M., and Dunne, J. 2013. A comparison of methods to determine phytoplankton bloom initiation. *Journal of Geophysical Research: Oceans*, 118: 2345–2357.
- Cetinic, I., Perry, M., Briggs, N., Kallin, E., D'Asaro, E., and Lee, C. 2012. Particulate organic carbon and inherent optical properties during 2008 North Atlantic bloom experiment. *Journal of Geophysical Research*, 117: C06028.
- Chiswell, S. 2011. Annual cycles and spring blooms in phytoplankton: don't abandon Sverdrup completely. *Marine Ecology Progress Series*, 443: 39–50.
- Chiswell, S., Bradford-Grieve, J., Hadfield, M., and Kennan, S. 2013. Climatology of surface chlorophyll *a*, autumn-winter and spring blooms in the southwest Pacific Ocean. *Journal of Geophysical Research*, 118: 1–16.
- Cole, H., Henson, S., Martin, A., and Yool, A. 2012. Mind the gap: the impact of missing data on the calculation of phytoplankton phenology metrics. *Journal of Geophysical Research*, 117: C08030.
- D'Asaro, E. 2003. Performance of autonomous Lagrangian floats. *Journal of Atmospheric and Oceanic Technology*, 20: 896–911.
- D'Asaro, E. 2008. Convection and seeding of the North Atlantic bloom. *Journal of Marine Systems*, 69: 233–237.
- D'Asaro, E., Farmer, D., Osse, J., and Dairiki, G. 1996. A Lagrangian float. *Journal of Atmospheric and Oceanic Technology*, 13: 1230–1246.
- Davis, R., Regier, L., Dufour, J., and Webb, D. 1992. The autonomous Lagrangian circulation explorer (ALACE). *Journal of Atmospheric and Oceanic Technology*, 9: 264–285.
- Deardorff, J. 1972. Numerical investigations of neutral and unstable planetary boundary layers. *Journal of Atmospheric Science*, 29: 91–115.
- Deardorff, J., and Willis, G. 1985. Further results from a laboratory model of the convective planetary boundary layer. *Boundary Layer Meteorology*, 32: 205–236.
- Denman, K., and Gargett, A. 1983. Time and space scales of vertical mixing and advection of phytoplankton in the upper ocean. *Limnology and Oceanography*, 28: 801–815.

- Edwards, M., and Richardson, J. 2004. Impact of climate change on marine pelagic phenology and trophic mismatch. *Nature*, 430: 881–884.
- Eriksen, C., Osse, T., Light, R., Wen, T., Lehman, T., Sabin, P., Ballard, J., *et al.* 2001. Seaglider: a long-range autonomous underwater vehicle for oceanographic research. *IEEE Journal of Oceanic Engineering*, 26: 424–436.
- Fennel, L., Cetinic, I., D'Asaro, E., Lee, C., and Perry, M. 2011. Autonomous data describe North ATLANTIC spring bloom. *Eos Transactions*, 92: 465–466.
- Fernando, H., Chen, R., and Boyer, D. 1991. Effects of rotation on convective turbulence. *Journal of Fluid Mechanics*, 228: 513–547.
- Follows, M., and Dutkiewicz, S. 2001. Meteorological modulation of the North Atlantic spring bloom. *Deep-Sea Research Part II*, 49: 321–344.
- Harcourt, R., Steffen, E., Garwood, R., and D'Asaro, E. 2002. Fully Lagrangian floats in Labrador Sea deep convection: comparison of numerical and experimental results. *Journal of Physical Oceanography*, 32: 493–510.
- Henson, S., Dunne, J., and Sarmiento, J. 2009. Decadal variability in North Atlantic phytoplankton blooms. *Journal of Geophysical Research*, 114: C04013.
- Henson, S., Robinson, I., Allen, J., and Waniek, J. 2006. Effect of meteorological conditions on interannual variability in timing and magnitude of the spring bloom in the Irminger Basin, North Atlantic. *Deep Sea Research Part I*, 53: 1601–1615.
- Hersbach, H. 2011. Sea surface roughness and drag coefficient as a function of neutral wind speed. *Journal of Physical Oceanography*, 41: 247–251.
- Holte, J., and Talley, L. 2009. A new algorithm for finding mixed layer depths with applications to Aego data and subantarctic mode water formation. *Journal of Atmospheric and Oceanic Technology*, 26: 1920–1939.
- Huisman, J., van Oostveen, P., and Weissing, F. 1999. Critical depth and critical turbulence: two different mechanisms for the development of phytoplankton blooms. *Limnology and Oceanography*, 44: 1781–1787.
- Kanamitsu, M., Ebisuzaki, W., Woollen, J., Yang, S.-K., Hnilo, J., Fiorino, M., and Potter, G. 2002. NCEP-DEO AMIP-II reanalysis (R-2). *Bulletin of the American Meteorological Society*, 83: 1631–1643.
- Koeller, P., Fuentes-Yaco, C., Platt, T., Sathyendranath, S., Richards, A., Ouellet, P., Orr, D., *et al.* 2009. Basin-scale coherence in phenology of shrimps and phytoplankton in the North Atlantic Ocean. *Science*, 324: 791–793.
- Krahmann, G., Visbeck, M., Smethie, W., D'Asaro, E., Rhines, P., Clarke, R., Lazier, J., *et al.* 2003. The Labrador Sea deep convection experiment data collection. *Geochemistry Geophysics Geosystems*, 4: 4.
- Lavender, K., Davis, R., and Owens, W. 2000. Mid-depth recirculation observed in the interior Labrador and Irminger seas by direct velocity measurements. *Nature*, 407: 66–69.
- Letelier, R., Karl, D., Abbot, M., and Bidigare, R. 2004. Light driven seasonal patterns of chlorophyll and nitrate in the lower euphotic zone of the North Pacific subtropical gyre. *Limnology and Oceanography*, 49: 508–519.
- Lutz, M., Caldeira, K., Dunbar, R., and Behrenfeld, M. 2007. Seasonal rhythms of net primary production and particulate organic flux to depth describe the efficiency of the biological pump in the global ocean. *Journal of Geophysical Research*, 112: C10011.
- Mahadevan, A., D'Asaro, E., Lee, C., and Perry, M. 2012. Eddy-driven stratification initiates North Atlantic spring phytoplankton blooms. *Science*, 337: 54–58.
- Massey, F. 1951. The Kolmogorov-Smirnov test for goodness of fit. *Journal of the American Statistical Association*, 46: 68–78.
- McDougall, T., and Barker, P. 2011. Getting started with TEOS-10 and the Gibbs Seawater (GSW) Oceanographic Toolbox.
- Molemaker, M., and Dijkstra, H. 1997. The formation and evolution of a diffusive interface. *Journal of Fluid Mechanics*, 331: 199–229.
- Morel, A., Huot, Y., Gentili, B., Werdell, P., Hooker, S., and Brayan, A. 2007. Examining the consistency of products derived from various ocean color sensors in open ocean (case 1) waters in the perspective of a multi-sensor approach. *Remote Sensing of Environment*, 111: 69–88.
- Phillips, O. 1977. *The Dynamics of the Upper Ocean*. Cambridge University Press, Cambridge, UK, and New York.
- Platt, T., Fuentes-Yaco, C., and Frank, K. 2003. Spring algal bloom and larval fish survival. *Nature*, 423: 398–399.
- Platt, T., White, G., 3rd, Zhai, L., Sathyendranath, S., and Roy, S. 2009. The phenology of phytoplankton blooms: ecosystem indicators from remote sensing. *Ecological Modeling*, 220: 3057–3069.
- Racault, M., Le Quéré, C., Buitenhuis, E., Sathyendranath, S., and Platt, T. 2012. Phytoplankton phenology in the global ocean. *Ecological Indicators*, 14: 152–163.
- Riley, J., and Lelong, M. 2000. Fluid motions in the presence of strong stable stratification. *Annual Reviews of Fluid Mechanics*, 32: 613–657.
- Sabine, C., Feely, R., Gruber, N., Key, R., Lee, K., Bullister, J., Wanninkhof, R., *et al.* 2004. The oceanic sink for anthropogenic CO₂. *Science*, 305: 367–371.
- Sapiano, M., Brown, C., Schollaert Uz, S., and Vargas, M. 2012. Establishing a global climatology of marine phytoplankton phenological characteristics. *Journal of Geophysical Research*, 117: C028026.
- Siegel, D., Doney, S., and Yoder, J. 2002. The North Atlantic spring phytoplankton bloom and Sverdrup's critical depth hypothesis. *Science*, 296: 730–733.
- Steffen, E., and D'Asaro, E. 2002. Deep convection in the Labrador Sea as observed by Lagrangian floats. *Journal of Physical Oceanography*, 32: 475–492.
- Stramska, M., Dickey, T., Plueddemann, A., Weller, R., Langdon, C., and Marra, J. 1995. Bio-optical variability associated with phytoplankton dynamics in the North Atlantic Ocean during spring and summer of 1991. *Journal of Geophysical Research*, 100: 6621–6632.
- Sverdrup, H. 1953. On conditions for the vernal blooming of phytoplankton. *Journal du Conseil International Pour L'Exploration de la Mer*, 18: 287–295.
- Taylor, J., and Ferrari, R. 2011. Shutdown of turbulent convection as a new criterion for the onset of spring phytoplankton blooms. *Limnology and Oceanography*, 56: 2293–2307.
- Townsend, D., Keller, M., Sieracki, M., and Ackleson, S. 1992. Spring phytoplankton blooms in the absence of vertical water column stratification. *Nature*, 360: 59–62.
- Wang, W., and Huang, R. 2003. Wind energy input the Ekman layer. *Journal of Physical Oceanography*, 34: 1267–1275.
- Yu, L., and Weller, R. 2007. Objectively analyzed air-sea heat fluxes for the global ice-free oceans (1981–2005). *Bulletin of the American Meteorological Society*, 88: 527–539.

Handling editor: Shubha Sathyendranath



Contribution to the Themed Section: 'Revisiting Sverdrup's Critical Depth Hypothesis' Original Article

Onset, intensification, and decline of phytoplankton blooms in the Southern Ocean

Joan Llorc^{1*}, Marina Lévy¹, Jean-Baptiste Sallée^{1,2}, and Alessandro Tagliabue³

¹Sorbonne Universités (UPMC, Univ Paris 06)-CNRS-IRD-MNHN, LOCEAN Laboratory, 4 Place Jussieu, Paris F-75005, France

²British Antarctic Survey, Madingley Road, High Cross, Cambridge CB30ET, UK

³Department of Earth, Ocean and Ecological Sciences, School of Environmental Sciences, University of Liverpool, Liverpool L69 3GP, UK

*Corresponding author: e-mail: joan.llorc@locean-ipsl.upmc.fr

Llorc, J., Lévy, M., Sallée, J.-B., and Tagliabue, A. Onset, intensification, and decline of phytoplankton blooms in the Southern Ocean. – ICES Journal of Marine Science, 72: 1971–1984.

Received 17 September 2014; revised 4 March 2015; accepted 10 March 2015; advance access publication 14 April 2015.

The seasonal cycle of phytoplankton biomass in the Southern Ocean (SO) is characterized by a period of rapid accumulation, known as bloom, that is typical of high-latitude regions. Recent studies have illustrated how spatial and temporal dynamics of blooms in the SO are more complex than in other oceans. This complexity is likely related to differences in vertical mixing and the iron availability. In this work, we examine the sensitivity of bloom dynamics to changes in vertical mixing and iron availability using a biogeochemical model. Under idealized physical forcing, we produce seasonal cycles of phytoplankton for an ensemble of SO scenarios and we describe the bloom dynamics in terms of the net biomass accumulation rate. Based on this metric, we define three crucial bloom phases: the onset, the climax, and the apex. For the ensemble of modelled blooms, onsets always occur in winter and can be either bottom-up (increase in productivity) or top-down (decrease in grazing) controlled. Climaxes are mostly found in spring and their magnitudes are bottom-up controlled. Apexes are always found in late spring and strongly top-down controlled. Our results show that while a "strict" onset definition is consistent with a winter onset, the surface spring bloom is associated with the climax of the integrated bloom. Furthermore, we demonstrate that onset phase can be distinguished from climax phase using appropriate bloom detection methods based on surface satellite-based products. The ensemble of these results suggests that Sverdrup's blooming conditions are not indicative of the bloom onset but of the climax. We conclude that the recent bloom onset debate may partly be due to a confusion between what is defined here as the bloom onset and the climax, and that the SO observed complexity is due to the factors that control the climax.

Keywords: bloom onset, iron, Sverdrup, Southern Ocean.

Introduction

The Southern Ocean (SO) is the largest high-nutrient low-chlorophyll region in the world's ocean. Its relatively low productivity has been attributed to a combination of iron scarcity (Martin *et al.*, 1990), elevated grazing, and light limitation (Boyd and Ellwood, 2010). Despite these unfavourable biological growth conditions, large accumulations of phytoplankton biomass, or blooms, are observed in surface waters each spring over wide areas of the SO (Thomalla *et al.*, 2011). The distribution of these blooms is very patchy in space and time. Hot-spots of phytoplankton accumulation are mainly seen where sources of iron are significant, i.e. in the lee of Islands (Moore and Abbott, 2000; Arrigo *et al.*, 2008). Additionally, the bloom onset dates are rather spread in time,

from October to January (Thomalla *et al.*, 2011), and do not show a clear latitudinal pattern. This is unlike the pattern for North Atlantic spring bloom which is zonal and propagates from South to North (Siegel, 2002; Lévy *et al.*, 2005). The variability of bloom dynamics in the SO in terms of their amplitude, timing and location has been mainly documented from ocean-colour observations (Moore and Abbott, 2000; Arrigo *et al.*, 2008; Thomalla *et al.*, 2011). However, the drivers of the observed variability remains unclear. We hypothesize that patchy environmental conditions, involving zonally asymmetric mixed-layer distributions (Sallée *et al.*, 2010) combined with equally complex dissolved iron distributions (Tagliabue *et al.*, 2011, 2014) are mostly responsible for the complex SO patterns.

Our current understanding of phytoplankton bloom dynamics mainly comes from works based on the North Atlantic. In this region, the mixed-layer, nutrient, and atmospheric environment are largely different from in the southern hemisphere. Historically, the emergence of blooms in the North Atlantic has been related to thinning of the ocean surface layer where turbulence is active (hereafter referred to as “turbulent or mixing-layer”, or *XLD*, to be distinguished from the usual “mixed-layer depth”, or *MLD*, which represents the upper-layer where hydrographical properties are well mixed; Franks, 2015). This thinning implied an increase of averaged exposure of phytoplankton cells to light (Gran and Braarud, 1935; Riley, 1942). Along with this bottom-up view, Sverdrup (1953) proposed that bloom would start when surface mixing-layer crosses a critical depth above which integrated phytoplankton growth would overcome phytoplankton losses (Siegel, 2002). It must be emphasized to note that Sverdrup (1953)’s hypothesis (also known as the Critical Depth hypothesis) is founded on the assumption that “within the top layer the turbulence is strong enough to distribute the plankton organisms evenly through the layer” (Sverdrup, 1953). This assumption is crucial to understand the Critical Depth hypothesis as points out that what matters for phytoplankton is the vertical profile of turbulent mixing, rather than the hydrographical properties of the water column. Indeed, the relevant parameter for the Sverdrup (1953)’s hypothesis is the *XLD* rather than the *MLD* (Franks, 2015).

As an alternative to the bottom-up understanding of ocean blooms, a top-down view has also appeared. This view proposes that, in essence, the causes of phytoplankton concentrations cannot be fully understood without considering the role of their main predator, zooplankton (Banse, 1994). The top-down hypothesis has gained interest recently via a series of papers that challenged the prevailing “bottom-up” paradigm (Behrenfeld and Boss, 2013). Using various tools (satellite data: Behrenfeld, 2010; float data: Boss and Behrenfeld, 2010; and model estimates: Behrenfeld et al., 2013), it has been suggested that the North Atlantic spring bloom does not initiate in spring alongside thinning mixing-layers, but rather in winter when mixing-layer is deepening. This winter initiation is consistent with the hypothesis that dilution enables phytoplankton to better escape their predators and accumulate biomass (Evans and Parslow, 1985; Yoshie et al., 2003; Marra and Barber, 2004).

In this context, our primary objective is to examine the drivers of phytoplankton blooms over the full range of SO environmental conditions. In particular, we examine how different environmental conditions (mixing-layer depth, ferricline, and solar radiation) result in bottom-up or top-down control. To that end, we extend a framework in which the rate of net biomass accumulation (r) results from a competition between growth (μ) and loss (l) of phytoplankton: $r = \mu - l = (1/P)(dP/dt)$, with P the total biomass of phytoplankton present in the water column (Riley, 1942; Sverdrup, 1953; Behrenfeld, 2010). At equilibrium, phytoplankton growth and loss are in balance and phytoplankton population remains stable. This balance can be disturbed by a sudden change in iron supply, light conditions, or stratification in isolation or in combination, which would then likely affect μ and l in different ways (Behrenfeld et al., 2013). Our overarching question is how such perturbations modify μ and l at seasonal scale, and which term is the most sensitive to a given perturbation and the most effective at driving variations in r (i.e. phytoplankton population fluctuations). One of the key aspects of our approach is that we examine three important phases in the annual cycle of blooms: the bloom onset, climax, and apex. Using time evolution of r , we define these bloom phases as follows:

1. The bloom *onset* is when total biomass starts to accumulate.
2. The bloom *climax* occurs when the rate of biomass accumulation is maximal. After this instant, accumulation of phytoplankton continues but at a slower rate because ecosystem has yet started its way to readjustment (i.e. to recoupling).
3. Finally, the bloom *apex* marks the peak in total biomass, i.e. the time after which $l > \mu$ (recoupling is actually achieved) and accumulation starts decreasing.

Figure 1 illustrates these three phases associated with the time of minimum integrated biomass (onset), of maximum slope of integrated biomass (climax), and of maximum integrated biomass (apex). This distinction complements previous studies on bloom dynamics that focused either exclusively on onset (Sverdrup, 1953; Behrenfeld, 2010) or on climax (Lozier et al., 2011; Ferrari et al., 2014).

We address the question of bloom drivers in the SO in the framework of a numerical model. This model uses a state-of-the-art biogeochemical network (Aumont and Bopp, 2006) within a vertically discretized 1D water column configuration where vertical mixing is the main physical process. Aiming to examine the full range of SO conditions, we perform statistical analyses using an ensemble of 1200 model simulations with distinct seasonal cycles of mixing-layer depth, ferricline, and solar radiation. Bloom onset, climax, and apex dates are diagnosed for each run in the ensemble. Simultaneously, the distributions of variables such as iron supply, mixing-layer depth, light, phytoplankton growth, and loss rates for each of the three bloom phases are attributed to drivers. We investigate when bottom-up or top-down controls prevailed. This model allows us to test existing theories on bloom onset in an idealized and comprehensive framework, and to discuss them in the context of the SO. Furthermore, the completeness of the model data allows us to compare the onset and climax dates with the dates at which two different satellite-based bloom detection methods identify bloom initiation. These bloom detection methods are also compared with the date of the bloom onset predicted by Sverdrup (1953)’s hypothesis with the aim to evaluate at which point the validation (or refusal) of this hypothesis is influenced by the bloom detection method.

Methods

Biogeochemical model

The model was set up to represent the Permanent Open Ocean Zone (POOZ) of the SO, away from ice formation and melting, where nitrate and silica do not limit productivity. Our goal in this study is to untangle how the different phases of a bloom (onset, climax, and apex) are controlled by their physical and biogeochemical environment. As such, we deliberately chose to reduce the complexity of the problem by considering a 1D physical framework (e.g. lateral advection is neglected). Varying vertical diffusion reproduces seasonal cycle of the mixing-layer depth. Along with this idealized physical configuration, we model the associated biogeochemical activity with the model PISCES (Aumont and Bopp, 2006). PISCES contains 24 biogeochemical tracers with five nutrients able to limit phytoplankton growth: nitrate, phosphate, ammonium, iron, and silicate. The iron pool is explicitly modelled and controlled by a range of processes such as phytoplankton uptake, bacterial uptake, zooplankton, and bacterial recycling, remineralization and scavenging. In addition, four living pools are represented: two phytoplankton size classes (small and large) and two zooplankton size classes (microzooplankton and mesozooplankton). Large phytoplankton differs

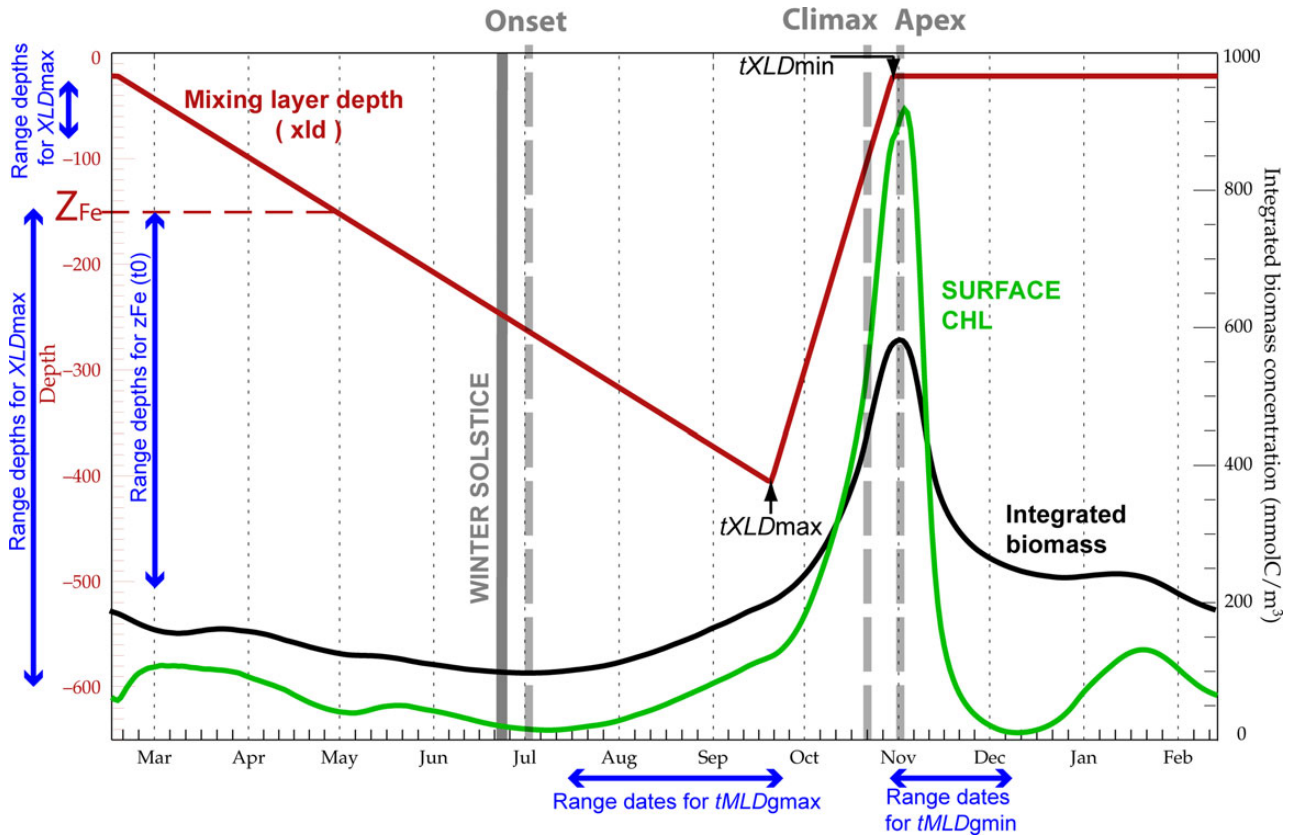


Figure 1. Seasonal cycle of the mixing depth (XLD; red line), integrated phytoplankton biomass (black line) and surface chlorophyll (green line) for one of the modelled blooms. The red horizontal dashed line marks the depth of summer ferricline (Z_{Fe}). The dates of the maximal and the minimal depth ($tXLD_{max}$ and $tXLD_{min}$, respectively) are indicated with a black arrow. The vertical grey solid line marks the date of the winter solstice (21 June) while vertical grey dashed lines mark the three bloom stages: onset, climax, and apex. Blue arrows show the range of values sampled for each of the five physical parameters: maximal and minimal mixing dates (XLD_{max} and XLD_{min}), its corresponding dates ($tXLD_{max}$ and $tXLD_{min}$) and the summer ferricline (Z_{Fe}).

from the small phytoplankton by higher requirements in iron and a greater iron half-saturation constant. Grazing pressure on each phytoplankton is also differentiated by size: microzooplankton (Z) preferentially grazes small phytoplankton while mesozooplankton (M) preferentially grazes the larger phytoplankton but also microzooplankton.

Prognostic equation for each phytoplankton group ($i = 1, 2$) is:

$$\frac{\partial P_i}{\partial t} = \mu_i P_i - g^Z(P_i)Z - g^M(P_i)M - m_i P_i + \frac{\partial}{\partial z} \left[\kappa_z \frac{\partial P_i}{\partial z} \right], \quad (1)$$

$i = 1, 2,$

where P_i is the phytoplankton biomass, μ_i is the growth rate, g_i represents the grazing rate, and m_i is the mortality rate. The last right hand side term is the effect of vertical diffusion over biomass due to vertical mixing of intensity κ_z . The growth rate (μ_i) is computed as follows:

$$\mu_i = \mu_{max} f_i(T) h(z) \left(1 - \exp \left(\frac{-\alpha_i Q_i^{Chl} PAR_i}{\mu_{max} f_i(T) L_i} \right) \right) L_i, \quad i = 1, 2 \quad (2)$$

where $f_i(T)$ is the dependence of the growth rate with temperature (Eppley, 1972), $h(z)$ is a penalization term for deep mixing, PAR_i is function of the shortwave radiation at the surface, α_i is the

initial slope of the photosynthesis-irradiance curve, Q_i^{Chl} the Chl:C quota for each phytoplankton, and L_i is the nutrient limitation. Nutrients limitation in our set-up can only be due to Fe, so $L_i \equiv L_i^{Fe}$, where

$$L_i^{Fe} = \min \left(1, \max \left(0, \frac{Q_i^{Fe} - Q_{i,min}^{Fe}}{Q_{i,opt}^{Fe}} \right) \right). \quad (3)$$

Iron limitation is formulated following a Quota approach (McCarthy, 1980; Droop, 1983) with the term $Q_{i,opt}^{Fe}$ allowing luxury uptake (as in Buitenhuis, 2010). Grazing rate by zooplankton is computed as a Michaelis–Menton parametrization with a phytoplankton feeding threshold (Aumont and Bopp, 2006). It can be formulated as follows:

$$g^Z(P_i) = g_m^{0,Z} f_Z(T) \frac{\gamma_{P_i}^Z}{K_{graz}^Z + \sum_{P_i} \gamma_{P_i}^Z P_i} F_{threshold}^{Z,P_i}, \quad (4)$$

where Z stands for both micro- and mesozooplankton, $g_m^{0,Z}$ is the maximum grazing rate at $0^\circ C$, $f_Z(T)$ is a temperature-dependent function, K_{graz}^Z is the corresponding half-saturation constant, $\gamma_{P_i}^Z$ is the preference of each zooplankton for each phytoplankton, and $F_{threshold}^{Z,P_i}$ is a function computing the corresponding feeding thresholds

for each couple phyto/zoo. Encounter probability between grazers and phytoplankton is not explicitly computed but results from the volumetric concentration of the four biological compartments.

The model equations were computed on a regular vertical grid of $74 + 1$ vertical levels (constant spacing of 7 m for the first 74 levels and a last one of 500 m depth) and a time step of 20 min. The vertical mixing coefficient (κ_z), temperature and surface photosynthetic available radiation (PAR) were analytically prescribed every 6 h. Vertical mixing coefficient were assumed to be constant and equal to $1 \text{ m}^2 \text{ s}^{-1}$ within a surface mixing layer of depth XLD , and equal to $10^{-5} \text{ m}^2 \text{ s}^{-1}$ below. Hence, in this study, XLD was not calculated but imposed through the κ_z vertical profile. The extremely large value of κ_z within the XLD guaranteed that turbulence was strong enough to homogeneously distribute phytoplankton (i.e. Sverdrup, 1953s assumption). Following Lévy (2015), who highlighted the need to represent the full seasonal cycle of the XLD to study the bloom, we imposed an idealized seasonal cycle of the XLD divided into three phases (red curve in Figure 1):

- A fall/winter phase of convection and progressive XLD deepening.
- A spring phase where cessation of convection led to the thinning of the XLD .
- A summer phase with a relatively shallow and constant XLD .

To ensure that the timing of these phases and the magnitude of the XLD were relatively realistic, we used data estimates derived from Argo data (Sallée et al., 2010). These data provided us with an estimate of the depth of the seasonal thermocline in the SO, which we assumed to reflect the mixing depth. Sub-seasonal variability in the XLD was not accounted for. For temperature and surface PAR, we used a smoothed climatological seasonal cycle constructed from observations (DFS3-ERA40; Broderau et al., 2008) averaged over the 40–60°S latitudinal band.

The summer initial condition for dissolved Fe profile was constructed by assuming low concentrations (0.03 nMolFe/l) above a prescribed ferricline depth (Z_{Fe}), and larger concentrations (0.5 nMolFe/l) below. The depth of the ferricline for the initial condition iron profile is one of the parameters we varied in our set of simulations. It is generally understood that the summer Fe profile is set by a combination of remineralization, scavenging and physical supplies by lateral sources. While remineralization and scavenging are parametrized in PISCES, there remains a large degree of uncertainty in the parameterization. In addition, lateral supplies were not explicitly accounted for. To overcome these issues and to allow the model to reach a repeating and stationary seasonal cycle, the dissolved iron profile was restored towards its initial value at the end of each summer.

Initial vertical profiles for macronutrient (i.e. nitrates, phosphates, and silicates) were constructed based on the winter mean profiles collected during the KERFIX project (Jeandel et al., 1998). This project aimed to monitor ocean-atmosphere CO_2 and O_2 exchanges and related processes with a time-series station (called KERFIX station) located at 50°40'S–68°25'E, 60 miles southwest of the Kerguelen Islands (SO). From January 1990 to March 1995, regular monthly measurements of physical and biogeochemical water properties were carried out at KERFIX station. As for iron, macronutrients were restored to the initial profiles at the end of each summer. Initial conditions for the four living compartments were set to low values for the first year. The simulations were

integrated for 3 years, starting in austral summer (15 February), with outputs saved at daily frequency. A repeating seasonal cycle was reached after 2 years and results are based on the third year of simulation. As an example, Figure 1 shows a complete seasonal cycle of integrated biomass (black curve), surface Chl (green), XLD (red), and summer Z_{Fe} , for one of these runs.

Ensemble runs

An ensemble of runs was performed by varying the XLD and summer Z_{Fe} in the range of values found in the POOZ. Specifically, these XLD and Z_{Fe} were modified based on the following variables:

- The winter maximal mixing depth (XLD_{\max})
- The summer minimal mixing depth (XLD_{\min})
- The date at which XLD_{\max} was reached ($tXLD_{\max}$)
- The date at which XLD_{\min} was reached ($tXLD_{\min}$)
- The summer ferricline depth, Z_{Fe}

The variables i–v were set based on a discrete set of observed values, with equal weight given to each discrete value (see ranges in Figure 1, blue arrows). The ranges for Z_{Fe} were established based on a recent compilation of dissolved iron measurements (Tagliabue et al., 2011), the ranges of values used to set XLD were based on >500 000 density profiles sampled in the SO by Argo floats data (Sallée et al., 2010). Our choice of variables led to an ensemble of almost 1200 different scenarios that combine different values of the above parameters i–v covering a wide range of XLD and Z_{Fe} observed in the SO.

In our model, the amount of Fe injected at the surface each year was not prescribed: Fe was entrained in the mixing layer during the deepening phase. Thus, the Fe supply depended on the relative depths of the ferricline and XLD_{\max} (Figure 2). The relationship between both variables was however non-linear, due to the effects of consumption/remineralization by the biological community and the rate of stratification/destratification. A peculiarity of the SO is that the ferricline depth is often found below the maximum

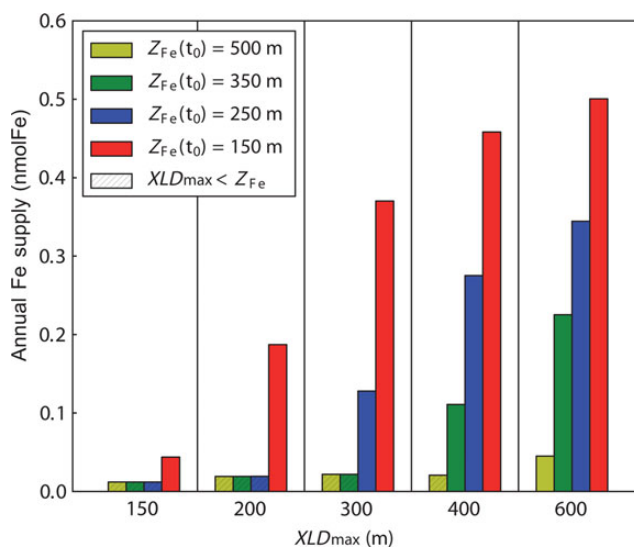


Figure 2. Histogram of the total amount of Fe supplied to the 0–50 m surface layer as a function of the XLD_{\max} and the summer ferricline (colours).

winter mixed-layer depth (Tagliabue *et al.*, 2014), implying some regions permanently Fe-limited despite strong and deep winter mixing. In our scenarios, this situation occurred when Z_{Fe} was greater than XLD_{max} (Figure 2). Note that this is different from other high-latitude productive regions such as the North Atlantic, where nitrate is the main limiting nutrient. In the North Atlantic, the depth of winter mixing and the convective nitrate supplies are more tightly correlated than its SO counterpart (depth of winter mixing and convective Fe supplies).

Bloom onset, climax, and apex

The bloom phenology was decomposed into three main events defined by the rate of net biomass accumulation (r), which writes as:

$$r = \frac{1}{P^{int}} \frac{dP^{int}}{dt}, \quad \text{with} \quad P^{int} = \int_0^H P dz \quad (5)$$

where H is the depth of the water column. For simplicity, hereinafter we will refer to P^{int} as P . From the seasonal evolution of r , we defined the bloom onset (total biomass starts to increase: P_{min} , $r = 0$, and $r' > 0$; hereafter all temporal derivatives are marked by a prime, i.e. $r' = \partial r / \partial t$); the bloom climax (the rate of accumulation is maximum: $r = r_{max}$ and $r' = 0$) and the bloom apex (bloom peaks in total biomass: $P = P_{max}$, $r = 0$ and $r' < 0$). See Figure 1 where the three steps are reported. We note here that r was computed in our study from a total water column integral, which slightly differs from what is done in Sverdrup (1953) or Behrenfeld (2010) where P was integrated down to the base of the mixing layer. As Chiswell (2013) pointed out, mixing layer integration of P might be misleading when the mixing layer restratifies as plankton is not conserved in the XLD . Integrating over the whole water column overcomes the discontinuity issue pointed out by Chiswell (2013).

Integrating Equation (1) and dividing all terms by P , r can be written as the integrated balance between phytoplankton source (i.e. growth rate, μ) and sinks (i.e. grazing and mortality rates, g and m , respectively):

$$r = \mu - g - m. \quad (6)$$

Hence, the evolution of modelled ecosystem in the water column can be synthesized as:

$$r = \mu - l, \quad (7)$$

where μ is the mean growth rate of the total depth integrated phytoplankton community, and l is the sum of grazing and mortality.

Bloom timing

In our set of experiments, the time of the deepest convection ($tXLD_{max}$) can vary by up to 2 months between experiments, and the time at which summer stratification is reached ($tXLD_{min}$) by 1 month (Figure 1). To account for this variability, the timing of the different bloom phases was not only measured relatively to the day of the year but also relatively to the phase of the physical forcing (i.e. relative to the time of $tXLD_{min}$ and $tXLD_{max}$). In this sense, bloom phases before $tXLD_{max}$ occurred in “winter”, when the mixing layer is still deepening. Similarly, bloom phases occurring between $tXLD_{max}$ and $tXLD_{min}$ are occurred during the spring thinning of the mixing layer.

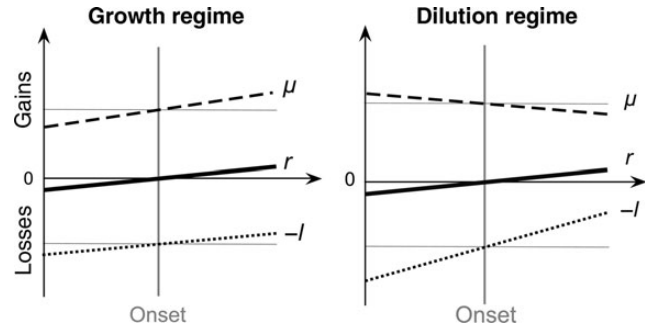


Figure 3. Diagram of the two mechanisms able to trigger the bloom in winter. In growth (dashed), net accumulation (solid) and losses (dotted) rates are represented for the (a) Growth Regime and (b) the Dilution Regime. Losses rate is represented as negative ($-l$) to illustrate the balance $r = \mu - l$. The vertical grey line marks the date of onset at which r becomes greater than zero.

Bottom-up vs. top-down control

In this paper, we aim at investigating whether the bloom seasonal cycle is controlled by bottom-up or top-down processes. Here, we detail how the relative intensity of μ' and l' can be used to link onset, climax, and apex to their bottom-up or top-down controls.

Onset ($r = 0$, $r' > 0$) occurs when gains first overcome losses. At onset integrated phytoplankton biomass is minimal and losses are always decreasing. Under these circumstances, two possible mechanisms can cause the bloom onset (Figure 3):

1. *Growth regime*: The growth rate has already started to increase while the loss rate is still decreasing or stable. The growth will then become larger than loss at some point leading to the initiation of net biomass accumulation in the water column (i.e. $r > 0$). The onset is controlled by the growth (i.e. light and nutrients) and therefore is bottom-up driven. Analytically, this regime can be expressed as:

$$\mu' > 0, l' \leq 0 \Rightarrow r' > 0. \quad (8)$$

2. *Dilution regime*: Growth and loss rate are decreasing due to nutrients depletion, low light conditions, and XLD deepening. The latter causes the dilution of plankton (both, phyto- and grazers) when increasing the volume of water in the mixing layer. This process strongly decreases the prey–predator encounter probability causing a faster decrease on loss rate than on growth rate. The grazing pressure relaxation allows phytoplankton ecosystem to start increasing. This regime is top-down controlled and it corresponds to bloom onset scenario described in Marra and Barber (2004), Behrenfeld (2010), and Boss and Behrenfeld (2010). It can be analytically expressed by

$$l' < \mu' < 0 \Rightarrow r' > 0. \quad (9)$$

Climax ($r = r_{max}$, $r' = 0$) marks the instant of the fastest population increase. Consequently, climax is the inflection point in the seasonal evolution of biomass:

$$r = r_{max} \Rightarrow r' = 0 \quad \text{where} \quad P' \propto r'. \quad (10)$$

From an ecosystem point of view, this means that the trend in loss rate overcomes the trend in growth rate ($l' \geq \mu'$). Therefore, the

bloom climax marks the beginning of the recoupling process that leads to the re-equilibrium of the system. Climax can be achieved in two different ways: either μ' becoming negative due to nutrient limitation (bottom-up control) or l' becoming greater than μ' (top-down control).

Finally, *apex* ($r = 0, r' < 0$) marks the actual time of recoupling, when losses first equals gains. At apex, losses are always increasing $l' > 0$. Apex can be reached when growth is still increasing, and biomass accumulation is stopped by grazers (i.e. $l' > \mu'$ with $\mu' > 0$); we refer to this case as the top-down controlled. In the bottom-up case, the apex is mainly due to change on the growth rate trend (i.e. $\mu' < 0$). This situation is often caused by the nutrients depletion in the mixing layer. We note that both top-down and bottom-up controls can mutually act together. Our analysis only points out the dominant process at play.

Bloom onset detection and Sverdrup's hypothesis

With the aim to evaluate how onset and climax phases can be detected using ocean-colour data, we applied two different bloom detection methods to model outputs. Several bloom detection methods exist in the literature and it has been shown that bloom detection dates can strongly differ depending on which method is applied (Ji *et al.*, 2010; Brody *et al.*, 2013). Here we use two methods, a surface biomass- (sP) and a surface chlorophyll- (sChl) based methods, that have already been implemented in literature with ocean-colour data (Behrenfeld, 2010; Brody *et al.*, 2013). Despite these methods are designed to be applied with ocean-colour data, in our case bloom detection dates are obtained from modelled sP and sChl and compared to the actual onset and climax computed from the full vertical profile. The two bloom detection methods are defined as follows:

1. P^* -method: date at which $P^{*'} > 0$ Behrenfeld (2010), where:

$$P \approx P^* = sP \times XLD \text{ while } t < tXLD_{\max}. \quad (11)$$

2. sChl-method: Date of maximal sChl" (Sallée *et al.*, 2015)

The P^* -method is based on a depth integrated view of the bloom: it estimates the amount of biomass within the water column assuming that phytoplankton is homogeneously mixed in the ocean upper layer and that the amount of biomass below is negligible. Onset is then detected when integrated biomass starts to increase. On the other hand, the sChl-method is only based on the surface imprint of the bloom and onset detection is based on the rate of change of sChl. Interestingly, when used in the literature, the P^* -method resulted on bloom onset detected in winter (Behrenfeld, 2010) while sChl-method detects bloom onsets mostly in spring (White *et al.*, 2009; Sallée *et al.*, 2015).

A number of studies have addressed high-latitude blooms using ocean-colour data with the aim to validate (or to reject) Sverdrup (1953)'s hypothesis (Siegel, 2002; Behrenfeld, 2010; Chiswell, 2011). Here, we aim to quantify at which point the validation (or refusal) of the Sverdrup (1953)'s hypothesis depends on the bloom detection method implemented. We took advantage of the model data completeness to compute the critical depth (Z_c) based on the two main Sverdrup (1953)'s assumptions: strongly turbulent surface layer and constant mortality (assumed to be the main loss term in winter-early spring). The formal expression of Sverdrup

(1953) critical depth (as presented in Lévy, 2015)

$$\frac{\alpha I_0}{kZ_c} (1 - e^{-kZ_c}) = m \quad (12)$$

can be approximated to

$$Z_c \approx \left(\frac{1}{k}\right) \frac{\mu_0}{m}, \quad (13)$$

where μ_0 is the phytoplankton growth rate at surface (i.e. $\mu_0 = \alpha I_0$), k is the light attenuation coefficient (in m^{-1}), and m is the mortality rate. The variable Z_c is computed at each time step using the model outputs for μ_0 , m averaged from August to October and a light attenuation coefficient of $k = 0.05 \text{ m}^{-1}$, constant throughout the year (i.e. no phytoplankton shelf-shading; Lévy, 2015). Determining the date at which $XLD = Z_c$ for each modelled bloom, we are able to investigate whether Sverdrup's bloom conditions are satisfied or not for the two surface bloom detection methods presented above (P^* -method and sChl-method).

Results

Abrupt and smooth blooms

Two types of bloom phenology emerge from our 1200 runs ensemble: abrupt blooms, characterized by a sudden and very strong intensification of biomass accumulation, and smooth blooms, which display a smoother biomass accumulation. In fact, there is a continuous range of possible phenologies between these two bloom types and, hence, no objective method that distinguishes them. Nevertheless, as abrupt blooms reach, by definition, a higher value of r at climax, the 20% of blooms with the largest r_{\max} were identified as abrupt, and the remaining 80% as smooth in the following analysis. Importantly, these two types of SO bloom phenologies are also identifiable from ocean-colour observations (Sallée *et al.*, 2015).

For illustrative purpose, we will describe an example of an abrupt and smooth bloom taken from our results (Figure 4). In the abrupt case example (Figure 4a, c, and e), the XLD reaches 400 m in winter and the summer ferricline is located at 150 m. This deep winter mixing causes strong light limitation over 6 months of the year (from May to October; yellow surface in Figure 4e). Simultaneously, Fe limitation (red surface in Figure 4e) declines as XLD becomes deeper than Z_{Fe} and entrains Fe to the surface. The bloom onset occurs around 1 July and is followed by 2.5 months of a low and stable positive r during which the XLD continues to progressively deepen. We will refer to this period as the *plateau*. Then, when $tXLD_{\max}$ is reached and the XLD starts shallowing, r rapidly increases until climax (r_{\max}) is reached on 20 October. In this scenario, the climax is an abrupt and strong peak that occurs during the period of XLD restratification. This date also marks the start of a large and rapid increase in both integrated biomass (P) and surface chlorophyll (sChl) (black and green lines in Figure 4a). Apex is reached 10 days after the climax (1 November) associated to a rapid decline in r , which is driven by decreasing μ as Fe-limitation becomes important, as well as increasing losses ($l' \gg 0$). Following apex, growth/loss equilibrium ($r \approx 0$) is re-established over the summer (i.e. grazers-prey recoupling). This type of bloom is characteristic of high-latitude regions like the North Atlantic and iron rich waters of the SO (Waniek, 2003).

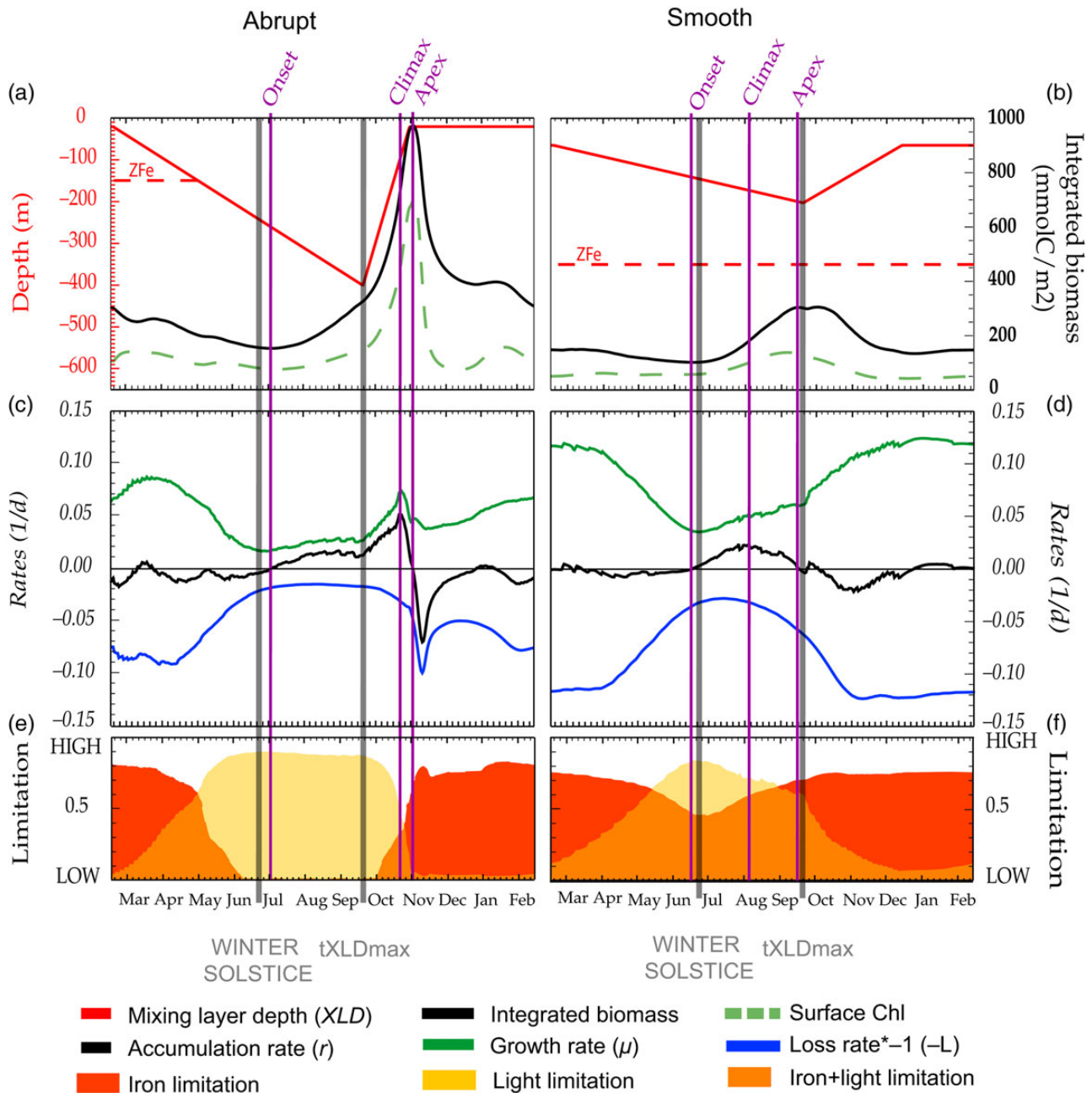


Figure 4. Seasonal cycle of the forcing XLD (red line) and model outputs of integrated biomass (black line) and surface chlorophyll (green line) for (a) an abrupt bloom and (b) a smooth bloom. Summer Z_{Fe} is indicated by a horizontal red dashed line. The seasonal cycle of the accumulation rate (r , black line), the growth rate (μ , green line), and losses rate (l , blue line) for both runs are represented in panels (c) and (d). Losses rate is represented as negative ($-l$) to illustrate the balance $r = \mu - l$. Limitation due to Fe and light are shaded in red and yellow areas; orange areas stands for the time at which both factors are limiting. Winter solstice date and XLD_{max} date are indicated by a vertical grey line. Onset, climax, and apex dates for each run are marked by a light blue dashed line.

In the smooth bloom case example (Figure 4b, d, and f), XLD reaches 200 m in winter, with a long period of restratification (>2 months) and a relatively deep mixing during summer (65 m). The variable Z_{Fe} is deeper than XLD_{max} , so mixing does not reach the largest Fe stocks, which maintains a significant Fe limitation all year-round. As for abrupt bloom case, onset occurs in mid-June and is followed by a *plateau* phase which lasts during XLD deepening. In contrast to the abrupt bloom (Figure 4a, c, and e), the *plateau* has

a much smoother shape and, instead of switching to a high r phase, is followed by a phase where r declines slowly. Climax is in late-July, in the midst of the *plateau* and just before $tXLD_{max}$; the accumulation intensity at climax is almost four times lower than for the abrupt bloom case ($r_{max}^{smooth} = 0.02 \text{ d}^{-1}$ compared with $r_{max}^{abrupt} = 0.075 \text{ d}^{-1}$). Restratification is not associated with an increase in accumulation, which is likely due to prevailing Fe limitation. The climax lead to the beginning of recoupling and apex is

reached after 2 months (around mid-September), associated to a strong grazing pressure that overcomes the steady increase in growth rate (at $r = 0 : l' > \mu' > 0$, Figure 4b–d). Overall, the temporal changes in r are much less pronounced than for the abrupt case (Figure 4a–c) and the apex seems to arise from the long process of re-equilibrium that begins just after the onset, due to maintained top-down control. The variables P and sChl display a weak seasonal cycle with maximal values between September and October. The maximal value of sChl is reached just before P_{\max} , which in contrast to the abrupt bloom case, has a broader and lower peak. This second type of bloom are often observed in subtropical regions and low iron concentration areas of the SO.

Bloom seasonal cycle: onset, climax, and apex

Onset

A remarkably consistent result over our 1200 simulations is that in 100% of the situations that we have explored, the bloom onset always occurs in winter, when the mixing layer is deepening (Figure 5a). The median value of the onset date is ~ 2 months before $tXLD_{\max}$ and 4 months before $tXLD_{\min}$. Abrupt blooms tend to

initiate earlier than smooth blooms, and the spread of the time of initiation is wider for smooth blooms than for abrupt blooms.

As introduced above, these winter onsets can either be growth or dilution driven. Here we assess each of the blooms in terms of the rate of change in losses and growth (l' and μ' , respectively) at the time of onset (Figure 6). In this way, we can discriminate between the bottom-up (increase in growth rate or Growth regime) and top-down (decrease in grazing or Dilution regime) control. Overall, across the 1200 scenarios of our study we find an equal distribution between Growth regimes ($\mu' > 0$, red quadrant in Figure 6) and Dilution regimes ($\mu' < 0$, blue semi-quadrant in Figure 6). No significant differences in the onset regime are found for abrupt blooms (represented by triangles in Figure 6).

In terms of absolute timing, all onsets occurring after the winter solstice are associated to Growth regimes and those occurring before the winter solstice, to the Dilution regime (see colour bar in Figure 6). Thus, in our simulations (and unlike the results of Behrenfeld *et al.*, 2013 in a model of the North Atlantic) dilution is not always efficient enough to initiate the bloom. We found that the efficiency of dilution at initiating the bloom is related to the speed of destratification of the mixing layer. Dilution is efficient

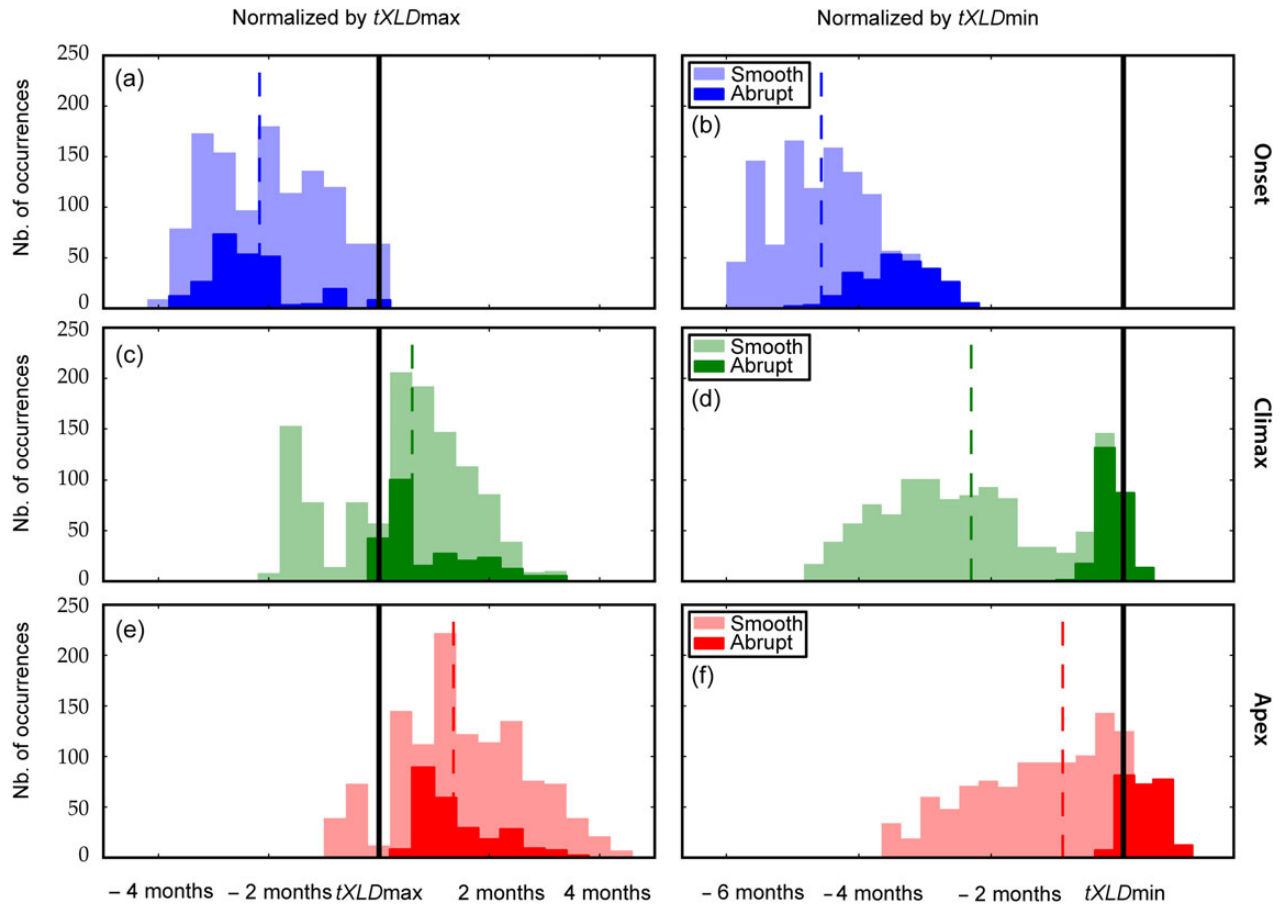


Figure 5. Bloom onset, climax, and apex dates for each modelled bloom have been normalized by the corresponding $tXLD_{\max}$ (left column) and $tXLD_{\min}$ (right column). In the figure, the histogram of the ensemble of modelled blooms representing: (a) the onset date normalized to the $tXLD_{\max}$ date, (b) the onset date normalized to the $tXLD_{\min}$ date, (c) the climax date normalized to the $tXLD_{\max}$ date, (d) the climax date normalized to the $tXLD_{\min}$ date, (e) the apex date normalized to the $tXLD_{\max}$ date and (f) the apex date normalized to the $tXLD_{\min}$ date. Median value is represented by a vertical dashed line. Abrupt blooms distribution are in dark colour and smooth blooms distribution in light colour. Normalization allows to identify the link the bloom phase with the dynamics of the XLD. For instance, independently of the absolute onset date, negative values represent onsets occurring before $tXLD_{\max}$ (i.e. before the start of stratification) while positive values indicate that bloom starts after $tXLD_{\min}$ (i.e. during stratification).

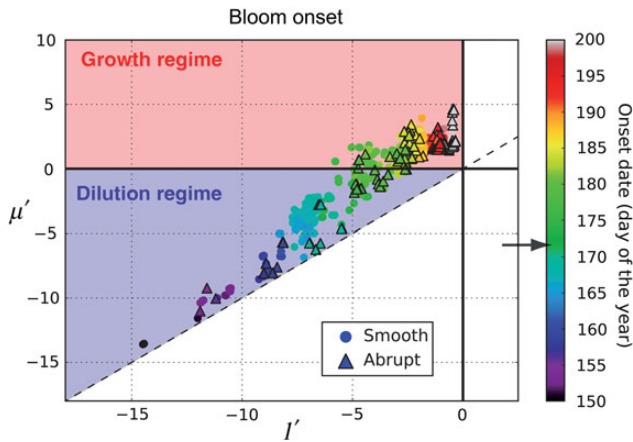


Figure 6. Growth and losses rate trends at the date of onset for the ensemble of modelled blooms. Circles stand for smooth blooms and triangles for abrupt blooms. Growth Regime quadrant (background red shade) and Dilution regime semi-quadrant (background blue shade). The absolute onset date (day of the year) is represented by coloured symbols. Austral winter solstice date (21 of June, day of the year 172) is marked with an arrow on the colour bar.

when the destratification is strong enough to dilute predators, but weak enough to retain favourable light conditions for phytoplankton. In our simulations, we find a threshold between dilution and Growth regimes of at $\approx 2 \text{ m d}^{-1}$ (not shown). When the destratification rate is greater than $\approx 2 \text{ m d}^{-1}$, the decrease in losses due to dilution is not strong enough to overcome the decrease in growth and to cause the bloom to onset. In this case, the onset is delayed until light conditions become more favourable (i.e. after winter solstice), switching to a Growth regime. Alternatively, when the destratification rate is less than $\approx 2 \text{ m d}^{-1}$ the opposite occurs, favouring Dilution regime.

Climax

After the bloom onset, biomass accumulation increases until it reaches a maximum rate that we define as the climax (time of $r = r_{\text{max}}$). We note here that this date is different from the date of maximal biomass stock: accumulation continues until r switches back to a negative value. Instead, climax refers to the maximum increase rate of integrated biomass. In contrast to the bloom onset, for the large majority of blooms ($\approx 80\%$), climax is reached during the phase of XLD retreat, i.e. after XLD_{max} (Figure 5c). The remaining 20% of blooms are characterized by a climax before or when the mixing-layer reaches its maximum depth. However, all these blooms with a climax before XLD_{max} are smooth blooms. Abrupt blooms, associated with, by definition, a large (i.e. an “intense” climax) have their climax occurring after XLD_{max} .

Interestingly, for all seasonal cycles analysed, we found the accumulation reaches its maximum before the surface layer re-stratifies to its minimal value (Figure 5d). In summary, we find that in 80% of our simulation climax occurs during the spring stratification (i.e. before $tXLD_{\text{min}}$ and after $tXLD_{\text{max}}$). In addition, climax associated with all the abrupt blooms occurs at the time where the mixing layer reaches its minimal value (i.e. at $tXLD_{\text{min}}$ and after $tXLD_{\text{max}}$; dark green in Figure 6c and d). These results suggest a relationship between climax date and intensity, and the surface layer re-stratification period, which in turns points out the possible importance of light on biomass accumulation rate. Therefore, we find

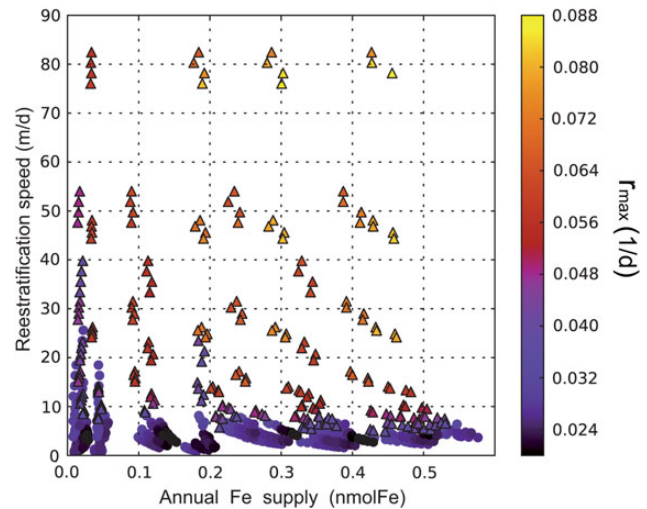


Figure 7. The climax intensity (or r_{max} ; in d^{-1}) is represented in colour as a function of the vertical iron supply and the re-stratification speed. Circles stand for smooth blooms and triangles for abrupt blooms.

that the faster is the re-stratification of the surface layer, the larger is the maximum accumulation rate (Figure 7), with the total Fe input playing a secondary role. We note that for a given re-stratification speed (except for the very low re-stratification, slower than 5 m d^{-1}), r_{max} is tightly linked to the total Fe input in the surface layer. We interpret the tight relationship between r_{max} and the re-stratification as an indication of bottom-up control: a rapid improvement in light conditions leads to a parallel increase in growth rate (μ), which quickly translates into a rapid elevation of r , as grazers are not able to respond at the same rate. The amount of Fe available in winter thus works as a catalyst, allowing phytoplankton to take an optimal benefit of the increase in light conditions.

Apex

The apex date is reached when loss rate first overcomes growth rate ($l = \mu$) causing biomass accumulation to arrest ($r = 0$). For 90% of the scenarios we analysed, apex occurs after the mixing layer reaches its maximum (median value ~ 1.5 months later; Figure 5e). In addition, apex is reached, in $>75\%$ of bloom scenarios, before the date of minimum mixing depth (median value ~ 1 month before; Figure 5f). However, apex for abrupt blooms occurs after $tXLD_{\text{min}}$ (hence also after $tXLD_{\text{max}}$; Figure 5e and f). Such blooms can be viewed as examples of “bloom and bust” dynamics occurring during a rapid re-stratification that causes a sudden drop in r following the climax (compare Figure 5d and f; dark colours, or example of Figure 4b).

By assessing the state of the ecosystem at the apex date, we can better understand the processes leading to this stage. At apex, l is always positive (Figure 8), which means grazing pressure is increasing. In contrast, μ' can be either positive (but necessarily lower than l) or negative (Figure 8). Over the ensemble of scenarios, 68% have an increase in growth ($\mu' > 0$) at the time of apex, and 32% have a decrease in growth ($\mu' < 0$) at the time of apex. However, l is always greater than μ' (up to a factor 10 in some cases) indicating strong top-down control for our entire suite of scenarios. The earliest apex dates are always associated with $\mu' > 0$ (Figure 8), while after around day 260 (\sim mid-September), μ' can be either positive or negative at recoupling. The highest loss rates ($l > 100 \text{ d}^{-1}$) are always associated to abrupt blooms (see triangles in Figure 8).

Relating bloom phases and bloom detection methods based on surface Chl

Many of the seasonal cycles generated by our model are characterized by a plateau phase, with positive, but weak and relatively

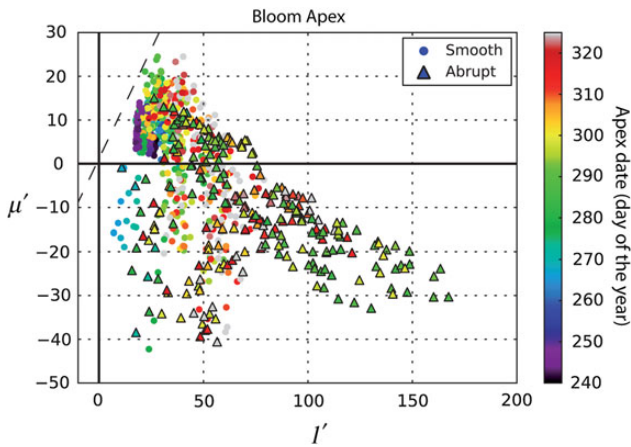


Figure 8. Growth and losses rate trends at the date of the apex for the ensemble of modelled blooms. Circles stand for smooth blooms and triangles for abrupt blooms. The absolute apex date (day of the year) is represented by coloured symbols.

constant accumulation between onset and climax (see Section Abrupt and smooth blooms and Figure 4). While in terms of biomass accumulation, the bloom has definitely started (i.e. r), there is little accumulation of chlorophyll at the ocean surface (sChl; see examples in Figure 4, green dashed curve). Clearly, detecting bloom onset from surface chlorophyll observations would be challenging in such cases. In this section, we aim to evaluate two bloom detection methods that have been previously applied to surface observations of Chl accumulation (e.g. Behrenfeld, 2010; Brody et al., 2013), see what phase of the bloom they detect (onset or climax) and if they comply to the critical depth hypothesis or to the dilution/recoupling hypothesis.

The biomass-based bloom detection method (P^* -method; see Section Methods for details) detects dates that coincide, for 85% of blooms, to the onset computed from the full vertical profile (Figure 9a). This result is not surprising given the model set-up: in our model, the mixing layer is very strongly mixed, so we expect P to be relatively constant over XLD and very weak below the mixing layer (so $P^* \approx P$). The accuracy of the P^* -method is therefore strongly tied to the choice of the mixing depth over which P^* is computed: it must be a strongly mixed surface layer which is not always well described by typical mixed-layer depth criterion (e.g. Taylor and Ferrari, 2011). Arguably, P^* -method will work better during the convective phase of the surface layer, when mixed-layer actively mixes. The P^* -method detects onset dates ~ 2 months before the climax

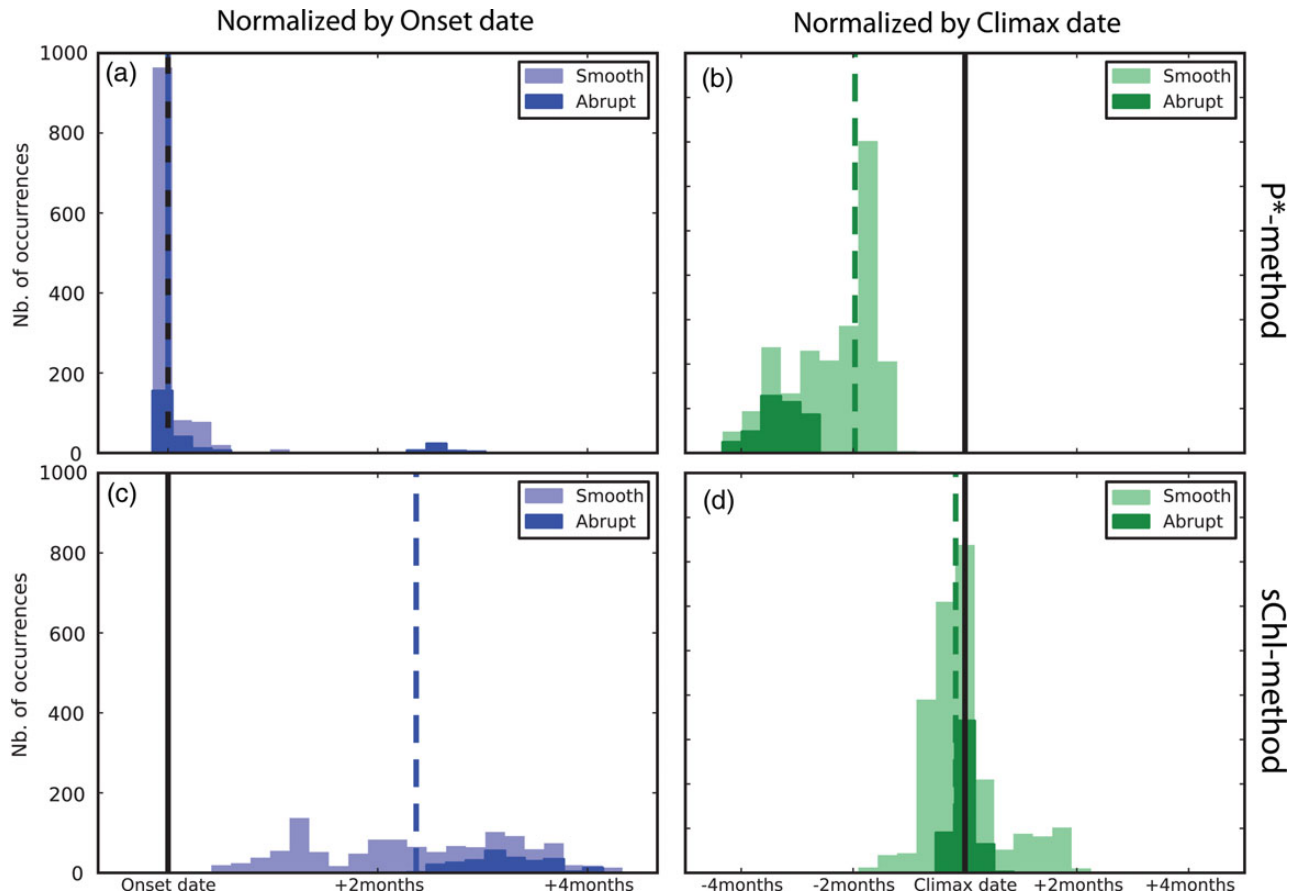


Figure 9. The histogram of the ensemble of modelled blooms representing: (a) bloom detection date using P^* -criterion normalized to the actual onset date, (b) bloom detection date using sChl-criterion normalized to the actual onset date, (c) bloom detection date using P^* -criterion normalized to the actual climax date, (d) bloom detection date using sChl-criterion normalized to the actual climax date. Median value is represented by a vertical dashed line. Abrupt blooms distribution are in dark colour and smooth blooms distribution in light colour.

(Figure 9b), in agreement with the typical time difference found between onset and climax (Figure 5a and c). On the other hand, the sChl-method detects dates that are only very weakly related to the actual onsets in our model scenarios (Figure 9c). Onset dates derived from this method are 1–4 months later than the actual onset, with a median value of ~ 2.5 months later. Interestingly, the dates detected by sChl-method are more closely related to the bloom climax (Figure 9d), with this bias even clearer for abrupt blooms (dark green on Figure 9d).

From these results, we conclude that, usually, the P^* -method is reliable on detecting the bloom onset while the sChl-method mainly detects the bloom climax.

Evaluating Sverdrup's bloom conditions from space

A significant part of the recent works that contributed to the bloom onset debate is based on ocean-colour data (Siegel, 2002; Behrenfeld, 2010; Chiswell, 2011). However, some authors have shown how bloom detection from ocean-colour data may be strongly influenced by the time-series data gaps (Cole *et al.*, 2012) and specially by the detection method applied (Ji *et al.*, 2010; Brody *et al.*, 2013). With the aim to evaluate at which point the choice on the detection method influence the validation or refusal of the Sverdrup (1953)'s hypothesis, here used model data to compare the dates of bloom detection with the bloom onset date predicted by the critical depth hypothesis (Figure 10). Such a comparison was done in a similar way as for bloom phases: normalizing the dates of detection by the date at which XLD reaches the critical depth (i.e. $XLD = Z_c$).

This comparison shown that the P^* -method detected dates 2–4.5 months before Sverdrup (1953)'s conditions were satisfied (median value ~ 3.6 months before; Figure 10a). Similarly, close to 95% of the dates associated with sChl-method were before XLD became shallower than Z_c . However, for abrupt blooms, the dates detected by the sChl-method were well distributed around the $XLD = Z_c$ date (Figure 10b, black bars).

Discussion

During the last 20 years, many studies based on SO bloom dynamics have been conducted. Most of them rely on satellite ocean-colour observations (Moore *et al.*, 1999; Venables *et al.*, 2007; Fauchereau *et al.*, 2011) except specific locations where mooring observations have been sampled (Jeandel *et al.*, 1998; Abbott *et al.*, 2000; Weeding and Trull, 2013), occasional oceanographic surveys (Boyd *et al.*, 2000; Pollard *et al.*, 2007; Blain *et al.*, 2007), and recent datasets obtained by elephant seals equipped with CTD and fluorescence sensors (Blain *et al.*, 2013). While *in situ* observations usually offer water column measurements, they are limited to specific regions and last for only a few weeks/months. In contrast, satellite-based chlorophyll data provide substantial spatial and temporal coverage. However, they are limited to interpret bloom dynamics solely based on its surface imprint.

Satellite-based analysis of high-latitude bloom onset often relate the increase of surface chlorophyll to the stratification of the mixed layer in spring. From this temporal correlation, authors conclude that alleviation of light limitation in the surface ocean layer is the main bloom trigger (Nelson and Smith, 1991; Siegel, 2002). Such results are based on the seminal concepts of Gran and Braarud (1935) and Riley (1942) and theoretically supported by Sverdrup's hypothesis (Sverdrup, 1953). More recently, combined analyses of satellite and model data identified onset based on its "strict" definition: the date at which integrated gains overcome losses (Behrenfeld, 2010). In this case, onset is systematically found in

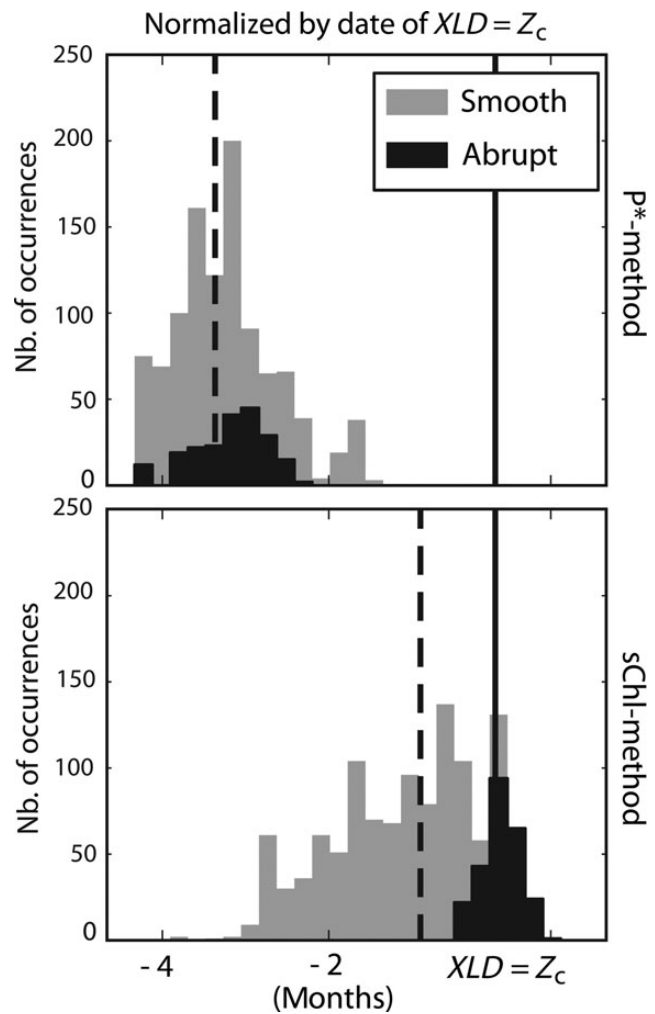


Figure 10. The histogram of the ensemble of modelled blooms representing: (a) bloom detection date using P^* -criterion normalized by the date at which Sverdrup's conditions are satisfied, (b) bloom detection date using sChl-criterion normalized by the date at which Sverdrup's conditions are satisfied. Median value is represented by a vertical dashed line. Abrupt blooms distribution are in dark colour and smooth blooms distribution in light colour.

winter presumably caused by a fast decrease on grazing pressure during MLD deepening. This apparent inconsistency between the two results is subject to much debate (Chiswell, 2011; Behrenfeld and Boss, 2013; Ferrari *et al.*, 2014).

Our results shed light on the current debate by describing the bloom as a sequence of three distinct phases: an onset, a climax, and an apex. While a "strict" onset definition is consistent with a winter onset (in agreement with Behrenfeld, 2010; Behrenfeld *et al.*, 2013) the surface spring bloom is associated with the climax of the integrated bloom, which is the rapid accumulation occurring after the winter onset.

One advantage of using a model approach is that it allows us to investigate the mechanisms that drive each of the bloom phases. Interestingly, two possible winter bloom triggers have been identified: grazer-prey dilution and winter net growth (Figure 6). In addition, we find that dilution is only efficient when the destratification of the mixing layer is not too fast. When destratification is rapid, grazers are diluted, but the phytoplankton growth is reduced even

more strongly due to light limitation. In such cases, the winter onset is delayed to later in the season, when light conditions improve following the winter solstice. Furthermore, the climax phase is clearly bottom-up controlled and is the only phase of the bloom for which we identified a significant role of iron (enhancing the speed at which phytoplankton accumulates). Finally, the date at which net accumulation stops (i.e. the apex) is strongly top-down controlled (Figure 8). The complete recoupling and the thereafter re-adjustment is influenced by many complex biogeochemical processes involving remineralization, aggregation of particles or virus infection (Boyd *et al.*, 2012). We want to stress here that any given model, even if containing a significant level of complexity, would be suspect in the representation of these processes, which are still poorly understood. This is particularly true in the SO, where the complex cycle of iron is involved.

To complement the idealized study on the bloom dynamics and with the aim to evaluate our conclusions in satellite-based studies, we showed that it is possible to differentiate onset and climax phases using two different bloom detection methods (Figure 9a and b). In Sallée *et al.* (2015), these two detection methods have been used to estimate onset and climaxes dates from ocean-colour data in the SO. However, it must be noted here that (as discussed in Chiswell, 2013; Sallée *et al.*, 2015) the method proposed to detect the onset ($P^* = MLD \times sP$, Behrenfeld, 2010) can only be successfully applied during winter destratification if three conditions are satisfied: ocean-colour satellite data are available in winter, the timing and magnitude of *MLD* can be accurately estimated, and the *MLD* is actively mixed (i.e. $MLD \approx XLD$).

In the final part of this paper, we investigated at which point bloom detection methods agree with critical depth hypothesis. To do so, we computed the critical depth (Z_c) using model outputs and we compared the date at which *XLD* crosses Z_c to the dates of bloom detection. Our results showed that Sverdrup (1953)'s blooming conditions coincided well with the dates detected by sChl-method for the case of abrupt blooms (Figure 10b), and hence with the climax phase (which was proven to be mainly top-down driven; Figure 7). Altogether, our results suggest that the top-down mechanisms identified by Gran and Braarud (1935), Riley (1942), and Sverdrup (1953) are not indicative of the bloom onset, but they are still crucial to bloom dynamics as they presumably control the climax phase. We therefore suggest that much of the debate regarding winter vs. spring onset mostly results from confusions on the definition of the word "onset". It must be emphasized to note that what originally made blooms such an attractive phenomenon was "the sudden appearance of an enormous numbers of diatoms in early spring" (Bigelow, 1926). Therefore, in our opinion, the key phase of the bloom is arguably the climax, not the onset. Indeed, it is the bloom climax (and its associated surface signal) what actually defines the observed spatial heterogeneity of SO blooms (Thomalla *et al.*, 2011). We conclude then that the observed differences on spatial distribution of surface spring blooms between the North Atlantic and the SO regions are indicative of differences on the factors that control the climax phase; i.e. the *XLD* dynamics in spring and the nutrient limitation (iron for the SO). This conclusion is coherent with the fact that these two factors, and specially the coupling between them, present unique characteristics in the SO (Tagliabue *et al.*, 2014).

Our results and conclusions are based on an idealized model where strong assumptions were applied to minimize the degrees

of freedom and ease results interpretation. These simplifications and assumptions must be taken into account when interpreting the results. First of all, the seasonal cycle is modelled in a 1D water column where lateral advection is not considered. Even if this may have important consequences on nutrients/iron transport, our approach is supported by recent works on iron supply in the SO (Tagliabue *et al.*, 2011, 2014). Second, in our model vertical mixing is assumed to be very strong and homogeneous from the surface to a depth level (*XLD*) and very low below. This highly turbulent mixing layer is a reasonable assumption for the SO where winds are generally strong and sustain efficient turbulent vertical mixing. However, we did not address the sources of vertical mixing and the possible sub-seasonal variations in mixing. We note here that in the present study we analysed bloom in relation to the mixing layer depth (*XLD*) which is not necessarily the same as the mixed-layer depth. While Sverdrup (1953) referred to the seasonal thermocline (classically associated to the mixed layer), recent studies have focused the interest on the upper-layer mixing (based on the critical turbulence hypothesis of Huisman *et al.*, 1999) and the mechanisms able to reduce it: positive heat fluxes (Taylor and Ferrari, 2011; Ferrari *et al.*, 2014), wind reduction (Chiswell, 2011), or sub-mesoscale eddies (Lévy *et al.*, 2001; Mahadevan *et al.*, 2012). In our study, we avoided such controversy by imposing a very strong mixed upper-layer with no sub-seasonal variability. In the real ocean (and especially in the SO), the phytoplankton activity (and therefore, the bloom dynamics) is highly affected by atmospheric and oceanic physical events ranging from synoptic (Waniek, 2003) to sub-mesoscale (Swart *et al.*, 2014) scales and from day to week. Such events are arguably an important source of variability when addressing the phytoplankton seasonal cycle with ocean-colour satellite data.

The idealized seasonal cycle of *XLD* used in this study is based on Argo observations and present three main phases during the seasonal cycle: a deepening phase (autumn–winter), a quicker shallowing phase (spring) and a transition phase (in summer) between the shallowing and the deepening. This transition phase present stable or slightly decreasing *MLD* (Sallée *et al.*, 2010; Figure 1c). However, the evolution of *XLD* throughout the seasonal cycle is actually more complex in the SO (e.g. Swart *et al.*, 2014), with short (i.e. sub-seasonal) and rapid (days to weeks) deepening/shallowing events. Such events are likely to influence the integrated accumulation of phytoplankton and the dates at which the onset, climax, and apex are reached. Among the three phases, the climax is by far the most sensitive to rapid changes on stratification (Figure 7). On the other hand, our results suggest that sub-seasonal *XLD* variability may weakly affect the onset and apex dates. The reason is that onset and apex controls (grazers dilution or low net growth for the former, and grazing pressure for the latter) are mainly related to the phytozooplankton coupling which is much less sensitive to rapid (\sim day) changes in mixing depth.

Finally, it must be emphasized to point out that in our set of experiments the limiting nutrient was always dissolved iron while it is known that in Fe-rich water of the SO, diatoms can also be limited by silicic acid (Boyd and Ellwood, 2010). We therefore note that our results should not be extrapolated to any other location or SO regions where main iron supply is not winter mixing (in the lee of Island and shallow plateaus), where silicic acid is a limiting factor, nor to higher latitudes ($>70^\circ\text{S}$) where the role of light and ice seasonal cycle can be critical on the phytoplankton bloom phenology.

Conclusions

Implementing an ensemble of >1200 idealized physical scenarios for an isolated water column, a complex biogeochemical model has been forced with the aim to reproduce the plankton seasonal cycle for a collection of open waters/ice-free SO spots. Daily frequency model outputs covering a large spectra of the variables involved in the phytoplanktonic bloom allowed us to target the question of bloom formation mechanisms from different focus.

Three crucial stages of bloom seasonal evolution have been defined: onset, climax, and apex date. All onsets occurred in winter and a large majority (~80%) of the climax, in spring. For the onset, upper-layer mixing (or *XLD*) appeared as a key component on tilting the system to be bottom-up or top-down controlled. For climax, the amount of Fe (and thus the relative depth between mixing layer and ferricline) seemed to play a secondary but significant role on the intensity of accumulation. Concerning apex, permanent top-down control was identified.

Two bloom detection criteria were tested using model surface chlorophyll and mixed-layer integrated biomass estimated from surface values. The biomass-based method appeared as a good proxy for detecting bloom onset while the method based on surface chlorophyll was reliable on detecting the climax. Finally, we compared the date at which *XLD* crosses the critical depth with the dates of bloom detection by the biomass- and the sChl-based methods. Sverdrup (1953)'s blooming conditions fairly coincided with the dates of detection using the sChl-method, and therefore with the bloom climax.

Our results suggest the existence of bottom-up as well as top-down drivers of the different phases of the blooms. It also enlightens the apparent controversy between onset/surface bloom detection and it shows that how different criteria can be used to answer different questions.

Acknowledgements

The authors thank J. LeSommer and L. Bopp for their suggestions, comments, and discussions at several stages of this study. We are grateful to A. Albert, C. Ethé, S. Ayata, and O. Aumont for their invaluable help on the technical aspects and setting up of model configuration. This study was possible thanks to the research staff exchange SOCCLI program (FP7-PEOPLE-2012-IRSES). We also thank the two anonymous reviewers for their comments that improved the final manuscript.

References

Abbott, M. R., Richman, J. G., Letelier, R. M., and Bartlett, J. S. 2000. The spring bloom in the Antarctic polar frontal zone as observed from a mesoscale array of bio-optical sensors. *Deep Sea Research Part II: Topical Studies in Oceanography*, 47: 3285–3314.

Arrigo, K. R., van Dijken, G. L., and Bushinsky, S. 2008. Primary production in the southern ocean, 1997–2006. *Journal of Geophysical Research*, 113: C38004.

Aumont, O., and Bopp, L. 2006. Globalizing results from ocean in situ iron fertilization studies. *Global Biogeochemical Cycles*, 20: GB2017.

Banase, K. 1994. Grazing and zooplankton production as key controls of phytoplankton production in the open ocean. *Oceanography*, 7: 13–20.

Behrenfeld, M. J. 2010. Abandoning Sverdrup's critical depth hypothesis on phytoplankton blooms. *Ecology*, 91: 977–989.

Behrenfeld, M. J., and Boss, E. S. 2013. Resurrecting the ecological underpinnings of ocean plankton blooms. *Annual Review of Marine Science*, 6:167–194.

Behrenfeld, M. J., Doney, S. C., Lima, I., Boss, E. S., and Siegel, D. A. 2013. Annual cycles of ecological disturbance and recovery underlying the subarctic Atlantic spring plankton bloom. *Global Biogeochemical Cycles*, 27: 526–540.

Bigelow, H. B. 1926. Plankton of the offshore waters of the Gulf of Maine. US Government Printing Office, 40: 1–509.

Blain, S., Quéguiner, B., Armand, L., Belviso, S., Bombled, B., Bopp, L., Bowie, A., *et al.* 2007. Effect of natural iron fertilization on carbon sequestration in the southern ocean. *Nature*, 446: 1070–1074.

Blain, S., Sophie, R., Xiaogang, X., Hervé, C., and Christophe, G. 2013. Instrumented elephant seals reveal the seasonality in chlorophyll and light-mixing regime in the iron fertilized southern ocean. *Chlorophyll and light in Southern Ocean*. *Geophysical Research Letters*, 40: 6368–6372.

Boss, E., and Behrenfeld, M. 2010. In situ evaluation of the initiation of the North Atlantic phytoplankton bloom. *Geophysical Research Letters*, 37: L18603.

Boyd, P., Watson, A., Law, C., Abraham, E., Trull, T., Murdoch, R., Bakker, D., *et al.* 2000. A mesoscale phytoplankton bloom in the polar southern ocean stimulated by iron fertilization. *Nature*, 407: 695–702.

Boyd, P. W., and Ellwood, M. J. 2010. The biogeochemical cycle of iron in the ocean. *Nature Geoscience*, 3: 675–682.

Boyd, P. W., Strzepek, R., Chiswell, S., Chang, H., DeBruyn, J. M., Ellwood, M., Keenan, S., *et al.* 2012. Microbial control of diatom bloom dynamics in the open ocean. *Geophysical Research Letters*, 39: L18601.

Broderau, L., Treguier, A. M., Penduff, T., and Gulev, S. 2008. An ERA40-based atmospheric forcing for global ocean circulation models. *Ocean Modelling*, 31: 88–104.

Brody, S. R., Lozier, M. S., and Dunne, J. P. 2013. A comparison of methods to determine phytoplankton bloom initiation. *Journal of Geophysical Research: Oceans*, 118: 2345–2357.

Buitenhuis, E. T., and Geider, R. J. 2010. A model of phytoplankton acclimation to iron-light colimitation. *Limnology and Oceanography*, 55: 714–724.

Chiswell, S. 2011. Annual cycles and spring blooms in phytoplankton: don't abandon Sverdrup completely. *Marine Ecology Progress Series*, 443: 39–50.

Chiswell, S. M. 2013. Comment on “annual cycles of ecological disturbance and recovery underlying the subarctic atlantic spring plankton bloom”. *Global Biogeochemical Cycles*, 27: 1291–1293.

Cole, H., Henson, S., Martin, A., and Yool, A. 2012. Mind the gap: the impact of missing data on the calculation of phytoplankton phenology metrics. *American Geophysical Union*, 117: C08030.

Droop, M. R. 1983. 25 years of algal growth kinetics a personal view. *Botanica Marina*, 26: 99–112.

Eppley, R. W. 1972. Temperature and phytoplankton growth in the sea. *Fish Bulletin*, 4: 1063–1085.

Evans, G. T., and Parslow, J. S. 1985. A model of annual plankton cycles. *Biological Oceanography*, 3: 327–347.

Fauchereau, N., Tagliabue, A., Bopp, L., and Monteiro, P. M. S. 2011. The response of phytoplankton biomass to transient mixing events in the southern ocean. *Geophysical Research Letters*, 38: L17601.

Ferrari, R., Merrifield, S. T., and Taylor, J. R. 2014. Shutdown of convection triggers increase of surface chlorophyll. *Journal of Marine Systems*, 0924-7963. <http://www.sciencedirect.com/science/article/pii/S0924796314000384> (last accessed 6 April 2015).

Franks, J. S. 2015. Has Sverdrup's critical depth hypothesis been tested? Mixed layers vs. turbulent layers. *ICES Journal of Marine Science*, 72: 1897–1907.

Gran, H. H., and Braarud, T. 1935. A quantitative study of the phytoplankton in the Bay of Fundy and the Gulf of Maine (including observations on hydrography, chemistry and turbidity). *Journal of the Biological Board of Canada*, 1: 279–467.

Huisman, J., van Oostveen, P., and Weissing, F. J. 1999. Critical depth and critical turbulence: two different mechanisms for the

- development of phytoplankton blooms. *Limnology and Oceanography*, 7: doi:10.4319/lo.1999.44.7.1781.
- Jeandel, C., Ruiz-Pino, D., Gjata, E., Poisson, A., Brunet, C., Charriaud, E., Dehairs, F., *et al.* 1998. KERFIX, a time-series station in the southern ocean: a presentation. *Journal of Marine Systems*, 17: 555–569.
- Ji, R., Edwards, M., Mackas, D. L., Runge, J. A., and Thomas, A. C. 2010. Marine plankton phenology and life history in a changing climate: current research and future directions. *Journal of Plankton Research*, 32: 1355–1368.
- Lozier, M. S., Dave, A. C., Palter, J. B., Gerber, L. M., and Barber, R. T. 2011. On the relationship between stratification and primary productivity in the North Atlantic. *Geophysical Research Letters*, 38: L18609.
- Lévy, M. 2015. Exploration of the critical depth hypothesis with a simple NPZ model. *ICES Journal of Marine Science*, 72: 1916–1925.
- Lévy, M., Klein, P., and Treguier, A. M. 2001. Impact of sub-mesoscale physics on production and subduction of phytoplankton in an oligotrophic regime. *Journal of Marine Research*, 59: 535–565.
- Lévy, M., Lehahn, Y., André, J. M., Mémery, L., Loisel, H., and Heifetz, E. 2005. Production regimes in the northeast Atlantic: a study based on sea-viewing wide field-of-view sensor (SeaWiFS) chlorophyll and ocean general circulation model mixed layer depth. *Journal of Geophysical Research*, 110: 1978–2012, C07S10.
- Mahadevan, A., D'Asaro, E., Lee, C., and Perry, M. J. 2012. Eddy-driven stratification initiates north Atlantic spring phytoplankton blooms. *Science*, 337: 54–58.
- Marra, J., and Barber, R. T. 2004. Phytoplankton and heterotrophic respiration in the surface layer of the ocean. *Geophysical Research Letters*, 31: L09314.1–L09314.4.
- Martin, J. H., Fitzwater, S. E., and Gordon, R. M. 1990. Iron deficiency limits phytoplankton growth in Antarctic waters. *Global Biogeochemical Cycles*, 4: 5–12.
- McCarthy, J. J. 1980. The kinetics of nutrient utilization. In *Physiological Bases of Phytoplankton Ecology*. Ed. by T. Piatt. Canadian Bulletin of Fisheries and Aquatic Sciences, 210: 211–233.
- Moore, J. K., and Abbott, M. R. 2000. Phytoplankton chlorophyll distributions and primary production in the southern ocean. *Journal of Geophysical Research*, 105: 28–709.
- Moore, J. K., Abbott, M. R., Richman, J. G., Smith, W. O., Cowles, T. J., Coale, K. H., Gardner, W. D., *et al.* 1999. SeaWiFS satellite ocean color data from the southern ocean. *Geophysical Research Letters*, 26: 1465–1468.
- Nelson, D. M., and Smith, W. O. 1991. Sverdrup revisited: critical depths, maximum chlorophyll levels, and the control of southern ocean productivity by the irradiance-mixing regime. *Limnology and Oceanography*, 36: 1650–1661.
- Pollard, R., Sanders, R., Lucas, M., and Statham, P. 2007. The Crozet natural iron bloom and export experiment (CROZEX). *Deep Sea Research Part II: Topical Studies in Oceanography*, 54: 1905–1914.
- Riley, G. 1942. The relationship of vertical turbulence and spring diatom flowerings. *Journal of Marine Research*, 5.1: 67–87.
- Sallée, J. B., Llorc, J., Tagliabue, A., and Lévy, M. 2015. Characterisation of distinct bloom phenology regimes in the Southern Ocean. *ICES Journal of Marine Science*, 72: 1985–1998.
- Sallée, J. B., Speer, K., Rintoul, S., and Wijffels, S. 2010. Zonally asymmetric response of the Southern Ocean mixed-layer depth to the Southern Annular Mode. *Nature Geoscience*, 3: 273–279.
- Siegel, D. A. 2002. The North Atlantic spring phytoplankton bloom and Sverdrup's critical depth hypothesis. *Science*, 296: 730–733.
- Sverdrup, H. U. 1953. On conditions for the vernal blooming of phytoplankton. *Journal du Conseil*, 18: 287–295.
- Swart, S., Thomalla, S. J., and Monteiro, P. M. S. 2014. The seasonal cycle of mixed layer dynamics and phytoplankton biomass in the sub-Antarctic zone: a high-resolution glider experiment. *Journal of Marine Systems*, doi:10.1016/j.jmarsys.2014.06.002.
- Tagliabue, A., Mtshali, T., Aumont, O., Bowie, A. R., Klunder, M. B., Roychoudhury, A. N., and Swart, S. 2011. A global compilation of over 13 000 dissolved iron measurements: focus on distributions and processes in the southern ocean. *Biogeosciences Discussions*, 8: 11489–11527.
- Tagliabue, A., Sallée, J. B., Bowie, A. R., Lévy, M., Swart, S., and Boyd, P. 2014. Surface-water iron supplies in the southern ocean sustained by deep winter mixing. *Nature Geoscience*, 7: 314–320.
- Taylor, J. R., and Ferrari, R. 2011. Shutdown of turbulent convection as a new criterion for the onset of spring phytoplankton blooms. *Limnology and Oceanography*, 56: 2293–2307.
- Thomalla, S. J., Fauchereau, N., Swart, S., and Monteiro, P. M. S. 2011. Regional scale characteristics of the seasonal cycle of chlorophyll in the southern ocean. *Biogeosciences*, 8: 2849–2866.
- Venables, H., Pollard, R., and Popova, E. 2007. Physical conditions controlling the development of a regular phytoplankton bloom north of the crozet plateau, southern ocean. *Deep Sea Research Part II: Topical Studies in Oceanography*, 54: 1949–1965.
- Waniek, J. J. 2003. The role of physical forcing in initiation of spring blooms in the northeast Atlantic. *Journal of Marine Systems*, doi:10.1016/S0924-7963(02)00248-8.
- Weeding, B., and Trull, T. W. 2013. Hourly oxygen and total gas tension measurements at the southern ocean time series site reveal winter ventilation and spring net community production. *Journal of Geophysical Research: Oceans*, 119: 348–358.
- White, M. A., de Beurs, K. M., Didan, K., Inouye, D. W., Richardson, A., Jensen, O. P., O'Keefe, J., *et al.* 2009. Intercomparison, interpretation, and assessment of spring phenology in North America estimated from remote sensing for 1982–2006. *Global Change Biology*, 15.10: 2335–2359.
- Yoshie, N., Yamanaka, Y., Kishi, M. J., and Saito, H. 2003. One dimensional ecosystem model simulation of the effects of vertical dilution by the winter mixing on the spring diatom bloom. *Journal of Oceanography*, 59.5: 563–571.

Handling editor: Rubao Ji



Contribution to the Themed Section: 'Revisiting Sverdrup's Critical Depth Hypothesis' Original Article

Characterization of distinct bloom phenology regimes in the Southern Ocean

Jean-Baptiste Sallée^{1,2*}, J. Llorc¹, A. Tagliabue³, and M. Lévy¹

¹Sorbonne Universités (UPMC Univ.), UMR 7159, LOCEAN-IPSL Institute, F-75005 Paris, France

²British Antarctic Survey, High Cross, Madingley Road, Cambridge CB30ET, UK

³Department of Earth, Ocean and Ecological Sciences, School of Environmental Sciences, University of Liverpool, Liverpool, UK

*Corresponding author: e-mail: jbsallee@gmail.com

Sallée, J-B., Llorc, J., Tagliabue, A., and Lévy, M. Characterization of distinct bloom phenology regimes in the Southern Ocean. – ICES Journal of Marine Science, 72: 1985–1998.

Received 17 September 2014; accepted 31 March 2015; advance access publication 14 June 2015.

In this study, we document the regional variations of bloom phenology in the Southern Ocean, based on a 13-year product of ocean colour measurements co-located with observation-based estimates of the mixed-layer depth. One key aspect of our work is to discriminate between mixed-layer integrated blooms and surface blooms. By segregating blooms that occur before or after the winter solstice and blooms where integrated and surface biomass increase together or display a lag, we define three dominating Southern Ocean bloom regimes. While the regime definitions are solely based on bloom timing characteristics, the three regimes organize coherently in geographical space, and are associated with distinct dynamical regions of the Southern Ocean: the subtropics, the subantarctic, and the Antarctic Circumpolar Current region. All regimes have their mixed-layer integrated onset between autumn and winter, when the daylength is short and the mixed layer actively mixes and deepens. We discuss how these autumn–winter bloom onsets are controlled by either nutrient entrainment and/or reduction in prey-grazer encounter rate. In addition to the autumn–winter biomass increase, the subantarctic regime has a significant spring biomass growth associated with the shutdown of turbulence when air–sea heat flux switches from surface cooling to surface warming.

Keywords: bloom, chlorophyll, seasonal cycle, Southern Ocean.

Introduction

Satellite observations and studies based on *in situ* observations have shown that phytoplankton distribution in the Southern Ocean displays patchy regional variability (Figure 1a) and a wide range of distinct seasonal cycle regimes (e.g. Moore and Abbott, 2002; Arrigo *et al.*, 2008; Thomalla *et al.*, 2011; Chiswell *et al.*, 2013; Frants *et al.*, 2013; Carranza and Gille, 2015). While phytoplankton biomass and the associated primary productivity fluctuate according to season (e.g. Arrigo *et al.*, 2008) and location, the environmental conditions that drive these patterns are poorly understood. This hampers our ability to constrain how seasonality might be modified in the future (e.g. Henson *et al.*, 2013) and the associated implications for Southern Ocean foodwebs and biogeochemical cycling.

A unique aspect of the Southern Ocean circulation is the presence of a strong eastward, circumpolar current, the Antarctic Circumpolar

Current (ACC). On the northern edge of the ACC, subtropical gyres flow anticlockwise, and their intense and energetic western boundary currents join the northern branches of the ACC in the western Atlantic, Indian, and Pacific basins. The ACC and the western boundary currents have a profound influence on the physical and biogeochemical characteristics of the Southern Ocean (Rintoul *et al.*, 2001). They form meridional dynamical barriers (Sallée *et al.*, 2008), which split the Southern Ocean into a number of distinct zones. Four main zones can be described, from north to south: the subtropical region, around 30°S, characterized by stratified surface layers (Figure 1c), and relatively weak wind and buoyancy forcing; the subantarctic region, directly north of the ACC, which is characterized by very deep mixed layers (Figure 1c), intense winds, large buoyancy forcing, and the presence of the energetic western boundary currents; the ACC region, characterized by the top-to-bottom and large circumpolar

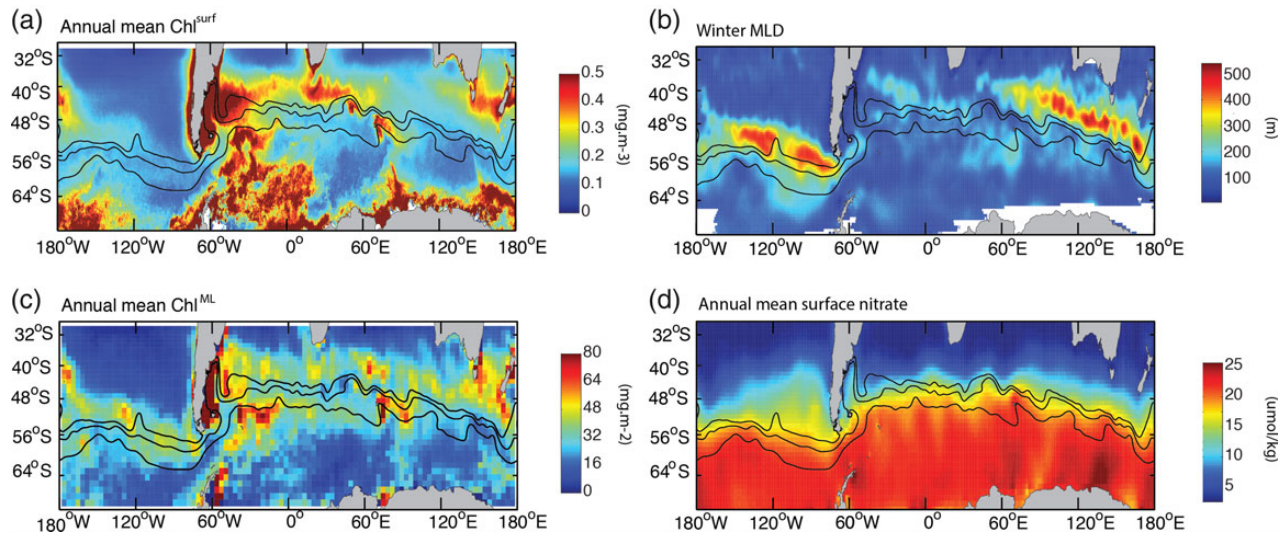


Figure 1. Climatological (a) annual mean of surface chlorophyll (Chl^{surf} ; mg m^{-3}); (b) winter (September) MLD from estimated from the observational dataset; (c) annual mean mixed-layer integrated chlorophyll (Chl^{ML} ; mg m^{-2}); and (d) annual mean surface nutrient concentration ($\mu\text{mol kg}^{-1}$) from the World Ocean Atlas 2009. In (a–d), the three black lines represent the approximate climatological position of the three main ACC branches, from south to north: Polar Front, subantarctic front, and northern branch of the subantarctic front following Sallée et al. (2008).

current; and the subpolar region, south of the ACC, characterized by the seasonal presence of sea ice, and a relatively stratified surface layer.

These dynamical zones of the Southern Ocean correspond to specific biogeochemical regions (e.g. Longhurst et al., 1995). The surface layers of the subtropical region have low macronutrient concentrations (Figure 1d), the subantarctic, ACC, and subpolar regions are generally considered as macronutrient rich, iron-limited regions (e.g. Martin et al., 1990; Boyd, 2002), although silicic acid is notably much lower in the subantarctic region than the ACC (e.g. Sarmiento et al., 2004). Another notable aspect of the subantarctic zone is that it contains many continental sources of iron (Boyd and Ellwood, 2010), with the presence of continental plateau and many subantarctic islands, in the lee of the western boundary currents flowing eastward.

At present, it is not clear how the specific dynamical and biogeochemical regions of the Southern Ocean relate to the patchy phytoplankton distribution in the Southern Ocean (Figure 1; e.g. Thomalla et al., 2011; Chiswell et al., 2013).

The aim of this study is to use a range of physical and biochemical observational products to document the general chlorophyll bloom patterns in the Southern Ocean, and link these patterns to the distinct dynamical and biogeochemical regions of the Southern Ocean. Our aim of describing regional variability of the Southern Ocean phytoplankton seasonal cycle falls within the more general context of the mechanisms associated with the onset and duration of phytoplankton blooms. These mechanisms remain much debated despite decades of research (e.g. Sverdrup, 1953; Ryther and Hulbert, 1960; Evans and Parslow, 1985; Townsend et al., 1992; Huisman et al., 1999; Behrenfeld, 2010; Taylor and Ferrari, 2011a, b; Mahadevan et al., 2012; Ferrari et al., 2014). This debate arises from the wide diversity, and often inter-related, factors that control phytoplankton blooms, which range from physical (e.g. solar irradiance and the intensity of surface layer mixing), biological

(e.g. growth or grazing rates), to chemical (e.g. availability or cycling of nutrients) factors.

The founding conceptual model of bloom dynamics, which arose in the first half of the last century, is the “critical depth” theory (Gran and Braarud, 1935; Riley, 1946; Sverdrup, 1953), which proposes that blooms should commence when the ocean surface mixed-layer restratifies in spring. Recently, the extent to which the mixed-layer depth (MLD) shallowing explains phytoplankton blooms has been questioned (e.g. Behrenfeld, 2010; Taylor and Ferrari, 2011a, b; Chiswell et al., 2013). For instance, several authors have proposed that surface layer turbulence (primarily driven by wind and air–sea buoyancy flux) is one of the key factors for bloom onset (e.g. Huisman et al., 1999; Taylor and Ferrari, 2011a, b; Chiswell et al., 2013). Other works have proposed that blooms do not occur in spring, but instead in autumn or early winter, which seems to invalidate the basis of the critical depth theory (Behrenfeld, 2010; Boss and Behrenfeld, 2010). Instead, a new framework, the “disturbance-recoupling” hypothesis, has been proposed, which focuses on the balance between phytoplankton growth and grazing (Behrenfeld, 2010). Finally, some of the confusion in our understanding of phytoplankton blooms might arise from whether blooms are examined from the standpoint of water-column integrated biomass, or from surface observations (Llort et al., 2015).

After presenting the datasets and methods in the Material and methods section, we introduce examples of chlorophyll seasonal cycle in the Southern Ocean. An important point in our study is that we seek to discriminate between water-column integrated chlorophyll and surface chlorophyll by co-locating surface chlorophyll observations with physical observations of the water column. One necessary assumption here is that chlorophyll is well mixed in the mixed layer and that subsurface chlorophyll are relatively uncommon or small compared with mixed-layer imprint. We demonstrate that Southern Ocean blooms can be grouped

into a number of distinct regimes based on their phenology. We then discuss the seasonal cycle of each of these regimes, before finishing with a discussion of our results.

Material and methods

Surface ocean colour product

Surface chlorophyll (Chl^{surf}) over the Southern Ocean is investigated in this study. We define the Southern Ocean as the region between the latitude 70 and 30°S. Although remote sensing of Southern Ocean chlorophyll concentrations is effective in detecting large-scale chlorophyll bloom regime, the current algorithms for the Sea-viewing Wide Field-of-view Sensor (SeaWiFS, algorithm OC4v6), the Moderate Resolution Imaging Spectroradiometer (MODIS-Aqua, algorithm OC3M), and GlobColour significantly underestimate chlorophyll concentrations at high latitudes (Johnson *et al.*, 2013). Therefore, in this study, we use a new algorithm, specifically designed for the Southern Ocean that more accurately matches long-term *in situ* datasets (Johnson *et al.*, 2013). The new algorithm improves *in situ* vs. satellite chlorophyll coefficients of determination (R2) from 0.27 to 0.46, 0.26 to 0.51, and 0.25 to 0.27, for OC4v6, OC3M, and GlobColour, respectively, while also addressing the underestimation problem. We also compared our results with the Globcolour dataset and found the definition of the regimes and their characteristics to be very similar, giving us confidence in the broad reliability of our results. However, the absolute magnitudes of blooms are affected, and as the Johnson *et al.* (2013) algorithm best matches observations, we decided to present results using this algorithm. Overall, surface chlorophyll concentrations are available at a weekly resolution, at 9 km resolution, between the years 1998 and 2010, when cloud coverage allows.

Ocean interior

To investigate the role of ocean physics in driving phytoplankton blooms, we co-located ocean temperature and salinity observations with the satellite-derived estimates of Chl^{surf} . To do this, we utilize two different ocean interior datasets, as described below.

First, defined as the “observational dataset”, we use *in situ* observations of temperature/salinity profiles from a combination of the Argo float database and the ship-based Southern Ocean Data Base (SODB; see <http://woceSOatlas.tamu.edu> for more information). The Argo project contributes about half of the Southern Ocean profiles, fills the centre of ocean basins, and provides complete sampling over the austral winter (Sallée *et al.*, 2010). We use only profiles that have passed the Argo real-time quality control, containing information on their position, date, pressure, temperature (T), and salinity (S). Most Argo profiles sample T and S from the surface to 2000 m depth every 10 days. From this database, we extract information regarding the MLD. The advantage of this approach is that it provides ocean observations at the time and location of the Chl^{surf} concentration estimate from satellite. However, as the satellite coverage is much greater than the *in situ* temperature/salinity coverage, this co-location procedure reduces the number of Chl^{surf} estimates available.

Second, defined as the “reanalysis dataset”, we use a statistical reanalysis of ocean observation: the EN3 product produced by the UK Met-Office (<http://www.metoffice.gov.uk/hadobs/en3/>). The EN3 product consists of objective analyses formed from ship and Argo profile data. It provides monthly analysed fields of full-depth temperature and salinity profiles on a 1° grid. While the data are

provided from 1950, we only used data from the year 2002 onward, when the objective analysis is constrained by Argo observations in the Southern Ocean. Although not independent (as EN3 assimilates Argo profiles), we compared mixed layer obtained from direct Argo profiles and from EN3 profiles. The comparison gives a correlation of 0.7, which gives us confidence that EN3 reanalysis is reasonable. We note that a careful evaluation of EN3 would involve re-running EN3 reanalysis, leaving some Argo profiles out, which is beyond the scope of this study.

MLD was extracted from individual profiles of the observational dataset and the reanalysis dataset. We calculated the MLD with a surface-density-difference criterion of $\Delta\sigma \leq 0.03 \text{ kg m}^{-3}$ (de Boyer Montégut *et al.*, 2004; Sallée *et al.*, 2006). Sallée *et al.* (2006) tested a number of methods and show that this particular criterion is well adapted to find the base of the seasonal mixed layer in the Southern Ocean.

Where possible, we used the “observational dataset” to estimate MLD. However, when the analysis required the full length of the seasonal cycle (e.g. to reproduce the seasonal cycle of the mixed-layer integrated chlorophyll, or to compute the initiation date of the mixed-layer integrated chlorophyll), the “reanalysis dataset” was used.

For collocating the observational and reanalysis datasets to satellite-derived estimates of Chl^{surf} , we associated each Argo profiles or EN3 pixel to the closest (in space and time) pixel of ocean colour (so the largest distance in time is 4 d, and the largest distance in space is 6 km).

Water-column integrated chlorophyll

Although no observations of water-column integrated chlorophyll exist at large scales, in this study, we quantify this via the combination of surface satellite estimates of Chl^{surf} and interior ocean structure. We assume that chlorophyll is well mixed above the mixed-layer base, and that there is no chlorophyll below the mixed-layer base. Under such assumptions, we quantify the water-column integrated chlorophyll, Chl^{ML} , as:

$$\text{Chl}^{\text{ML}} = H \times \text{Chl}^{\text{surf}}, \quad (1)$$

where H is the MLD. We note that our assumptions may be questioned in spring when the MLD rapidly shallows, as under such conditions, some chlorophyll may be left below the mixed-layer base (e.g. Chiswell *et al.*, 2013; Franks, 2015). One therefore needs to be cautious of the interpretation of Chl^{ML} in spring.

We note that we assume here that Chl^{surf} and Chl^{ML} have the same seasonal pattern as, respectively, the surface biomass content and the mixed-layer integrated biomass content. In the Discussion section, we discuss the extent to which this is true by attempting to compute the carbon concentration from Chl^{surf} , based on the chlorophyll-to-carbon ratio, $\text{Chl}:\text{C}$ (Cloern *et al.*, 1995; Behrenfeld *et al.*, 2002): $\text{Chl}:\text{C} = \text{Chl} : C_{\text{min}} + [\text{Chl} : C_{\text{max}} - \text{Chl} : C_{\text{min}}]e^{-3I_{\text{g}}}$, where I_{g} is the mixed-layer integrated irradiance (in moles photons $\text{m}^{-2} \text{h}^{-1}$; calculation of I_{g} is described below, and is computed from NCEP Climate Forcing System Reanalysis outputs; see the Atmospheric fluxes section), $\text{Chl} : C_{\text{min}} = 0.004 \text{ mgChl}(\text{mgC})^{-1}$, and $\text{Chl} : C_{\text{max}} = 0.013 \text{ mgChl}(\text{mgC})^{-1}$ (Behrenfeld, 2010). We show that Chl^{surf} and C have very similar seasonal pattern.

Onset detection method

In this section, we describe the onset detection method that we apply to both Chl^{ML} and Chl^{surf} time-series. Hereafter, Chl^{ML} -onset will

refer to the date of onset detected on the Chl^{ML} time-series, and Chl^{surf} -onset to the date of onset detected on the Chl^{surf} time-series.

An important challenge is to identify the date of the start of intensification of chlorophyll (either Chl^{ML} or Chl^{surf}) in a manner that can be efficiently and accurately applied to a large datasets. Phenology studies currently use several methods to estimate the timing of a phytoplankton bloom. Ji *et al.* (2010) identify three broad categories of methods (see also Brody *et al.*, 2013): threshold method based on biomass; threshold method based on cumulative chlorophyll content; and rate of change methods. Threshold methods based on chlorophyll biomass define bloom initiation as the time at which a given threshold is reached (e.g. Siegel *et al.*, 2002; Vargas *et al.*, 2009; Thomalla *et al.*, 2011; Cole *et al.*, 2012; Sapiano *et al.*, 2012). Threshold methods based on cumulative chlorophyll biomass identify a bloom as the time at which a cumulative summation of chlorophyll biomass crosses a threshold percentile of the total biomass (e.g. Greve *et al.*, 2005; Mackas *et al.*, 2012). Finally, the rate of change methods estimate bloom initiation from the point of most rapid increase on a chlorophyll time-series or function fit to that time-series (e.g. Rolinski *et al.*, 2007; White *et al.*, 2009).

Brody *et al.* (2013) investigated the differences between these bloom detection methods. Their conclusion was that the first group of methods (chlorophyll biomass threshold) can be strongly biased for specific time-series and are well suited to investigating the match or mismatch between phytoplankton and upper trophic levels. The second group of methods (cumulative chlorophyll biomass threshold) is also very sensitive to the date used for the start of the time-series and thus cannot be implemented at the basin scale using a globally fixed start date (Brody *et al.*, 2013). Finally, the third group of methods (rate of change) identifies blooms when chlorophyll is increasing rapidly from the pre-bloom minimum, while absolute biomass levels may still remain low. These methods can be useful in examining the seasonal physical or biological mechanisms that create conditions in which a bloom can occur (Brody *et al.*, 2013).

Based on the analysis of Brody *et al.* (2013), we chose to apply a rate of change method that we designed and tuned for our dataset. At each grid-point of the chlorophyll dataset, a 13-year time-series (1998–2010) is extracted and linearly interpolated, and a fast Fourier transform low-pass filter is applied to remove any high-frequency (<3 months) variability irrelevant to seasonal time-scale and bloom onset. The bloom onset of one particular year is defined as the maximum of the second derivative of Chl (Chl_{tt}) in the time window where the derivative of Chl (Chl_t) (i) is positive, and (ii) contains a local maximum (here Chl is either Chl^{ML} or Chl^{surf}). If the bloom peak is below 1.2 times the seasonal minimum of Chl, we do not consider a bloom to have occurred. Our definition ensures that each defined onset is robust and exists as a bloom in the dataset. Additional constraints are applied to avoid unrealistic bloom detection: (i) the largest data-gap within the 4 months centred on the defined onset must be smaller than 45 d; (ii) the integrated amount of chlorophyll accumulated within 6 months before the onset must be <25% of the total amount of chlorophyll summed over the year, centred on the time of onset.

The Chl^{surf} -onset detection procedure nicely positions the Chl^{surf} -onset date at the start of the high Chl^{surf} season (Figure 2). We note however that in some instances, the detected Chl^{surf} -onset seems to be a bit late (e.g. Figure 2a in 2006; Figure 2a in 2010) compare with other cases where Chl^{surf} -onset appears detected in the very early days of the increasing season (e.g.

Figure 2b in 2008). All automatic detection methods will have such caveats and errors associated with it (Cole *et al.*, 2012; Brody *et al.*, 2013). Cole *et al.* (2012) estimate the error on such automatic detection method to ~ 30 d in the Southern Ocean, which appears, by eyes, as a correct order of magnitude on the specific examples shown in Figure 2. We acknowledge that a definition “by eye” would produce in many instances a more robust definition of onset. However, our goal is to define an objective definition as robust as possible that can consistently treat more than 1 million seasonal cycles and investigate general basin-scale phenomena. We applied the same detection method on the Chl^{ML} time-series as an estimate of the bloom Chl^{ML} -onset date. Similar to the Chl^{surf} -onset date, we found the method reliable in detecting Chl^{ML} -onset as the starting date of the increased Chl^{ML} season (Figure 2).

Atmospheric fluxes

Atmospheric winds, buoyancy, and short-wave forcings are obtained from NCEP Climate Forcing System Reanalysis (<http://cfs.ncep.noaa.gov/cfsr/>). We used atmospheric fields from this reanalysis for the year 1998–2010, consistent with surface chlorophyll dataset time frame. The winds of the reanalysis product are strongly constrained by assimilation of satellite wind observation. However, we note that buoyancy flux fields remain poorly known in the Southern Ocean, and are only weakly constrained in atmospheric reanalysis efforts. These constraints are even weaker for freshwater fluxes. We therefore approximate the buoyancy flux to its heat component, which is less uncertain. Photosynthetically active radiation (PAR) relates to solar irradiance (I_t) following $\text{PAR} = 0.473 \times I_t$ (Papaioannou *et al.*, 1993). Mixed-layer integrated irradiance, I_g , is computed from downward short wave flux (in W m^{-2}):

$$I_g = \int_0^H I_0 e^{-kz} dz, \quad (2)$$

where I_0 is the downward short wave flux at sea surface, k the attenuation coefficient in the surface layer, and H the MLD. Attenuation coefficient depends on both water attenuation (k_w) and chlorophyll self-shading attenuation (k_{chl}). In this paper, we use $k_w = 0.02 \text{ m}^{-1}$ and $k_{\text{chl}} = 0.0865 \text{ m}^{-1}$ (e.g. Nelson and Smith, 1991).

Results

Southern Ocean bloom Chl^{ML} -onset and Chl^{surf} -onset dates are estimated by a systematic method on more than 1 million seasonal cycles based on satellite-derived surface Chl^{surf} co-located with estimates of MLD (see the Material and methods section). Two time-series of Chl^{ML} and Chl^{surf} , and associated Chl^{ML} -onset and Chl^{surf} -onset dates are presented in Figure 2. These examples are chosen to represent two distinct regimes of blooms: one where Chl^{ML} is in phase with Chl^{surf} (Figure 2a), and one where Chl^{ML} and Chl^{surf} are slightly out of phase (Figure 2b).

The two time-series present a very marked seasonal cycle, with Chl^{surf} increasing by 3–5 times during the high activity season. The surface bloom clearly stands out as the period during which Chl^{surf} dramatically increases. Surface and mixed-layer integrated chlorophyll blooms have been described as tightly linked to the seasonal cycle of the MLD (e.g. Sverdrup, 1953; Behrenfeld, 2010). We therefore compare chlorophyll time-series with the collocated mixed-layer time-series (from the reanalysis dataset; see the Material and Methods section). The phasing between the

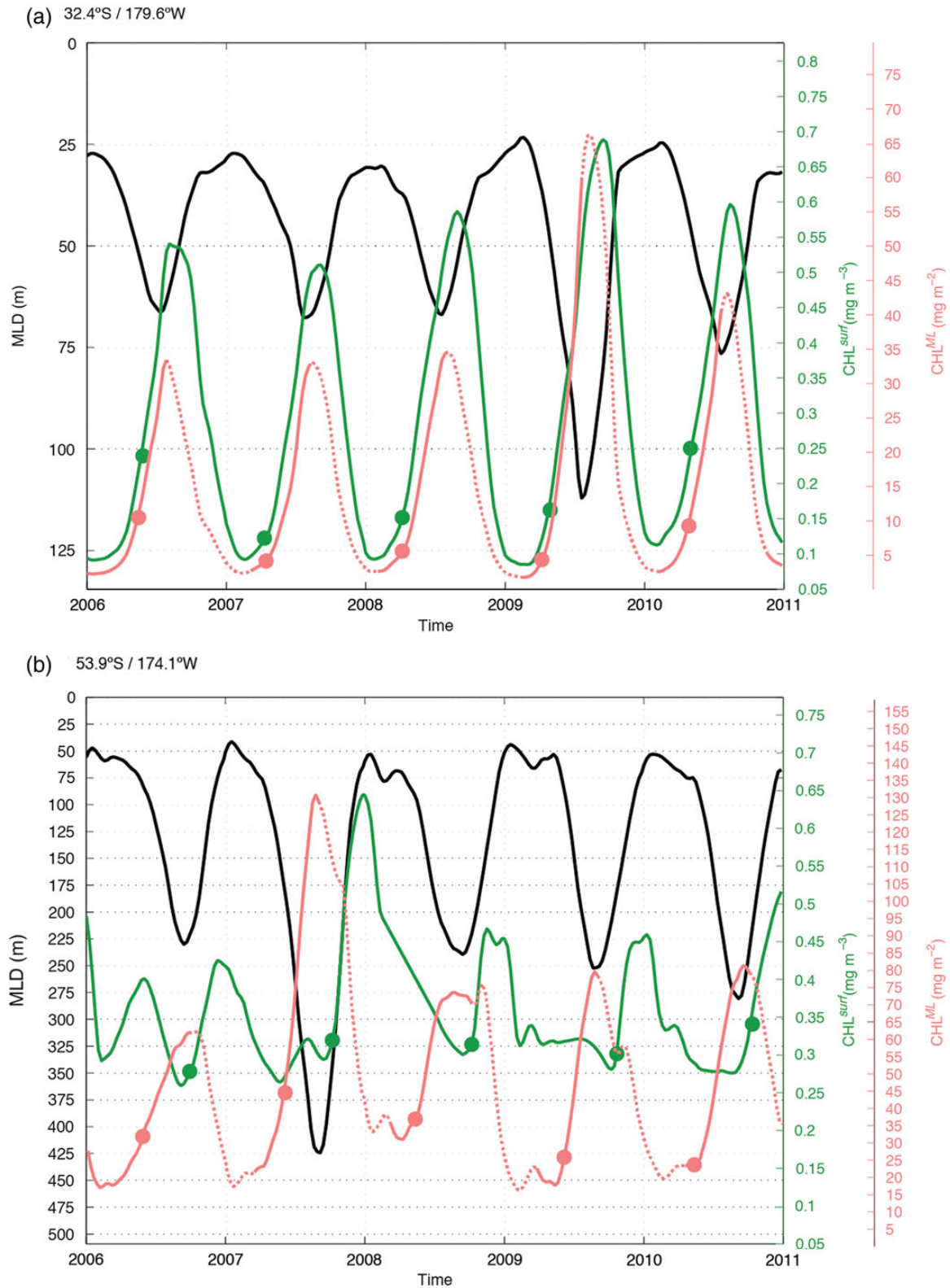


Figure 2. Two examples of time-series of (green) Chl_a in two distinct regions: (a) in a subtropical zone characterized by subtropical gyre circulation, at 32.4°S–179.6°W; and (b) in a subantarctic zone, influence by the ACC dynamics, at 53.9°S–174.1°W. Chl_a time-series is averaged over a region of 20×20 km centred on each location. For clarity, data are shown for 5 years, although the full time series are longer. Collocated (black) MLD and (pink) mixed-layer integrated chlorophyll time-series are superimposed on each panel. For each seasonal cycles at each location, green dots indicate the Chl^{surf} -onset date and pink dots the Chl^{ML} -onset date detected by our automatic procedure (see text for details). Chl^{ML} is shown as dashed line during the mixed-layer restratification phase to remind the reader that our estimate of Chl^{ML} is questionable during this period (see text for details).

mixed-layer and the chlorophyll seasonal cycles appears consistent for different years of a given location, but clearly varies depending on the location (Figure 2). For instance, in Figure 2a, the surface chlorophyll bloom is associated with a deepening of the mixed layer, while in Figure 2b, the surface bloom is associated with a shallowing of the mixed layer. These two strikingly different regimes recall the debate around autumn vs. spring blooms (Lévy *et al.*, 2005; Chiswell *et al.*, 2013).

In the two example of Figure 2, we find that Chl^{ML} -onset and Chl^{surf} -onset can either be almost instantaneous or separated by a few months. We note that Chl^{ML} -onset is, here, always found during the deepening phase of the mixed layer, i.e. when the mixed layer actively convects, and where the assumption of a well-mixed chlorophyll profile in the mixed layer is the most robust. In the following, we undertake a systematic analysis of bloom Chl^{ML} -onset and Chl^{surf} -onset on the entire dataset to define specific bloom regimes, and next, we describe the seasonal cycles associated with each of the regimes.

Southern Ocean regimes of surface bloom

Over the entire database of Southern Ocean, the Chl^{ML} -onset dates organize around two main modes (Figure 3a). One mode, centred on May, is associated with autumn blooms that have a Chl^{ML} -onset before the winter solstice (21 June); the other mode, centred on July, is associated with winter blooms that have a Chl^{ML} -onset after the winter solstice. The winter solstice is a key date in the year as it corresponds to the date where incoming irradiance switches from declining to increasing (note, however, that one may argue that chlorophyll cares about the mixed-layer integrated irradiance, which can be distinct to incoming irradiance). The modal structure in Chl^{ML} -onset date could possibly be due to an unstable detection method picking very early Chl^{ML} -onsets in some instances and late Chl^{ML} -onsets in others (for instance, Figure 2 suggests that some Chl^{ML} -onsets are detected slightly later than what we would have picked by eye). To test the “stability” or “sensitivity” of the Chl^{ML} -onset detection procedure, we investigate the amount of accumulated chlorophyll at Chl^{ML} -onset. The percentage of accumulated chlorophyll at Chl^{ML} -onset is consistent over the entire database, with a clear and unique mode centred on 12.6% (Figure 3c). This result gives us confidence that the Chl^{ML} -onset detection procedure is stable enough to investigate bloom regimes in the Southern Ocean.

We then turn to the time-lag between Chl^{ML} -onset and Chl^{surf} -onset over the entire database. Two very clear modes stand out, with a group of blooms being characterized by almost parallel Chl^{ML} -onset and Chl^{surf} -onset, and a second group characterized by a lag of several months between Chl^{surf} -onset and Chl^{ML} -onset (Figure 3b).

Based on these Chl^{ML} -onset and Chl^{surf} -onset histograms, we define four Southern Ocean regimes: (regime 1) blooms with Chl^{ML} -onset before the winter solstice, and nearly parallel Chl^{surf} -onset (within 2 months); (regime 2a) blooms with Chl^{ML} -onset before the winter solstice, and with a significant lag between Chl^{ML} -onset and Chl^{surf} -onset (>2 months); (regime 2b) bloom with Chl^{ML} -onset after the winter solstice, and with a long time-lag between Chl^{ML} -onset and Chl^{surf} -onset (more than 2 months); and (regime 3) blooms with Chl^{ML} -onset after the winter solstice, and nearly parallel Chl^{surf} -onset (within 2 months). Ultimately, we seek to segregate blooms that occur before or after the winter solstice and blooms where integrated and surface biomass increase together or display a lag. For simplicity, in the remainder of this paper, we combine regime 2a and 2b, in a

single “regime 2” since the regime 2a, and 2b did not show phenology different enough to be especially highlighted (not shown; regime 2 corresponds therefore to blooms with long time-lag between Chl^{ML} -onset and Chl^{surf} -onset). We remind the reader that we have, so far, made no assumption regarding geographic location, yet are able to group Southern Ocean chlorophyll blooms in three regimes. We now analyse the characteristics of each of these regimes.

We find that the three bloom regimes defined above display a coherent geographical organization (Figure 4). Blooms of regime 1 occur in a narrow zonal band between 30 and 40°S in the subtropics (except for the central Pacific basin, 80–160°W, that appears as an exception; Figure 4a) that are characterized by low surface nitrate concentrations (Figure 1d). Blooms of regime 2 are concentrated in the subantarctic region of the Southern Ocean: south of the subtropical front region and directly north of the Antarctic Circumpolar Fronts (Figure 4b). Finally, blooms of regime 3 are primarily associated with the fronts of the Antarctic Circumpolar (ACC; Figure 4c). Given the coherent geographical distribution associated with the three regimes, for convenience, we hereafter refer to them as “subtropical regime” for regime 1, “subantarctic regime” for regime 2, and “ACC regime” for regime 3. We note however that there are no clear geographical boundaries between the three regimes, which is consistent with the different blooms being driven by multiple processes (defined by a range of parameters, e.g. gyres, ACC, deep mixed-layers, iron inputs, etc.) rather than geographical bins.

The three regimes are associated with very distinct bloom characteristics. By definition, the subtropical regime has bloom Chl^{ML} -onsets centred in autumn (i.e. April–June; Figure 3a). Similarly, the ACC regime has bloom Chl^{ML} -onsets centred in winter (i.e. July–August; Figure 3a). Subantarctic regime Chl^{ML} -onset dates are mostly in autumn but some are in winter. All three regimes have their Chl^{ML} -onset during the period of convection, when air–sea heat fluxes are driving overturn of the surface layer (air–sea heat flux approximately -100 to -50 W m^{-2} at Chl^{ML} -onset; Figure 5a). In addition, the subantarctic and ACC regimes have their Chl^{ML} -onset when surface irradiance is low (short wave $\sim 50 \text{ W m}^{-2}$ at Chl^{ML} -onset; Figure 5b), and daylight length is short ($\sim 9 \text{ h d}^{-1}$; Figure 5c).

Before investigating the details of the seasonal cycles, it is instructive to discuss the typical physical and biogeochemical conditions of the regions where each regime falls. Subtropical regimes are located in the centre of subtropical gyres, which are characterized by surface-depleted macronutrients and shallow winter mixed-layers (averaged MLD_{max} of 86 m and average surface nitrate concentration of $0.7 \mu\text{mol kg}^{-1}$; Table 1 and Figure 1c and d). Therefore, we anticipate the availability of macronutrients will be the major regulator of blooms in these regions. In contrast, subantarctic and ACC regimes are located in the region of very deep winter mixed layers, much deeper than typical euphotic layers, and in regions richer in macronutrients (averaged MLD_{max} of 258 and 246 m, respectively, and average surface nitrate concentration of 11.8 and $11.9 \mu\text{mol kg}^{-1}$; Table 1 and Figure 1c and d). Subantarctic and ACC regions are also known as HNLC regions. We therefore anticipate that these blooms will be governed by light and iron availability.

Seasonal cycles

For each of the three bloom regimes, we compute the median seasonal cycle of mixed layer, Chl^{ML} and Chl^{surf} (Figure 6). To

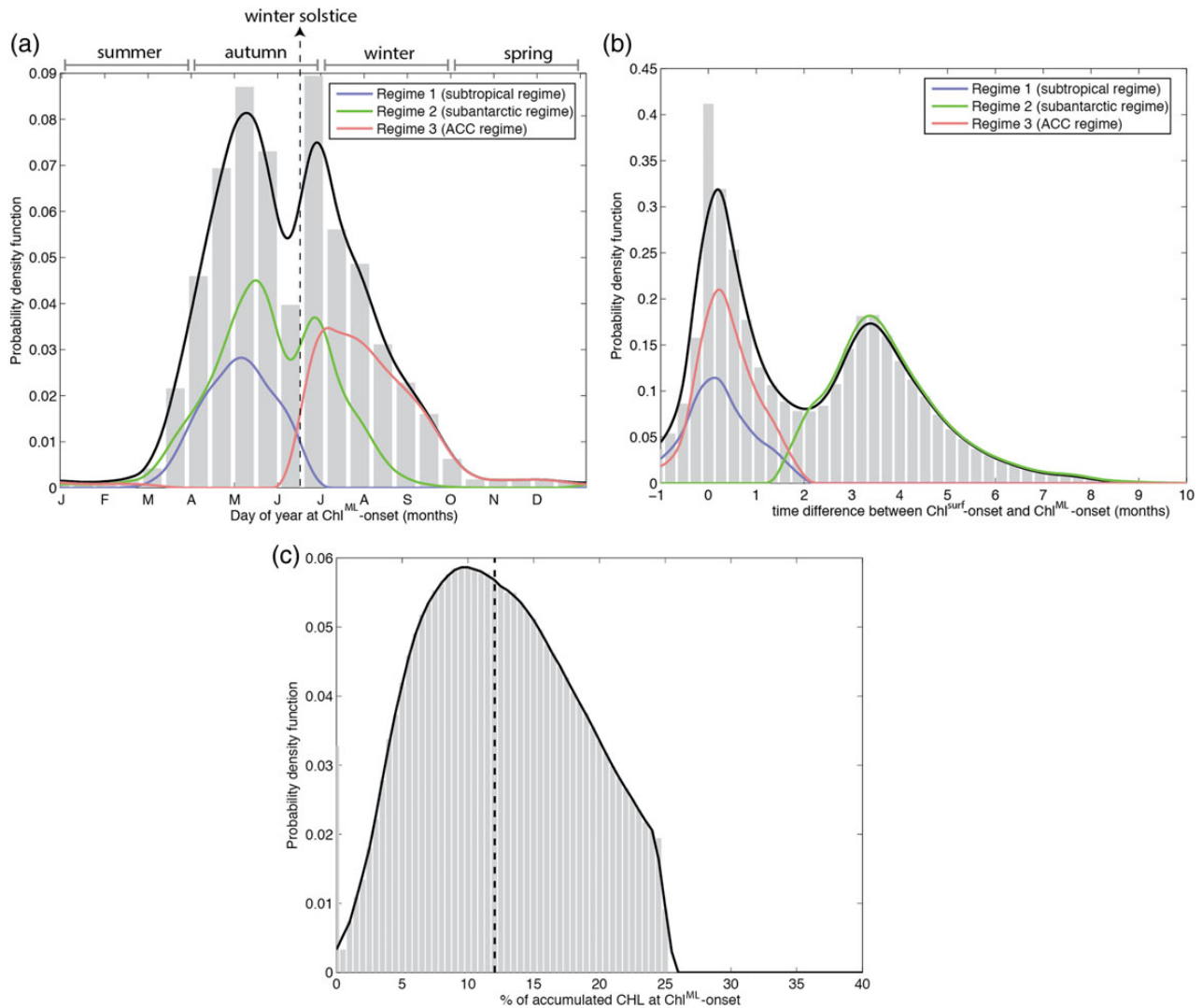


Figure 3. Probability density function (PDF) of the distribution of (a) the day of year of Chl^{ML} -onset; (b) the time difference between Chl^{ML} -onset and Chl^{surf} -onset; and (c) the percentage of accumulated chlorophyll at Chl^{ML} -onset. Grey bars show the PDF of the entire datasets. Smoothed PDF of (black) the entire dataset, and of (blue) regime 1, (green) regime 2, and (pink) regime 3 are superimposed on (a) and (b). Dashed line in (a) refers to the time of winter solstice. Dashed line in (c) denotes the median value of the distribution.

prevent the median from blurring Chl^{ML} -onset and the different phases of the bloom, we reference all seasonal cycles to their Chl^{ML} -onset date before averaging (see Supplementary material for more details). Similarly, we compute the mean seasonal cycle of air–sea heat flux, windstress, and downward short wave at ocean surface. We discuss the median seasonal cycle of each regime in turn, below.

The subtropical regime is marked by a Chl^{ML} -onset in autumn when the mixed layer deepens (Figure 6a). In this region, the Chl^{ML} -onset is parallel with the Chl^{surf} -onset. Chl^{ML} -onset occurs in a convective mixed layer (negative heat flux; Figure 6d) and when cycle of surface winds begins its seasonal increase. These characteristics rule out any control of Chl^{ML} -onset by a critical depth or critical stratification and points to control by the entrainment of macronutrients in the mixed layer associated with the deepening of the mixed layer. We note that the subtropical region is characterized by very low macronutrient concentrations in the surface layer (Table 1; Figure 1d), which supports the argument that the bloom

herein is limited by the availability of nutrients. In addition, we note that the subtropical region is characterized by relatively shallow mixed layers (MLD_{max} of 85 ± 77 m; Table 1; Figure 1c), so light availability is likely to play a minor role in regulating blooms in this region. Although the Chl^{ML} -onset occurs at the seasonal minimum of mixed-layer integrated irradiance, the irradiance at this time is notably much larger than for subantarctic and ACC regimes (yellow lines in Figure 6d–f). The bloom in the subtropical regime continues for the entire mixed-layer deepening period, and weakens when the mixed layer reaches its maximum depth. Overall, the bloom seen at surface remains in phase with the integrated bloom over the year.

In contrast to the subtropical regime, the subantarctic regime is not in regions of low surface nitrate (Table 1; Figure 1d). The subantarctic regime Chl^{ML} -onset occurs in autumn, when the mixed layer starts destratifying (Figure 6b). Interestingly, the autumn–winter increase in Chl^{ML} is not seen at surface (i.e. on Chl^{surf}), which suggests that the actual increase in chlorophyll biomass is

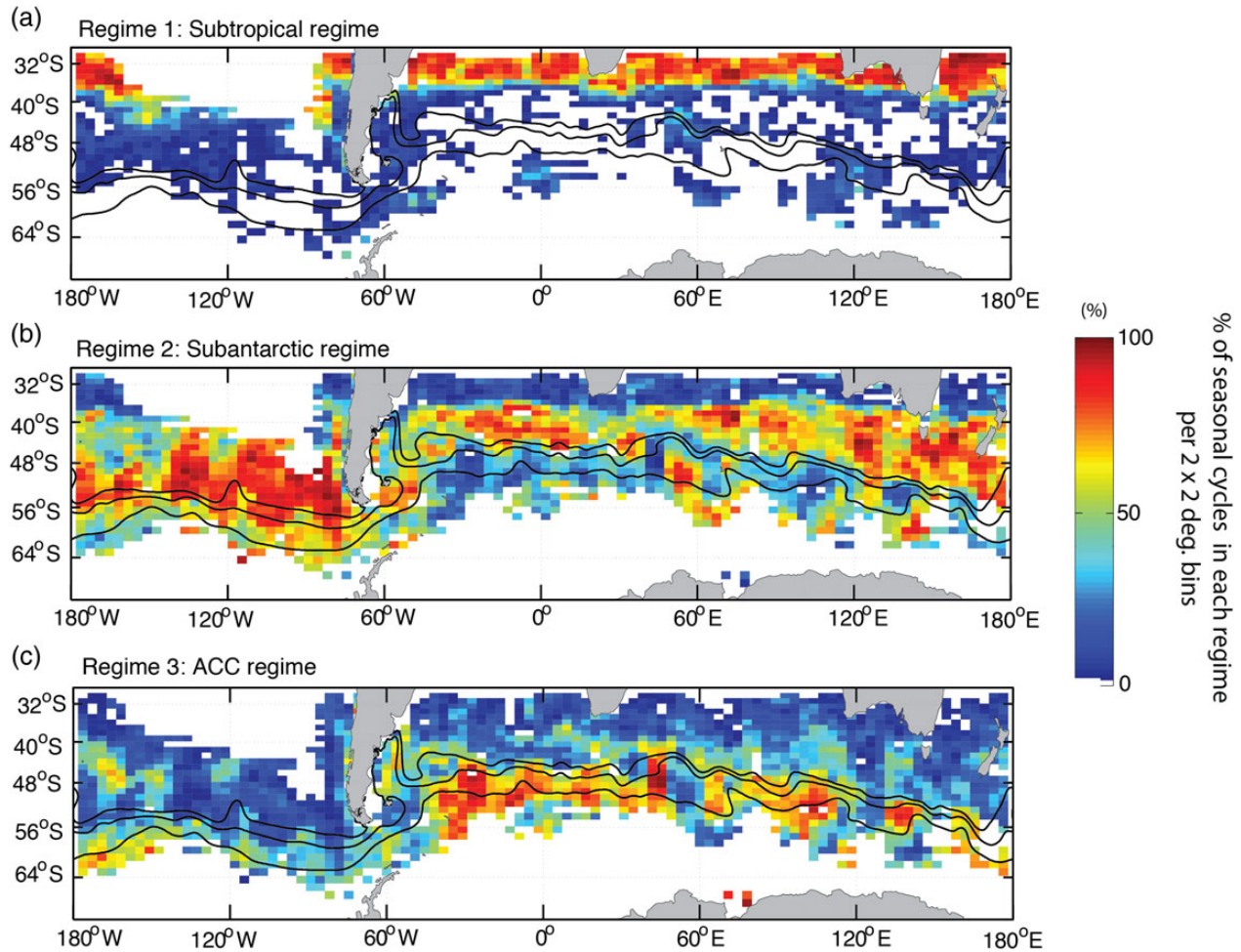


Figure 4. Geographical distribution of each bloom regime (see text for regime definition). The percentage of seasonal cycles associated with any given regime is gridded in $2 \times 2^\circ$: (a) regime 1: subtropical blooms; (b) regime 2: subantarctic bloom; (c) regime 3: ACC blooms. In (a–c), the three black lines represent the approximate climatological position of the three main ACC branches, from south to north: Polar Front, subantarctic front, and northern branch of the subantarctic front following Sallée et al. (2008).

diluted in the increasing volume of the surface layer associated with mixed-layer deepening. Chl^{ML} -onsets in the subantarctic regime occur at low irradiance and in convective mixed layers (Figure 6e and f). When the mixed layer reaches its maximum depth in winter, the increase in Chl^{ML} stops (see in August in Figure 6b), and a second increase phase starts in early spring (star in Figure 6b). This second phase of the bloom is associated with a large surface signal (i.e. on Chl^{surf}) and is associated with Chl^{surf} -onset. It occurs during the restratification phase of the mixed layer (Figure 6b) and when light conditions rapidly increase (Figure 6e). The spring increase in Chl^{ML} in the subantarctic regime is therefore consistent with a light control of the bloom. However, this spring increase in Chl^{ML} , possibly light controlled, can begin in very deep mixed layers (up to 400–600 m, Figure 7a), which should rule out control by critical depth. Interestingly, we find that subantarctic Chl^{surf} -onsets are associated with air–sea heat fluxes switching from surface cooling to surface warming (Figures 6e and 7b).

Similar to the two other regimes, the ACC regime Chl^{ML} -onset occurs during the destratification phase of the mixed layer (Figure 6c). However, ACC regime blooms have their Chl^{ML} -onset

in winter, later in the year compared with the other regimes. We note however that Chl^{ML} -onset of the ACC regime might be biased too late in the year, due to a weak bloom initiation. As such, one might say that Chl^{ML} -onset of ACC regime actually occurs in autumn (as the other regimes). However, the important point we wish to highlight is that the increase in integrated chlorophyll in autumn/winter in the ACC regime is, if anything, very low (Figure 6b and c). Chl^{surf} even decreases during autumn months (Figure 6b), suggesting that the autumnal growth is so low that it cannot compensate for the dilution associated with the deepening of the mixed-layer base. Then, in winter, when the MLD reaches its seasonal maximum, a very large and sudden increase in Chl^{ML} starts. In contrast to the subantarctic regime, the autumn–winter increase in Chl^{ML} happens at the end of the MLD deepening season, so the increase in integrated chlorophyll is not diluted in increasing volume of the surface layer. The chlorophyll increase signal translates therefore very clearly on Chl^{surf} (Figure 6b). This winter increase in Chl^{ML} and Chl^{surf} starts at low irradiance, in convective mixed layers (Figures 6f and 7b) and in deep mixed layers (up to 200–300 m; Figure 7a). The bloom continues over in spring when mixed layer restratifies and light condition improves.

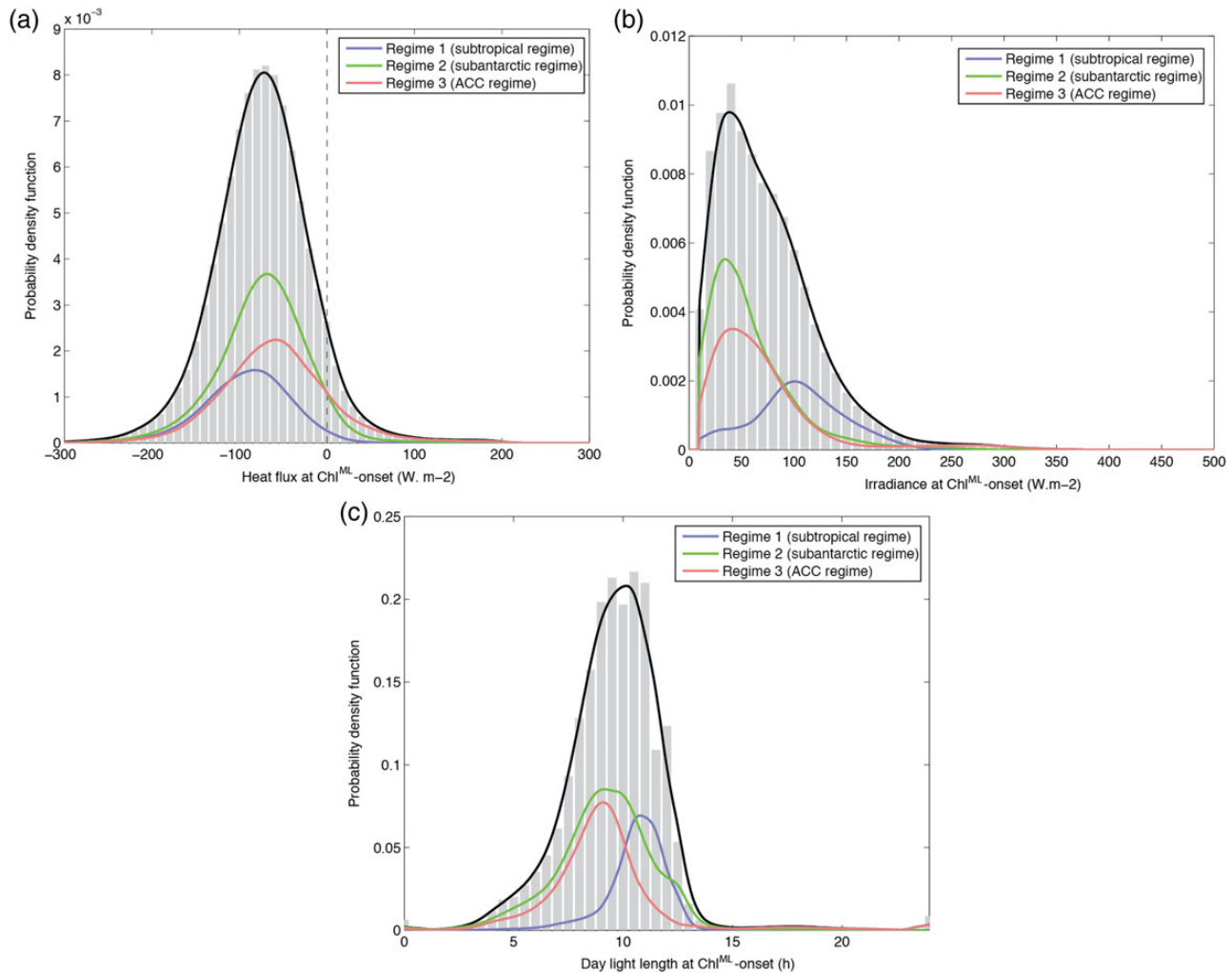


Figure 5. Probability density function (PDF) of the distribution of (a) daylight length at the time of Chl^{ML} -onset (h); (b) surface irradiance at Chl^{ML} -onset (W m^{-2}); and (c) the intensity of air–sea heat flux at Chl^{ML} -onset (negative denotes an ocean cooling; W m^{-2}). Grey bars show the PDF of the entire datasets. Smoothed PDF of (black) the entire dataset, and of (blue) regime 1, (green) regime 2, (pink) regime 3 are superimposed.

Table 1. Climatological mean biogeochemical and physical surface characteristics values in each of the three regimes.

	Subtropical regime	Subantarctic regime	ACC regime
MLD_{max} (m)	85.77 ± 27.71	257.80 ± 104.86	245.62 ± 105.67
Nitrate ($\mu\text{mol kg}^{-1}$)	0.71 ± 0.77	11.79 ± 6.44	11.91 ± 7.22

MLD_{max} refers to the climatological winter depth of mixed layer (from Argo; Sallée *et al.*, 2010). Nitrate are climatological mean surface values from World Ocean Atlas. Averages are weighted by the geographical distribution of the number of profiles for each regime.

Discussion

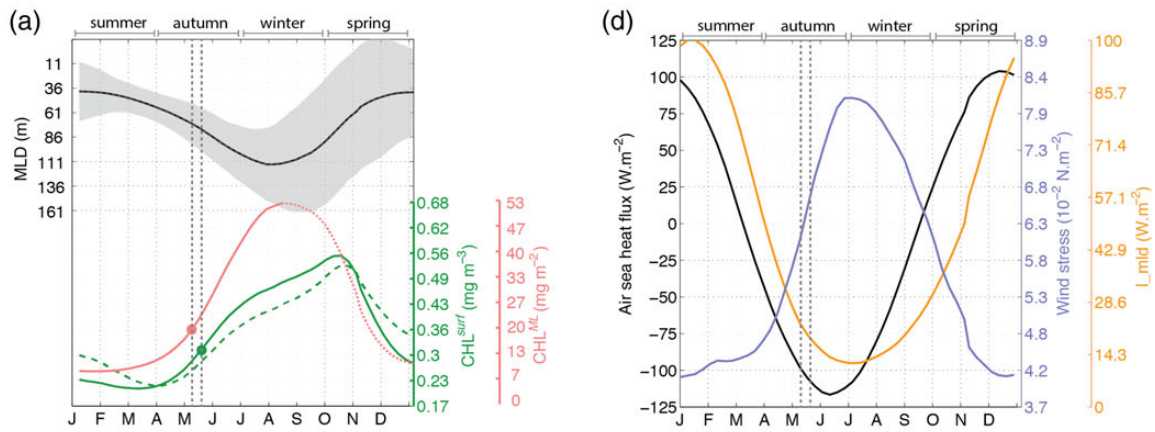
Overall, we find that all three regimes found in the present study have their Chl^{ML} -onset in autumn–winter when the solar irradiance is at its seasonal minimum, when daylight length is short, and when mixed layer actively mixes. While the phenological differences between the three regimes clearly stand out in our observational dataset, linking these differences to biological and physical control

is challenging from the available observations. The year-round biogeochemical water-column observations necessary to determine the factors that control the different phases of the bloom are currently not available. Nevertheless, we can speculate on the distinct controlling factors of each regime.

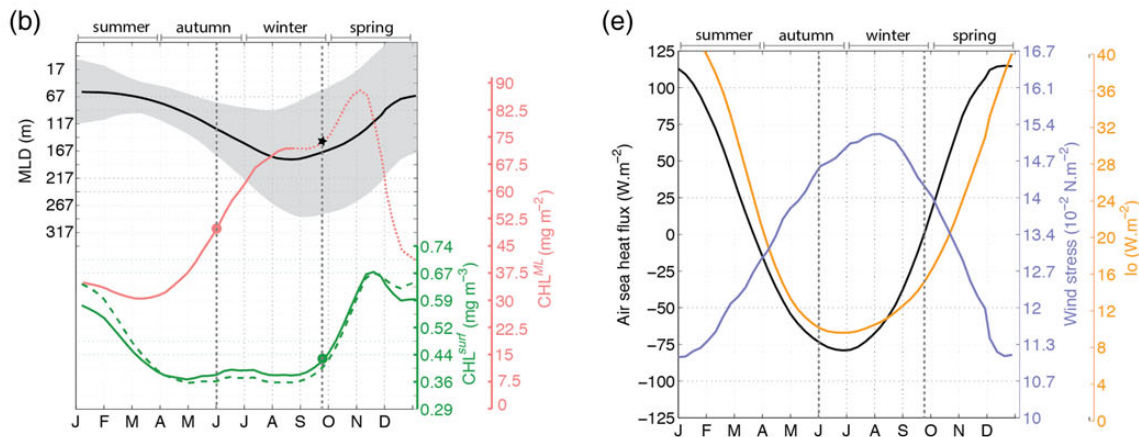
The subtropical regime is specific since it is located in a region of much stronger nitrate limitation (Table 1; Figure 1d) and relatively higher year-round light levels than the wider Southern Ocean. We find that the Chl^{ML} -onset in the subtropical regime occurs as soon as the mixed layer deepens in fall and entrains subsurface nitrate. The bloom then reaches its apex (i.e. date of maximum Chl^{ML}) when the MLD is maximal. While we cannot disentangle the potential roles of dilution and nutrients with our dataset, the strong degree of nitrate limitation in this region implies this is most likely to be a bloom controlled by nitrate entrainment. In that sense, the subtropical regime bloom Chl^{ML} -onsets can be considered to be in a bottom-up regime.

In the subantarctic regime, the deepening of the mixed-layer in autumn–winter dilutes the surface layer, which will reduce the prey-grazer encounter rate. However, for a bloom to be efficiently initiated by the reduction in the prey-grazer encounter rate, the

Regime 1: Subtropical regime



Regime 2: Subantarctic regime



Regime 3: ACC regime

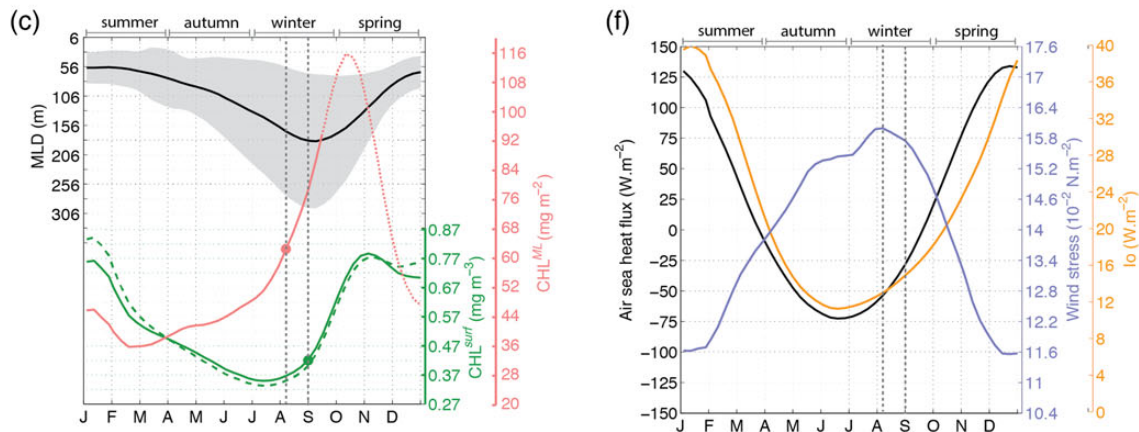


Figure 6. Median of all seasonal cycles falling in (a and d) subtropical regime; (b and e) subantarctic regime; (c and f) ACC regime. Before taking the mean, all seasonal cycles are centred on their date of Chl^{ML}-onset. (a–c) show the seasonal cycles of: (plain green) surface Chl_a (mg m⁻³); (dashed green) associated surface carbon biomass (mg C); (pink) mixed-layer integrated chlorophyll, Chl^{ML} (mg m⁻²); (black) MLD from collocated *in situ* observation (m). Surface carbon biomass reads on the surface Chl_a axis, and has been multiplied by the following values to scale with Chl_a: (a) 0.0124; (b) 0.0122; (c) 0.0098. (d–f) show the seasonal cycles of: (black) air–sea heat flux (W m⁻²); (purple) windstress (N m⁻²); and (yellow) mixed-layer averaged irradiance (W m⁻²). In (a–c), green dots indicate the median Chl_{surf}-onset date and pink dots the median Chl^{ML}-onset date detected by our automatic procedure (see text for details). Chl^{ML} is shown as a dotted line during the mixed-layer restratification phase because our estimate of Chl^{ML} is questionable during this period (see text for details). In (b), the black star on the Chl^{ML} curves denotes the time of Chl_{surf}-onset. Chl_{surf}-onset and Chl^{ML}-onset are reported on all panels by the vertical grey dashed lines. In (a–c), grey shadings denote the 1 s.d. envelop around the median value.

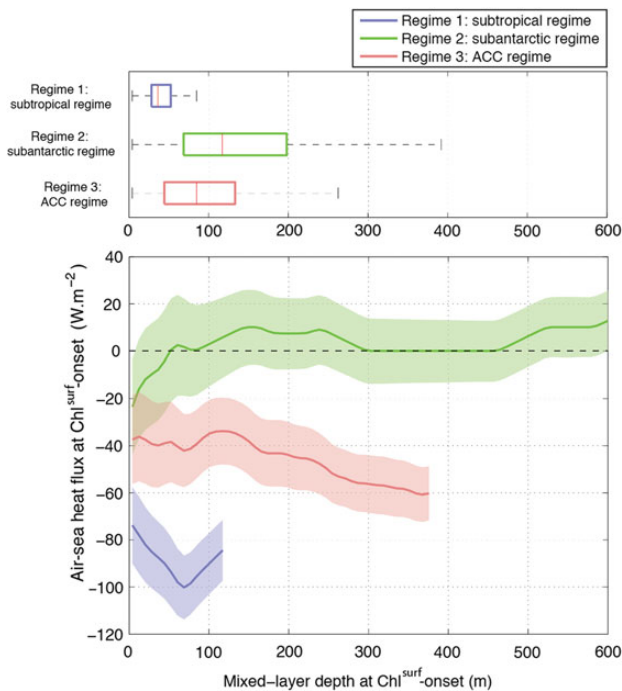


Figure 7. (a) Box plot of the mixed layer depth at $\text{Chl}^{\text{surf}}\text{-onset}$ for each regime. (b) Air–sea heat flux at $\text{Chl}^{\text{surf}}\text{-onset}$ vs. MLD at $\text{Chl}^{\text{surf}}\text{-onset}$: (plain curve) mean and (shading) standard deviation are shown for each regime. In both panels, the colour refers to bloom regime: (blue) subtropical regime; (green) subantarctic regime; and (pink) ACC regime.

system must at least be supporting some low levels of growth, or the growth must decline slower than the reduction in loss associated with the diminished prey-grazer encounter rate (e.g. Llort *et al.*, 2015). Again, this is difficult to assess, but we do observe a significant autumnal accumulation of integrated chlorophyll, which suggests some growth is occurring at the time of mixed layer deepening, or that losses are reducing faster than growth. In addition, Chl^{surf} remains constant in autumn (Figure 6b), while we know that the mixed layer is deepening at this seasons, which is an evidence that some growth must occur to balance the increase in the surface-layer volume. Therefore, perhaps dilution, lowering prey-grazer encounter rate, may stimulate this bloom and that the autumn–winter subantarctic regime bloom $\text{Chl}^{\text{ML}}\text{-onsets}$ are a top-down controlled regime.

The subantarctic regime is also noteworthy in that it contains a spring increase in Chl^{ML} after the autumn–winter increase. This spring increase translates into a large surface signal, and is therefore associated with $\text{Chl}^{\text{surf}}\text{-onset}$. Interestingly, this spring increase in Chl^{ML} can start in either deep or shallow mixed layers (Figure 7a). However, for mixed layer deeper than 50 m or so, it consistently starts when air–sea heat fluxes switch from cooling the surface layer to warming (Figure 7b). Taylor and Ferrari (2011a, b) proposed that the date at which air–sea heat flux switches from cooling to warming would be a good proxy for the date at which turbulence in the mixed layer would drop. Indeed, as mixed-layer turbulence ceases the degree of light limitation reduces (e.g. Huisman *et al.*, 1999). This improvement of the light environment associated with a more stable mixed layer can explain spring Chl^{ML} increase in this regime. When mixed layers are very shallow (below 50 m or so),

light is not limiting, and spring increase starts earlier (in negative air–sea heat fluxes).

In the ACC regime, the autumn–winter dilution is not able to initiate the bloom. Instead, there is very little chlorophyll accumulation in autumn, suggestive of chronic limitation of growth and ruling out a strong role for dilution (Llort *et al.*, 2015). A large integrated chlorophyll accumulation only starts when the mixed layer reaches its winter maximum. In the absence of dilution, a plausible explanation is that strong iron limitation in the ACC regime prevents the autumnal dilution from triggering the bloom. It is only when the mixed layers reach deep iron reservoir in winter that iron limitation is alleviated (e.g. Tagliabue *et al.*, 2014). In parallel, light conditions start to improve and we therefore speculate that the combination of light and iron initiates a short and intense bottom-up controlled bloom in the ACC regime.

An implication of our interpretation is that the subantarctic regime is assumed to be less iron-limited than the ACC regime, which allows for some autumnal growth (permitting therefore the top-down controlled autumn–winter bloom) and permits the spring secondary bloom not seen in the ACC. This may manifest itself due to differences between the two regions in total iron inputs or in iron recycling (Boyd *et al.*, 2012; Tagliabue *et al.*, 2014). At present, we do not have enough observations of dissolved iron, particularly at the times of seasonal transitions (Tagliabue *et al.*, 2012), nor do we have a broad enough understanding of the seasonal patterns of iron limitation (e.g. Moore *et al.*, 2013; Tagliabue *et al.*, 2014) to address this at basin scale and over the full length of seasonal cycle. However, it is notable that the subantarctic regime contains the largest number of continental sources of iron in the Southern Ocean (e.g. South America, Falkland Islands, South Africa, Crozet Island, Tasmania, New Zealand; the only notable exception being Kerguelen Island). This consistently translates into the presence of large blooms and maximum iron utilization in the subantarctic region, downstream of the major western boundary currents flowing on the northern edge of the ACC, as estimated from satellite imagery (Figure 1a; e.g. Sokolov and Rintoul, 2007; Thomalla *et al.*, 2011; Boyd *et al.*, 2012).

Llort *et al.* (2015) found that onset identified from Chl^{ML} corresponded in more than 85% of cases to the bloom onset detected from the actual water-column integrated biomass of their model (see also Sverdrup, 1953; Behrenfeld *et al.*, 2010). In addition, they found that $\text{Chl}^{\text{surf}}\text{-onset}$ is associated with the climax of the bloom, which corresponds to the date of maximum integrated chlorophyll increase. $\text{Chl}^{\text{ML}}\text{-onset}$ and $\text{Chl}^{\text{surf}}\text{-onset}$, which we use to describe bloom regimes, are therefore associated with two distinct key dates of bloom phenology. As noted by Llort *et al.* (2015), some confusion in our understanding of chlorophyll bloom might have arisen from the use of the same word “onset” to refer to either $\text{Chl}^{\text{ML}}\text{-onset}$ (e.g. Sverdrup, 1953; Behrenfeld *et al.*, 2010) or $\text{Chl}^{\text{surf}}\text{-onset}$ (e.g. Lozier *et al.*, 2011; Ferrari *et al.*, 2014). Indeed, our results clearly indicate that $\text{Chl}^{\text{ML}}\text{-onset}$ and $\text{Chl}^{\text{surf}}\text{-onset}$ refer to different phases of the bloom with arguably distinct controlling factors (see also Llort *et al.*, 2015).

One potential caveat in studying chlorophyll blooms from surface estimate of Chl^{surf} is that an increase in Chl^{surf} can be produced by photoadaptation rather than an increase in biomass. To test this, we computed the carbon concentration from Chl^{surf} based on the chlorophyll-to-carbon ratio, $\text{Chl}:\text{C}$ (e.g. Cloern *et al.*, 1995; Behrenfeld *et al.*, 2002; see the Material and methods section). We find that in all three regimes, the increase in surface

chlorophyll does coincide with the increase in carbon biomass (Figure 6a–c). Another important assumption in our study is that chlorophyll is well mixed in the mixed layer. We note that the three regimes described in this paper do not rely only on Chl^{ML} , but are also clearly identified as three distinct patterns on surface chlorophyll (Figure 6a–c). In addition, Chl^{ML} -onsets are detected in the deepening phase of the mixed layer, when active convection occurs and where we are confident that phytoplankton are actively mixed over the MLD. Subsurface chlorophyll directly beneath the base of the surface layer when the mixed layer is shallow in summer has been observed in the ocean (e.g. Holm-Hansen and Hewes, 2004), which would question our assumption regarding the vertical structure of chlorophyll, and could cause an increase in surface chlorophyll without increase in biomass through resuspension of a subsurface chlorophyll maximum. Although the presence of such subsurface chlorophyll would affect our results, we note that summer mixed layer in the subantarctic and ACC regions are of order of 50–100 m (e.g. Sallée et al., 2010), so we are confident that light limitation in these regions would prevent chlorophyll to be maintained year-round under the base of the mixed layer. Making these assumptions has allowed us to identify three main bloom regimes of the Southern Ocean, as well as their distinct phenologies (autumn, winter, and spring blooms). Future work will however need to be dedicated to the study of these regimes from *in situ* datasets. The growing bio-argo programme that reports concomitant biological and physical observations, year-round, will no doubt be of great help in assessing the details of the three main regimes identified in this paper.

Conclusion

The bloom Chl^{ML} -onset and Chl^{surf} -onset in the Southern Ocean have been estimated from satellite-derived products and observation-based estimates of MLD. Our automatic procedure was applied systematically over a large dataset, which allows us to illustrate basin scale regimes of bloom dynamics. The phenology of phytoplankton blooms appears organized into three distinct regimes when analysing Chl^{ML} -onset and Chl^{surf} -onset dates. These regimes are associated with three specific geographic locations: (i) autumn Chl^{ML} -onset (i.e. before winter solstice) blooms in a single phase (i.e. almost parallel Chl^{surf} -onset and Chl^{ML} -onset) are found in the subtropics, (ii) autumn–winter blooms with a second increase in spring (i.e. Chl^{surf} -onset and Chl^{ML} -onset separated by a few months) are found in the subantarctic zone (between the ACC and the subtropics), and (iii) winter Chl^{ML} -onset (i.e. after winter solstice) blooms in a single phase (i.e. almost parallel Chl^{surf} -onset and Chl^{ML} -onset) are found in the ACC region. It is notable that these three regimes organize themselves coherently in geographical space that is mostly zonal (except the central Pacific basin, 80–160°W, that appears as an exception for the subtropical regime, with almost no bloom in the region; Figure 4). However, the subantarctic and ACC regimes clearly follow the known meridional deviations and standing meanders of the ACC. Our findings suggest that the three regimes are fundamentally controlled by distinct mixed-layer and nutrient characteristics.

In summary, we find that autumn–winter blooms in the subtropical and ACC regimes are bottom-up controlled, associated with entrainment of nutrient (nitrate for the subtropical regime, and iron for the ACC regime). The autumn bloom in the subantarctic regime is top-down controlled, associated with a reduction in

prey-grazer encounter when the mixed-layer destratifies. This subantarctic regime autumn bloom is followed by a bottom-up controlled spring bloom, associated with rapid light improvement in the surface layer, which is caused by a reduction in surface-layer turbulence.

Supplementary data

Supplementary material is available at *ICESJMS* online version of the manuscript.

Acknowledgements

We thank two anonymous reviewers and R. Johnson for their comments and suggestions that improved the manuscript. We thank R. Johnson for kindly providing his reprocessed ocean colour dataset, specifically treated for the Southern Ocean. R. Johnson originally used satellite data provided by NASA Goddard Space Flight Centre and the ESA GlobColour Project. We also thank J. Le Sommer and L. Bopp for the interesting discussions that partly motivated this work. The Argo float data were collected and made freely available by the International Argo Program (<http://www.argo.ucsd.edu>). J-BS received support from Agence Nationale de la Recherche (ANR), ANR-12-PDOC-0001, as well as from the British Antarctic Survey as a BAS Fellow.

References

- Arrigo, K. R., van Dijken, G. L., and Bushinsky, S. 2008. Primary production in the Southern Ocean, 1997–2006. *Journal of Geophysical Research*, 113: C08004.
- Behrenfeld, M. J. 2010. Abandoning Sverdrup's critical depth hypothesis on phytoplankton blooms. *Ecology*, 91: 977–989.
- Behrenfeld, M. J., Marañón, E., Siegel, D. A., and Hooker, S. B. 2002. Photoacclimation and nutrient-based model of light-saturated photosynthesis for quantifying oceanic primary production. *Marine Ecology Progress Series*, 228: 103–117.
- Boss, E., and Behrenfeld, M. 2010. In situ evaluation of the initiation of the North Atlantic phytoplankton bloom. *Geophysical Research Letters*, 37: L18603.
- Boyd, P. W. 2002. The role of iron in the biogeochemistry of the Southern Ocean and equatorial Pacific: a comparison of in situ iron enrichments. *Deep Sea Research II: Topical Studies in Oceanography*, 49: 1803–1821.
- Boyd, P. W., Arrigo, K. R., Strzepek, R., and van Dijken, G. L. 2012. Mapping phytoplankton iron utilization: insights into Southern Ocean supply mechanisms. *Journal of Geophysical Research*, 117: C06009.
- Boyd, P. W., and Ellwood, M. J. 2010. The biogeochemical cycle of iron in the ocean. *Nature Geoscience*, 3: 675–682.
- Brody, S. R., Lozier, M. S., and Dunne, J. P. 2013. A comparison of methods to determine phytoplankton bloom initiation. *Journal of Geophysical Research: Oceans*, 118: 2345–2357.
- Carranza, M., and Gille, S. T. 2015. Southern Ocean wind-driven entrainment enhances satellite chlorophyll-a through the summer. *Journal of Geophysical Research: Oceans*, 120: 304–323.
- Chiswell, S. M., Bradford-Grieve, J., Hadfield, M. G., and Kennan, S. C. 2013. Climatology of surface chlorophyll a, autumn–winter and spring blooms in the southwest Pacific Ocean. *Journal of Geophysical Research: Oceans*, 118: 1003–1018.
- Cloern, E. J., Grenz, C., and Videgar-Lucas, L. 1995. An empirical model of the phytoplankton chlorophyll:carbon ratio—the conversion factor between productivity and growth rate. *Limnology and Oceanography*, 40: 1313–1321.

- Cole, H., Henson, S., Martin, A., and Yool, A. 2012. Mind the gap: the impact of missing data on the calculation of phytoplankton phenology metrics. *Journal of Geophysical Research*, 117: C08030.
- de Boyer Montégut, C., Madec, G., Fischer, A. S., Lazar, A., and Iudicone, D. 2004. Mixed layer depth over the global ocean: an examination of profile data and a profile-based climatology. *Journal of Geophysical Research*, 109: C12003.
- Evans, G. T., and Parslow, J. S. 1985. A model of annual plankton cycles. *Biological Oceanography*, 3: 327–347.
- Ferrari, R., Merrifield, S., and Taylor, J. 2014. Shutdown of convection triggers increase of surface chlorophyll. *Journal of Marine Systems*, 1–32. doi:10.1016/j.jmarsys.2014.02.009.
- Franks, P. J. S. 2015. Has Sverdrup's critical depth hypothesis been tested? Mixed layers vs. turbulent layers. *ICES Journal of Marine Science*, 72: 1897–1907.
- Frants, M., Gille, S. T., Hatta, M., Hiscock, W. T., Kahru, M., Measures, C. I., Mitchell, B. G., *et al.* 2013. Analysis of horizontal and vertical processes contributing to natural iron supply in the mixed layer in southern Drake Passage. *Deep Sea Research II: Topical Studies in Oceanography*, 90: 68–76.
- Gran, H. H., and Braarud, T. 1935. A quantitative study of the phytoplankton in the Bay of Fundy and the Gulf of Maine (including observations on hydrography, chemistry and turbidity). *Journal of the Biological Board of Canada*, 1: 279–467.
- Greve, W., Prinage, S., Zidowitz, H., Nast, J., and Reiners, F. 2005. On the phenology of North Sea ichthyoplankton. *ICES Journal of Marine Science*, 62: 1216–1223.
- Henson, S., Cole, H., Beaulieu, C., and Yool, A. 2013. The impact of global warming on seasonality of ocean primary production. *Biogeosciences*, 10: 4357–4369.
- Holm-Hansen, O., and Hewes, C. D. 2004. Deep chlorophyll-a maxima (DCMs) in Antarctic waters. *Polar Biology*, 27: 699–710.
- Huisman, J., van Oostveen, P., and Weissing, F. J. 1999. Critical depth and critical turbulence: two different mechanisms for the development of phytoplankton blooms. *Limnology and Oceanography*, 44: 1781–1787.
- Ji, R., Edwards, M., Mackas, D. L., Runge, J. A., and Thomas, A. C. 2010. Marine plankton phenology and life history in a changing climate: current research and future directions. *Journal of Plankton Research*, 32: 1355–1368.
- Johnson, R., Strutton, P. G., Wright, S. W., McMinn, A., and Meiners, K. M. 2013. Three improved satellite chlorophyll algorithms for the Southern Ocean. *Journal of Geophysical Research: Oceans*, 118: 3694–3703.
- Lévy, M., Lehahn, Y., Andre, J.-M., Mémerly, L., Loisel, H., and Heifetz, E. 2005. Production regimes in the northeast Atlantic: a study based on Sea-viewing Wide Field-of-view Sensor (SeaWiFS) chlorophyll and ocean general circulation model mixed layer depth. *Journal of Geophysical Research*, 110: C07S10.
- Llort, J., Lévy, M., Sallée, J. B., and Tagliabue, A. 2015. Onset, intensification and decline of phytoplankton blooms in the Southern Ocean. *ICES Journal of Marine Science*, 72: 1971–1984.
- Longhurst, A., Sathyendranath, S., Platt, T., and Caverhill, C. 1995. An estimate of global primary production in the ocean from satellite radiometer data. *Journal of Plankton Research*, 17: 1245–1271.
- Lozier, S., Dave, A. C., Palter, J., Gerber, L. M., and Barber, R. T. 2011. On the relationship between stratification and primary productivity in the North Atlantic. *Geophysical Research Letters*, 38: L18609.
- Mackas, D. L., Greve, W., Edwards, M., Chiba, S., Tadokoro, K., Eloire, D., Mazzocchi, M. G., *et al.* 2012. Changing zooplankton seasonality in a changing ocean: comparing time series of zooplankton phenology. *Progress in Oceanography*, 97–100: 31–62.
- Mahadevan, A., Dasaro, E., Lee, C., and Perry, M. J. 2012. Eddy-driven stratification initiates North Atlantic spring phytoplankton blooms. *Science*, 337: 54–58.
- Martin, J. H., Fitzwater, S. E., and Gordon, R. M. 1990. Iron deficiency limits phytoplankton growth in Antarctic waters. *Global Biogeochemical Cycles*, 4: 5–12.
- Moore, C. M., Mills, M. M., Arrigo, K. R., Berman-Frank, I., Bopp, L., Boyd, P. W., Galbraith, E. D., *et al.* 2013. Processes and patterns of oceanic nutrient limitation. *Nature Geoscience*, 6: 701–710.
- Moore, J. K., and Abbott, M. R. 2002. Surface chlorophyll concentrations in relation to the Antarctic Polar Front: seasonal and spatial patterns from satellite observations. *Journal of Marine Systems*, 37: 69–86.
- Nelson, D. M., and Smith, W. O. 1991. Sverdrup revisited: critical depths, maximum chlorophyll levels, and the control of Southern Ocean productivity by the irradiance-mixing regime. *Limnology and Oceanography*, 36: 1650–1661.
- Papaioannou, G., Papanikolaou, N., and Retalis, D. 1993. Relationships of photosynthetically active radiation and shortwave irradiance. *Theoretical and Applied Climatology*, 48: 23–27.
- Riley, G. A. 1946. Factors controlling phytoplankton populations on Georges Bank. *Journal of Marine Research*, 6: 54–73.
- Rintoul, S. R., Hughes, C. W., and Olbers, D. 2001. The Antarctic circumpolar current system. *In Ocean Circulation and Climate*, pp. 271–302. Ed. G. Siedler, J. Church, and J. Gould. Academic Press, New York.
- Rolinski, S., Horn, H., Petzoldt, T., and Paul, L. 2007. Identifying cardinal dates in phytoplankton time series to enable the analysis of long-term trends. *Oecologia*, 153: 997–1008.
- Ryther, J. H., and Hulbert, E. M. 1960. On winter mixing and the vertical distribution of phytoplankton. *Limnology and Oceanography*, 5: 337–338.
- Sallée, J. B., Speer, K., and Morrow, R. 2008. Response of the Antarctic Circumpolar Current to atmospheric variability. *Journal of Climate*, 21: 3020–3039.
- Sallée, J. B., Speer, K., Rintoul, S., and Wijffels, S. 2010. Southern Ocean thermocline ventilation. *Journal of Physical Oceanography*, 40: 509–529.
- Sallée, J. B., Wienders, N., Speer, K., and Morrow, R. 2006. Formation of subantarctic mode water in the southeastern Indian Ocean. *Ocean Dynamics*, 56: 525–542.
- Sapiano, M. R. P., Brown, C. W., Schollaert Uz, S., and Vargas, M. 2012. Establishing a global climatology of marine phytoplankton phenological characteristics. *Journal of Geophysical Research*, 117: C08026.
- Sarmiento, J. L., Gruber, N., Brzezinski, M. A., and Dunne, J. P. 2004. High-latitude controls of thermocline nutrients and low latitude biological productivity. *Nature*, 427: 56–60.
- Siegel, D. A., Doney, S. C., and Yoder, J. A. 2002. The North Atlantic spring phytoplankton bloom and Sverdrup's critical depth hypothesis. *Science*, 296: 730.
- Sokolov, S., and Rintoul, S. R. 2007. On the relationship between fronts of the Antarctic Circumpolar Current and surface chlorophyll concentrations in the Southern Ocean. *Journal of Geophysical Research*, 112: C07030.
- Sverdrup, H. U. 1953. On conditions for the vernal blooming of phytoplankton. *Journal du Conseil International pour l'Exploration de la Mer*, 18: 287–295.
- Tagliabue, A., Mtshali, T., Aumont, O., Bowie, A. R., Klunder, M. B., Roychoudhury, A. N., and Swart, S. 2012. A global compilation of dissolved iron measurements: focus on distributions and processes in the Southern Ocean. *Biogeosciences*, 9: 2333–2349.
- Tagliabue, A., Sallée, J. B., Bowie, A. R., Lévy, M., Swart, S., and Boyd, P. W. 2014. Surface-water iron supplies in the Southern

- Ocean sustained by deep winter mixing. *Nature Geoscience*, 7: 314–320.
- Taylor, J. R., and Ferrari, R. 2011a. Ocean fronts trigger high latitude phytoplankton blooms. *Geophysical Research Letters*, 38: L23601.
- Taylor, J. R., and Ferrari, R. 2011b. Shutdown of turbulent convection as a new criterion for the onset of spring phytoplankton blooms. *Limnology and Oceanography*, 56: 2293–2307.
- Thomalla, S. J., Fauchereau, N., Swart, S., and Monteiro, P. M. S. 2011. Regional scale characteristics of the seasonal cycle of chlorophyll in the Southern Ocean. *Biogeosciences*, 8: 2849–2866.
- Townsend, D. W., Kelle, M. D., Sieracki, M. E., and Ackleson, S. G. 1992. Spring phytoplankton blooms in the absence of vertical water column stratification. *Nature*, 360: 59–62.
- Vargas, M., Brown, C. W., and Sapiano, M. R. P. 2009. Phenology of marine phytoplankton from satellite ocean color measurements. *Geophysical Research Letters*, 36: L01608.
- White, M. A., de Beurs, K. M., Didan, K., Inouye, D. W., Richardson, A. J., Jensen, O. P., O’Keefe, J., *et al.* 2009. Intercomparison, interpretation, and assessment of spring phenology in North America estimated from remote sensing for 1982–2006. *Global Change Biology*, 15: 2335–2359.

Handling editor: Rubao Ji



Contribution to the Themed Section: 'Revisiting Sverdrup's Critical Depth Hypothesis' Original Article

High-resolution view of the spring bloom initiation and net community production in the Subantarctic Southern Ocean using glider data

Sandy J. Thomalla^{1,2*}, Marie-Fanny Racault³, Sebastiaan Swart^{1,2}, and Pedro M. S. Monteiro²

¹Southern Ocean Carbon and Climate Observatory, CSIR, PO Box 320, Stellenbosch 7599, South Africa

²Department of Oceanography, Marine Research Institute, University of Cape Town, Rondebosch 7701, South Africa

³Plymouth Marine Laboratory, Prospect Place, The Hoe, Plymouth PL1 3DH, UK

*Corresponding author: tel: +27 21 658 2764; e-mail: sthomalla@csir.co.za

Thomalla, S. J., Racault, M-F., Swart, S., and Monteiro, P. M. S. High-resolution view of the spring bloom initiation and net community production in the Subantarctic Southern Ocean using glider data. – ICES Journal of Marine Science, 72: 1999–2020.

Received 12 December 2014; revised 6 May 2015; accepted 16 May 2015; advance access publication 8 June 2015.

In the Southern Ocean, there is increasing evidence that seasonal to subseasonal temporal scales, and meso- to submesoscales play an important role in understanding the sensitivity of ocean primary productivity to climate change. This drives the need for a high-resolution approach to resolving biogeochemical processes. In this study, 5.5 months of continuous, high-resolution (3 h, 2 km horizontal resolution) glider data from spring to summer in the Atlantic Subantarctic Zone is used to investigate: (i) the mechanisms that drive bloom initiation and high growth rates in the region and (ii) the seasonal evolution of water column production and respiration. Bloom initiation dates were analysed in the context of upper ocean boundary layer physics highlighting sensitivities of different bloom detection methods to different environmental processes. Model results show that in early spring (September to mid-November) increased rates of net community production (NCP) are strongly affected by meso- to submesoscale features. In late spring/early summer (late-November to mid-December) seasonal shoaling of the mixed layer drives a more spatially homogenous bloom with maximum rates of NCP and chlorophyll biomass. A comparison of biomass accumulation rates with a study in the North Atlantic highlights the sensitivity of phytoplankton growth to fine-scale dynamics and emphasizes the need to sample the ocean at high resolution to accurately resolve phytoplankton phenology and improve our ability to estimate the sensitivity of the biological carbon pump to climate change.

Keywords: bloom initiation, glider, net community production, primary production, respiration, Subantarctic, sverdrup critical depth model.

Introduction

Phytoplankton blooms are ecological hot spots (Hjort, 1926; Ryther, 1969; Chassot *et al.*, 2010), such that their timing and location dictate the life cycles and migration patterns of many zooplankton grazers and fish larvae (Longhurst, 2007). Therefore, changes in bloom phenology may have profound implications for higher trophic levels (Platt *et al.*, 2003; Edwards and Richardson, 2004; Mackas *et al.*, 2007; Koeller *et al.*, 2009; Kahru *et al.*, 2011). In addition, phytoplankton blooms play an important role in biogeochemical cycling as they result in substantial transport of organic material from the surface waters to the oceans interior which contributes to the oceans net annual uptake of CO₂ (Takahashi *et al.*, 2009). Despite the importance of phytoplankton production and its

relation to the biogenic flux of CO₂ (Arrigo *et al.*, 1998), particularly in the Southern Ocean (3 PgC yr⁻¹, 33% of global organic carbon flux; Schlitzer, 2002), our understanding of phytoplankton seasonal distribution, rates of production, and carbon export remains poorly constrained.

The conditions necessary for phytoplankton bloom development and high growth rates in the Southern Ocean are the presence of a favourable light environment (Sverdrup, 1953), Iron (Fe) availability (Martin *et al.*, 1990) and low grazing pressure relative to algal growth rates (Smetacek and Passow 1990; Sakshaug *et al.*, 1991; Boyd *et al.*, 1999; Boyd, 2002; Dandonneau *et al.*, 2004; Arrigo *et al.*, 2008). It is the seasonal cycle that sets much of the environmental variability in

these factors and as such ascribes the growing conditions that phytoplankton are exposed to over an annual cycle. The seasonal cycle is also a mode of variability that couples the physical mechanisms of climate forcing to ecosystem response in production, diversity, and carbon export (Monteiro *et al.*, 2011). An understanding of the seasonal evolution of phytoplankton production can thus provide a sensitive index of climate variability through their dependence on physical processes that transport nutrients and control the exposure of phytoplankton to sunlight (Sommer and Lengfellner, 2008; Henson *et al.*, 2009; Lavigne *et al.*, 2013).

In addition to the importance of the seasonal cycle in characterizing phytoplankton phenology, submesoscale features (baroclinic instabilities from enhanced lateral density gradients; 1–10 km in size) have been shown to account for up to 50% of the variance observed in primary production (*PP*) estimates (Lévy *et al.*, 2001; Glover *et al.*, 2008). At similar spatial scales, variance in vertical velocity (which modulates nutrient supply and carbon export) shows a tenfold increase when numerical simulation resolutions increase from 6 to 1 km (Klein *et al.*, 2008). If researchers are to accurately predict the seasonal timing of phytoplankton blooms forced by climate forecast models and improve our understanding of the sensitivities of the biological carbon pump to changes in climate forcing factors (both needed for predicting long-term trends), the Southern Ocean ecosystem has to be investigated at the appropriate scales that link the physical drivers to the biogeochemistry (Lévy *et al.*, 2001; Le Quére *et al.*, 2007; Klein *et al.*, 2008; Doney *et al.*, 2009; Thomalla *et al.*, 2011; Racault *et al.*, 2012; Joubert *et al.*, 2014; Swart *et al.*, 2014; Carranza and Gille, 2015). These include the temporal scales extending from seasonal to subseasonal and the spatial scale ranging from the mesoscale to the submesoscale.

To date, analyses of open ocean phytoplankton phenology have mostly relied on observations made by Continuous Plankton Recorders (Edwards and Richardson, 2004; Racault *et al.*, 2014; Raitos *et al.*, 2014), a limited number of open ocean stations with continuous long-term time series (e.g. Hawaii Ocean Time series and Bermuda Atlantic Time Series) (Johnson and Howd, 2000; Brix *et al.*, 2004), and satellite-measured chlorophyll data (e.g. Siegel *et al.*, 2002; Henson *et al.*, 2006; Platt *et al.*, 2009; Zhai *et al.*, 2011; Thomalla *et al.*, 2011; D'Ortenzio *et al.*, 2012; Sapiano *et al.*, 2012; González Taboada and Anadón, 2014; Racault *et al.*, 2014). The high-sampling frequency and large spatial and temporal coverage gained with satellite observations are clear. However, remotely detected water-leaving radiances emanate from only the first optical ocean layer and require some assumptions to be made about their representativeness of the vertical structure of the water column. Autonomous platforms (e.g. floats and gliders) on the other hand are able to profile the water column (0–1000 m) and characterize the vertical structure at the relevant time scales (subseasonal to seasonal) and spatial scales (meso- to submesoscale) that are necessary to link physical forcing mechanisms of climate drivers to biogeochemical responses. Given their growing importance in the trajectory of ocean ecosystem research, it must be emphasized that we maximize the output from these multi-sensor platforms to improve our understanding of regional contrasts in the timing of the onset and evolution of phytoplankton blooms.

The formation of phytoplankton blooms has traditionally been defined with Sverdrup's critical depth model where the mixed layer shoals above a critical light depth due to warming associated with enhanced seasonal radiation. This allows phytoplankton to reside within increasingly shallow depths where they experience higher light levels, and, as a result, begin to bloom (Sverdrup,

1953). Recent studies have challenged this explanation however, proposing instead that bloom initiation is driven by (i) eddy-induced stratification that shoals the *MLD* to create a favourable light environment before seasonal warming (Mahadevan *et al.*, 2012); (ii) the stratification-onset model where convective overturning shuts down in spring, decreasing the depth of mixing (despite a still deep seasonal *MLD*) allowing phytoplankton blooms to form in shallow near-surface layers that deepen with the onset of thermal stratification (Chiswell, 2011; Chiswell *et al.*, 2013); (iii) a shutdown of turbulent convective mixing when net heat fluxes become positive, increasing the residence times of phytoplankton in the euphotic zone (Taylor and Ferrari, 2011); (iv) a decrease in the dominant mixing length scales when negative heat fluxes weaken and shift the mixing mechanism from convection to wind, allowing phytoplankton to gain sufficient light exposure to bloom (Brody and Lozier, 2014); and (v) the disturbance-recovery hypothesis, where physical dilution during winter mixed layer deepening decreases grazing pressure driving subtle imbalances between phytoplankton division and loss rates allowing positive biomass accumulation to result in a bloom (Behrenfeld, 2010; Boss and Behrenfeld, 2010; Behrenfeld *et al.*, 2013). In this study, we use 5.5 months of continuous, high-resolution glider data (3 h, 2 km horizontal resolution) from spring to summer in the Atlantic Subantarctic Zone (SAZ) to investigate; (i) the phytoplankton spring bloom initiation and time-scale sensitivity in the region and (ii) the seasonal evolution of water column production and respiration.

Conventionally, using surface chlorophyll time series from satellite, bloom initiation dates have been estimated based on threshold criteria (e.g. Siegel *et al.*, 2002) or based on fitting a model to the data and estimating the phenological metrics from the model equations (e.g. Platt *et al.*, 2009). These methods may allow for the detection of one to two phytoplankton blooms per year (e.g. Sapiano *et al.*, 2012; Ardyna *et al.*, 2014; González Taboada and Anadón, 2014; Racault *et al.*, 2015). Here, we apply a number of these methods to glider-surface chlorophyll time series and for the first time, using glider vertical profile data, to mixed layer integrated chlorophyll. Specifically, bloom initiation dates were identified by implementing five different methods of detection, four of which have previously been applied to *in situ* and ocean-colour remote-sensing datasets to investigate phytoplankton phenological variability. The methods include a median threshold criterion approach (e.g. Siegel *et al.*, 2002), a cumulative sum approach (Brody *et al.*, 2013), a rate of change method (Wiltshire *et al.*, 2008; Brody *et al.*, 2013); and a cumulative sum of anomalies approach (Racault *et al.*, 2015). In addition, we developed a novel method of bloom detection based on the cumulative sum of anomalies of mixed layer phytoplankton growth rates.

The bloom initiation dates identified by the different mathematical methods of detection and regions of high growth rates were analysed in the context of upper ocean boundary layer physics. Such analysis is important to enhance our understanding of how blooms (and different detection methods), may relate to the underlying physical changes occurring in the environment.

Furthermore, the bloom initiation dates estimated using the different methods in conjunction with ancillary glider data, allowed us to implement a *PP* model (Platt *et al.*, 1980; Platt and Sathyendranath, 1993), and to compute Sverdrup's critical depth model, generating the first time series of glider-estimated rates of *PP*, respiration and net community production (*NCP*). Another possible method (worth noting but not used in this study) of attaining *NCP* (and community losses) is the bio-optical method of Claustre *et al.* (2008), which analyses the diel cycle of particulate

organic carbon (POC) from high-frequency measurements of beam attenuation (or backscattering). The variable PP reflects the total amount of carbon fixed during photosynthesis while NCP , calculated as the difference between production and respiration, is used to define the trophic balance of a biological community and to characterize its “potential for organic export” (Hansell and Carlson, 1998). Together, estimates of these variables from high-resolution glider datasets provide important insights into the carbon cycle and allows us to assess the biogeochemical responses (in production and export potential) to physical forcing mechanisms at the required time and space scales for informing climate response research.

Data and methods

Experimental set up and glider deployment

An autonomous Seaglider (SG573) was deployed in the Southeast Atlantic Ocean in the central SAZ region of the Southern Ocean at 42.4°S, 9.9°W (Figure 1) as part of the Southern Ocean Seasonal

Cycle Experiment (SOSCEX; Swart *et al.*, 2014). The aim of SOSCEX was to improve our understanding of the links between climate drivers, ecosystem productivity, and climate feedbacks in the Southern Ocean by investigating physical forcing mechanisms and biogeochemical responses at the relevant time (subseasonal to seasonal) and space (meso- to submesoscale) scales (Swart *et al.*, 2012).

The glider was deployed on 20 September 2012 and retrieved on 15 February 2013 resulting in continuous sampling for 148 d (or ~ 5.5 months) covering a total distance of 1537 km. The glider measured a suite of parameters that include conductivity, temperature, pressure, dissolved oxygen, fluorescence, photosynthetically active radiation (PAR), and optical backscattering at two wavelengths ($\lambda = 470$ and 700). Each dive cycle of the glider took ~ 5 h to complete and covered an average horizontal distance of 2.8 km, rendering a temporal resolution of 2.5 h and spatial resolution of 1.4 km between profiles. This spatial resolution covers both meso- (10–200 km) and submesoscale (1–10 km) ranges in the ocean. Data were transmitted

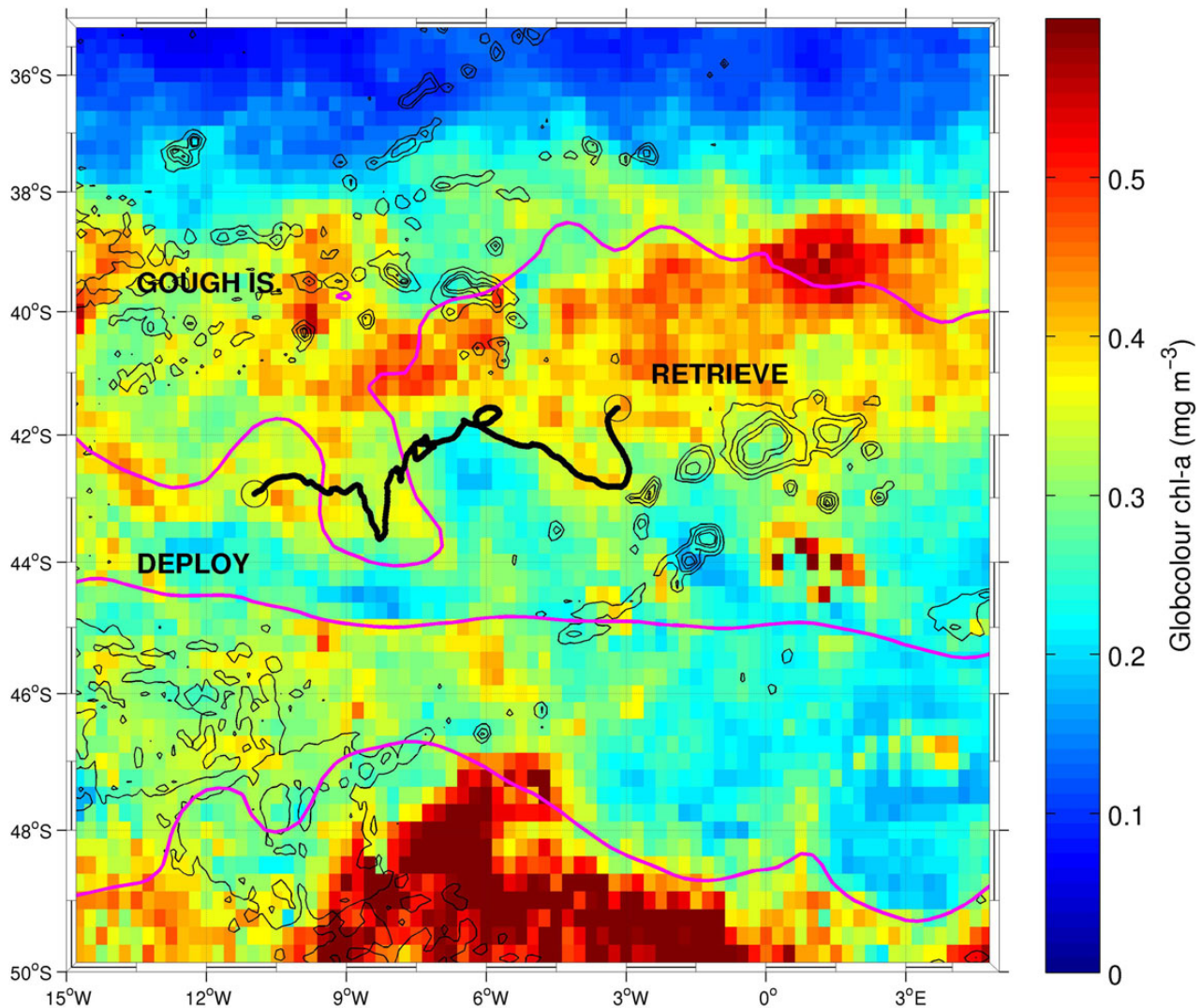


Figure 1. Mean satellite chlorophyll-*a* concentration (mg m^{-3}) (from GlobColour Case I water product: www.globcolour.info) for the temporal period of SOSCEX (25 September 2012–2015 February 2013) showing the trajectory of the glider. The mean ACC front locations for the period of SOSCEX, as defined using satellite altimetry, are plotted (magenta lines) from north to south: Subtropical Front, Subantarctic Front, and Antarctic Polar Front. The bathymetry for the region is overlaid using black contours (500, 1000, 2000, and 3000 m isobaths). This figure is available in black and white in print and in colour at ICES *Journal of Marine Science* online.

in real time via the Iridium satellite upon reaching the surface after each dive. At the deployment and retrieval site of each glider, ship-based Conductivity Temperature Depth (CTD) cross-calibration casts were carried out (all within 3 km and 4 h or each other) yielding two independent inter-calibrations between glider and CTD sensors as well as bottle samples of chlorophyll-*a*, salinity, and dissolved oxygen. Glider data were interpolated onto a 6-h grid allowing extraction of daily midday profiles which were used for models of production.

Glider datasets

Glider fluorescence was dark corrected by subtracting the median fluorescence value <300 m. All daylight fluorescence profiles were corrected for quenching using optical backscattering based on the methods described in [Sackmann et al. \(2008\)](#). In the rare occasion when backscattering was unavailable (due to intermittent sensor malfunction), fluorescence was corrected by extrapolating the maximum fluorescence value within the mixed layer to the surface ([Xing et al., 2012](#)). Glider fluorescence was converted to chlorophyll using the manufacturer's instrument-specific chlorophyll conversion factor then adjusted with a statistically significant regression from 83 co-located glider chlorophyll and *in situ* chlorophyll samples (slope = 4.12, intercept = -0.21, $r^2 = 0.66$) (see [Swart et al., 2014](#) for more detail). Integrated chlorophyll was obtained by integrating chlorophyll (trapezoidal rule) from the surface to the mixed layer depth (MLD); defined as the depth where the temperature difference exceeds 0.2°C in reference to the temperature at 10 m ($\Delta T_{10m} = 0.2^\circ\text{C}$) following the criterion of [de Boyer Montégut \(2004\)](#).

The instrument-specific dark count was subtracted from glider PAR which was then divided by the scaling factor to get the correct units ($\mu\text{E cm}^{-2} \text{s}^{-1}$). An additional dark correction was performed by subtracting an *in situ* dark count calculated from the mean of all midnight profiles. Daily surface PAR was calculated by fitting an exponential curve to the top 50 m of each midday PAR profile and extrapolating it to the surface to get PAR at 0 m. The exponential fit similarly generated the vertical attenuation coefficient of irradiance (k_d).

Spikes were separated from raw backscattering ($\lambda = 470$ and 700) using a seven-point running median filter ([Briggs et al., 2011](#)). Raw digital counts were converted into particulate backscattering (b_{bp}) according to the following equation:

$$b_{bp} = 2\pi \chi_p [S(C - D) - \beta_{sw}], \quad (1)$$

where χ_p is equal to 1.1 and the factor used to convert β_p (at a central angle of 117°) into b_∞ ([Boss and Pegau, 2001](#)), S is the instrument-specific scaling factor, C is the digital counts ($\lambda = 470$ and 700), D is the dark counts, β_{sw} is the volume scattering of pure water estimated using the models of [Zhang and Hu \(2009\)](#) and [Zhang et al. \(2009\)](#), and $[S(C - D)]$ and $[S(C - D)\beta_{sw}]$ are the total and particle volume scattering functions, β and β_p , respectively ([Dall'Olmo et al., 2009](#)). Remaining spikes in particulate backscattering were removed with a threshold in shallow ($b_{bp} > 0.0048$) and deep ($b_{bp} > 0.0025$) waters. Bad profiles with high mean backscattering ($b_{bp} > 0.001$) in deep water (>150 m) were identified and discarded.

Phytoplankton-specific carbon biomass (see Supplementary Figure S1) was estimated from b_{bp} according to [Behrenfeld et al. \(2005\)](#):

$$C_{phyto} = 13\,000 \times (b_{bp} - 0.00035), \quad (2)$$

where C_{phyto} is phytoplankton-specific carbon (mg C m^{-3}),

0.00035 (m^{-3}) is a background value representing a global estimate of backscattering by stable heterotrophic and detrital components of the surface particle population ([Behrenfeld et al., 2005](#)), and 13 000 (mg C m^{-3}) is a scalar that has been shown to give satellite chlorophyll-to-carbon ratio consistent with laboratory results and an average phytoplankton contribution to total POC of $\sim 30\%$, consistent with field estimates ([Eppley, 1992](#); [Durand et al., 2001](#); [Gundersen et al., 2001](#)).

Satellite-derived datasets

The satellite chlorophyll product was obtained from the ESA Ocean Colour CCI (OC-CCI) project that merged chlorophyll data from ocean-colour remote sensors' MERIS (processed with Polymer algorithm, [Steinmetz et al., 2011](#)), SeaWiFS, and MODIS (processed with SeaDAS chlorophyll retrieval algorithm). Further information about the project is available at <http://www.esa-oceancolour-cci.org>. The description of the processing version 0.95 used in the present analysis is presented in the Product User Guide at http://www.esa-oceancolour-cci.org/?q=webfm_send/318. The OC-CCI surface chlorophyll data were extracted at monthly resolution in the region covered by the glider transect (40.9°S – 43.7°S , 11°W – 2.9°W). Chlorophyll climatology was computed using OC-CCI data from September 1997 to April 2013. The chlorophyll annual cycle over the period from May 2012 to April 2013 (encompassing the timing of the glider deployment from September 2012 to February 2013) was also computed. It can be noted that from May 2012–onwards, only MODIS ocean-colour satellite data were available and therefore were included in the OC-CCI product. This product was used to visualize the annual cycle of chlorophyll with respect to the glider and was not used in any of the model calculations.

Wind data were sourced from SeaWinds, a blended product from observations of sea surface vector winds (at 10 m above sea level reference height) from multiple satellites microwave radiometers and scatterometers (QuickSCAT), SSMIs, TMI, and AMSR-E ([Zhang et al., 2006](#), <ftp://eclipse.ncdc.noaa.gov/pub/seawinds/>) to produce global 6-h, 0.25° resolution, and gridded fields. The [Large and Pond \(1981\)](#) method was applied to convert the windspeed to a windstress product. The windstress data were collocated with the gliders in space and time using two-dimensional bilinear interpolation.

Heat flux data were sourced from the NCEP/DOE AMIP-II Reanalysis-2 model where the 6-h mean of net incoming heat flux was calculated as net downwards heat flux minus (net upwards + latent + sensible heat flux) at the ocean surface (for more details, see [Kanamitsu et al., 2002](#)). Heat flux data were collocated with the gliders in space and time using two-dimensional bilinear interpolation.

Bloom initiation detection methods

Four of the five bloom initiation detection methods listed below rely on the median of the annual cycle of chlorophyll. Since the glider dataset presented here only covers 5.5 months of the annual cycle, a median calculated using the glider-chlorophyll time series measured during spring and summer only, would overestimate the median value relative to that estimated from the entire annual cycle. To circumvent this, a box of satellite surface chlorophyll from OC-CCI time series was extracted spanning the spatial coverage of the glider transect and a full annual cycle coinciding with the timing of the glider deployment (see description in Satellite-derived datasets). Using these satellite chlorophyll data, the median of the annual time series (May 2012–April 2013) was calculated and

compared with the median of the glider sampling period (September 2012 to February 2013). The comparison showed that the satellite-chlorophyll median estimated from the annual time series (12 months) was 10% lower than the satellite-chlorophyll median estimated over the glider sampling period (5.5 months). Hence, in the bloom detection methods described below, the glider-chlorophyll annual median threshold was approximated to

$$\tilde{C}_{\text{annual}} = 0.9\tilde{C}_{5.5}, \quad (3)$$

where $\tilde{C}_{\text{annual}}$ is the annual glider-chlorophyll median value and $\tilde{C}_{5.5}$ is the 5.5 months glider-chlorophyll median value.

Threshold method

The date of phytoplankton bloom initiation is estimated as the first day that surface and *MLD*-integrated chlorophyll exceeds 5% of the annual median. This threshold has been used successfully in previous studies based on ocean-colour remote sensing observations in the North Atlantic (e.g. Siegel *et al.*, 2002; Brody *et al.*, 2013) and in the Southern Ocean (Thomalla *et al.*, 2011; Racault *et al.*, 2012; see Supplementary Figure S2a and b).

Cumulative sum method

The date of phytoplankton bloom initiation is estimated as the first day that the cumulative summation of surface and *MLD*-integrated chlorophyll exceeded 15% of the maximum cumulative sum of the glider-chlorophyll time series. This method has been previously applied to zooplankton time series (Greve *et al.*, 2005) and to ocean-colour remote sensing observations (Batten and Mackas, 2009; Brody *et al.*, 2013) (see Supplementary Figure S2c and d).

Rate of change method

The date of phytoplankton bloom initiation is estimated as the day(s) on which the daily rate of change of surface and *MLD*-integrated chlorophyll increased 15% above the annual median rate of change and remained above this threshold for a minimum of 8 d (Brody *et al.*, 2013). The daily rate of change was calculated as the daily difference in surface and *MLD*-integrated chlorophyll. A 60-d filter was applied to the dataset to smooth the time series and reduce noise (see Supplementary Figure S2e and f).

Cumulative sum of anomalies method

The date of phytoplankton bloom initiation is estimated as the day of the largest step change in the cumulative sum of the anomalies of surface and *MLD*-integrated chlorophyll (Racault *et al.*, 2015). In this method, a step change is observed when the trend in the cumulative sum of anomalies changes direction (from a decreasing trend to an increasing trend). The timing of the change in direction indicates the date that the chlorophyll concentration in the time series is equal to the median chlorophyll concentration of the annual time series (see Supplementary Figure S2g and h).

Cumulative sum of anomalies of positive growth rates method

The date of phytoplankton bloom initiation is estimated as the day of the largest step change in the cumulative sum of the anomalies of positive daily rates of change in integrated chlorophyll. Net population growth rates can be calculated from two measures of biomass separated by a period and were here calculated as the daily difference or slope of *MLD*-integrated chlorophyll. Positive daily growth rates (positive slopes) infer positive *NCP*, whereas negative growth rates (negative slopes) infer net community loss. Consecutive daily

rates of change in the same direction were averaged over the number of consecutive days. The cumulative sum of the anomalies of the positive slopes highlights changes in trends in positive net population growth rates of the glider time series, whereas the cumulative sum of the anomalies of the negative slopes shows adjustments in trends of community losses. The bloom initiation date was selected as the date of maximum change in positive daily growth rates indicative of a regime shift towards a phase of positive net community growth (see Supplementary Figure S2i).

Primary production

Water column *PP* rates were calculated according to Platt *et al.* (1980) and Platt and Sathyendranath (1993) using the following equations:

$$PP_0 = P_{\text{max}} \times (1 - e^{-\alpha I_0^m / P_{\text{max}}}), \quad (4)$$

where PP_0 is *PP* in $\text{mg C m}^{-2} \text{d}^{-1}$ at the surface, P_{max} is the assimilation number defined as the height of the production–irradiance ($P-I$) curve, α is the initial slope of the $P-I$ curve, and I_0^m is daily *PAR* at the surface. To convert midday *PAR* to daily *PAR*, surface midday *PAR* was extrapolated over daylight hours by using maximum *PAR* at midday and assuming zero *PAR* at sunrise and sunset (given the assumption of a constant gradient of light between sunrise and midday and back to sunset). The parameters P_{max} and α are estimated from power law regression functions between P_{max} and chlorophyll ($R^2 = 0.84$) and between α and chlorophyll ($R^2 = 0.76$) based on a compilation of $P-I$ incubation experiments from the Southern Ocean (Dower and Lucas, 1993; Hiscock, 2004; Hiscock *et al.*, 2008; E.A. Kean, unpublished data) (see Supplementary Figure S3a and b).

The light adaptation parameter of the $P-I$ curve I_k is defined by the identity

$$I_k = \frac{P_{\text{max}}}{\alpha}. \quad (5)$$

Then, to generalize our results we normalized the surface irradiance by calculating I_*^m , the dimensionless daily surface irradiance

$$I_*^m = \frac{I_0^m}{I_k}. \quad (6)$$

The dimensionless function $f(I_*^m)$ for daily *PP* was solved analytically by Platt *et al.* (1980) as

$$f(I_*^m) = 0.7576 \ln I_*^d + 0.5256. \quad (7)$$

The values of $f(I_*^m)$ from the above analytic solution were tabulated for the range for $0.2 \leq I_*^m \leq 20$ by Platt and Sathyendranath (1993; their Table A1).

The *PP* integrated over the entire water column PP_{wc} ($\text{mg C m}^{-2} \text{d}^{-1}$) is calculated as follows:

$$PP_{\text{wc}} = PP_0 \times \frac{f(I_*^m)}{k_d}, \quad (8)$$

where k_d is the vertical attenuation coefficient of irradiance calculated from an exponential fit to each midday glider *PAR* profile.

The variable *PP* integrated within the mixed layer PP_{mld} ($\text{mg C m}^{-2} \text{d}^{-1}$) was calculated by subtracting *PP* estimated from the bottom of the mixed layer to the lower end of the water column.

Phytoplankton-specific growth rate

Phytoplankton-specific growth rate, expressed in the time dimension (d^{-1}), was calculated by dividing PP integrated within the euphotic depth PP_{wc} with integrated phytoplankton carbon biomass (POC_{int}) ($mg\ C\ m^{-2}$) estimated from glider midday phytoplankton-specific carbon (C_{phyto}) integrated from the surface to the deeper of MLD and z_{eu} (i.e. when $z_{eu} > z_{mld}$ then POC_{int} is integrated from surface to z_{eu} and vice versa), such that

$$\mu = \frac{PP_{wc}}{POC_{int}}. \quad (9)$$

Net community production and respiration

With the rates of PP calculated as above, together with knowledge of bloom initiation dates, MLD , and surface irradiance, we can resolve the critical depth model of Sverdrup (1953). This model, which is described step by step below, allows us to generate a compensation irradiance for each bloom initiation date (see also Siegel et al., 2002) and to output an ensemble of time series of daily rates of plankton community respiration and NCP for the glider transect.

In the ocean water column, irradiance levels decrease exponentially with depth:

$$I(z) = I_0 e^{-k_d z}, \quad (10)$$

where $I(z)$ is PAR at depth z , I_0 is surface irradiance, and k_d is the vertical attenuation coefficient of irradiance. Sverdrup's critical depth model assumes, at the start of the spring bloom, that PP is linearly related to the level of PAR such that PP is described to decrease exponentially with depth:

$$PP(z) = \propto I(z) = \propto I_0 e^{-k_d z} = PP_0 e^{k_d z}, \quad (11)$$

where $PP(z)$ is PP at depth z . Community respiration is assumed to remain constant with depth:

$$R(z) = R_0, \quad (12)$$

where $R(z)$ is community respiration at depth z and R_0 is community respiration at the surface. The minimum level of irradiance required for production to compensate community respiration at a particular depth is defined as community compensation irradiance I_c , which occurs at the compensation depth z_c :

$$I_c = I_0 e^{-k_d z_c}. \quad (13)$$

At compensation depth z_c production and respiration are equal:

$$R_0 = PP_0 e^{-k_d z_c}. \quad (14)$$

Hence, I_c can be defined as

$$I_c = \frac{I_0 R_0}{PP_0}. \quad (15)$$

The integrated production from the surface to z_{mld} is

$$PP_{mld} = PP_0 \int_0^{z_{mld}} e^{-k_d z} dz = \frac{PP_0}{k_d} (1 - e^{-k_d z_{mld}}). \quad (16)$$

The integrated respiration in the mixed layer is

$$R_{mld} = R_0 \int_0^{z_{mld}} dz = R_0 z_{mld}. \quad (17)$$

The depth at which rates of integrated production and respiration are equal is defined as the critical depth z_{cr} :

$$PP_{z_{cr}} = R_{z_{cr}}. \quad (18)$$

Sverdrup's necessary condition for initiation of the phytoplankton bloom is that integrated mixed layer production must compensate for respiration such that net positive growth can occur. This allows the critical depth to be defined as the depth where

$$\frac{1}{k_d z_{cr}} (1 - e^{-k_d z_{cr}}) = \frac{R_0}{PP_0} = \frac{I_c}{I_0}. \quad (19)$$

According to Sverdrup's hypothesis, at the time of the bloom initiation, depth-integrated production compensates exactly for respiration when the depth of the mixed layer z_{mld} coincides with the critical depth z_{cr} . The variables in Equation (19) are now available to solve for I_c . From glider transect data, we can compute a time series of critical depth z_{cr} based on Equation (19) assuming that I_c remains constant over time:

$$\frac{1}{k_d z_{cr}} (1 - e^{-k_d z_{cr}}) - \frac{I_c}{I_0} = 0. \quad (20)$$

All the variables are then available to solve for daily respiration along the glider transect using Equation (15).

Finally, NCP is calculated as

$$NCP = PP_{mld} - R_{mld}. \quad (21)$$

Biomass accumulation

The biomass accumulation rate of a phytoplankton population (r) can be calculated from two measures of biomass separated by a period ($\Delta t = t_2 - t_1$) according to Boss and Behrenfeld (2010):

$$r = \frac{\ln(Chl_{mean_{t_1}}/Chl_{mean_{t_0}})}{\Delta t} \quad (22)$$

if MLD is shoaling and $MLD > z_{eu}$ and

$$r = \frac{\ln(Chl_{int_{t_1}}/Chl_{int_{t_0}})}{\Delta t}, \quad (23)$$

in all other cases, where Chl_{int} is daily midday chlorophyll integrated from the surface to the deeper of MLD and z_{eu} . The variable Chl_{int} is the daily midday mean chlorophyll concentration in the mixed layer, and $\Delta t = 1$ d.

Results and discussion

Bio-optical sensors on autonomous platforms (e.g. gliders and floats) provide highly cost-effective measurements at the relevant time (subseasonal to seasonal) and space scales (meso- to submesoscale) to link the physical forcing mechanisms associated with climate change to ecosystem responses in primary productivity.

Given the growing importance of autonomous platforms in the trajectory of Southern Ocean ecosystem understanding, it is necessary that we maximize the value of these multi-sensor observations by developing appropriate applications and interpretations. This study shows how an ~ 5.5 -month high-resolution glider transect in the SAZ can be used to characterize the biological seasonal cycle through phytoplankton biomass distribution, phenological metrics of bloom initiation as well as seasonal changes in *PP*, respiration, and *NCP*. To help us understand some of the environmental drivers of these biological variables, the physical variables of *MLD*, stratification, mean *PAR* in the mixed layer, mean daily net heat flux, and surface windstress are concurrently investigated at high space and time resolution during the sampling period from spring through summer in the SAZ.

We are mindful that the not fully Lagrangian sampling nature of the gliders raises the possibility that meso- to submesoscale features, crossed by the gliders could influence our interpretation of the data as a Lagrangian time series. A study by Swart *et al.* (2014) addressed this issue by investigating the variability of mixed layer characteristics (*MLD* and stratification) between the glider data presented in this study and a second glider that was simultaneously sampling the SAZ. Their results (their Supplementary Figure S1) showed temporal coherence in *MLD* between both gliders at varying spatial separation scales (up to 213 km apart). These results support the view that subseasonal *MLD* variability was primarily forced by synoptic-scale windforcing (and not submesoscale features) particularly in the summer (*MLD* difference < 20 m). Since the spatial scale of the dominant mode of variability in the physics is synoptic (10's to 1000's of km) and the glider is sampling at an ~ 3 km spatial scale, the data during this period can be interpreted as quasi-Lagrangian.

However, weak stratification combined with the presence of meso- to submesoscale features in spring (September–October) resulted in a more variable influence of the windfield and accounts for the greater *MLD* differences observed between the two gliders (often > 100 m) at the beginning of the time series. To investigate this issue further, a continuous wavelet transform (CWT) of the surface (mean in top 20 m) salinity, chlorophyll, and *MLD* time series was used to investigate the dominant scales of variability (Supplementary Figure S4a–c). The CWT of surface salinity, used here as an indicator of water mass variations, shows that the dominant temporal scales of variability occur at periods > 4 d (particularly within the second half of the time series, > 16 d) (Supplementary Figure S4a). There is little evidence of mesoscale activity (2–4 d) driving the variability with only one noteworthy feature observed on Days 50–70 in mid-October. On the contrary, variability in surface chlorophyll is dominated by short period (< 8 d) variability (Supplementary Figure S4b) throughout the time series, which are strongly linked to *MLD* variability (Supplementary Figure S4c) in response to synoptic wind events as shown by Swart *et al.* (2014). To summarize: (i) since the glider is resolving fine temporal (6 h) and spatial (~ 3 km) scales; (ii) since the primary scales of variability observed in the physics are not feature-driven adjustments on the meso- or submesoscale, except for some explicit examples in spring (Swart *et al.*, 2014), (iii) since *MLD* variability is driven largely by large-scale synoptic wind events; then (iv) although there may be instances where the observations are affected by spatial aliasing the dominant signal of variability is considered to be driven by temporal evolution at time scales resolved by the glider sampling.

Surface layer physics and chlorophyll distribution

To illustrate the evolution of the biogeophysical data, we present time-series measurements of temperature, ocean stratification (using the Brunt-Väisälä frequency, *BVF*, also known as buoyancy frequency), *MLD*, and chlorophyll (Figure 2a–c).

In spring (September–November), the upper ocean physical structure is characterized by variable *MLD* ranging between 12 and 272 m (mean = 80 ± 52 m) (Figure 2a). The *BVF* shows that variable *MLD* is associated with a weakly stratified upper layer (*BVF* ~ 0), which extends to the “seasonal” pycnocline (the depth of the stratification maximum), found between 200 and 300 m from September to October and between 50 and 150 m from November to December (Figure 2b) (Swart *et al.*, 2014). These episodic events of rapid *MLD* shoaling (> 160 m d^{-1}) were synonymous with relatively short lived (~ 1 week) increases in stratification ($1-2 \times 10^{-5} \text{ s}^{-2}$) that could not be explained by surface warming-induced buoyancy increases (net heat flux was too weak to initiate observed rates of stratification, $> 3 \times 10^{-5} \text{ s}^{-2} \text{ d}^{-1}$, see Swart *et al.*, 2014). These events were instead assigned to feature-driven stratification from slumping of the lateral density gradient during periods of low windstress (Mahadevan *et al.*, 2012; Swart *et al.*, 2014). In particular, the elevated doming of the pycnocline and maximum stratification (> 200 m) seen in the first 2 weeks of the time series is related to the crossing of the centre of a cold-core mesoscale cyclone (approximate diameter 200 km from satellite sea surface height observations) (Swart *et al.*, 2014). From the end of November onwards, a consistent increase in stratification in the upper 150 m is observed (Figures 2b and 4b) together with increasing surface temperatures and decreasing surface densities (see Swart *et al.*, 2014 their Figure 8a and b) that are believed to result from seasonal surface heating (Swart *et al.*, 2014). At the end of November (around 28 November), the surface mixed layer merges and remains coupled with the deeper seasonal thermocline for the rest of the time series. In summer, December to February, surface waters undergo a consistent warming (Figure 2b) caused by increased solar radiation and positive air-sea heat flux. During these months, stratification in the upper 150 m increases continually as the gradient in the thermocline sharpens with the warming surface waters (Figure 4b). The *MLD* becomes shallower (mean = 40 ± 16 m) and shows relatively large variations at meso- to submesospatial scales and subseasonal time scales.

A comparison of the glider-surface chlorophyll with the satellite chlorophyll time-series places the timing of the glider time series into context of a full annual time series (Figure 3). Standard satellite algorithms are known to underestimate chlorophyll-*a* concentrations by two to three times in the Southern Ocean (Mitchell and Kahru, 2009; Kahru and Mitchell, 2010). Although the glider was not able to sample the seasonal minimum in August, its outset in late September captures the beginning of the spring bloom and extends well into summer, following which a sustained bloom is evident in the satellite chlorophyll concentrations that extend into June (Figure 3). At the beginning of the transect (September–October), chlorophyll is generally low ($< 0.4 \text{ mg m}^{-3}$), except for an ~ 7 -d period from 6 to 13 October where higher chlorophyll concentrations ($0.4-0.5 \text{ mg m}^{-3}$) coincide with shallower *MLDs* (~ 15 m) (Figure 2c). On 2 November, shallow *MLDs* (~ 20 m) once again coincide with higher chlorophyll ($> 0.4 \text{ mg m}^{-3}$) this time persisting and generally increasing with high-frequency variability into summer (December–February), where chlorophyll concentrations are considerably higher ($> 0.6 \text{ mg m}^{-3}$) and sustained

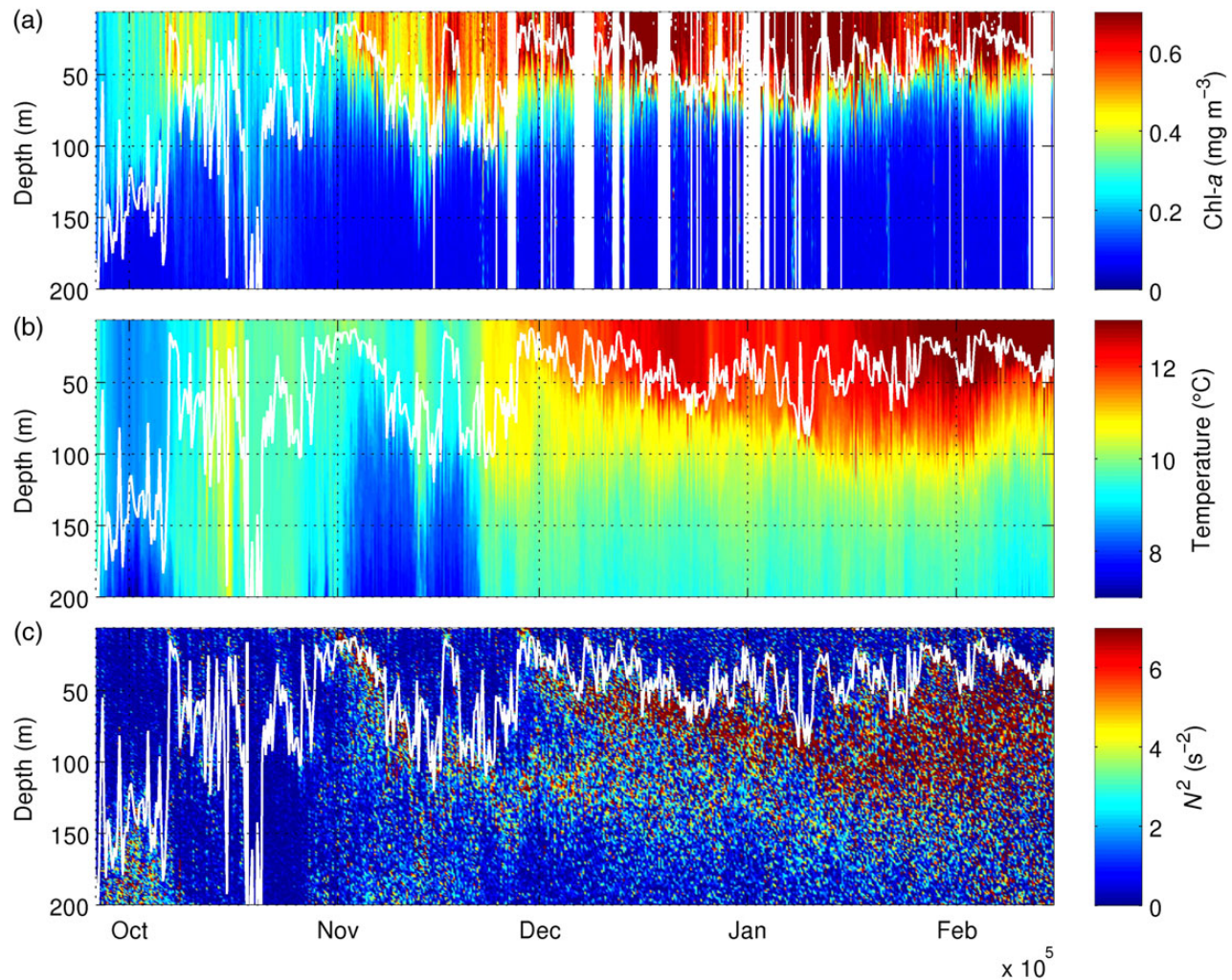


Figure 2. Sections for the glider time series from 25 September 2012 to 15 February 2013 of (a) chlorophyll-*a* concentration (mg m^{-3}), (b) temperature ($^{\circ}\text{C}$), and (c) Brunt-Väisälä frequency (s^{-2}) used as an index for stratification. The MLD, where $\Delta T_{10\text{m}} = 0.2^{\circ}\text{C}$, is overlaid in white. This figure is available in black and white in print and in colour at *ICES Journal of Marine Science* online.

through to the end of the transect. The distribution of chlorophyll is discussed in more detail in *Swart et al. (2014)*. This study expands on this research by providing a stronger focus on interpreting *PP*, respiration, and *NCP* (in the sections below) in terms of the underlying physical drivers, highlighting the important time scales of variability that characterize the seasonal cycle.

Bloom initiation and time-scale sensitivity

The concept of a bloom is qualitatively agreed upon as a condition of increased phytoplankton biomass (*Behrenfeld and Boss, 2014*) however; blooms can result from rapid growth (*Platt et al., 1991*) or can develop over long periods (*Behrenfeld, 2010*). Similarly, a bloom can be short lived and intermittent or sustained over a growing season. Although the onset of phytoplankton blooms has undergone increasing research focus in the last decade (especially with the availability of continuous, high resolution and high frequency, repeat remote-sensing chlorophyll time series), important debate remains as to what processes are most important (and at which time scales) for high growth rates that prompt bloom onset. In this study, five methods (described in Section 2.6) were applied to both the glider-surface and *MLD*-integrated chlorophyll time series to estimate dates

of phytoplankton bloom onset and the community compensation irradiance at the time of bloom initiation (Tables 1 and 2), which was then used to initialize Sverdrup's critical depth model (see Methods). The motivation to estimate the bloom initiation dates based on both surface and *MLD*-integrated time series was twofold: (i) the analysis of surface chlorophyll can be compared with remotely sensed observations and (ii) to examine and resolve subsurface dynamics using profile glider data, which is not possible when using only satellite remote-sensing measurements. On the occasions when the estimated initiation dates fell within 3 d of each other, the dates were "rounded-off", and in the end, a total of six distinct bloom initiation dates were identified from the two time series (Figures 4a and 1a).

Five of the six bloom initiation dates were estimated in spring (from 28 September to 25 November) and one in early summer (12 December). Given that it was only after the end of November that there was sufficient heat flux to explain observed increases in stratification, only the last two bloom initiations in the time series (25 November and 12 December) would appear to strictly adhere to Sverdrup's critical depth hypothesis, where seasonal surface heating is considered the primary driver of shallower mixed layers, which then allows for biomass accumulation and high

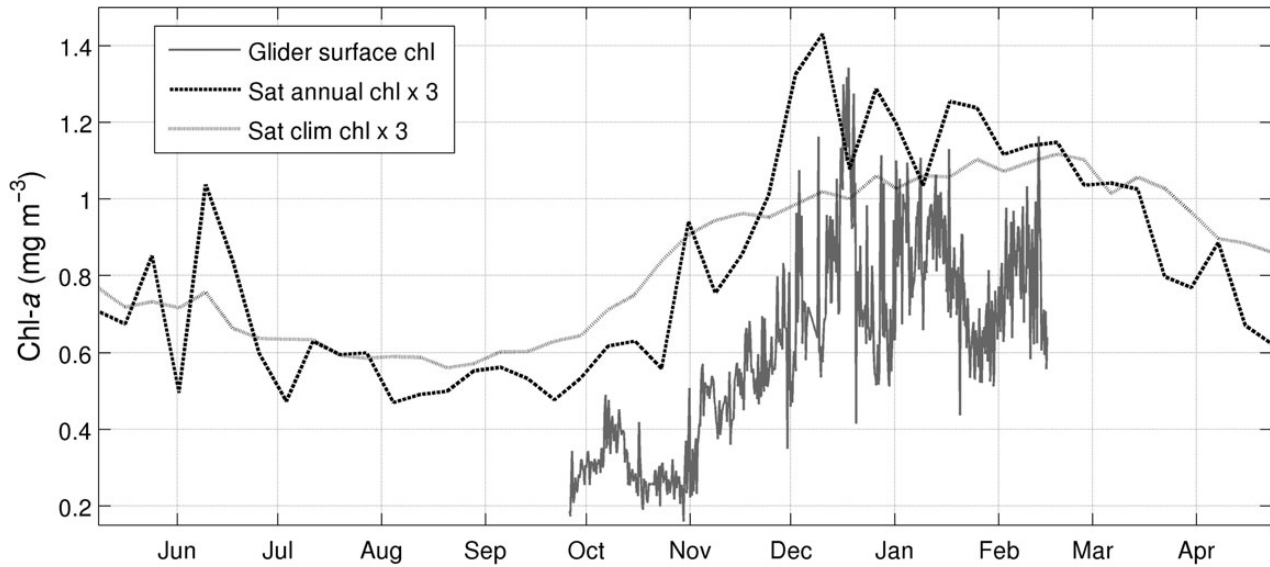


Figure 3. Seasonal cycle of glider-surface chlorophyll (mg m^{-3}) and satellite surface chlorophyll (mg m^{-3}) multiplied by 3 to facilitate display on a single axis. Dark grey solid line: glider 6 h surface chlorophyll time series; black dotted line: OC-CCI satellite surface chlorophyll data averaged over the region $40.9\text{--}43.7^\circ\text{S}$, $11\text{--}2.9^\circ\text{W}$ (encompassing the spatial coverage of the glider transect) for the period September 2012–September 2013 (coinciding with the timing of the glider deployment); light grey solid line: OC-CCI satellite surface chlorophyll climatology (September 1997–April 2013) averaged over the region $40.9\text{--}43.7^\circ\text{S}$, $11\text{--}2.9^\circ\text{W}$.

Table 1. Bloom initiation dates and compensation irradiances (I_c) from five different bloom initiation detection methods applied to surface chlorophyll and MLD-integrated chlorophyll time series.

Bloom initiation detection method	Surface chlorophyll	I_c ($\mu\text{E m}^{-2} \text{s}^{-1}$)	MLD-integrated chlorophyll	I_c ($\mu\text{E m}^{-2} \text{s}^{-1}$)
Threshold	17 November	1036	26 September	36
Cumulative sum	06 November	116	15 October	51
Rate of change	29 September, 13 December	75, 280	18 November, 11 December	445, 796
Cumulative sum of anomalies	17 November	1036	08 November	171
Cumulative sum of anomalies of positive growth rates			24–25 November	338

Table 2. When bloom initiations fell within 3 d of each other the dates were “rounded-off” to give six distinct bloom initiation dates identified using both the surface and MLD-integrated chlorophyll time series.

Bloom initiation detection methods	Bloom Initiation dates	Rounded off bloom initiation dates
Threshold (MLD), rate of change (surf)	26–29 September	28 September
Cumulative sum (MLD)	15 October	15 October
Cumulative sum (surf), cumulative sum of anomalies (MLD)	06–08 November	07 November
Threshold (surf), cumulative sum of anomalies (surf), rate of change (MLD)	17–18 November	17 November
Cumulative sum of anomalies of positive growth rates (MLD)	24–25 November	25 November
Rate of change (surf and MLD)	11–13 December	12 December

growth rates. The first four bloom initiation dates (28 September, 15 October, 7 November, and 17 November) on the other hand are more likely explained by an extension of Sverdrup’s hypothesis, where bloom initiation is invoked by a shoaling of the mixed layer above a critical depth through feature-driven stratification (Mahadevan *et al.*, 2012), and to potential decreases in the dominant mixing length scales (Brody and Lozier, 2014) as well as decreased rates of turbulent mixing that allow phytoplankton to gain sufficient light exposure to bloom even when seasonal mixed layers are deep (Chiswell, 2011; Taylor and Ferrari, 2011; Chiswell *et al.*, 2013).

Interestingly, none of the methods of bloom detection were sensitive to selecting the high chlorophyll region associated with the

mesoscale feature-driven stratification (Mahadevan *et al.*, 2012) observed during the second week of October (Figure 2c). These results suggest that the bloom detection methods implemented here may be more sensitive to characterizing biological and physical processes occurring on seasonal timescales. In addition, the mathematical procedures inherent in the methods themselves make interpreting the bloom initiation dates in terms of the underlying physical environment (observed at the time of the estimated bloom initiation date) challenging. For example, both the threshold and cumulative sum methods of bloom detection depend on a percentage biomass relative to a threshold criterion (e.g. median chlorophyll concentration) and appear insensitive to subseasonal feature-driven

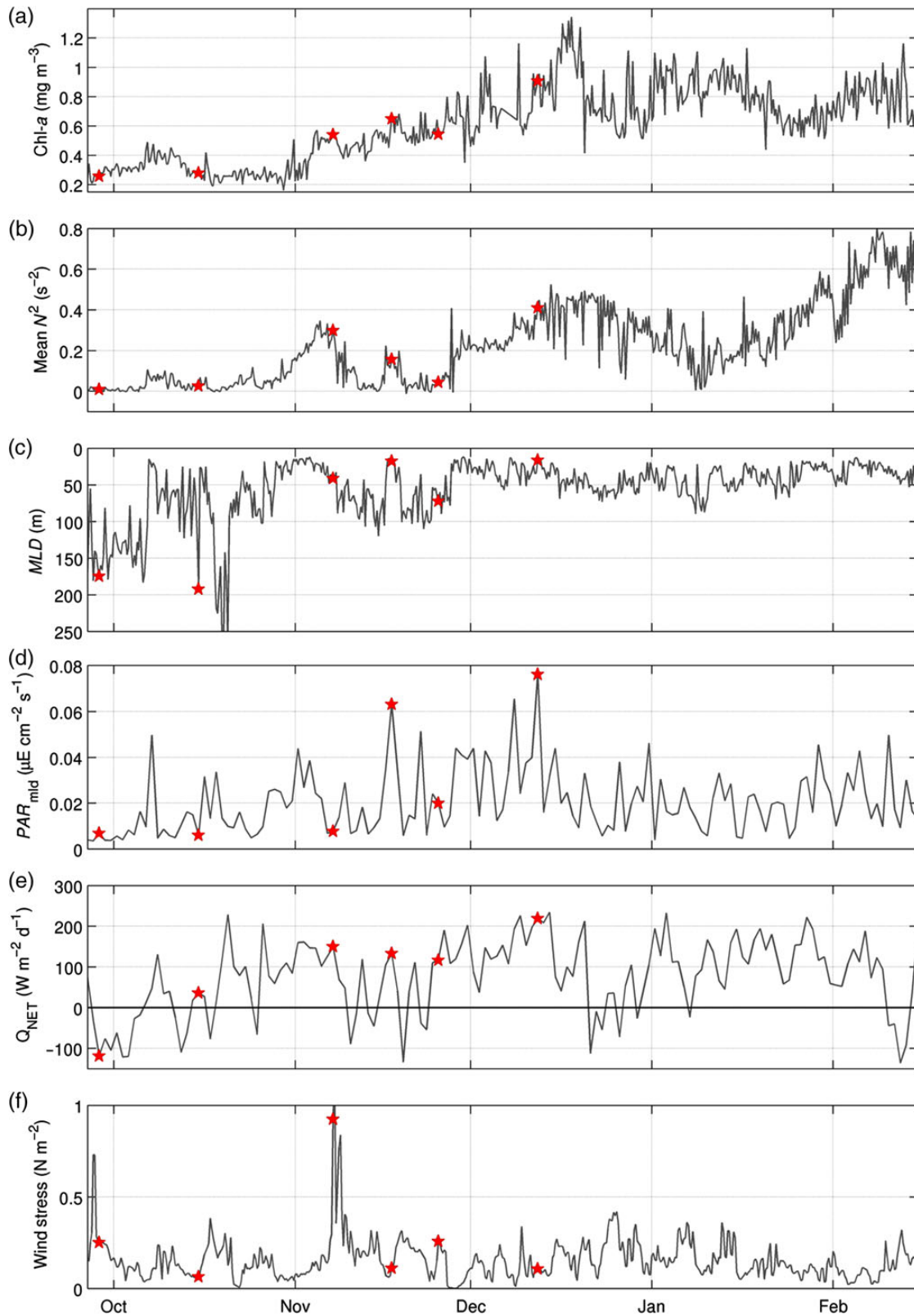


Figure 4. Time series of (a) surface chlorophyll-*a* concentration (mg m^{-3}), (b) mean Brunt-Väisälä frequency (s^{-2}) in the top 100 m, (c) MLD (m), where $\Delta T_{10\text{m}} = 0.2^\circ\text{C}$, (d) mean PAR ($\mu\text{E cm}^{-2} \text{s}^{-1}$) in the MLD, (e) net incoming heat flux ($\text{W m}^{-2} \text{d}^{-1}$), and (f) surface windstress (N m^{-2}). Bloom initiation dates are overlaid as red stars. This figure is available in black and white in print and in colour at *ICES Journal of Marine Science* online.

adjustments in biomass observed in this high-resolution glider time series both. Similarly, both the cumulative sum of anomalies methods that select the most evident regime shift in the time series is likely to be insensitive to intermittent patchy blooms associated with feature-driven adjustments in stratification seen early in the season. Rather, these methods are designed for identifying the start of the sustained growing period which can be used as a key ecological indicator to characterize marine ecosystems and are specifically not sensitive to sporadic and patchy blooms, typical of highly variable systems, that if included, create a high standard deviation around the bloom initiation date and can make it difficult to systematically monitor the state of the ecosystem.

On the other hand, the rate of change method of detecting a bloom, which is able to select multiple initiation dates within a time series (provided the selection criteria are met), is likely to be sensitive to mesoscale feature-driven blooms such as the one evidenced here (second week of October). However, Supplementary data, Figure S2e shows that despite consistently higher surface chlorophyll concentrations ($\sim 0.4 \mu\text{g l}^{-1}$) associated with the eddy-driven stratification and *MLD* shoaling in the second week of October, the most rapid rate of change of surface chlorophyll (indicative of phytoplankton growth) was evidenced earlier in the time series over the ~ 10 d transitioning September to October, where chlorophyll concentrations increase from 0.2 to $\sim 0.4 \mu\text{g l}^{-1}$. Hence, the rate of change method selects 28 September as the bloom initiation date and not the high chlorophyll region associated with the mesoscale feature in the second week of October. This highlights the point that population growth rates (the change in biomass with time) can be high even if biomass is low and vice versa. This can occur in many ways, first, high cell division rates can drive high growth rates even if phytoplankton biomass is low (but increasing), or population growth rates can increase independent of phytoplankton division rates if there is a reduction in losses (e.g. a decrease in grazing through dilution associated with *MLD* deepening Behrenfeld and Boss, 2014). Similarly, in high biomass areas, high phytoplankton division rates can be equally matched by high grazing rates to result in low population growth rates. Although *MLDs* are deep, this particular bloom (28 September) is associated with an *MLD* shoaling (Figure 4c) and high rates of PP (Figure 6), suggesting that increased division rates (and not a reduction in grazing) are responsible for the increased rates of population growth observed over this period. Finally, the newly developed bloom detection method (cumulative sum of anomalies of positive growth rates) appears to provide a robust approach to identifying the bloom initiation that is associated with a regime shift towards a phase of positive net community growth. This was in fact the only method which selected a date that coincides with the date of transition from the spring blooming phase to summer sustained phase described by Swart *et al.* (2014).

To summarize, the concurrent examination of mathematically defined timings of initiation together with changes occurring in the physical environment highlights different time-scale sensitivities of the different bloom detection methods. More specifically, each method appears prone to detect more subtle or more persistent changes in the chlorophyll time series, occurring in response to different physical processes. Statistical methods (e.g. threshold and cumulative sum) appear not to be sensitive to sporadic blooms observed in the glider time series and hence these methods may perform better when characterizing the phenology of marine ecosystems by identifying the start of sustained growing periods. The rate of change method on the other hand appears sensitive to patchy

blooms, typical of highly variable systems, and can select multiple blooms within a time series. It must be emphasized to note that although some of the bloom detection methods may not be sensitive to detecting patchy blooms earlier in the season; these blooms can make a major contribution to the regions seasonally integrated phytoplankton biomass and can lead to a substantial overall increase in carbon fixation (Mahadevan *et al.*, 2012; Swart *et al.*, 2014).

The bimodal nature of the spring bloom observed here (i.e. spring blooming phase vs. summer sustaining phase; Swart *et al.*, 2014) is of particular scientific interest. It shows that the spatially and temporally heterogeneous blooms in early spring (September to mid-November) are controlled by subseasonal changes in the physical forcing which do not maintain sufficient stability in the structure of the water column to preserve positive growth rates (Platt *et al.*, 2003). Whereas, on seasonal timescales, it appears that water column stability, driven by synoptic-scale shoaling of the mixed layer through seasonal surface heating, is the most important factor controlling the accumulation of biomass and high growth rates that are sustained into a prolonged growing period as shown in the more spatially homogenous bloom observed late in spring/early summer (late-November to mid-December).

Seasonal variability in primary production

In this study, the model of Platt *et al.* (1980) and Platt and Sathyendranath (1993) is applied to the glider data to generate a high-resolution transect of *PP*. This model describes phytoplankton photosynthesis as a continuous function of available light based on an initial linear response to light availability through to light saturating conditions. By definition, *PP* is the amount of photosynthetically fixed carbon available to the first heterotrophic level and, as such, is a relevant metric for addressing environmental questions ranging from trophic energy transfer to the influence of biological processes on carbon cycling (Linderman, 1991). One of the most important steps when implementing a *PP* model is the assignment of the photosynthesis-irradiance parameters. In the present study, these parameters were estimated based on empirical relationships with chlorophyll concentration derived from *in situ* measurements. This approach has been previously demonstrated for instance in the Black Sea (Finenko *et al.*, 2004). More advanced and complete methods to estimate photosynthesis-irradiance parameters have been developed that include: (i) empirical relationships between the assimilation number and variables of light, temperature, and nutrients (Saux Picart *et al.*, 2013) empirical relationships between the assimilation number and variables of light, temperature, and chlorophyll concentration (Saux Picart *et al.*, 2013); (ii) a nearest-neighbour method that assigns the photosynthesis-parameters according to chlorophyll concentration and surface temperature by searching a regional *in situ* database (Platt *et al.*, 2008); and (iii) functional relationships between photosynthesis-irradiance parameters, environmental variables, and phytoplankton community structure (Huot *et al.*, 2013). In the present study, the availability of concurrent *in situ* measurements of photosynthesis-irradiance parameters, environmental and community structure variables were limited and it was not possible to implement the latter two methods. However, it is anticipated that a refined estimation of the photosynthesis-irradiance parameters would help to reduce the uncertainty of glider estimates of phytoplankton *PP* by up to 20% (Platt *et al.*, 1995).

Relatively low rates of *PP* ($\sim 150 \text{ mg C m}^{-2} \text{ d}^{-1}$) were generally observed in early spring (September through October) (Figure 6) likely driven by limited light availability ($< 0.02 \mu\text{E cm}^{-2} \text{ s}^{-1}$, Figure 4d) in a predominantly deep mixed layer ($> 100 \text{ m}$,

Figure 4c) associated with low rates of surface warming, which are consistent with early spring solar radiation and low air-sea heat exchange (Figure 4e). In the first week of October, a slight increase in PP ($\sim 200 \text{ mg C m}^{-2} \text{ d}^{-1}$) was apparent in association with a cold-core mesoscale eddy (see Swart *et al.*, 2014). Higher PP values were found towards the centre of the eddy where $MLDs$ were deep ($\sim 150 \text{ m}$) (Figure 4c) and chlorophyll concentrations low ($\sim 0.3 \mu\text{g l}^{-1}$) (Figure 4a). Phytoplankton growth in deep mixed layers has been shown to be possible when the full mixed layer is not actively mixing due to a reduction in turbulent mixing (Huisman *et al.*, 1999; Chiswell, 2011; Taylor and Ferrari, 2011). On crossing the edge of the eddy, an increase in stratification (Figures 2b and 4b) is characterized by considerably shallower $MLDs$ (Figure 4c) hypothesized to be driven by water mass layering or slumping of the sharper lateral density gradients. Similar conditions were observed by Mahadevan *et al.* (2012) in the North Atlantic, who showed that mixed layer eddies may initiate blooms earlier in the season than surface heating alone. In our study, increased rates of PP were not particularly evident in association with the eddy-driven stratification and MLD shoaling (Figure 4b and c, respectively) despite increased concentrations of chlorophyll biomass (Figure 2c).

At the end of October/beginning of November a dramatic shoaling of the MLD for 10 d from ~ 100 to $\sim 25 \text{ m}$ (Figure 2c), driven by a combination of decreased windstress (Figure 2f), increased heating (Figure 4e) and resultant relaxation of the lateral buoyancy gradient associated with wind-front dynamics (Mahadevan *et al.*, 2012; Swart *et al.*, 2014), accounts for the stark contrast between MLD -integrated PP ($\sim 50 \text{ mg C m}^{-2} \text{ d}^{-1}$) and water column PP ($\sim 250 \text{ mg C m}^{-2} \text{ d}^{-1}$) (Figure 6). The drop in MLD -integrated PP is a consequence of the loss of chlorophyll from the mixed layer through rapid shoaling (~ 100 to $\sim 20 \text{ m}$ in 4 h). However, this chlorophyll is still viable and remained within the euphotic zone actively photosynthesizing and contributing to the observed increase in water column-integrated PP , reaching values of up to $\sim 250 \text{ mg C m}^{-2} \text{ d}^{-1}$ (Figure 6). Both MLD - and water column-integrated PP rates continued to increase during the month of November until mid-December, with high sub-seasonal variability, reaching a maximum of $\sim 500 \text{ mg C m}^{-2} \text{ d}^{-1}$ in mid-December. This increasing trend in PP (Figure 6) is associated with an increase in heat flux (Figure 4e), stratification (Figure 4b), a shoaling of the mixed layer (Figure 4c) consistent with the progression from spring into summer and results in increased concentrations of chlorophyll from $\sim 0.5 \mu\text{g l}^{-1}$ at the beginning of November to maximum surface concentrations of $\sim 1.2 \mu\text{g l}^{-1}$ in mid-December (Figures 2c and 4a).

Towards the end of the time series in summer, integrated PP rates fluctuated rapidly (~ 4 – 6 d) between ~ 200 and $\sim 400 \text{ mg m}^{-2} \text{ d}^{-1}$ from mid-December to mid-January and between ~ 100 and $\sim 200 \text{ mg m}^{-2} \text{ d}^{-1}$ from mid-January to mid-February. In a study by Swart *et al.* (2014) on the same glider dataset, enhanced stratification in summer was shown to prevent significant deepening of the MLD (to $> 80 \text{ m}$), which remained highly variable at subseasonal time scales, fluctuating around a threshold of $\sim 40 \text{ m}$. These MLD variations were shown to be driven by the combined effect of elevated windstress from synoptic (4- to 9-d) storm events that deepened the MLD , followed by rapid shoaling during quiescent periods driven by buoyancy forcing from strong horizontal density gradients associated with meso- and submesoscale features. Their study, together with a study by Joubert *et al.* (2014), proposed that this mechanism was responsible for maintaining the balance between iron and light supply at appropriate time scales for phytoplankton growth

culminating in a sustained summer bloom (> 2.5 months longer than that found in the Polar Frontal Zone). These findings have more recently been corroborated in a study by Carranza and Gille (2015) that uses correlation analysis between chlorophyll, MLD , and temperature in the Southern Ocean to conclude that transient MLD deepening through wind mixing (from storms $< 10 \text{ d}$) leads to nutrient entrainment to support enhanced chlorophyll observed through summer (particularly in the SAZ). The sustained high PP rates observed by the glider in summer with high subseasonal variability (~ 4 – 6 d) supports the hypothesis of a mechanism of subseasonal Fe and light supply through MLD fluctuations in the SAZ that occur at time scales appropriate for phytoplankton growth.

Seasonal respiration and net community production

Understanding the nature of the trophic balance between oceanic production and respiration is key to predicting how climate change will affect air-sea CO_2 flux. Although estimates of PP have been extensively investigated over the last 30 years, estimates of loss rates are extremely difficult to measure and knowledge of community respiration and NCP is still relatively limited (del Giorgio and Duarte, 2002; Robinson and Williams, 2005; Robinson, 2008). A key question when trying to understand the global carbon cycle is whether regions of the ocean are a net source or sink of carbon. This will depend on the production of organic matter relative to their decomposition due to biological respiration (del Giorgio and Duarte, 2002). The difference between photosynthesis and respiration in the euphotic zone is set by the export term. Only a small fraction of organic matter produced during PP is exported to depth and sequestered away from the atmosphere for hundreds of thousands of years (Henson *et al.*, 2011), the bulk of organic matter being produced is instead remineralized in the upper ocean through biological respiration (Ducklow, 1995).

NCP is a measure of the metabolic balance between PP and the sum of auto- and heterotrophic respiration. At steady-state or over large spatial and temporal scales, NCP is equivalent to new production (Cassar *et al.*, 2011). Since storage of organic carbon in the mixed layer is modest with respect to production (Ducklow *et al.*, 2007), NCP can provide an estimate of the net amount of carbon removed from the atmosphere via the biological pump (Falkowski *et al.*, 2003; Stanley *et al.*, 2010; Huang *et al.*, 2012). Sverdrup's NCP model assumes that phytoplankton are homogeneously mixed throughout the upper mixed layer, that specific losses are constant with depth, and that specific growth rates are proportional to the amount of light in the water column. This means that as light increases with seasonal increases in PAR , the critical depth will deepen while the opposite is true for when losses increase, for example, increased grazing following a bloom will cause the critical depth to shoal (Supplementary Figure S6). Sverdrup's model was applied to satellite-derived data by Siegel *et al.* (2002) and Henson *et al.* (2006) in the North Atlantic and Lavigne *et al.* (2013) in the Mediterranean Sea to estimate a time series of the critical depth. Their results verified the critical depth model and showed that the spring bloom did not start while the MLD was deeper than the critical depth, highlighting the essential requirement for phytoplankton to receive, on average, a minimum critical light level to bloom.

Sverdrup's necessary condition for a bloom initiation is that integrated mixed layer production must compensate for respiration such that net positive growth occurs when the mixed layer is shallower than a critical depth. In other words, at the time of bloom initiation, the mixed layer depth must coincide with the critical depth. Despite the following: (i) that the mathematical methods of

detecting blooms do not necessarily reflect *in situ* physical drivers of the growing conditions that phytoplankton is exposed to on the day and (ii) that reduced turbulence (Chiswell, 2011; Taylor and Ferrari *et al.*, 2011; Chiswell *et al.*, 2013) and reduced mixing length scales (Brody and Lozier, 2014) can contribute to spring blooms even when seasonal mixed layers are deep; we initiate Sverdrup's critical depth model using all bloom initiation dates defined by the five methods (Table 1). As such we imply that all bloom initiations reflect Sverdrup conditions where the *MLD* is at a depth critical for net positive growth. Although not necessarily true, doing so allows us to determine a range of community compensation irradiances and hence to model an ensemble of time series of daily respiration and *NCP* along the glider time series (Supplementary Figure S5a and b) (see Methods). This approach also allows us to investigate the sensitivity of Sverdrup's model to different compensation irradiance levels and hence to different methods of bloom detection (Figure 5a).

Including all bloom dates to initiate the model, as opposed to selecting only the ones where *MLDs* were presumed to be shallow enough to adhere to Sverdrup's critical depth criteria, prevents any subjective bias, increases the possible range of calculated respiration rates and provides a more robust calculation of mean rates of *NCP* for the time series. In addition, inclusion of all bloom initiation dates to generate a standard mean error (Figure 3b and c) highlights periods in the time series when standard mean errors are low and confidence levels in the interpretation of the community as net heterotrophic (negative *NCP*) or net autotrophic (positive *NCP*) are increased. The single time series of respiration and *NCP* generated from the 25 November bloom initiation (selected using the cumulative sum of anomalies of positive growth rates method developed by the authors) is however included in the figures and discussion as the authors feel that this date best represents Sverdrup conditions (seasonal *MLD* < Z_{cr} driven by seasonal warming) (Figure 3b and c). Interestingly, the compensation irradiance generated by this bloom initiation ($338 \mu\text{E cm}^{-2} \text{s}^{-1}$) is close to the mean I_c from all bloom initiation dates ($398 \mu\text{E cm}^{-2} \text{s}^{-1}$) accounting for the strong similarity observed between the respiration and *NCP* time series generated from the 25 November bloom and the mean of all-time series discussed below (Figure 6 b and c).

Bloom detection dates that generate high-compensation irradiances (e.g. 11 December and 17 November) result in a time series with lower mean *NCP* (-144 and $-253 \text{ mg C m}^{-2} \text{d}^{-1}$, respectively) and a much greater range of variability distributed toward more negative *NCP* (Figure 5a; Supplementary Figure S5b and c). Lower compensation irradiances on the other hand (e.g. 26 September, 29 September, and 15 October) showed higher mean *NCP* (183 – $200 \text{ mg C m}^{-2} \text{d}^{-1}$) with a low range of variability that extends more towards positive *NCP* (Figure 5a; Supplementary Figure S5b and c). It is noteworthy that the compensation irradiances generated from the different bloom initiation dates are not driven by seasonal progression (i.e. decreasing I_c is not chronological) nor necessarily by the choice of bloom detection method (e.g. different methods can select similar bloom initiation dates (11 December and 13 December) with very different compensation irradiances (280 and $796 \mu\text{E m}^{-2} \text{s}^{-1}$) and hence mean *NCP* (-144 and $-253 \text{ mg C m}^{-2} \text{d}^{-1}$). Rather, compensation irradiance is sensitive to conditions experienced at the time of the selected bloom onset. A high I_c indicates that phytoplankton cells require a high minimum irradiance level to compensate for community respiration while the opposite is true for low I_c . High-compensation irradiances (associated with more variable and more negative

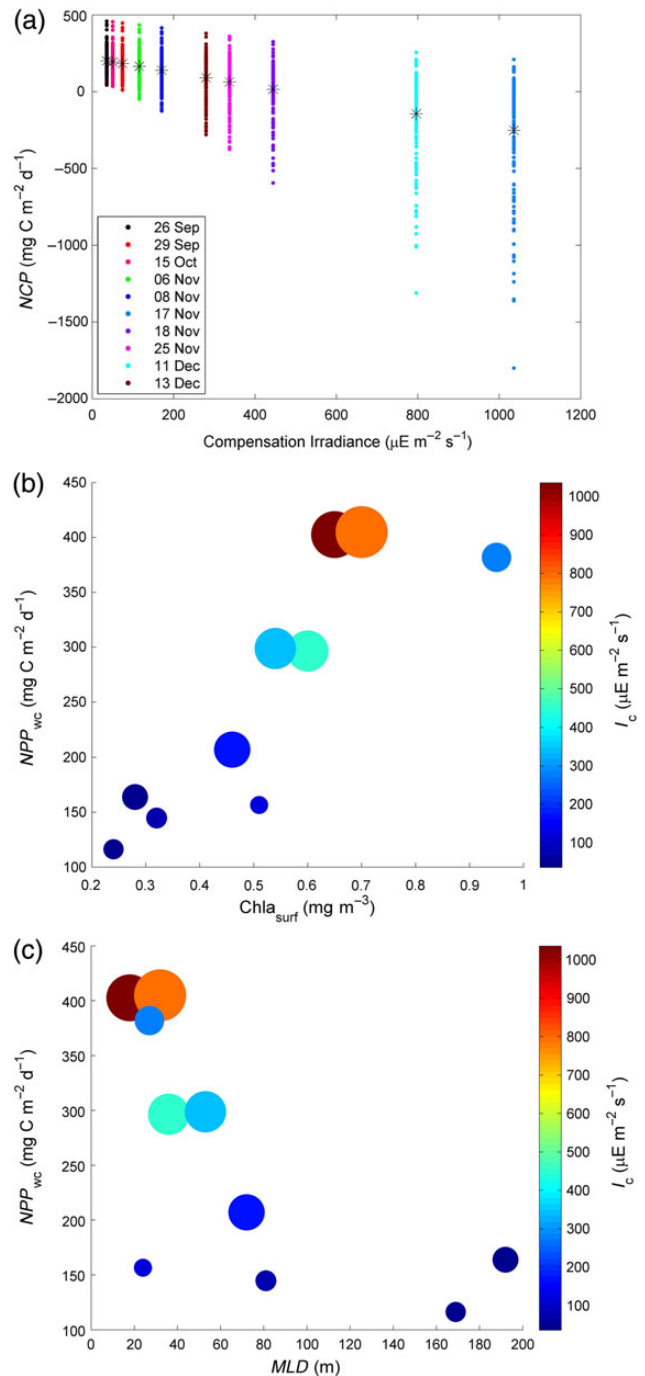


Figure 5. (a) Sensitivity of Sverdrup modelled *NCP* ($\text{mg C m}^{-2} \text{d}^{-1}$) to the range of compensation irradiances ($\mu\text{E m}^{-2} \text{s}^{-1}$) generated from the different bloom initiation dates (depicted in the legend), which have been selected from the various bloom detection methods. The mean *NCP* for each time series initiated with a different bloom initiation date appears as a black star. Figures (b) and (c) sensitivity of I_c ($\mu\text{E m}^{-2} \text{s}^{-1}$) (colour bar) to changes in surface PAR ($\mu\text{E m}^{-2} \text{s}^{-1}$) (size of the circles), *NPP*_{wc} ($\text{mg C m}^{-2} \text{d}^{-1}$) (y-axis), surface chlorophyll (mg m^{-3}) (x-axis b) and *MLD* (m) (x-axis c).

rates of *NCP*) were generated when bloom initiation dates coincided with shallow mixed layers, high surface PAR, high chlorophyll concentrations, and high rates of *PP*, while the opposite was true for low I_c (Figure 5b and c).

To allow comparison of compensation irradiances generated in this study with those from the literature, midday I_c ($\mu\text{E m}^{-2} \text{s}^{-1}$) was converted to daily rates ($\text{E m}^{-2} \text{d}^{-1}$) by assuming a constant gradient of change between maximum I_c at midday and zero I_c at sunrise and sunset (6 a.m. and 6 p.m., respectively). Daily compensation irradiances in this study ranged from 0.06 to $1.86 \text{ E m}^{-2} \text{d}^{-1}$, which is comparable with I_c values found in the literature (0.02– $3.5 \text{ E m}^{-2} \text{d}^{-1}$) (Table 3). Bloom detection methods that selected

initiation dates early in the time series (when mixed layers were deep and surface PAR was low) tended to have low I_c , suggesting that the presence of phytoplankton communities adapted to low irradiance levels (Marra, 2004).

Model results show very high mean respiration rates ($\sim 400 \text{ mg C m}^{-2} \text{d}^{-1}$) and low mean NCP ($-600 \text{ mg C m}^{-2} \text{d}^{-1}$) (Figures 6 and 7) at the start of the glider transect in late September coincident with negative net heat flux ($-100 \text{ W m}^{-2} \text{d}^{-1}$), weakly stratified waters ($BVF = 0$), and consequently deep MLDs ($>150 \text{ m}$) with low mean PAR ($<0.01 \mu\text{E cm}^{-2} \text{s}^{-1}$) (see Figure 2b–e). Respiration rates decrease rapidly into the first week of October (~ 450 – $150 \text{ mg C m}^{-2} \text{d}^{-1}$) coincident with an increase in NCP (~ -600 – $0 \text{ mg C m}^{-2} \text{d}^{-1}$) despite deep MLDs ($\sim 150 \text{ m}$) at the centre of the cold-core eddy identified by Swart et al. (2014). A study by Zhai et al. (2008) (on the continental shelf of Nova Scotia) showed normalized respiration rates that decreased by $\sim 50\%$ during the spring bloom supposedly driven by lower respiration rates in the typically diatom dominated spring bloom community. Respiration rates fluctuate $\sim 200 \text{ mg C m}^{-2} \text{d}^{-1}$ for the next ~ 3 weeks of October and do not return to September rates despite deep MLD fluctuations to $>250 \text{ m}$. The lack of a strong relationship between MLD and respiration in early spring highlights the complex role of multiple drivers

Table 3. Comparison of compensation irradiance (I_c) levels from this study with those from the literature.

Study	Method	I_c ($\text{E m}^{-2} \text{d}^{-1}$)
Langdon (1988) ^a	Laboratory cultures	0.1–3.0
Riley (1957)	<i>In situ</i>	3.5
Marra (2004) (@ 50 m) ^a	<i>In situ</i>	0.2–0.4
Marra (2004) (@ 150 m) ^a	<i>In situ</i>	0.02–0.09
Siegel et al. (2002) (zonal median)	Sverdrup model	0.96–1.75
Henson et al. (2006) (zonal means)	Sverdrup model	1.56–3.23
This study	Sverdrup model	0.06–1.86

^aPhytoplankton compensation irradiance as opposed to community compensation irradiance.

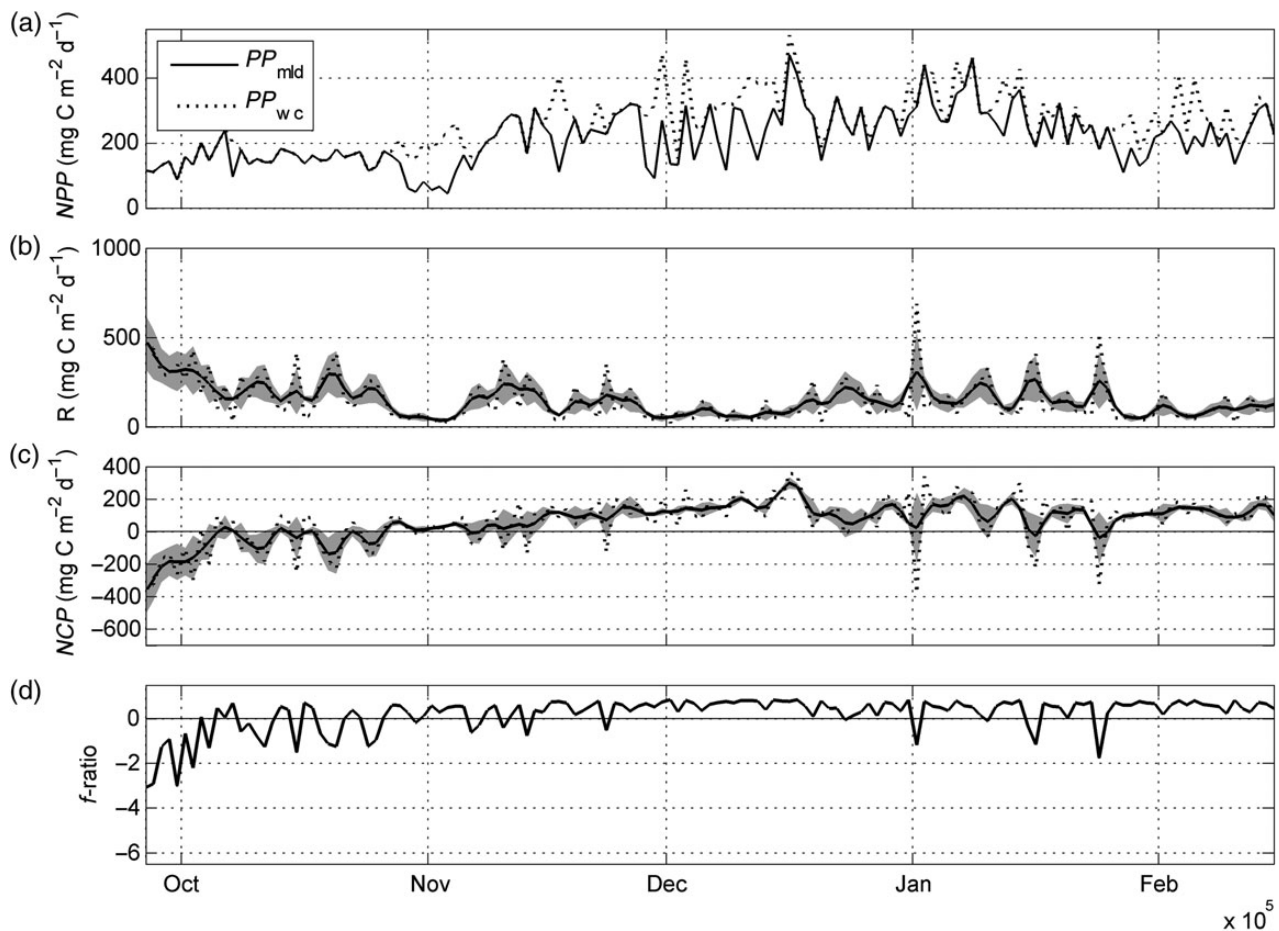


Figure 6. Time series of (a) modelled NPP ($\text{mg C m}^{-2} \text{d}^{-1}$) (Platt et al., 1980; Platt and Sathyendranath, 1993) integrated over the MLD (PP_{mld}) solid black line and the water column (PP_{wc}) dashed grey line. (b) modelled respiration ($\text{mg C m}^{-2} \text{d}^{-1}$) (Sverdrup 1953), from the mean of all-time series (solid line) with standard mean error (shaded area), time-series initiated with bloom initiation on 25 November (dashed line) (c) same as for (c) but for NCP ($\text{mg C m}^{-2} \text{d}^{-1}$), and (d) f -ratio approximation of the export efficiency ($PP/\text{mean NCP}$) (solid line).

of community respiration within the mixed layer, which include phytoplankton and zooplankton respiration (Sverdrup, 1953), plankton maintenance, dark respiration, micro- and macrozooplankton grazing, parasitism, excretion, and sedimentation losses (Platt *et al.*, 1991; Zhai *et al.*, 2008).

On crossing through the edge of the cold-core cyclone on the second week of October, the mixed layer shoals ($\sim 50 \pm 25$ m), causing a peak in mean light in the *MLD* (Figure 2d) that drives an increase in specific growth rates (Figure 7), which is not evidenced in *NCP* (Figure 6c) due to high respiration (possibly due to zooplankton grazing) (Figure 6b). Although rates of *NCP* for the rest of October are higher than in September, they remain predominantly negative (-300 to 0 $\text{mg C m}^{-2} \text{d}^{-1}$). Ocean domains where respiration in the photic layer exceeds *PP* are net heterotrophic and have the potential to be net source regions of CO_2 to the atmosphere. Respiration within a community is distributed between autotrophic plankton respiration, as that part of *PP* not available to the rest of the community, while the distribution of heterotrophic respiration is dominated by bacterioplankton and provides insight into ecosystem function (Robinson and Williams, 2005). Net heterotrophy in early spring requires an organic carbon subsidy to fuel the associated respiration (Williams *et al.*, 2013), possibly through excess production during summer and accumulation of dissolved organic carbon via microbial recycling.

On the cross over into November, there is a prolonged period of reduced windstress (~ 28 October–03 November) (Figure 4f), which likely results in water masses of different lateral densities to interleave and adjust the upper ocean buoyancy term (Swart *et al.*, 2014). This leads to coincidental increased stratification (Figure 4b) and an intense shoaling of the mixed layer to ~ 25 m, which is maintained for ~ 10 d (Figure 4c). These features result in an increase in mean *PAR* in the mixed layer (Figure 4d) that fuels *PP* (Figure 6a), which together with reduced respiration (Figure 6b) allows for persistent rates of positive *NCP* to occur (Figure 6c). Rates of *NCP* during November (mean = 74 $\text{mg C m}^{-2} \text{d}^{-1}$) compare well with spring (30 October–14 December) new production estimates (converted to carbon using Redfield stoichiometry) in the SAZ south of Australia (60 – 84 $\text{mg C m}^{-2} \text{d}^{-1}$) measured by Savoye *et al.* (2004) (Table 4). Despite high respiration rates for much of November (potentially related to deep *MLDs* and increased grazing response to available biomass), *NCP* continues to increase to the end of November (~ 25 November) where positive community production persists (Figure 6c). This date marks the point of transition to net autotrophy, where rates of mixed layer photosynthesis are greater than respiration and the potential to export organic carbon from the upper mixed layer is increased. This prolonged period of net autotrophy increases the capacity of

the region to take up atmospheric carbon and facilitates an efficient biological carbon pump in the SAZ. Maximum rates of *NCP* observed in summer (max = 361 $\text{mg C m}^{-2} \text{d}^{-1}$) are lower than those measured by Joubert *et al.* (2014) in the Atlantic SAZ (max = 686 $\text{mg C m}^{-2} \text{d}^{-1}$) and Cassar *et al.* (2011) in the Australian SAZ (max = 1286 $\text{mg C m}^{-2} \text{d}^{-1}$) based on O_2/Ar measurements converted to carbon using the photosynthetic quotient of Laws (1991) (Table 4). However, summertime rates of *NCP* are similar to ^{15}N new production estimates in the Australian SAZ (95 – 318 $\text{mg C m}^{-2} \text{d}^{-1}$) by Sambrotto and Mace (2000) and the South Atlantic SAZ (365 $\text{mg C m}^{-2} \text{d}^{-1}$) by Joubert *et al.* (2011) (Table 4).

The trend in increasing *NCP* (Figure 6c) appears related to improved light availability for photosynthesis through a combination of reduced turbulent mixing, lateral density gradient adjustments (slumping), which together with increased seasonal heat flux, favour shallower mixed layers, increased stratification and high but variable mean *PAR* in the *MLD* (Figure 2b–f). This combination of physical controls likely drives the observed increase in net primary production (*NPP*) and surface chlorophyll through a combination of available bloom theories (e.g. critical depth, critical turbulence, and eddy-driven stratification; see Section 4.2) which pose greater light exposure as the principal driver of positive community production (Sverdrup, 1953; Chiswell, 2011; Taylor and Ferrari, 2011; Mahadevan *et al.*, 2012; Brody and Lozier *et al.*, 2014). In addition to light availability, a study by Cassar *et al.* (2011) in the SAZ south of Australia highlighted the requirements for sufficient iron to support positive rates of *NCP* (from O_2/Ar ratio). Their results showed that in shallow mixed layers (< 50 m), *NCP* was positively correlated with phytoplankton variable fluorescence as a physiological indicator of iron limitation stress. These results highlight the dependence of positive *NCP* on both iron and light availability in the SAZ and suggest that the observed rates of *NCP* measured here were the result of sufficient light and Fe favouring net community growth.

According to Swart *et al.* (2014), the 28 November marks the date that separates the glider transect into the spring bloom initiation phase and the summer sustained bloom phase. The separation of the time series was identified by a difference in the mechanisms driving a shallower thermocline and increased stratification in summer (warming through solar radiation and air-sea heat exchange) vs. spring (meso- to submesoscale eddies and fronts). Maximum rates of *NCP* were observed from the end of November continually increasing to a maximum of ~ 300 $\text{mg C m}^{-2} \text{d}^{-1}$ in mid-December consistent with maximum rates of *PP* and surface chlorophyll concentrations (Figures 6 and 2c, respectively). Given that the shoaling of the mixed layer at this point in the time series

Table 4. Comparison of *NCP* and *f*-ratio results from this study with new production (from ^{15}N), *NCP* (from O_2/Ar ratio), and *f*-ratio results from the literature in the SAZ from spring through to late summer.

Paper	Region	Season	Method	<i>NCP</i> /new production ($\text{mg C m}^{-2} \text{d}^{-1}$)	<i>f</i> -ratio
This study	South Atlantic SAZ	Spring	Sverdrup	–357 to 198	0.1 ± 0.9
This study	South Atlantic SAZ	Summer	Sverdrup	–369 to 361	0.4 ± 0.5
Savoye <i>et al.</i> (2004)	Australian SAZ	Spring	^{15}N	60 to 84	0.5 ± 0.3
Sambrotto and Mace (2000)	Australian SAZ	Summer	^{15}N	95 to 318	0.1 ± 0.1
Joubert <i>et al.</i> (2014)	South Atlantic SAZ	Summer	O_2/Ar	–145 to 686	
Cassar <i>et al.</i> (2011)	Australian SAZ	Summer	O_2/Ar	0 to 1286	
Elskens (2002)	Australian SAZ	Summer	^{15}N	49 ± 18	0.3 ± 0.1
Joubert <i>et al.</i> (2011)	South Atlantic SAZ	Late summer	^{15}N	365	0.5
Thomalla <i>et al.</i> (2011)	South Indian SAZ	Late Summer	^{15}N	62 to 81	0.1 ± 0.03

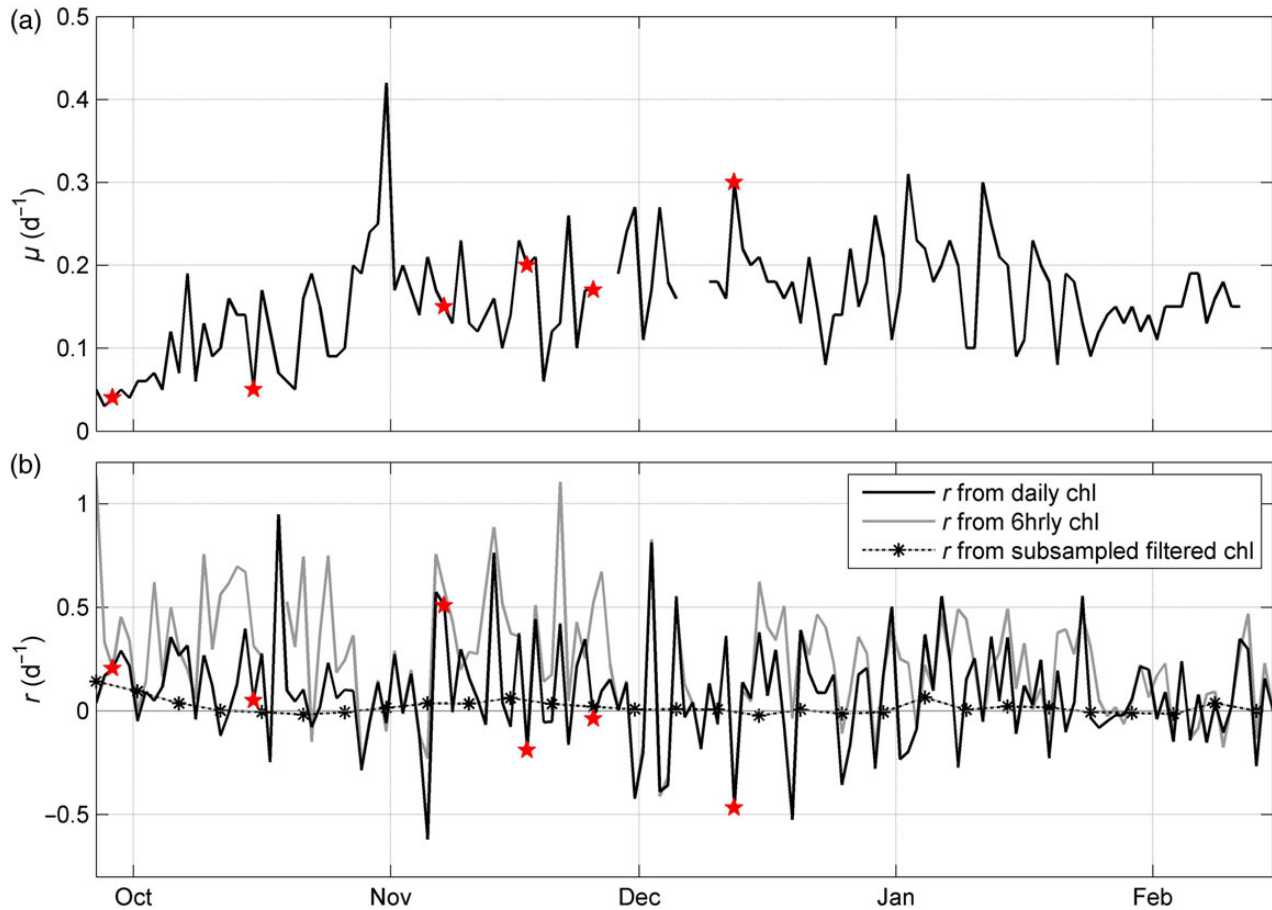


Figure 7. Time series of (a) specific growth rate (μ) (d^{-1}) (NPP/MLD-integrated POC) and (b) biomass accumulation rate (r) (d^{-1}) calculated according to Boss and Behrenfeld (2010) [Equations (22) and (23)]. The black solid line is r calculated from the glider daily (midday) time series with bloom initiation dates as red stars overlaid, the light grey line is r calculated from the glider 6 h time series and the starred dotted line is r calculated with a 5-d subsampled time series smoothed with a four-point box filter to facilitate direct comparison with results from Boss and Behrenfeld (2010). This figure is available in black and white in print and in colour at ICES Journal of Marine Science online.

is the result of seasonal warming (Swart *et al.*, 2014), it is likely that Sverdrup's critical depth hypothesis (Sverdrup, 1953) plays a primary role in driving the observed positive rates of NCP at the end of November. Furthermore, it appears that the method of bloom detection that is developed by the authors in this paper (the cumulative sum of anomalies of positive growth rates, Section 2.6.5), which identifies the 25 November as a bloom initiation, is sensitive to Sverdrup's hypothesis of synoptic adjustments to the mixed layer through seasonal-induced heating. A comparison of the respiration and NCP time series produced from the mean of the bloom initiation dates with that of the 25 November (Figure 6b and c) shows higher variability in the 25 November initiated time series when compared with the mean but a very similar range and distribution pattern.

From mid-December to the end of the time series, there is a reduction in mean PAR in the mixed layer despite continued increase in stratification and shallow mixed layers (mean = 40 m), which is likely the result of self-shading evidenced in high surface chlorophyll concentrations (Figures 2c and 4a). In addition, grazing is known to increase after a blooming period (Zhai *et al.*, 2008, 2010), which together with the consumption of nutrients (Chiswell, 2011), enhanced sinking rates, bacterial activity, and viral infection (Platt

et al., 1991; Llewellyn *et al.*, 2008; Pommier *et al.*, 2008) are the likely cause of decreased NCP observed in January/February compared with mid-December. Nonetheless, highly variable but generally positive rates of NCP are evident throughout January and February implying a sufficient Fe source to support net autotrophy well into summer (Cassar *et al.*, 2011). The studies of Swart *et al.* (2014) and Joubert *et al.* (2014) propose a subseasonal Fe supply from below the mixed layer driven by alternating states of synoptic-scale MLD deepening (from 4- to 9-d storm events) that leads to an entrainment of Fe, followed by restratification, allowing rapid growth in an iron replete, high light environment. The consequence of which is highly variable rates of production and respiration at the same subseasonal time scales as the wind events that drive the MLD deepening (increased respiration relative to production). Consequent NCP fluctuations between positive and negative $200 \text{ mg C m}^{-2} \text{ d}^{-1}$ are observed for much of January. A very limited separation in time is thus observed between net autotrophic and net heterotrophic phases during January. This is clearly evident in the MLD deepening events (50–80 m), which exceed the critical depth (Supplementary Figure S6) and coincide with peaks in respiration ($300\text{--}400 \text{ mg C m}^{-2} \text{ d}^{-1}$). In February, despite a likely shoaling of the critical depth through reduced mean PAR and increased

grazing rates (Chiswell, 2011), a reduction in the extent of the *MLD* deepening events (~ 50 m) (driven by increased stratification; Figure 4b) likely accounts for the less elaborate fluctuations observed in respiration and *NCP* rates that remain positive ($MLD < \text{critical depth}$) through February. The compact relationship between *NCP* and *MLD* highlights the important role that stratification plays in regulating *NCP* and enhancing export production. This has important implications when interpreting climate models that suggest an increase in stratification and alteration of the *MLD* in the Southern Ocean through increased freshening and an increase in atmosphere to ocean heat fluxes (Boyd, 2002).

Export ratio

The combination of *NCP* and *PP* data yields information on how tightly the system is recycling carbon. Previous studies have indicated that exportable production and the export efficiency (the *f*-ratio, defined by Eppley and Peterson, 1979) as the relative importance of new vs. regenerated production), can be regulated by a wide range of properties that includes temperature (Laws *et al.*, 2000), community structure (Ducklow *et al.*, 2001), light (Hannon *et al.*, 2001), and availability of nutrients (Pollard *et al.*, 2009). Since *NCP* approximates carbon export production (Falkowski *et al.*, 2003; Huang *et al.*, 2012), dividing *PP* by *NCP* along the glider transect gives an approximation of the export efficiency of the system over the time series (Figure 6d). Given the oftentimes heterotrophic conditions observed at the beginning of the time series, it is not surprising that *f*-ratios are lower in spring (mean = 0.1 ± 0.9) than in summer (mean = 0.4 ± 0.5) (Table 4). *f*-ratio estimates compare favourably with those measured in many other studies in the SAZ (using ^{15}N new production) which range from 0.1 to 0.5 from spring through to late summer (Sambrotto and Mace, 2000; Elskens, 2002; Savoye, 2004; Joubert *et al.*, 2011; Thomalla *et al.*, 2011) (Table 4). These results imply that the SAZ is a relatively efficient system exporting $\sim 40\%$ of its summer time production.

Comparison of Sverdrup's model and the dilution-recoupling hypothesis

The definition of a bloom initiation presented by Sverdrup is similar to those proposed by Taylor and Ferrari (2011), Chiswell (2011), and Mahadevan *et al.* (2012), whereby positive heat fluxes, a shut-down in turbulence and eddy-induced stratification, respectively, reduce the depth of the mixed layer or depth of mixing, such that the exposure of phytoplankton to light is increased, favouring production, and subsequent biomass accumulation.

These definitions of a phytoplankton bloom are different from the one described by Behrenfeld (2010), who defines the bloom initiation according to the time when phytoplankton population net growth rate (r) becomes positive (see also Boss and Behrenfeld, 2010; Behrenfeld *et al.*, 2013). According to Behrenfeld (2010), the bloom initiation in the North Atlantic occurs in mid-winter when light levels are minimal, near-surface mixing is deepest, and phytoplankton-specific division rates (μ) are declining. Hence, the dilution-recoupling hypothesis proposed by Behrenfeld (2010) de-emphasizes the role of light availability demonstrated in the critical depth model proposed by Sverdrup (1953), by instead suggesting a greater role in the balance between phytoplankton growth and loss rates through grazing. According to Behrenfeld (2010), positive accumulation rates are primarily driven by a reduction in predator–prey interactions (i.e. a reduction in population loss terms through physical dilution when mixed layers deepen) that allow for biomass accumulation to begin in

early winter, before the onset of mixed layer shoaling (Behrenfeld, 2010; Boss and Behrenfeld, 2010; Behrenfeld *et al.*, 2013; Behrenfeld and Boss, 2014). The dilution-recoupling hypothesis allows for winter phytoplankton population accumulation rates comparable with those observed in spring, with changes in phytoplankton biomass remaining largely independent of phytoplankton-specific growth rates.

In the studies by Behrenfeld (2010) and Behrenfeld *et al.* (2013), the biomass accumulation rates r calculated from satellite in the North Atlantic appear one to several orders of magnitude smaller ($r < 0.05 \text{ d}^{-1}$) than specific growth rates μ ($< 0.8 \text{ d}^{-1}$). Despite differences in the methods to calculate specific growth rates based on satellite *NPP* estimates from Vertically Generalized Production Model in Behrenfeld and Falkowski (1997) compared with glider *NPP* estimates in this study based on Platt *et al.* (1980) and Platt and Sathyendranath (1993), specific growth rates were within a similar order of magnitude ($\mu < 0.6 \text{ d}^{-1}$) (Figure 7a). Since biomass accumulation rates result from the difference between specific growth and loss rates ($r = \mu - l$), the extremely low values of r ($< 0.05 \text{ d}^{-1}$) observed by Behrenfeld (2010), meant that growth μ and loss rates l had to be nearly identical with each other so that a bloom (positive r) became the consequence of very subtle imbalances between two larger opposing rates (μ and l).

In this study, net biomass accumulation rates (r) (as calculated by Boss and Behrenfeld, 2010, Equations (22) and (23)) (Figure 7b) and specific growth rates (μ) (Equation (9)) (Figure 7a) were plotted for the glider time series. Figure 7a and b shows rates of r that range over an order of magnitude higher in this study (-0.5 – 1 d^{-1}) than when Boss and Behrenfeld (2010) calculated r for the North Atlantic (-0.02 – 0.06 d^{-1}) and generally higher than our specific growth rates (μ) (as opposed to several orders of magnitude smaller).

Although it is theoretically impossible for r to be larger than μ (since $r = \mu - l$), a comparison of their co-located trends in distribution with respect to the bloom initiation dates (Figure 7a) shows that all bloom initiation dates fell over the period where μ was positive and generally increasing (from ~ 0.03 to $\sim 0.3 \text{ d}^{-1}$). Although three of the bloom initiation dates were associated with a positive r (28 September, 15 October, and 07 November), the remaining three fell over periods of negative r (Figure 7b) implying that community loss rates were greater than growth rates, conditions that cannot theoretically support a bloom. These results are perhaps not surprising when one considers that the most the bloom detection methods are designed to select a period of increasing biomass that results from coincident increases in specific growth rates, whereas the dilution-recoupling hypothesis selects a bloom as the period when r becomes positive coincident with maximum mixed layer depths in winter (before our glider sampling). What is however surprising (over and above the difference in magnitude) is the lack of evidence of a seasonal cycle in r in the ~ 5.5 -month glider time series [which shows similar fluctuations around zero ($+ \text{ or } - \sim 0.5 \text{ d}^{-1}$) at high frequency (~ 5 d) over the entire time series], compared with the distinct seasonal signal observed in the North Atlantic. In other words, for these dataset, there is no tendency for r to consistently change over the season in response to the mixed layer as is shown in the North Atlantic where r tends to decrease (from max to min) in spring and increase (from min to zero) through summer becoming positive in winter when mixed layers are deepest.

The primary cause of the differences in magnitude and seasonality of r in the two datasets is likely due to the sensitivity of the

variability of chlorophyll to fine-scale dynamics. Satellite measurements of chlorophyll in Behrenfeld (2010) were averaged in time over 8 d and in space over large-scale 12.5° latitude \times 10° longitude bins, “chosen to minimize the influence of advection between eight-day periods while maintaining a sense of spatial variability in phytoplankton seasonal properties”. Similarly, in Boss and Behrenfeld (2010), the 5-d temporal sampling of the float dataset was filtered with a four-point box car filter, “chosen to minimize the effects of the mesoscale variance band” (which had a 20-d decorrelation scale). This temporal and spatial averaging removes the dominant signal of the interaction of synoptic and seasonal scale forcing with the meso- and submeso-spatial scales that drives the observed variability in chlorophyll. The effect of this is a smoothing of the chlorophyll time series removing the influence of small-scale variability and short-term events. As such, the difference between observational time-points when divided by Δt to get daily rates of change in biomass, results in very low rates of biomass accumulation ($r < 0.03$ and $r < 0.06 \text{ d}^{-1}$ in Behrenfeld (2010) and Boss and Behrenfeld (2010), respectively). A similar treatment of the glider time series to Boss and Behrenfeld (2010) before calculating r (i.e. 5-d subsampling to recreate the float time series smoothed with a four-point box filter) renders biomass accumulation rates in the same range of variability ($r < 0.1 \text{ d}^{-1}$) as those measured by Boss and Behrenfeld (2010) (Figure 7b).

An advantage of the unique, high-frequency sampling of the glider is that it allows us to resolve fine spatial and temporal scales of variability. When r is calculated from daily glider chlorophyll, the results show rates of biomass accumulation that are ten times higher ($r < 1 \text{ d}^{-1}$) than the 5-d subsampled 20-d filtered time series ($r < 0.1 \text{ d}^{-1}$) (Figure 7b). Since the glider is not Lagrangian but moves $\sim 12\text{--}15 \text{ km}$ in 24 h, it can be argued that the high biomass accumulation rates (calculated here from daily midday chlorophyll) were influenced by spatial aliasing and not the result of phytoplankton growth, i.e. in 24 h the glider could have moved into a new water mass with a different chlorophyll concentration driving a large change in biomass with time. A comparison of r (Figure 6b) with mean salinity in the top 100 m (as a proxy for mesoscale features) (Supplementary Figure S7) clearly shows that the time scales of variability in r ($\sim 5 \text{ d}$) cannot be driven by the time scales of mesoscale variability observed in salinity (several weeks). Where smaller submesoscale spatial variability playing a large role in modulating the amplitude of variability of daily r , one would expect a greater range of variability in calculations of r using daily sampling relative to 6 h sampling (since the glider only moves $\sim 3 \text{ km}$ in 6 h which is within submesoscale spatial variability). To test this, r (calculated from daily midday chlorophyll) was compared with r [calculated from a 6-h resolved time series (with midday z_{eu} interpolated)] (Figure 7b). These results show that (apart from relatively few instances) the range of variability of the daily sampled time series of r is the same as or greater than the 6 h time series of r (Figure 7b). Hence, submesoscale spatial aliasing is not playing a primary role in driving the observed rates of change in phytoplankton biomass. Rather, changes in biomass can be interpreted as the result of intrinsic variability in growth and loss rates of the phytoplankton community in response to environmental forcing (see also Supplementary Figure S4a–c and additional discussion Results and Discussion). These results highlight the importance of fine scales in driving system-scale variability and the need to sample at the relevant scales if we wish to accurately resolve daily rates of change and characterize the seasonal cycle.

Further comparison of Sverdrup’s model and the dilution-coupling hypothesis would require a full seasonal cycle of high-resolution profile deployments to include the maximum winter mixed layer extents. This research campaign is currently planned in the third SOSCEX III to commence in the SAZ in the austral winter of 2015. Finally, the implementation of the approach described by Zhai et al. (2010) to calculate net change in phytoplankton biomass in the mixed layer will also be an important task to help us further our understanding of the difference between mixed layer depth-integrated phytoplankton growth and total phytoplankton loss by respiration, mortality, grazing, sinking, and effects of advection and mixing.

Summary and conclusion

Surface ocean ecosystems and their associated carbon production and export are a basic part of the global carbon cycle. Understanding these processes is a daunting challenge since marine ecosystems are governed by complex interactions among living organisms, nutrients, and physical properties. This complexity drives the need for a high-resolution approach to resolving biogeochemical processes. Autonomous gliders and floats are proving to be an ideal platform for addressing this challenge. This study derives new information from glider data that enhances our understanding of the Subantarctic ecosystem and the importance of fine-scale dynamics in characterizing phytoplankton phenology. In summary, this study shows how high-resolution glider data can be used to identify phenological indicators of bloom initiation, to model PP, to resolve Sverdrup’s critical depth model, and finally to compute biomass accumulation and specific growth rates for comparison with current literature.

The timing of phytoplankton bloom initiation was estimated using five different methods of detection applied to glider-surface and MLD-integrated chlorophyll. One of these methods is based on the cumulative sum of anomalies of phytoplankton growth rates which is to our knowledge a novel method of bloom detection. This method identifies 25 November as the bloom initiation date marking the most evident transition in the trend of positive daily growth rates. This date coincides with the shoaling of the mixed layer driven by seasonal-induced heating and is consistent with Sverdrup’s critical depth hypothesis. The first four bloom initiation dates on the other hand were estimated to occur before MLD shoaling from seasonal heating and are instead thought to relate to shoaling of the MLD via feature induced stratification (Mahadevan et al., 2012; Swart et al., 2014) in addition to contributions from increased light exposure through decreased turbulence (Chiswell, 2011; Taylor and Ferrari, 2011; Chiswell et al., 2013) and a decrease in the dominant mixing length scales (Brody and Lozier 2014).

All bloom initiations in this study were associated with an increase in biomass resulting from coincident increases in specific growth rates driven primarily by increased light availability and in agreement with Sverdrup conditions. The different estimates of bloom initiation were used to run Sverdrup’s critical depth model to determine mean (\pm SE) daily respiration and NCP rates along the glider time series. Model results show that for the spatially and temporally heterogeneous blooms in early spring (September to mid-November), increased rates of NCP are strongly affected by meso- to submesoscale eddies and fronts, which drive vertical stratification and enhance light availability 1–2 months earlier than what would be expected by positive net heat flux alone (Mahadevan et al., 2012). In addition, enhanced light availability through reduced

mixing attributed either to a switch from negative to positive ocean-atmosphere heat fluxes (Taylor and Ferrari *et al.*, 2011) or lowered windstress (Chiswell, 2011; Chiswell *et al.*, 2013) likely contributes to increased rates of *NCP* observed in spring. Seasonal shoaling of the *MLD* at the end of November drives a more spatially homogenous bloom observed late in spring/early summer (late-November to mid-December) where maximum rates of *NCP* and chlorophyll are observed, following which a slight decrease in *NCP* is likely driven by increased grazing, nutrient consumption, and reduced *PAR* from self-shading. Highly variable *NCP* in summer is driven by subseasonal storms that alter the depth of the mixed layer thus regulating iron and light requirements at appropriate time scales for sustained net autotrophy well into summer (mid-February and beyond) in accordance with recent research (Joubert *et al.*, 2014; Swart *et al.*, 2014; Carranza and Gille., 2015).

A comparison of the biomass accumulation rates (r) derived from the high-resolution glider time series with those calculated from a smoothed float dataset by Boss and Behrenfeld (2010) highlights the sensitivity of phytoplankton growth to fine-scale dynamics. These results emphasize the need to sample the ocean at time and space scales relevant to ecosystem dynamics and phytoplankton growth if we wish to accurately resolve phytoplankton phenology and improve our ability to estimate the sensitivity of the biological carbon pump to climate change.

The observations presented in this research provides valuable insight into the sensitivity of the seasonal cycle of *NCP* and associated organic export potential in the SAZ due to surface boundary layer physics. Therefore, long-term changes in the characteristics of mixing (synoptic-scale storms) and buoyancy forcing will strongly impact the effectiveness of the Southern Ocean biological carbon pump. This study highlights the need for future research and climate models to resolve both meso- to submesoscale and subseasonal processes to accurately reflect the phenology of the phytoplankton community and understand the sensitivity of ocean productivity to climate change.

Supplementary data

Supplementary material is available at the *ICESJMS* online version of the manuscript.

Acknowledgements

This work was undertaken and supported through the Southern Ocean Carbon and Climate Observatory (SOCCO) Programme. The authors acknowledge the ESA Ocean Colour CCI team for providing OC-CCI chlorophyll data and Stéphane Saux Picart for technical support. This work was partially funded by the European Commission 7th framework programme through the GreenSeas Collaborative Project (265294 FP7-ENV-2010). This work was supported by CSIR's Parliamentary Grant funding (SNA2011112600001) and NRF-SANAP grants (SNA2011120800004 and SNA14071475720). We thank both the South African Maritime Safety Authority (SAMSA) the South African National Antarctic Programme (SANAP), the captain and officers of the MV SA Agulhas, and the RV SA Agulhas II for the successful completion of the research voyages pertaining to SOSCEX. We acknowledge the dedication and professionalism shown by oceanographic engineers, Derek Needham and André Hoek of Sea Technology Services, and the electronic engineering students Sinekhaya Bilana and Jean-Pierre Smit of Cape Peninsula University of Technology. Thanks is extended to the IOP team at the Applied Physics Laboratory, University of Washington, in particular to Geoff Shilling and Craig Lee.

References

- Ardyna, M., Babin, M., Gosselin, M., Devred, E., Rainville, L., and Tremblay, J. E. 2014. Recent Arctic Ocean sea-ice loss triggers novel fall phytoplankton blooms. *Geophysical Research Letters*, 41: 6207–6212.
- Arrigo, K. R., Robinson, D. H., Worthen, D. L., Schieber, B., and Lizotte, M. P. 1998. Bio-optical properties of the southwestern Ross Sea particle absorption coefficients. *Journal of Geophysical Research*, 103: 21683–21695.
- Arrigo, K. R., van Dijken, G. L., and Bushinsky, S. 2008. Primary production in the Southern Ocean, 1997–2006. *Journal of Geophysical Research*, 113: C08004, doi:10.1029/2007JC004551.
- Batten, S. D., and Mackas, D. L. 2009. Shortened duration of the annual *Neocalanus plumchrus* biomass peak in the Northeast Pacific. *Marine Ecology Progress Series*, 393: 189–198.
- Behrenfeld, M. J. 2010. Abandoning Sverdrup's critical depth hypothesis on phytoplankton blooms. *Ecology*, 91: 977–989.
- Behrenfeld, M. J., Boss, E., Siegel, D. A., and Shea, D. M. 2005. Carbon-based ocean productivity and phytoplankton physiology from space. *Global Biogeochemical Cycles*, 19, doi:10.1029/2004GB002299.
- Behrenfeld, M. J., and Boss, E. S. 2014. Resurrecting the ecological underpinnings of ocean plankton blooms. *Annual Review of Marine Science*, 6: 167–194.
- Behrenfeld, M. J., Doney, S. C., Lima, I., Boss, E. S., and Siegel, D. A. 2013. Annual cycles of ecological disturbance and recovery underlying the subarctic Atlantic spring plankton bloom. *Global Biogeochemical Cycles*, 27: 526–540.
- Behrenfeld, M. J., and Falkowski, P. G. 1997. Photosynthetic rates derived from satellite-based chlorophyll concentration. *Limnology and Oceanography*, 42: 1–20.
- Boss, E., and Behrenfeld, M. 2010. In situ evaluation of the initiation of the North Atlantic phytoplankton bloom. *Geophysical Research Letters*, 37: doi:10.1029/2010GL044174.
- Boss, E., and Pegau, W. S. 2001. Relationship of light scattering at an angle in the backward direction to the backscattering coefficient. *Applied Optics*, 40: 5503–5507.
- Boyd, P., LaRoche, J., Gall, M., Frew, R., and McKay, R. M. L. 1999. Role of iron, light, and silicate in controlling algal biomass in Subantarctic waters SE of New Zealand. *Journal of Geophysical Research Oceans*, 104: 13395–13408.
- Boyd, P. W. 2002. Review environmental factors controlling phytoplankton processes in the Southern Ocean. *Journal of Phycology*, 861: 844–861.
- Briggs, N., Perry, M. J., Cetinić, I., Lee, C., D'Asaro, E., Gray, A. M., and Rehm, E. 2011. High-resolution observations of aggregate flux during a sub-polar North Atlantic spring bloom. *Deep-Sea Research Part I: Oceanographic Research Papers*, 58: 1031–1039.
- Brix, H., Gruber, N., and Keeling, C. D. 2004. Interannual variability of the upper ocean carbon cycle at station ALOHA near Hawaii. *Global Biogeochemical Cycles*, 18: 1–18.
- Brody, S. R., and Lozier, M. S. 2014. Changes in dominant mixing length scales as a driver of subpolar phytoplankton bloom initiation in the North Atlantic. *Geophysical Research Letters*, 41: 3197–3203.
- Brody, S. R., Lozier, M. S., and Dunne, J. P. 2013. A comparison of methods to determine phytoplankton bloom initiation. *Journal of Geophysical Research: Oceans*, 118: 2345–2357.
- Carranza, M. M., and Gille, S. T. 2015. Southern Ocean wind-driven entrainment enhances satellite chlorophyll-a through the summer. *Journal of Geophysical Research*, 120, doi:10.1002/2014JC010203.
- Cassar, N., Difiore, P. J., Barnett, B. A., Bender, M. L., Bowie, A. R., Tilbrook, B., Petrou, K., *et al.* 2011. The influence of iron and light on net community production in the Subantarctic and Polar Frontal Zones. *Biogeosciences*, 8: 227–237.

- Chassot, E., Bonhommeau, S., Dulvy, N. K., Mélin, F., Watson, R., Gascuel, D., and Le Pape, O. 2010. Global marine primary production constrains fisheries catches. *Ecology Letters*, 13: 495–505.
- Chiswell, S. 2011. Annual cycles and spring blooms in phytoplankton: don't abandon Sverdrup completely. *Marine Ecology Progress Series*, 443: 39–50.
- Chiswell, S. M., Bradford-Grieve, J., Hadfield, M. G., and Kennan, S. C. 2013. Climatology of surface chlorophyll a, autumn-winter and spring blooms in the southwest Pacific Ocean. *Journal of Geophysical Research: Oceans*, 118: 1003–1018.
- Claustre, H., Huot, Y., Obernosterer, I., Gentili, B., Tailliez, D., and Lewis, M. 2008. Gross community production and metabolic balance in the South Pacific Gyre, using a non-intrusive bio-optical method. *Biogeosciences*, 5: 463–474.
- Dall'Olmo, G., Westberry, T. K., Behrenfeld, M. J., Boss, E., and Slade, W. H. 2009. Significant contribution of large particles to optical backscattering in the open ocean. *Biogeosciences*, 6: 947–967.
- Dandonneau, Y., Deschamps, P.-Y., Nicolas, J.-M., Loisel, H., Blanchot, J., Montel, Y., Thieuleux, F., et al. 2004. Seasonal and interannual variability of ocean color and composition of phytoplankton communities in the North Atlantic, equatorial Pacific and South Pacific. *Deep Sea Research Part II: Topical Studies in Oceanography*, 51: 303–318.
- De Boyer Montégut, C. 2004. Mixed layer depth over the global ocean: an examination of profile data and a profile-based climatology. *Journal of Geophysical Research*, 109: C12003.
- del Giorgio, P. A., and Duarte, C. M. 2002. Respiration in the open ocean [Review]. *Nature*, 420: 379–384.
- D'Ortenzio, F., Antoine, D., Martinez, E., and d'Alcala, M. R. 2012. Phenological changes of oceanic phytoplankton in the 1980s and 2000s as revealed by remotely sensed ocean-color observations. *Global Biogeochemical Cycles*, 26: doi: 10.1029/2011GB004269.
- Doney, S. C., Lima, I., Feely, R. A., Glover, D. M., Lindsay, K., Mahowald, N., Moore, J. K., et al. 2009. Mechanisms governing interannual variability in upper-ocean inorganic carbon system and air–sea CO₂ fluxes: physical climate and atmospheric dust. *Deep Sea Research Part II: Topical Studies in Oceanography*, 56: 640–655.
- Dower, K. M., and Lucas, M. I. 1993. Photosynthesis-irradiance relationships and production associated with a warm-core ring shep from the Agulhas Retroflection south of Africa. *Marine Ecology*, 95: 141–154.
- Ducklow, H., Steinberg, D., and Buesseler, K. 2001. Upper ocean carbon export and the biological pump. *Oceanography*, 14: 50–58.
- Ducklow, H. W. 1995. Ocean biogeochemical fluxes: new production and export of organic matter from the upper ocean. *Reviews of Geophysics Supplement (U.S. National Report to IUGG, Contributions in Ocean Sciences)*, 33: 1271–1276.
- Ducklow, H. W., Baker, K., Martinson, D. G., Quetin, L. B., Ross, R. M., Smith, R. C., Stammerjohn, S. E., et al. 2007. Marine pelagic ecosystems: the west Antarctic Peninsula. *Philosophical Transactions of the Royal Society of London. Series B, Biological Sciences*, 362: 67–94.
- Durand, M. D., Olson, R. J., and Chisholm, S. W. 2001. Phytoplankton population dynamics at the Bermuda Atlantic time-series station in the Sargasso Sea. *Deep-Sea Research Part II: Topical Studies in Oceanography*, 48: 1983–2003.
- Edwards, M., and Richardson, A. J. 2004. Impact of climate change on marine pelagic phenology and trophic mismatch. *Nature*, 430: 881–884.
- Elskens, M. 2002. N uptake conditions during summer in the Subantarctic and Polar Frontal Zones of the Australian sector of the Southern Ocean. *Journal of Geophysical Research*, 107: 3182.
- Eppley, R. W. 1992. Chlorophyll, photosynthesis and new production in the Southern California Bight. *Progress in Oceanography*, 30: 117–150.
- Eppley, R. W., and Peterson, B. J. 1979. Particulate organic matter flux and planktonic new production in the deep ocean. *Nature*, 282: 677–680.
- Falkowski, P. G., Laws, E., Barber, R., and Murray, J. 2003. Phytoplankton and their role in primary, new, and export production. *In Ocean Biogeochemistry*, pp. 99–121. Ed. by M. R. Fasham. Springer, Berlin Heidelberg, 978-3-642-62691-3.
- Finenko, Z. Z., Churilova, T. Y., and Sosik, H. M. 2004. Vertical distribution of phytoplankton photosynthetic characteristics in the Black Sea. *Oceanology*, 44: 205–218.
- Glover, D. M., Doney, S. C., Nelson, N. B., and Wallis, A. 2008. Submesoscale anisotropy (fronts, eddies, and filaments) as observed near Bermuda with ocean color data. Presented at Ocean Sci. Meet., Orlando.
- González Taboada, F., and Anadón, R. 2014. Seasonality of North Atlantic phytoplankton from space: impact of environmental forcing on a changing phenology (1998–2012). *Global Change Biology*, 20: 698–712.
- Greve, W., Prinage, S., Zidowitz, H., Nast, J., and Reiners, F. 2005. On the phenology of North Sea ichthyoplankton. *ICES Journal of Marine Science*, 62: 1216–1223.
- Gundersen, K., Orcutt, K. M., Purdie, D. A., Michaels, A. F., and Knap, A. H. 2001. Particulate organic carbon mass distribution at the Bermuda Atlantic time-series Study (BATS) site. *Deep Sea Research Part II*, 48: 1697–1718.
- Hannon, E., Boyd, P. W., Silviso, M., and Lancelot, C. 2001. Modeling the bloom evolution and carbon flows during SOIREE: implications for future in situ iron-enrichments in the Southern Ocean. *Deep Sea Research Part II*, 48: 2745–2773.
- Hansell, D. A., and Carlson, C. A. 1998. Net community production of dissolved organic carbon. *Global Biogeochemical Cycles*, 861: 844–861.
- Henson, S. A., Dunne, J. P., and Sarmiento, J. L. 2009. Decadal variability in North Atlantic phytoplankton blooms. *Journal of Geophysical Research*, 114: C04013, doi:10.1029/2008JC005139.
- Henson, S. A., Robinson, I., Allen, J. T., and Waniek, J. J. 2006. Effect of meteorological conditions on interannual variability in timing and magnitude of the spring bloom in the Irminger Basin, North Atlantic. *Deep Sea Research Part I: Oceanographic Research Papers*, 53: 1601–1615.
- Henson, S. A., Sanders, R., Madsen, E., Morris, P. J., Le Moigne, F., and Quartly, G. D. 2011. A reduced estimate of the strength of the ocean's biological carbon pump. *Geophysical Research Letters*, 38: doi:10.1029/2011GL046735.
- Hiscock, M. R. 2004. The regulation of primary productivity in the Southern Ocean. PhD thesis, Nicholas school of environmental and earth sciences, Duke University.
- Hiscock, M. R., Lance, V. P., Apprill, A. M., Bidigare, R. R., Johnson, Z. I., Mitchell, B. G., Smith, W. O., et al. 2008. Photosynthetic maximum quantum yield increases are an essential component of the Southern Ocean phytoplankton response to iron. *Proceedings of the National Academy of Sciences of the United States of America*, 105: 4775–4780.
- Hjort, J. 1926. Fluctuations in the year classes of important food fishes. *ICES Journal of Marine Science*, 1: 5–38.
- Huang, K., Ducklow, H., Vernet, M., Cassar, N., and Bender, M. L. 2012. Export production and its regulating factors in the West Antarctica Peninsula region of the Southern Ocean. *Global Biogeochemical Cycles*, 26: doi:10.1029/2010GB004028.
- Huisman, J., van Oostveen, P., and Weissing, F. J. 1999. Critical depth and critical turbulence: two different mechanisms for the development of phytoplankton blooms. *Limnology and Oceanography*, 44: 1781–1787.
- Huot, Y., Franz, B. A., and Fradette, M. 2013. Estimating variability in the quantum yield of Sun-induced chlorophyll fluorescence: a global analysis of oceanic waters. *Remote Sensing of Environment*, 132: 238–253.
- Johnson, Z., and Howd, P. 2000. Marine photosynthetic performance forcing and periodicity for the Bermuda Atlantic Time Series,

- 1989–1995. Deep-Sea Research Part I: Oceanographic Research Papers, 47: 1485–1512.
- Joubert, W. R., Swart, S., Tagliabue, A., Thomalla, S. J., and Monteiro, P. M. S. 2014. The sensitivity of primary productivity to intra-seasonal mixed layer variability in the sub-Antarctic Zone of the Atlantic Ocean. *Biogeosciences Discussions*, 11: 4335–4358.
- Joubert, W. R., Thomalla, S. J., Waldron, H. N., Lucas, M. I., Boye, M., Le Moigne, F. A. C., Planchon, F., *et al.* 2011. Nitrogen uptake by phytoplankton in the Atlantic sector of the Southern Ocean during late austral summer. *Biogeosciences*, 8: 2947–2959.
- Kahru, M., Brotas, V., Manzano-Sarabia, M., and Mitchell, B. G. 2011. Are phytoplankton blooms occurring earlier in the Arctic? *Global Change Biology*, 17: 1733–1739.
- Kahru, M., and Mitchell, B. G. 2010. Blending of ocean colour algorithms applied to the Southern Ocean. *Remote Sensing Letters*, 1: 119–124.
- Kanamitsu, M., Ebisuzaki, W., Woollen, J., Yang, S. K., Hnilo, J. J., Fiorino, M., and Potter, G. L. 2002. NCEP-DOE AMIP-II reanalysis (R-2). *Bulletin of the American Meteorological Society*, 83: 1631–1643+1559.
- Klein, P., Hua, B. L., Lapeyre, G., Capet, X., Le Gentil, S., and Sasaki, H. 2008. Upper ocean turbulence from high-resolution 3D simulations. *Journal of Physical Oceanography*, 38: 1748–1763.
- Koeller, P., Fuentes-Yaco, C., Platt, T., Sathyendranath, S., Richards, A., Ouellet, P., Orr, D., *et al.* 2009. Basin-scale coherence in phenology of shrimps and phytoplankton in the North Atlantic Ocean. *Science (New York, NY)*, 324: 791–793.
- Langdon, C. 1988. On the causes of interspecific differences in the growth-irradiance relationship for phytoplankton. II. A general review. *Journal of Plankton Research*, 10:1291–1312.
- Large, W., and Pond, S. 1981. Open ocean momentum flux measurements in moderate to strong winds. *Journal of Physical Oceanography*, 11:324–336.
- Lavigne, H., D'Ortenzio, F., Migon, C., Claustre, H., Testor, P., D'Alcalà, M. R., Lavezza, R., *et al.* 2013. Enhancing the comprehension of mixed layer depth control on the Mediterranean phytoplankton phenology. *Journal of Geophysical Research: Oceans*, 118: 3416–3430.
- Laws, E. A. 1991. Photosynthetic quotients, new production and net community production in the open ocean. *Deep-Sea Research Part A*, 38: 143–167.
- Laws, E. A., Falkowski, P. G., Smith, W. O., Ducklow, H., and McCarthy, J. J. 2000. Temperature effects on export production in the open ocean. *Global Biogeochemical Cycles*, 14: 1231–1246.
- Le Quéré, C., Rödenbeck, C., Buitenhuis, E. T., Conway, T. J., Langenfelds, R., Gomez, A., Labuschagne, C., *et al.* 2007. Saturation of the Southern Ocean CO₂ Sink Due to Recent Climate Change. *Science*, 316: 1735–1738.
- Lévy, M., Klein, P., and Treguier, A. M. 2001. Impact of sub-mesoscale physics on production and subduction of phytoplankton in an oligotrophic regime. *Journal of Marine Research*, 59: 535–565.
- Linderman, R. 1991. The trophic-dynamic aspect of ecology. *Bulletin of Mathematical Biology*, 53: 167–191.
- Llewellyn, C. A., Tarran, G. A., Galliene, C. P., Cummings, D. G., De Menezes, A., Rees, A. P., Dixon, J. L., *et al.* 2008. Microbial dynamics during the decline of a spring diatom bloom in the Northeast Atlantic. *Journal of Plankton Research*, 30: 261–273.
- Longhurst, A. R. 2007. Toward an Ecological Geography of the Sea. *In Ecological Geography of the Sea*, pp. 1–17.
- Mackas, D. L., Batten, S., and Trudel, M. 2007. Effects on zooplankton of a warmer ocean: Recent evidence from the Northeast Pacific. *Progress in Oceanography*, 75: 223–252.
- Mahadevan, A., D'Asaro, E., Lee, C., and Perry, M. J. 2012. Eddy-driven stratification initiates North Atlantic spring phytoplankton blooms. *Science (New York, N.Y.)*, 337: 54–58.
- Marra, J. 2004. The compensation irradiance for phytoplankton in nature. *Geophysical Research Letters*, 31: doi:10.1029/2003GL018881.
- Martin, J. H., Gordon, R. M., and Fitzwater, S. E. 1990. Iron in Antarctic waters. *Nature*, 345: 156–158.
- Mitchell, B. G., and Kahru, M. 2009. Bio-optical algorithms for ADEOS-, GLI. *Journal of the Remote Sensing Society of Japan*, 29: 80–85.
- Monteiro, P. M. S., Boyd, P., and Bellerby, R. 2011. Role of the seasonal cycle in coupling climate and carbon cycling in the subantarctic zone. *EOS, Transactions, American Geophysical Union*, 92: 235–236.
- Platt, T., Bird, D. F., and Sathyendranath, S. 1991. Critical depth and marine primary production. *Proceedings of the Royal Society B: Biological Sciences*, 246: 205–217.
- Platt, T., Broomhead, D., Sathyendranath, S., Edwards, A., and Murphy, E. 2003. Phytoplankton biomass and residual nitrate in the pelagic ecosystem. *Proceedings of the Royal Society of London, Series A*, 459: 1063–1073.
- Platt, T., Gallegos, C. L., and Harrison, W. G. 1980. Photoinhibition of photosynthesis in natural assemblages of marine phytoplankton. *Journal of Marine Research*, 38: 687–701.
- Platt, T., and Sathyendranath, S. 1993. Estimators of primary production for interpretation of remotely-sensed data on ocean color. *Journal of Geophysical Research: Oceans*, 98: 14561–14576.
- Platt, T., Sathyendranath, S., Forget, M. H., White, G. N., Caverhill, C., Bouman, H., Devred, E., *et al.* 2008. Operational estimation of primary production at large geographical scales. *Remote Sensing of Environment*, 112: 3437–3448.
- Platt, T., Sathyendranath, S., and Longhurst, A. 1995. Remote-sensing of primary production in the ocean – promise and fulfillment. *Philosophical Transactions of the Royal Society of London Series B-Biological Sciences*, 348: 191–201.
- Platt, T., White, G. N., Zhai, L., Sathyendranath, S., and Roy, S. 2009. The phenology of phytoplankton blooms: ecosystem indicators from remote sensing. *Ecological Modelling*, 220: 3057–3069.
- Pollard, R. T., Salter, I., Sanders, R. J., Lucas, M. I., Moore, C. M., Mills, R. A., Statham, P. J., *et al.* 2009. Southern ocean deep-water carbon export enhanced by natural iron fertilization. *Nature*, 457: 577–580.
- Pommier, J., Michel, C., and Gosselin, M. 2008. Particulate organic carbon export in the upper twilight zone during the decline of the spring bloom. *Marine Ecology Progress Series*, 356: 81–92.
- Racault, M. F., Le Quéré, C., Buitenhuis, E., Sathyendranath, S., and Platt, T. 2012. Phytoplankton phenology in the global ocean. *Ecological Indicators*, 14: 152–163.
- Racault, M. F., Platt, T., Sathyendranath, S., Ağırbaş, E., Martínez Vicente, V., and Brewin, R. 2014. Plankton indicators and ocean observing systems: support to the marine ecosystem state assessment. *Journal of Plankton Research*, 36: 621–629.
- Racault, M-F., Raitos, D. E., Berumen, M. L., Brewin, R. J. W., Platt, T., Sathyendranath, S., and Hoteit, I. 2015. Phytoplankton phenology indices in coral reef ecosystems: application to ocean-colour observations in the Red Sea. *Remote Sensing of Environment*, 160: 222–234.
- Raitos, D. E., Pradhan, Y., Lavender, S. J., Hoteit, I., Mcquatters-Gollop, A., Reid, P. C., and Richardson, A. J. 2014. From silk to satellite: half a century of ocean colour anomalies in the Northeast Atlantic. *Global Change Biology*, 20: 2117–2123.
- Riley, G. A. 1957. Phytoplankton of the North Central Sargasso Sea, 1950–52. *Limnology and Oceanography*, 2:252–270.
- Robinson, C. 2008. Heterotrophic bacterial respiration. *In Microbial Ecology of the Oceans*, 2nd edn, Ed. by D.L. Kirchman Wiley-Liss, Hoboken, NJ, pp. 299–334.
- Robinson, C., and Williams, P. 2005. Respiration and its measurement in surface marine waters. *In Respiration in Aquatic Ecosystems*, pp. 147–180. Ed. by P. del Giorgio, and P. Williams Oxford University Press, Oxford.

- Ryther, J. H. 1969. Photosynthesis and fish production in the sea. *Science* (New York, NY), 166: 72–76.
- Sackmann, B. S., Perry, M. J., and Eriksen, C. C. 2008. Seaglider observations of variability in daytime fluorescence quenching of chlorophyll-a in Northeastern Pacific coastal waters. *Biogeosciences Discussions*, 5: 2839–2865.
- Sakshaug, E., Slagstad, D., and Holm-Hansen, O. 1991. Factors controlling the development of phytoplankton blooms in the Antarctic Ocean – a mathematical model. *Marine Chemistry*, 35: 259–271.
- Sambrotto, R. N., and Mace, B. J. 2000. Coupling of biological and physical regimes across the Antarctic Polar Front as reflected by nitrogen production and recycling. *Deep-Sea Research Part II: Topical Studies in Oceanography*, 47: 3339–3367.
- Sapiano, M. R. P., Brown, C. W., Schollaert Uz, S., and Vargas, M. 2012. Establishing a global climatology of marine phytoplankton phenological characteristics. *Journal of Geophysical Research: Oceans*, 117: doi:10.1029/2012JC007958.
- Saux Picart, S., Sathyendranath, S., Dowell, M., Moore, T., and Platt, T. 2013. Remote sensing of assimilation number for marine phytoplankton. *Remote Sensing of Environment*, 146: 87–96.
- Savoie, N. 2004. Regional variation of spring N-uptake and new production in the Southern Ocean. *Geophysical Research Letters*, 31: L03301.
- Savoie, N., Dehairs, F., Elskens, M., Cardinal, D., Kopczynska, E. E., Trull, T. W., Wright, S., et al. 2004. Regional variation of spring N-uptake and new production in the Southern Ocean. *Geophysical Research Letters*, 31: L03301.
- Schlitzer, R. 2002. Carbon export fluxes in the Southern Ocean: results from inverse modeling and comparison with satellite-based estimates. *Deep Sea Research Part II: Topical Studies in Oceanography*, 49: 1623–1644.
- Siegel, D. A., Doney, S. C., and Yoder, J. A. 2002. The North Atlantic spring phytoplankton bloom and Sverdrup's critical depth hypothesis. *Science* (New York, NY), 296: 730–733.
- Smetacek, V., and Passow, U. 1990. Spring bloom initiation and sverdrup's critical-depth model. *Limnology and Oceanography*, 35:228–234.
- Sommer, U., and Lengfellner, K. 2008. Climate change and the timing, magnitude, and composition of the phytoplankton spring bloom. *Global Change Biology*, 14: 1199–1208.
- Stanley, R. H. R., Kirkpatrick, J. B., Cassar, N., Barnett, B. A., and Bender, M. L. 2010. Net community production and gross primary production rates in the western equatorial Pacific. *Global Biogeochemical Cycles*, 24: doi:10.1029/2009GB003651.
- Steinmetz, F., Deschamps, P.-Y., and Ramon, D. 2011. Atmospheric correction in presence of sun glint: application to MERIS. *Optics Express*, 19: 9783–9800.
- Sverdrup, H. 1953. On conditions for the vernal blooming of phytoplankton. *Journal du Conseil*, 18: 287–295.
- Swart, S., Chang, N., Fauchereau, N., Joubert, W., Lucas, M., Mtshali, T., Roychoudhury, A., et al. 2012. Southern ocean seasonal cycle experiment 2012: seasonal scale climate and carbon cycle links. *South African Journal of Science*, 108: 3.
- Swart, S., Thomalla, S. J., and Monteiro, P. M. S. 2014. The seasonal cycle of mixed layer dynamics and phytoplankton biomass in the Sub-Antarctic Zone: a high-resolution glider experiment. *Journal of Marine Systems*: doi:10.1016/j.jmarsys.2014.06.002.
- Takahashi, T., Sutherland, S. C., Wanninkhof, R., Sweeney, C., Feely, R. A., Chipman, D. W., Hales, B., et al. 2009. Climatological mean and decadal change in surface ocean pCO₂, and net sea–air CO₂ flux over the global oceans. *Deep Sea Research Part II: Topical Studies in Oceanography*, 56: 554–577.
- Taylor, J. R., and Ferrari, R. 2011. Shutdown of turbulent convection as a new criterion for the onset of spring phytoplankton blooms. *Limnology and Oceanography*, 56: 2293–2307.
- Thomalla, S. J., Fauchereau, N., Swart, S., and Monteiro, P. M. S. 2011. Regional scale characteristics of the seasonal cycle of chlorophyll in the Southern Ocean. *Biogeosciences*, 8: 2849–2866.
- Williams, P. J. L. B., Quay, P. D., Westberry, T. K., and Behrenfeld, M. J. 2013. The oligotrophic ocean is autotrophic. *Annual Review of Marine Science*, 5: 535–549.
- Wiltshire, K. H., Malzahn, A. M., Wirtz, K., Greve, W., Janisch, S., Mangelsdorf, P., Manly, B. F. J., et al. 2008. Resilience of North Sea phytoplankton spring bloom dynamics: an analysis of long-term data at Helgoland roads. *Biological Sciences*, 53: 1294–1302.
- Xing, X., Claustre, H., Blain, S., D'Ortenzio, F., Antoine, D., Ras, J., and Guinet, C. 2012. Quenching correction for in vivo chlorophyll fluorescence acquired by autonomous platforms: a case study with instrumented elephant seals in the Kerguelen region (Southern Ocean). *Limnology and Oceanography Methods*, 10: 483–495.
- Zhai, L., Platt, T., Tang, C., Dowd, M., Sathyendranath, S., and Forget, M.-H. 2008. Estimation of phytoplankton loss rate by remote sensing. *Geophysical Research Letters*, 35: L23606.
- Zhai, L., Platt, T., Tang, C., Sathyendranath, S., Fuentes-Yaco, C., Devred, E., and Wu, Y. 2010. Seasonal and geographic variations in phytoplankton losses from the mixed layer on the Northwest Atlantic Shelf. *Journal of Marine Systems*, 80: 36–46.
- Zhai, L., Platt, T., Tang, C., Sathyendranath, S., and Hernández Walls, R. 2011. Phytoplankton phenology on the Scotian Shelf. *ICES Journal of Marine Science*, 68: 781–791.
- Zhang, H. M., Bates, J. J., and Reynolds, R. W. 2006. Assessment of composite global sampling: sea surface wind speed. *Geophysical Research Letters*, 33: L17714.
- Zhang, X., and Hu, L. 2009. Scattering by pure seawater at high salinity. *Optics Express*, 17: 12685–12691.
- Zhang, X. D., Hu, L., and He, M. X. 2009. Scattering by pure seawater: effect of salinity. *Optics Express*, 17: 5698–5710.

Handling editor: Rubao Ji



Contribution to the Themed Section: 'Revisiting Sverdrup's Critical Depth Hypothesis' Original Article

Phytoplankton bloom phenomena in the North Atlantic Ocean and Arabian Sea

John F. Marra^{1*}, Tommy D. Dickey², Albert J. Plueddemann³, Robert A. Weller³,
Christopher S. Kinkade⁴, and Malgorzata Stramska⁵

¹Earth and Environmental Sciences Department, Brooklyn College (CUNY), Brooklyn, NY, USA

²Ocean Physics Laboratory, University of California Santa Barbara, Santa Barbara, CA, USA

³Physical Oceanography Department, Woods Hole Oceanographic Institution, Woods Hole, MA, USA

⁴NOAA National Ocean Service, Silver Spring, MD 20910, USA

⁵Institute of Oceanology of the Polish Academy of Sciences, Sopot 81-712, Poland

*Corresponding author: tel: +1 718 951 5000x2594; fax: +1 718 951 4753; e-mail: jfm7780@brooklyn.cuny.edu

Marra, J. F., Dickey, T. D., Plueddemann, A. J., Weller, R. A., Kinkade, Christopher S., and Stramska, M. Phytoplankton bloom phenomena in the North Atlantic Ocean and Arabian Sea. – ICES Journal of Marine Science, 72: 2021–2028.

Received 1 June 2014; revised 25 October 2014; accepted 5 December 2014; advance access publication 8 January 2015.

We review bio-optical and physical data from three mooring experiments, the Marine Light–Mixed Layers programme in spring 1989 and 1991 in the Iceland Basin (59°N/21°W), and the Forced Upper Ocean Dynamics Experiment in the central Arabian Sea from October 1994 to 1995 (15.5°N/61.5°E). In the Iceland Basin, from mid-April to mid-June in 1989, chlorophyll-*a* concentrations are sensitive to small changes in stratification, with intermittent increases early in the record. The spring increase occurs after 20 May, coincident with persistent water column stratification. In 1991, the bloom occurs 2 weeks earlier than in 1989, with a background of strong short-term and diurnal variability in mixed layer depth and minimal horizontal advection. In the Arabian Sea, the mixing response to the northeast and southwest monsoons, plus the response to mesoscale eddies, produces four blooms over the annual cycle. The mixed layer depth in the Arabian Sea never exceeds the euphotic zone, allowing interactions between phytoplankton and grazer populations to become important. For all three mooring experiments, change in water column stratification is key in producing phytoplankton blooms.

Keywords: Arabian Sea, critical depth, North Atlantic, spring bloom, Sverdrup, zooplankton grazing.

Introduction

There has been a resurgence of interest in Sverdrup's (1953) critical depth hypothesis in recent years (e.g. Behrenfeld, 2010; Chiswell, 2011; Taylor and Ferrari, 2011), as exemplified by a special session at a recent Ocean Sciences Meeting (February 2014) and by this issue of the *Journal of Marine Science*. The most recent contributions indicate an ongoing interest in what has been called "one of the largest transient events on the planet" (Gillis, 1991): the North Atlantic spring bloom is the rapid increase in phytoplankton biomass that occurs in spring months because of the interacting conditions of high nutrients and the seasonal increasing solar irradiance.

There are few datasets that can be used to understand the initiation of the North Atlantic spring bloom. *In situ* data on hydrographic structure and biological response are sparse or non-existent

for winter or early spring, before seasonal restratification of the water column. Here, we reanalyse observational data from two moorings deployed in 1989 and in 1991 in the Iceland Basin (59°N/21°W) (Figure 1a) that help illuminate the causes of the initiation of the North Atlantic spring bloom. We also use data from the Forced Upper Ocean Dynamics Experiment in the Arabian Sea in 1994–1995 (15.5°N and 61.5°E; Figure 1b). The Arabian Sea is a monsoon-dominated regime, with two energetic surface forcing seasons, and unlike the North Atlantic, has near-constant surface irradiance over the year and a more modest seasonal temperature range (20–30°C). In these respects, the Arabian Sea serves as a useful contrast to the North Atlantic. The moorings recorded both physical (e.g. irradiance and temperature) and biological (e.g. chlorophyll-*a*) properties at high temporal resolution

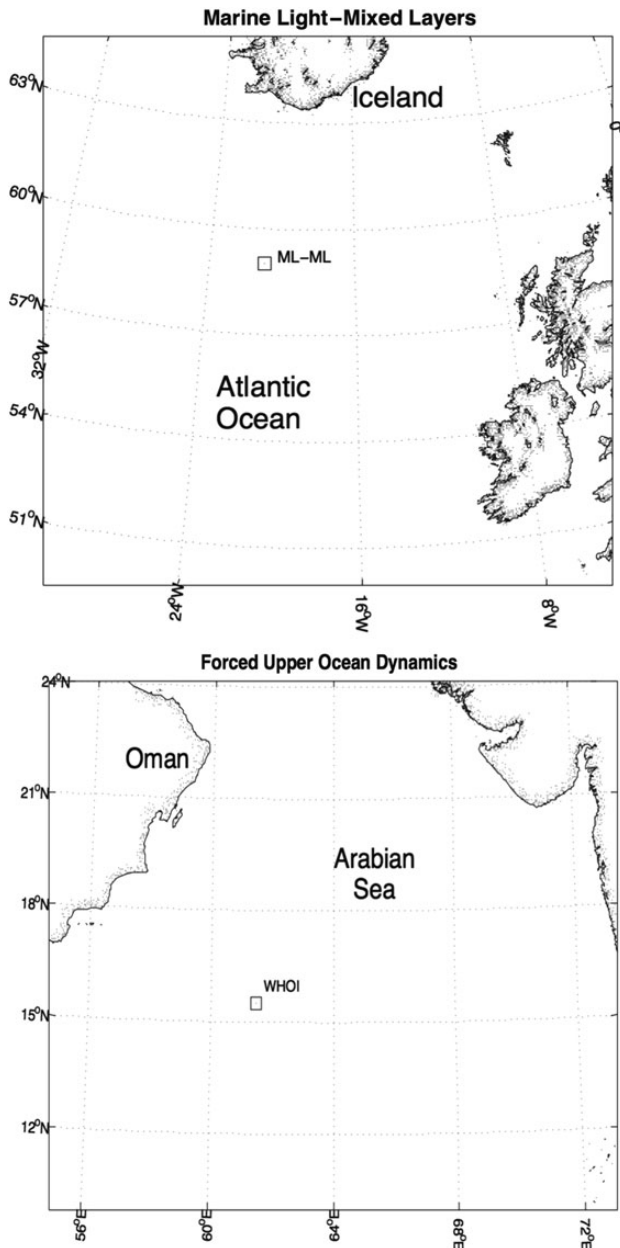


Figure 1. (a) Site of the Marine Light—Mixed Layers (“ML–ML”) mooring experiments in 1989 and 1991. (b) Map showing the site of the Forced Upper Ocean Dynamics Experiment in 1994–1995. The mooring data come from the marker designated as “WHOI” at 15.5°N/61.5°E [see Rudnick *et al.* (1997)].

(minutes and hours), allowing the covariability between physical and biological properties to be examined as the structure of the water column evolved from late winter to spring.

Data sources

Marine Light—Mixed Layers, 1989, Iceland Basin

The first Marine Light—Mixed Layers (ML–ML) mooring experiment took place in spring, 1989 (hereafter, “MLML89”; much of the data are publicly available, with assistance from the authors, at <http://www.ideo.columbia.edu/research/biology-paleo-environment/bioinfo>). The mooring was deployed from 15 April (year day, or yd, 105) to 10 June (yd 161). Details of the mooring design, instrumentation, sensor

Table 1. Array of relevant instrumentation on the three moorings, MLML89, MLML91 (Iceland Basin), and the Forced Upper Ocean Dynamics Experiment in the Arabian Sea. ‘Meas’ refers to measurement type.

Relevant measurements in upper 250 m

MLML89		MLML91		Arabian Sea	
Meas	Depth	Meas	Depth	Meas	Depth
Temp	2	Temp	2	Temp	1.5
MVMS	10	MVMS	10	Temp	5
MVMS	30	MVMS	30	MVMS	10
MVMS	50	MVMS	50	Temp	15
MVMS	90	MVMS	70	Temp	20
MVMS	110	Temp	80	Temp	25
MVMS	150	Temp	102	Temp	30
Temp	200	Temp	118	MVMS	35
MVMS	250	Temp	150	Temp	40
		Temp	166	Temp	45
		Temp	182	Temp	50
		Temp	198	Temp	55
		Temp	214	Temp	60
		Temp	230	MVMS	65
				Temp	72.5
				MVMS	80
				Temp	90
				Temp	100
				Temp	125
				Temp	150
				Temp	175
				Temp	200
				Temp	225
				Temp	250

MVMS, Multivariate Moored Sensor; temp, temperature sensor package.

calibration, and methods can be found in Stramska and Dickey (1992) and Dickey *et al.* (1994). Multivariate Moored Sensors (MVMSs; Dickey *et al.*, 1994) were put at 10, 30, 50, 90, 150, and 250 m. (See Table 1 for the array of sensors relevant to the data discussed. Sensors at 70 and 110 m failed, and are not included in the analysis.) Bio-optical observations at these depths included chlorophyll-*a* fluorescence, beam attenuation coefficient, and photosynthetic active radiation (PAR). Temperature and current velocities were measured at these same depths; salinity was measured only at 10 and 250 m. Meteorological data were collected at a surface buoy. We do not have data for all these variables for the full deployment period; but overall, the data retrievals were good.

Marine Light—Mixed Layers, 1991, Iceland Basin

The mooring for MLML91 collected data from 30 April (yd 120) until 6 September (yd 249), although we consider only data through yd 155. For MLML91, MVMSs were deployed at 10, 30, 50, 70, and 90 m. Temperature sensors were placed approximately every 20 m, starting at the surface, to 250 m (Table 1). Key references for background, methods, instrumentation, and mooring design are Plueddemann *et al.* (1993, 1995), Stramska *et al.* (1995), and Weller *et al.* (1990).

Forced Upper Ocean Dynamics Experiment, 1994–1995, Arabian Sea

The mooring for the Arabian Sea was similar in design to that deployed in MLML91, with MVMS units deployed at 10, 35, 65,

and 80 m, and temperature sensors placed at depth intervals of 5–10 m throughout the upper 250 m (Table 1). The mooring discussed here (Figure 1b) was at the central point of an array of five moorings, also part of the Forced Upper Ocean Dynamics Experiment. There were two deployments of 6 months each, the first from 16 October 1994 to 21 April 1995, and the second from 23 April to 25 October 1995. Key references for this programme are Rudnick *et al.* (1997), Dickey *et al.* (1998), Kinkade *et al.* (2001), and Weller *et al.* (2002).

Results

MLML89

The time evolution of the temperature and chlorophyll-*a* distributions from the various sampled depths are shown in Figure 2. Temperature (Figure 2a) is marked by periods of intermittent stratification and isothermal layers, culminating in spring restratification beginning about yd140 (May 20), and remains so for the remainder of the record.

There are periods of stratification early in the series (April to early May), followed by a few days where the sensors recorded nearly uniform temperatures, suggesting vertical mixing. The water column then begins to restratify, punctuated by a shallow

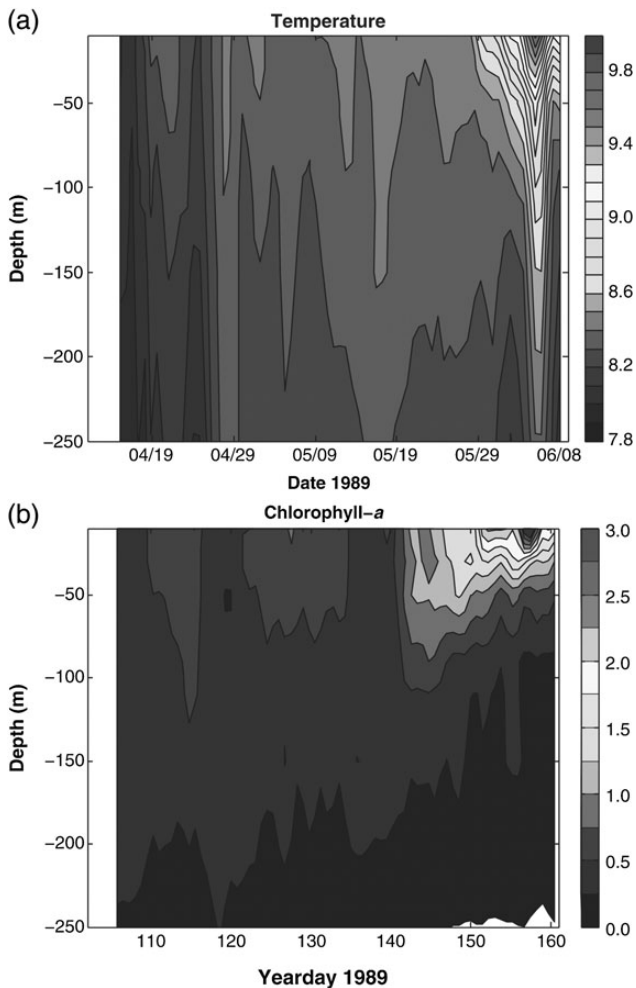


Figure 2. Contour plots of (a) temperature ($^{\circ}\text{C}$) and (b) chlorophyll-*a* ($\mu\text{g l}^{-1}$) for the MLML89 mooring experiment. There are no data from 110 m for chlorophyll-*a*. Time is presented as calendar dates (mm/dd) in (a) and as yd in (b).

mixing event (0–150 m) around May 18 (yd138). By yd145, the water column becomes stratified and remains so for the remainder of the record. Winds and windstress were highly variable throughout the time-series; the mixing event during May 18–May 20 (yd 138–140) was associated with the windstress event [see Dickey *et al.* (1994)].

The chlorophyll-*a* record (Figure 2b) essentially follows the temperature in character. There are early periods of vertical stratification where chlorophyll-*a* increases at all depths except the deepest (150 and 250 m), followed by a brief periods where chlorophyll values are nearly uniform. After this, the spring increase is almost completely confined to the shallowest three depths, 10, 30, and 50 m, with the values at 10 m exceeding for a short time, $3 \mu\text{g chlorophyll-}a \text{ l}^{-1}$. The increases in near-surface chlorophyll-*a* near the end of the record (late May, early June, where June 1 is yd 152) come at the expense of chlorophyll-*a* deeper in the water column, an example of self-shading of the population [see Marra (2004)].

Contour plots are always an interpretation. The two episodic stratification events are best viewed with time-series plots of data from each of the depths to span the period covering both events

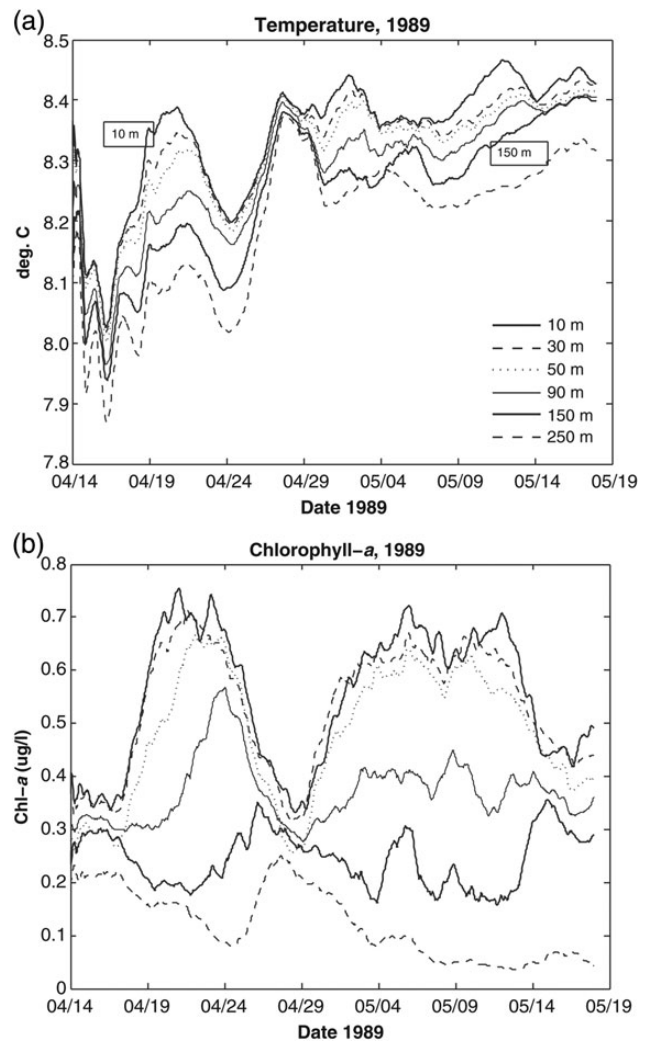


Figure 3. Time-series from individual depths for mid-April to mid-May in Figure 2 with (a) temperature ($^{\circ}\text{C}$) and (b) chlorophyll-*a* ($\mu\text{g l}^{-1}$). The data have been smoothed, for clarity. The unsmoothed data are shown in Marra (2004).

(Figure 3). In both instances, the water column becomes progressively warmer at all depths, and subsequently becomes more uniform in temperature, producing near-isothermal conditions as a function of depth. For the first event, the water column becomes increasingly stratified until yd113 (April 23), after which vertical mixing occurs to 50 m, followed by a near-isothermal water column over the full range of observed depths (10–250 m) by April 28. Chlorophyll-*a* concentrations (Figure 3b) increase coincident with stratification of the upper ocean at April 17 down to 90 m, then declines as the upper 50 m become isothermal, with roughly constant levels (within $\pm 0.1 \mu\text{g chlorophyll-}a \text{ l}^{-1}$) by April 28, from 10 to 150 m. Following this episode, chlorophyll-*a* at the shallowest three depths (10, 30, and 50 m) increases until the next time the water column mixes in mid-May.

It is likely that the increases in chlorophyll-*a* in the near-surface records (10, 30, and 50 m) are from phytoplankton growth. Certainly, estimates of the increase in chlorophyll-*a*, of about a doubling per day, are reasonable. Deeper than this the evidence is less clear. As the water column becomes isothermal, chlorophyll-*a* concentration at all depths declines except the two deepest depths (150 and 250 m), perhaps because concentrations at these depths increase as a result of mixing from above. Integrated over 10–250 m, however, chlorophyll-*a* declines by 30% from April 24 to 29 (data not shown). The increases shown for the 150 and 250 m depths are not enough to compensate for the losses shallower in the water column. The integrals may be inaccurate because of the limited depth resolution, because chlorophyll had been mixed deeper than our deepest sensor (250 m), or else because local currents (which were otherwise relatively weak during this period: Dickey *et al.*, 1994) play a role in the variability. [Unfortunately, satellite altimetry data are unavailable for the period of our experiment, and satellite sea surface temperatures are not sufficiently resolved to identify mesoscale features. See Dickey *et al.* (1994).] The water column becomes isothermal over all depths by April 28 (yd118), and chlorophyll-*a* does as well. Nevertheless, temperature differences of less than a few tenths of a degree between adjacent instruments allow an increase chlorophyll-*a* concentrations by a factor of two during the first half of the record.

Daily PAR in the water column is shown in Figure 4. It is fairly constant at $20\text{--}30 \text{ mol photons m}^{-2} \text{ d}^{-1}$ until the wind event (May 18–May 20), and declines thereafter as the bloom develops. Daily-averaged net heat flux is also relatively constant over the course of the experiment [see Dickey *et al.* (1994)].

MLML91

The experiment in 1991 shows similar temperature variability, but very different biological behaviour than in 1989 (Figure 5). We had the benefit of extensive sampling from shipboard that we did not have in MLML89, and that allowed phytoplankton and zooplankton species to be identified.

Compared with 1989, the major chlorophyll-*a* increase over the water column occurred much earlier in 1991, and during the incipient stratification from yd125 to yd140 (May 5–20). The first stage of the bloom was interrupted by a storm (yd128–130, May 8–10), as recorded at the mooring's surface meteorological sensors (Plueddemann *et al.*, 1995). Shipboard observations during two ML–ML cruises, covering the period May 7–24 [see Marra *et al.* (1995)], identified the bloom occurring then as *Phaeocystis pouchetii*, an unusual occurrence south of Iceland. After a major storm on May 22 (yd142), with $>70 \text{ knot}$ (35 m s^{-1}) winds, the *Phaeocystis* bloom was no longer observed.

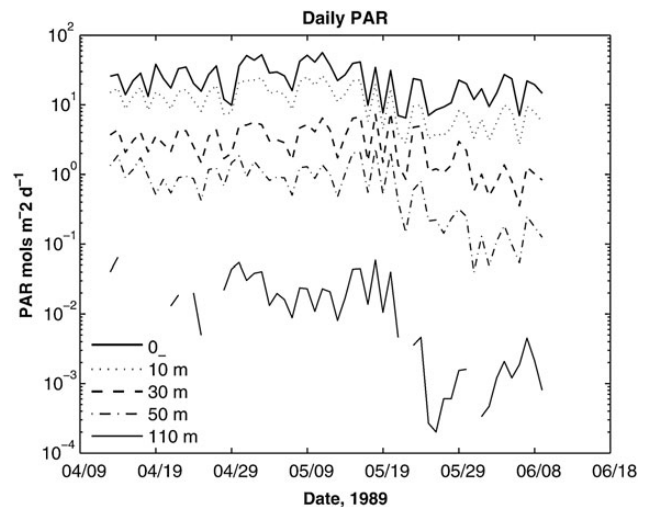


Figure 4. Daily PAR in the water column. $E(0)^{-}$ is calculated as the intercept from the linear regression of $\ln \text{PAR}(z)$.

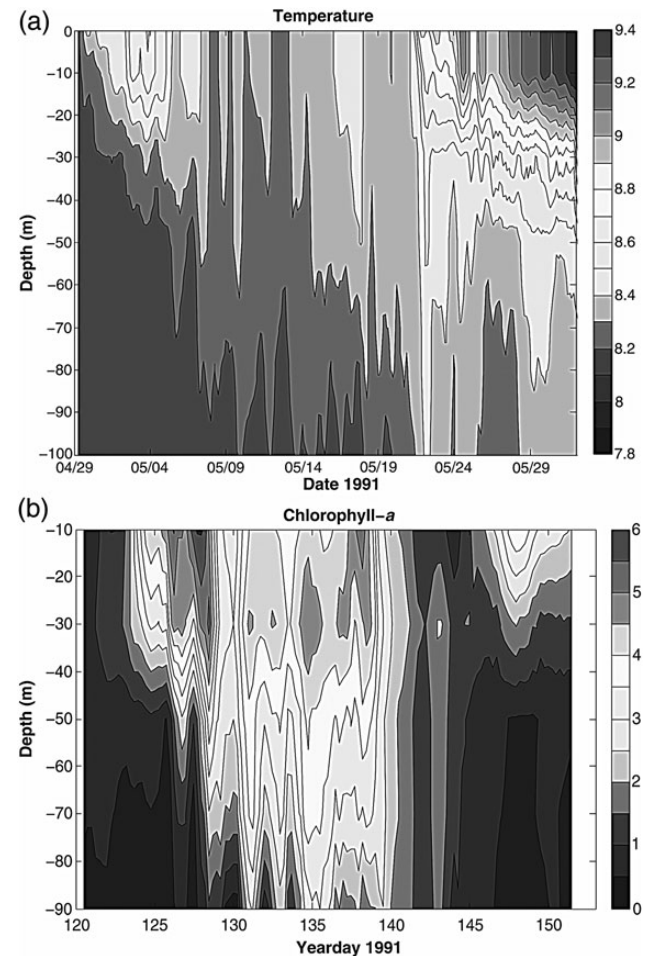


Figure 5. Contour plots of (a) temperature ($^{\circ}\text{C}$) and (b) chlorophyll-*a* ($\mu\text{g l}^{-1}$) for the MLML91 spring data. There is more detail in the temperature plot because of the higher sampling resolution with depth. Depths for temperature sensors begin at the surface, then with $\sim 20 \text{ m}$ spacing until 310 m. Depths for chlorophyll-*a* sensors are 10, 30, 50, 70, and 90 m. Time is presented as calendar dates (mm/dd) in (a) and as yd in (b).

The water column quickly stratified under clear skies (total daily irradiance of $60 \text{ mol photons m}^{-2} \text{ d}^{-1}$; Marra *et al.*, 1995), and diatoms and copepods appeared in the surface layers (Cowles and Fessenden, 1995). Chlorophyll-*a* levels had declined by nearly an order of magnitude after the storm, and recovered only partially thereafter. At this time, nitrate concentrations in the upper water column ranged from 6 to $8 \text{ } \mu\text{M}$ (Marra *et al.*, 1995); therefore, nutrients were likely not a factor in the development of the bloom.

Forced Upper Ocean Dynamics Experiment, Arabian Sea, 1994–1995

The Arabian Sea mooring experiment extended an entire year, from October 1994 to 1995. The seasonal cycle is dominated by monsoons, with within-season effects from mesoscale eddies. The moored observations captured both the northeast (December 1994–February 1995) and southwest (June–August 1995) monsoons. The seasonal cycle in the vertical structure of temperature and areal chlorophyll-*a* (Figure 6) is reported in Kinkade *et al.* (2001), compiled from both mooring and shipboard data. This is the most complete description of the physical setting and biological response determined for the Arabian Sea. In the one-dimensional sense, convective cooling occurs during the northeast monsoon, as the winds from Asia blow over the northern Arabian Sea (Fischer *et al.*, 2002). The result is vertical, convective, mixing resulting in deepening the mixed layer. In contrast, the mixing during the southwest monsoon is mechanical, and caused by windstress at the

surface. In neither case, however, does the mixing extend to great depth, never reaching $>100 \text{ m}$, and perhaps never exceeding the euphotic zone (Barber *et al.*, 2001). The biological response to the southwest monsoon was greater than for the northeast monsoon, but for reasons that are not clear (Barber *et al.*, 2001).

Perhaps enhanced activity at the mesoscale, associated with the southwest monsoon, provides a source of nutrients (Keen *et al.*, 1997) to support the greater productivity during the southwest monsoon. Fischer *et al.* (2002), using data from the array of five moorings and data from Sea Soar tows, show that cool and nutrient-rich waters are brought from the coastal upwelling regime out to the central mooring. In autumn of 1994, there is evidence of two mesoscale eddies at the mooring location (Figure 6a), one when the mooring was first deployed, and the second about a month later. In these cases, the increase in chlorophyll-*a* is associated with relatively shallow mixed layers, and the strong temperature contrast with depth suggests an enhanced nutrient supply that supports surface productivity. Over the year, there are four episodes of phytoplankton increases observed in the Arabian Sea, two occurring as a result of each of the monsoon periods, and two associated with the passage of mesoscale eddies in autumn of 1994.

Discussion

Sverdrup's (1953) critical depth hypothesis is a mathematical derivation of ideas presented earlier by Gran and Braarud (1935) and Riley (1942). These earlier authors recognized that since autotrophic respiration (R) was, perhaps, 20% of gross production (G), the phytoplankton cells could be mixed to five times the depth of the compensation irradiance (i.e. where $G = R$) without incurring a population decline [see Mills (1989)]. Conceptually, this is sound. The balance between net production by phytoplankton and the vertical mixing that they are subject to, should determine the fate of phytoplankton populations in a variety of environments. This is especially so in the late-winter North Atlantic where Sverdrup (1953) tested his ideas. The North Atlantic, unlike many other ocean regimes, convectively mixes during winter, producing mixed layers $>600 \text{ m}$ deep (Robinson *et al.*, 1979; Monterey and Levitus, 1997), and in effect, resetting the seasonal production cycle.

The critical depth hypothesis has achieved wide acceptance, becoming a core tenet of biological oceanography, but it has had few, if any, actual tests. Later, there were critiques. Smetacek and Passow (1990) note that actual critical depths may exceed winter mixing depths, anyway, and further that phytoplankton communities are capable of overwintering [see, e.g., Backhaus *et al.* (2003)]. They also remind that stratification occurs from the surface, and that there are difficulties in accounting for other losses (e.g. zooplankton grazing). They conclude that the critical depth hypothesis serves a little practical value. Behrenfeld (2010) takes a similar position, noting that there is significant biomass during winter in the boreal North Atlantic, and highlighting the balance between growth and grazing. This balance would be disrupted by seasonal restratification in favour of a spring bloom. Behrenfeld's (2010) evidence, however, comes from satellite ocean colour estimates of chlorophyll-*a*, which can be subject to error during winter at high latitudes, and carry no information on vertical structure.

While we do not have winter data, our records for the North Atlantic are from before the seasonal restratification of the water column, and indicate the initiation of the spring bloom. We cannot provide a direct test of the critical depth hypothesis; however, we can point to factors that are important for bloom initiation. For the Arabian Sea, we show how mixed layer dynamics

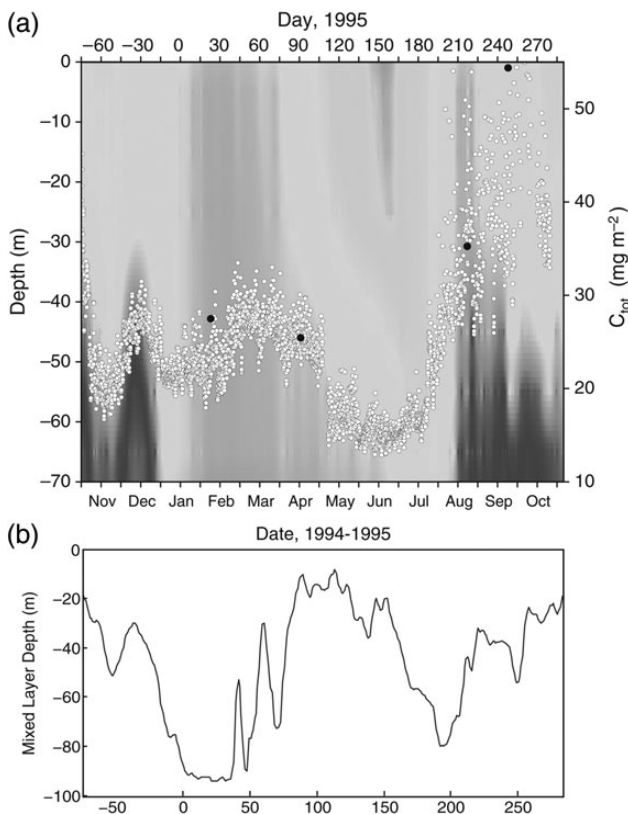


Figure 6. (a) Contour plot of temperature overlain with areal chlorophyll-*a* (C_{tot} , mg m^{-2}) from the mooring (open circles) and from shipboard hydrographic casts (filled circles), and (b) mixed layer depth. Mixed layer depths were estimated as a temperature difference of 0.1°C from the surface temperature.

affect chlorophyll-*a* for a situation where the mixed layer never exceeds the critical depth.

North Atlantic

For both the 1989 and 1991 programmes, the moorings provide a good realization of the temporal dynamics of bloom development for the Iceland Basin in the North Atlantic. Dickey *et al.* (1994) note that current velocities during the restratification period were weak and barotropic. For the 1991 experiment, Plueddemann *et al.* (1995) show that the spring evolution of the temperature structure in the upper water column could successfully be simulated by a one-dimensional mixed layer model. Thus, for 1989 and 1991, we conclude that we observed the temporal evolution of the spring bloom.

It is clear from the time-series observations of temperature and chlorophyll-*a* that stratification of the water column instigated the bloom. In 1989, there are two early, incipient episodes of stratification that elicit a chlorophyll-*a* response, followed by vertical mixing (isothermal periods). When the water column becomes persistently stratified, chlorophyll-*a* increases in the top 150 m. In both 1989 and 1991, there are periods of weak stratification interspersed with water column mixing, the result of wind events (1989) or major storms (1991), with the stratified periods associated with strong increases in chlorophyll-*a*. The timing of the blooms in 1989 and 1991 are within two weeks of each other. The seasonal restratification (Figures 2 and 5) begins at yd135–140 (May 15–20) in 1989, and yd140–143 (May 20–23) in 1991. Stramska and Dickey (1993) have pointed out that chlorophyll-*a* is very sensitive to water column stratification. A vertical difference of a few tenths of a degree celsius within the top layers is enough to stabilize the surface layers and thereby allow increases in chlorophyll-*a*. Similarly, mixing those top layers disperses the chlorophyll-*a*.

We can try to interpret our data using the critical depth idea, to make an inference as to what happens earlier in the season (before our observations), and whether it is a useful guide for the initiation of the bloom. We use a simplification of Sverdrup's (1953) equation, presented in Lalli and Parsons (1993), whereby

$$Z_{cr} = \frac{E(0)}{(k \cdot E_c)}$$

Here, Z_{cr} is the critical depth, $E(0)$ is the solar irradiance penetrating the surface, k is the vertical diffuse attenuation coefficient for PAR, and E_c the compensation irradiance. The 1989 observations show that $E(0)$ is $\sim 20\text{--}30$ mol photons $\text{m}^{-2} \text{d}^{-1}$ (Figure 4), with a vertical diffuse attenuation coefficient of 0.06 m^{-1} . Marra (2004) has estimated that E_c for the data from 1989 is $0.1\text{--}0.3$ mol photons $\text{m}^{-2} \text{d}^{-1}$ based on the time and depth changes in chlorophyll-*a* at the height of the bloom. If we assume a surface irradiance of 10 mol photons $\text{m}^{-2} \text{d}^{-1}$ to represent times earlier in the year than our observations, then the critical depth will have a calculated range from 600 to 1600 m. This depth range is large, but comparable to, or greater than, prior estimates of the late-winter mixed layer depths (Monterey and Levitus, 1997; see also Smetacek and Passow, 1990). The depth range also suggests that the critical depth will be greater than the mixed layer depth for the observations in MLML89 and MLML91. As the season progresses, and $E(0)$ increases, the critical depth will increase accordingly. We do not have data for the late-winter population of phytoplankton; however, it is unlikely that the balance between photosynthesis

and respiration, as suggested by Sverdrup (1953), is a primary factor to the initiation of the bloom.

Thus, we conclude that seasonal restratification of the water column drives the change in chlorophyll-*a* concentration in surface waters from midwinter lows to spring highs. The change in stratification may be episodic, and the spring bloom may therefore proceed episodically, and be spatially heterogeneous. We recognize that there are other processes at work that we cannot account for with our dataset. For example, perhaps there is advection of more stratified water past the mooring. However, 1D models (Stramska and Dickey, 1994; Plueddemann *et al.*, 1995; Stramska *et al.*, 1995) support the notion that air–sea interaction processes could explain the change in water stratification that we observe. Recently, Mahadevan *et al.* (2012) suggest that mixed layer “slumping” produces stratification that can affect the timing of spring bloom. Our data do not contradict that assessment. Our data support the view that it is a decrease in mixing intensity followed by the development of water column stratification that is the driver for the changes in chlorophyll-*a* concentration observed.

Another control on biomass (although not on physiology) is grazing. Sverdrup (1953) considered this as a significant loss term in his analysis of spring bloom, and it has been considered so in subsequent treatments (e.g. Platt *et al.*, 1991; Behrenfeld, 2010). Behrenfeld (2010) regards grazing as a strong control of overwintering phytoplankton populations in the North Atlantic. Although we do not have the appropriate measurements to assess the impact of grazing for the 1989 dataset, there are shipboard observations for the MLML91 experiment, for the period of May 17–24 (yd137–144). During the *Phaeocystis* bloom, there are few mesozooplankton, but they become abundant after the seasonal stratification, after May 23 (Cowles and Fessenden, 1995). Despite that abundance, these authors calculate that the grazing impact by copepods after 23 May is $\sim 5\%$ of primary production. The impact of grazing by microzooplankton is higher, but as well, only after the onset of persistent stratification (Gifford *et al.*, 1995). To be sure, there are no data earlier in the season than this, but the sequence suggests that grazing only becomes important after the bloom is established, and plays little role in the initial stages. Finally, incubation estimates of primary production (^{14}C assimilation and ΔO_2) are roughly comparable to changes in *in situ* biomass, calculated from diurnal changes in beam attenuation (Marra *et al.*, 1995). This is further evidence that grazing is not a large loss process during the spring bloom in the North Atlantic.

Arabian Sea

In the Arabian Sea, unlike in the North Atlantic, there is not a dominant annual cycle. Incoming shortwave radiation, expressed as PAR, averages $\sim 30 \pm 5$ mol photons $\text{m}^{-2} \text{d}^{-1}$ over the year, with summertime values dropping significantly below that because of cloudiness (Marra *et al.*, 1998; Weller *et al.*, 1998). Sea surface temperature lacks a summer peak, instead showing cooling during both summer and winter (Weller *et al.*, 1998) from the effects of the two monsoons. The Arabian Sea, like most other ocean areas, also has mesoscale variability and advective transports that are at times significant contributors to local water column properties. Like many tropical areas (e.g. Lukas and Lindstrom, 1991), vertical mixing in the Arabian Sea does not extend deeper than 100 m (Dickey *et al.*, 1998; Weller *et al.*, 2002). Because of these attributes, we can expect that biological interactions, most prominently zooplankton grazing on phytoplankton, will be relevant to the dynamics in the Arabian Sea.

One way to ascertain the importance of grazing is to compare photosynthetic carbon assimilation in incubations (Barber *et al.*, 2001) with the variability of chlorophyll-*a* from the moored fluorometers (Figure 6a). The largest change in *in situ* chlorophyll-*a* occurs with the southwest monsoon. The data are scattered towards the end of the monsoon period, but the realized increase in chlorophyll-*a* from July to September (~ 90 d) is $0.3\text{--}0.5\text{ mg m}^{-2}\text{ d}^{-1}$. Assuming a (high) carbon : chlorophyll-*a* ratio of 100, this daily increase amounts to $30\text{--}50\text{ mg C m}^{-2}\text{ d}^{-1}$, about a factor of 20 smaller than the daily photosynthetic carbon assimilation measured during the southwest monsoon (Barber *et al.*, 2001). Still, zooplankton grazing does not completely regulate phytoplankton biomass in the Arabian Sea; biomass variations are observed. The argument made by Marra and Barber (2005) and also by Marra and Moore (2009) is that the monsoons affect more strongly micrograzer populations than the phytoplankton, since the phytoplankton are not mixed to depths greater than their capacity for positive production. Thus, in the Arabian Sea, we have a situation where vertical mixing may apply more to heterotrophs than autotrophs.

In conclusion, our observations from moorings in the Iceland Basin (1989 and 1991) support the idea that water column stratification is the trigger for the spring phytoplankton bloom in the North Atlantic. Before the observed spring increase, calculations of the critical depth suggest that the phytoplankton are capable of maintaining themselves through winter, with perhaps small episodic increases of biomass with transient stratification events. The Arabian Sea serves as a useful contrast to the North Atlantic, in that vertical mixing does not extend beneath the euphotic zone (and certainly not to a critical depth). Thus, for the Arabian Sea, vertical mixing affects grazer populations to a greater extent than the phytoplankton.

References

- Backhaus, J. O., Hegseth, E. N., Wehde, H., Irigoien, X., Hatten, K., and Logemann, K. 2003. Convection and primary production in winter. *Marine Ecology Progress Series*, 251: 1–14.
- Barber, R. T., Marra, J., Bidigare, R. R., Codispoti, L. A., Halpern, D., Johnson, Z., Latasa, M., *et al.* 2001. Primary productivity and its regulation in the Arabian Sea during 1995. *Deep-Sea Research II*, 48: 1127–1172.
- Behrenfeld, M. J. 2010. Abandoning Sverdrup's Critical Depth Hypothesis on phytoplankton blooms. *Ecology*, 91: 977–989.
- Chiswell, S. M. 2011. Annual cycles and spring blooms in phytoplankton: don't abandon Sverdrup completely. *Marine Ecology Progress Series*, 443: 39–50.
- Cowles, T., and Fessenden, L. 1995. Copepod grazing and fine-scale distribution patterns during the Marine Light–Mixed Layers experiment. *Journal of Geophysical Research*, 100: 6677–6686.
- Dickey, T., Marra, J., Sigurdson, D. E., Weller, R. A., Kinkade, C. S., Zedler, S. E., Wiggert, J. D., *et al.* 1998. Seasonal variability of bio-optical and physical properties in the Arabian Sea: October 1994–October 1995. *Deep-Sea Research II*, 45: 2001–2025.
- Dickey, T., Marra, J., Stramska, M., Langdon, C., Granata, T., Weller, R., Plueddemann, A., *et al.* 1994. Bio-optical and physical variability in the sub-arctic North Atlantic Ocean during the spring of 1989. *Journal of Geophysical Research*, 99: 22541–22556.
- Fischer, A. S., Weller, R. A., Rudnick, D. L., Eriksen, C. C., Lee, C. M., Brink, K. H., Fox, C. A., *et al.* 2002. Mesoscale eddies, coastal upwelling, and the upper-ocean heat budget in the Arabian Sea. *Deep-Sea Research II*, 49: 2231–2264.
- Gifford, D., Fessenden, L., Garrahan, P., and Martin, E. 1995. Grazing by microzooplankton and mesozooplankton in the high-latitude North Atlantic Ocean: spring versus summer dynamics. *Journal of Geophysical Research*, 100: 6665–6675.
- Gillis, A. M. 1991. Why can't we balance the globe's carbon budget? *BioScience*, 41: 442–447.
- Gran, H. H., and Braarud, T. 1935. A quantitative study of the phytoplankton in the Bay of Fundy and the gulf of Maine (including observations on hydrography, chemistry, and turbidity). *Journal of the Biological Board of Canada*, 1: 279–433.
- Keen, T. R., Kindle, J. C., and You, D. K. 1997. The interaction of southwest monsoon upwelling, advection and primary production in the northwest Arabian Sea. *Journal of Marine Systems*, 13: 61–82.
- Kinkade, C. S., Marra, J., Dickey, T. D., and Weller, R. 2001. An annual cycle of phytoplankton biomass in the Arabian Sea, 1994–1995, as determined by moored optical sensors. *Deep-Sea Research II*, 48: 1285–1301.
- Lalli, C., and Parsons, T. R. 1993. *Biological Oceanography: An Introduction*. Pergamon, Oxford, UK.
- Lukas, R., and Lindstrom, E. 1991. The mixed layer of the western equatorial Pacific Ocean. *Journal of Geophysical Research*, 96: 3343–3357.
- Mahadevan, A., D'Asaro, E., Lee, C., and Perry, M. J. 2012. Eddy-driven stratification initiates North Atlantic spring phytoplankton Blooms. *Science*, 337: 54–58.
- Marra, J. 2004. The compensation irradiance for phytoplankton in nature. *Geophysical Research Letters*, 31: L06305.
- Marra, J., and Barber, R. T. 2005. Primary productivity in the Arabian Sea: a synthesis of JGOFS data. *Progress in Oceanography*, 65: 159–175.
- Marra, J., and Moore, T. S., II. 2009. Monsoons, islands, and eddies: their effects on phytoplankton in the Indian Ocean. *In* *Indian Ocean Biogeochemical Processes and Ecological Variability*, pp. 57–70. *Geophysical Monograph Series* 185.
- Marra, J., Langdon, C., and Knudson, C. 1995. Primary production, water column changes and the demise of a *Phaeocystis* bloom at the ML-ML site in the northeast Atlantic Ocean. *Journal of Geophysical Research*, 100: 6633–6643.
- Marra, J., Dickey, T. D., Ho, C., Kinkade, C. S., Sigurdson, D. E., Weller, R. A., and Barber, R. T. 1998. Variability in primary production as observed from moored sensors in the central Arabian Sea in 1995. *Deep-Sea Research II*, 45: 2253–2267.
- Mills, E. L. 1989. *Biological Oceanography: An Early History, 1870–1960*. Cornell University Press, Ithaca, NY.
- Monterey, G., and Levitus, S. 1997. Seasonal Variability of Mixed Layer Depth for the World Ocean. NOAA Atlas NESDIS 14.
- Platt, T., Bird, D., and Sathyendranath, S. 1991. Critical depth and marine primary production. *Proceedings of the Royal Society of London, Series B*, 246: 205–217.
- Plueddemann, A. J., Weller, R. A., Stramska, M., Dickey, T. D., and Marra, J. 1995. The vertical structure of the upper ocean during the Marine Light–Mixed Layer experiment. *Journal of Geophysics Research*, 100: 6605–6619.
- Plueddemann, A. J., Weller, R. A., Stramska, M., Dickey, T. D., Marra, J., Tupper, G. H., Way, B. S., *et al.* 1993. *The Marine Light–Mixed Layers Cruise and Data Report*. Tech. Rep. WHOI-93–33, Woods Hole Oceanographic Institution, Woods Hole, MA. 116 pp.
- Riley, G. A. 1942. The relationship of vertical turbulence and spring diatom flowerings. *Journal of Marine Research*, 5: 67–87.
- Robinson, M. K., Bauer, R. A., and Schroeder, E. H. 1979. *Atlas of North-Atlantic-Indian-Ocean Monthly Mean Temperatures and Mean Salinities of the Surface Layer*. US Naval Oceanographic Office, Ref. Pub. 18.
- Rudnick, D. L., Weller, R. A., Eriksen, C. C., Dickey, T. D., Marra, J., and Langdon, C. 1997. Moored instruments weather Arabian Sea monsoons yield data. *EOS*, 78: 117–121.
- Smetacek, V., and Passow, U. 1990. Spring bloom initiation and Sverdrup's critical-depth model. *Limnology and Oceanography*, 35: 228–234.

- Stramska, M., and Dickey, T. 1992. Variability of bio-optical properties of the upper ocean associated with diel cycles in phytoplankton population. *Journal of Geophysical Research*, 97: 17873–17887.
- Stramska, M., and Dickey, T. 1993. Phytoplankton bloom and the vertical thermal structure of the upper ocean. *Journal of Marine Research*, 51: 819–842.
- Stramska, M., and Dickey, T. 1994. Modeling phytoplankton dynamics in the northeast Atlantic during the initiation of the spring bloom. *Journal of Geophysical Research*, 99: 10241–10253.
- Stramska, M., Dickey, T., Marra, J., Plueddemann, A., Langdon, C., and Weller, R. 1995. Bio-optical variability associated with phytoplankton dynamics in the North Atlantic. *Journal of Geophysical Research*, 100: 6621–6632.
- Sverdrup, H. U. 1953. On the conditions for the vernal blooming of phytoplankton. *Journal du Conseil/Conseil Permanent International pour l'Exploration de la Mer*, 18: 287–295.
- Taylor, J. R., and Ferrari, R. 2011. Shutdown of turbulent convection as a new criterion for the onset of spring phytoplankton blooms. *Limnology and Oceanography*, 56: 2293–2307.
- Weller, R., Fischer, A. S., Rudnick, D. L., Eriksen, C. C., Dickey, T., Marra, J., Fox, C., *et al.* 2002. Moored observations of upper_ocean response to the monsoons in the Arabian Sea during 1994–1995. *Deep Sea Research II*, 49: 2195–2230.
- Weller, R. A., Baumgartner, M. F., Josey, S. A., Fischer, A. S., and Kindle, J. C. 1998. Atmospheric forcing in the Arabian Sea during 1994–1995: observations and comparisons with climatology. *Deep Sea Research II*, 45: 1961–1999.
- Weller, R. A., Rudnick, D. L., Payne, R. E., Dean, J. P., Pennington, N. J., and Trask, R. P. 1990. Measuring near-surface meteorology over the ocean from an array of surface moorings in the subtropical convergence zone. *Journal of Atmospheric and Oceanic Technology*, 7: 85–103.

Handling editor: Howard Browman



Contribution to the Themed Section: 'Revisiting Sverdrup's Critical Depth Hypothesis' Original Article

Basin-wide mechanisms for spring bloom initiation: how typical is the North Atlantic?

Harriet S. Cole^{1,2}, Stephanie Henson³, Adrian P. Martin³, and Andrew Yool³

¹Ocean and Earth Science, National Oceanography Centre Southampton, University of Southampton Waterfront Campus, European Way, Southampton SO14 3ZH, UK

²Now at Marine Laboratory, Marine Scotland Science, 375 Victoria Road, Aberdeen AB11 9DB, UK

³National Oceanography Centre, University of Southampton Waterfront Campus, European Way, Southampton SO14 3ZH, UK

*Corresponding author: tel: +1 224 295508; fax: +1 224 295511; e-mail: h.cole@marlab.ac.uk

Cole, H. S., Henson, S., Martin, A. P., and Yool, A. Basin-wide mechanisms for spring bloom initiation: how typical is the North Atlantic? – ICES Journal of Marine Science, 72: 2029–2040.

Received 30 May 2014; revised 28 November 2014; accepted 4 December 2014; advance access publication 7 January 2015.

The annual phytoplankton bloom is a key event in pelagic ecosystems. Variability in the timing, or phenology, of these blooms affects ecosystem dynamics with implications for carbon export efficiency and food availability for higher trophic levels. Furthermore, interannual variability in phytoplankton bloom timing may be used to monitor changes in the pelagic ecosystem that are either naturally or anthropogenically forced. The onset of the spring bloom has traditionally been thought to be controlled by the restratification of the water column and shoaling of the mixed layer, as encapsulated in Sverdrup's critical depth hypothesis. However, this has been challenged by recent studies which have put forward different mechanisms. For example, the critical turbulence hypothesis attributes bloom initiation to a reduction in turbulent mixing associated with the onset of positive net heat fluxes (NHF). To date, the majority of studies on bloom initiation mechanisms have concentrated on North Atlantic datasets leaving their validity in other subpolar regions unknown. Here, we use chlorophyll output from a model that assimilates satellite ocean colour data to calculate bloom initiation timing and examine the basin-wide drivers of spatial and interannual variability. We find that the date that the NHF turns positive is a stronger predictor for the date of bloom initiation, both spatially and interannually, across the North Atlantic than changes in the mixed layer depth. However, results obtained from the North Pacific and Southern Ocean show no such basin-wide coherence. The lack of consistency in the response of the subpolar basins indicates that other drivers are likely responsible for variability in bloom initiation. This disparity between basins suggests that the North Atlantic bloom initiation processes are unique and therefore that this region may not be a suitable model for a global, theoretical understanding of the mechanisms leading to the onset of the spring bloom.

Keywords: bloom initiation, critical depth, critical turbulence, phytoplankton phenology.

Introduction

Phenology is the study of the timing of periodic biological events, such as the annual phytoplankton bloom, and has led to a number of ecological and biogeochemical insights. For example, the timing of greatest food availability is important for grazers in addition to food abundance as summarized in the match–mismatch hypothesis (Cushing, 1990). This hypothesis states that interannual variability in the timing of the bloom results in years where the bloom coincides with larval hatching (a match) and years where their timing is not synchronous (mismatch). This affects larval survival and recruitment rates of several commercially important species (Cushing, 1990;

Platt *et al.*, 2003; Fuentes-Yaco *et al.*, 2007; Koeller *et al.*, 2009; Kristiansen *et al.*, 2011). Furthermore, phytoplankton seasonality has impacts on the magnitude and efficiency of carbon export. The bloom duration has been linked to carbon export efficiency with short, but highly productive, blooms producing less refractory material (Lutz *et al.*, 2007), though exporting larger quantities of organic carbon (Eppley and Peterson, 1979; Francois *et al.*, 2002).

The expected subpolar ocean response to climate change is stronger stratification of the water column, occurring earlier in the year and breaking down later (Sarmiento *et al.*, 2004). Based on this prediction, primary production in subpolar regions is expected to

increase as the longer period of stratification extends the growing season with blooms starting earlier and ending later (Doney, 2006). In contrast, productivity in the subtropics is expected to decrease as nutrient limitation will be more severe and longer lasting. Thus, bloom timing metrics can be used as additional monitoring indicators to detect changes in the pelagic ecosystem (Platt et al., 2009). However, before trying to predict these changes we must first understand the drivers of contemporary interannual variability.

Several recent studies have related the observed variability in bloom initiation to annual, seasonal, or shorter term means in a physical parameter. In the North Atlantic, bloom initiation is reported to vary by 2–3 weeks relative to the mean and has been related to the winter mean net heat flux (NHF) and windspeed (Henson et al., 2006) as well as the windspeed during the bloom (Ueyama and Monger, 2005). Variability in initiation timing has also been linked to large-scale climate indices such as the North Atlantic Oscillation (Henson et al., 2009; Zhai et al., 2013). In the Arctic, bloom initiation has been related to the timing of sea ice melt, changes in which have driven an advance in bloom timing of 50 d since 1997 (Kahru et al., 2011).

In the North Pacific, several drivers of bloom timing variability have been identified. Sasaoka et al. (2011) found bloom initiation varied by ~5 weeks in the coastal subpolar North Pacific and was related to the winter Southern Oscillation Index. In *El Niño* years (negative SOI), sea surface temperature (SST) in these regions is warmer than average consistent with earlier stratification and alleviated light limitation resulting in an earlier bloom. Conversely, in open ocean regions of the North Pacific blooms occurred earlier in *La Niña* years when SST was cooler, mixing stronger, and iron and nutrient entrainment greater. Additionally, bloom timing variability has been linked to large-scale climate indices such as the Pacific Decadal Oscillation and changes in SST and mixed layer depth (MLD; Sasaoka et al., 2011; Chiba et al., 2012).

Bloom initiation variability in the Southern Ocean has only recently been examined, and seasonal and intraseasonal variability in MLD, heat fluxes, and iron supply have been identified as potential drivers (Thomalla et al., 2011). Other regions have been shown to be more variable, especially boundary regions between subpolar and subtropical gyres. In these areas, bloom initiation dates vary by ~20 weeks in the North Atlantic (Henson et al., 2009) and Southern Ocean (Thomalla et al., 2011).

Studying the drivers of variability in bloom initiation may also provide insights into the mechanisms that lead to the onset of the spring bloom in the first place. Additionally, using interannual variability in the timing of the bloom is likely to be a stronger test of theories of bloom initiation than using a single year, which may have experienced anomalous conditions. Currently, there are several theories concerning the conditions that cause the bloom to start in subpolar regions. The critical depth hypothesis states that the bloom starts when the MLD shoals to a point where the average irradiance in the mixed layer is high enough for net growth to occur in the phytoplankton population (i.e. photosynthesis > respiration; Sverdrup, 1953). An extension of this, the critical turbulence hypothesis states that blooms may start when mixed layers are still very deep, if the rate of near surface vertical mixing has reduced sufficiently. This means that phytoplankton are no longer rapidly mixed out of the euphotic zone and are able to accumulate and grow in the near surface (Huisman et al., 1999; Taylor and Ferrari, 2011). Turbulent mixing may be reduced through an increase in the heat flux into the ocean or a reduction in windspeed. A further theory is the dilution-recoupling hypothesis, which states that the bloom starts

when the mixed layer is at its maximum depth, when phytoplankton and grazers are sufficiently diluted so encounter rates are minimal and growth can overcome grazing losses (Behrenfeld, 2010; Boss and Behrenfeld, 2010). On smaller spatial scales, eddies have been observed to play a role in starting the spring bloom by restratifying the water column in spring, earlier and more quickly than by solar heating alone (Mahadevan et al., 2012).

Significantly, all these hypotheses were developed using observations from the North Atlantic. However, each of the subpolar basins present their own character and are hydrodynamically different from each other; the North Atlantic has very deep winter mixed layers, the North Pacific has a permanent halocline and is iron limited, as is the Southern Ocean. Thus, although the theories discussed above are mechanisms that may be present across all the basins, there may not be a single globally consistent mechanism for bloom initiation. This begs the question of whether the dominant mechanism for bloom initiation is the same everywhere, or if our view of spring bloom initiation is skewed by the dominance of studies focused on the North Atlantic.

This study aims to use satellite-derived chlorophyll data and output from a data-assimilating model to quantify variability in the date of bloom initiation in the subpolar North Atlantic, North Pacific, and Southern Oceans. The bloom initiation dates will be used to identify dominant, basin-wide drivers of variability in the onset of the bloom and to assess if bloom timing responds to interannual variability in forcing in a similar manner. In this way, we will address the question, “How typical is the North Atlantic?”

Data and methods

Datasets

Bloom initiation timing was calculated from a satellite-derived chlorophyll dataset, GlobColour, and from the output of the NASA Ocean Biogeochemistry Model (NOBM). Both bloom metric datasets were regridded to $1 \times 1^\circ$ grid to match the physical datasets. The GlobColour dataset was available at $1 \times 1^\circ$ resolution and as 8 d composites and was downloaded from <http://globcolour.info>. It combines data from three ocean colour sensors: SeaWiFS, MODIS, and MERIS. Data covering the period 2002–2009 are used here as all three sensors were operational over this period and to match the availability of the other datasets being used. GlobColour is reported to perform better than the individual sensors when compared with the SeaWiFS Bio-optical Archive and Storage System (SeaBASS) database, an *in situ* dataset used for comparison with remote sensing products (Durand, 2007). For GlobColour chlorophyll, the match up statistics with *in situ* data are similar to SeaWiFS with a root mean square log error of 30% (SeaWiFS: 31%) and a coefficient of determination of 0.73 (SeaWiFS: 0.76; Gregg and Casey, 2004; Durand, 2007). However, GlobColour improves coverage in both space and time, since it includes three datasets (Durand, 2007).

NOBM is a dynamic plankton ecosystem model that assimilates SeaWiFS data as surface chlorophyll. The ability of NOBM to reproduce seasonal blooms in chlorophyll was assessed by Cole et al. (2012). NOBM shows high fidelity to seasonal characteristics, although absolute concentrations of chlorophyll can be slightly different (Cole et al., 2012). This means that while the magnitude of the bloom in NOBM may be different from that recorded by SeaWiFS, the timing of the bloom remains the same in both datasets. Since the bloom timing is based on the relative change in chlorophyll concentration, accuracy in the timing rather than the magnitude is of greater consequence for this study.

The analysis was performed on both the GlobColour and NOBM chlorophyll datasets. The GlobColour dataset extends further towards the poles giving wider global coverage and spans more years (2002–2009) than NOBM (2002–2007). However, NOBM is used here to more accurately determine interannual variability in bloom timing (as it is a gap-free dataset vs. the satellite-derived GlobColour which has missing data), as well as to provide a second estimate and thus improve the robustness of this study. The chlorophyll output from NOBM has previously been used to quantify the impact of missing data in the satellite record on the accuracy of bloom initiation and peak dates (Cole *et al.*, 2012). Cole *et al.* (2012) found that missing data resulted in errors of ~30 d in bloom initiation timing further justifying the use of NOBM output in this analysis. All the physical datasets used were observational and were used in conjunction with bloom timing dates from both GlobColour and NOBM.

The physical parameters considered were NHF, MLD, and mean mixed layer photosynthetically active radiation (PAR_{ML}). The NHF data were downloaded from the WHOI OAflux project website (<http://oaflux.whoi.edu>) as a $1 \times 1^\circ$ dataset and with daily temporal resolution, which was averaged to 8 d to match the chlorophyll data. The MLD was calculated from a global dataset of regularly gridded temperature and salinity profiles, obtained from the Coriolis project (<http://www.coriolis.eu.org>). These profiles were collected from ARGO floats, expendable bathythermographs, conductivity temperature and depth, profiles and moorings. These were available on a $1/10$ by $1/10^\circ$ grid but were regridded to $1 \times 1^\circ$ to match the other datasets. Density was calculated from the regridded profiles and the MLD was defined as the depth at which the density had increased by 0.03 kg m^{-3} relative to a reference depth of 10 m to avoid diurnal effects. PAR data were downloaded from the MODIS ocean colour webpage (<http://oceancolor.gsfc.nasa.gov>) as 8 d composites and were regridded to a spatial resolution of $1 \times 1^\circ$. The attenuation coefficient at 490 nm was obtained from the GlobColour webpage and is derived from the chlorophyll concentrations (Barrot, 2010). This was converted to Kd_{PAR} (attenuation coefficient for all PAR wavelengths) using the conversion detailed in Morel *et al.* (2007). The mean irradiance in the mixed layer was calculated using Equation (1).

$$PAR_{ML} = \left(\frac{PAR_0}{KD} \right) (1 - e^{-KD}), \quad (1)$$

where PAR_0 is the surface photosynthetically available irradiance,

k the attenuation coefficient (Kd_{PAR}), and D the depth of the mixed layer as described above.

Subpolar regions were identified using correlations between the chlorophyll and MLD climatological annual cycles at each pixel (as in Henson *et al.*, 2009). Pixels poleward of 40°N/S with a negative correlation (shallower MLD associated with higher chlorophyll) were defined as being subpolar. Pixels without a strong seasonal cycle, defined as having a coefficient of variation (CV – variance/mean) value of 0.35 or lower, were excluded from the analysis (Cole *et al.*, 2012). Defining the subpolar regions was necessary as some subtropical regions have a strong seasonal cycle but the mechanisms underlying it are different from subpolar blooms.

Timing of bloom initiation

The initiation date was defined as the date on which the chlorophyll concentration exceeded a threshold value more than 5% of the annual median. This criterion has been frequently used previously to define the bloom initiation date (Siegel *et al.*, 2002; Henson *et al.*, 2009; Racault *et al.*, 2012; Brody *et al.*, 2013). As January is not always an appropriate date from which to start a “bloom year” (e.g. in the southern hemisphere), the date of the peak (defined as the date of the maximum chlorophyll value in each year) was used as a reference point and the date of bloom initiation is found in the preceding 6 months. The bloom initiation was found by searching backwards in time from the peak identifying the last datum before the threshold value was exceeded. The bloom initiation date was calculated for each year at each pixel in the North Atlantic, North Pacific, and Southern Ocean.

Physical timing metrics

Many of the previous studies discussed in the introduction that address bloom initiation processes focus on seasonal or annual means in parameters such as MLD, NHF, or windspeed. Here, the focus will be on the relationships between interannual variability in bloom initiation and the timing of a change in the physical environment (e.g. timing of MLD shoaling). Strong correlations between the interannual variability in bloom timing and physical forcing may lead to alternative insights into the mechanisms that control bloom initiation.

A suite of physical timing metrics (see Table 1 for definitions) were devised based on extant theories. The timing metrics were calculated for each year at each pixel. In the Southern Ocean, time-series were adjusted to run from July to June before calculating the metric dates to match the seasonal chlorophyll cycle.

Table 1. Description of physical metrics.

Metric name	Definition	Reference
Maximum MLD	Date on which the maximum (deepest) MLD value occurs	Behrenfeld (2010), Boss and Behrenfeld (2010)
MLD shoaling	The date of steepest gradient in MLD (i.e. becoming shallower) which occurred between the maximum and minimum MLD	Sverdrup (1953)
NHF turns positive	The date on which the NHF became positive was defined as the date it first exceeds zero for at least 16 d (two consecutive time-steps)	Huisman <i>et al.</i> (1999), Taylor and Ferrari (2011)
PAR_{ML} starts to increase	The date the gradient in PAR_{ML} became positive. This must occur between the beginning of the annual cycle and the date of the peak value of PAR_{ML}	
Fastest rise in PAR_{ML}	The date of largest increase in PAR_{ML} between the beginning of the annual cycle and the maximum PAR_{ML} value	
MLD becomes shallower than euphotic depth (MLD < Z_{eu})	Date on which the MLD becomes shallower than the euphotic depth (define as 1% of surface irradiance) for at least 16 d (two time-steps). This served as a proxy for the MLD crossing the critical depth and light levels ceasing to be limiting	Sverdrup (1953)

From the annual cycle of MLD the dates of maximum MLD and MLD shoaling were calculated. From the NHF annual cycle, the date the NHF became positive was calculated. This latter metric is a proxy for a change from winter convection to less turbulent conditions (Taylor and Ferrari, 2011). The dates of interest from the annual cycle of PAR_{ML} include the date PAR_{ML} starts to increase and the date of fastest rise in PAR_{ML} . These are proxies for when light levels become favourable for growth and when light is most rapidly becoming less limiting. Additionally, the depth of the euphotic zone, defined as the depth at which 1% of the surface PAR still remained, was calculated. This was used to calculate the date on which the MLD became shallower than the euphotic zone depth as another proxy for the alleviation of light limitation.

Latitudinal means of the physical and bloom timing metrics were calculated for each degree of latitude across the three basins. In addition, each ocean basin was split into a number of 10° longitude by 10° latitude boxes, for which interannual anomalies in the physical and bloom metric dates were calculated (Figure 1). The size of these boxes was chosen to filter out mesoscale features and to focus on large-scale variability. Averaging the metric dates over these large boxes also removes the effect of temporal autocorrelation on the correlations. Similarly, the effect of spatial autocorrelation is reduced for the correlations of the latitudinal means due to the coarse resolution averaging used. For all basins, the anomalies in bloom and physical metric dates were approximately normally distributed.

Results

Generally, the date of bloom initiation in all three basins becomes progressively later towards the poles (Figure 1). In the North Atlantic, blooms initiate during February–March at ~ 40 – 45° N progressing to initiation dates in May, June, and July at higher latitudes. In the North Pacific, although on average blooms occur later at higher latitudes, blooms are seen to initiate earlier (April/May) near the coast progressing to later blooms offshore (June/July). In the Southern Ocean, bloom timing gets progressively later towards the pole, with blooms starting in August/September at 40° S and January/February south of 65° S.

As an example of the degree to which the timing of the bloom and physical metrics coincide, average time-series from the North Atlantic (45 – 80° N -60 to 0° E), North Pacific (50 – 70° N -120 to 120° E), and Southern Ocean (-80 to -50° N -180 to 180° E) are shown in Figure 2. Broadly speaking, bloom initiation occurred just after the NHF turns positive, the MLD was shoaling and PAR_{ML} was increasing in all three basins except for the Southern Ocean. There are clear differences in the variability of the physical parameters between the three basins though the NHF annual cycle was fairly similar between the three basins ranging from -200 to 200 $W\ m^{-2}$. The largest inter-basin differences were seen in the maximum depth reached by the mixed layer. In the North Atlantic, the mean maximum MLD varied between 150 and 200 m was ~ 50 m at its deepest in the North Pacific and ~ 110 m in the Southern Ocean. The maximum

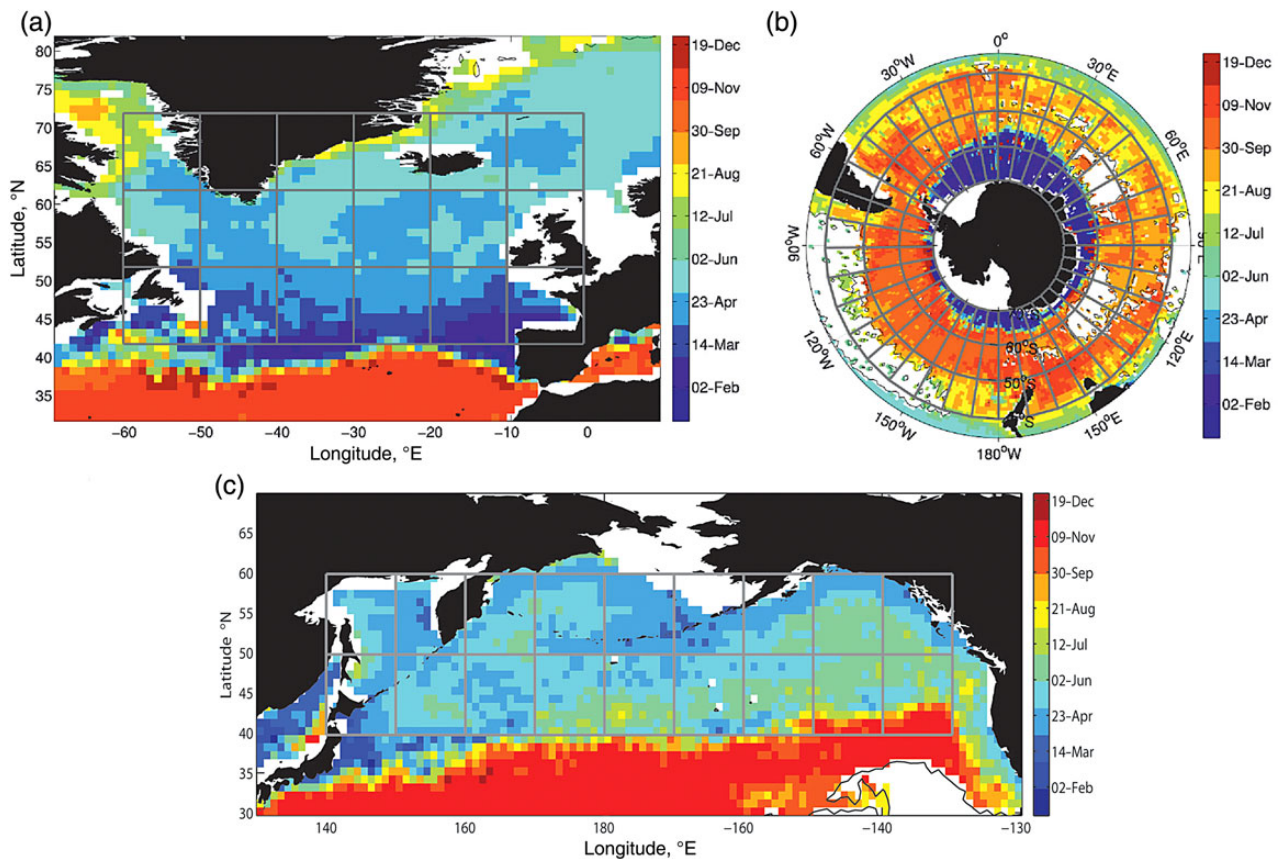


Figure 1. Map of the mean date of bloom initiation (2002–2009) in (a) the North Atlantic, (b) Southern Ocean, and (c) the North Pacific. Each map show the location of the boxes used to calculate interannual anomalies in the date of bloom initiation. Each box is 10° longitude by 10° latitude. White regions bounded by the black contour are regions of low seasonality. Other white regions are areas of permanent sea ice cover. A colour version of this figure is available online.

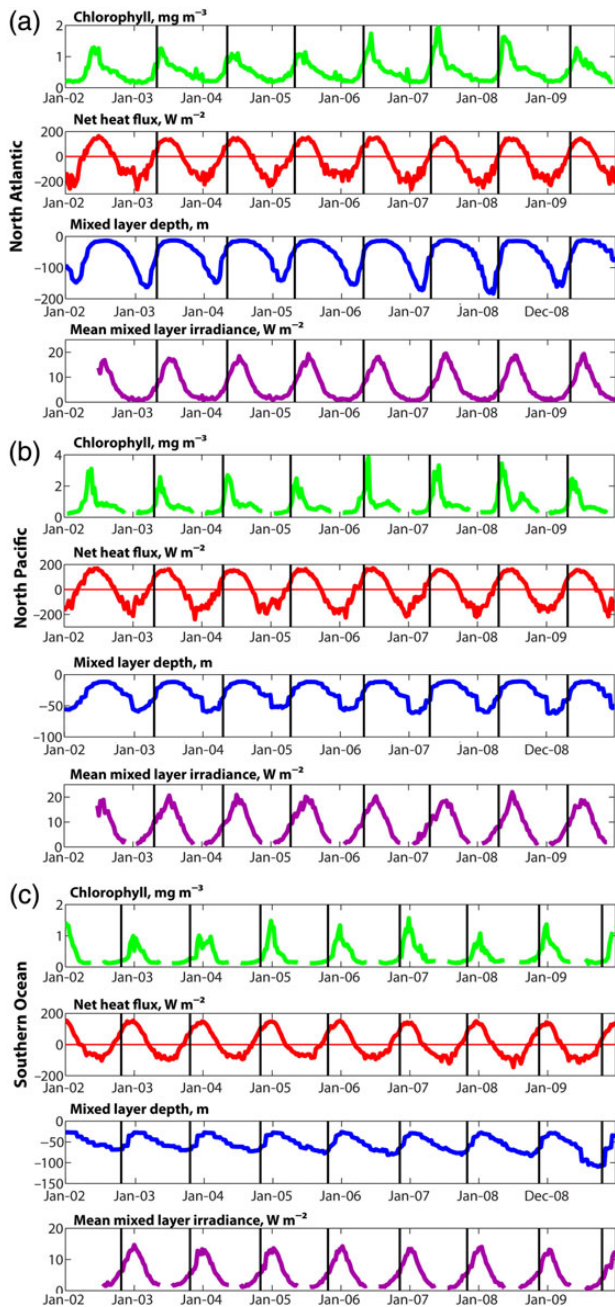


Figure 2. Mean time-series (2002–2009) across the (a) North Atlantic, (b) North Pacific, and (c) Southern Ocean for GlobColour chlorophyll (mg m^{-3}), NHF (W m^{-2}), MLD (m), and mean mixed layer irradiance (W m^{-2}). The black vertical line represents the mean bloom initiation date (years 2003–2009). The mean bloom initiation dates are calculated from averaging the metric dates in each year across the basin (i.e. they are not calculated from the chlorophyll time-series above). A colour version of this figure is available online.

PAR_{ML} was lowest in the Southern Ocean ($\sim 15 \text{ W m}^{-2}$) but similar in the North Atlantic and North Pacific ($\sim 20\text{--}23 \text{ W m}^{-2}$).

The critical depth and critical turbulence hypothesis both indicate that if a physical timing event is a driver of spatial variability in bloom timing then the two metrics are likely to occur at similar times in a given year, though potentially with a lag, and have similar latitudinal gradients (Figure 3; Table 2, see Supplementary

Figure S2 for plots of further physical metrics). In the North Atlantic, the date of bloom initiation closely follows the progression of the date the NHF turns positive and progresses polewards at a similar rate (initiation: 5.72 km d^{-1} , NHF turns positive: 6.72 km d^{-1}) and they are strongly correlated ($r = 0.95$). The bloom initiation also has very similar timing to the date the ML irradiance starts to increase and the date of MLD shoaling. Both are strongly correlated ($r = 0.87$ and $r = 0.86$, respectively). The other physical timing metrics are also highly correlated with bloom initiation (most have $r \geq 0.67$ and are statistically significant; Table 2) in the North Atlantic. However, in the North Pacific, the metrics do not match well and are generally weakly correlated ($r \leq 0.32$), except the date at which the MLD becomes shallower than the euphotic depth ($r = 0.52$). In the Southern Ocean, the date of bloom initiation has a similar progression to that of the date the NHF turns positive, is highly correlated ($r = 0.98$), and progresses towards the pole at similar speeds (initiation: -2.54 km d^{-1} , NHF turns positive: -2.53 km d^{-1}). Furthermore, the date the PAR starts to rise is also highly correlated with bloom initiation and progresses at a similar speed (Table 2; $r = 0.98$, speed = -2.84 km d^{-1}).

On an interannual basis, mostly weak correlations are seen between the interannual anomalies in bloom initiation and in the physical timing metrics. However, a reasonable correlation ($r = 0.61$) is seen between interannual variability in the timing of bloom initiation and the date at which the NHF turns positive in the North Atlantic (Figure 4, Table 3, see Supplementary Figure S3 for scatterplots of further physical metrics). Weak but significant ($p < 0.05$) correlations with bloom initiation timing are also seen with the date of maximum MLD ($r = 0.21$) and MLD shoaling ($r = 0.25$), $MLD > Z_{eu}$ ($r = 0.29$), and PAR starts to increase ($r = 0.29$) in the North Atlantic. No strong positive correlations were seen in the North Pacific. The only significant, positive correlation seen in the Southern Ocean was with the date of NHF turning positive but was very weak (< 0.12).

Discussion

Drivers of variability in bloom initiation

In the North Atlantic, the timing of bloom initiation coincides with the period of increasing stratification and decreasing mixing as the NHF becomes positive, the MLD shoals, and PAR_{ML} increases (Figure 2). This suggests that they may potentially be prominent drivers for interannual variability in bloom initiation. This is supported by the synchronous timing and high correlation in the latitudinal progression of bloom initiation, NHF turning positive, MLD shoaling, and the date the PAR_{ML} starts to increase.

In comparison, bloom initiation in the North Pacific had neither high correlation, nor synchronous timing with, any of the physical timing metrics. However, it was moderately correlated and had synchronous timing, with the date the MLD becomes shallower than the euphotic depth. This suggests that variability in the date of bloom initiation is weakly driven by the alleviation of light limitation as the MLD shoals and the surface irradiance increases as spring progresses.

Similar to the North Atlantic, the date the NHF turns positive and the PAR_{ML} starts to increase are indicated as drivers of bloom timing variability in the Southern Ocean. Though many of the other metrics in the North Atlantic and Southern Ocean were moderately to highly correlated, not all had synchronous timing across the whole basin.

It should be noted that at higher latitudes in the Southern Ocean the uncertainty in bloom initiation date due to missing data was

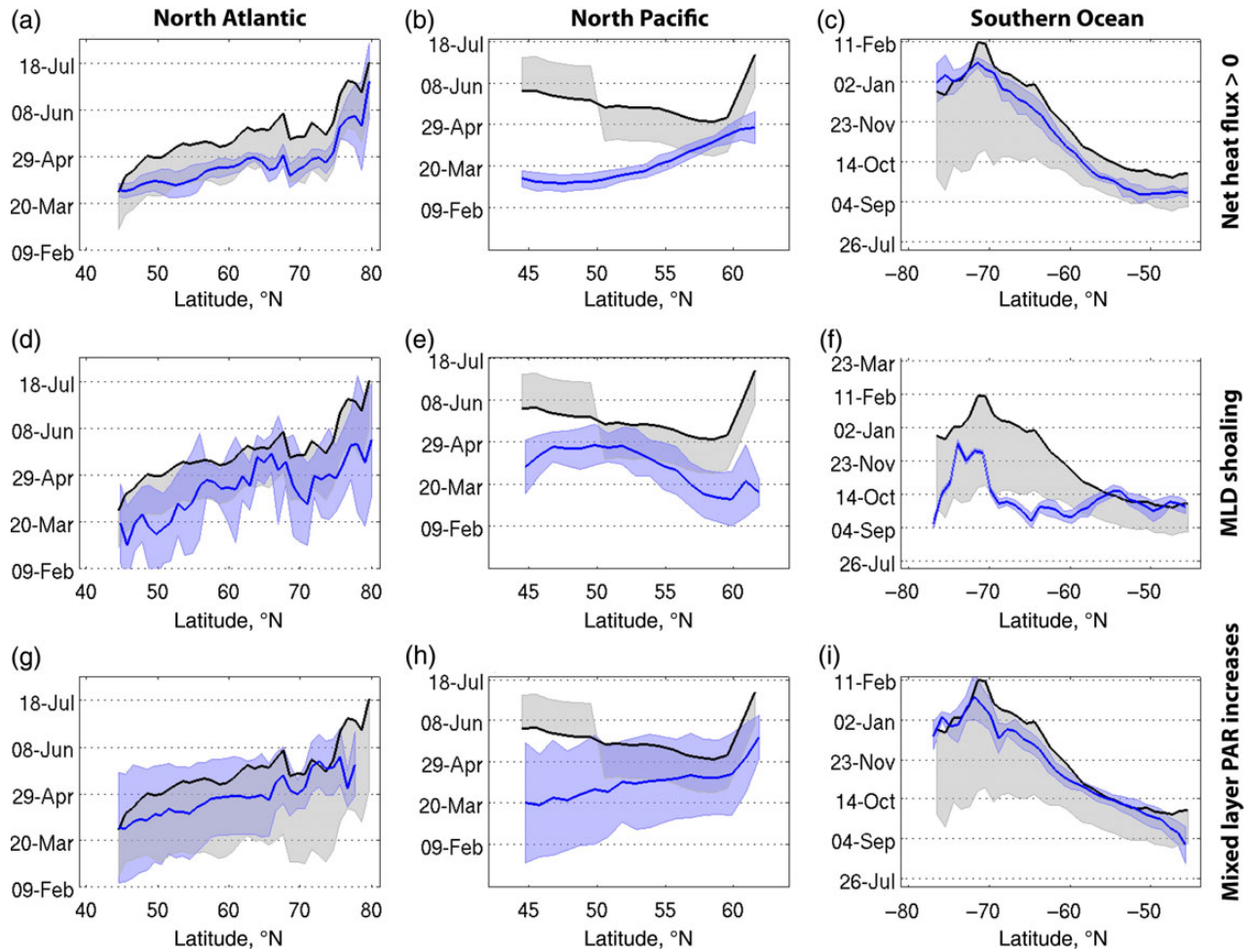


Figure 3. Latitudinal mean date for bloom initiation (black line with light grey shading) and the physical timing metrics [grey line with dark grey shading (blue in online colour version)] (a–c) date of NHF becoming positive, (d–f) MLD shoaling, (g–i) PAR_{ML} begins to increase for each of the three subpolar basins. The light grey shaded area associated with the mean bloom initiation date represents the uncertainty in bloom initiation date arising from missing data in the chlorophyll time-series from which bloom initiation is calculated (Cole et al., 2012). The dark grey (blue in online colour version) shaded regions around the mean physical timing dates represent the variability (1 s.d.) in the physical timing metric dates at that latitude. Pixels with shallow bathymetry (<200 m) or without a significant seasonal cycle (coefficient of variation <0.35) were removed before longitudinal averaging. The vertical axis in all panels is the average metric date (dd-mmm). A colour version of this figure is available online.

Table 2. Correlation coefficients and latitudinal speeds for bloom initiation and associated physical timing metrics in the subpolar basins for GlobColour chlorophyll dataset

	Bloom initiation	NHF positive	MLD max	MLD shoaling	MLD < Zeu ^a	Fastest rise in PAR_{ML}	PAR_{ML} starts to increase
North Atlantic							
Correlation coefficient ^b		0.95*	0.72*	0.86*	0.67*	0.59*	0.87*
Latitudinal speed (km day ⁻¹) ^c	5.72	6.72	13.37	5.29	3.99	5.05	7.29
North Pacific							
Correlation coefficient ^b		0.08	0.20	0.06	0.52	0.15	0.32
Latitudinal speed (km d ⁻¹) ^c	-6.47	3.53	-13.31	-4.65	-2.70	9.30	5.59
Southern Ocean							
Correlation coefficient ^b		0.98*	0.61*	0.45*	0.90*	0.98*	0.98*
Latitudinal speed (km day ⁻¹) ^c	-2.54	-2.53	-3.84	-3.53	-4.31	-5.77	-2.84

^aMLD < Zeu stands for the date the MLD becomes shallower than the euphotic depth.

^bAn asterisk indicates correlation coefficients which are statistically significant at the 95% confidence interval. Correlations were calculated between the bloom initiation latitudinal mean date and the physical metric latitudinal mean date. Mean dates were calculated over the years 2002–2009 for GlobColour.

^cLatitudinal speeds were calculated by regressing the metric dates on latitude (latitude = $a + b \times$ date) and then multiplying the linear coefficient (b) by 111.19493 km/°latitude. Negative numbers indicate that bloom dates get earlier with more northerly latitudes.

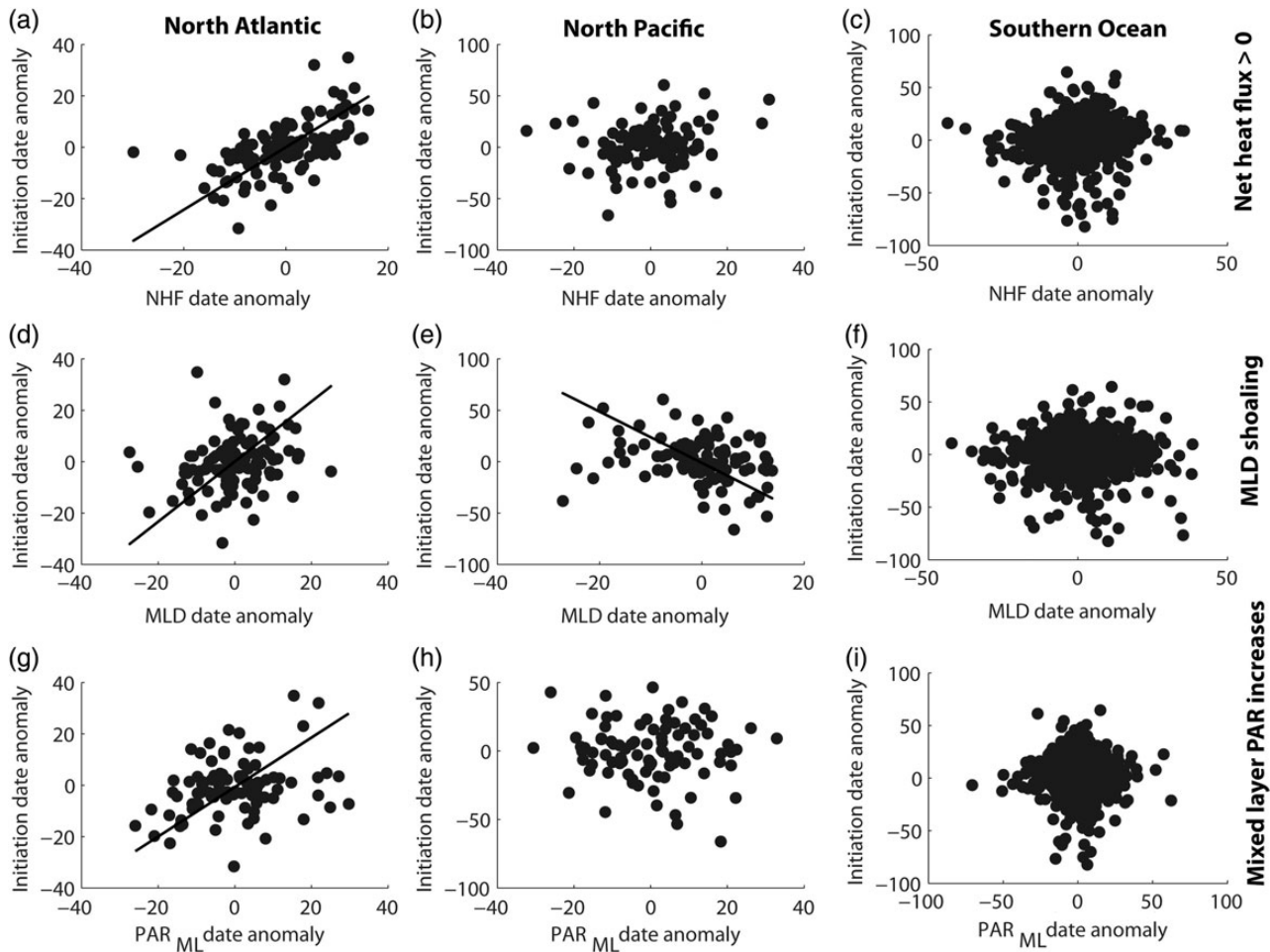


Figure 4. Scatterplots of interannual anomalies in bloom initiation date and associated physical metric (a–c) NHF turns positive, (d–f) MLD shoals, and (g–i) PAR_{ML} starts to increase, for subpolar regions: North Atlantic, North Pacific, and Southern Ocean. Anomalies were calculated using the 10×10^3 boxes shown in Figure 1; each box has 6 datapoints. Fitted lines are shown for statistically significant correlations and are generated using a type II regression which accounts for variability in both x and y parameters.

Table 3. Correlation coefficients between interannual variability in bloom initiation and physical timing metrics in the subpolar basins^a.

	NHF positive	MLD max	MLD shoaling	PAR_{ML} starts to increase	Fastest rise in PAR_{ML}	MLD < Z_{eu} ^b
North Atlantic	0.61*	0.21*	0.25*	0.29*	0.03	0.29*
North Pacific	0.12	-0.08	-0.28*	-0.06	0.04	-0.18
Southern Ocean	0.12*	-0.04	-0.01	0.03	0.02	-0.03

^aAn asterisk indicates correlation coefficients which are statistically significant at the 95% confidence interval.

^bMLD < Z_{eu} stands for the date the MLD becomes shallower than the euphotic depth.

high. However, uncertainty in the date may also arise from the definition used to calculate bloom initiation. The definition used here for bloom initiation was found to be similar to other definitions of bloom timing (Supplementary Figure S1).

Not all the metrics identified as strong drivers of spatial variability were strong drivers of interannual variability. The majority of the physical timing metrics were only weakly correlated with interannual variability in bloom initiation, if at all. The strongest relationships were seen in the North Atlantic where the date that the NHF turns positive was seen to be a strong predictor for the bloom initiation date (Figure 4). The date that the NHF turns positive explains ~37% of the variability in bloom initiation date. In comparison, the relationship between NHF turning positive and bloom initiation was

very weak in the North Pacific and Southern Ocean. The other metric identified as a consistent driver of spatial variation in bloom initiation was the date PAR_{ML} starts to rise in both the North Atlantic and Southern Ocean. However, only a weak (if significant) relationship with interannual variability in bloom initiation was found in the North Atlantic, whereas there was no relationship between these metrics in the other two ocean basins. Other weak correlations were seen with the date of MLD shoaling, maximum MLD, and MLD < Z_{eu} , though only in the North Atlantic.

Spatial vs. interannual variability in bloom onset

Interestingly, many of the dominant drivers of latitudinal variability are not found to be dominant drivers of interannual variability

and even then not consistently across the basins. Similarly, in the subpolar North Atlantic, [Follows and Dutkiewicz \(2002\)](#) found that the relationships between proxies for mixing (e.g. bloom period NHF and windspeed) were strongly correlated with bloom period chlorophyll concentration spatially, but not on an interannual basis. [Follows and Dutkiewicz \(2002\)](#) proposed that this lack of correlation was due to a number of factors such as changes in insolation, mesoscale variability, and grazing pressure having a stronger influence on interannual variability in bloom magnitude. Thus, the lack of an obviously dominant driver of interannual variability in bloom initiation may be because a combination of variables is responsible but that each, individually, only has a small influence on the initiation date or that noise in the datasets used here obscure the interannual relationship. There are many variables not included in this set of timing metrics, especially those representing ecological/biogeochemical processes such as grazing or micronutrient availability which may also have an influence on the interannual variability in timing of bloom onset. Alternatively, a lack of strong relationships in both spatial and interannual variability may indicate that these physical timing metrics are not drivers of bloom timing.

Mechanisms for subpolar bloom initiation

Two of the main theories for bloom initiation are the critical depth hypothesis ([Sverdrup, 1953](#)), for which MLD shoaling is a proxy, and the critical turbulence hypothesis ([Taylor and Ferrari, 2011](#)), for which NHF turning positive is a proxy. Both the date of NHF turning positive and MLD shoaling were strongly related to bloom initiation, in a latitudinal sense, in the North Atlantic. This was also seen in the Southern Ocean though the date of MLD shoaling showed a weaker relationship than in the North Atlantic. However, only the North Atlantic shows a basin-wide interannual

relationship between the NHF turning positive and bloom initiation. This nevertheless suggests that the critical turbulence hypothesis is a better description of the processes that lead to a bloom than the critical depth hypothesis, at least for the North Atlantic.

To investigate the role of MLD and NHF in bloom initiation further, the conditions in the North Atlantic at the time of bloom initiation were examined in more detail (Figure 5 and Table 4). The median conditions in the North Atlantic when blooms started were a low and positive NHF ($\sim 31 \text{ W m}^{-2}$), a relatively shallow MLD

Table 4. Conditions at bloom initiation for the North Atlantic, North Pacific, and Southern Oceans^a.

	North Atlantic	North Pacific	Southern Ocean
NHF			
Min	-406.54	-237.16	-421.80
Max	219.84	237.22	284.09
Median	31.41	122.33	47.40
MAD	44.94	33.16	57.18
MLD			
Min	10.09	10.01	10.59
Max	1 011.81	172.03	690.88
Median	80.04	20.67	58.42
MAD	50.38	8.08	32.73
Mean mixed layer PAR			
Min	0.17	0.78	0.19
Max	37.52	38.67	39.77
Median	2.74	10.68	4.61
MAD	1.61	4.91	2.79

^aMinimum, maximum, median, and median absolute difference (MAD) for the NHF, MLD, and mean mixed layer PAR at bloom initiation in the three subpolar basins. Median and MAD values were calculated from pixel values weighted by area.

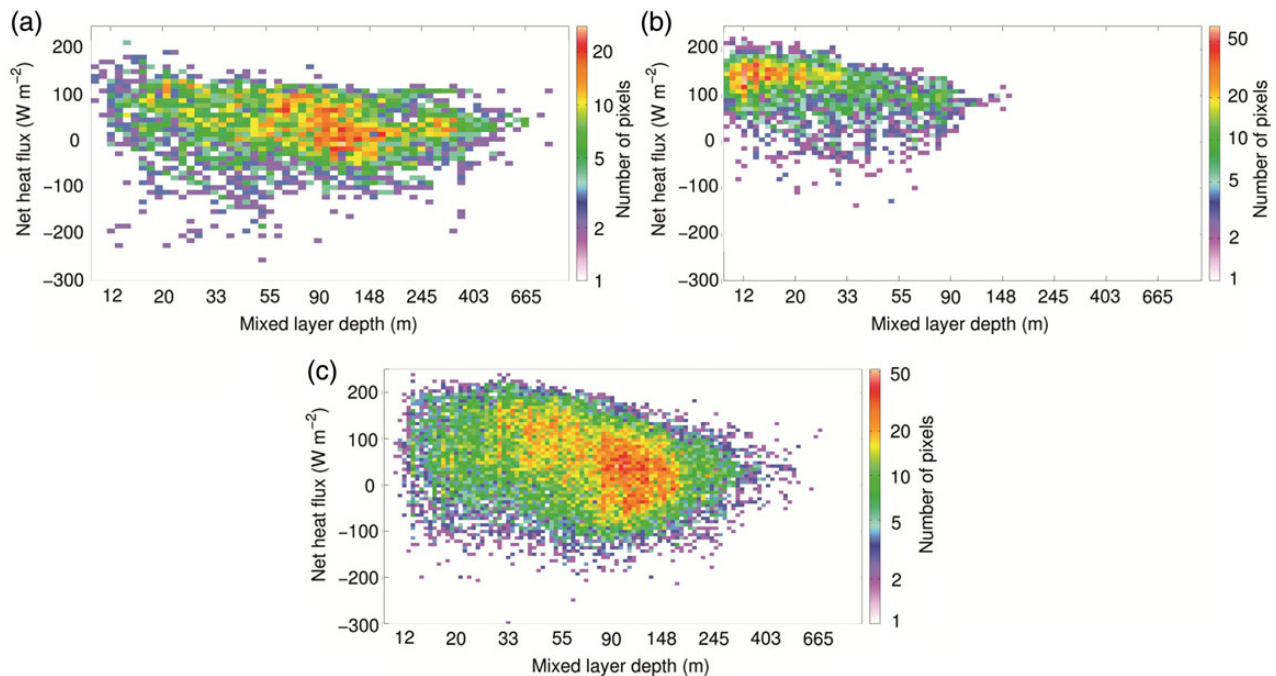


Figure 5. Conditions at bloom initiation for all pixels in the (a) subpolar North Atlantic, (b) North Pacific, and (c) Southern Ocean showing the relationship between NHF and MLD. Data are binned for plotting purposes with the colour bar indicating the number of pixels in each bin. Larger numbers of pixels in a bin indicate a larger number of blooms initiation under these conditions. Note that the colour bar is on a log scale. A colour version of this figure is available online.

(~ 80 m), and low PAR_{ML} (~ 3 $W\ m^{-2}$). In accordance with the critical turbulence hypothesis, a number of blooms (19%) were seen to start in deep mixed layers (deeper than median value) but when the NHF was low and positive (~ 25 $W\ m^{-2}$) (Figure 5). Conversely, 19% of the blooms were also seen to start when MLDs were shallow (shallower than median value) with NHF mostly ranging from 0 to 100 $W\ m^{-2}$. The greatest number of blooms (51%) occurs when the NHF ranges from ~ 50 to 150 $W\ m^{-2}$ and the MLD is between 40 and 240 m deep (the red pixels in Figure 5a). Additionally, PAR_{ML} at the start of the bloom was seen to range from very low values, indicating deep MLD, to very high values when the MLD was very shallow. Based on these results, it would seem that there is evidence to support both the critical depth and critical turbulence hypotheses. However, though MLDs are shallow when the bloom starts the NHF is also typically close to zero. This suggests that the critical turbulence hypothesis could also be valid where both a reduction in turbulence and MLD shoaling come together to initiate a bloom.

The distribution in PAR_{ML} values allows further examination of the critical depth hypothesis. The compensation irradiance is the irradiance at which photosynthesis is equal to respiration. Assuming that at bloom initiation, the MLD is equal to the critical depth, the mean mixed layer irradiance (PAR_{ML}) will be equal to the community compensation irradiance, as this is the light level needed for phytoplankton growth to overcome community losses and rapidly increase phytoplankton standing stocks, according to the critical depth hypothesis (Sverdrup, 1953).

The large range (0.17 – 37.52 $W\ m^{-2}$) in PAR_{ML} at bloom initiation across the North Atlantic suggests that the critical depth hypothesis is not a complete description of the conditions necessary for initiating a bloom. This is because bloom initiation does not seem to be dependent on the mean mixed layer irradiance reaching a certain threshold level that is sufficient for net population growth as bloom initiation occurs under a large range of PAR_{ML} values. Blooms starting in low PAR_{ML} suggest that phytoplankton are not necessarily mixed throughout the whole mixed layer, due to low turbulence mixing, so that their exposure to sufficient irradiance levels

for net growth is increased relative to if they were evenly distributed throughout the ML. Conversely, some blooms initiated when PAR_{ML} was higher than average. This suggests that another limiting factor delayed the start of the bloom since the mean mixed layer irradiance would not be expected to be limiting at these levels.

In the North Pacific, there is weak evidence supporting the critical turbulence hypothesis. Interannual relationships between NHF turning positive and bloom initiation are very weak and bloom initiation occurs in a small number (8%) of pixels when NHF is low and positive (~ 25 $W\ m^{-2}$) and the MLD still relatively deep (Figure 5b). Furthermore, the median value of NHF at bloom initiation is much higher than in the Atlantic (~ 122 $W\ m^{-2}$), MLD much shallower (~ 21 m), and PAR_{ML} much higher (~ 11 $W\ m^{-2}$). This suggests that for the majority of the basin the initiation of the bloom is delayed compared with the North Atlantic, occurring later in the season when ocean warming is more advanced, the MLD shallower and as a result the PAR_{ML} higher. This is supported by the higher NHF values (>100 $W\ m^{-2}$) and shallower MLD (<33 m) under which the majority of blooms in the North Pacific occur (red pixels in Figure 5b). Furthermore, this is reflected in the map of mean bloom initiation dates in Figure 1.

In the Southern Ocean, the median values for NHF (~ 47 $W\ m^{-2}$), MLD (~ 58 m), and PAR_{ML} (~ 5 $W\ m^{-2}$) at bloom initiation were more similar to the North Atlantic values than the North Pacific. This similarity was seen again in Figure 5c with evidence of some blooms (16%) initiating in deep mixed layers when the NHF is low and positive (~ 25 $W\ m^{-2}$). The largest concentration of blooms ($\sim 33\%$) occurs with MLD ranging from 80 to 200 m and NHF ranging from -75 to 150 $W\ m^{-2}$. Similar to the North Atlantic, there are many (29%) blooms that initiate in shallow MLD (30–80 m) and positive NHF (0 – 200 $W\ m^{-2}$). These two bloom groups form coherent patches in the Southern Ocean with the first group dominating open ocean regions and the second marking the shelf and the subpolar/subtropical boundary region. Though this implies that the critical depth and critical turbulence hypotheses may be applicable in different regions of the Southern Ocean,

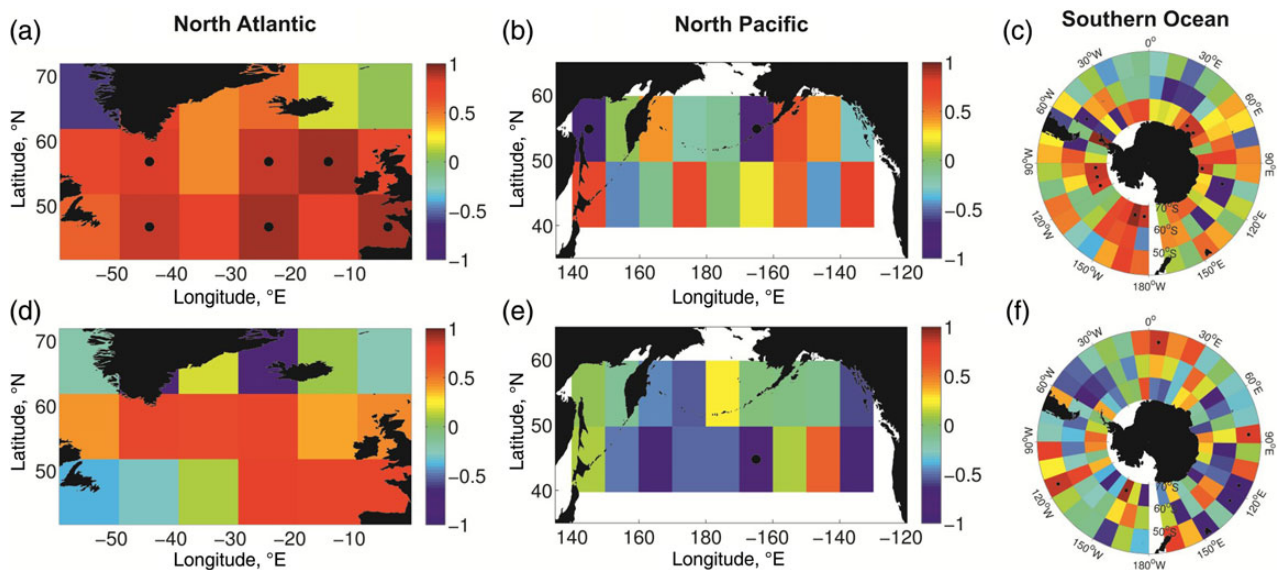


Figure 6. Maps showing the correlation coefficient in each $10 \times 10^\circ$ box between anomalies in the date of bloom initiation and date of NHF turning positive (a–c) and MLD shoaling (d–f) for the North Atlantic, North Pacific, and Southern Ocean. Boxes with a statistically significant correlation are indicated with the black dot. A colour version of this figure is available online.

neither the MLD shoaling nor NHF turning positive were strongly correlated with interannual variability in the bloom initiation date.

Overall, the NHF turning positive is a stronger predictor for the date of bloom initiation than the shoaling of the MLD but this relationship is seen to dominate the whole basin only in the North Atlantic. The strength of the relationship between NHF turning positive and bloom initiation in the North Atlantic is again obvious in its spatial pattern (mean correlation = 0.60) (Figure 6) where strong and significant positive correlations occur across the basin. Conversely, there is no coherent pattern in the correlations between the onset of positive NHF and bloom initiation in the North Pacific. In the Southern Ocean, strong and significant positive correlations occur in larger patches near the Antarctic landmass. In all three basins, the correlations with the onset of positive NHF are more likely to be stronger and positive than the correlations with the shoaling of the MLD.

How typical is the North Atlantic?

Our results raise the question: why do the other basins behave differently from the North Atlantic? Several theories exist for the differences in bloom dynamics between the basins. The bloom in the North Pacific occurs later in the year compared with the North Atlantic. This has been previously reported and several hypotheses have been proposed to explain this observation (Heinrich, 1962; Miller, 1993; Fasham, 1995; Balse and English, 1999; Boyd and Harrison, 1999). Some have focused on the role of grazing on bloom development. The life history of the dominant copepod species in the Pacific means that adults emerge from winter hibernation and immediately lay their eggs, ensuring that their larvae are ready to feed once the bloom starts, whereas in the North Atlantic the adult copepods need to feed on the bloom before being able to lay eggs (Parsons and Lalli, 1988). The differences in the dominant copepod between the basins results from a combination of environmental factors and the differences in phytoplankton production and species composition (Parsons and Lalli, 1988). Alternatively, the elevated light levels resulting from the relatively shallow winter MLD in the North Pacific may sustain primary production over winter. This allows microzooplankton populations to be maintained at levels high enough to graze down the bloom as soon as it starts (Evans and Parslow, 1985; Fasham, 1995; Boyd and Harrison, 1999).

Another theory has suggested that iron limitation may play a role in limiting phytoplankton growth in spring in both the North Pacific and Southern Ocean. Both of these oceans are high nutrient-low chlorophyll regions, and so processes that deliver iron to these regions may dictate the start date of the bloom by increasing growth rates to a point where phytoplankton can escape grazing pressure (Landry et al., 1993; Balse and English, 1999).

The role of wind mixing has not been assessed here but is another parameter that modulates turbulence and may also be a significant driver of bloom timing. A reduction in windspeed may lead to a drop in turbulent mixing and a shoaling MLD and has previously been reported as a predictor for bloom onset around New Zealand and in the Irminger Basin (Henson et al., 2006; Chiswell et al., 2013).

Finally, large differences in the physical environments in the three basins have been observed here. For example, there is a deeper winter MLD in the North Atlantic, although the NHF annual cycle is broadly the same across the basins. The North Atlantic is saltier than the North Pacific due to the northward advection of warm and salty water from the subtropics by the Atlantic Meridional Overturning Circulation (Schmittner et al., 2005).

This makes it easier for cooling to overturn the water column, giving a deeper MLD in the Atlantic.

The North Atlantic may in fact be a poor model system for theoretical understanding of bloom initiation. This is because the North Atlantic results presented here identify the onset of positive NHF as a basin wide driver of variability in bloom initiation though a similar result is not seen in the North Pacific or Southern Ocean. Furthermore, the timing of MLD shoaling was uncorrelated in the North Pacific and Southern Ocean but showed a weak relationship with bloom initiation timing in the North Atlantic. Thus, it would seem that observations from the majority of the world's subpolar regions do not support either the critical turbulence or critical depth hypothesis and that the North Atlantic response may be unique. Further evaluation of the current theories on bloom initiation in the North Pacific and Southern Ocean is needed to properly explain the observed differences from the North Atlantic. This could include the differences in the character of atmospheric forcing, underlying oceanographic conditions (e.g. saltier vs. fresher), physical heterogeneity across the basins, seasonal differences in micronutrient availability and in grazing pressure. This may lead to a greater understanding of the mechanisms that lead to the onset of the spring bloom.

To definitively identify the mechanisms that initiate the spring bloom, *in situ* measurements of additional parameters (e.g. turbulence, nutrients, grazing rates) would be needed. Alternatively, future work could examine the role of mechanisms in different regions using appropriately validated, high resolution, free-running models. Additionally, three-dimensional spatial scale processes at the mesoscale may also influence bloom timing. For example, the results of Mahadevan et al. (2012) demonstrate the role of frontal slumping as a mechanism for restratifying the water column and initiating the bloom. Furthermore, the exact mechanisms for the survival of phytoplankton over winter are still not known in great detail which, if examined further, may help to identify mechanisms for bloom initiation. One such theory is that although phytoplankton are convectively mixed down to great depths they are also returned to the surface euphotic zone with sufficient frequency that production can be sustained over winter (Backhaus et al., 1999; Backhaus et al., 2003). Alternatively, the mixed layer eddies observed by Mahadevan et al. (2012) may sustain production in winter by intermittently stratifying some of the water column.

Limitations

This study has used global datasets of NHF and MLD but it is important to note that the datasets are not "equal" in their relationship with the bloom timing metrics. The NHF dataset is measured synoptically from satellite and reanalysis products with each pixel being an areal average. Conversely, the MLD was calculated from sporadic, non-uniform point samples of temperature and salinity. Thus, they cannot be easily ranked against each other because the way the datasets are derived may result in a limit on the variability that one dataset can show. Furthermore, since many of the physical metrics are interdependent, it is difficult to separate out the effects of just one on bloom timing. As the NHF starts to increase from its winter minimum, the MLD begins to shoal as well because the reduction in cooling and mixing encourages restratification of the water column (Huisman et al., 1999). The results here show that the MLD shoaling occurs, on average, within ± 20 d of the NHF turning positive. Thus, it is difficult to definitively say which mechanism, MLD shoaling or a reduction in mixing, starts the bloom. In a comparison study of three different bloom timing metric

definitions, Brody *et al.* (2013) demonstrated that all three gave bloom initiation dates that were approximately synchronous with the NHF turning positive. This suggests that our result is robust (to some extent) to the choice of bloom metric definition, although a slightly different period and different datasets are used here (note that the range in bloom initiation date with latitude calculated in this study from different metric definitions can be seen in Supplementary Figure S1).

Conclusion

In conclusion, evidence has been presented that the critical turbulence hypothesis is the most likely mechanism for bloom initiation in the North Atlantic. The influence of this mechanism appears much weaker in the North Pacific and Southern Ocean though smaller areas of the Southern Ocean did show strong correlation with NHF becoming positive. This lack of consistency in bloom timing response across these three subpolar regions indicates that the North Atlantic is not a universal model system for developing a general theoretical understanding of the mechanisms that lead to the onset of the spring bloom. Further investigation of the environmental and ecological differences between the subpolar basins may lead to a greater understanding of the environmental controls on bloom timing.

Supplementary data

Supplementary material is available at the ICESJMS online version of the manuscript.

Acknowledgements

GlobColour data were provided by ACRI-ST GlobColour service, supported by EU FP7 MyOcean & ESA GlobColour Projects, using ESA ENVISAT MERIS data, NASA MODIS, and SeaWiFS data. The NASA Ocean Biogeochemical Model output was obtained using the Giovanni online data system, developed and maintained by the NASA GES DISC. The temperature and salinity objective analysis datasets were provided by and made freely available by the Coriolis project and programmes that contribute to it (<http://www.coriolis.eu.org>). The global ocean net heat flux product was made freely available by the WHOI OAFlux project (<http://oafux.whoi.edu>) funded by the NOAA Climate Observations and Monitoring (COM) program. This work was funded by the UK Natural Environment Research Council (NERC) as part of an Ocean and Earth Science postgraduate research programme at the University of Southampton (NE/I528626/1). In addition, this work was supported by NERC National Capability funding for SAH, APM, and AY.

References

Backhaus, J. O., Hegseth, E. N., Wehde, H., Irigoien, X., Hatten, K., and Logemann, K. 2003. Convection and primary production in winter. *Marine Ecology Progress Series*, 251: 1–14.

Backhaus, J. O., Wehde, H., Hegseth, E. N., and Kämpf, J. 1999. “Phyto-convection”: the role of oceanic convection in primary production. *Marine Ecology Progress Series*, 189: 77–92.

Banase, K., and English, D. C. 1999. Comparing phytoplankton seasonality in the eastern and western subarctic Pacific and the western Bering Sea. *Progress in Oceanography*, 43: 235–287.

Barrot, G. 2010. Product User Guide. GlobCOLOUR: an EO based service supporting global ocean carbon cycle research. European Space Agency.

Behrenfeld, M. J. 2010. Abandoning Sverdrup’s Critical Depth Hypothesis on phytoplankton blooms. *Ecology*, 91: 977–989.

Boss, E., and Behrenfeld, M. 2010. In situ evaluation of the initiation of the North Atlantic phytoplankton bloom. *Geophysical Research Letters*, 37: L18603.

Boyd, P., and Harrison, P. J. 1999. Phytoplankton dynamics in the NE subarctic Pacific. *Deep Sea Research II: Topical Studies in Oceanography*, 46: 2405–2432.

Brody, S. R., Lozier, M. S., and John, P. D. 2013. A comparison of methods to determine phytoplankton bloom initiation. *Journal of Geophysical Research: Oceans*, 118: 2345–2357.

Chiba, S., Batten, S., Sasaoka, K., Sasai, Y., and Sugisaki, H. 2012. Influence of the Pacific Decadal Oscillation on phytoplankton phenology and community structure in the western North Pacific. *Geophysical Research Letters*, 39: L15603.

Chiswell, S. M., Bradford-Grieve, J., Hadfield, M. G., and Kennan, S. C. 2013. Climatology of surface chlorophyll a, autumn-winter and spring blooms in the south-west Pacific Ocean. *Journal of Geophysical Research: Oceans*, 118: 1003–1018.

Cole, H., Henson, S., Martin, A., and Yool, A. 2012. Mind the gap: the impact of missing data on the calculation of phytoplankton phenology metrics. *Journal of Geophysical Research*, 117: C08030.

Cushing, D. H. 1990. Plankton production and year-class strength in fish populations - an update of the match mismatch hypothesis. *Advances in Marine Biology*, 26: 249–293.

Doney, S. 2006. Oceanography: plankton in a warmer world. *Nature*, 444: 695–696.

Durand, D. 2007. Full Validation Report. GlobCOLOUR: an EO based service supporting global ocean carbon cycle research. European Space Agency.

Eppley, R. W., and Peterson, B. J. 1979. Particulate organic matter flux and planktonic new production in the deep ocean. *Nature*, 282: 677–680.

Evans, G. T., and Parslow, J. S. 1985. A model of annual plankton cycles. *Biological Oceanography*, 3: 327–347.

Fasham, M. J. R. 1995. Variations in the seasonal cycle of biological production in subarctic oceans: a model sensitivity analysis. *Deep Sea Research I: Oceanographic Research Papers*, 42: 1111–1149.

Follows, M., and Dutkiewicz, S. 2002. Meteorological modulation of the North Atlantic spring bloom. *Deep Sea Research II: Topical Studies in Oceanography*, 49: 321–344.

Francois, R., Honjo, S., Krishfield, R., and Manganini, S. 2002. Factors controlling the flux of organic carbon to the bathypelagic zone of the ocean. *Global Biogeochemical Cycles*, 16: 34–31–34–20.

Fuentes-Yaco, C., Koeller, P. A., Sathyendranath, S., and Platt, T. 2007. Shrimp (*Pandalus borealis*) growth and timing of the spring phytoplankton bloom on the Newfoundland-Labrador Shelf. *Fisheries Oceanography*, 16: 116–129.

Gregg, W. W., and Casey, N. W. 2004. Global and regional evaluation of the SeaWiFS chlorophyll data set. *Remote Sensing of Environment*, 93: 463–479.

Heinrich, A. K. 1962. The life histories of plankton animals and seasonal cycles of plankton communities in the oceans. *Journal du Conseil International Pour l’Exploration de la Mer*, 27: 15–25.

Henson, S. A., Dunne, J. P., and Sarmiento, J. L. 2009. Decadal variability in North Atlantic phytoplankton blooms. *Journal of Geophysical Research*, 114: C04013.

Henson, S. A., Robinson, I., Allen, J. T., and Waniek, J. J. 2006. Effect of meteorological conditions on interannual variability in timing and magnitude of the spring bloom in the Irminger Basin, North Atlantic. *Deep Sea Research I: Oceanographic Research Papers*, 53: 1601–1615.

Huisman, J., Oostveen, P. v., and Weissing, F. J. 1999. Critical depth and critical turbulence: two different mechanisms for the development of phytoplankton blooms. *Limnology and Oceanography*, 44: 1781–1787.

Kahru, M., Brotas, V., Manzano-Sarabia, M., and Mitchell, B. G. 2011. Are phytoplankton blooms occurring earlier in the Arctic? *Global Change Biology*, 17: 1733–1739.

- Koeller, P., Fuentes-Yaco, C., Platt, T., Sathyendranath, S., Richards, A., Ouellet, P., Orr, D., *et al.* 2009. Basin-scale coherence in phenology of shrimps and phytoplankton in the North Atlantic Ocean. *Science*, 324: 791–793.
- Kristiansen, T., Drinkwater, K. F., Lough, R. G., and Sundby, S. 2011. Recruitment variability in North Atlantic cod and match-mismatch dynamics. *PLoS One*, 6: e17456.
- Landry, M. R., Monger, B. C., and Selph, K. E. 1993. Time-dependency of microzooplankton grazing and phytoplankton growth in the subarctic Pacific. *Progress in Oceanography*, 32: 205–222.
- Lutz, M. J., Caldeira, K., Dunbar, R. B., and Behrenfeld, M. J. 2007. Seasonal rhythms of net primary production and particulate organic carbon flux to depth describe the efficiency of biological pump in the global ocean. *Journal of Geophysical Research-Oceans*, 112: C10011.
- Mahadevan, A., D'Asaro, E., Lee, C., and Perry, M. J. 2012. Eddy-driven stratification initiates North Atlantic spring phytoplankton blooms. *Science*, 337: 54–58.
- Miller, C. B. 1993. Pelagic production in the Subarctic Pacific. *Progress in Oceanography*, 32: 1–15.
- Morel, A., Yannick, H., Bernard, G., Werdell, P. J., Stanford, B. H., and Bryan, A. F. 2007. Examining the consistency of products derived from various ocean color sensors in open ocean (Case 1) waters in the perspective of a multi-sensor approach. *Remote Sensing of Environment*, 111: 69–88.
- Parsons, T. R., and Lalli, C. M. 1988. Comparative oceanic ecology of the plankton communities of the subarctic Atlantic and Pacific oceans. *Oceanography and Marine Biology: an Annual Review*, 26: 317–359.
- Platt, T., Fuentes-Yaco, C., and Frank, K. 2003. Marine ecology: spring algal bloom and larval fish survival. *Nature*, 423: 398–399.
- Platt, T., White, G. N., Zhai, L., Sathyendranath, S., and Roy, S. 2009. The phenology of phytoplankton blooms: ecosystem indicators from remote sensing. *Ecological Modelling*, 220: 3057–3069.
- Racault, M.-F., Le Quéré, C., Buitenhuis, E., Sathyendranath, S., and Platt, T. 2012. Phytoplankton phenology in the global ocean. *Ecological Indicators*, 14: 152–163.
- Sarmiento, J. L., Slater, R., Barber, R., Bopp, L., Doney, S. C., Hirst, A. C., Kleypas, J., *et al.* 2004. Response of ocean ecosystems to climate warming. *Global Biogeochemical Cycles*, 18: GB3003.
- Sasaoka, K., Chiba, S., and Saino, T. 2011. Climatic forcing and phytoplankton phenology over the subarctic North Pacific from 1998 to 2006, as observed from ocean color data. *Geophysical Research Letters*, 38: L15609.
- Schmittner, A., Latif, M., and Schneider, B. 2005. Model projections of the North Atlantic thermohaline circulation for the 21st century assessed by observations. *Geophysical Research Letters*, 32: L23710.
- Siegel, D. A., Doney, S. C., and Yoder, J. A. 2002. The North Atlantic spring phytoplankton bloom and Sverdrup's critical depth hypothesis. *Science*, 296: 730–733.
- Sverdrup, H. U. 1953. On conditions for the vernal blooming of phytoplankton. *ICES Journal of Marine Science*, 18: 287–295.
- Taylor, J. R., and Ferrari, R. 2011. Shutdown of turbulent convection as a new criterion for the onset of spring phytoplankton blooms. *Limnology and Oceanography*, 56: 2293–2307.
- Thomalla, S. J., Fauchereau, N., Swart, S., and Monteiro, P. M. S. 2011. Regional scale characteristics of the seasonal cycle of chlorophyll in the Southern Ocean. *Biogeosciences*, 8: 2849–2866.
- Ueyama, R., and Monger, B. C. 2005. Wind-induced modulation of seasonal phytoplankton blooms in the North Atlantic derived from satellite observations. *Limnology and Oceanography*, 50: 1820–1829.
- Zhai, L., Platt, T., Tang, C., Sathyendranath, S., and Walne, A. 2013. The response of phytoplankton to climate variability associated with the North Atlantic Oscillation. *Deep Sea Research II: Topical Studies in Oceanography*, 93: 159–168.

Handling editor: Rubao Ji



Contribution to the Themed Section: 'Revisiting Sverdrup's Critical Depth Hypothesis' Original Article

Sverdrup critical depth and the role of water clarity in Norwegian Coastal Water

D. L. Aksnes*

Department of Biology, University of Bergen and Hjort Centre for Marine Ecosystem Dynamics, Bergen N-5020, Norway

*Corresponding author: tel: +47 5558 4478; fax: +47 5558 4450; e-mail: dag.aksnes@bio.uib.no

Aksnes, D. L. Sverdrup critical depth and the role of water clarity in Norwegian Coastal Water. – ICES Journal of Marine Science, 72: 2041–2050.

Received 30 July 2014; revised 30 January 2015; accepted 4 February 2015; advance access publication 25 February 2015.

The critical depth concept was first recognized by Gran and Braarud (1935). During summer, in the Bay of Fundy, they observed an unexpected no bloom situation. Their interpretation was that high amounts of detritus of terrestrial origin caused too murky water and insufficient light for the tidally mixed phytoplankton. Almost 20 years later, this was elaborated by Sverdrup (1953) into a hypothesis for the initiation of the spring bloom in the North Atlantic Water (NAW) masses. Since then, variations in mixed layer depth have been a key in phytoplankton modelling. As illustrated by the study of Gran and Braarud, variation in the non-phytoplankton light attenuation coefficient is also a key to understand phytoplankton bloom conditions. Due to lack of accurate parameterizations, however, non-phytoplankton light attenuation is often assumed invariant in phytoplankton modelling. Here, I report spatial variation in a proxy for the pre-bloom light attenuation in Norwegian Coastal Water (NCW). It is shown that this variation can be partially accounted for by variations in salinity and dissolved oxygen. The light attenuation coefficient at 440 nm increased by 0.041 and 0.032 m^{-1} with drops in salinity and dissolved oxygen of 1PSU and 1 $\text{ml O}_2 \text{ l}^{-1}$, respectively. Consequences for the euphotic depth, Sverdrup critical depth, and the nutricline depth are discussed. I conclude that phytoplankton modelling, particularly across coastal and oceanic waters, such as NCW and NAW, needs to account for variations in the non-phytoplankton light attenuation and that salinity might be a useful proxy for regional parameterizations.

Keywords: light attenuation, oxygen, phytoplankton modelling, proxy, salinity, water column.

Introduction

Sverdrup's "critical depth" is commonly associated with the initiation of the spring bloom in clear oceanic water. This concept originated, however, from observations made in a murky inshore location, the Bay of Fundy (Gran and Braarud, 1935). There, elevated non-phytoplankton light attenuation, in combination with strong tidal mixing, was likely responsible for a no bloom situation at a time when both nutrients and incoming irradiance were at high levels (Figure 1). Based on a detailed study of phytoplankton and hydrography in the Gulf of Maine and the Bay of Fundy, Gran and Braarud (1935) concluded: "Although our material is insufficient for accurate calculations, we have come to the conclusion that for these reasons the extraordinary turbulence and turbidity conditions of the Bay of Fundy waters are the main factors for

limiting their production of phytoplankton. No other explanation could be found, as the surface waters at the least productive seasons, as in June, contain a surplus of nutrient salts, and the zooplankton feeding upon the phytoplankton is not as rich in the Bay of Fundy as in the gulf of Maine". This reasoning was translated (Sverdrup, 1953) into a mathematical expression for the critical depth (Z_{cr}) that has become a cornerstone, although questioned by some (e.g. Behrenfeld, 2010), in biological oceanography:

$$\frac{Z_{cr}}{1 - e^{-KZ_{cr}}} = \frac{1}{K} \frac{E_0}{E_c}, \quad (1)$$

where, in modern notation, K is the attenuation coefficient for downwelling irradiance, E_0 and E_c the average daily (24 h) irradiances, respectively, below the surface and at the compensation

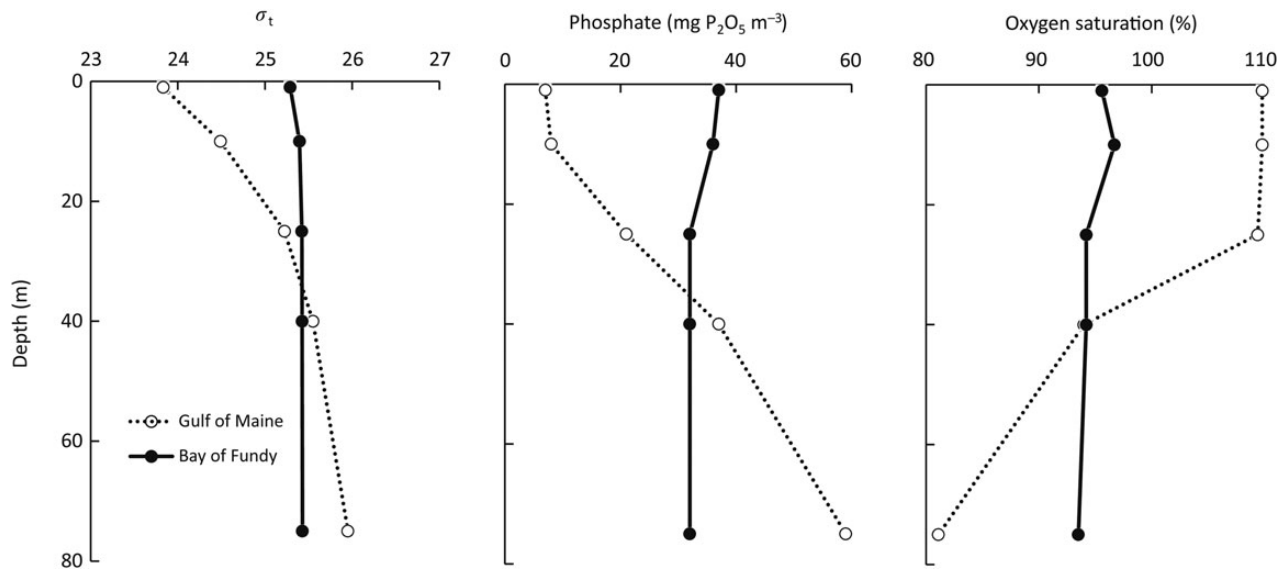


Figure 1. Birth of the critical depth concept. This concept originates from observations in the Bay of Fundy (Gran and Braarud, 1935), a location with high non-phytoplankton light attenuation and consequently a critical depth that might have been shallower than 50 m (see text). Compared with the Gulf of Maine, the Bay of Fundy was characterized by less stability (as indicated by σ_t), high nutrients and low oxygen saturation (i.e. low photosynthesis) throughout the water column. Gran and Braarud (1935) concluded that the phytoplankton in Bay of Fundy was limited by tidal mixing below a shallow compensation depth caused by limited light penetration. The observations for Gulf of Maine and Bay of Fundy are from June at station 24A and 37, respectively, and are taken from the tables in Gran and Braarud (1935).

depth, i.e. the depth where photosynthetic production equals “all” losses, not just respiration, during a 24-h cycle (see clarification by Chiswell, 2011). From Equation (1), we see that all coefficients in the critical depth formulation are associated with light and that the critical depth is particularly sensitive to variations in K . The frequently used phytoplankton bloom condition of Sverdrup (1953) can be formulated: if there exists a thoroughly mixed top layer of thickness D , D must be shallower than Z_{cr} in order for a bloom to develop.

Gran and Braarud (1935) noted that the high turbidity of the Bay of Fundy was due to detritus washed out by rivers at the head of the bay. They refer to an experiment on photosynthesis and respiration indicating that the compensation depth (Z_c) was not deeper than 10 m. If this depth, often equated with the euphotic depth, equals 1% light depth (i.e. $Z_c = -\ln(0.01)/K$), it can be seen that K must have been higher than 0.46 m^{-1} . This value indicates a critical depth shallower than 50 m, and it seems plausible that the lack of bloom in the Bay of Fundy indeed was in accordance with the critical depth hypothesis, i.e. that the mixed layer depth was deeper than the critical depth. Nevertheless, the observations of Gran and Braarud (1935) emphasize that natural variations in the non-phytoplankton light attenuation are critically important to phytoplankton bloom conditions. Sverdrup (1953) chose an oceanic test location, at Weather Ship M in the Norwegian Sea, with much higher water clarity than the Bay of Fundy. One challenge with this location, however, was the lack of observations of the pre-bloom light attenuation coefficient and Sverdrup had to assume values for this coefficient. Lack of accurate parameterizations of the non-phytoplankton light attenuation coefficient is still a challenge in ecosystem modeling in general as well as in coastal and oceanic areas off Norway (e.g. Schrum *et al.*, 2006; Hjøllø *et al.*, 2012; Samuelsen *et al.*, 2014).

Here, I quantify variations in the pre-bloom light attenuation in water masses along the coast of Norway (Table 1, Figure 2). These

water masses spanned salinities from 16.6 to 35.2. Norwegian Coastal Water (NCW) is transported with the Norwegian Coastal Current (NCC) from south to north (Figure 2) along the Norwegian coast (Sætre, 2007). NCW, characterized by salinity < 34.5 (Sætre, 2007), forms a wedge between the coastline and the North Atlantic Water (NAW, salinity > 34.5). Both NCW and NAW, which are located below the NCW, extend into the many deep fjords situated along the Norwegian coast on its way towards the Barents Sea. The freshwater content of the NCW originates from the brackish Baltic Sea, the rivers entering the North Sea, and drainage from Norway (Sætre, 2007). Many previous studies have shown that Chromophoric Dissolved Organic Matter (CDOM) of terrestrial origin is an important light absorber in the Baltic Sea, Kattegat, Skagerrak, and Danish coastal waters. This light absorption correlates negatively with salinity (e.g. Højerslev *et al.*, 1996; Stedmon *et al.*, 2000; Kowalczyk *et al.*, 2005), and as also reviewed by Nelson and Siegel (2013), CDOM absorption decreases linearly with increasing salinity if the mixing of offshore and terrestrial end-member water masses is the only process affecting CDOM. Based on this concept, I estimate an empirical model where salinity, but also dissolved oxygen (see below), serve as proxy for the non-phytoplankton NCW light attenuation.

Methods

During the unproductive winter season, locations along the Norwegian coast with bottom depth of several hundred meters (Table 1) contain relatively small amounts of organic and inorganic particles in the water column. Under these conditions, spectrophotometric measurements of light absorption in unfiltered samples have been used as proxy for the light attenuation of downwelling irradiance (Aksnes *et al.*, 2009). A benefit is that measurements can be obtained regardless of sunlight conditions and from large depths. All together, 375 measurements were obtained from 40 different locations along

Table 1. Sampling locations along the Norwegian coast in 2008.

Station number	Distance (km)	Location	Date	Latitude (North)	Longitude (East)	Bottom depth (m)
1102	0	Bunnefjorden	9 November	59°51.27	10°44.36	73
1100	25	Oslofjorden, Drøbak	8 November	59°38.38	10°37.50	194
1099	45	Breiangen	8 November	59°28.03	10°28.75	196
1097	101	Larvikfjorden	7 November	59°00.75	10°03.71	117
1095	128	Frierfjorden	7 November	59°06.36	9°37.05	89
1094	141	Eidangerfjorden, Brevik	7 November	59°01.33	9°44.81	107
1092	167	Off Kragerø	7 November	58°50.75	9°27.07	131
1091	184	Off Risør	6 November	58°44.26	9°15.34	183
1103	385	Gansfjorden	12 November	58°55.66	5°46.53	242
1105	414	Lysefjorden	13 November	59°00.20	6°16.54	454
1110	471	Sandsfjorden	13 November	59°30.64	6°15.41	422
1111	499	Nedstrandsfjorden	13 November	59°18.73	5°56.80	691
1112	527	Boknafjorden	13 November	59°09.99	5°33.11	574
1114	647	Hardangerfjorden, Tyssedal	15 November	60°07.29	6°32.87	150
1115	670	Hardangerfjorden, Ullensvang	15 November	60°19.51	6°38.00	353
1120	760	Fensfjorden	20 November	60°45.70	5°14.44	594
1123	773	Masfjorden	20 November	60°52.02	5°21.95	471
1127	813	Sognefjorden	21 November	61°08.52	5°49.92	1258
1128	900	Davikfjorden	24 November	61°54.63	5°34.78	576
1129	918	Hundvikfjorden	24 November	61°52.22	5°55.21	358
1130	946	Innvikfjorden	24 November	61°49.22	6°26.70	436
1133	1013	Vanylvsfjorden	25 November	62°08.09	5°20.99	254
1141	1030	Syvdsfjorden	26 November	62°10.99	5°39.24	375
1145	1071	Storfjorden 1	26 November	62°24.73	6°26.19	402
1146	1101	Storfjorden 2	26 November	62°26.74	6°50.06	669
1148	1143	Geirangerfjorden	26 November	62°05.48	7°03.88	185
1151	1209	Romsdalsfjorden	29 November	62°40.76	7°04.95	471
1154	1243	Langfjorden	30 November	62°43.55	7°45.27	353
1157	1273	Tingsvollfjorden	1 December	62°56.41	8°07.08	308
1160	1289	Freifjorden	1 December	63°01.03	7°50.80	135
1162	1304	Talgsjøen	2 December	63°08.90	7°52.16	327
1163	1413	Trondheimsfjorden	3 December	63°37.24	9°46.97	600
1166	1483	Beistadfjorden	4 December	63°55.12	11°02.57	239
1205	1642	Tosenfjorden	16 December	65°10.19	12°37.81	525
1202	1656	Bindalsfjorden	15 December	65°10.31	12°18.74	699
1196	1743	Vefsnfjorden	14 December	65°51.52	13°10.52	151
1191	1804	Ranafjorden	13 December	66°15.07	13°44.39	425
1185	1867	Glomfjorden	11 December	66°49.10	13°37.05	372
1175	1963	Follafjorden	8 December	67°33.03	14°46.42	487
1184	2055	Ofotfjorden	10 December	68°16.34	15°50.72	608

Distance is the approximate distances from station 1102.

the Norwegian coast (Table 1, Figure 2) between 58°N and 68°N during a cruise with RV “Håkon Mosby” in the period from 6 November to 16 December 2008. This period of the year was chosen to minimize the effect from phytoplankton on light attenuation. Depending on the bottom depth (Table 1), 6–12 water samples were collected between the surface and 700-m depth with rosette mounted Niskin water collectors attached to a CTD system (Seabird SBE 911). Absorbance on the unfiltered water samples (A_{un}) was measured at 400, 420, 440, 450, 460, 480, 500, and 550 nm with a spectrophotometer (UV/VIS Spectrometer Lambda 2, Perkin Elmer). Absorbance readings were made for four subsamples placed in a 10-cm quartz cuvette that was acclimatized to room temperature. Distilled freshwater purified with a Millipore Simplicity 185 Water Purification System was used as blank control. As in studies of light absorption (e.g. Højerslev *et al.*, 1996), I calculated a quantity (in units of m^{-1}) from the absorbance readings; $a_{\text{un}}(\lambda) = 2.303A_{\text{un}}(\lambda)/0.1$, where λ is the wavelength. I fitted the exponential function, $a_{\text{un}}(\lambda) = Ce^{-k\lambda}$, to the observations by log-linear regression (Bricaud *et al.*, 1981). Here, C is a constant

and k is the spectral slope factor. Throughout the present study, I use a_{un} at 440 nm, which was obtained by insertion of $\lambda = 440$ in the estimated regression equations. This wavelength was chosen because it is approximately the midpoint of the waveband peak that most classes of algae have in their photosynthetic action spectrum (Kirk, 2011). Similar to the attenuation of downwelling irradiance, K , the a_{un} measurements are affected by scattering and absorption from potential particles, such as phytoplankton, as well as from dissolved matter of the water samples. Thus, below I avoid to use the notation of absorption (a) and instead use K_p to emphasize that the measurements are used as an “approximation” for the attenuation coefficient (K) for downwelling irradiance (at 440 nm), i.e. $K \approx K_p = a_{\text{un}}(440)$. This approximation ignores that K is an apparent optical property that depends on the angular distribution of the underwater light field. The ability of the proxy, K_p , to predict measured light penetration is tested for a NAW and a NCW location (see below).

Dissolved oxygen was determined from the water samples by a standard Winkler technique, and salinity was obtained from the CTD system simultaneously with the collection of water. Water

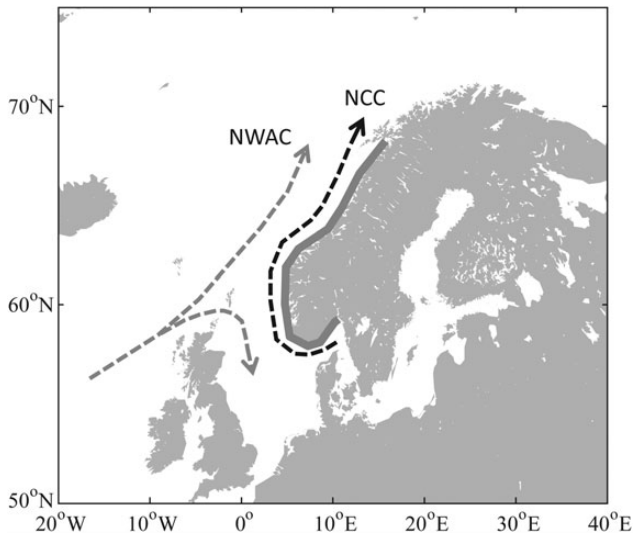


Figure 2. The Norwegian Atlantic Current (NWAC) transports saline NAW into the Norwegian Sea, whereas the NCC transports less-saline NCW northwards along the Norwegian coast. The shaded area indicates the area covered by the stations listed in Table 1.

samples (100 ml) were also filtered through 0.45 μm Sartorius filters, and the filters were frozen for later determination of Chl *a* by the use of acetone extraction (Holm-Hansen *et al.*, 1965).

Model used in estimation

The chlorophyll concentrations were generally low (see below), but chlorophyll (Chl) will nevertheless affect the proxy for light attenuation K_p . I apply the following model:

$$K_p = K_{\text{non}} + f(\text{Chl}), \quad (2)$$

where K_{non} is the non-phytoplankton light attenuation and $f(\text{Chl})$ the attenuation from algal cells (see Table 2 for a summary of symbols).

I assume that the water samples of NCW are a mixture of two end-member water masses; oceanic water (NAW) and freshwater (FW). Furthermore, it is assumed that K_{non} is determined by the mixing ratio of the two water masses and the respective non-phytoplankton attenuations, K_{NAW} and K_{FW} , according to:

$$K_{\text{non}} = gK_{\text{NAW}} + (1 - g)K_{\text{FW}} + K_{\text{loc}}, \quad (3)$$

where g and $1 - g$ are the fractions of NAW and FW, respectively (as given by salinity, see below). This model is similar to conservative mixing of, e.g. CDOM of two end-member water masses, which gives rise to a negative linear relationship between CDOM absorption and salinity (Aarup *et al.*, 1996; Kowalczyk *et al.*, 2003; Stedmon and Markager, 2003; Nelson and Siegel, 2013). Equation (3) is a simplification since the freshwater sources and their content of persistent light attenuating substances are diverse and include many different riverine inputs to the Baltic Sea, the North Sea, as well as directly to the NCW. The third term of Equation (3), K_{loc} , is introduced to reflect locally produced non-phytoplankton light attenuating substances from heterotrophic activity. Previous oceanic (Yamashita and Tanoue, 2008; Nelson and Siegel, 2013) and fjord (Aksnes *et al.*, 2009) studies suggest that heterotrophic consumption of dissolved oxygen, i.e. apparent oxygen utilization (AOU, Nelson and Siegel, 2013), might serve as proxy for light absorption in some

Table 2. Symbols used in the text.

A_{un}		Observed light absorbance of unfiltered water samples
a_{un}	m^{-1}	Light absorption of unfiltered water samples
Chl	mg m^{-3}	Concentration of chlorophyll <i>a</i>
FW		Freshwater draining to NCW
g		Fraction of NAW in NCW (=Sal/35.2)
h		= Oxy/7.1
Λ	nm	Wavelength
K	m^{-1}	Attenuation coefficient for downwelling irradiance
K_p	m^{-1}	Proxy for K [$K_p = a_{\text{un}}(440)$]
K_{non}	m^{-1}	Non-chlorophyll light attenuation coefficient
K_{FW}	m^{-1}	Non-chlorophyll light attenuation of the FW source
K_{NAW}	m^{-1}	Non-chlorophyll light attenuation of the NAW source
K_{loc}	m^{-1}	Non-chlorophyll light attenuation of local substances
$K_{\text{Oxy}=0}$	m^{-1}	Non-chlorophyll light attenuation associated with no dissolved oxygen
NAW		North Atlantic Water
NCC		Norwegian Coastal Current
NCW		Norwegian Coastal Water
Oxy	ml l^{-1}	Dissolved oxygen concentration
Oxy_{max}	ml l^{-1}	The maximal dissolved oxygen in the dataset (7.1 ml l^{-1})
Sal		Salinity

areas. The present study includes hypoxic fjord basins and it is hypothesized that bacterial degradation of particulate organic matter produces local light attenuating DOM in proportion with the removal of dissolved oxygen. Such relationship between light attenuation and AOU is parameterized as follows: for a water mass high in dissolved oxygen ($\text{Oxy} = \text{Oxy}_{\text{max}}$), $K_{\text{loc}} = 0$ is assumed. When $\text{Oxy} < \text{Oxy}_{\text{max}}$, K_{loc} is assumed to increase linearly with the decrease in Oxy, i.e. $K_{\text{loc}} = (1 - h)K_{\text{Oxy}=0}$, where $h = \text{Oxy}/\text{Oxy}_{\text{max}}$ and $K_{\text{Oxy}=0}$ is the hypothetical non-phytoplankton light attenuation of water without dissolved oxygen. Equation (3) then becomes:

$$K_{\text{non}} = gK_{\text{NAW}} + (1 - g)K_{\text{FW}} + (1 - h)K_{\text{Oxy}=0}. \quad (4)$$

Estimation of model parameters

The salinity of the NAW end-member is set equal to the highest salinity (35.2) observed in the present study and the salinity of FW end-member is set to zero. Then, $g = \text{Sal}/35.2$, where Sal is the salinity of the water sample in question. Similarly, Oxy_{max} is set equal to the highest dissolved oxygen concentration in the dataset (7.1 ml l^{-1}) and consequently $h = \text{Oxy}/7.1$.

The water samples were collected during a period of presumably low biological productivity (November and December), but Chl *a* was present (average 0.23 and s.d. 0.49 mg m^{-3}) particularly in the southernmost locations (see the ‘‘Results’’ section). Out of the 375 samples, 324 contained concentrations less than 0.5 mg m^{-3} and 26 samples had concentrations on the range 1–3.6 mg m^{-3} . The effect of chlorophyll on K is known to be non-linear (Morel and Maritorena, 2001). To keep the number of parameters to be estimated low, however, I assume that the effect of chlorophyll (Chl) on K_p is linear and Equation (2) becomes $K_p = K_{\text{non}} + k_3\text{Chl}$. Combination with Equation (4) and elimination of

g and h by insertion of $g = \text{Sal}/35.2$ and $h = \text{Oxy}/7.1$ provide the following model:

$$K_p = k_0 + k_1 \text{Sal} + k_2 \text{Oxy} + k_3 \text{Chl}, \quad (5a)$$

where k_0 , k_1 , and k_2 are:

$$k_0 = K_{\text{FW}} + K_{\text{Oxy}=0}, \quad (5b)$$

$$k_1 = \frac{K_{\text{NAW}} - K_{\text{FW}}}{35.2}, \quad (5c)$$

$$k_2 = \frac{-K_{\text{Oxy}=0}}{7.1}. \quad (5d)$$

Estimates of k_0 , k_1 , k_2 , and k_3 were obtained by fitting Equation (5a) to the observations of K_p , Sal, Oxy, and Chl. This equation corresponds to a linear multiple regression model and the software Statistica was applied. Estimates of K_{NAW} , K_{FW} , and $K_{\text{Oxy}=0}$ were obtained by solving Equations (5b)–(5d).

Observed and predicted light penetration in pre-bloom NAW and NCW

Measurements of underwater irradiance (Trios RAMSES ACC hyperspectral radiometer), salinity, dissolved oxygen, and fluorescence in NCW and NAW were available from two field studies. In the first, measurements were taken at a coastal location (60.41°N 5.10°E, 9 February 2010) during a cruise with RV “H. Mosby”. The second included measurements from a cruise with RV “G.O. Sars” at a station in the Norwegian Sea (65.03°N 0.51°W, 7 May 2013). The observed light penetration was compared with that predicted from the proxy, K_p . Values for K_p as a function of depth were obtained from Equation (5a) by use of observed depth distributions of salinity, dissolved oxygen, and chlorophyll as input. The predicted irradiance, E , as a function of depth (z) was calculated:

$$E = E_0 \exp\left(-\int_0^z K_p(\sigma) d\sigma\right). \quad (6)$$

Here, E_0 is the irradiance just below the surface and σ is an integration variable accounting for the observed non-uniform depth distributions of K_p (being a function of salinity, dissolved oxygen, and chlorophyll).

Results

The variations in salinity, oxygen, and chlorophyll accounted for 62% ($R = 0.79$) of the observed variation in the light attenuation proxy, K_p , and the statistical effects of all three variables were significant (Figure 3 and Table 3). Increases of 0.041 ± 0.003 and $0.032 \pm 0.004 \text{ m}^{-1}$ in K_p are associated with a 1 PSU drop in salinity and a 1 ml l^{-1} drop in dissolved oxygen, respectively (Table 3). The estimated effect of chlorophyll corresponds to an increase of $0.073 \pm 0.011 \text{ m}^{-1}$ for an increase of $1 \text{ mg Chl } a \text{ m}^{-3}$ (Table 3). The estimated non-phytoplankton light attenuation of the freshwater source was $K_{\text{FW}} = 1.47 \pm 0.05 \text{ m}^{-1}$. The corresponding value for the North Atlantic source water was $K_{\text{NAW}} = 0.03 \pm 0.07 \text{ m}^{-1}$.

Overall, the observed K_p tends to decrease with latitude and depth (Figure 4), and this pattern is also well reflected by the model predicted K_p (Figure 5a). Figure 5b–d illustrates how the predicted K_p is associated with variations in chlorophyll, salinity, and dissolved oxygen, respectively. Except for the surface water of the southernmost locations, chlorophyll concentrations were generally

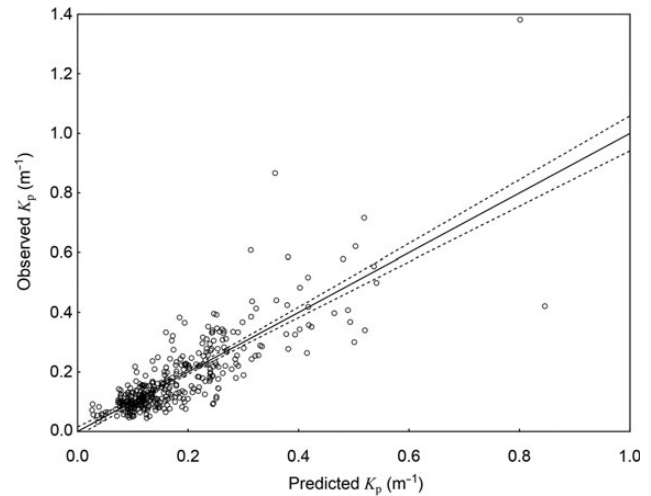


Figure 3. Model predicted vs. observed K_p at 440 nm. The model predictions are: $K_p = 1.70 + 0.073 \text{ Chl} - 0.041 \text{ Sal} - 0.032 \text{ Oxy}$, $r = 0.79$, $p < 10^{-5}$, $n = 375$ (Table 3). Dotted lines represent 95% CI.

Table 3. Statistical effects of salinity, oxygen, and chlorophyll on K_p (440 nm) estimated with multiple regression analysis according to the model in Equation (5).

Coefficient and unit	Estimates	β
$k_0 \text{ m}^{-1}$	1.70 ± 0.09	
$k_1 \text{ m}^{-1}(\text{PSU})^{-1}$	-0.041 ± 0.003	-0.62 ± 0.04
$k_2 \text{ m}^{-1}(\text{ml O}_2 \text{ l}^{-1})^{-1}$	-0.032 ± 0.004	-0.27 ± 0.03
$k_3 \text{ m}^{-1}(\text{mg Chl } a \text{ m}^{-3})^{-1}$	0.073 ± 0.011	0.27 ± 0.04
$K_{\text{Oxy}=0} \text{ m}^{-1}$	0.23 ± 0.03	
$K_{\text{FW}} \text{ m}^{-1}$	1.47 ± 0.05	
$K_{\text{NAW}} \text{ m}^{-1}$	0.03 ± 0.07	

All effects were statistically significant ($p < 10^{-5}$). The multiple R was 0.79. The β is the regression coefficient that is obtained when all variables are standardized to a mean of 0 and an s.d. of 1. This coefficient compares the relative contribution of each independent variable (salinity, dissolved oxygen, and Chl a) in the prediction of K_p . The indicated uncertainties are \pm standard error. The estimates are based on 375 records where the ranges of the variables were K_p 0.03–1.4 m^{-1} (mean 0.18), salinity 16.6–35.2 (mean 33.4), chlorophyll 0.0–3.6 $\text{mg Chl } a \text{ m}^{-3}$ (mean 0.23), and dissolved oxygen 0.1–7.1 ml l^{-1} (mean 5.21).

low and therefore accounted for a small part of the variations in K_p in the model (Figure 5b). The variations in salinity accounted for the largest variations in K_p (Figure 5c), except for some intermediate and large depths where variations in oxygen, particularly in the south, accounted for the largest part of the variations in K_p (Figure 5d).

The derived model was verified by measurements obtained at an NCW and an NAW location (Figure 6). Light penetrations, standardized as the fraction of observed irradiance at 2-m depth, are shown in Figure 6a. The sensitivity of the radiometer allowed irradiance measurements down to 80 m at the NCW location and to 170 m in the clearer NAW location. Linear regression analysis on the ln-transformed irradiances (not shown in Figure 6a) gave attenuation coefficients (K) of 0.182 m^{-1} (s.e. = 0.002, $r^2 = 0.99$, $n = 17$) and 0.0600 m^{-1} (s.e. = 0.0007, $r^2 = 0.99$, $n = 22$) for the NCW and the NAW location, respectively.

The light penetration [Equations (5) and (6)] predicted from the observed distributions of salinity (Figure 6b), dissolved oxygen

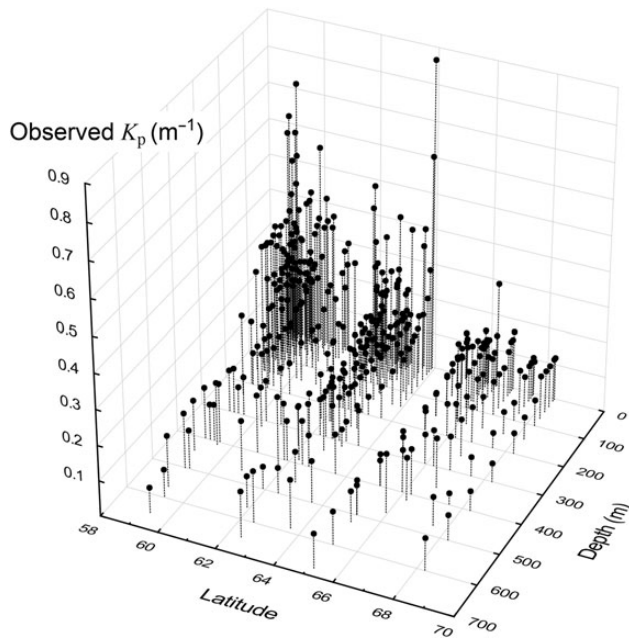


Figure 4. Observations of K_p at 440 nm as a function of latitude and depth. One observation, $K_p = 1.38 \text{ m}^{-1}$ (Figure 3), is outside the scale and not shown.

(Figure 6c), and fluorescence (Figure 6d) is shown by the lines in Figure 6a. The average of the predicted attenuation coefficients (i.e. K_p) are 0.185 and 0.064 m^{-1} for NCW (0–80 m) and NAW (0–170 m), respectively, which are close to the measured values.

The fluorescence measurements (Figure 6d) indicate chlorophyll concentrations below 0.05 and $0.22 \text{ mg Chl } a \text{ m}^{-3}$ at the NCW and the NAW location, respectively. An estimate of the non-phytoplankton attenuation, K_{non} , is obtained by setting $\text{Chl} = 0$ in Equation (5a):

$$K_{\text{non}} = 1.70 - 0.041\text{Sal} - 0.032\text{Oxy}. \quad (7)$$

This provides K_{non} values of 0.183 m^{-1} and 0.054 for the NCW and the NAW location, respectively.

The average salinity was 35.12 and 32.55 for NAW (upper 170 m) and NCW (upper 80 m), respectively (Figure 6b). According to the proxy model, $\sim 80\%$ of the elevated K_{non} at the NCW location was associated with the lower salinity, whereas the remaining 20% was associated with lower dissolved oxygen at this location (Figure 6c).

The effect of chlorophyll on K has been estimated by Morel and Maritorena (2001) and for 440 nm this effect corresponds to $K_{\text{Chl}} = 0.11 \text{ Chl}^{0.67}$. It should be noted that this expression also includes effects of constituents other than chlorophyll like CDOM produced by algal cells. Subtraction of this effect (insertion of average chlorophyll of the observed profiles in Figure 6d) from the measured K values provides K_{non} values of 0.168 and 0.032 m^{-1} for the NCW and NAW location, respectively, which is lower than those indicated by the proxy.

Discussion

The present study provides a model to estimate variations in the non-phytoplankton light attenuation in coastal waters of Norway in relation to the variations in salinity and dissolved oxygen.

Because the largest salinity variation is generally found in upper water, salinity appears to be a useful proxy for K_{non} in the euphotic zone. The largest variation in dissolved oxygen is normally found at intermediate and large depths, i.e. where hypoxia is common, and has been applied as proxy for the light conditions in the mesopelagic zone (Aksnes *et al.*, 2009). Salinity has previously been applied as proxy for non-phytoplankton light attenuation in phytoplankton modelling, e.g. in Florida shelf water (Walsh *et al.*, 2003) and in the Gulf of St Lawrence (Mei *et al.*, 2010). These studies report salinity coefficients, which corresponds to $k_1 = -0.041 \pm 0.003 \text{ m}^{-1} \text{ PSU}^{-1}$ (Table 3), on the ranges -0.095 to -0.003 (for 443 nm) and -0.02995 to $-0.01392 \text{ m}^{-1} \text{ PSU}^{-1}$ (for PAR). The present study suggests that salinity also might be a useful proxy for K_{non} in phytoplankton modelling in coastal waters of Norway. Below, I discuss some implications of variation in K_{non} on the euphotic depth, the critical depth, and the nutricline depth spanning a salinity range from 28 to 35 (Figure 7).

Implications of variation in the non-phytoplankton light attenuation of NCW

If the depth of the euphotic zone is defined as the depth where 1% of the surface light penetrates, the euphotic depth of NCW₂₈ (i.e. salinity is 28) is 98 m shallower than in NAW₃₅ (14 and 112 m, respectively, Figure 7) for a water column devoid of chlorophyll and with a dissolved oxygen concentration of 7 ml l^{-1} . According to the assumptions underlying Figure 7 (see legend), the deepening of the critical depth associated with a move from NCW₂₈ to NAW₃₅ is 427 m (from 61 to 488 m). Note, however, that the actual shoaling in a bloom situation will also be affected by the phytoplankton shading.

Elevated non-phytoplankton attenuation shoals the euphotic zone and consequently also the phytoplankton and nutrient distributions (Urtizberea *et al.*, 2013). This optical effect is strong and can be quantified by the analytical expression for the steady-state nutricline depth (Z_n); $Z_n = -\ln(\psi K)/K$ [Equation (3) in Aksnes *et al.*, 2007], where ψ is a scaled quantity reflecting biological nutrient uptake rate, vertical transport of the nutrient, and the actual definition of the nutrient concentration at Z_n . For $\psi = 0.014 \text{ m}$ (Figure 1 in Aksnes *et al.*, 2007), nutricline depths corresponds to 16 and 182 m for the K_{non} values calculated for NCW₂₈ and NAW₃₅, respectively (Figure 7). This calculation is based solely on the change in K_{non} and ignores the effect of phytoplankton self-shading. Nevertheless, it illustrates that spatial variations in K_{non} are likely to have large implications for the vertical distribution of nutrients in NCW during the productive season.

The simple analytical sensitivity analysis in Figure 7 illustrates that the largest variations (in meters) in euphotic depth, critical depth, and nutricline depth are to be expected at salinity variations in the upper range (i.e. between 34 and 35). This is in line with previous sensitivity analyses involving numerical ecosystem models (e.g. Fasham *et al.*, 1990; Urtizberea *et al.*, 2013) showing that the outcome of these models, particularly at small values of K_{non} (i.e. close to pure water), is very sensitive to variation in K_{non} . This can be illustrated by assumptions made by Sverdrup (1953). He assumed values in the range 0.075 – 0.10 m^{-1} for his critical depth estimates for the Norwegian Sea. A value of 0.05 m^{-1} , which appears realistic for the NAW pre-bloom situation (see above), provides critical depths that are 50–100% deeper than those indicated by Sverdrup and will, for a given mixed layer depth, indicate earlier spring bloom initiation than in Sverdrup (1953).

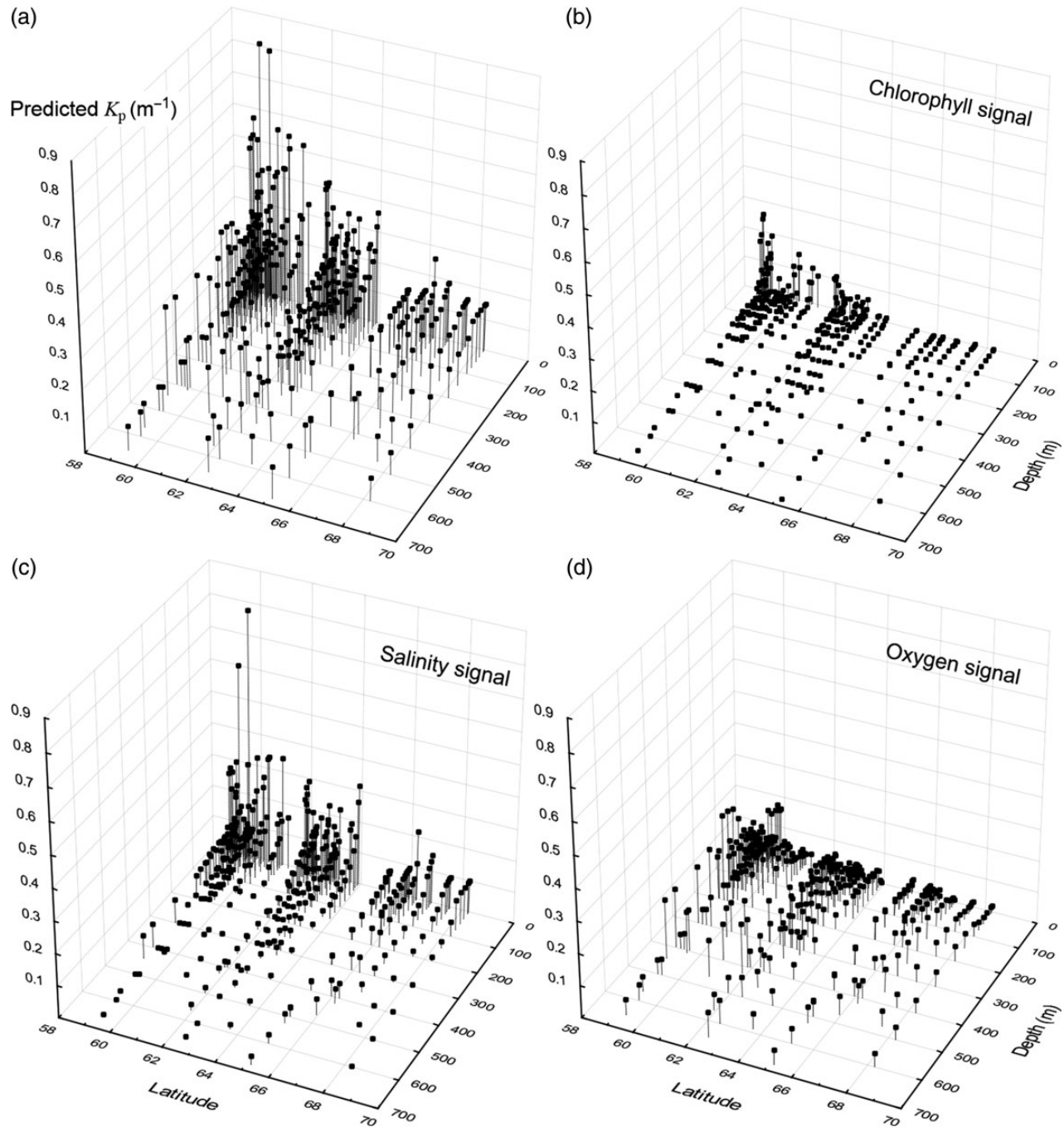


Figure 5. The model predicted K_p values at 440 nm [Equation (5a), estimated coefficients in Table 3] as a function of latitude and depth (a), and how much of these values that could be accounted for by chlorophyll (b), salinity (c), and dissolved oxygen (d).

Salinity as proxy for non-phytoplankton attenuation in ecological modelling

According to Sarmiento and Gruber (2006) and Fujii *et al.* (2007), most ecosystem models that have been developed to study the ocean's biogeochemical properties use simple formulations to describe light penetration. In such formulations (Sarmiento and Gruber, 2006), K is often a function of the simulated phytoplankton concentration added to the contribution from clear water (K_w) and non-phytoplankton constituents (K_x), i.e. $K = K_w + K_x + k_p P$, where $k_p P$ is the contribution from phytoplankton ($K_w + K_x$ here

corresponds to K_{non}). The effect of pure water is often set close to 0.04 m^{-1} for PAR, while, according to Sarmiento and Gruber (2006), K_x is generally ignored. Some ecological modelling studies do include the optical effects (and thereby K_x) of constituents such as CDOM (Bissett *et al.*, 1999; Fujii *et al.*, 2007; Mouw *et al.*, 2012; Alver *et al.*, 2014). A reason why the more advanced bio-optical approaches are underrepresented in ecosystem models is likely due to the difficulty and uncertainties in translating model outputs accurately into optical properties. Given that there exists a robust relationship between non-phytoplankton light

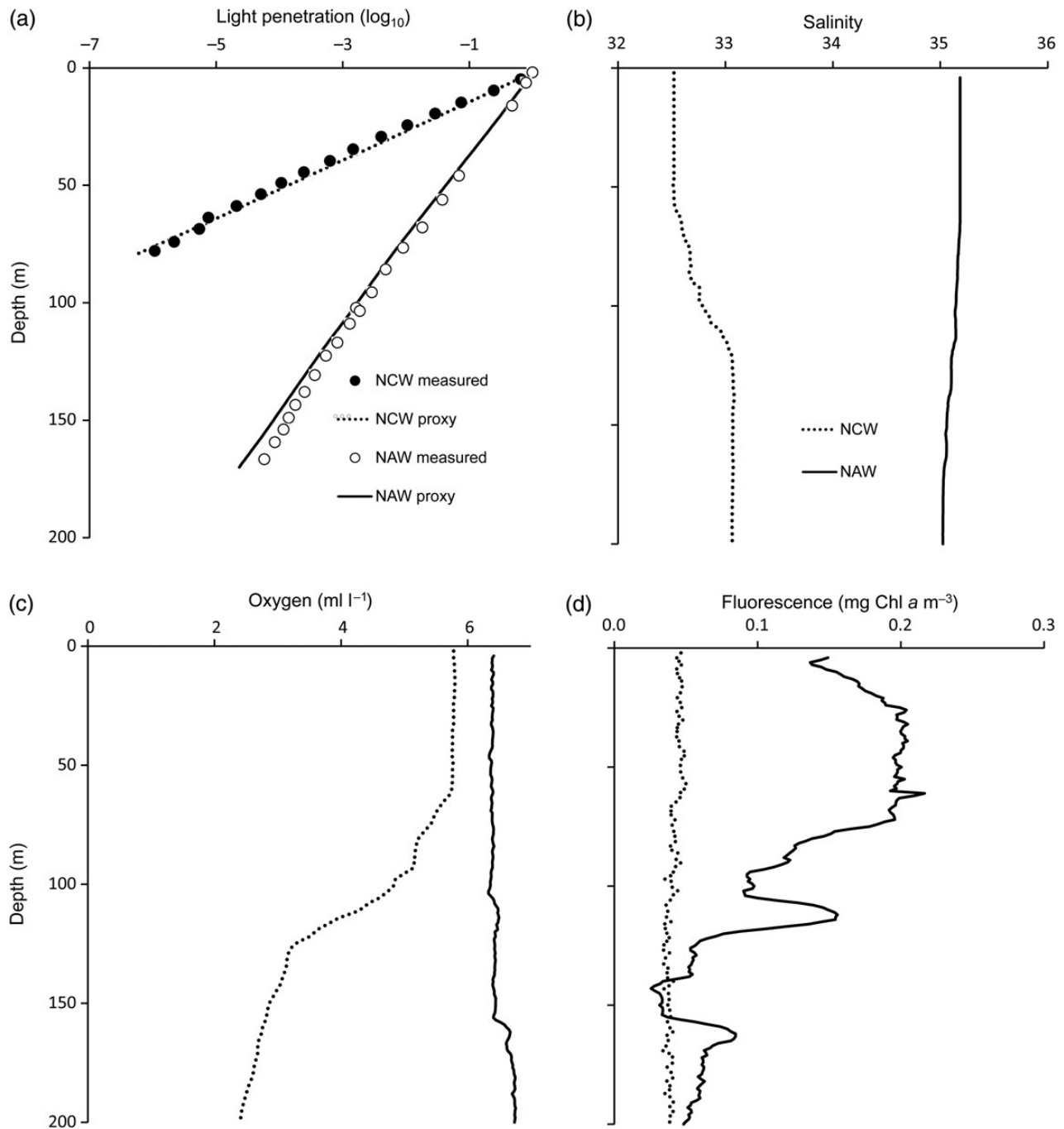


Figure 6. Observed and model predicted light penetration (a) in NAW (65.03°N 0.51°W on 7 May 2013) and in NCW (60.41°N 5.10°W on 9 February 2010). Light penetration is given as a fraction; $E(z)/E(2)$, where $E(z)$ and $E(2)$ are the observed downwelling irradiance at depth z and 2 m, respectively. The model predicted light penetration was obtained by using Equation (5a) (estimated coefficients in Table 3) and the observed distributions of salinity (b), dissolved oxygen (c), and chlorophyll (d).

attenuation and salinity for certain areas (e.g. Walsh *et al.*, 2003; Mei *et al.*, 2010), salinity proxies for non-phytoplankton attenuation are likely to be useful. This is particularly true if assumption of invariant K_{non} is the alternative. It should be noted, however, that there is no universal relationship between the non-phytoplankton light attenuation and salinity and that Equation (7) has been derived specifically for the pre-bloom situation in Norwegian coastal areas.

Latitudinal variations in non-phytoplankton light attenuation

A large fraction (38%) of the variation in the light attenuation proxy is not accounted for by the variations in salinity, oxygen, and chlorophyll (Table 3 and Figure 3). The measurements were obtained between the surface and 700-m depth along a coastline that spans 2000 km (Table 1). Variation in attenuation properties of the

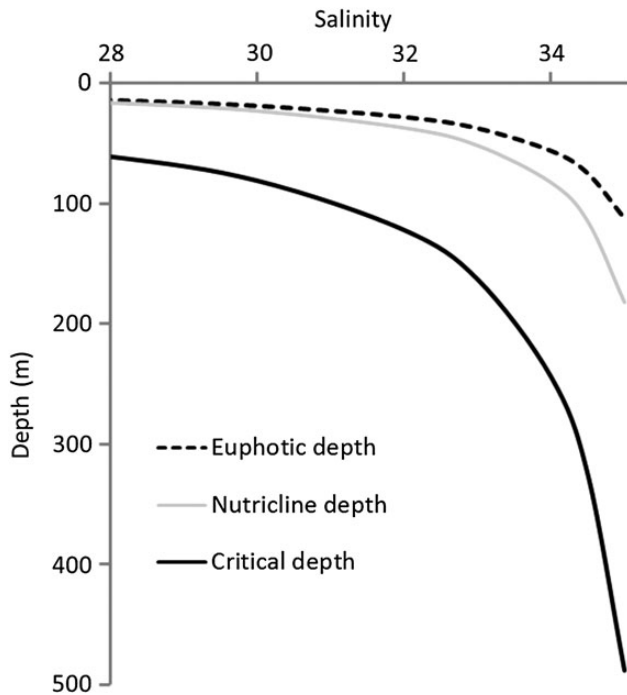


Figure 7. Predicted variations in euphotic, nutricline, and critical depth as a function of salinity in a gradient from NCW₂₈ to NAW₃₅. Euphotic depth was calculated according to $-\ln(0.01)/K$, nutricline depth according to $-\ln(0.014K)/K$ (see text), and critical depth according to Equation (1), where $E_0/E_c = 20$ (see text). K was derived from salinity according to the proxy equation (7) where dissolved oxygen was set constant ($Oxy = 7 \text{ ml l}^{-1}$).

different freshwater sources along this coastline is likely to have affected the observations, but also variations in the oceanic waters that mix in along the coast. Such effects have not been accounted for in the present analysis and have likely increased the error term of the estimation model. If the distance along the coast from south to north (Table 1) is included *ad hoc* in Equation (5a), this effect, as well as the other three, becomes statistically significant ($p < 10^{-5}$), and the unexplained fraction drops from 38 to 33%. The distance effect is negative, -0.058 m^{-1} per 1000 km. This might indicate that the non-phytoplankton light attenuation of the freshwater and/or the oceanic sources drops northward along the coast. This suggestion, however, needs to be addressed in studies where the optical properties of these sources are targeted.

Effects of terrestrial CDOM on non-phytoplankton light attenuation in NCW

CDOM has received increased attention in the last decades due to its role in the global carbon budget, but also because it changes the colour (brownification) and light conditions in rivers and streams (Roulet and Moore, 2006), in lakes (Larsen *et al.*, 2011), and in coastal waters (Branco and Kremer, 2005; Frigstad *et al.*, 2013). Increased amounts of organic carbon in Scandinavian lakes have been related to increased precipitation, warming, and associated changes in the terrestrial vegetation (Larsen *et al.*, 2011). Long-term Secchi depth shoaling off Southern Norway, in the North Sea, and in the Baltic Sea has been reported (Fleming-Lehtinen and Laamanen, 2012; Dupont and Aksnes, 2013) and associated with long-term ecosystem changes (Haraldsson *et al.*, 2012), but it is unclear to what extent this shoaling has been caused by increased phytoplankton or CDOM of

terrestrial origin. Predictions based on climate change scenarios suggest future increase in organic carbon in lakes and rivers in Scandinavia (Larsen *et al.*, 2011) and consequently to an increase in the coefficient K_{FW} of the mixing model. In that case, K_{non} increases and is likely to cause shoaling and narrowing of NCW photic zones in the coming years. In the words of Gran and Braarud (1935): “The amount was so considerable that it seemed obvious that the detritus essentially must lower the light supply of subsurface localities”.

Acknowledgements

Thanks to Mette Hordnes for cruise participation, sampling, and laboratory analyses, to Rita Amundsen (University of Oslo) for Chl *a* analyses, to Else Torstensen (Institute of Marine Research) for cruise cooperation, and to two anonymous reviewers for valuable suggestion. This study was financially supported from the Norwegian Research Council (Project no. 196444/S40).

References

- Aarup, T., Holt, N., and Højerslev, N. K. 1996. Optical measurements in the North Sea-Baltic Sea transition zone. 2. Water mass classification along the Jutland west coast from salinity and spectral irradiance measurements. *Continental Shelf Research*, 16: 1343–1353.
- Aksnes, D. L., Dupont, N., Staby, A., Fiksen, Ø., Kaartvedt, S., and Aure, J. 2009. Coastal water darkening and implications for mesopelagic regime shifts in Norwegian fjords. *Marine Ecology Progress Series*, 387: 39–49.
- Aksnes, D. L., Ohman, M. D., and Riviere, P. 2007. Optical effect on the nitracline in a coastal upwelling area. *Limnology and Oceanography*, 52: 1179–1187.
- Alver, M. O., Hancke, K., Sakshaug, E., and Slagstad, D. 2014. A spectrally-resolved light propagation model for aquatic systems: steps toward parameterizing primary production. *Journal of Marine Systems*, 130: 134–146.
- Behrenfeld, M. J. 2010. Abandoning Sverdrup’s critical depth hypothesis on phytoplankton blooms. *Ecology*, 91: 977–989.
- Bissett, W. P., Carder, K. L., Walsh, J. J., and Dieterle, D. A. 1999. Carbon cycling in the upper waters of the Sargasso Sea: II. Numerical simulation of apparent and inherent optical properties. *Deep Sea Research I: Oceanographic Research Papers*, 46: 271–317.
- Branco, A. B., and Kremer, J. N. 2005. The relative importance of chlorophyll and colored dissolved organic matter (CDOM) to the prediction of the diffuse attenuation coefficient in shallow estuaries. *Estuaries*, 28: 643–652.
- Bricaud, A., Morel, A., and Prieur, L. 1981. Absorption by dissolved organic matter of the sea (yellow substance) in the UV and visible domains. *Limnology and Oceanography*, 26: 43–53.
- Chiswell, S. M. 2011. Annual cycles and spring blooms in phytoplankton: don’t abandon Sverdrup completely. *Marine Ecology Progress Series*, 443: 39–50.
- Dupont, N., and Aksnes, D. L. 2013. Centennial changes in water clarity of the Baltic Sea and the North Sea. *Estuarine Coastal and Shelf Science*, 131: 282–289.
- Fasham, M. J. R., Ducklow, H. W., and McKelvie, S. M. 1990. A nitrogen-based model of plankton dynamics in the oceanic mixed layer. *Journal of Marine Research*, 48: 591–639.
- Fleming-Lehtinen, V., and Laamanen, M. 2012. Long-term changes in Secchi depth and the role of phytoplankton in explaining light attenuation in the Baltic Sea. *Estuarine Coastal and Shelf Science*, 102–103: 1–10.
- Frigstad, H., Andersen, T., Hessen, D. O., Jeansson, E., Skogen, M., Nautsvoll, L. J., Miles, M. W., *et al.* 2013. Long-term trends in carbon, nutrients and stoichiometry in Norwegian coastal waters: evidence of a regime shift. *Progress in Oceanography*, 111: 113–124.
- Fujii, M., Boss, E., and Chai, F. 2007. The value of adding optics to ecosystem models: a case study. *Biogeosciences*, 4: 817–835.

- Gran, H. H., and Braarud, T. 1935. A quantitative study of the phytoplankton in the Bay of Fundy and the Gulf of Maine (including observations on hydrography, chemistry and turbidity). *Journal of the Biological Board of Canada*, 1: 279–467.
- Haraldsson, M., Tönnesson, K., Tiselius, P., Thingstad, T. F., and Aksnes, D. L. 2012. Relationship between fish and jellyfish as a function of eutrophication and water clarity. *Marine Ecology Progress Series*, 471: 73–85.
- Hjøllo, S. S., Huse, G., Skogen, M. D., and Melle, W. 2012. Modelling secondary production in the Norwegian Sea with a fully coupled physical/primary production/individual-based *Calanus finmarchicus* model system. *Marine Biology Research*, 8: 508–526.
- Holm-Hansen, O., Lorenzen, C., Holmes, R., and Strickland, J. 1965. Fluorometric determination of chlorophyll. *ICES Journal of Marine Science*, 30: 3–15.
- Højerslev, N. K., Holt, N., and Aarup, T. 1996. Optical measurements in the North Sea–Baltic Sea transition zone. 1. On the origin of the deep water in the Kattegat. *Continental Shelf Research*, 16: 1329–1342.
- Kirk, J. T. O. 2011. *Light and Photosynthesis in Aquatic Ecosystems*. Cambridge University Press, Cambridge.
- Kowalczyk, P., Cooper, W., Whitehead, R., Durako, M., and Sheldon, W. 2003. Characterization of CDOM in an organic-rich river and surrounding coastal ocean in the South Atlantic Bight. *Aquatic Sciences*, 65: 384–401.
- Kowalczyk, P., Olszewski, J., Darecki, M., and Kaczmarek, S. 2005. Empirical relationships between coloured dissolved organic matter (CDOM) absorption and apparent optical properties in Baltic Sea waters. *International Journal of Remote Sensing*, 26: 345–370.
- Larsen, S., Andersen, T., and Hessen, D. O. 2011. Climate change predicted to cause severe increase of organic carbon in lakes. *Global Change Biology*, 17: 1186–1192.
- Mei, Z. P., Saucier, F. J., Le Fouest, V., Zakardjian, B., Sennville, S., Xie, H. X., and Starr, M. 2010. Modeling the timing of spring phytoplankton bloom and biological production of the Gulf of St. Lawrence (Canada): effects of colored dissolved organic matter and temperature. *Continental Shelf Research*, 30: 2027–2042.
- Morel, A., and Maritorena, S. 2001. Bio-optical properties of oceanic waters: a reappraisal. *Journal of Geophysical Research: Oceans*, 106: 7163–7180.
- Mouw, C. B., Yoder, J. A., and Doney, S. C. 2012. Impact of phytoplankton community size on a linked global ocean optical and ecosystem model. *Journal of Marine Systems*, 89: 61–75.
- Nelson, N. B., and Siegel, D. A. 2013. The global distribution and dynamics of chromophoric dissolved organic matter. *Annual Review of Marine Science*, 5: 447–476.
- Roulet, N., and Moore, T. R. 2006. Environmental chemistry - browning the waters. *Nature*, 444: 283–284.
- Samuelsen, A., Hansen, C., and Wehde, H. 2014. Tuning and assessment of the HYCOM NORWECOM V2.1 modeling System. *Geoscientific Model Development Discussion*, 7: 8399–8432.
- Sætre, R. 2007. *The Norwegian Coastal Current - Oceanography and Climate*. Tapir Academic Press, Trondheim.
- Sarmiento, J. L., and Gruber, N. 2006. *Ocean Biogeochemical Dynamics*. Princeton University Press, Princeton.
- Schrum, C., Alekseeva, I., and St John, M. 2006. Development of a coupled physical-biological ecosystem model ECOSMO - Part I: model description and validation for the North Sea. *Journal of Marine Systems*, 61: 79–99.
- Stedmon, C. A., and Markager, S. 2003. Behaviour of the optical properties of coloured dissolved organic matter under conservative mixing. *Estuarine Coastal and Shelf Science*, 57: 973–979.
- Stedmon, C. A., Markager, S., and Kaas, H. 2000. Optical properties and signatures of chromophoric dissolved organic matter (CDOM) in Danish coastal waters. *Estuarine Coastal and Shelf Science*, 51: 267–278.
- Sverdrup, H. U. 1953. On conditions for the vernal blooming of phytoplankton. *Journal du Conseil Permanent International pour l'Exploration de la Mer*, 18: 287–295.
- Urtizberea, A., Dupont, N., Rosland, R., and Aksnes, D. L. 2013. Sensitivity of euphotic zone properties to CDOM variations in marine ecosystem models. *Ecological Modelling*, 256: 16–22.
- Walsh, J. J., Weisberg, R. H., Dieterle, D. A., He, R. Y., Darrow, B. P., Jolliff, J. K., Lester, K. M., *et al.* 2003. Phytoplankton response to intrusions of slope water on the West Florida Shelf: Models and observations. *Journal of Geophysical Research-Oceans*, 108: 1–23.
- Yamashita, Y., and Tanoue, E. 2008. Production of bio-refractory fluorescent dissolved organic matter in the ocean interior. *Nature Geoscience*, 1: 579–582.

Handling editor: Shubha Sathyendranath



Contribution to the Themed Section: 'Revisiting Sverdrup's Critical Depth Hypothesis' Original Article

An experimental demonstration of the critical depth principle

Sebastian Diehl^{1,2*}, Stella A. Berger^{1,3}, Quentin Soissons¹, Darren P. Giling³, and Herwig Stibor^{1,4}

¹Department of Biology II, Ludwig-Maximilians-University Munich, Grosshaderner Str. 2, Planegg-Martinsried 82152, Germany

²Department of Ecology and Environmental Science, Umeå University, Umeå 90187, Sweden

³Department of Experimental Limnology, Leibniz-Institute of Freshwater Ecology and Inland Fisheries (IGB), Alte Fischerhütte 2, Stechlin 16775, Germany

⁴European Institute for Marine Studies, LEMAR, Technopole Brest-Iroise, Place Nicolas Copernic, Plouzané 29280, France

*Corresponding author: tel: +46 90 7865738; fax: +46 90 7866705; e-mail: sebastian.diehl@emg.umu.se

Diehl, S., Berger, S. A., Soissons, Q., Giling, D. P., and Stibor, H. An experimental demonstration of the critical depth principle. – ICES Journal of Marine Science, 72: 2051–2060.

Received 4 August 2014; revised 28 January 2015; accepted 10 February 2015; advance access publication 2 March 2015.

Sverdrup's critical depth hypothesis, which has had an almost canonical status in biological oceanography, has recently been challenged as a universal explanation for the formation of oceanic spring blooms, and several alternative hypotheses have been proposed. Arguments pro and contra alternative explanations have so far relied on theoretical considerations and purely observational data. In this paper, we propose that mesocosm experiments with natural plankton communities could make important contributions to the resolution of the issue. We first briefly review the foundations of the critical depth concept and derive an approximate relationship that relates optically scaled critical depth (= "critical optical depth", i.e. the product of the light attenuation coefficient and the critical depth) to light-dependent phytoplankton production in the mixed surface layer. We describe how this relationship can be used to scale experimental mesocosms such that they reproduce ambient light conditions of natural water columns from the surface down to the critical depth and beyond. We illustrate the power of the approach with a mesocosm study in which we experimentally controlled the onset of the spring bloom of a lake plankton community through the manipulation of optically scaled mixed-layer depth. This experiment may be the first experimental demonstration of the critical depth principle acting on a natural plankton community. Compensation light intensity (= minimum average mixed-layer light intensity required to trigger a bloom of the ambient plankton community) could be constrained to be somewhat above 3.2 moles PAR m⁻² d⁻¹, corresponding to a critical optical depth of 10.5. We compare these numbers to estimates from marine systems and end with a discussion of how experiments could be designed to (i) more accurately determine the critical depth in a given system and (ii) resolve among competing hypotheses for vernal bloom onset.

Keywords: compensation light intensity, critical optical depth, dimensional analysis, mesocosm experiment, phytoplankton spring bloom, scaling.

Introduction

Phytoplankton blooms are regular and often spectacular phenomena in many lakes, estuaries, coastal seas, and oceanic regions. Most prominent is the spring bloom, which is an annual occurrence in most freshwater and many marine systems above 45° latitude. It is commonly believed that the spring bloom is triggered by a combination of biotic and abiotic factors creating an opportunity for phytoplankton to temporarily outgrow grazing losses. These factors include an extended period of declining phytoplankton and grazer densities during fall and winter, a nutrient pulse created by deep, convective mixing of the water column during fall overturn, and a subsequent increase in light availability in the mixed surface layer caused by seasonally increasing surface irradiation and concomitant

thermal stratification and shallowing of the surface layer. The above components are widely agreed upon cornerstones of conceptual models such as the Plankton Ecology Group model of seasonal plankton succession in freshwater ecology and the critical depth concept in biological oceanography (Sverdrup, 1953; Sommer *et al.*, 1986, 2012a; Siegel *et al.*, 2002).

Phytoplankton spring blooms make large contributions to annual primary and secondary production and to biogeochemical processes such as the biological carbon pump (Körtzinger *et al.*, 2008; Chassot *et al.*, 2010; Martin *et al.*, 2011). Much effort has therefore been directed towards the study of spring blooms. In a recent review, Behrenfeld and Boss (2014) highlight three mechanisms that can trigger a spring bloom: (i) the critical depth hypothesis,

which proposes that vertical mixing of the surface layer must stay above a critical depth beyond which phytoplankton has negative growth because of light limitation (Sverdrup, 1953); (ii) the critical turbulence hypothesis, which proposes that surface blooms can be triggered in the absence of significant vertical density gradients when turbulent vertical transport is weak (Huisman et al., 1999; Taylor and Ferrari, 2011), and (iii) the dilution-recoupling hypothesis, which proposes that winter mixing stays above the critical depth and that the bloom onset is triggered during autumn and winter mixing by a decrease in grazing pressure when phytoplankton become diluted in the deepening mixed layer (Behrenfeld, 2010). Although the critical depth hypothesis has had an almost canonical status in biological oceanography for decades, recent studies have cast doubt on its legitimacy as a universal explanation for the occurrence of oceanic spring blooms (Behrenfeld, 2010; Taylor and Ferrari, 2011). The latter has spurred controversy that needs to be resolved (Chiswell, 2011; Behrenfeld and Boss, 2014; Fischer et al., 2014). In this paper, we propose that carefully designed experiments can make important contributions to the resolution of this issue.

Oceanography has a long history of studying vernal phytoplankton blooms based on observation. Over recent decades, the geographical and temporal coverage of observation has reached unprecedented levels with the advent of remote sensing from satellites (Behrenfeld et al., 2006; Henson et al., 2009; Boyce et al., 2010). In combination with data-driven mathematical modelling of ocean physics and mixed-layer climatology, this wealth of data has been used to descriptively parameterize elements of the critical depth hypothesis and/or to find support for alternative bloom explanations (Siegel et al., 2002; Behrenfeld, 2010; Taylor and Ferrari, 2011). Large-scale, high-resolution data and coupled biogeochemical-physical ocean models are clearly indispensable to the accurate description of blooms and to the validation of potential mechanisms explaining their occurrence (or absence!). Yet, when it comes to discriminating among competing ecological hypotheses, nothing is more compelling than evidence from carefully designed field experiments (Hairton, 1989). Although spring bloom formation has been studied experimentally at the community level in some marine systems (e.g. Sommer et al., 2012b), to our knowledge, the critical depth concept has not yet been explicitly addressed with field experiments.

Irrespective of which hypothesis correctly describes the mechanisms underlying spring bloom formation, the “concept” of a critical depth is clearly relevant to the resolution of the issue. It would therefore be extremely useful if the critical depth in a given field situation could be experimentally determined. In this paper, we describe how appropriately designed mesocosm experiments with ambient plankton communities can be used to accomplish this goal. We first briefly review the foundations of the critical depth concept and derive an approximate relationship that relates optically scaled critical depth to light-dependent phytoplankton production in the mixed surface layer. We describe how this relationship can be used to scale experimental mesocosms such that they reproduce ambient light conditions of natural water columns from the surface down to the critical depth and beyond. We illustrate the power of the approach by briefly summarizing a decade of relevant experiments from our own lab and by describing in detail a mesocosm study in which we experimentally controlled the onset of the spring bloom through the manipulation of optically scaled mixed-layer depth. We end with a discussion of how experiments could be designed to most accurately measure the critical depth as well as to resolve among alternative hypotheses for vernal bloom onset.

Optically scaled critical depth

In the context of this manuscript, we define a spring bloom as a vernal increase in the volumetric density of phytoplankton in the mixed surface layer, the depth z_{mix} of which may vary over time [note that this definition deviates from the area-based definition used in the dilution-recoupling hypothesis (Behrenfeld, 2010)]. Sverdrup’s critical depth hypothesis for spring bloom initiation builds on three explicit assumptions: (i) turbulent mixing is strong enough to evenly distribute the plankton within the mixed surface layer; (ii) phytoplankton growth within the mixed surface layer is not limited by nutrients and is linearly dependent (with slope α) on the ambient photon flux density $I(z)$ of PAR at depth z ; (iii) the light attenuation coefficient K is constant within the mixed surface layer. An obvious fourth, but implicit, assumption is that a bloom can only develop when specific growth exceeds specific losses R . Losses were not specified by Sverdrup but must reasonably encompass all loss processes including density and mixing depth-dependent processes such as grazing, sinking, and dilution in a deepening mixed layer. Under these assumptions, the specific rate of change of phytoplankton biomass density P in the mixed surface layer is described by

$$\frac{1}{P} \frac{dP}{dt} = \frac{\alpha}{z_{\text{mix}}} \int_0^{z_{\text{mix}}} I(z) dz - R = \alpha I_{\text{mix}} - R, \quad (1)$$

where $I_{\text{mix}} = \alpha I_0(1 - e^{-Kz_{\text{mix}}})/(Kz_{\text{mix}})$ is average PAR in the mixed surface layer and I_0 is incident PAR at the water surface, averaged over a day–night cycle (see Table 1 for an overview of symbols, units, and descriptions). Sverdrup hypothesized that the phytoplankton net rate of change is negative under conditions of winter mixing but would eventually turn positive (and initiate a bloom) when incident radiation I_0 increases and depth of the mixed surface layer z_{mix} becomes shallower as the season progresses. From Equation (1) follows that initiation of a bloom ($dP/dt > 0$) requires that $z_{\text{mix}}/(1 - e^{-Kz_{\text{mix}}}) < \alpha I_0/(KR)$, which during winter mixing (when Kz_{mix} is large and $e^{-Kz_{\text{mix}}}$ approaches zero) is well approximated by

$$z_{\text{mix}} \approx z_{\text{cr}} < \frac{\alpha I_0}{KR}, \quad (2)$$

Table 1. Definition of symbols used in model equations.

Symbol	Commonly used units	Description
α	$\text{m}^2 (\text{mol photons})^{-1}$	Specific growth coefficient of phytoplankton
I	$\text{mol photons m}^{-2} \text{d}^{-1}$	Photosynthetically active radiation (PAR)
I_0	$\text{mol photons m}^{-2} \text{d}^{-1}$	Daily mean incident PAR at water surface
I_c	$\text{mol photons m}^{-2} \text{d}^{-1}$	Compensation irradiance
I_{mix}	$\text{mol photons m}^{-2} \text{d}^{-1}$	Daily mean PAR in mixed surface layer
K	m^{-1}	Light attenuation coefficient
P	g carbon m^{-3} or $\text{mg chl } a \text{ m}^{-3}$	Phytoplankton biomass density
R	d^{-1}	Daily mean specific loss rate of phytoplankton
z	m	Depth below water surface
z_{cr}	m	Critical depth
z_{mix}	m	Depth of mixed surface layer

where z_{cr} is the critical depth, i.e. the maximum depth of the mixed surface layer that allows for positive phytoplankton growth. Inequality (2) can be rearranged and expressed in terms of an optically scaled, dimensionless critical depth Kz_{cr} as

$$Kz_{\text{cr}} < \frac{\alpha I_0}{R} = \frac{I_0}{I_c}, \quad (3)$$

where I_c is the compensation irradiance, i.e. the PAR intensity at which production equals losses defined by $\alpha I_c - R = 0$ (note that this differs from the physiological definition of a compensation irradiance which includes phytoplankton respiration as the only loss process). Equation (3) contains three physical variables (I_0 , K , z_{mix}) that are relatively easy to measure (though different authors may use different operational definition of z_{mix}) and two biological variables (α and R , or their ratio $R/\alpha = I_c$) that are notoriously difficult to constrain. Consequently, empirical estimates of the compensation irradiance I_c differ by more than an order of magnitude (Smetacek and Passow, 1990; Townsend *et al.*, 1992), which likely reflects both real spatial and temporal variation in α and R but also an inability to accurately determine compensation depth from purely observational data.

The concept of an optical depth is well established in phytoplankton ecology (Reynolds, 1984; Kirk, 1994). We emphasize it here because extending it to the definition of a “critical optical depth” (Kz_{cr} , Equation 3) opens up for the possibility of determining critical depths experimentally by use of optically scaled mesocosms. In the following sections, we first describe such an experimental system that we have used for the manipulation of optical depth in several field experiments and briefly highlight a few relevant results from these studies.

An experimental system of optically deep mesocosms

For over a decade, our lab has performed field experiments in which we studied the influence of optically scaled mixed water column depth on phytoplankton and zooplankton dynamics in mesocosms. Common to most experiments were the following design features.

(i) The experiments were performed in Lake Brunnsee, a small, deep, oligotrophic clear-water lake close to the University of Munich’s Limnological Research Station at Seon 90 km east of Munich, Germany. Lake Brunnsee has a maximum depth of 19 m, total phosphorus concentrations are year-round $< 0.3 \mu\text{M}$, while concentrations of dissolved inorganic nitrogen and silicon exceed $70 \mu\text{M}$ each, and Secchi depth ranges from 7 to 15 m.

(ii) Mesocosms consisted of cylindrical plastic bags made from transparent Tricoron (RKW Wasserburg, Germany). Mesocosms had an inner diameter of 0.95 m, were sealed at the bottom but open to the atmosphere (and thus exposed to direct sunlight), and were suspended from a wooden frame attached to a raft such that they extended 0.2 m above the lake surface (Figure 1). Mesocosms were made optically deep by surrounding them with light absorbing silage film. Depending on the pigmentation of the silage film the light attenuation coefficient inside a mesocosm could range from 0.77 [white, slightly translucent silage film, Diehl *et al.* (2002)] to 1.3 m^{-1} (black, opaque silage film, this study). For comparison, the attenuation coefficient in the lake typically ranges from 0.25 to 0.45 m^{-1} .

(iii) At the beginning of each experiment, all mesocosms were filled with 30–50 μm filtered lake water containing the natural community of phyto- and microzooplankton but excluding crustaceans. In some experiments, we deliberately excluded the latter group to keep grazing pressure on phytoplankton low. In other experiments,

we subsequently re-stocked mesocosms with crustacean grazers. In most experiments, we fertilized mesocosms with an initial pulse of 0.25–1 μM inorganic phosphorus to mimic nutrient replete spring conditions and/or accentuate response patterns.

(iv) The total vertical extent of a mesocosm could range from 1 to 15 m depending on the experiment. Depth of the mixed water column inside a mesocosm was controlled by intermittently blowing compressed air to the desired depth using battery driven compressors. Depending on the question, we either mixed the entire water column inside a mesocosm or only its upper part (Figure 1, left panel).

(v) Mixing was highly effective but produced temperature differences between treatments differing in mixing depth (Diehl *et al.*, 2002), because more deeply mixed water columns extend deeper into colder parts of the thermally stratified lake. To manipulate mixed-layer depth independently of temperature, we surrounded mesocosms by a large, permanently mixed outer bag (Figure 1). Mesocosms suspended inside this destratified water bath have identical mixed-layer temperatures and exhibit negligible vertical temperature gradients in non-mixed parts of the water column (e.g. Jäger *et al.*, 2008a, b). Because the destratified water bath takes on the average, depth integrated temperature of the surrounding stratified lake, water temperatures in shallow mixed layers differ between mesocosms inside and outside the water bath. We exploited this in several experiments in which we manipulated temperature independently of mixing depth (Figure 1, Berger *et al.*, 2007, 2010, 2014, this study).

A glance on 10+ years of experimental manipulations of mixed water column depth

Early experiments performed in the described mesocosm facility focused on long-term (equilibrium) responses of late summer phytoplankton communities to mixed water column depth. Very generally, these experiments corroborate theoretical predictions about the influence of mixed-layer depth on light vs. nutrient limitation of phytoplankton (Diehl, 2002; Huisman and Sommeijer, 2002; Berger *et al.*, 2006; Jäger *et al.*, 2010) and support oceanographic theory on the influence of mixed layer deepening in different oceanic regions (Le Quéré *et al.*, 2003; Doney, 2006). Specifically, we found that steady state phytoplankton biomass has a maximum at an intermediate mixed-layer depth. Biomass decreases towards both deeper mixed layers where light limitation becomes increasingly severe (as in high-latitude oceans during winter) and towards shallower mixed layers where algal sinking losses and concurrent nutrient depletion become increasingly important (as in tropical oceans) (Diehl *et al.*, 2002, 2005; Ptacnik *et al.* 2003).

The above experiments support a body of process oriented theory that does not only explain equilibrium responses of phytoplankton to mixed-layer depth but is equally relevant to the formation of transient blooms. In subsequent experiments, we have therefore focused on seasonal plankton dynamics under spring conditions. Because water columns are nutrient replete at the onset of spring, phytoplankton concentrations during transient spring peaks are predicted to be the higher the shallower the mixed layer (i.e. at higher average mixed-layer PAR), except for extremely shallow layers where sinking losses are so high as to very rapidly deplete nutrients (Jäger *et al.*, 2008a). In accordance with these predictions, spring peak heights of both phytoplankton and zooplankton were found to decrease over realistic ranges of increasing mixed-layer depth (Berger *et al.*, 2007, 2010, 2014). Also in accordance with theory (Jäger *et al.*, 2008a; Peeters *et al.*, 2013),

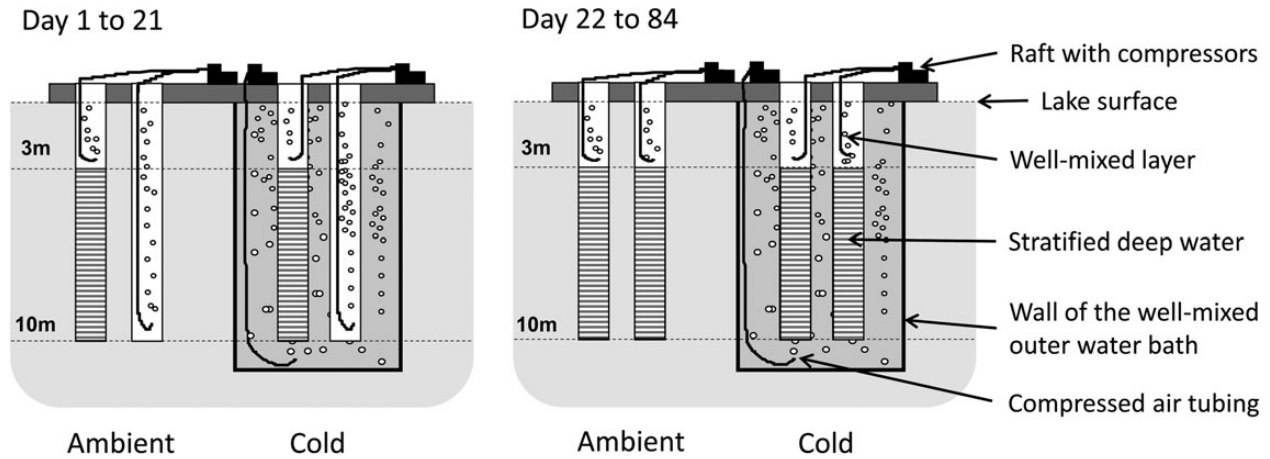


Figure 1. Schematic drawing of the experimental set-up. Shown is one mesocosm of each treatment and the compressed air system used to mix the mesocosms to the desired depths. The lake stratified thermally at 3–4 m depth. “Ambient” mesocosms were placed directly in the lake. “Cold” mesocosms were placed inside a well-mixed outer water bath with $\sim 3^{\circ}\text{C}$ colder water compared with the surface layer of the lake. “Early” stratification treatments were well mixed down to 3 m and stratified below from day 1 onward. “Late” stratification treatments were well mixed down to 10 m until day 21 and stratified at 3 m thereafter. Dots (symbolizing air bubbles) indicate the well-mixed water masses. Horizontal hatching indicates the stratified deepwater.

phytoplankton grew faster and reached the peak of the spring bloom earlier the shallower the mixed layer (Berger *et al.*, 2007, 2010, 2014).

An experimental demonstration of the critical depth principle

In this section, we describe a mesocosm study that explored the effects of water temperature and the timing of stratification on spring plankton dynamics by independently manipulating both factors. Specifically, we cross-classified (i) early and late water column stratification with (ii) ambient and reduced water temperature (Figures 1 and 2). Incidentally, this study provides an experimental demonstration of the critical depth principle and illustrates how the optically scaled critical depth can be estimated for a natural plankton community. Note, however, that estimation of the optically scaled critical depth was not the primary purpose of this experiment and that we would target the latter with a different experimental approach (described in the “Discussion” section). Below, we describe the experimental and analytical methods and the observed treatment effects, with special emphasis on the timing of the phytoplankton spring bloom and its quantitative relationship with mixed-layer light climate.

Methods

The experimental protocol followed the general recipe described above. Below, we emphasize additional details that are specific to this experiment. The mesocosm facility was set up in Lake Brunsee in April 2006 soon after ice-out. At this time, the phytoplankton community was dominated by small centric diatoms (*Cyclotella* sp.) and cryptophytes (*Rhodomonas minuta*). On 16 April, when the lake had just started to thermally stratify, a total of 12 mesocosms (3 replicates per treatment) was filled with ambient, 30 μm filtered lake water containing the natural community of microplankton but excluding larger mesozooplankton. Mimicking natural recruitment from overwintering resting eggs,

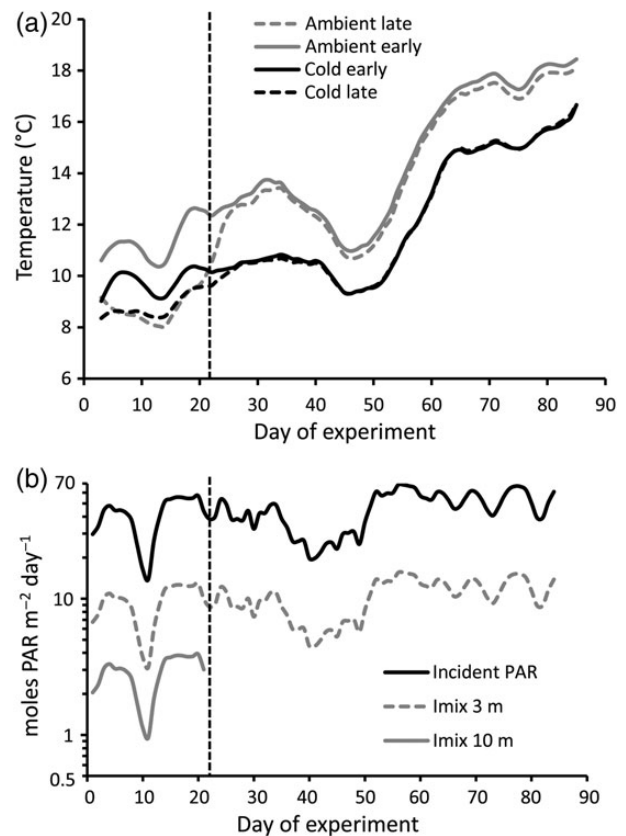


Figure 2. Temporal development of (a) daily mean water temperature in the mixed layers of the four different treatments and (b) of estimated daily PAR. Shown are 3-d running means of incident PAR at the water surface and of depth-averaged PAR [= I_{mix} in Equation (5)] in mixed layers of 3- and 10-m depth, respectively. Dashed vertical lines indicate the onset of “late” stratification on day 22.

mesocosms were stocked on 18, 24, and 30 April with small, equal aliquots of *Daphnia hyalina* (in total 0.3 ind. l⁻¹) that had been isolated from the lake and pre-cultivated in the lab. Mesocosms extended 10 m below the water surface and were made optically deep by an outer layer of light absorbing, black, opaque silage film. To enhance the annual nutrient pulse following spring overturn, we fertilized all mesocosms once with KH₂PO₄ to a total phosphorus concentration of 0.8 μM P. Throughout the experiment, we logged water temperature in all mesocosms every 30 min at a depth of 15 cm.

A schematic drawing of the experimental set-up is given in Figure 1. Before the start of the experiment, mesocosms were fully mixed by intermittently blowing compressed air to their bottom (5 min every 35 min). “Early” stratification was accomplished by raising the outlet of compressed air from a depth of 10–3 m on 18 April (day 1). “Late” stratification treatments were completely mixed for another three weeks and stratified at 3 m on day 22 (Figure 1). On 3 May, we measured vertical profiles of PAR with a spherical quantum sensor (LICOR LI-139SA) in all mesocosms and calculated the light attenuation coefficient *K* as the slope of linear regressions of log-transformed PAR against depth. In mesocosms that were close to starting conditions (2.3 μg chl *a* l⁻¹) *K* was 1.3 m⁻¹, which yields values of optical mixed-layer depth *Kz*_{mix} of 13 before stratification and 3.9 thereafter. For comparison, these values correspond to physical depths of 260 and 78 m, respectively, in water columns with a light attenuation coefficient of 0.05 m⁻¹, which is a typical value for the North Atlantic before the onset of the spring bloom (Wroblewski, 1989; Henson, 2005).

The “ambient” temperature treatment consisted of mesocosms that were freely suspended and thus exposed to the lake’s seasonal temperature regime (Figure 2a). In contrast, mesocosms with reduced temperature (hereafter “cold”) were placed inside a 12 m deep, permanently mixed outer bag that served as a destratified water bath. The latter took on the vertically averaged temperature of the surrounding lake. Water temperatures in “cold” treatments thus followed the seasonal temperature trajectory in the lake, but once all mesocosms were stratified at 3 m, the mixed layers of the “cold” treatments remained ~3°C colder than “ambient” mixed layers throughout the rest of the experiment (Figure 2a).

The experiment was maintained for 84 d (until 10 July) to allow for the typical seasonal sequence of a phytoplankton spring bloom followed by a *Daphnia* peak and a clear-water phase with low phytoplankton biomass. We sampled phytoplankton and mesozooplankton twice weekly from the mixed surface layer and, where applicable, at mid-depth from the stratified water column below. Phytoplankton biomass was estimated as chlorophyll *a* concentration measured from *in vivo* fluorescence (TD 700, Turner Designs) of 250 μm filtered water immediately after sampling. The abundance of mesozooplankton (almost exclusively *D. hyalina*) was estimated from vertical hauls with a 55-μm plankton net. We also took vertical profiles of temperature, dissolved oxygen, and alkalinity from the surface to 10-m depth about once a week using a multiprobe LT1/T (WTW, Weilheim, Germany).

Knowledge of incident PAR is required to relate phytoplankton dynamics to depth-averaged PAR in the mixed layer. Continuous measurements of incident PAR are, however, not available for Lake Brunnsee. We therefore estimated incident PAR for each day of the experiment from daily sunshine hours recorded at Amerang 10 km to the west (www.dwd.de/WESTE) using the relationship

$$I_0 = [0.2468 + 1.1924o/c - 0.43791924(o/c)^2]Q \quad (4)$$

where *I*₀ is incident PAR at the water surface (mol PAR m⁻² d⁻¹), *o* the observed sunshine hours, *c* the sunshine hours under a clear sky, and *Q* is incident PAR under a clear sky (Qin *et al.*, 2012). Values for *c* and *Q* for the latitude of Lake Brunnsee were obtained from solar radiation tables assuming that 50% of solar radiation is PAR and that PAR energy converts to photon flux density as 4.56 μmol photons s⁻¹ W⁻¹ (McCree, 1972). Monthly solar radiation sums calculated from Equation (4) consistently overestimated incident radiation by a factor of 1.26–1.29 compared with (spatially interpolated) monthly global radiation sums for the geographical location of Lake Brunnsee (available at www.dwd.de/WESTE). We therefore corrected our estimates of daily PAR by a factor 1/1.28. Incident PAR was converted to depth-averaged PAR in the mixed layer *I*_{mix} as

$$I_{\text{mix}} = I_0 \frac{1 - e^{-Kz_{\text{mix}}}}{Kz_{\text{mix}}}, \quad (5)$$

where optical mixed-layer depth *Kz*_{mix} was 14.5 and 4.35 before and after stratification, respectively. The time courses of incident PAR and mixed-layer PAR are shown in Figure 2b.

Data analyses

We estimated the timing of the onset, peak, and end of the phytoplankton spring bloom in each mesocosm by fitting a unimodal 6-parameter Weibull function to each chlorophyll *a* time-series using the “carditates” package in R (Rolinski *et al.*, 2007; R Development Core Team, 2014). The function allows for non-zero baselines before the onset of the bloom and after its end as well as for lagged and different slopes in the increasing and decreasing sections (Figure 3). Neighbouring maxima were considered separate peaks only when the relative height of an intervening pit was <0.1 times the lower maximum. The beginning and end of a bloom were determined separately for the periods before and after the fitted peak (i.e. the left and right branch of the curve) as the date of the 10% quantile of the area under the curve before the maximum and the date of the 90% quantile of the area under the curve after the maximum, respectively (Rolinski *et al.*, 2007).

Effects of temperature (“ambient” and “cold”) and stratification (“early” and “late”) treatments on the timing of the onset and the peak of the bloom (as determined from the Weibull fits) were statistically analysed with two-factor analysis of variance (ANOVA) in R (R Development Core Team, 2014). We also attempted to delineate a bound to the compensation light intensity (*I*_c) by visually identifying periods of zero phytoplankton net growth in each replicate and comparing them with concomitant estimates of average mixed-layer PAR.

Results

Phytoplankton dynamics

Similar to other experiments with stratified water columns (Berger *et al.*, 2010, 2014), water chemistry and phytoplankton indicated that dynamics in the surface layer were unaffected by processes in deeper water. We therefore report phytoplankton data only from the mixed surface layer. The 6-parameter Weibull function gave a very good to excellent fit to the chlorophyll *a* time-series (*R*² ≥ 0.76, Figure 3). In “early” stratification treatments, phytoplankton had a brief lag phase (likely caused by the initial disturbance of pumping lake water into the mesocosms) but grew exponentially within a week from the start of the experiment, reaching peak densities in weeks 3–4 (Figure 3, left panels). In contrast, chlorophyll

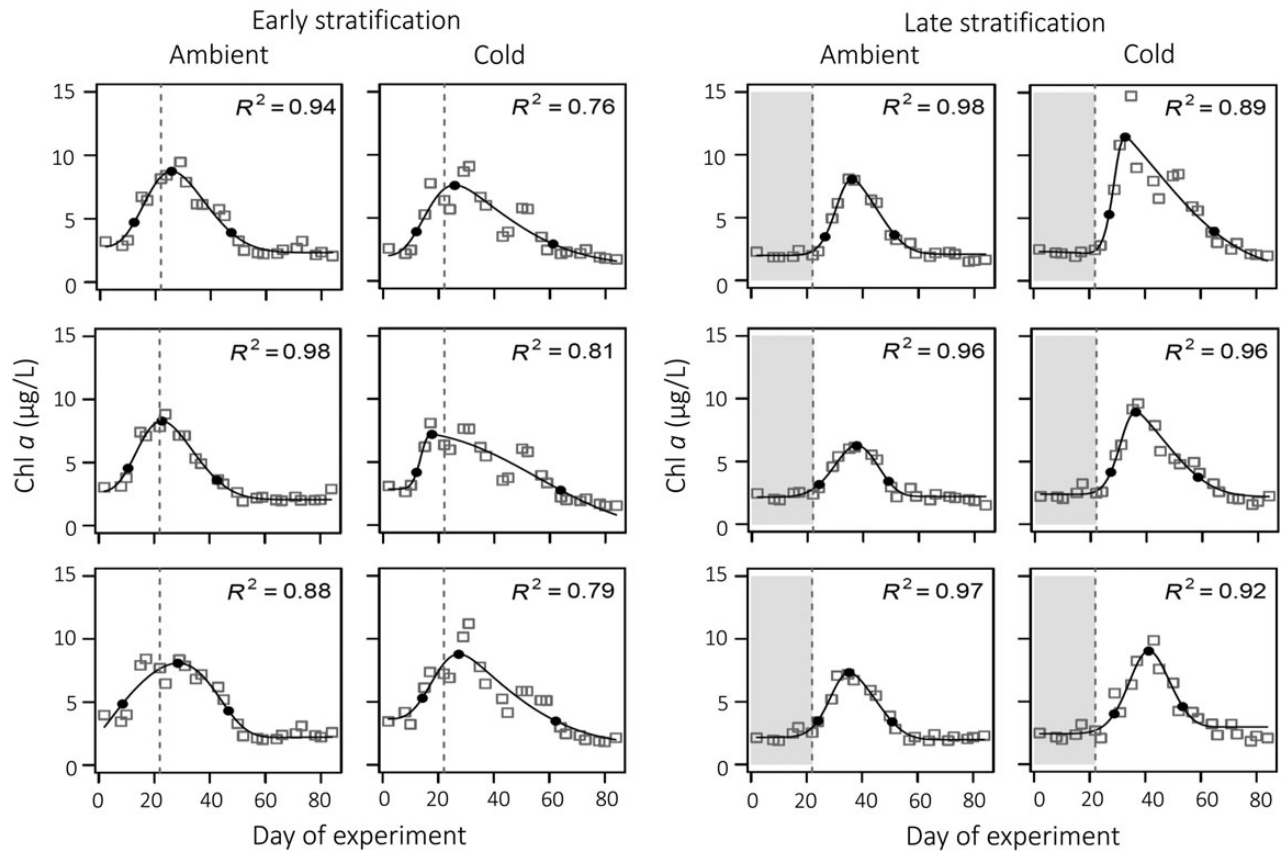


Figure 3. Time course of phytoplankton biomass (as chlorophyll *a* concentration) in the mixed layers of individual “ambient” and “cold” mesocosms that where stratified “early” (day 1, left panels) and “late” (day 22, right panels). Panels show data points (open squares), Weibull fits (solid lines), and R^2 values of the Weibull fits. Filled circles indicate the estimated beginning, peak, and end of the bloom in each mesocosm. For comparison, the date of late stratification is indicated in all panels (dashed vertical lines). The period of deep mixing of the “late” stratification treatments is highlighted in grey.

concentrations remained constant during the first 3 weeks in the “late” stratification treatments and did not start to increase until the mesocosms were stratified on day 22 (Figure 3, right panels). Chlorophyll concentrations in the “late” treatments peaked in weeks 5–6. On average, the onset of the phytoplankton bloom occurred 15 d earlier and the peak of the bloom occurred 12 d earlier in “early” than in “late” stratification treatments (Figure 4; ANOVA, effect of stratification timing, $p \leq 0.001$). In “cold” treatments, the onset, but not the peak, of the bloom was slightly delayed compared with “ambient” treatments (Figure 4; ANOVA, effect of temperature, $p = 0.007$ and $p > 0.7$, respectively).

At the time of the onset of the spring bloom, *Daphnia* densities were still very low (< 1 ind. l^{-1}) in all mesocosms. Average *Daphnia* density before bloom onset was slightly higher in the treatment with the earliest bloom onset (“ambient-early”, 0.55 ind. l^{-1}) than in the remaining treatments (0.33 ind. l^{-1} ; ANOVA, $p = 0.02$). If grazing had been significant, it should rather have delayed phytoplankton development, suggesting that the influence of grazing on bloom initiation was weak. Once phytoplankton blooms peaked (weeks 3–6), *Daphnia* densities increased rapidly and subsequently reached own peak densities > 80 ind. l^{-1} in weeks 7–10. The latter are likely responsible for the low chlorophyll levels during the second half of the experiment (Figure 3). After the onset of stratification, very few *Daphnia* were caught below the mixed surface layer. Further details of the zooplankton dynamics will be described elsewhere.

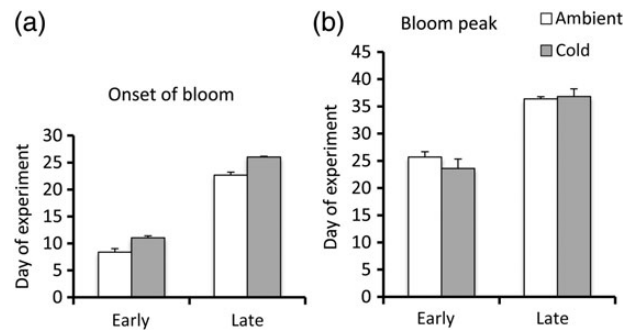


Figure 4. Timing of (a) the onset and (b) the peak of the phytoplankton spring bloom as estimated from the Weibull fits in Figure 3. Shown are means \pm 1 SE.

Phytoplankton growth in relation to the light and temperature environment

Water temperature in the mixed surface layers of the “early” stratification treatments followed the temporal trends of incident PAR in a dampened and time-lagged manner (Figure 2), fluctuating from 10.5 to 14°C (“ambient early”) and from 9 to 10.5°C (“cold early”) during the period when the phytoplankton blooms occurred (up to day 50). Due to a miscalculation, the outer bag surrounding

the “cold” treatments was only mixed to a depth of 7 m (instead of 11 m). As a consequence, mixed layers in “cold early” treatments (3 m deep from day 1 on) were $\sim 1\text{--}1.5^\circ\text{C}$ warmer than in “cold late” treatments (10 m deep until day 21) during the first 3 weeks of the experiment, but quickly converged in temperature after the latter were stratified at 3 m on day 22 (Figure 2a).

Although these early differences in temperature slightly confound the interpretation of the phytoplankton growth data, it is obvious that the large differences in timing of the onset and peak of the spring bloom between “early” and “late” stratification treatments were primarily related to differences in light climate (Figures 2b and 4). In the “early” stratification treatments, estimated mean PAR in the mixed surface layer (I_{mix}) was $10.22 \text{ moles m}^{-2} \text{ d}^{-1}$ before the onset of the bloom (days 1–8) but dropped to an average value of $5.12 \text{ moles m}^{-2} \text{ d}^{-1}$ during a period of overcast (days 9–12, Figure 2b). Despite this temporary reduction in PAR, phytoplankton in “early” stratification treatments grew fast during this period and had doubled to tripled by day 15 (Figure 3). In contrast, phytoplankton did not show any net growth in “late” stratification treatments before stratification. Average PAR during this initial period of deep mixing was $3.2 \text{ moles m}^{-2} \text{ d}^{-1}$ (days 1–21) but shifted to a value of $9.67 \text{ moles m}^{-2} \text{ d}^{-1}$ on the day of stratification (day 22), triggering an almost instant net growth response (Figures 2b and 3).

Together, these data suggest that an average mixed-layer photon flux density of $3.2 \text{ moles m}^{-2} \text{ d}^{-1}$ was insufficient to trigger a phytoplankton bloom, whereas a photon flux density of $5.12 \text{ moles m}^{-2} \text{ d}^{-1}$ allowed for rapid growth. The compensation light intensity (I_c) of the plankton community of Lake Brunnsee in spring 2006 can thus be estimated to be somewhat above $3.2 \text{ moles PAR m}^{-2} \text{ d}^{-1}$. Using an average incident PAR value of $33.5 \text{ moles m}^{-2} \text{ d}^{-1}$ (the mean for April 2006), this yields an estimate of the critical “optical” depth [K_{z_c} , Equation (3)] of the Lake Brunnsee community of somewhat below 10.5 in 2006.

Discussion

Pelagic mesocosms provide a near natural environment in which complex plankton communities can be maintained and manipulated for many weeks, while simultaneously enabling detailed monitoring of the pools and fluxes of the components under study (Petersen *et al.*, 2003). If properly designed and scaled, pelagic mesocosm experiments therefore allow strong inference on underlying processes, scaling-up to larger ecosystems, and discrimination among competing hypotheses (Petersen *et al.*, 2009). Not surprisingly, the experimental study of plankton dynamics in mesocosms has a long history in marine science (McAllister *et al.*, 1961; Grice *et al.*, 1977; Davies *et al.*, 1979; Banse, 1982). Yet, the use of mesocosms has been largely restricted to estuarine and sheltered ecosystems and has only very recently been added to the toolbox of biological oceanography (Sommer *et al.*, 2007; Riebesell *et al.*, 2013).

Reasons for this absence are likely twofold. First, mesocosm experiments in the open ocean pose severe technical and logistical challenges. It is not until very recently that mesocosms have been developed that withstand the mechanical strain exerted by waves and currents in the open ocean (Riebesell *et al.*, 2013). Moreover, mesocosm experiments require continuous maintenance and frequent sampling and thus entail costly ship time if performed in remote oceanic regions. Second, ocean stratification, productivity, and biogeochemistry are all strongly affected by turbulent hydrodynamic forces acting at multiple spatial scales many times larger than the enclosed systems under study (Falkowski *et al.*, 1998; McGillicuddy *et al.*, 2007; Mahadevan *et al.*, 2010). It may therefore seem difficult to justify approaching large-scale phenomena such as

the North Atlantic spring bloom with costly experimentation on enclosed, local communities. The latter is, however, in principle no different from the general scaling issues inherent to all kinds of mesocosm experiments, and methods such as dimensional analysis are available to accommodate many of these issues (Perez *et al.*, 1977; Petersen and Hastings, 2001; Petersen and Englund, 2005).

For example, despite the complex, three-dimensional nature of hydrodynamical forces in the ocean, the three hypotheses on mechanisms triggering vernal plankton blooms described in the introduction do only include physical and biological structure in the “vertical” dimension (Behrenfeld and Boss, 2014). This means that principles of vertical gradient compression (Petersen and Kemp, 2009) can be applied to scale mesocosms that are used in experimental hypothesis testing. We have already described how a deepwater light environment can be simulated in relatively shallow mesocosms and have developed the concept of a “critical optical depth” from this approach.

Our experimental estimate of the compensation light intensity I_c of closely above $3.2 \text{ moles PAR m}^{-2} \text{ d}^{-1}$ for the plankton community of Lake Brunnsee in spring 2006 is similar to Riley’s (1957) classical estimate of $3.5 \text{ moles PAR m}^{-2} \text{ d}^{-1}$ for the Sargasso Sea [recalculated by Siegel *et al.* (2002)] and consistent with a mesocosm study in which an experimental doubling of the ambient mixed-layer light dose from 2 to $4 \text{ moles PAR m}^{-2} \text{ d}^{-1}$ triggered a bloom of a Baltic Sea plankton community (Sommer *et al.*, 2011). It is also within the range of local (1° by 1° grid cell) estimates of I_c for the North Atlantic spring bloom in 1998–2000 calculated from satellite data and oceanic climatologies (Figure 1d in Siegel *et al.*, 2002) but about a factor 2–3 higher than regionally averaged estimates (Siegel *et al.*, 2002).

We emphasize that, compared with the many assumptions that go into the estimation of local compensation light intensities from satellite data, our experimentally determined estimates are likely more reliable. In particular, the physical mixing depths and the dates of the onset of the phytoplankton bloom could be almost exactly determined in each experimental mesocosm. Yet, perhaps our method overestimates the true compensation light intensity. Incident radiation at the water surface was probably lower inside than outside the mesocosms, because the opaque, black walls extended 0.2 m above the water surface. Second, our vertical light measurements did not take into account horizontal light gradients inside the mesocosms. We attempted to measure PAR at a central location of the mesocosm cross section, where light levels are typically appreciably higher than close to walls. Although we did not gather data to quantify these biases, it would be easy to do so.

Although our mesocosm study may be the first experimental demonstration of the critical depth principle acting on a natural plankton community, a precise estimate of the critical optical depth (and thus I_c) was not the primary goal of the study. To that end, we would suggest a gradient design that covers a broad range of optical depth treatments. The reason is that near the critical optical depth phytoplankton biomass and net growth rate are very low and thus difficult to measure with precision. Instead, because the relationship between gross primary production and average PAR in the mixed surface layer I_{mix} is approximately linear at the onset of a spring bloom (Equation 1), the compensation light intensity can be estimated as the x -axis intercept of a regression of experimentally determined phytoplankton net growth rates vs. I_{mix} . We illustrate this with a hypothetical example of a mesocosm experiment performed under conditions similar to the onset of the North Atlantic spring bloom (Figure 5). In the example we

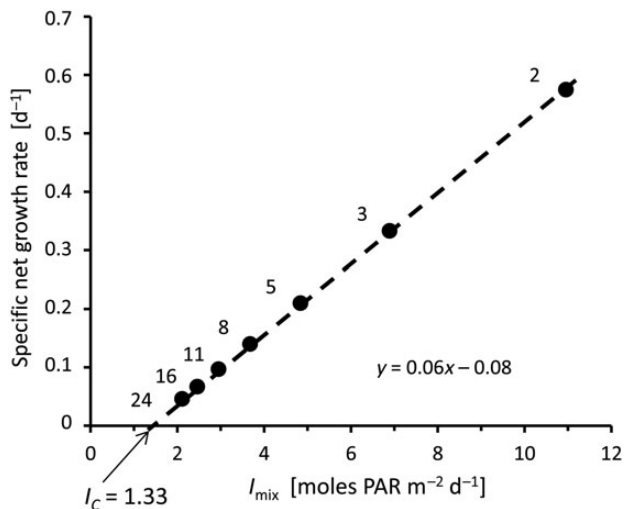


Figure 5. An experimental approach to the determination of the compensation irradiance. The (hypothetical) example assumes that seven optically scaled mesocosms, covering a range of physical mixed-layer depths from 1–7 m (regularly spaced at 1 m intervals), were filled with water containing the plankton community of a well-mixed oceanic water column near the onset of the spring bloom. Initial chlorophyll P_0 was $0.1 \text{ mg chl } a \text{ m}^{-3}$ and its net rate of change followed Equation (1), with $I_0 = 20$, $\alpha = 0.06$, $R = 0.08$, $z_{mix} =$ mesocosm depth, and $K = K_{bg} + k_p P$ with chlorophyll-specific attenuation coefficient $k_p = 0.05$. Light attenuation is dominated by the mesocosm walls (background attenuation coefficient $K_{bg} = 1.35$). The remaining parameter values are representative of the onset of the North Atlantic spring bloom (Bricaud et al., 1995; Siegel et al., 2002; Behrenfeld, 2010; see Table 1 for units). Specific net growth rate in each mesocosm was estimated as $(\ln P_0 - \ln P_t)/t$, where t is the time required for chlorophyll to increase to $P_t = 0.3 \text{ mg chl } a \text{ m}^{-3}$ (assuming that an increase from 0.1 to $0.3 \text{ mg chl } a \text{ m}^{-3}$ is required for a precise measurement of the change in P). Feedback from self-shading is minimal under these conditions and growth is near exponential if R is constant over time t . Shown are specific net growth rates from the seven mesocosms plotted against average PAR in the mixed layer I_{mix} . The compensation irradiance I_c is equal to the x -axis intercept of a linear regression of the specific growth rate against average mixed layer PAR I_{mix} (broken line). Numbers next to data points indicate the time t required to reach $0.3 \text{ mg chl } a \text{ m}^{-3}$ (in days).

assume that an increase in chlorophyll a from an initial value of 0.1 mg m^{-3} to a concentration of 0.3 mg m^{-3} is required to yield sufficient measurement precision. Note that, since specific production and losses (and thus bloom timing, Figure 4a) depend on temperature, one must ensure that the experimental I_{mix} gradient does not co-vary with temperature.

The approach described in Figure 5 is exact only if phytoplankton net growth is exponential over the measurement period. This requires two things. First, the measurement period should be short enough that specific losses R remain approximately constant. Perhaps counter-intuitively, measurements of net growth taken at I_{mix} much higher than I_c are therefore likely to be more reliable than ones taken near I_c (because it takes very much longer to reach measurable phytoplankton biomass changes at low light levels, Figure 5). Second, negative feedback from self-shading should be minimal over the measurement period. The latter condition is well met in experimentally compressed light gradients, where background light attenuation can be easily tuned to be 1–2 orders of

magnitude higher than the contribution of phytoplankton self-shading. Note, however, that self-shading is significant in clear oceanic waters. In other circumstances, the absence of feedback from self-shading may therefore be a limitation of experimentally compressed light gradients. For example, if the longer-term balance of phytoplankton production vs. grazing losses is a study focus (as would be relevant to the dilution-recoupling hypothesis), insignificant self-shading may artificially allow phytoplankton to outgrow more slowly changing grazing losses.

Looking forward, we suggest that mesocosm experiments should be performed that can simultaneously address two or more of the competing hypotheses for vernal spring blooms proposed by Behrenfeld and Boss (2014). For example, it should be feasible to test the principal working of the dilution-recoupling hypothesis with experiments in (optically scaled) mesocosms in which autumnal deepening of a mixed surface layer into a deepwater mass is simulated, followed by simulated vernal re-stratification. Observed plankton dynamics could be related to the critical depth hypothesis by using control treatments without re-stratification or a gradient of re-stratification depth treatments. Similarly, it should be feasible to assess the relative influences of critical depth and critical turbulence mechanisms on plankton dynamics by using appropriately scaled optical depth and turbulence treatments. For example, a finely tunable mixing mechanism can in principle be scaled to any compressed light gradient such as to realistically mimic natural PAR fluctuations experienced by phytoplankters in different turbulence regimes (Sanford, 1997; Petersen and Kemp, 2009).

To be quantitatively most relevant to plankton blooms in the open ocean, mesocosm experiments could be conducted in coastal regions that harbour near oceanic water and plankton communities [see Stibor et al. (2004) and Thingstad et al. (2008) for examples from western Norway and Svalbard]. It is, however, also conceivable to design ship borne systems. Although the construction of on-board plankton towers may appear daunting (and likely pose challenges to the simulation of low turbulence regimes), vertical ocean gradients can be approximated on board with sets of linked, discrete compartments representing different depth strata (Petersen and Kemp, 2009). The latter could be seeded with water and plankton from relevant depths and exposed to depth-specific light and temperature regimes, while exchange rates between neighbouring compartments could be tuned to simulate different turbulence regimes. Clearly, there is much room for creative, hypothesis-driven experimentation in mesocosms in biological oceanography, and we expect that such experimentation will yield crucial insights into the causes and consequences of oceanic plankton dynamics.

Acknowledgements

We thank Angelika Wild, Achim Weigert, Miriam Ruhenstroth, Gabriele Trommer, Florian Hantzschke, and Tanja Weibulat for laboratory analyses and/or help with fieldwork, Margit Feissel, Maria Stockenreiter, and Michaela Baumgartner for culturing *Daphnia* and/or help during the preparation of the experiment, and three anonymous reviewers for very helpful comments. The work was financially supported by the German Science Foundation (DFG) within the priority program AQUASHIFT through grant DI 745/5-1.

References

- Banase, K. 1982. Experimental marine ecosystem enclosures in a historical perspective. In *Marine Mesocosms*, pp. 11–24. Ed. by G. D. Grice, and M. R. Reeve. Springer-Verlag, New York.

- Behrenfeld, M. J. 2010. Abandoning Sverdrup's critical depth hypothesis on phytoplankton blooms. *Ecology*, 91: 977–989.
- Behrenfeld, M. J., and Boss, E. S. 2014. Resurrecting the ecological underpinnings of ocean plankton blooms. *Annual Review of Marine Science*, 6: 167–194.
- Behrenfeld, M. J., O'Malley, R. T., Siegel, D. A., McClain, C. R., Sarmiento, J. L., Feldman, G. C., Milligan, A. J., *et al.* 2006. Climate-driven trends in contemporary ocean productivity. *Nature*, 444: 752–755.
- Berger, S. A., Diehl, S., Kunz, T. J., Albrecht, D., Oucible, A. M., and Ritzer, S. 2006. Light supply, plankton biomass and seston stoichiometry in a gradient of lake mixing depths. *Limnology and Oceanography*, 51: 1898–1905.
- Berger, S. A., Diehl, S., Stibor, H., Sebastian, P., and Scherz, A. 2014. Separating effects of climatic drivers and biotic feedbacks on seasonal plankton dynamics: no sign of trophic mismatch. *Freshwater Biology*, 59: 2204–2220.
- Berger, S. A., Diehl, S., Stibor, H., Trommer, G., and Ruhenstroth, M. 2010. Water temperature and stratification depth independently shift cardinal events during plankton spring succession. *Global Change Biology*, 16: 1954–1965.
- Berger, S. A., Diehl, S., Stibor, H., Trommer, G., Ruhenstroth, M., Wild, A., Weigert, A., *et al.* 2007. Water temperature and mixing depth affect timing and intensity of events during spring succession of the plankton. *Oecologia*, 150: 643–654.
- Boyce, D. G., Lewis, M. R., and Worm, B. 2010. Global phytoplankton decline over the past century. *Nature*, 466: 591–596.
- Bricaud, A., Babin, M., Morel, A., and Claustre, H. 1995. Variability in chlorophyll-specific absorption coefficients of natural phytoplankton: analysis and parameterization. *Journal of Geophysical Research*, 100: 13321–13332.
- Chassot, E., Bonhommeau, S., Dulvy, N. K., Mélin, F., Watson, R., Gascuel, D., and Le Pape, O. 2010. Global marine primary production constrains fisheries catches. *Ecology Letters*, 13: 495–505.
- Chiswell, S. M. 2011. Annual cycles and spring blooms in phytoplankton: don't abandon Sverdrup completely. *Marine Ecology Progress Series*, 443: 39–50.
- Davies, J. M., Gamble, J. C., Morris, R. J., and Wilson, J. G. 1979. Experiments with large enclosed ecosystems. *Philosophical Transactions of the Royal Society London, Series B*, 286: 523–544.
- Diehl, S. 2002. Phytoplankton, light, and nutrients in a gradient of mixing depths: theory. *Ecology*, 83: 386–398.
- Diehl, S., Berger, S., Ptacnik, R., and Wild, A. 2002. Phytoplankton, light, and nutrients in a gradient of mixing depths: field experiments. *Ecology*, 83: 399–411.
- Diehl, S., Berger, S. A., and Wöhrl, R. 2005. Flexible nutrient stoichiometry mediates environmental influences on phytoplankton and its abiotic resources. *Ecology*, 86: 2931–2945.
- Doney, S. C. 2006. Oceanography: plankton in a warmer world. *Nature*, 444: 695–696.
- Falkowski, P. G., Barber, R. T., and Smetacek, V. 1998. Biogeochemical controls and feedbacks on ocean primary production. *Science*, 281: 200–206.
- Fischer, A. D., Moberg, E. A., Alexander, H., Brownlee, E. F., Hunter-Cevera, K. R., Pitz, K. J., Rosengard, S. Z., *et al.* 2014. Sixty years of Sverdrup: a retrospective of progress in the study of phytoplankton blooms. *Oceanography*, 27: 222–235.
- Grice, G. D., Reeve, M. R., Koeller, P., and Menzel, D. W. 1977. The use of large volume, transparent, enclosed sea-surface water columns in the study of stress on plankton ecosystems. *Helgoländer Wissenschaftliche Meeresuntersuchungen*, 30: 118–133.
- Hairton, N. G. 1989. *Ecological experiments: purpose, design and execution*. Cambridge University Press, New York.
- Henson, S. A. 2005. Physical controls on spring bloom dynamics in the Irminger basin, North Atlantic. PhD thesis, University of Southampton.
- Henson, S. A., Dunne, J. P., and Sarmiento, J. L. 2009. Decadal variability in North Atlantic phytoplankton blooms. *Journal of Geophysical Research*, 114: C04013.
- Huisman, J., and Sommeijer, B. 2002. Maximal sustainable sinking velocity of phytoplankton. *Marine Ecology Progress Series*, 244: 39–48.
- Huisman, J., van Oostveen, P., and Weissing, F. J. 1999. Critical depth and critical turbulence: two different mechanisms for the development of phytoplankton blooms. *Limnology and Oceanography*, 44: 1781–1787.
- Jäger, C. G., Diehl, S., and Emans, M. 2010. Physical determinants of phytoplankton production, algal stoichiometry, and vertical nutrient fluxes. *American Naturalist*, 175: E91–E104.
- Jäger, C. G., Diehl, S., Matauschek, C., Klausmeier, C. A., and Stibor, H. 2008a. Transient dynamics of pelagic producer-grazer systems in a gradient of nutrients and mixing depths. *Ecology*, 89: 1272–1286.
- Jäger, C. G., Diehl, S., and Schmidt, G. 2008b. Influence of water column depth and mixing on phytoplankton biomass, community composition, and nutrients. *Limnology and Oceanography*, 53: 2361–2373.
- Kirk, J. T. O. 1994. *Light and photosynthesis in aquatic ecosystems*, 2nd edn. Cambridge University Press, Cambridge, UK.
- Körtzinger, A., Send, U., Lampitt, R. S., Hartman, S., Wallace, D. W. R., Karstensen, J., Villagarcia, M. G., *et al.* 2008. The seasonal $p\text{CO}_2$ cycle at $49^\circ\text{N}/16.5^\circ\text{W}$ in the northeastern Atlantic Ocean and what it tells us about biological productivity. *Journal of Geophysical Research*, 113: C04020.
- Le Quéré, C., Aumont, O., Monfray, P., and Orr, J. 2003. Propagation of climatic events on ocean stratification, marine biology, and CO_2 : case studies over the 1979–1999 period. *Journal of Geophysical Research*, 108: 3375–3389.
- Mahadevan, A., Tandon, A., and Ferrari, R. 2010. Rapid changes in mixed layer stratification driven by submesoscale instabilities and winds. *Journal of Geophysical Research—Oceans*, 115: C03017.
- Martin, P., Lampitt, R. S., Perry, M. J., Sanders, R., Lee, C., and D'Asaro, E. 2011. Export and mesopelagic particle flux during a North Atlantic spring diatom bloom. *Deep Sea Research I*, 58: 338–349.
- McAllister, C. D., Parsons, T. R., Stephens, K., and Strickland, J. D. H. 1961. Measurements of primary production in coastal sea water using a large-volume plastic sphere. *Limnology and Oceanography*, 6: 237–258.
- McCree, K. J. 1972. Test of current definitions of photosynthetically active radiation against leaf photosynthesis data. *Agricultural and Forest Meteorology*, 10: 443–453.
- McGillicuddy, D. J., Jr, Anderson, L. A., Bates, N. R., Bibby, T., Buesseler, K. O., Carlson, C. A., Davis, C. S., *et al.* 2007. Eddy/wind interactions stimulate extraordinary mid-ocean plankton blooms. *Science*, 316: 1021–1026.
- Peeters, F., Kerimoglu, O., and Straile, D. 2013. Implications of seasonal mixing for phytoplankton production and bloom development. *Theoretical Ecology*, 6: 115–129.
- Perez, K. T., Morrison, G. M., Lackie, N. F., Oviatt, C. A., Nixon, S. W., Buckley, B. A., and Heltsche, J. F. 1977. The importance of physical and biotic scaling to the experimental simulation of a coastal marine ecosystem. *Helgoländer Wissenschaftliche Meeresuntersuchungen*, 30: 144–162.
- Petersen, J. E., and Englund, G. 2005. Dimensional approaches to designing better experimental ecosystems: a practitioner's guide with examples. *Oecologia*, 145: 216–224.
- Petersen, J. E., and Hastings, A. 2001. Dimensional approaches to scaling experimental ecosystems: designing mousetraps to catch elephants. *American Naturalist*, 157: 324–333.
- Petersen, J. E., and Kemp, W. M. 2009. Dimensional analysis. *In* *Enclosed Experimental Ecosystems and Scale: Tools for Understanding and Managing Coastal Ecosystems*, pp. 145–160. Ed. by J. E. Petersen, V. S. Kennedy, W. C. Dennison, and W. M. Kemp. Springer, New York.
- Petersen, J. E., Kemp, W. M., Bartleson, R., Boynton, W. R., Chen, C.-C., Cornwell, J. C., Gardner, R. H., *et al.* 2003. Multiscale experiments in

- coastal ecology: improving realism and advancing theory. *BioScience*, 53: 1181–1197.
- Petersen, J. E., Kennedy, V. S., Dennison, W. C., and Kemp, W. M. (eds.). 2009. *Enclosed Experimental Ecosystems and Scale: Tools for Understanding and Managing Coastal Ecosystems*. Springer, New York.
- Ptácnik, R., Diehl, S., and Berger, S. A. 2003. Patterns of abundance of phytoplankton species along an experimental mixing depth gradient. *Limnology and Oceanography*, 48: 1903–1912.
- Qin, J., Yang, K., Liang, S., and Tang, W. 2012. Estimation of daily mean photosynthetically active radiation under all-sky conditions based on relative sunshine data. *Journal of Applied Meteorology and Climatology*, 51: 150–160.
- R Development Core Team. 2014. *R: a language and environment for statistical computing*. R Foundation for Statistical Computing, Vienna, Austria. ISBN 3-900051-07-0, <http://www.R-project.org>.
- Reynolds, C. S. 1984. *The Ecology of Freshwater Phytoplankton*. Cambridge University Press, Cambridge, UK.
- Riebesell, U., Czerny, J., von Bröckel, K., Boxhammer, T., Büdenbender, J., Deckelnick, M., Fischer, M., *et al.* 2013. Technical note: a mobile sea-going mesocosm system—new opportunities for ocean change research. *Biogeosciences*, 10: 1835–1847.
- Riley, G. A. 1957. Phytoplankton of the North Central Sargasso Sea. *Limnology and Oceanography*, 2: 252–270.
- Rolinski, S., Horn, H., Petzoldt, T., and Paul, L. 2007. Identifying cardinal dates in phytoplankton time series to enable the analysis of long-term trends. *Oecologia*, 153: 997–1008.
- Sanford, L. P. 1997. Turbulent mixing in experimental ecosystem studies. *Marine Ecology-Progress Series*, 161: 265–293.
- Siegel, D. A., Doney, S. C., and Yoder, J. A. 2002. The North Atlantic spring bloom and Sverdrup's critical depth hypothesis. *Science*, 296: 730–733.
- Smetacek, V., and Passow, U. 1990. Spring bloom initiation and Sverdrup's critical depth model. *Limnology and Oceanography*, 35: 228–233.
- Sommer, U., Aberle, N., Engel, A., Hansen, T., Lengfellner, K., Sandow, M., Wohlers, J., *et al.* 2007. An indoor mesocosm system to study the effect of climate change on the late winter and spring succession of Baltic Sea phyto- and zooplankton. *Oecologia*, 150: 655–667.
- Sommer, U., Aberle, N., Lengfellner, K., and Lewandowska, A. M. 2012b. The Baltic Sea spring phytoplankton bloom in a changing climate: an experimental approach. *Marine Biology*, 159: 2479–2490.
- Sommer, U., Adrian, R., de Senerpont Domis, L., Elser, J. J., Gaedke, U., Ibelings, B., Jeppesen, E., *et al.* 2012a. Beyond the Plankton Ecology Group (PEG) model: mechanisms driving plankton succession. *Annual Review of Ecology, Evolution, and Systematics*, 43: 429–448.
- Sommer, U., Gliwicz, Z. M., Lampert, W., and Duncan, A. 1986. The peg-model of seasonal succession of planktonic events in fresh waters. *Archiv für Hydrobiologie*, 106: 433–471.
- Sommer, U., Lengfellner, K., and Lewandowska, A. M. 2011. Experimental induction of a coastal spring bloom early in the year by intermittent high-light episodes. *Marine Ecology Progress Series*, 446: 61–71.
- Stibor, H., Vadstein, O., Diehl, S., Gelzleichter, A., Hantzschke, F., Katschik, A., Lippert, B., *et al.* 2004. Copepods act as a switch between alternative trophic cascades in marine food webs. *Ecology Letters*, 7: 321–328.
- Sverdrup, H. U. 1953. On conditions for the vernal blooming of phytoplankton. *Journal du Conseil International pour l'Exploration de la Mer*, 18: 287–295.
- Taylor, J. R., and Ferrari, R. 2011. Shutdown of turbulent convection as a new criterion for the onset of spring phytoplankton blooms. *Limnology and Oceanography*, 56: 2293–2307.
- Thingstad, T. F., Bellerby, R. G. J., Bratbak, G., Børsheim, K. Y., Egge, J. K., Heldal, M., Larsen, A., *et al.* 2008. Counterintuitive carbon-to-nutrient coupling in an Arctic pelagic ecosystem. *Nature*, 455: 387–390.
- Townsend, D. W., Keller, M. D., Sieracki, M. E., and Ackleson, S. G. 1992. Spring phytoplankton blooms in the absence of vertical water column stratification. *Nature*, 260: 59–62.
- Wroblewski, J. S. 1989. A model of the spring bloom in the North Atlantic and its impact on ocean optics. *Limnology and Oceanography*, 34: 1563–1571.

Handling editor: Rubao Ji



Contribution to the Themed Section: 'Revisiting Sverdrup's Critical Depth Hypothesis' Review Article

Interactive effects of temperature and light during deep convection: a case study on growth and condition of the diatom *Thalassiosira weissflogii*

B. Walter^{1*}, J. Peters¹, J. E. E. van Beusekom^{1,2}, and M. A. St. John³

¹Institute for Hydrobiology and Fisheries Science, University of Hamburg, Hamburg, Germany

²Institute for Coastal Research Helmholtz-Zentrum, Geesthacht, Germany

³National Institute of Aquatic Resources, Technical University of Denmark, Copenhagen, Denmark

*Corresponding author: tel: +49 40 428386648; fax: +49 40 428386618; e-mail: bettina.walter@uni-hamburg.de

Walter, B., Peters, J., van Beusekom, J. E. E., and St. John, M. A. Interactive effects of temperature and light during deep convection: a case study on growth and condition of the diatom *Thalassiosira weissflogii*. – ICES Journal of Marine Science, 72: 2061–2071.

Received 5 June 2014; revised 2 November 2014; accepted 4 November 2014; advance access publication 26 November 2014.

Aim of this study was to expose phytoplankton to growth conditions simulating deep winter convection in the North Atlantic and thereby to assess changes in physiology enabling their survival. Growth rate, biochemical composition, and photosynthetic activity of the diatom *Thalassiosira weissflogii* were determined under two different light scenarios over a temperature range of 5–15°C to simulate conditions experienced by cells during winter deep convection. These metrics were examined under a low light scenario (20 $\mu\text{mol m}^{-2} \text{s}^{-1}$, 12/12 h light/dark), and compared with a scenario of short light pulses of a higher light intensity (120 $\mu\text{mol m}^{-2} \text{s}^{-1}$, 2/22 h light/dark). Both experimental light conditions offered the same daily light dose. No growth was observed at temperatures below 8°C. Above 8°C, growth rates were significantly higher under low light conditions compared with those of short pulsed light exposures, indicating a higher efficiency of light utilization. This could be related to (i) a higher content of Chl *a* per cell in the low light trial and/or (ii) a more efficient transfer of light energy into growth as indicated by constantly low carbohydrate levels. In contrast, pulsed intense light led to an accumulation of carbohydrates, which were catabolized during the longer dark period for maintaining metabolism. Light curves measured via Chl *a* fluorescence indicated low light assimilation for the algae exposed to short pulsed light. We postulate that our trial with short light pulses did not provide sufficient light to reach full light saturation. In general, photosynthesis was more strongly affected by temperature under pulsed light than under low light conditions. Our results indicate that model estimates of primary production in relation to deep convection, which are based on average low light conditions, not considering vertical transportation of algae will lead to an overestimation of *in situ* primary production.

Keywords: deep convection, diatoms, growth rate, light acclimation, temperature.

Introduction

The spring phytoplankton bloom of the northern North Atlantic is one of the largest biological events on earth influencing biogeochemical cycles and the marine foodweb (Platt *et al.*, 2003; Feng *et al.*, 2009). A common model for predicting the onset of a phytoplankton spring bloom is the “critical depth” model of Sverdrup (1953). This model assumes that net primary production is only possible when the mixed layer depth is shallower than a critical mixing depth, where depth-integrated phytoplankton production

equals the loss, for example, by respiration and grazing. Many model and observational studies have supported Sverdrup's hypothesis (Platt *et al.*, 1991; Obata *et al.*, 1996; Falkowski and Raven, 1997). However, new observations (Townsend *et al.*, 1992; Backhaus *et al.*, 2003; Behrenfeld, 2010) and modelling studies (e.g. Huisman *et al.*, 1999; Nagai *et al.*, 2003; Ross *et al.*, 2011; Mahadevan *et al.*, 2012) identify flaws in Sverdrup's critical depth model based on the development of a spring bloom before the onset of stratification.

One of the processes potentially influencing winter light conditions and thus winter production is the occurrence of deep convection (Backhaus *et al.*, 2003). During deep convection, cells can be transported to depths of several hundred metres before potentially being returned to the surface (Marshall and Schott, 1999). Within such a convective cell phytoplankton, cells are exposed to short pulses of light and long periods of darkness (MacIntyre *et al.*, 2000).

Individual-based model results suggest that phytoplankton cells in a convective cell have the potential to frequently visit the euphotic layer with a return rate of 1–2 d (Backhaus *et al.*, 1999, 2003; D'Asaro, 2008). Furthermore, it has been suggested that neglecting vertical mixing in an ecosystem model can lead to an overestimation of primary production due to the effect of turbulence on the photo-adaptive properties (Barkmann and Woods, 1996).

Typically, in the development of light parameterizations for phytoplankton growth models, laboratory and field experiments are carried out to determine growth rates under different light intensities (e.g. Falkowski and Owens, 1980; Cosper, 1982; Sakshaug and Holm-Hansen, 1986) and temperatures (e.g. Berges *et al.*, 2002) or a combination of both factors (e.g. Fawley, 1984; Bouterfas *et al.*, 2002; Hammer *et al.*, 2002). For the development of parameterizations for winter conditions, studies typically focus on acclimatization to low light (e.g. Post *et al.*, 1984; Cullen and Lewis, 1988; Anning *et al.*, 2000) using light exposures of 8 h or more. These experimental set-ups allow algae to acclimatize to low light intensities, for example, by increasing their Chl *a* content. During deep convection, phytoplankton may not have sufficient time to acclimatize to the fluctuating light conditions, for example, by an increase in Chl *a* concentration. Other acclimation processes such as the activation of Rusisco can occur in time-scales from seconds to few minutes (MacIntyre *et al.*, 2000). Experiments with fluctuating light have shown lower phytoplankton growth rates than under continuous irradiance with the same number of photons during light exposure (Nicklisch, 1998; Shatwell *et al.*, 2012). However, these experiments were mainly carried out under daylength of 12 h. Interestingly, cellular resources, i.e. carbohydrate content, is affected by a change in light availability due to mixing. The assumption is that more carbohydrates are necessary for the maintenance of the metabolism during prolonged periods of darkness (Raven and Geider, 1988).

A second factor influencing winter phytoplankton growth is temperature. Spring bloom development in the North Atlantic has been related to the survival of the phytoplankton winter stock, which was effected by winter temperatures (Wiltshire *et al.*, 2008). Temperature within the winter mixed layer is relatively constant on a daily temporal scale, with temperature changing seasonally due to the input of solar energy. Predictions for the North Atlantic suggest an average sea surface temperature increase of 2–4°C by 2100 due to climate change (Houghton *et al.*, 2001).

It is well known that phytoplankton species have an optimum growth temperature (e.g. Li, 1980). Up to this optimum, temperature increases led to higher enzymatic activity and photosynthesis rate as well as nutrient uptake. These increases in vital rates, in turn, lead to higher growth rates (Raven and Geider, 1988; Falkowski and Raven, 1997). Furthermore, temperature increases can also enhance the kinetics of activation and deactivation of the photosynthetic apparatus and thus influence the acclimation potential (Davison, 1991). Conversely, an increase in temperature can have a negative effect on dark survival of some diatom species (Antia, 1976) and may lead to an increased dark respiration (Verity, 1982; Lombard *et al.*, 2009). The result of the interplay between these processes on growth and survival of phytoplankton

cells is unclear with the effect of rising temperatures on the growth rate under short light and long dark periods are present unknown.

Short-term pulsed changes in light availability represent a challenge for estimating marine primary production with ecosystem models, a process which is seldom implemented within these models (Ross *et al.*, 2011; Lindemann *et al.*, 2015). However, Lagrangian-based individual models can simulate the environmental conditions experienced by phytoplankton cells in the mixed layer and thereby examine the potential importance of changes in light intensity and duration (Woods *et al.*, 2005).

With this background, and a clear need to better understand algal physiology under the influence of exposure to short-term light pulses, we conducted laboratory experiments using the marine diatom *Thalassiosira weissflogii* as a model organism. The results of the study we propose have the potential to improve primary production models for the testing of deep convection scenario's in relation to climate change.

Material and methods

Algae cultures

Non-axenic cultures of the diatom *T. weissflogii* (strain CCMP 1336) were obtained from the Provasoli-Guillard National Centre for the Culture of Marine Phytoplankton. Before the experiment, a stock culture of algae was maintained in autoclaved, GF/F filtered and f/2 (Guillard and Ryther, 1962) enriched North Sea water (salinity 32) at a temperature of 15°C. Biolux neon lamps (Osram) were used as a light source providing 160–180 $\mu\text{mol m}^{-2} \text{s}^{-1}$ light over a 12/12 h light/dark cycle. Algae were maintained under these conditions for at least 3 weeks before the commencement of the experiments. The stock cultures were continuously bubbled with filtered air to minimize self-shading and sedimentation as well as to ensure a sufficient supply of CO₂ and O₂. Growth rate was determined during the exponential growth phase.

Experimental set-up

Experiments were carried out under two different light scenarios offering the same daily light dose, exposed in different light/dark cycles and light intensity combinations. The two different light scenarios were:

- (i) a low light trial (labelled as LL for long exposure and low light intensity) offering a light intensity of 20 $\mu\text{mol m}^{-2} \text{s}^{-1}$ over photoperiod of 12/12 h (light/dark) and
- (ii) a short light trial (labelled as SH for short exposure and high light intensity) with a light intensity of 120 $\mu\text{mol m}^{-2} \text{s}^{-1}$ over a photoperiod of 2/22 h (light/dark).

The daily light dose in both trials was 0.86 $\text{mol m}^{-2} \text{d}^{-1}$ [2.16 W m^{-2} converted by the formula of Cloern *et al.* (1995)]. Osram Biolux lamps were used as the light source, with intensity controlled by the distance of the sample from the lamps.

Both trials were run in a thermal gradient table (Thomas *et al.*, 1963) with a temperature gradient between 5.5 and 14.6°C (5.5, 7.8, 10.1, 12.3, and 14.6 \pm 0.2°C for LL) and 5 and 12.5°C (4.9, 6.7, 8.5, 10.3, and 12.5 \pm 0.4°C for SH). Three replicates were performed for each temperature. Algae from the initial stock culture were diluted with autoclaved, GF/C filtered North Sea water enriched with 0.5 ml f/2 stock solution per litre seawater to a final concentration of 6000–10 000 cells ml^{-1} , and put into covered 1 l glass beakers. The cultures were bubbled with filtered air to ensure

a homogeneous cell distribution within the beakers. Samples were brought to experimental temperatures within 24 h.

For each light trial, two identical experiments were carried out. In one experiment, all measurements were made at the end of the photophase, whereas in the second experiment samples were taken at the end of the scotophase. Triplicate samples for cell counts were taken after 2, 4, and 6 d. Cell number samples were always taken after 48 h. Aliquots of 30 ml were taken from each beaker with a similar volume of medium added to maintain the sample at a constant volume. Sample aliquots were fixed with Lugol (final concentration of 1%) and measured within 3 d using a Multisizer 3 (Coulter Counter). Cell number in each sample was determined in triplicate. The specific growth rate was calculated using the equation:

$$\mu = \ln \frac{N_2/N_1}{t_2 - t_1}, \quad (1)$$

where μ is the specific growth rate (d^{-1}) and N_1 and N_2 are cell numbers at time 1 (t_1) and time (t_2), respectively. Chl *a* fluorescence emission for each of the triplicates was measured using pulse amplitude modulation (PAM) fluorometry with a Water PAM (WALZ, Germany). As the two different light scenarios were never tested simultaneously with algae coming from the same stock culture, an additional experiment was carried out allowing a comparison of low and short light effects to validate the previous results and exclude potential temporal effects. This experiment was only carried out at 15°C in a temperature-controlled chamber. In every trial samples for cell number, biochemical analysis and PAM fluorometry were taken from each replicate at the end of the photo- and scotophases after 6 d of exposure to the experimental conditions. Furthermore, an additional (third) SH experiment was performed under comparable conditions. The aim of this experiment was to—by an increase in the number of samples—reduce the range of variability of growth rates, and to extend the temperature range examined to 5.6 and 14.6°C, and to evaluate the direct comparison experiment. These experiments were carried out with algae maintained under the same stock culture conditions as the earlier trials.

For a more detailed view of the potential for short-term acclimation, PAM measurements were carried out during a light/dark cycle of 5 h light and 7 h darkness at a light intensity of 120 $\mu\text{mol m}^{-2} \text{s}^{-1}$ at three different temperatures (5, 10, and 15°C). Algae came from the same stock culture conditions than used for the main experiments and were acclimatized to different exposure temperatures for 24 h in darkness. PAM measurements were carried out in time-steps between 5 min and 1 h over a period of ~12 h.

Biochemistry

Samples for biochemical analyses were obtained either at the end of the photo- or scotophase on the last day of the experiment (Day 6). Duplicate samples of 70 ml volume were filtered onto pre-combusted Whatman GF/C filters and frozen at -20°C for Chl *a* or -80°C for carbohydrate analyses. Chl *a* was extracted in 90% acetone and analysed photometrically after Jeffrey and Humphrey (1975).

Total carbohydrates were determined after Dubois *et al.* (1956) and Herbert *et al.* (1971) Furan derivatives were formed by adding 96% sulphuric acid to the sample and pentoses were converted to α -furfurylaldehyde, while hexoses are transformed to 5-(hydroxymethyl)-furfural. These aldehydes react with phenol to

produce characteristically coloured products. Measurements of carbohydrates were expressed as glucose equivalents. A D-(+)-glucose monohydrate solution was used as a primary standard and samples were measured photometrically at 490 nm.

Chl *a* fluorometry

Chl *a* fluorescence was measured with a Water PAM (WALZ, Germany). A light saturation pulse was applied with $>10\,000 \mu\text{mol photons m}^{-2} \text{s}^{-1}$ for 0.8 s. Algae were dark adapted for 5 min before estimating rapid light curves (RLCs) and the maximum quantum yield of the photosystem II (PSII) (Genty *et al.*, 1989) was determined:

$$\frac{F_v}{F_m} = \frac{F_m - F_o}{F_m}, \quad (2)$$

where F_v is the difference of the maximum fluorescence (F_m) measured after a saturating light pulse and the minimum fluorescence (F_o) emitted as a result of the measuring light only. F_v/F_m requires dark adaptation. Whereas, the effective quantum yield of PSII: $\Phi_{\text{PSII}} = \Delta F/F'_m = (F'_m - F)/F'_m$ requires light adaptation.

Immediately after F_v/F_m , a RLC was measured as described in Cosgrove and Borowitzka (2006). Each treatment involved nine consecutive, 30 s intervals of actinic light pulses of increasing intensity with an accompanying yield measurement at the end of each actinic interval. Blue light emitting diodes provided the actinic light at levels of 0, 86, 124, 190, 281, 399, 556, 922, and 1381 $\mu\text{mol photons m}^{-2} \text{s}^{-1}$ of photosynthetically active radiation (PAR) and the electron transport rate (ETR) was calculated as:

$$\text{ETR} = \Phi_{\text{PSII}} \times \text{PAR}. \quad (3)$$

Empirical data for the establishment of photosynthesis (P) at every measured light intensity were fitted to the function of Platt *et al.* (1980) including photoinhibition and using a Marquardt–Levenberg regression algorithm:

$$P = P_s(1 - e^{-(\alpha \text{Ed}/P_s)} \times e^{-(\beta \text{Ed}/P_s)}), \quad (4)$$

where P_s is a scaling factor defined as the maximum potential rETR, α is the initial slope of the RLC, Ed is the downwelling irradiance (400–700 nm), and β characterizes photoinhibition.

The two main parameters of the RLC were determined using (i) the maximum relative electron transport rate (rETR_{max}) and (ii) the minimum saturating irradiance (E_k). rETR_{max} is the asymptote of the curve and gives evidence of the ability of the photosystems to utilize the absorbed light energy (Marshall *et al.*, 2000). E_k is determined by the intercept α with the maximum photosynthetic rate (Sakshaug *et al.*, 1997). These parameters were estimated following the equation (Ralph and Gademann, 2005):

$$\text{rETR}_{\text{max}} = P_s \left(\frac{\alpha}{\alpha + \beta} \right) \left(\frac{\beta}{\alpha + \beta} \right)^{\beta/\alpha}, \quad (5)$$

$$E_k = \text{rETR}_{\text{max}}/\alpha. \quad (6)$$

Data analysis and statistics

Growth rate was determined in triplicate, and Chl *a* and carbohydrates in duplicate measurements for every independent sample.

Mean values were determined and used for plotting and statistical analysis. PAM data were determined only once for each replicate. Data of all parameters were combined into temperature ranges (5°C range: 4.9–5.6°C; 8°C range: 6.7–8.8°C; 10°C range: 10.1–10.6°C, 12°C range: 12.1–12.5°C, and 15°C range: 14.5–14.7°C) and used for statistical analysis.

The growth rates from the two experiments (end the photo- and scotophases) of each tested light condition were combined ($n = 6$). Chl *a*, carbohydrates, and PAM data were treated separately for each experimental trial ($n = 3$). Significance differences between the two different light conditions (LL and SH) and each determination time (end the photo- and scotophases) were tested for the defined temperature ranges using a one-way ANOVA. The effect of temperature was tested using Spearman correlations. Data were assumed to be significantly different at $p < 0.05$. Statistical analyses were carried out using the SPSS 15.0 software.

To describe the correlation between growth rate and temperature, data were fitted to linear regression equation $f = y_0 + a \times x$, where y_0 is the intercept and a is the slope of the curve, using Sigma Plot 11. The slopes of the curves were compared using a *t*-test.

A potential temperature impact on the saturation curves of $rETR_{max}$ during the light period of the experiment exposing a higher temporal resolution was determined using non-linear regression. Logistic models (for each temperature and for all temperatures combined) were compared using a second-order Akaike's information criterion (AIC, corrected for small sampling sizes).

Results

Growth

Two concurrent experiments were carried out to investigate the impact of different light regimes (LL: long light exposure of low light intensity and SH: short light exposure of higher light intensity) on the growth of *T. weissflogii* at different temperatures (Figure 1). At temperatures below 8°C, growth rates were not different from zero

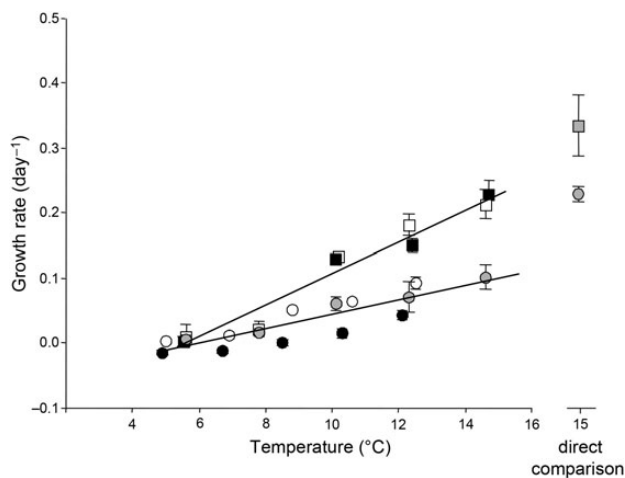


Figure 1. Averaged growth rate of *T. weissflogii* under different temperatures and light scenarios: 12/12 h light/dark cycles with $20 \mu\text{mol m}^{-2} \text{s}^{-1}$ (squares) and 2/22 h light/dark with $120 \mu\text{mol m}^{-2} \text{s}^{-1}$ (circles). White: measured at the end of the light phase; black: end of the dark phase (first experiment). Grey: second experiment end of the light phase. Mean values with error bars of standard deviation ($n = 3$). Lines describe the linear model fitting the data.

under both light conditions. Above this temperature, growth rates increased with increasing temperature under both light conditions (Figure 1).

The temperature growth relation was described by a linear model. For SH, the linear model had the best fit ($r^2 = 0.7524$). The LL treatment had a better fit for the linear model ($r^2 = 0.9317$); however, a three-parameter sigmoid curve had a best fit ($r^2 = 0.9438$). Due to Montagnes *et al.* (2003), we choose the linear fitting for both trials. The slopes of the two regressions are significantly different ($p < 0.001$), where the slope of the LL is higher than that of the SH trial. These results were confirmed by the statistical tests on the different temperature ranges (5°C: 4.9–5.6°C; 8°C: 6.7–8.8°C; 10°C: 10.1–10.6°C, 12°C: 12.1–12.5°C, and 15°C: 14.5–14.7°C). At all tested temperatures above 8°C growth rate was significantly higher under LL than under SH conditions ($p < 0.02$).

The highest measured growth rates of 0.23 ± 0.02 (LL) and 0.10 ± 0.02 (SH) were determined at the highest tested temperature (14.5°C). Growth rates were determined after 48 h for each experiment. The measured growth rate do not give any information about the time of the day when growth occurred.

For logistic reasons, all experiment had to be carried out consecutively. To exclude any stock cultural effects on the growth rates, the effect of the different light conditions was directly compared in one follow up experiment at 15°C. The results (shown separately in Figure 1) confirmed that growth rate was significantly higher ($p < 0.0001$) under the LL than under SH conditions.

Biochemical components

Chl *a* start values from the algae stock cultures used for the different trials varied between 4.5 and 5.4 pg cell^{-1} (shaded area in Figure 2a). During the LL trial, the Chl *a* content per cell increased during the experimental time of 6 d and was always higher than the initial value. The Chl *a* content per cell during the SH trial remained in the range of the initial values independent of temperature. At every temperature ranges, the Chl *a* content under LL conditions was significantly higher than under the comparable SH conditions, for both determination times end of the photo- and scotophases, with one exception (10°C; after the scotophase). In the two light trials, the Chl *a* content, measured at the end of the photo- or scotophases, was only significantly different at two temperatures under LL conditions (10 and 12°C).

Temperature had a significant effect on the Chl *a* content at the end of the photophase of the SH trial. The lowest Chl *a* content was found at the lowest temperature. The experiment directly comparing the light treatments at 15° substantiated that the Chl *a* content per cell was significantly higher after the LL than SH conditions.

The carbohydrate contents per cell under SH conditions measured at the end of the photophase were always higher than at the end of the scotophase (maximum $0.94 \text{ pg cell}^{-1}$ at 6.7°C at the end of the photophase; minimum 0.33 ± 0.06 at 5°C at the end of the scotophase; Figure 2b). During the LL trial, the values were constantly low (about 0.5 pg cell^{-1}) with no significant effect of sampling time (end of the photo- or scotophase) with one exception at 10°C. These results were substantiated by the direct comparison experiment, where the carbohydrate content was also significantly higher under SH conditions. Temperature had a significant effect on the carbohydrate content at all tested treatments beside the once measured at the end of the photophase of the SH trial.

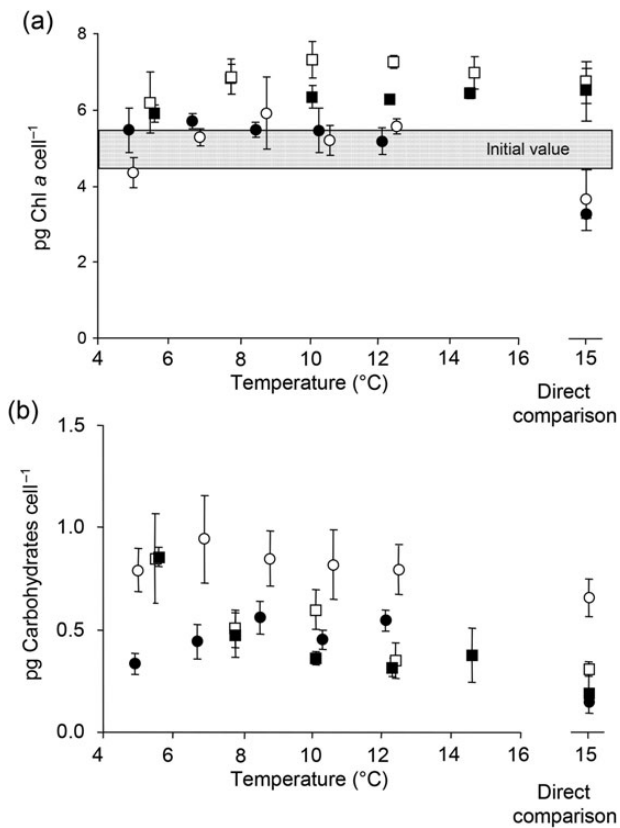


Figure 2. Cell components (pg cell^{-1}) under different temperatures and light scenarios: Chl *a* (a) and carbohydrate (b). Squares: 12/12 h light/dark cycles with $20 \mu\text{mol m}^{-2} \text{s}^{-1}$ and circles: 2/22 h light/dark with $120 \mu\text{mol m}^{-2} \text{s}^{-1}$. White: measured at the end of the light phase; black: end of the dark phase. Mean values with error bars of standard deviation ($n = 3$).

Chlorophyll *a* fluorometry

The following metrics of phytoplankton photosynthetic status were determined via Chl *a* fluorescence: the maximal quantum yield (F_v/F_m , Figure 3a) and two different parameters inferred from RLCs: $r\text{ETR}_{\text{max}}$ and E_k (Figure 3b and c). The algae stock cultures in 2011 did not differ significantly in their PAM parameters (F_v/F_m : 0.63 ± 0.02 relative values, $r\text{ETR}_{\text{max}}$: 58.2 ± 4.4 relative values, and E_k : $107 \pm 12 \mu\text{mol m}^{-2} \text{s}^{-1}$).

Parameters of the RLC from the direct comparison experiment performed in 2012 were significantly different from start values ($p < 0.05$) and can therefore not be compared directly with the measurements of 2011.

During the LL trial, F_v/F_m values increased up to the highest observed value of 0.73 ± 0.01 at 14.7°C (Figure 3a), whereas during the SH experiment F_v/F_m never increased above the initial value. All values measured during the LL were higher than during the SH trial. But only at temperatures below 12°C , the differences were significant ($p < 0.005$).

Temperature had a significant effect on F_v/F_m during the SH trial ($p < 0.03$). The value decreased with decreasing temperature especially at the end of the 22 h dark period. During this trial, we also determined the lowest value of 0.35 ± 0.03 at 5°C . During the LL trial, temperature only affected F_v/F_m measured at the end of the photophase ($p < 0.001$). Differences between the F_v/F_m measured

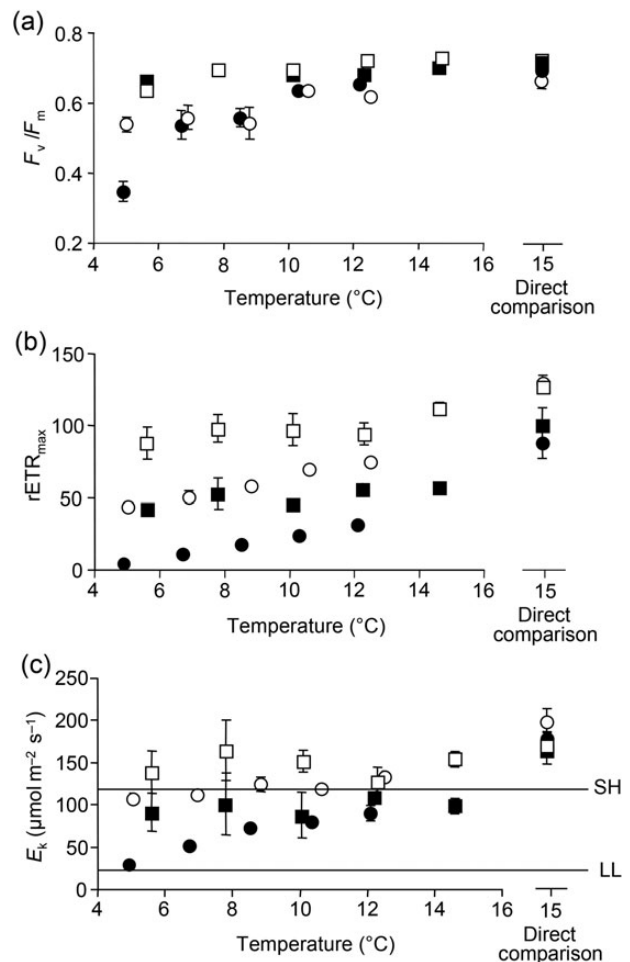


Figure 3. Effect of temperature and light availability on PAM data. Squares: 12/12 h light/dark cycles; $20 \mu\text{mol m}^{-2} \text{s}^{-1}$ and circles: 2/22 h light/dark; $120 \mu\text{mol m}^{-2} \text{s}^{-1}$. F_v/F_m (a), $r\text{ETR}_{\text{max}}$ (b), and E_k (c) at experimental Day 6. White: measured at the end of the light phase; black: end of the dark phase. Mean values with error bars of standard deviation ($n = 3$). Lines (c) mark the experimental light intensity ($\mu\text{mol m}^{-2} \text{s}^{-1}$).

at the end of the photo- or the scotophase were only evident for the SH trial at 5°C .

$r\text{ETR}_{\text{max}}$ ranged between a maximum of 94.5 ± 7.8 at 14.7°C at the end of the photophase under LL conditions and 4.6 ± 0.8 at 5°C at the end of the scotophase under SH conditions (Figure 3b). RLCs were more strongly influenced by the different light conditions than F_v/F_m . $r\text{ETR}_{\text{max}}$ decreased during the scotophase. Under both light conditions, at every tested temperature, $r\text{ETR}_{\text{max}}$ was significantly higher at the end of the photo- than scotophase (LL: $p < 0.01$; SH: $p < 0.0001$). Furthermore, all $r\text{ETR}_{\text{max}}$ values measured under LL conditions were significantly higher than the corresponding SH data (end of photo- $p < 0.02$ and scotophase $p < 0.0001$). Temperature had a significant effect on $r\text{ETR}_{\text{max}}$ during SH ($p < 0.02$), but not during LL, conditions. Delta $r\text{ETR}_{\text{max}}$ at the end of the photo- and scotophases (of ~ 40) was similar for both light scenarios.

$r\text{ETR}_{\text{max}}$ values of the two light scenarios of the “direct comparison” experiment were not significantly different. However, the value at the end of the photo- and scotophases for each scenario was significantly different.

E_k is $rETR_{max}/\alpha$, where data of α are not shown. Comparable to the results of $rETR_{max}$ and E_k α was higher under LL than under SH conditions, whereas during the LL trial delta at the end of the photo- and scotophases was less extended than during the SH trial. Treatment behaviour of α was comparable to the one of E_k . Owing to the higher physiological relevance of E_k , we decided to only show these values.

E_k values were always higher at the end of the photo- than at the end of the scotophase. This effect was always significant for the results of the SH trial ($p < 0.008$), but only significant at 10°C ($p = 0.003$) and 15°C ($p = 0.002$) during the LL trial. Temperature only had a significant effect on the E_k values at the end of the scotophase of the SH trail.

The values described relative to the experimental light intensity give important physiological information (experimental light intensities are marked as lines in Figure 3c). Under LL conditions, E_k was always higher than the experimental light condition of $20 \mu\text{mol m}^{-2} \text{s}^{-2}$, with the lowest measured value of $87 \pm 27 \mu\text{mol m}^{-2} \text{s}^{-1}$ at the end of the scotophase. In contrast, at the end of the long dark period of the SH trial, E_k was always lower than the experimental light intensity of $120 \mu\text{mol m}^{-2} \text{s}^{-1}$ (between 29.8 ± 5.1 and $90.1 \pm 8.8 \mu\text{mol m}^{-2} \text{s}^{-1}$).

The temporal evolution of $rETR_{max}$ measured during a light/dark cycle of 5 h light and 7 h darkness (Figure 4) was investigated for three temperatures. All results show a continuous increase of $rETR_{max}$ from the beginning of the light phase. The increase was stronger at higher temperatures. After 5 h of irradiance with a light intensity of $120 \mu\text{mol m}^{-2} \text{s}^{-1}$, saturation was not reached as indicated by the E_k values (results not shown). During the subsequent dark period, $rETR_{max}$ decreased and stabilized after about 4 h. Temperature had a significant positive effect on $rETR_{max}$ levels based on the lower corrected AIC ($\Delta AIC_{corr} = 34$) for the model including a temperature impact. The slopes of the decrease during darkness were low comparable to the increase in light and not significantly different. After an initial decrease during the first 10 h, the values remained more or less constant for the following 20 h (data not shown).

Methodological issues

Due to logistics and equipment availability, each experiment had to be carried out separately. To separate between treatment effects and a potential bias of different start cultures, two additional

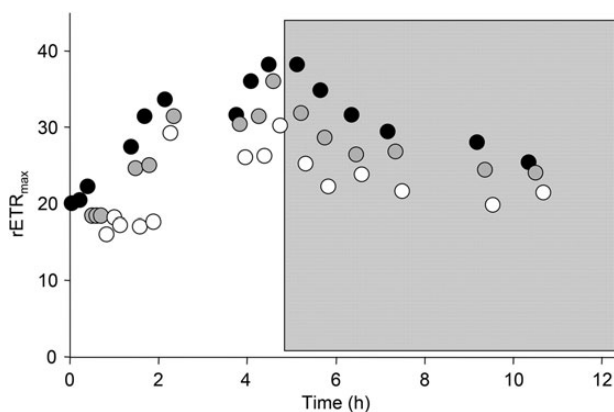


Figure 4. $rETR_{max}$ over time in light and darkness (grey box) at three different temperature (white: 5°C; grey: 10°C, and black: 15°C).

experiments were carried out. The complete SH experiment was repeated at this time (with sampling only for growth rate at the end of the photophase) plus an experiment to test the direct effect of the two light treatments at one temperature. To account for potential set-up effects, data from the “direct comparison” experiment are always presented separately and were not used for curve fitting of the temperature growth curve. These validation experiments show that observed differences in growth rate and biological composition were caused by light treatment and not by differences in start conditions. Chl *a* fluorescence measurements on the other hand deviated from the pattern observed in the previous experiments. Start values of the RLC parameters were higher in later experiment and light conditions affected fluorescence parameters less than in former.

Chl *a* fluorescence is generally a good tool for showing photophysiological differences. Furthermore, many studies have shown a high correlation with primary production (Morris and Kromkamp, 2003, Goto *et al.*, 2008), although this approach cannot be used as a direct measure for primary production.

Discussion

Winter deep convection plays an important role in the seasonal dynamics of phytoplankton by maintaining a viable community in the water column and thereby sustaining the spring seed population while its retreat the pre-spring bloom particle fluxes seen in sediment traps (e.g. Honjo *et al.*, 1988, D’Asaro, 2008). In our study, we examined the effect of different light scenarios presumed to be experienced by phytoplankton cells during deep winter convection on phytoplankton growth and physiology. The basis for our experimental design comes from a model study of Lindeman *et al.* (2015) who simulated an average exposure time of 2.1 h for cells experiencing deep convection in early spring in the North Atlantic with a mixed layer depth of 500 m. The light conditions we tested included a classical low light scenario (12/12 h light/dark cycle of $20 \mu\text{mol m}^{-2} \text{s}^{-1}$) assuming the retention of cells in a subsurface chlorophyll *a* maximum layer and a scenario with short intervals of higher light intensity (2/22 h light/dark of $120 \mu\text{mol m}^{-2} \text{s}^{-1}$) simulating a simplified deep convection situation. Both scenarios offered the same daily light dose of $0.86 \text{ mol m}^{-2} \text{ d}^{-1}$.

The temperature range of 5–15°C was chosen around the observed winter temperature of 9.4°C in the North Atlantic.

Growth rates

In this study, above a critical temperature of 8°C, growth rates of *T. weissflogii* increased with increasing temperature under all experimental conditions. However, in the long exposure, low light trial (LL) growth rates were always higher than those observed during the short exposure high light trial (SH). Notably, all experimental conditions above 8°C elicited a positive growth response in our experimental algae. The growth response was best fitted using a linear model comparable to Eppley (1972) and Montagnes *et al.* (2003). Although a sigmoid model would describe the biological processes including a temperature limitation below 8°C and an anticipated maximal growth rate at a certain temperature. The maximum growth rates obtained in our study ($< 0.23 \text{ d}^{-1}$) were below those observed by Montagnes and Franklin (2001) for *T. weissflogii* who observed growth rates of $0.5\text{--}0.6 \text{ d}^{-1}$, when exposed at $50 \mu\text{mol m}^{-2} \text{ s}^{-1}$ over a day/night cycle of 14/10 h at a temperature range of 12–20°C. Our temperature growth behaviour does not show a clear temperature optimum under either light condition.

Hence, an optimal growth temperature under our experimental conditions cannot be determined.

Furthermore, based on our two levels of light exposure, we found a clear effect of exposure duration on growth rates especially at higher temperatures. Thompson (1999) also tested the effect of different daily light doses and temperature on *Thalassiosira pseudonana*. He found in contrast to our findings no temperature effect on the initial slope of a daily light dose–growth relationship. In addition, he found that daily light doses below $1 \text{ mol m}^{-2} \text{ d}^{-1}$ day-length did not affect growth, when testing light cycles within a range of continuous light and the shortest light period of 4 h. Despite the daily light dose in our experiment being lower than Thompson (1999) ($0.86 \text{ mol m}^{-2} \text{ d}^{-1}$), we did find an effect of exposure time. We suggest that a shorter light period of 2 h does not allow the cell to use the available light.

Similar to our findings, Verity (1982) showed an effect of day-length on growth only at higher temperatures. The shortest day-length examined during this study was 9/15 h light/dark. To our knowledge, our study represents the only examination of the effects of light exposure at a period of 2 h light. 3/21 h light/dark cycle has been the shortest light period tested to date (Foy, 1983; Bouterfas *et al.*, 2006).

Acclimatization

The algae in our experiment were not acclimated to the experimental light or temperature conditions. Rather, the study was designed to examine the ability of a cell to function during transition from a fall stratified situation to a regime of deep convection. Allowing the cells time to acclimatize due to prolonged exposure to specific light and temperature conditions will select for different genotypes and allowing the cell to optimize its internal environment (e.g. Chlorophyll *a* content) and as a result will lead to different physiological responses. This change can be considered to be an adaptation, a change which occurs over generations when compared with acclimation, which is the response of the individual. Hence, our focus was on the cells short-term ability to acclimatize due to changes in Chl *a* metabolism (periods of 10^4 – 10^3 s) and Rubisco activity (MacIntyre *et al.*, 2000).

The potential for phytoplankton species to adapt to changing environmental temperatures is still not well understood. For example, a correlation between changing environmental temperature and optimal growth temperature was found (Boyd *et al.*, 2013), whereas conversely no clear relationship has been observed between (Thomas *et al.*, 2012). To address the issue of adaptation, a longer term study would be required examining changes in response over generations. This is beyond the scope of this study, but represents a key issue for understanding the evolution of the phytoplankton community as influenced by climate change.

Biochemical compounds

Light availability has a clear effect on phytoplankton biochemistry. For example, lower light intensities induce an increase in Chl *a* content to optimize light harvesting capacity (Post *et al.*, 1984; Cullen and Lewis, 1988; Anning *et al.*, 2000; Wagner *et al.*, 2006; Dimier *et al.*, 2009; Milligan *et al.*, 2012). Our findings support this as an increased Chl *a* content was observed under the LL, but not under SH, conditions. In contrast to other studies (Post *et al.*, 1984; Fábregas *et al.*, 2002), we did not observe diel changes in the Chl *a* content. Chl *a* content during the SH scenario was comparable to the initial value independent of temperature. Hence, light limitation due to a short period light dose did not cause an increase in the

Chl *a* content. Changes in the Chl *a* content have been observed under fluctuating light experiments. Most likely, the duration of low light intensities was more important than the period of high light intensities (e.g. Fietz and Nicklisch, 2002; van Leeuwe *et al.*, 2005; Dimier *et al.*, 2009). During these experiments, the increased Chl *a* content did not affect growth rate (Fietz and Nicklisch, 2002; Dimier *et al.*, 2009). In contrast, our findings showed higher growth rates at higher Chl *a* concentrations.

Carbohydrates are the main energy reserve in marine algae and can be accumulated under high light irradiances (Granum *et al.*, 2002). Temperature has a twofold influence on carbohydrate dynamics influencing anabolism during periods of light (Varum *et al.*, 1986) and catabolism during dark respiration (Raven and Geider, 1988; Falkowski and Raven, 1997). In our study, *T. weissflogii* accumulated high amounts of carbohydrates during the short light intervals in the SH trial. Interestingly, given the low growth rates observed, this surplus energy was not transformed into growth, but consumed during dark respiration. The constant carbohydrate content during the LL experiment over the day/night cycle may reflect more balanced conditions supporting higher growth rates. Halsey *et al.* (2011, 2013) observed higher polysaccharide accumulation at higher growth rates. In these studies, nutrients were the growth limiting factor. Growth rates during our experiment were generally low and light limited. The high carbohydrate accumulation we observed during the light phase of the SH trial did not result into higher growth rates, but could enable a longer period of survival during dark periods as survival during darkness depends on the reserve carbon availability (Furusato and Asaeda, 2009; Talmy *et al.*, 2014).

Metrics of photobiology

PAM metrics such as the maximal quantum yield (F_v/F_m), photosynthetic capacity (relative maximum ETR; $rETR_{max}$), and minimum saturation irradiance (E_k) are often used as indicators of the fitness or to describe photoacclimation of algae (Cullen and Davis, 2003; Franklin *et al.*, 2009; McMinn *et al.*, 2010).

In our study, the F_v/F_m was generally high especially under LL conditions, indicating a good physiological state of the algae. Only long dark periods in combination with low temperatures negatively affected F_v/F_m . Low temperatures also had a negative effect on $rETR_{max}$ under SH conditions. In contrast, these parameters in the LL trial were not affected by temperature. A decrease in temperatures reduces light saturation because the light reaction of photosynthesis is temperature independent in contrast to the dark reaction (Davison, 1991). A lower light saturation level most likely leads to an earlier appearance of photodamage (Falkowski and La Roche, 1991; Demmig-Adams and Adams, 1992). The lower light intensities during the LL trial did not seem to induce damage at any of the tested temperatures.

In contrast to our study, several previous studies have identified lower $rETR_{max}$ and E_k values for algae exposed to lower light intensity (e.g. Ralph and Gademann, 2005). In our study, algae exposed to higher light intensity (SH) showed a typical low light response with lower $rETR_{max}$ and E_k values. Values decreased during the long dark periods and the short pulsed light exposures were not sufficient to induce an increase of the photosynthetic capacity. E_k results from $rETR_{max}$ and the slope of the RLC α (data not shown). In our case, temperature and light dependence of α was more strongly related to E_k than $rETR_{max}$.

The minimum saturation irradiance (E_k) is the most representative parameter to explain photosynthetic efficiency and potential

damage. This index, in combination with the ambient light intensity, gives important information about light utilization potential (Behrenfeld *et al.*, 2004). During the long dark phase of the SH scenario, E_k decreased below the experimental light intensity of $120 \mu\text{mol m}^{-2} \text{s}^{-1}$. Thus, especially at the beginning of the light period, photons could not be completely used for photosynthesis. Excess energy during this period could lead to photodamage thus necessitating the activation of cell apparatus for repair and thereby reducing growth efficiency, causing the decreased values of F_v/F_m and rETR_{max} , especially at low temperatures.

At the end of the short light period, the minimum saturation irradiance was comparable to the experimental light intensity, which suggests high photosynthetic capacity but at a level which could still induce more damage than lower intensities (Aro *et al.*, 1993). In contrast, under LL conditions, E_k was always higher than the experimental light intensity. Hence, the available light could immediately be used completely for photosynthesis and most likely caused less damage.

Photoacclimation is a time-dependent process. Moore *et al.* (2006) found a strong correlation between E_k and the ambient light conditions in stratified waters, in contrast to deep mixed water, potentially because mixing rate was faster than acclimation time. During this study, algae showed comparable values to surface populations with a high light acclimation. In our study, algae exposed to conditions that simulated deep mixed conditions are low light acclimated. Both observations might be a result of insufficient acclimation time.

In our study, characterization of the time dependence of photoacclimation was performed by following the temporal evolution of rETR_{max} during the changes between light and darkness at three different temperatures. rETR_{max} followed a light and dark rhythm has been described for benthic diatoms in field (Seródio *et al.*, 2005). For *T. weissflogii* in our study, rETR_{max} increased continuously during the first 5 h of the photophase. No saturation could be observed within the tested light period. During darkness, the decrease of rETR_{max} stabilized after about 4 h. Hence, the decrease of rETR_{max} was similar during both light scenarios. This supports our finding that 2 h light are just not sufficient to reach full photosynthetic capacity. In contrast, Nymark *et al.* (2013) found after 48 h of darkness that the diatom *Phaeodactylum tricornutum* found that of rETR_{max} recovered to a value even higher than the start value during the first 30 min, with no further increase during the following 24 h of light. Thus, we postulate that recovery of the rETR_{max} after dark incubation may be species-specific.

Implications

The goal of this study was to assess the potential for individual phytoplankton cells to remain viable in the deep convective circulations occurring during winter in the North Atlantic. Our results clearly identify that cells can maintain positive, albeit low growth rates in conditions simulating those they would experience. Our study showed a 50% higher growth rate under constant low light than under pulsed light simulating conditions. The analyses of carbohydrate content and Chl *a* fluorescence indicate that cells experiencing periods of short pulses of light can use those light windows for growth if temperature is not limiting even if growth rates are very low. Furthermore, accumulated carbohydrates could allow the cells to survive for longer periods due to these reserves. These findings are particularly important for understanding the role of deep convection in maintaining an integrated phytoplankton biomass of the same magnitude as it was found in the spring bloom

(Li, 1980; Backhaus *et al.*, 2003) as well as providing the seed population for the spring bloom in the North Atlantic.

In conclusion, our experiment showed that a calculation of primary production with growth rates coming from laboratory experiments with constant low light intensities, as often assumed in ecosystem models, could lead to an overestimation of primary production in well-mixed water bodies. Earlier studies have focused on the difference between constant and fluctuating light (Marra 1978; Barkmann and Woods, 1996; Anning *et al.*, 2000; Ross *et al.*, 2011). These results have been inconclusive with an underestimation of primary production of 87% (Marra, 1978) to an overestimation of 40% (Barkmann and Woods, 1996) when comparing fluctuating and fixed light incubations. The latter model calculation did not take into account that particles within the whole mixed layer have the same ability to short ephemeral visits in the euphotic zone to use the short available light windows for growth as shown by Lindemann *et al.* (2015).

Rapidly changing light exposures are a challenge for autotrophic organisms. Many studies focus on the photoprotection mechanism activated due to quickly rising light intensities (Dimier *et al.*, 2009; Alderkamp *et al.*, 2011). However, a rapid rise in light saturation after long dark periods, as occurring during deep convection, is rarely explored. Studies focusing on photoacclimation under unsaturated conditions, including this study, have illustrated that low light intensity primarily triggers processes such as Chl *a* anabolism, changes in enzyme activity, or light harvesting complexes to increase growth. Algae exposed to short light intervals have a limited potential to raise their capacity to use the incoming light, and have higher losses due to dark respiration thus leading to lower growth rates. Our experiments have for the first time demonstrated positive growth under short temporal periods of only 2 h light per day in the laboratory. This scenario was taken from model calculations by Lindemann *et al.* (2015) and illustrates that, if temperature limitation does not occur, in contrast to Sverdrup's assumption primary production in the convective mixed layer of the North Atlantic is possible during winter, even if the mixed layer depth is much deeper than the critical depth (Backhaus *et al.*, 2003; Behrenfeld, 2010). Furthermore, our findings bring into question the use of daily light doses for phytoplankton growth or critical light boundaries. In a next step, our findings should be implemented into an IBM thereby allowing for phytoplankton growth even under unfavourable winter conditions. We suggest that future laboratory studies should focus on more fluctuating light conditions including photoinhibition under short light term light exposure. Finally, to understand the future evolution of the North Atlantic phytoplankton community and their contributions to biogeochemical and ecosystem services, understanding future changes winter deep convection and the response of the phytoplankton community is critical.

Acknowledgements

We thank Antje Gimple and Martina Wichmann for support in the laboratory and André Eckhardt for technical support. Support for the first author was provided by the Cluster of Excellence "CliSAP", University of Hamburg, funded through the German Science Foundation (DFG). Support for MSJ was provided by EC seventh Framework programme; EURO-BASIN Integrated Project on Basin-Scale Analysis, Synthesis, and Integration is funded by Framework Programme 7 (contract 264933). A further thanks goes to the two anonymous reviewers for their helpful comments.

References

- Alderkamp, A., Garçon, V., de Baar, H. J. W., and Arrigo, K. R. 2011. Short-term photoacclimation effects on photoinhibition of phytoplankton in the Dark Passage (Southern Ocean). *Deep Sea Research I*, 58: 943–955.
- Anning, T., MacIntyre, H. L., Pratt, S. M., Sammes, P. J., Gibb, S., and Geider, R. J. 2000. Photoacclimation in the marine diatom *Skeletonema costatum*. *Limnology and Oceanography*, 45: 1807–1817.
- Antia, N. J. 1976. Effects of temperature on the dark survival of marine macro-planktonic algae. *Microbial Ecology*, 3: 41–54.
- Aro, E.-M., Virgin, I., and Andersson, B. 1993. Photoinhibition of photosystem II. Inactivation, protein damage and turnover. *Biochimica et Biophysica Acta (BBA) - Bioenergetics*, 1143: 113–134.
- Backhaus, J. O., Hegseth, E. N., Wehde, H., and Kaempf, J. 2003. Convection and primary production in winter. *Marine Ecology Progress Series*, 251: 1–14.
- Backhaus, J. O., Henning, W., Hegseth, E. N., and Kämpf, J. 1999. “Phyto-convection”: the role of oceanic convection in primary production. *Marine Ecology Progress Series*, 189: 77–92.
- Barkmann, W., and Woods, J. D. 1996. On using a Lagrangian model to calibrate primary production determined from in vitro incubation measurements. *Journal of Plankton Research*, 18: 767–788.
- Behrenfeld, M. J. 2010. Abandoning Sverdrup’s critical depth hypothesis on phytoplankton blooms. *Ecology*, 91: 977–989.
- Behrenfeld, M. J., Prasil, O., Babin, M., and Bruyant, F. 2004. In search of a physiological basis for covariations in light-limited and light-saturation photosynthesis. *Journal of Phycology*, 40: 4–25.
- Berges, J. A., Varela, D. E., and Harrison, P. J. 2002. Effects of temperature on growth rate, cell composition and nitrogen metabolism in the marine diatom *Thalassiosira pseudonana* (Bacillariophyceae). *Marine Ecology Progress Series*, 225: 139–146.
- Bouterfas, R., Belkoura, M., and Dauta, A. 2002. Light and temperature effects on the growth rate of three freshwater algae isolated from a eutrophic lake. *Hydrobiologia*, 489: 207–217.
- Bouterfas, R., Belkoura, M., and Dauta, A. 2006. The effects of irradiance and photoperiod on the growth rate of three freshwater green algae isolated from a euphotic lake. *Limnologia*, 25(3): 647–656.
- Boyd, P. W., Rynearson, T. A., Armstrong, E. A., Fu, F., Hayashi, K., Hu, Z., and Hutchins, D. A. 2013. Marine phytoplankton temperature versus growth responses from polar to tropical waters—outcome of a Scientific Community-Wide Study. *PLoS ONE*. doi:10.1371/journal.pone.0063091
- Cloern, J. E., Grenz, C., and Videgar-Lucas, L. 1995. An empirical model of the phytoplankton chlorophyll: carbon ratio—the conversion factor between productivity and growth rate. *Limnology and Oceanography*, 40: 1313–1321.
- Cosgrove, J., and Borowitzka, M. 2006. Applying pulse amplitude modulation (PAM) fluorometry to microalgae suspensions: stirring potentially impacts fluorescence. *Photosynthesis Research*, 88: 343–350.
- Cosper, E. 1982. Effects of variations in light intensity on the efficiency of growth of *Skeletonema costatum* (Bacillariophyceae) in a cyclostate. *Journal of Phycology*, 18: 360–368.
- Cullen, J. J., and Davis, R. F. 2003. The blank can make a big difference in oceanographic measurements. *Limnology and Oceanography Bulletin*, 12: 29–56.
- Cullen, J. J., and Lewis, M. R. 1988. The kinetics of algal photoadaptation in the context of vertical mixing. *Journal of Plankton Research*, 10: 1039–1063.
- D’Asaro, E. A. 2008. Convection and the seeding of the North Atlantic bloom. *Journal of Marine Systems*, 69: 233–237.
- Davison, I. R. 1991. Environmental effects on algal photosynthesis: temperature. *Journal of Phycology*, 27: 2–8.
- Demmig-Adams, B., and Adams, W. W., III. 1992. Photoprotection and other responses of plants to high light stress. *Annual Review of Plant Physiology and Plant Molecular Biology*, 43: 599–626.
- Dimier, C., Brunet, C., Geider, R. J., and Raven, J. 2009. Growth and photoregulation dynamics of the picoeukaryote *Pelagomonas calceolata* in fluctuating light. *Limnology and Oceanography*, 54: 823–836.
- Dubois, M., Gilles, K. A., Hamilton, J. K., Rebers, P., and Smith, F. 1956. Colorimetric method for determination of sugars and related substances. *Analytical Chemistry*, 28: 350–356.
- Eppley, R. 1972. Temperature and phytoplankton growth in the sea. *Fish Bull*, 70: 1063–1085.
- Fábregas, J., Maseda, A., Domínguez, A., Ferreira, M., and Otero, A. 2002. Changes in the cell composition of the marine microalga, *Nannochloropsis gaditana*, during a light:dark cycle. *Biotechnology Letters*, 24: 1699–1703.
- Falkowski, P. G., and La Roche, J. 1991. Acclimation to spectral irradiance in algae. *Journal of Phycology*, 27: 8–14.
- Falkowski, P. G., and Owens, T. G. 1980. Light—shade adaptation: two strategies in marine phytoplankton. *Plant Physiology*, 66: 592–595.
- Falkowski, P. G., and Raven, J. A. 1997. *Aquatic Photosynthesis*. Blackwell, Science, Oxford.
- Fawley, M. W. 1984. Effects of light intensity and temperature interactions on growth characteristics of *Phaeodactylum tricorutum* (Bacillariophyceae). *Journal of Phycology*, 20: 67–72.
- Feng, Y., Hare, C. E., Leblanc, K., Rose, J. M., Zhang, Y., DiTullio, G. R., Lee, P. A., et al. 2009. Effects of increased pCO₂ and temperature on the North Atlantic spring bloom I: the phytoplankton community and biogeochemical response. *Marine Ecology Progress Series*, 388: 13–25.
- Fietz, S., and Nicklisch, A. 2002. Acclimation of the diatom *Stephanodiscus neoastraea* and the cyanobacterium *Planktothrix agardhii* to simulated natural light fluctuations. *Photosynthesis Research*, 72: 95–106.
- Foy, B. 1983. Interaction of temperature and light on the growth rates of two planktonic Oscillatoria species under a short photoperiod regime. *British Journal*, 18: 267–273.
- Franklin, D. J., Choi, C. J., Hughes, C., Malin, G., and Berges, J. 2009. Effect of dead phytoplankton cells on the apparent efficiency of photosystem II. *Marine Ecology Progress Series*, 382: 35–40.
- Furusato, E., and Asaeda, T. 2009. A dynamic model of darkness tolerance for phytoplankton: model description. *Hydrobiologia*, 619: 67–88.
- Genty, B., Briantais, J.-M., and Baker, N. R. 1989. The relationship between the quantum yield of photosynthetic electron transport and quenching of chlorophyll fluorescence. *Biochimica et Biophysica Acta*, 990: 87–92.
- Goto, N., Miyazaki, H., Nakamura, N., Terai, H., Ishida, N., and Mitamura, O. 2008. Relationships between electron transport rates determined by pulse amplitude modulated (PAM) chlorophyll fluorescence and photosynthetic rates by traditional and common methods in natural freshwater phytoplankton. *Fundamental and Applied Limnology*, 172: 121–134.
- Granum, E., Kirkvold, S., and Mykkestad, S. M. 2002. Cellular and extracellular production of carbohydrates and amino acids by the marine diatom *Skeletonema costatum*: diel variations and effects of N depletion. *Marine Ecology Progress Series*, 242: 83–94.
- Guillard, R. R. L., and Ryther, J. H. 1962. Studies of marine planktonic diatoms. I. *Cyclotella nana* Hustedt and *Detonula confervacea* Cleve. *Canadian Journal of Microbiology*, 8: 229–239.
- Hammer, A., Schumann, R., and Schubert, H. 2002. Light and temperature acclimation of *Rhodomonas salina* (Cryptophyceae): photosynthetic performance. *Aquatic Microbial Ecology*, 29: 287–296.
- Halsey, K., Milligan, A., and Behrenfeld, M. J. 2011. Linking time-dependent carbon-fixation efficiencies in *Dunaliella tertiolecta* to underlying metabolic pathways. *Journal of Phycology*, 47: 66–76.

- Halsey, K., O'Malley, R., Graff, J., Milligan, A., and Behrenfeld, M. J. 2013. A common partitioning strategy for photosynthetic products in evolutionarily distinct phytoplankton species. *New Phytologist*, 198: 1030–1038.
- Herbert, D., Phipps, P. J., and Strangem, R. E. 1971. Chemical analysis of microbial cells. *In Methods in Microbiology*, pp. 209–344. Ed. by J. R. Norris, and D. W. Ribbons. Academic Press, London.
- Honjo, S., Manganini, S. J., and Wefer, G. 1988. Annual particle flux and a winter outburst of sedimentation in the northern Norwegian Sea. *Deep Sea Research I*, 35: 1223–1234.
- Houghton, J. T., Ding, Y., Griggs, D. J., Noguer, M., van der Linden, P. J., and Dia, X. (Eds) 2001. The scientific basis: contribution of working group I to the third assessment report of the intergovernmental panel on climate change. *In Climate Change*, pp. 525–582. Cambridge University Press, Cambridge.
- Huisman, J. E. F., van Oostveen, P., and Weissing, F. J. 1999. Critical depth and critical turbulence: two different mechanisms for the development of phytoplankton blooms. *Limnology and Oceanography*, 44: 1781–1787.
- Jeffrey, S. W., and Humphrey, G. R. 1975. New spectrophotometric equations for determining chlorophylls *a*, *b*, *c*₁ and *c*₂ in higher plants, algae and natural phytoplankton. *Biochimie und Physiologie der Pflanzen*, 16: 191–194.
- Li, W. K. W. 1980. Temperature adaptation in phytoplankton: cellular and photosynthetic characteristics. *In Primary production in the sea*, pp. 259–279. Ed. by P. G. Falkowski. Plenum Press, New York and London.
- Lindemann, C., Backhaus, J. O., and St John, M. A. 2015. Physiological constrains on Sverdrup's Critical-Depth-Hypothesis: the influences of dark respiration and sinking. *ICES Journal of Marine Science*, 72: 1942–1951.
- Lombard, F., Erez, J., Michel, E., and Labeyrie, L. 2009. Temperature effect on respiration and photosynthesis of the symbiont-bearing planktonic foraminifera *Globigerinoides ruber*, *Orbulina universa*, and *Globigerinella siphonifera*. *Limnology and Oceanography*, 54: 210–218.
- MacIntyre, H. L., Kana, T. M., and Geider, R. J. 2000. The effect of water motion on short-term rates of photosynthesis by marine phytoplankton. *Trends Plant Science*, 5:12–17.
- Mahadevan, A., D'Asaro, E., Lee, C., and Perry, M. J. 2012. Eddy-driven stratification initiates North Atlantic spring phytoplankton blooms. *Science*, 337: 54–58.
- Marra, J. 1978. Phytoplankton photosynthetic response to vertical movement in a mixed layer. *Marine Biology*, 46: 203–208.
- Marshall, H. J., Geider, R. J., and Flynn, K. J. 2000. A mechanistic model of photoinhibition. *New Phytologist*, 145: 347–359.
- Marshall, J., and Schott, F. 1999. Open-ocean convection: observations, theory, and models. *Reviews of Geophysics*, 37: 1–64.
- McMinn, A., Martin, A., and Ryan, K. G. 2010. Phytoplankton and sea ice algal biomass and physiology during the transition between winter and spring. (McMurdo Sound, Antarctica). *Polar Biology*, 33: 1547–1556.
- Milligan, A., Aparicio, U., and Behrenfeld, M. 2012. Fluorescence and non-photochemical quenching responses to simulated vertical mixing in the marine diatom *Thalassiosira weissflogii*. *Marine Ecology Progress Series*, 448: 67–78.
- Montagnes, D. J., and Franklin, D. J. 2001. Effect of temperature on diatom volume, growth rate, and carbon and nitrogen content: reconsidering some paradigms. *Limnology and Oceanography*, 46: 2008–2018.
- Montagnes, D. J., Kimmance, S. A., and Atkinson, D. 2003. Using Q^{10} : can growth rates increase linearly with temperature? *Aquatic Microbial Ecology*, 32: 307–313.
- Moore, C. M., Suggett, D. J., Hickman, A. E., Kim, Y.-N., Tweddle, J. F. S., et al. 2006. Phytoplankton photoacclimation and photoadaptation in response to environmental gradients in a shelf sea. *Limnology and Oceanography*, 51: 936–949.
- Morris, E. P., and Kromkamp, J. C. 2003. Influence of temperature on the relationship between oxygen- and fluorescence-based estimates of photosynthetic parameters in a marine benthic diatom (*Cylindrotheca closterium*). *European Journal of Phycology*, 38:133–142.
- Nagai, T., Yamazaki, H., and Kamykowski, D. 2003. A Lagrangian photoresponse model coupled with 2nd-order turbulence closure. *Marine Ecology Progress Series*, 265: 17–30.
- Nicklisch, A. 1998. Growth and light absorption of some planktonic cyanobacteria, diatoms and chlorophyceae under simulated natural light fluctuations. *Journal of Plankton Research*, 20: 105–119.
- Nymark, M., Valle, K. C., Hancke, K., Winge, P., Andersen, K., Johnsen, G., and Bones, A. M. 2013. Molecular and photosynthetic responses to prolonged darkness and subsequent acclimation to re-illumination in the diatom *Phaeodactylum tricoratum*. *PLoS ONE*, 8: 1–19.
- Obata, A., Ishizaka, J., and Endoh, M. 1996. Global verification of critical depth theory for phytoplankton bloom with climatological in situ temperature and satellite ocean color data. *Journal of Geophysical Research*, 101: 657–667.
- Platt, T., Bird, D. F., and Sathyendranath, S. 1991. Critical depth and marine primary production. *Proceedings of the Royal Society of London Series B: Biological Sciences*, 246: 205–217.
- Platt, T., Gallegos, C. L., and Harrison, W. G. 1980. Photoinhibition of photosynthesis in natural assemblages of marine phytoplankton. *Journal of Marine Research*, 38: 687–701.
- Platt, T., Fuentes-Yaco, C., and Frank, K. T. 2003. Spring algal bloom and larval fish survival. *Nature*, 423: 398–399.
- Post, A. F., Dubinsky, Z., Wyman, K., and Falkowski, P. G. 1984. Kinetics of light-intensity adaptation in a marine planktonic diatom. *Marine Biology*, 83: 231–238.
- Ralph, P. J., and Gademann, R. 2005. Rapid light curves: a powerful tool to assess photosynthetic activity. *Aquatic Botany*, 82: 222–237.
- Raven, J., and Geider, R. 1988. Temperature and algae growth. *New Phytologist*, 110: 441–461.
- Ross, O., Geider, R., Berdalet, E., Artigas, M., and Piera, J. 2011. Modelling the effect of vertical mixing on bottle incubations for determining in situ phytoplankton dynamics. I. Growth rates. *Marine Ecology Progress Series*, 435: 13–31.
- Sakshaug, E., Bricaud, A., Dandonneau, Y., Falkowski, P. G., Kiefer, D. A., Legendre, L., Morel, A., et al. 1997. Parameter of photosynthesis: definitions, theory and interpretation results. *Journal of Plankton Research*, 19: 1637–1670.
- Sakshaug, E., and Holm-Hansen, O. 1986. Photoadaptation in Antarctic phytoplankton: variations in growth rate, chemical composition and P versus I curves. *Journal of Plankton Research*, 8: 459–473.
- Seródio, J., Vieira, S., Cruz, S., and Barroso, F. 2005. Short-term variability in the photosynthetic activity of microphytobenthos as detected by measuring rapid light curves using variable fluorescence. *Marine Biology*, 146: 903–914.
- Shatwell, T., Nicklisch, A., and Köhler, J. 2012. Temperature and photo-period effects on phytoplankton growing under simulated mixed layer light fluctuations. *Limnology and Oceanography*, 57: 541–553.
- Sverdrup, H. U. 1953. On conditions for the vernal blooming of phytoplankton. *Journal du Conseil*, 18: 287–295.
- Talmy, D., Blackford, J., Hardman-Mountford, N., Polimene, L., Follows, M., and Geider, R. 2014. Flexible C:N ratio enhances metabolism of large phytoplankton when resource supply is intermittent. *Biogeosciences*, 11: 5179–5214.
- Thomas, M., Kremer, C., Klausmeier, C. A., and Litchman, E. 2012. A global pattern of thermal adaptation in marine phytoplankton. *Science*, 338:1085–1088.
- Thomas, W. H., Scotten, H. L., and Bradshaw, J. S. 1963. Thermal gradient incubation for small aquatic organisms. *Limnology and Oceanography*, 8: 357–360.

- Thompson, P. 1999. The response of growth and biochemical composition to variations in daylength, temperature, and irradiance in the marine diatom *Thalassiosira pseudonana* (Bacillariophyceae). *Journal of Phycology*, 35: 1215–1223.
- Townsend, D. W., Keller, M. D., Sieracki, M. E., and Ackleson, S. G. 1992. Spring phytoplankton blooms in the absence of vertical water column stratification. *Nature*, 60: 59–62.
- van Leeuwe, M. A., van Sikkelerus, B., Gieseke, W. W. C., and Stefels, J. 2005. Taxon-specific differences in photoacclimation to fluctuating irradiance in an Antarctic diatom and a green flagellate. *Marine Ecology Progress Series*, 288: 9–19.
- Varum, K. M., Ostgaard, K., and Grimsrud, K. 1986. Diurnal rhythms in carbohydrate metabolism of the marine diatom *Skeletonema costatum* (Grev.) Cleve. *Journal of Experimental Marine Biology and Ecology*, 102: 249–256.
- Verity, P. G. 1982. Effects of temperature, irradiance, and daylength on the marine diatom *Leptocylindrus danicus* Cleve. IV. Growth. *Journal of Experimental Marine Biology and Ecology*, 60: 197–222.
- Wagner, H., Jakob, T., and Wilhelm, C. 2006. Balancing the energy flow from captured light to biomass under fluctuating light conditions. *New Phytologist*, 169: 95–108.
- Wiltshire, K. H., Malzahn, A., Greve, W., Wirtz, K., Janisch, S., *et al.* 2008. Resilience of North Sea phytoplankton spring blooms dynamics: an analysis of long term data at Helgoland Roads. *Limnology and Oceanography*, 53: 1294–1302.
- Woods, J., Perilli, A., and Barkmann, W. 2005. Stability and predictability of a virtual plankton ecosystem created with an individual-based model. *Progress in Oceanography*, 67: 43–83.

Handling editor: Rubao Ji